Modélisation multi-échelle des structures composites, comportement en compression et lien avec les procédés

Sylvain Drapier

Dossier présenté pour l'obtention de

l'**Habilitation à Diriger les Recherches de l'Université Jean Monnet**

Spécialité : Sciences pour l'Ingénieur - Mécanique

par

Sylvain Drapier

Docteur de l'Université de Metz

Maître Assistant à l'École Nationale Supérieure des Mines de Saint-Étienne

---

Modélisation multi-échelle des structures composites, comportement en compression et lien avec les procédés

---

Soutenue le 17 octobre 2002 à Saint-Étienne, devant le jury composé de :

O.Allix	École Normale Supérieure de Cachan (Rapporteur)
J.-M. Bergheau	École Nationale d'Ingénieurs de Saint-Étienne (Rapporteur)
R. De Borst	TU Delft - The Netherlands
D. Marquis	Institut Français de Mécanique Avancée - Clermont-Ferrand
M. Potier-Ferry	Université de Metz
M. Touratier	École Nationale Supérieure des Arts et Métiers - Paris (Rapporteur)
A. Vautrin	École Nationale Supérieure des Mines de Saint-Étienne

Département Mécanique et Matériaux
Centre Science des Matériaux et des Structures
École Nationale Supérieure des Mines de Saint-Étienne

À Joséphine,
À Valentin

Remerciements

Ce manuscrit est une synthèse de mes activités de recherche menées depuis le début de ma thèse de doctorat en 1993 à l'université de Metz, et poursuivies en 1996 à l'université de Bristol, et enfin depuis 1997 à l'École Nationale Supérieure des Mines de Saint-Étienne. C'est essentiellement au département Mécanique et Matériaux de l'ENSM.SE que j'ai pu mettre progressivement en place mes propres activités de recherche à travers le co-encadrement de thèses, en collaboration avec le professeur Alain Vautrin, directeur de ce département. Je tiens à adresser à Laurent Dufort et Lionel Léotoing mes remerciements amicaux pour avoir contribué, par leur travail de thèse, au développement de ces activités de recherche. J'associe à ces remerciements Alexandre Pagot et Bénédicte Régis, étudiants de DEA, et enfin Othmane Elbouazzaoui, Issam Gaied et Marco Gigliotti dont je co-encadre actuellement les thèses.

Ces (co-)encadrements n'ont été possibles que grâce à la confiance que m'a accordée le professeur Alain Vautrin. Je lui adresse donc mes plus vifs remerciemens, pour m'avoir donné les moyens matériels et humains de mettre en œuvre mes idées, mais aussi pour m'avoir apporté de précieux conseils tout au long de ces cinq dernières années. C'est à ses côtés que j'ai pu m'initier à l'encadrement et à la formation de chercheurs. Pour tout ceci je lui exprime ma plus profonde reconnaissance.

Le professeur René De Borst de la T.U. de Delft, aux Pays-Bas, a bien voulu accepter de présider le jury de cette Habilitation à Diriger les Recherches. Je lui en suis extrêmement reconnaissant. Les professeurs Olivier Allix de l'ENS de Cachan, Jean-Michel Bergheau de l'ENISE, et Maurice Touratier de l'ENSAM de Paris ont accepté d'apporter leur jugement sur ce travail. Je les remercie d'avoir bien voulu prendre en charge cette lourde tâche de rapporteur. Le professeur Didier Marquis a accepté spontanément, malgré ses occupations liées à sa fonction de directeur de l'IFMA, de faire partie de ce jury. Je tiens à lui exprimer ici mes plus vifs remerciements.

Enfin, le professeur Michel Potier-Ferry, mon directeur de thèse au LPMM à l'université de Metz, m'a fait le plaisir de participer à ce jury et je l'en remercie chaleureusement. J'associe à ces remerciements le professeur Jean-Claude Grandidier, maintenant à l'université de Poitier, mon co-directeur de thèse, et qui me fait la joie de partager mon amitié. La vie professionnelle qui est la mienne aujourd'hui résulte en grande partie de ma rencontre avec ces deux enseignants-chercheurs exceptionnels de compétences et de qualités humaines, dont l'enthousiasme communicatif n'a pu que renforcer mon souhait de m'orienter vers la recherche.

De façon plus générale, je tiens à remercier l'ensemble des personnes que j'ai côtoyé depuis 1993. En premier lieu, je pense au professeur Michael R. Wisnom qui m'a fait confiance en me proposant de collaborer avec lui pendant un an, à l'université de Bristol. Ensuite, je souhaite remercier l'ensemble des membres du département Mécanique et Matériaux et plus généralement du centre SMS. Je tiens particulièrement à exprimer au professeur Roland Fortunier toute mon amitié et ma reconnaissance pour ses conseils avisés. Enfin, ceux que je n'ai pu citer en particulier se retrouveront dans ces derniers remerciements adressés à tous ceux qui ont contribué à rendre possible mes activités de recherche et d'enseignement à l'ENSM.SE.

D'un point de vu plus personnel, je tiens à exprimer ici toute ma gratitude à mes parents. J'adresse enfin un grand merci à mon épouse Joséphine pour m'avoir soutenu durant toutes ces années. Il est évident que Joséphine et notre petit Valentin ont largement contribué à ce que je puisse mener sereinement ces activités d'enseignant-chercheur. Qu'ils reçoivent ici toute mon affection.

Préface

Ce document est une synthèse des activités de recherche que j'ai menées depuis maintenant neuf ans. C'est d'abord de 1993 à 1996 pour ma thèse de doctorat de l'université de Metz, puis pendant mon séjour post-doctoral à l'université de Bristol en 1996/1997 que j'ai mené une partie de ces recherches. Depuis octobre 1997, je suis maître assistant à l'École Nationale Supérieure des Mines de Saint-Étienne, au département Mécanique et Matériaux du centre Science des Matériaux et des Structures, et j'ai pu à ce titre co-encadrer des doctorants et des étudiants de DEA.

Ce document se divise en trois parties distinctes. La première partie est, à proprement parler, une synthèse de ces activités de recherche qui traite de deux thématiques relativement indépendantes pour l'instant et que je souhaite rapprocher : la **modélisation multi-échelle des comportements instables dans les composites**, et les **procédés d'élaboration des composites**. Les seconde et troisième partie du document sont des annexes à cette synthèse, ce sont respectivement une notice individuelle et une compilation d'articles issus de ces activités de recherche.

Table des matières

- 1 -

Introduction

Les matériaux composites à fibres longues et les structures sandwichs sont généralement utilisés dans une optique de réduction de masse des éléments de structure, notamment dans le domaine des transports. Actuellement, plus que les freins technico-économiques que peuvent encore rencontrer ces matériaux nouveaux, c'est le manque d'*outils de conception et d'optimisation adaptés, de nature numérique et expérimentale*, qui nuit à l'utilisation plus large des solutions composites et à leur pénétration dans de nouveaux secteurs industriels.

Le développement d'outils de conception, et donc d'analyse, propres aux composites est indispensable mais ne peut se faire par simple transposition des approches maîtrisées pour les matériaux homogènes macroscopiquement. En effet, les matériaux composites à fibres longues et les structures sandwichs résultent, à divers échelles d'observation, de l'*assemblage modulable* de constituants de nature très différente tant en termes de combinaisons de renforts et de liants, que d'orientations des renforts, ou encore de formats des semi-produits (plis UniDirectionnels pré-imprégnés, tissus, renforts multiaxiaux, ...). Le choix de ces constituants et de leur combinaison introduit, par rapport aux matériaux plus standards, des degrés de liberté supplémentaires dans le processus de conception. Si bien que le matériau composite peut être *conçu spécifiquement* pour chaque application. De plus, le matériau n'existe dans sa configuration définitive (solide) que lorsque la structure est réalisée. *Le matériau n'est donc pas dissociable de la structure qu'il constitue*. Dans ce cas, la notion même de matériau tend à disparaître au profit d'une définition de *structure multi-échelle* dans laquelle les propriétés mécaniques macroscopiques de la structure dépendent intimement, et de façon souvent complexe, des propriétés mésoscopiques anisotropes, à l'échelle des plis, elles-mêmes conditionnées par les propriétés microscopiques anisotropes, à l'échelle des constituants de base.

Ces dépendances inter-échelles sont particulièrement exacerbées dans le cas de certains comportements dits *critiques* où la réponse des structures composites et sandwichs devient instable. Ces comportements sont caractérisés par des propriétés ultimes approchées, associées à des coefficients

de sécurité conséquents, reflétant l'impossibilité d'appréhender correctement ces comportements aussi bien par des *approches matériaux (locales)* que par des *approches structures (globales)*. La compression dans le plan par exemple, propriété dimensionnante par excellence dans le domaine des transports, pose de nombreux problèmes tant au niveau de la prévision que de la mesure de la résistance. Sous ce chargement, seule une approche *structurelle* est en mesure d'expliciter la ruine de la structure, résultant du comportement instable piloté par l'*interaction de mécanismes à plusieurs échelles*. Ces mécanismes clefs sont contrôlés notamment par le couplage d'*imperfections géométriques* et des *comportements matériaux locaux*, que ces imperfections soient générées pendant l'élaboration, ou liées au choix des renforts.

En effet, l'architecture (géométrie, distribution des propriétés mécaniques) aux différentes échelles d'observation, dont dépendent fortement les comportements critiques, est de fait conditionnée par les spécificités des procédés de fabrication employés, et donc par la qualité qui en découle. Cette dépendance peut être directe, c'est le cas lorsque les imperfections sont générées pendant l'élaboration, ou indirecte dans le cas de renforts choisis, au moins en partie, en fonction du procédé utilisé. La conséquence directe de cette dépendance est la nécessité de maîtriser, en vue de les optimiser, les paramètres d'élaboration qui contrôlent l'architecture finale. La compréhension fine des phénomènes couplés thermo-mécaniques et physico-chimiques, mis en jeu lors de l'élaboration, est donc essentielle et passe nécessairement par la *modélisation des procédés*. Il faut de plus noter qu'aujourd'hui, l'optimisation des procédés répond également à un souci croissant visant à réduire, pour des raisons économiques, les phases de mise au point des cycles et méthodes de fabrication. Dans ce cadre, la caractérisation des propriétés matériaux contrôlant la qualité de l'élaboration est également un élément clef.

Finalement, la *conception des structures composites* est intrinsèquement *multi-échelle* et doit, de plus, intégrer très en amont les contraintes liées à l'*élaboration de la structure*. L'*utilisation rationnelle* des matériaux composites repose donc sur des *outils d'aide à la conception et à l'optimisation*, s'appuyant d'une part sur des modélisations mécaniques décrivant de manière convenable les *comportements critiques*, et d'autre part sur des *modélisations du procédé*. À plus long terme, le couplage de ces deux approches, aujourd'hui distinctes, devrait conduire à l'*optimisation simultanée des conditions d'élaboration et des matériaux* vis-à-vis notamment des comportements critiques. Soulignons que le terme modélisation s'entend ici comme une *approche complémentaire simulations / identifications*, point clef de la compréhension fine des mécanismes mis en jeu.

Le premier volet de l'approche globale présentée ci-dessus, c'est-à-dire la prévision des comportements critiques, est développé dans la première partie de ce mémoire. Cette première partie est consacrée aux *instabilités couplées aux effets d'échelle*. Plus précisément, à ce jour la plus grande partie de mes recherches s'est concentrée sur l'étude des *comportements critiques en compression dans les structures composites et sandwichs*, comportements qui ne peuvent être représentés par

une approche continue classique mais doivent s'appuyer sur des représentations de type *milieux à longueur interne*. Ces travaux de recherche ont permis d'apporter des réponses quantitatives à la prévision de la résistance en compression, d'abord dans les composites stratifiés, puis dans les semi-produits dits *NCF*s, et enfin dans les sandwichs. Le couplage de ces approches mises en place à l'échelle des plis et à l'échelle des sandwichs devrait permettre, à moyen terme, de proposer une approche de dimensionnement multi-échelle des structures sandwichs à peaux composites vis-à-vis du comportement en compression à l'échelle des constituants, des plis, et de la structure.

Pour mettre en place cette approche multi-échelle, il reste actuellement à quantifier les grandeurs géométriques initiales à l'échelle des constituants qui contrôlent en grande partie le comportement en compression. Dans le cadre spécifique des semi-produits *NCF*s où la géométrie mésoscopique dépend essentiellement du choix des constituants de base et de leur assemblage, un premier lien avec les comportements critiques a pu être proposé. Mais le choix de ces assemblages étant par ailleurs dicté, au moins partiellement, par des contraintes liées aux technologies d'élaboration elles-mêmes, la compréhension fine des procédés est tout de même nécessaire.

L'étude de ces procédés est développée dans la seconde partie de ce mémoire qui porte sur ce *thème émergent*, débuté récemment à travers deux projets de recherche complémentaires de la thématique *procédés*. D'une part, des simulations de type physico-chimique et thermo-mécanique sont mises en œuvre, indépendamment pour le moment, dans le cadre de la *modélisation de l'élaboration par voie liquide* de composites à base de nouveaux renforts multiaxiaux. Ce projet s'appuie également sur la caractérisation et le suivi in-situ de l'imprégnation et de la consolidation des préformes. D'autre part, la prévision des champs de pression générés par des *tricots élastomériques en grandes déformations* nécessite de mettre en œuvre des simulations s'apparentant à de la *mise en forme*, car faisant intervenir des grandes déformations couplées à des problèmes de contact. Ici encore, la caractérisation est essentielle car le comportement hyperélastique de ces matériaux particuliers doit être identifié au préalable, en recourant notamment à des méthodes d'identification sans contact.

Enfin, je conclurai cette synthèse de mes travaux de recherche en exposant les perspectives, à moyen et long terme, de cette démarche qui vise à *établir des liens forts entre élaboration et propriétés dimensionnantes*.

- 2 -

Instabilités et effets d’échelle dans les composites et les sandwichs

Dans l’objectif de mener des calculs de structures par exemple, le comportement des matériaux composites et des structures sandwich, ou plus généralement des matériaux hétérogènes, est souvent décrit à partir d’une approche de type ’milieu homogène équivalent’. Pour construire ce type de modèle, il est aujourd’hui classique de recourir aux techniques d’homogénéisation permettant de construire le comportement macroscopique des matériaux, en petites déformations, en partant de leur méso ou microstructure. Dans ce cadre linéaire géométrique, ces techniques s’appliquent assez bien aux matériaux composites et aux sandwichs, et peuvent fréquemment, en première approximation, se résumer à des lois de mélanges pour les propriétés courantes. On observe cependant que, sous des chargements déstabilisants tels que la compression ou encore le cisaillement interlaminaire, les techniques d’homogénéisation classiques ne semblent plus en mesure de représenter correctement le comportement réel des composites et des sandwichs. En effet, sous ces chargements la caractérisation des propriétés ultimes est très problématique, tant du point de vue de la modélisation que de la mesure expérimentale. Dans le domaine des transports, les difficultés à caractériser les propriétés ultimes en compression viennent se superposer aux contraintes de dimensionnement déjà très fortes liées à cette sollicitation intrinsèquement critique. Actuellement, la résistance en compression est sans conteste *la propriété dimensionnante* des structures composites. La compréhension de cette propriété, qui en fait masque des comportements complexes où interagissent les paramètres à diverses échelles, passe par la mise en place de modèles englobant plusieurs échelles d’observation dans ces matériaux.

En effet, comme nous l’avons décrit en introduction, intrinsèquement les matériaux composites et sandwichs sont des ’structures multi-échelles’ : association de renforts et de liant dans le cas des composites, et des peaux très fines et rigides associées à une âme épaisse et peu rigide dans le cas des sandwichs. Dans ces matériaux, l’hétérogénéité géométrique et mécanique des consti-

tuants de base est telle que sous ces chargements déstabilisants les renforts (les 'phases' les plus rigides) développent un comportement instable géométriquement tandis que les constituants les plus souples peuvent subir un écoulement plastique. C'est le développement de ces instabilités à l'échelle des constituants qui conduit finalement à la ruine de l'ensemble de la structure. L'interaction forte qui existe entre le comportement macroscopique et les instabilités locales, c'est-à-dire les *effets d'échelle*, est un élément primordial conditionnant la réponse en compression de ces matériaux. D'un point de vue empirique, on peut par exemple tenter d'approcher ces comportements complexes en identifiant le comportement macroscopique, pondéré par des coefficients dépendant de manière plus ou moins complexe des micro ou mésostructures étudiées. Toutefois, si de telles approches semblent satisfaisantes dans un premier temps, elles ne peuvent en aucun cas conduire à la compréhension fine du comportement, étape préliminaire pourtant indispensable. En conséquence, l'utilisation optimale des composites et des sandwichs est freinée en partie par le manque de compréhension des phénomènes contrôlant les comportements instables aux diverses échelles. Ceci essentiellement du fait de l'absence de modèles 'inter-échelles' capables de rendre compte de l'interaction de ces mécanismes.

La difficulté de ces approches 'inter-échelles', dans le cas des comportements instables, est de développer des outils prédictifs complets basés sur des formulations spécifiques induisant des coûts de calculs numériques ou analytiques très faibles, mais permettant de rendre compte de l'apparition d'instabilités à diverses échelles d'observation. Typiquement, de tels modèles sont basés sur des représentations de type milieu continu, pour les comportements 'matériaux' (locaux), associées à des approches de type mécanique des structures capables de rendre compte du caractère instable du point de vue géométrique des constituants les plus rigides. Dans le cadre de mes activités de recherche, ce type d'approche a d'abord été développé lors de ma thèse de doctorat dans le cas des composites à fibres longues dont le comportement mésoscopique dépend à la fois des paramètres à l'échelle des constituants, mais également de paramètres à l'échelle des plis, voire du stratifié. Ensuite, pendant mon post-doctorat le comportement en compression et en cisaillement interlaminaire de renforts multiaxiaux pour composites structuraux, caractérisés par une échelle d'observation supplémentaire, a été décrit par des modèles numériques établis à l'échelle des multiaxiaux, basés sur l'utilisation de cellules représentatives. Enfin, pour les poutres sandwich une approche originale analytique, puis numérique, a été développée dans la thèse de Lionel Léotoing, elle a permis de rendre compte de l'apparition d'instabilités à deux échelles différentes dans ces structures particulières, et de leur intéraction.

C'est principalement du point de vue de la modélisation que ces effets d'échelle couplés aux instabilités ont été abordés. Cependant, la confrontation prévisions théoriques / résultats expérimentaux est indispensable à la mise au point de modèles et d'expériences bien fondés. Ainsi, depuis deux ans la problématique de la résistance en compression des composites à fibres longues est dans une moindre mesure abordée expérimentalement. Elle devrait être rapidement étendue aux

sandwichs.

2.1 Approche structurelle du microflambage plastique

La résistance en compression dans le sens des fibres des composites à fibres longues a, depuis le milieu des années soixante [Rosen, 1964], sans cesse soulevé de nombreuses interrogations. En effet, alors que l'augmentation de la résistance en traction des fibres conduisait à des résistances en traction des stratifiés améliorées, la résistance en compression stagnait dans le meilleur des cas. Ainsi, cette résistance est devenue un critère dimensionnant, dont la mesure pose de nombreux problèmes. En tentant de répondre à ce souci de caractérisation, on a montré au début des années 90 ([Grandidier et al., 1992], [Grandsire-Vinçon, 1993], [Wisnom, 1991]) que la résistance en compression des composites à fibres longues dépendait non seulement des constituants, mais également de paramètres structuraux à l'échelle du stratifié. Cet *effet de structure*, est lié au gradient de chargement à travers l'épaisseur (Figure 2.1-a), et à la position des plis UDs dans les séquences d'empilement testées (Figure 2.1-b).

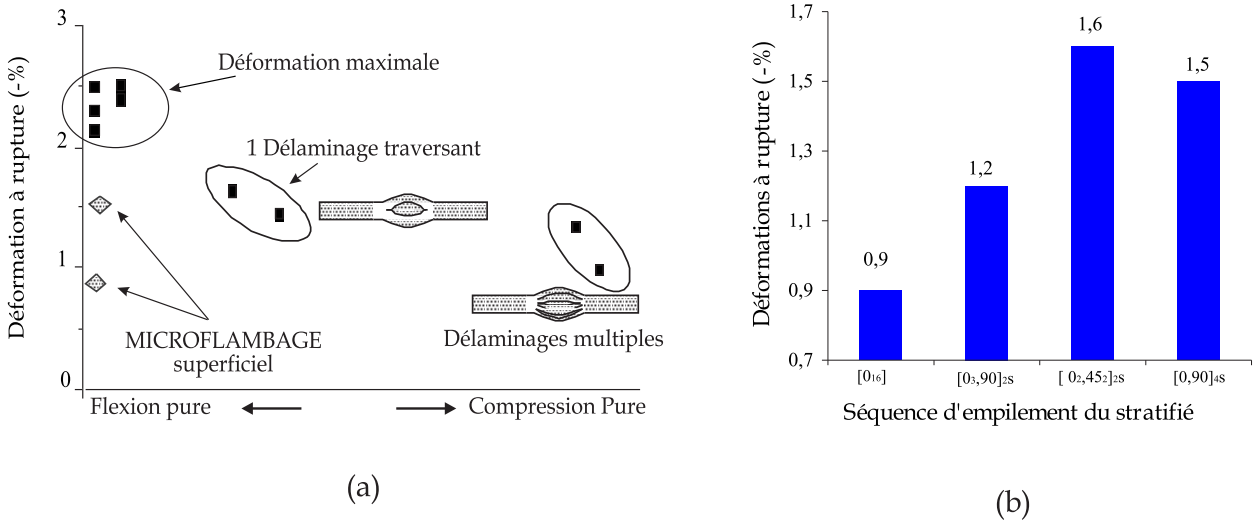

FIG. 2.1: Déformation à rupture en compression pour des UDs : (a) en fonction du gradient de chargement dans l'épaisseur pour des UDs verre E/914 [Grandidier et al., 1992], et de la séquence d'empilement pour des stratifiés T400/6376 [Grandsire-Vinçon, 1993].

Par ailleurs, du point de vue de la modélisation de la résistance en compression, de nombreux travaux ont été menés à l'échelle des constituants depuis Rosen [Rosen, 1964]. Les approches de ce type les plus récentes proposent de relier la rupture en compression à l'apparition d'une instabilité géométrique à l'échelle des fibres, appelée *microflambage*, qui dépend essentiellement de la présence d'un défaut d'alignement initial des fibres et du comportement plastique de la matrice. Il faut noter que ces non-linéarités locales ont été introduites notamment pour tenter de rapprocher les prévisions et les résistances expérimentales, identifiées avec de grosses difficultés à l'aide

d'essais de compression directe. Toutefois, ces approches permettent de proposer un scénario des mécanismes conduisant à la rupture en compression, dont le faciès typique est appelé *kink-band* : un chargement de compression est appliqué sur les fibres possédant un défaut d'ondulation initial, ce qui conduit à une flexion coopérative d'un ensemble de fibres, il en résulte un écoulement plastique en cisaillement de la matrice présente entre ces fibres.Une instabilité plastique se développe, qui finalement conduit à une courbure des fibres élevée limitée par la rupture en traction des fibres, formant *in fine* une bande de pliage.

Mais ces modèles restent intrinsèquement limités à des études locales. Les études de nature analytique [Budiansky, 1983] sont limitées de par l'échelle d'observation considérée, tandis que les études numériques [Kyriakides et al., 1995] ne peuvent être étendues, elles nécessitent pour quelques dizaines de fibres la résolution de problèmes de l'ordre de 30 à 40 000 ddls en non-linéaire géométrique et non-linéaire matériau. Finalement, ces modélisation ne peuvent en aucun cas rendre compte de l'effet de structure qui est pourtant essentiel puisque les résistances peuvent varier du simple au double selon le chargement par exemple (Figure 2.1-a). Il faut donc *mettre en place une approche capable de prendre en compte les effets d'un défaut d'alignement initial et du caractère plastique de la matrice, tout en conservant des temps de calculs suffisamment faibles pour représenter les effets des paramètres structuraux*.

2.1.1 Modélisation de l'effet de structure

Afin de rendre compte de l'effet de structure, Grandidier, Gardin et Potier-Ferry (voir par exemple [Grandidier et al., 1992], [Gardin and Potier-Ferry, 1992]) ont proposé un modèle bidimensionnel à l'échelle mésoscopique, dans l'épaisseur des plis UDs à 0°, *i.e.* orientés dans la direction du chargement (*cf* Figure 2.2). Ce modèle de milieu homogène équivalent (MHE), de type *Cosserat*, est capable de représenter l'apparition d'instabilités élastiques au niveau des fibres. La cinématique à la base de ce modèle a été établie à l'aide d'une analyse asymptotique d'un empilement bidimensionnel de couches raides et souples, basée sur la méthode des échelles multiples [Gardin and Potier-Ferry, 1992]. Cette cinématique a été également validée par l'étude des champs de déplacement obtenus lors du calcul des modes de flambage élastiques d'empilements discrétisés à l'échelle des constituants (Drapier *et al.*, 1996 [1] - Annexe 2.1[2]). Dans ce modèle de MHE, la matrice possède un comportement de milieu bidimensionnel, tandis que les fibres ont un comportement de poutre de Bernoulli. Pour construire le modèle, on recourt aux conditions de continuité des contraintes entre fibre et matrice, et pour la fibre, la partie membrane et la partie flexion peuvent être séparées, la part de flexion étant répartie sur le domaine entier. La partie quadratique de l'énergie potentielle associée à ce modèle homogénéisé, suffisante pour l'étude de la

[1] (XX) : références à des publications dont je suis (co-)auteur, *cf* **Production scientifique**, chapitre F de l'**Annexe 1 - Notice individuelle**, page 77

[2] Annexe 2.x : article contenu dans l'**Annexe 2 - articles représentatifs**

stabilité d'un domaine bidimensionnel tel que représenté sur la Figure 2.2, s'écrit :

$$P_2(\mathbf{u}) = \frac{1}{2}\int_\Omega < \varepsilon > \mathbf{L}_{equiv}^{homog}(x_2) < \varepsilon > \, d\Omega + \frac{1}{2}\int_\Omega f E_f r_{gf}^2 \left(\frac{\partial^2 v(\mathbf{x})}{\partial x_1^2}\right)^2 d\Omega \qquad (2.1)$$
$$-\lambda \int_\Omega < S_{11}^d(x_2) > \frac{1}{2}\left(\frac{\partial v(\mathbf{x})}{\partial x_1}\right)^2 d\Omega$$

où le premier terme représente l'énergie de déformation de membrane de l'ensemble fibre-matrice, le second terme est l'énergie de flexion des fibres seules répartie sur le domaine, et le troisième terme est le chargement imposé sur le domaine entier dans le cadre d'un pré-flambage linéaire. La notation $< \cdot >$ désigne une moyenne par rapport à la hauteur d'un assemblage élémentaire fibre-matrice, ε est la partie linéaire du tenseur des déformations de Green-Lagrange en 2D, $\mathbf{L}_{equiv}^{homog}(x_2)$ est le tenseur de rigidité du *MHE* (Eq. 2.2), f est la fraction volumique de fibres, E_f désigne le module d'Young des fibres, r_{gf} est le rayon de gyration des fibres défini par le rapport de l'inertie à la surface $r_{gf}^2 = \frac{I_f}{S_f}$, $v(\mathbf{x})$ est la composante du déplacement selon $\mathbf{e}_2$, λ est le facteur de proportionnalité du chargement extérieur, et $< S_{11}^d >$ est la seule composante non nulle du second tenseur de Piola-Kirchhoff des contraintes extérieures appliqué sur le domaine. Le tenseur de rigidité de membrane du *MHE*, constitué de matériaux isotropes, est anisotrope, il est donné en contraintes planes dans la base $(\mathbf{e}_1, \mathbf{e}_2)$ par :

$$\begin{Bmatrix} < S_{11} > \\ < S_{22} > \\ < S_{12} > \end{Bmatrix} = \begin{bmatrix} fE_f + (1-f)\dfrac{E_m}{1-\nu_m^2} & \dfrac{E_m \nu_m}{1-\nu_m^2} & 0 \\ \dfrac{E_m \nu_m}{1-\nu_m^2} & \dfrac{E_m}{(1-f)(1-\nu_m^2)} & 0 \\ 0 & 0 & \dfrac{G_m}{1-f} \end{bmatrix} \begin{Bmatrix} < \varepsilon_{11} > \\ < \varepsilon_{22} > \\ < \varepsilon_{12} > \end{Bmatrix} \qquad (2.2)$$

où E_m, ν_m et G_m désignent respectivement le module d'Young, le coefficient de Poisson et le module de cisaillement de la matrice.

En utilisant ce modèle, la position du pli à travers l'épaisseur du stratifié, c'est-à-dire la séquence d'empilement, est prise en compte via les conditions aux limites cinématiques imposées sur les bords du pli : déplacements libres pour un pli situé en surface d'un stratifié, ou déplacements nuls prenant en compte la présence de plis croisés voisins pour un pli situé dans le stratifié. Les modes de microflambage élastiques calculés par éléments finis à partir de ce modèle sont validés par les calculs menés sur les mêmes stratifiés mais discrétisés à l'échelle des constituants (Drapier *et al.*, 1996 - Annexe 2.1).

Cette approche apporte des résultats tout à fait probants quant à l'effet du chargement et des séquences d'empilement sur les contraintes critiques et les longueurs d'onde associées. Toutefois, dans l'objectif de proposer des comparaisons *quantitatives*, notamment avec des résultats expérimentaux, cette approche doit être enrichie afin de prendre en compte les non-linéarités au niveau des constituants. Le travail de recherche débuté dans le cadre de ma thèse au LPMM à l'université

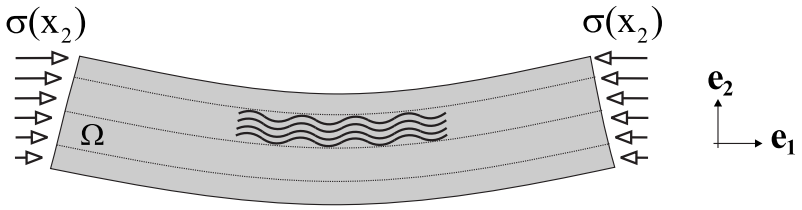

FIG. 2.2: Représentation schématique de la formulation locale (mésoscopique) du problème de microflambage dans un stratifié en flexion.

de Metz, et poursuivi dans une moindre mesure jusqu'à récemment, a consisté à quantifier l'effet des paramètres structuraux à l'échelle du stratifié (*mm*), sur la résistance en compression des plis pilotée par l'apparition de microflambage plastique (μm).

2.1.2 Formulation mésoscopique du problème de microflambage plastique

Le microflambage plastique

Afin de prendre en compte les éléments essentiels à l'échelle des constituants que sont le défaut initial d'ondulation des fibres, et le comportement non-linéaire matériau de la matrice, le problème de microflambage à l'échelle des plis doit être reformulé (Drapier, 1996, Drapier *et al.*, 1997 - Annexe 2.2, Drapier *et al.*, 1998). À partir de l'équation 2.1, on peut écrire de façon générale l'équilibre de ce milieu bidimensionnel (Figure 2.2), en utilisant le PPV par exemple :

$$-\int_{\Omega}\left\{fE_f r_{gf}^2 v'' \delta v'' + \mathbf{S}(\gamma).\delta\gamma\right\} d\Omega + <\mathbf{F},\delta\mathbf{u}>=0, \quad \forall\,\delta\mathbf{u} \tag{2.3}$$

avec les dérivations par rapport à x_1 notées $(')$, γ le tenseur de Green-Lagrange complet, $\mathbf{F}$ le vecteur de chargement extérieur et $\delta\mathbf{u}(\mathbf{x})$ le champ de déplacement virtuel quelconque. La loi de comportement non-linéaire du *MHE* ($\mathbf{S}(\gamma)=\mathbf{L}(\gamma)\cdot\gamma$) reste à préciser.

Dans ce problème de microflambage, les chargements sont principalement uniaxiaux. Si de plus nous représentons le défaut d'ondulation initial des fibres par un 'champ de défaut' d'ondulations $v_0(\mathbf{x})$, après quelques simplifications dues aux ordres de grandeurs des déformations et des courbures (voir Drapier *et al.*, 1999 - Annexe 2.2), le tenseur des déformations s'écrit : $\gamma(\mathbf{u})=\frac{1}{2}(\nabla\mathbf{u}+{}^t\nabla\mathbf{u})+\left(\frac{1}{2}v'^2+v'v_0'\right)\mathbf{e_1}\otimes\mathbf{e_1}$.

L'équilibre d'un milieu bidimensionnel dans lequel est susceptible de se développer du microflambage plastique est formulé. Partant de cette formulation, la résolution est possible, par exemple en discrétisant par éléments finis cette équation 2.3. Toutefois, une telle discrétisation n'est pas directe, essentiellement à cause de la présence du terme de flexion des fibres. En effet, la longueur d'onde de microflambage élastique, évaluée dans les études précédentes, est de l'ordre de quelques centaines de microns, ce qui est cohérent avec les largeurs de bande mesurées de l'ordre de 100 à 250 μm pour des composites carbone/époxyde courants [Kyriakides et al., 1995]. Du point de

vue de la discrétisation, ceci implique un maillage raffiné pour représenter correctement ce terme essentiel de flexion des fibres. Ce qui, dans un cadre non-linéaire géométrique et matériau, conduit rapidement à des calculs conséquents. Pour pallier à ces difficultés, nous recourrons à la formulation locale de ce problème de microflambage plastique.

Approche mésoscopique

Pour formuler le problème local, nous employons un cinématique à double échelle qui se justifie par le caractère local du microflambage, comme le montrent par exemple les expériences de [Grandidier, 1991] où du flambage surperficiel peut être observé. La solution du problème de microflambage est cherchée sous la forme d'un champ de déplacement évoluant à l'échelle de la structure (noté $\mathbf{u_G}$), *modulé très localement* par un champ de déplacement évoluant à l'échelle du pli (noté $\mathbf{u_L}$). Après quelques simplifications déduites des variations lentes et rapides respectivement pour le champ de déplacement global et le champ local, le tenseur des déformations se simplifie et se découple en deux termes indépendants pour chaque échelle : $\gamma(\mathbf{u}) = \gamma_G(\mathbf{u}_G) + \gamma_L(\mathbf{u}_L)$ (voir Drapier *et al.*, 1999 - Annexe 2.2).

L'équilibre de la structure peut alors s'écrire en injectant ces grandeurs dans l'équation 2.3. Mais, ce qui présente un intérêt pour nous ici est la détermination de l'apparition du microflambage des fibres, phénomène purement local, donc caractérisé par un équilibre local. On peut voir cet équilibre comme la différence entre l'équilibre de la structure dans laquelle le microflambage se développe, et l'équilibre de la structure 'saine'. Finalement, en supposant l'équilibre global réalisé, soit $\mathbf{u}_G(\mathbf{x})$ donné, le microflambage est caractérisé par l'équation 2.4 dont le champ de déplacement local $\mathbf{u}_L(\mathbf{x})$ est solution :

$$\int_\Omega \left\{ f E_f r_{gf}^2 \, v_L'' \delta v_L'' + \mathbf{S_L}(\gamma_G, \gamma_L).\delta\gamma_L + S_{11}(\gamma_G)(v_L' \, v_{0L}') \, \delta v_L' \right\} d\Omega = 0, \; \forall \delta \mathbf{u_L} \qquad (2.4)$$

avec la contrainte locale définie comme la différence des contraintes dues au champ de déplacement total et celles dues au champ global : $\mathbf{S_L}(\gamma_G, \gamma_L) = \mathbf{S}(\gamma_G + \gamma_L) - \mathbf{S}(\gamma_G)$. Cet équilibre local correspond à la réponse locale sous un chargement global donné à travers la contrainte macroscopique $\mathbf{S}(\gamma_G)$. Dans les cas qui nous intéressent, cette contrainte macroscopique sera principalement uniaxiale, et compte tenu des raideurs des composites courants, ne dépendra principalement que de la déformation uniaxiale $\gamma_{11}^d(x_2)$ qui peut par conséquent représenter le chargement extérieur de flexion-compression dans ce problème local.

Mise en œuvre de la formulation

Le problème mésoscopique incluant un défaut est clairement formulé, il reste à préciser la loi de comportement utilisée pour la matrice, et l'approximation numérique du problème continu (Eq. 2.4). Ceci est décrit plus en détails dans Drapier *et al.*, 1999 - Annexe 2.2.

Dans cette nouvelle formulation, nous choisissons de considérer la non-linéarité matériau uniquement pour la matrice, ce qui permet une étude fine du mécanisme de microflambage, mais implique par contre de connaître les déformations locales dans la matrice seule, et de reconstruire le comportement non-linéaire anisotrope du *MHE* à partir du comportement non-linéaire isotrope de la matrice. Mais la localisation des déformations s'exprimant analytiquement par des considérations micro-mécaniques, et l'homogénéisation des propriétés étant définie explicitement en fonction des caractéristiques de la matrice, par une expression proche de celle du *MHE* présentée précédemment (Eq. 2.2), au final toutes les opérations de localisation-homogénéisation sont analytiques, ce qui réduit considérablement le traitement de cette loi locale. Nous choisissons de représenter ce comportement de la matrice sous la forme d'un loi élastique non-linéaire dite J_2 *deformation* qui donne, dans le cas de chargements strictement croissants, *i.e.* sans décharge élastique, des résultats comparables à des lois plastiques plus complexes à mettre en œuvre [Hutchinson, 1974]. Dans notre cas, cette loi de comportement sera représentée soit par une loi continue de type Ramberg-Osgood, soit par une loi expérimentale donnée sous forme discrète.

Finalement, le problème est entièrement posé, il reste à choisir une approximation numérique du champ de déplacement. Dans le cadre des instabilités cellulaires, cette approximation est choisie comme le produit d'amplitudes à travers l'épaisseur du stratifié avec quelques fonctions d'une base de Ritz. Les fonctions de la base de Ritz sont choisies telles que les modes de microflambage élastique obtenus dans Drapier *et al* 1996 - Annexe 2.1 puissent être reproduits, et qu'une contrainte de flambage constante puisse être obtenue. Les amplitudes du champ de déplacement sont quant à elles discrétisées avec des éléments finis quadratiques de type Lagrange. L'imperfection $v_0(\mathbf{x})$ est représentée de la même manière que la composante $v(\mathbf{x})$. Il n'y a ainsi aucune limitation aux répartitions de déformations et de défauts à travers l'épaisseur du stratifié, ce point est essentiel pour rendre compte de l'influence des paramètres structuraux sur l'apparition du microflambage plastique.

Cette hypothèse d'instabilités cellulaires permet également une réduction du domaine d'étude bidimensionnel à une seule longueur d'onde dans la direction des fibres, ce qui réduit considérablement les temps de calculs. Par contre, la répartition de l'écoulement plastique de la matrice sera hétérogène, et une répartition bidimensionnelle de points de Gauss est utilisée afin de rendre compte de ces hétérogénéités. Enfin, le problème est résolu classiquement en utilisant une linéarisation de Newton associée à une méthode incrémentale, pilotée avec une méthode à longueur d'arc choisie pour sa robustesse et pour sa capacité à passer les points de rebroussements. Le tout est implémenté dans un code de calcul spécifiquement développé. Au final le calcul de la réponse complète non-linéaire géométrique et matériau d'un stratifié est de l'ordre de quelques minutes, la taille du problème à résoudre étant typiquement de l'ordre d'une centaine de ddls pour environ 250 points de Gauss.

2.1.3 Résultats

Mécanisme de microflambage plastique

Grâce aux temps de calculs très réduits, des études paramétriques complètes ont permis dans un premier temps de décrire très finement le mécanisme de microflambage plastique dans des composites UDs choisis suffisamment épais pour minimiser l'influence des conditions cinématiques aux limites du pli. La réponse typique d'un pli T300/914 contenant 60% de fibres est représentée sur la Figure 2.3 par exemple. On voit que cette réponse est fortement sous-critique dès lors qu'une loi de comportement non-linéaire est considérée. L'apparition de l'instabilité correspond, d'un point de vue expérimental, à la ruine du composite car ni un contrôle en déplacement, ni un contrôle en force ne permettent d'atteindre un équilibre après ce point de rebroussement. En conséquence, la contrainte et la déformation associées à l'apparition de cette instabilité sont les contrainte et déformation à rupture.

Il ressort de l'étude locale du microflambage plastique (Drapier *et al.*, 2001 - Annexe 2.3) que le mécanisme de rupture en compression est caractérisé par deux régimes différents selon que le défaut est faible ou plus important (Figure 2.3). Mais dans les deux cas l'équilibre entre la rigidité de flexion des fibres et la rigidité de la matrice est à la base de l'apparition du microflambage plastique, c'est la façon dont la matrice atteint sa phase plastique qui diffère. Pour les défauts faibles, l'apparition de la plasticité est due en grande partie à la contrainte de compression, alors que pour les défauts plus importants, elle a pour origine le cisaillement induit par l'ondulation progressive des fibres.

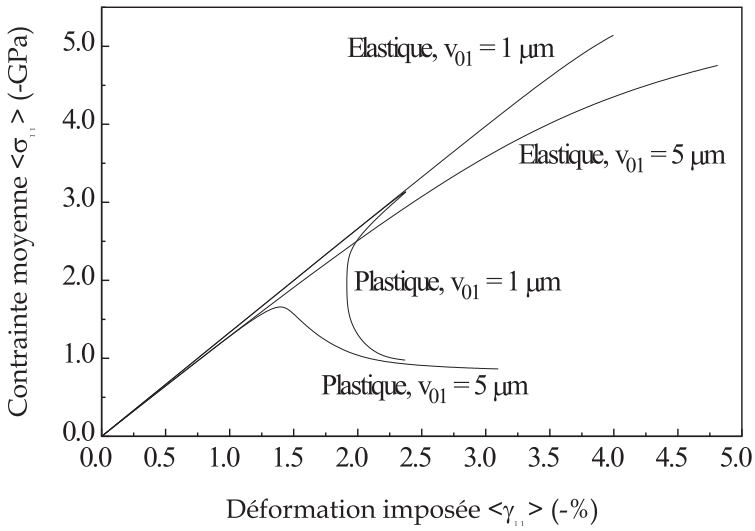

FIG. 2.3: Réponse élastique et plastique d'un pli UD T300/914 de 5 *mm* d'épaisseur affecté de deux défauts harmoniques d'amplitude constante 1 et 5 μm et de longueur d'onde 0,63 *mm*.

Le défaut initial des fibres est un paramètre clef de la rupture par microflambage plastique. Il peut être caractérisé par l'angle de désalignement maximum ϕ_0, mesuré entre la fibre et son axe

théorique, où se produit la localisation des déformations plastiques qui conduit à la rupture du pli. Toutefois, cette simplification du défaut n'est valable que dans une plage de longueurs d'onde pour lesquelles les déformations à rupture sont minimales et restent quasiment constantes pour un angle du défaut initial donné. On vérifie de plus qu'une répartition constante dans l'épaisseur du défaut pris sur le mode élastique conduit aux résistances les plus faibles. L'influence de la flexion des fibres quant à elle justifie la résistance accrue lorsque la longueur d'onde du défaut initial devient petite.

L'étude paramétrique des constituants valide l'approche de nombreux auteurs pour lesquels le couplage du défaut des fibres avec la plasticité de la matrice est un paramètre central de la rupture par microflambage plastique (Figure 2.3). L'utilisation de la loi de Ramberg-Osgood nous permet par contre de remettre en cause le rôle central de la limite élastique proposé par de nombreux auteurs. En effet, l'instabilité est principalement influencée par l'évolution de la rigidité tangente, qui est fonction des caractéristiques mécaniques de la matrice, mais également de l'état tridimensionnel des contraintes qui règne lors de l'apparition de la plasticité et qui diffère pour les petits et les grands défauts. Ceci est explicité en détails dans Drapier *et al.*, 2001 - Annexe 2.3. La rigidité du pli est quant à elle directement liée au module des fibres qui agit également, mais dans une moindre mesure, sur la résistance à rupture.

Effet de structure

L'étude locale du microflambage plastique est étendue ici aux paramètres structuraux (Drapier *et al.*, 1998, Drapier *et al.*, 1999 - Annexe 2.2, Drapier *et al.*, 2001 - Annexe 2.3). Pour ces simulations, une loi de comportement identifiée expérimentalement [Wisnom, 1993] est utilisée afin de pouvoir comparer quantitativement nos prévisions et les mesures expérimentales.

La position du pli dans la séquence d'empilement est schématisée par les conditions aux limites cinématiques imposées sur ses faces. L'observation de la répartition des contraintes près des bords montre qu'au voisinage d'une face bloquée les contraintes sont faibles et homogènes (Figure 2.4-b). La contrainte la plus élevée au voisinage du bord est dans ce cas la contrainte transverse S_{22} due au déplacement transverse d'une partie des fibres vers le bord bloqué. En revanche prés d'un bord libre (Figure 2.4-a), une couche limite est visible, comme le laissaient prévoir les calculs des modes élastiques de Drapier *et al.*, 1996 - Annexe 2.1, et le microflambage se développe dans cette zone où les déformations plastiques se localisent. Ceci entraîne une chute conséquente de la résistance. Finalement, ces deux types de conditions cinématiques pilotent la répartition des déformations et des contraintes dans tout le pli (Figure 2.4).

Le chargement quant à lui a pour effet de solliciter tout le pli ou une partie seulement. Il apparaît clairement sur la Figure 2.4-b que seule la moitié supérieure du pli est sollicitée, réduisant ainsi la zone de développement du microflambage plastique, avec comme conséquence une augmentation de la résistance. Finalement, on montre clairement ce qui est observé expérimentalement, les plis

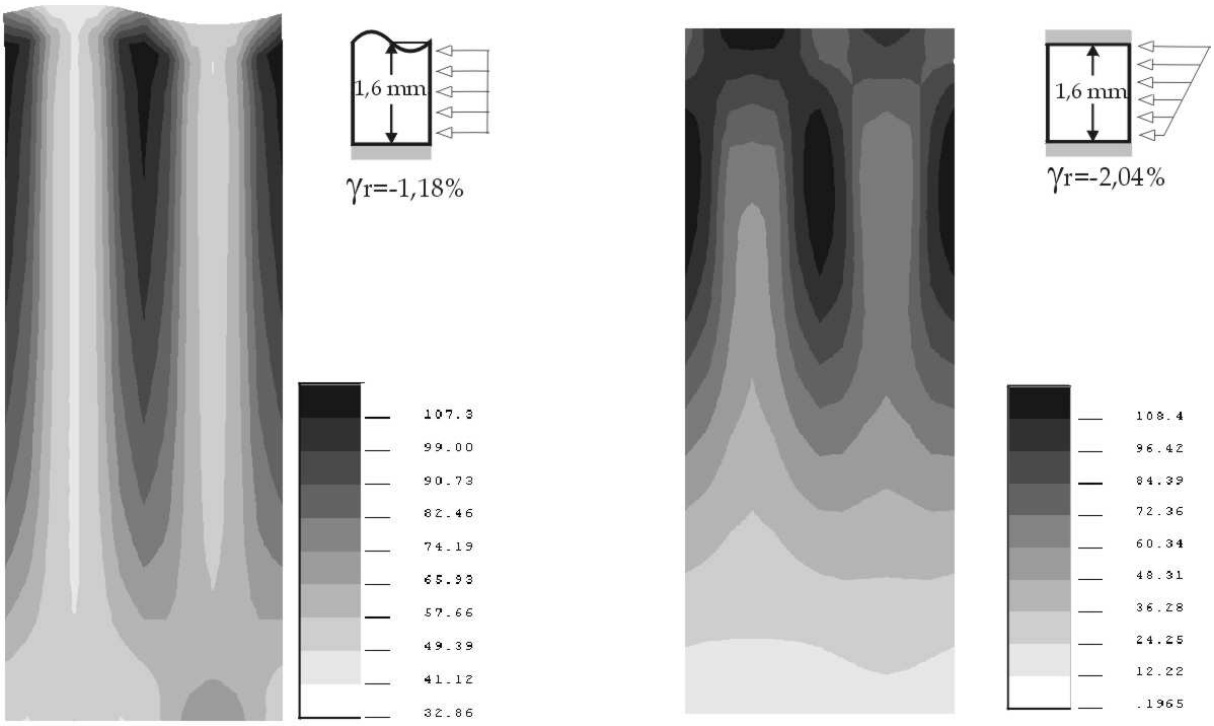

(a) (b)

FIG. 2.4: Distribution des contraintes de von-Mises dans la matrice pour un pli de 1,6 *mm* d'épaisseur (a) en compression bloqué-libre et (b) en flexion bloqué-bloqué. Le défaut est de 1°, sa longueur d'onde 0,63 mm, et le chargement correspond à la déformation à rupture γ_r - déformées $\times$ 10.

à l'intérieur des stratifiés possèdent une résistance plus élevée que les plis en surface des stratifiés. L'effet de la position du pli étant encore accentué sous des chargements de flexion.

Un effet supplémentaire, mais qui en fait se combine avec l'effet du chargement, est l'influence de l'épaisseur du pli testé. Plus le pli est fin, plus sa résistance est élevée. Les simulations ont été réalisées ici sur des plis complets, c'est-à-dire avec des conditions aux limites libre-libre (Figure 2.5). On vérifie également sur cette figure que les résistances mesurées par [Wisnom, 1991] pour différentes épaisseurs sont bien représentées par nos simulations. En résumé, la clef de l'augmentation de la résistance en compression repose en fait, du point de vue des paramètres structuraux, sur la capacité à limiter les déplacements transverses, et donc le développement du microflambage dans l'épaisseur des plis.

Comparaison avec des résultats expérimentaux

Nous avons indiqué en introduction de ce travail, qu'en plus de la position du pli dans la séquence d'empilement, le gradient de déformation dans l'épaisseur était l'autre paramètre de structure important. Le gradient de chargement peut idéalement être modulé expérimentalement en utilisant un montage de flambage rotulé équipé d'un blocage en rotation des têtes qui permet de

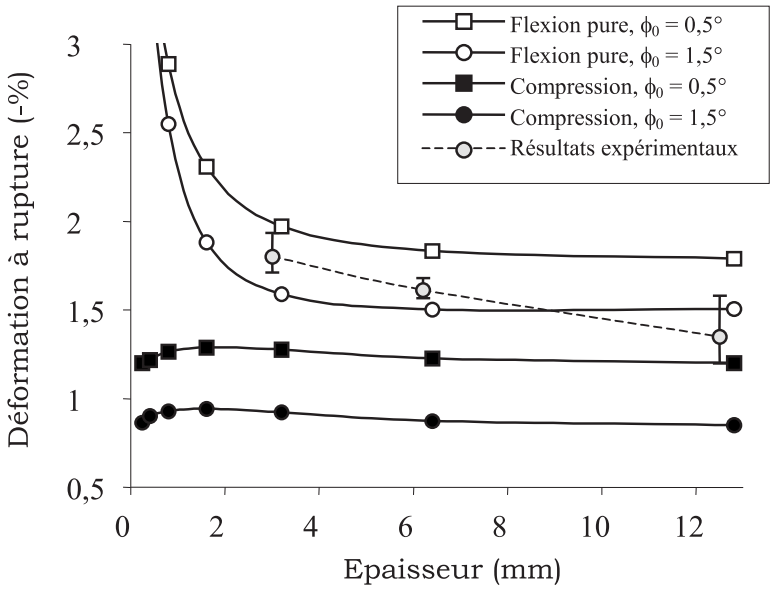

FIG. 2.5: Résistance à rupture en compression, simulée et mesurée [Wisnom, 1991], pour des plis UDs XAS/913 en fonction du chargement et de l'épaisseur.

modifier le rapport de compression et flexion dans le chargement appliqué au composite. Les résultats expérimentaux obtenus avec ce montage sont venus récemment conforter quantitativement et qualitativement les résistances prévues pour des composites modélisés dans toute leur épaisseur, avec des conditions de bord libre sur les deux faces. On voit par exemple sur la Figure 2.6 que pour des défauts d'alignement initiaux de l'ordre de ceux mesurés sur des composites ($0,5^\circ < \phi_0 < 1,5^\circ$), les prévisions pour des UDs T300/DA5208 encadrent parfaitement les mesures expérimentales réalisées avec un montage de flambage rotulé. On notera également dans ces résultats, le niveau de déformations atteint, de l'ordre de 2 à 2,5%, tandis qu'on attribue généralement une résistance en compression de l'ordre de 1% aux composites de ce type.

L'effet de la séquence d'empilement est quant à lui représenté sur la Figure 2.7. Les modélisations ont été menées sur les séquences d'empilement complètes, en approchant le comportement des plis transverses par leur rigidité de membrane équivalente. Dans le cas de plis croisés, la validité de cette approche a été établie en comparant la résistance de plis $[0,90]_s$ libre-libre et de plis [0] bloqué-libre. On peut, ici aussi, noter le niveau de déformation élevé mesuré avec un montage de flambage rotulé par [Anthoine-Rahier, 1998].

2.1.4 Conclusions et perspectives

L'approche présentée ici, est à ce jour la seule, à notre connaissance, capable de prédire quantitativement la résistance en compression des composites à fibres longues. Le point clef de cette approche originale est d'avoir pu prendre en compte, dans un modèle unique, les paramètres à l'échelle du stratifié et l'instabilité plastique à l'échelle des constituants, leurs effets respectifs sur

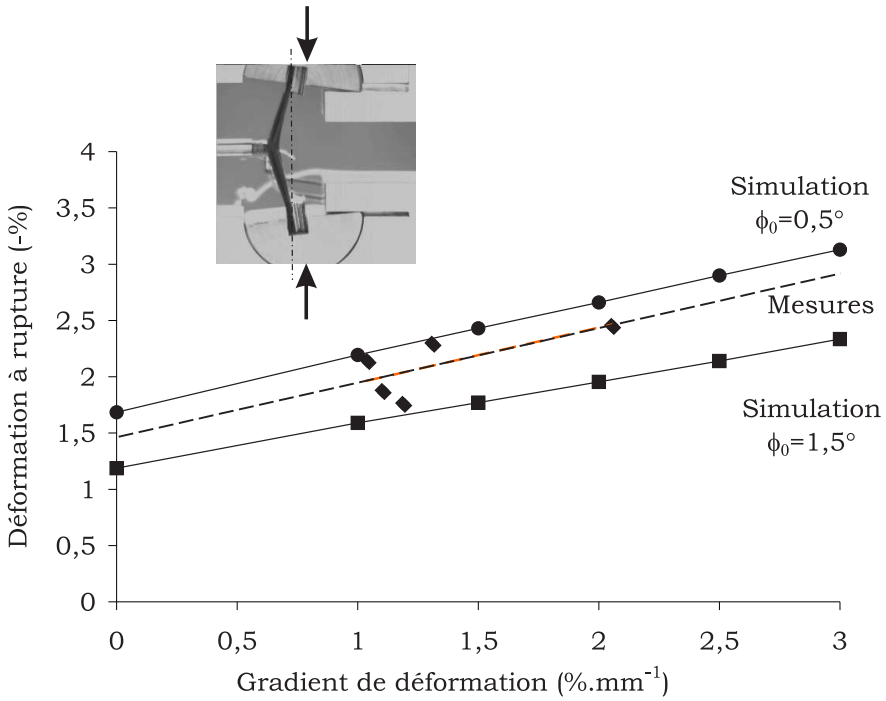

FIG. 2.6: Résistance à rupture en compression, simulée et mesurée avec un montage de flambage rotulé, en fonction du gradient de déformation appliqué, pour des unidirectionnels T300/DA5208.

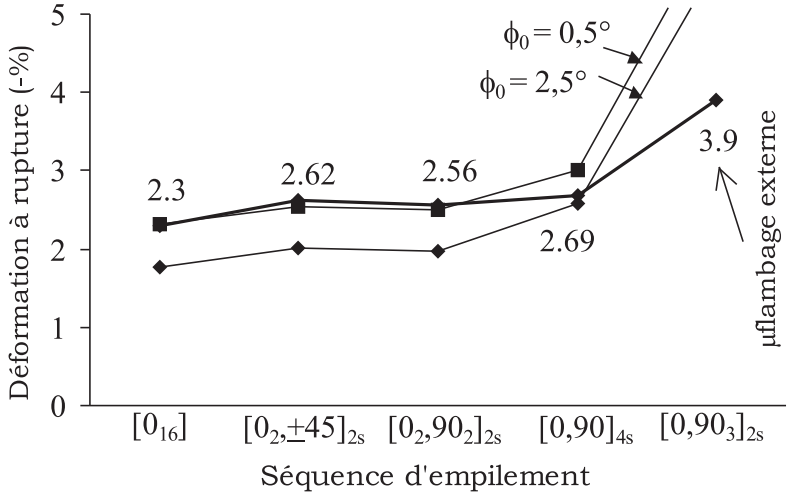

FIG. 2.7: Comparaison des prévisions de notre modèle et de mesures expérimentales de [Anthoine-Rahier, 1998] sur des stratifiés T300/DA508 en utilisant un montage de flambage rotulé.

la résistance étant cumulatifs et d'égale importance. On peut noter, de plus, que seule une formulation spécifique telle que celle adoptée ici garantit des temps de calcul suffisamment faibles, permettant de mener des études complètes à ces deux échelles.

L'étude paramétrique du mécanisme de microflambage plastique a confirmé l'influence ma-

jeure de la combinaison défauts des fibres et plasticité de la matrice sur le développement local de l'instabilité. De plus, nous avons apporté une connaissance plus fine de ce mécanisme, en montrant que le défaut des fibres ne peut pas systématiquement être représenté seulement par un angle de désalignement, et que le caractère plastique de l'instabilité doit être attribué à la rigidité tangente de la matrice. De façon plus essentielle, nous avons montré clairement que l'effet de structure s'explique assez simplement par l'influence des paramètres structuraux susceptibles de modifier la distribution des déplacements transverses dans l'épaisseur du pli, et par conséquent la distribution des déformations plastiques qui sont à l'origine de l'apparition du microflambage. Ces paramètres essentiels sont le gradient de chargement et la position du pli dans la séquence d'empilement. Les prévisions de résistance ont été, de plus, confirmées par les essais, notamment en recourant à un montage de flambage rotulé.

Il faut noter que dans nos essais de flambage rotulé, les déformations ultimes mesurées sont jusqu'à trois fois plus élevées que celles identifiées habituellement avec des essais de compression directe. Ces essais nécessitant, de plus, une mise en œuvre méticuleuse sous peine d'obtenir des dispersions importantes et des ruptures prématurées [Anthoine-Rahier et al., 1998]. On comprend mieux alors l'intérêt de développer en parallèle des modèles spécifiques, capables de décrire finement l'effet des paramètres aux deux échelles, et des systèmes de mesure adaptés. On peut d'ailleurs rappeler que la résistance en compression des composites à fibres longues a pendant très longtemps soulevé de nombreuses interrogations quant aux différences importantes observées entre les prévisions fournies par des modèles à l'échelle des constituants et les mesures effectuées à l'aide d'essais de compression directe, peu fiables jusqu'à très récemment. Le corollaire du travail de recherche présenté ici est que l'utilisation rationnelle des composites passe par des approches globales de ce type, intégrant des modèles complets mais également des essais bien fondés. Les essais pouvant révéler des effets nouveaux, et les modèles étant utilisés aussi pour la conception de ces outils de caractérisation.

Dans ce travail de recherche, les simulations sur les stratifiés complets ont permis de dégager les premiers résultats. Cette approche doit être généralisée au 3D pour être incluse dans une approche multi-échelle globale, développée plus longuement dans les perspectives de la thématique 'Instabilités et effets d'échelle' exposées ci-après (page 39). Cette extension au 3D est envisagée, mais il est nécessaire de mettre en balance ce raffinement du modèle par rapport, notamment, à l'approximation du défaut, dont l'influence sur la résistance à rupture est très forte, et pour lequel nous ne disposons que de peu de données. L'apparition des ondulations de fibres au cours de l'élaboration du composite a été abordée à l'échelle locale par [Jochum, 1999] ([Jochum et al., 1999], également présenté dans Drapier *et al.*, 2000). Les résultats obtenus sur des éprouvettes monofilamentaire sont concluants, les mesures expérimentales recoupent les prévisions d'un modèle d'instabilité géométrique établi à l'échelle d'une fibre soumise à un chargement compressif induit par la contraction volumique de la résine qui l'entoure. Mais actuellement, le manque de moyens

de caractérisation couplant microscopie et reconstruction tridimensionnelle est un frein pour les mesures à ces échelles lorsqu'un nombre important de fibres est considéré. De plus, on peut, au vu des résultats présentés ici, s'interroger quant à l'influence de la position des plis dans le stratifié et de leur épaisseur sur la répartition des ondulations des fibres. L'adaptation, au cas du microflambage d'origine thermo-mécanique, du modèle présenté ici peut constituer un élément de réponse à l'effet des paramètres structuraux sur la répartition des défauts.

Ce dernier point rejoint la problématique centrale que j'essaie de mettre en place sur le long terme dans mes travaux de recherche, c'est-à-dire l'influence de l'élaboration des composites sur leur comportement critique. Comme nous avons pu le voir à travers ce travail, c'est essentiellement au niveau des imperfections que cette relation s'établit. En conséquence, un premier lien entre élaboration et propriétés critiques peut être proposé dans le cas des renforts multiaxiaux pour composite structuraux, dans lesquels les imperfections géométriques mésoscopiques sont plus liées à l'assemblage des renforts secs qu'à l'élaboration du composite elle-même. Ce travail de recherche est présenté dans la partie suivante du mémoire.

2.2 Modélisation du comportement en compression et en cisaillement interlaminaire des *NCF*s

Aujourd'hui, l'élaboration de structures composites à partir de plis UniDirectionnels pré--imprégnés (UDs pre-pregs) reste la référence en terme de qualité d'élaboration et donc de propriétés finales, sauf peut-être en terme de résistances transverses particulièrement critiques dans les composites épais. Ce procédé d'élaboration coûteux a pendant très longtemps été le seul reconnu pour les applications hautes performances, notamment dans le domaine de l'aéronautique. Or, les structures aéronautiques deviennent de plus en plus épaisses ($\simeq 50$ *mm*), et les coûts matière/fabrication sont maintenant des éléments de sélection, au même titre que les propriétés mécaniques finales. Depuis quelques années, la réduction des coûts d'élaboration a donné lieu au développement de procédés dits *par voie liquide* dans lesquels les renforts peuvent être mis en forme, puis imprégnés de résine avant de subir un cycle de pression-température destiné à amener la résine dans son état solide. L'utilisation de renforts multiaxiaux, associés à des procédés de ce type, apporte désormais des réponses pertinentes à la réduction des coûts, notamment grâce à l'utilisation de nappes multiaxiales de fort grammage (donc épaisses), mais permet également d'améliorer les résistances transverses par l'introduction de coutures (Figure 2.8). Sur ce dernier point, des études expérimentales ont montré que la bonne résistance après impact des semi-produits dits Non Crimped Fabrics (*NCF*) est liée à l'hétérogénéité de leur mésostructure, dans laquelle le délaminage ne peut progresser qu'en contournant les mèches de fibres, augmentant ainsi la surface de fracture [Backhouse, 1998]. En contrepartie, certaines autres propriétés mécaniques de ces multiaxiaux sont moins bonnes que celles d'UDs pre-pregs. C'est notamment le cas des compor-

tements critiques en compression et cisaillement interlaminaire, très sensibles aux hétérogénéités de la micro et/ou mésostructure comme nous l'avons vérifié également dans le cas des composites à fibres longues.

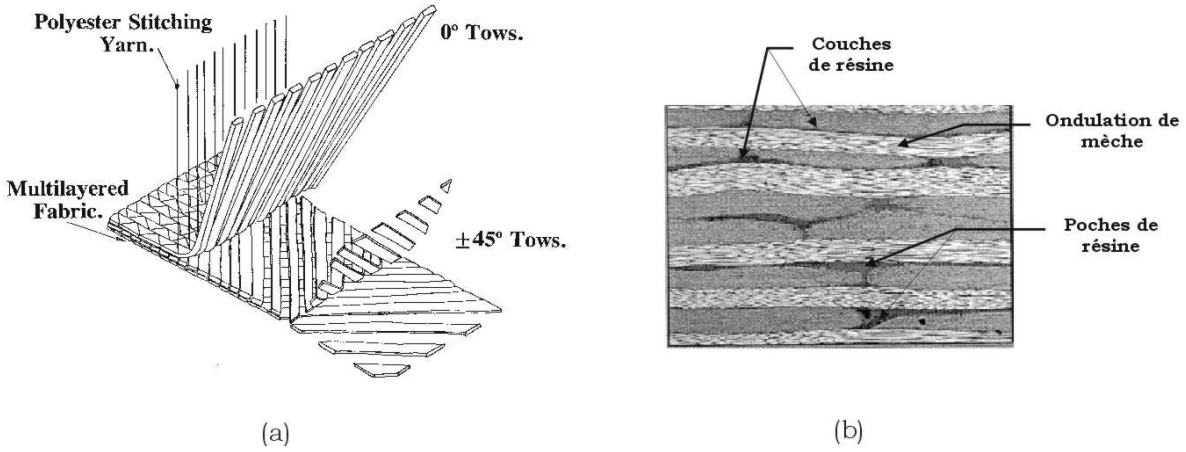

FIG. 2.8: (a) Élaboration d'un *NCF* à partir de mèches de fibres (tiré de [Backhouse, 1998]) et (b) mésostructure d'un *NCF* biaxial (extrait de [Miller, 1996]).

L'objectif étant d'utiliser encore plus largement ces nouvelles solutions composites, il est donc essentiel de pouvoir comprendre quels sont les paramètres susceptibles de modifier les propriétés mécaniques finales de ces multiaxiaux, et plus particulièrement les propriétés critiques. Dans ce travail mené lors de mon séjour post-doctoral d'un an à l'université de Bristol (GB) au département d'*Aerospace Engineering*, en 1996-97, j'ai développé des modèles numériques du comportement de *NCF*s. Ces recherches entraient dans le cadre d'un projet national intitulé INnovative Fabrics for Aircraft Composite Structures (*INFACS*) regroupant des partenaires universitaires et industriels (British Aerospace / Airbus, Hexcel Composites, Tech Textiles, University of Bristol, Imperial College, Queen Mary and Westfield College, Cranfield University, ...), pendant lequel ces semi-produits ont été développés et testés, en premier lieu à l'université de Cranfield en association avec British Aerospace ([Backhouse, 1998], [Miller, 1996]). Ces *NCF*s sont élaborés par un procédé breveté par Liba (Figure 2.8) : les renforts multiaxiaux sont obtenus par un empilement de nappes UDs, elles-mêmes reconstituées en plaçant côte à côte des mèches (ou torons) contenant de 3 à 64 000 fibres, l'ensemble étant cousu à travers l'épaisseur (Figure 2.8-a).

Dans ce programme nous étions plus particulièrement concernés par l'activité intitulée *Guidelines for Preform/Fabric Structure*. La modélisation mise en place avait donc pour objectif de comprendre en détail le lien entre les caractéristiques géométriques et mécaniques des *NCF*s aux diverses échelles d'observation, et les comportements mécaniques critiques en compression et cisaillement interlaminaire des structures utilisant ces renforts multiaxiaux. Le but final étant d'optimiser les choix des matériaux de base (mèches) et leur assemblage (coutures) dans les *NCF*s par rapport aux propriétés mécaniques finales visées, en tenant compte des contraintes de fabrication.

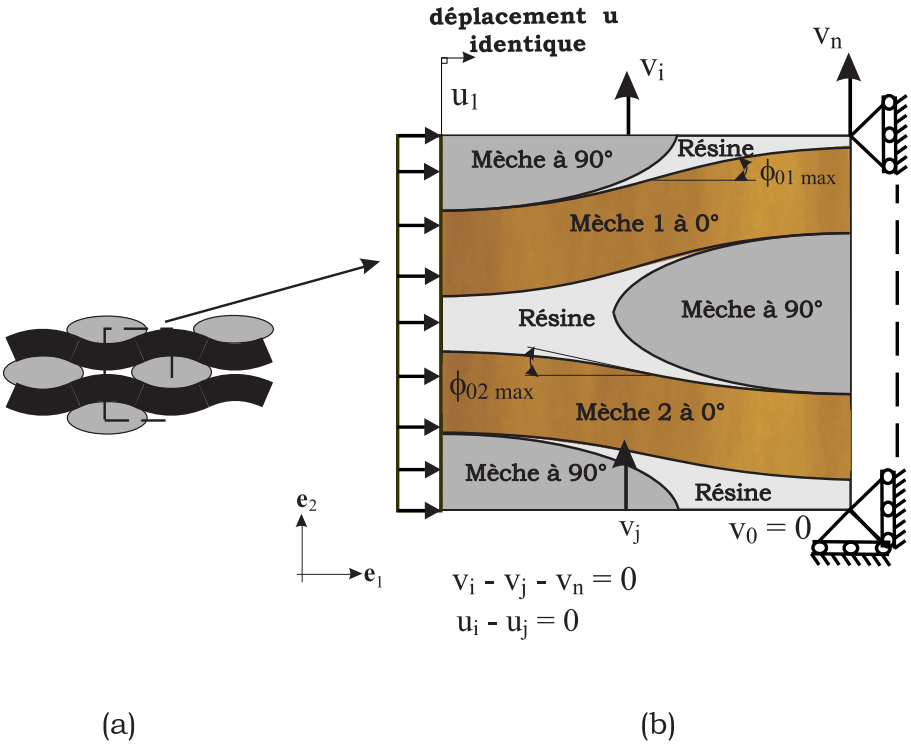

FIG. 2.9: Modélisation à l'échelle mésoscopique d'un *NCF* biaxial [0,90] en compression : (a) idéalisation du *nesting*, et (b) cellule de base avec défauts d'alignement pour les mèches à 0°.

2.2.1 Modélisation à l'échelle des nappes

La mise en place de la modélisation de ces matériaux spécifiques, caractérisés par quatre échelles d'observation, passe d'abord par la détermination des paramètres géométriques et matériaux pertinents. Ces matériaux ont été très peu étudiés du point de vue de la modélisation, mais on sait par contre, d'un point de vue général [Dransfield et al., 1994], que l'effet de la couture introduite principalement pour améliorer la maniabilité des semi-produits et augmenter les propriétés mécaniques dans la direction transverse, est souvent source de perturbation dans la mésostructure. De plus, le rapprochement des mesures morphologiques des *NCF*s et des résistances en compression [Miller, 1996] montrent une relation forte entre l'ondulation des mèches de fibres orientées dans la direction du chargement et la résistance en compression. Ces ondulations des mèches sont en fait reliées directement à l'architecture du semi-produit (Figure 2.9-a). Sous l'action de la pression imposée pendant l'élaboration, les mèches fléchissent dans les espaces libérés entre les mèches transverses (*nesting*) au moment de la formation des nappes (Figure 2.8-a/-b). Suivant la taille des torons utilisés, du type de couture utilisé et de la tension du fil de couture, ces défauts varient. On note en effet, que lorsque les fils de couture sont retirés avant l'imprégnation, les ondulations ne sont plus visibles dans le stratifié final [Miller, 1996].

Cellule de base

Finalement, compte-tenu de l'effet prépondérant des paramètres à cette échelle mésoscopique, un modèle a été mis en place à l'échelle des mèches, pour des nappes biaxiales [0,90] dans lesquelles les mécanismes seront les plus clairement identifiés. L'idée ici est assez similaire à celle proposée dans les recherches sur les composites à fibres longues, à savoir se placer à une échelle intermédiaire. Mais il n'est pas question, dans cette première approche, de prendre en compte les effets de structure tel que présenté précédemment.

Afin de réduire les temps de calcul des simulations par éléments finis, et compte-tenu de la faible variation des propriétés dans la direction transverse, une modélisation bidimensionnelle en déformations planes généralisées a été mise en place dans la hauteur et la longueur de la nappe (Figure 2.9). L'effet du fil de couture sur le comportement mécanique est négligé, son effet principal sera dans notre cas pris en compte par la modification de la section des mèches avec la tension de la couture. Les temps de calcul sont encore réduits en définissant une cellule représentative, basée sur le phénomène de nesting (Figure 2.9-a), qui permet de représenter, avec des conditions aux limites adéquates, le comportement d'un empilement de dimension finie de *NCF*s (Figure 2.9-b). Dans l'objectif de conduire une étude paramétrique, nous choisissons de représenter dans cette cellule deux mèches à 0 ˚afin de vérifier l'effet de défauts d'alignement antagonistes ou en phase. Le chargement imposé est un effort réparti sur une des faces de la cellule.

Modélisation des mèches

Nous avons choisi de nous placer à l'échelle des nappes, par conséquent les mèches sont vues comme des milieux homogènes. Pourtant, suite aux travaux menés sur le mécanisme de microflambage plastique, il est clair que le comportement des mèches à 0 ˚, *i.e.* dans la direction du chargement, doit être finement représenté dans notre modèle. En effet, sous un chargement de compression, on peut retrouver ici un mécanisme proche du microflambage, dans lequel la résine subit un écoulement plastique suite au désaxement coopératif de paquets de fibres par rapport à la direction de chargement.

Comme dans les recherches sur le microflambage, nous devons représenter un comportement homogène équivalent dans lequel l'instabilité plastique peut se développer. On pourrait modifier le modèle développé au LPMM à Metz mais la durée très limitée de la collaboration nous a poussé à reconstituer ce comportement à l'aide d'éléments finis standards. Nous connectons, en définissant les degrés de liberté de membrane communs, des éléments de poutre de type Hermite à chaque élément plan bi-quadratique du maillage [Wisnom, 1993]. La loi de comportement homogène orthotrope non-linéaire est ensuite reconstituée dans une subroutine utilisateur (UMAT) du code ABAQUS utilisé pour les simulations (Drapier & Wisnom, 1999 a - Annexe 2.4). Afin de réduire encore les temps de calculs, la loi de comportement non-linéaire en cisaillement de l'élément

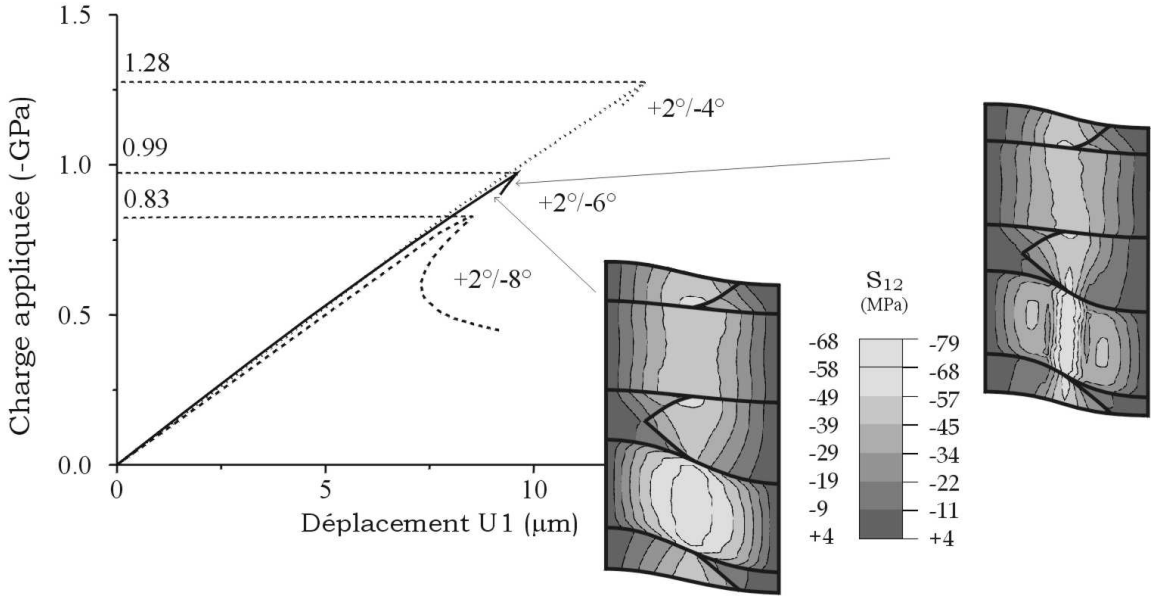

FIG. 2.10: Réponse en compression d'un *NCF* biaxial T300/914 pour différents défauts de la mèche 2 (-4˚, -6˚, -8˚) et distribution des contraintes de cisaillement avant et après le point de bifurcation - déformées $\times$ 10.

plan est reconstituée par de simples relations analytiques en partant du comportement de la résine, et la loi de comportement non-linéaire des plis à 90˚est également reconstituée analytiquement, via des considérations micromécaniques similaires à celles ayant permis d'établir le modèle de *MHE* de microflambage.

2.2.2 Réponses des *NCF*s et premiers liens avec l'élaboration

Utilisant ces modèles numériques, les comportements en compression (Drapier & Wisnom, 1999 a - Annexe 2.4) et en cisaillement interlaminaire (Drapier & Wisnom, 1999 b - Annexe 2.5) des *NCF*s ont été étudiés. Dans ces simulations, les dimensions des mèches et la longueur d'onde du défaut correspondent aux mesures de [Miller, 1996].

Comportement en compression

On peut voir sur la Figure 2.10 la réponse en compression d'une nappe biaxiale T300/914 contenant 55% de fibres. Comme on pouvait l'attendre, plus les défauts sont importants, plus la bifurcation sous-critique, et donc la rupture, apparaît pour un chargement faible. La répartition des contraintes de cisaillement montre que ce sont bien les mèches à 0˚qui contrôlent l'apparition de ce *mésoflambage* : le désaxement des renforts par rapport au chargement induit des déformations de cisaillement plastique, d'abord dans la mèche à 0˚possédant le défaut de plus grande amplitude, puis dans les mèches à 90˚, et enfin dans l'autre mèche à 0˚, ce qui conduit finalement à l'apparition de l'instabilité globale. Après le point de bifurcation, ces contraintes se localisent au centre de la

cellule, ce qui induit la perte de rigidité observée. Le mésoflambage est bien le mécanisme qui contrôle la résistance en compression. En conséquence, les paramètres qui ont une influence sur cette instabilité sont, dans l'ordre d'importance (Drapier & Wisnom, 1999 a - Annexe 2.4) : le désalignement des mèches à 0˚, le comportement en cisaillement de la résine, et la taille des mèches à 90˚qui seules s'opposent au mésoflambage. La rigidité globale est quant à elle directement liée à la rigidité des fibres.

Finalement, l'amélioration de la résistance en compression passe par la diminution des imperfections et l'*épanouissement* des mèches à 90˚qui se traduira par l'augmentation du recouvrement des mèches à 0˚. L'augmentation des propriétés de la résine en cisaillement est également une nécessité pour améliorer cette résistance. En résumé, en ce qui concerne la résistance en compression, la mésostructure doit tendre vers celle des stratifiés classiques (géométrie et fraction volumique de fibres), et une résine haut module doit être utilisée. Du point de vue des paramètres d'élaboration, le changement de résine peut être considéré rapidement. Quant à la géométrie, l'augmentation de la tension des mèches lors de la réalisation des nappes, et l'utilisation d'une tension de couture faible, devraient contribuer à limiter le nesting, et permettre également aux mèches de s'épanouir et ainsi de mieux supporter le mésoflambage des mèches à 0 ˚. Cette dernière indication concernant la tension de couture est confirmée par des études expérimentales confidentielles [Backhouse, 1998] qui montrent que la résistance en compression augmente quand la tension des fils est élevée.

Comportement en cisaillement interlaminaire

Pour cette étude du cisaillement interlaminaire, la cellule de base est doublée en taille afin de représenter ce phénomène antisymétrique par rapport au centre de la cellule. Le chargement est un déplacement homogène imposé sur son contour (Drapier & Wisnom, 1999 b - Annexe 2.5).

La réponse en cisaillement interlaminaire tracée sur la Figure 2.11 montre clairement que le comportement du *NCF* est contrôlé par le cisaillement de la résine (module et limite élastique), plus précisément par la résine dans les mèches à 0˚puisque la réponse du *NCF* est très proche de celle d'un pli UD de même type. Sur cette même figure on observe que les déformations de cisaillement se localisent dans les poches de résine, et plus particulièrement dans les zones à fort gradient de propriétés mécaniques où, par continuité des contraintes, les déformations varient en conséquence. Pour des raisons de limite de temps, nous ne pouvons proposer une approche maîtrisée de la résistance, par contre la présence des déformations maximales correspond très probablement aux endroits où la rupture sera initiée. Plus globalement, lorsque les déformations de cisaillement sont élevées, la cellule se comporte comme un empilement de couches raides (mèches 0˚) et souples (résine+mèches 90˚).

Comme pour la compression, en cisaillement les mèches à 90 ˚offrent un support aux mèches à 0˚. Par contre, à l'inverse de la compression, ici les défauts d'alignement des mèches à 0˚n'altèrent de façon significative ni la réponse globale ni la répartition des déformations. Une augmentation de

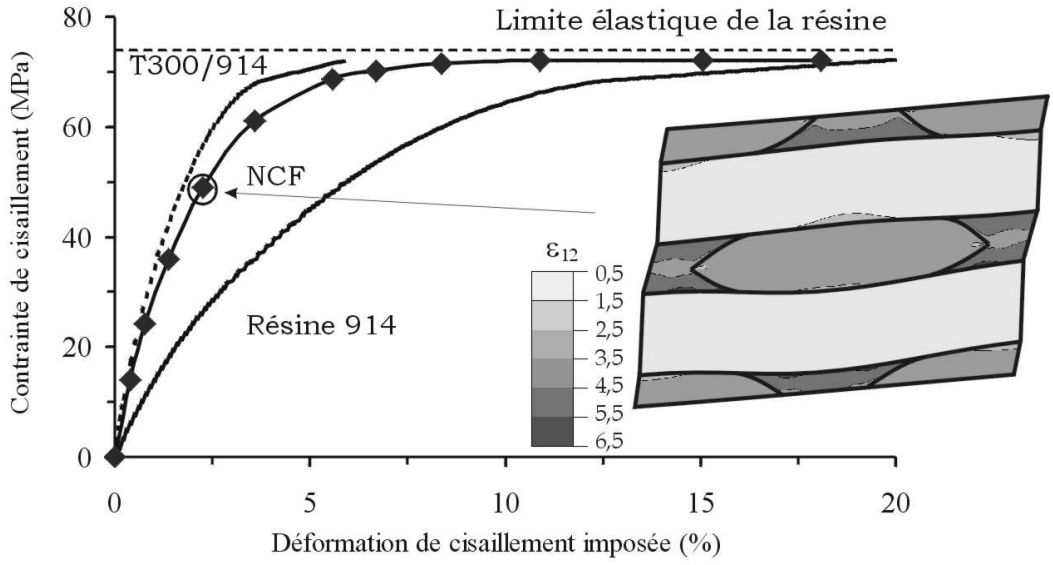

FIG. 2.11: Réponse en cisaillement interlaminaire de la cellule de base (+2 ˚/-6 ˚) et répartition des déformations de cisaillement pour un chargement de 50 MPa - déformée $\times$ 10.

la fraction volumique de fibres permettra par contre d'homogénéiser la distribution des déformations, tout comme l'utilisation d'une résine possédant une rigidité et une limite élastique accrues qui permettra de limiter la localisation des déformations dans les poches. Un dernier paramètre essentiel dans l'étude du cisaillement interlaminaire est la présence de couches résiduelles de résine, comme on peut les observer par exemple sur la Figure 2.8-b. C'est à travers ces couches que le chargement de cisaillement est transmis entre les mèches à 0 ˚et 90 ˚. Leur présence élimine presque totalement l'amélioration qui résulte de l'utilisation d'une résine à plus haut module. Les prévisions de nos simulations sont en accord avec les mesures expérimentales [Miller, 1996] qui montrent que la résistance en cisaillement interlaminaire est directement proportionnelle à l'épaisseur de ces couches de résine.

Nous avons montré que la résine joue un rôle essentiel par la présence de poches de résine, et par ses propriétés mécaniques. La forme des mèches à 90 ˚ainsi que la présence de couches de résine entre les mèches contribuent également à diminuer la résistance au cisaillement interlaminaire. Au final, l'amélioration des propriétés en cisaillement passe donc par la réduction de déformations de cisaillement élevées. Ceci peut être traité lors de l'élaboration en utilisant une résine possédant une limite élastique et un module élevés, et en limitant la tension des coutures pour permettre un bon épanouissement des mèches. Le point essentiel qu'il reste à lever concerne la réduction, lors de l'élaboration, des couches de résine entre les nappes.

2.2.3 Conclusions

Nous avons vu dans ces simulations du comportement des *NCF*s que la modélisation à l'échelle mésoscopique permet de décrire finement les mécanismes mis en jeu sous des chargements de compression et de cisaillement interlaminaire, et d'en déduire les premiers liens avec l'élaboration. C'est en effet la géométrie mésoscopique qui contrôle ces réponses, notamment la taille des mèches utilisées et la tension des coutures conditionne fortement l'amplitude et la longueur caractéristique des défauts géométriques dont l'effet sur la réponse en compression est critique (Figure 2.10). Par conséquent le choix de la taille des mèches utilisées a un effet direct sur la résistance en compression des *NCF*s. Un autre paramètre essentiel est la présence de poches de résine, corollaire de la présence de défauts de fortes amplitudes. C'est en effet dans ces poches que se produit la localisation des déformations plastiques de la résine qui contrôle la rigidité, et très probablement la résistance, en cisaillement interlaminaire. En résumé, l'amélioration des propriétés mécaniques des *NCF*s sera effective lorsque la mésostructure sera la plus homogène possible, réduisant la localisation des déformations.

Enfin, le dernier paramètre qui pénalise fortement le comportement en cisaillement est la présence de couches de résine résiduelles. Il paraît légitime de penser que le comportement en compression doit également être pénalisé par ces couches de résine, puisque le mésoflambage conduira à la localisation des déformations en cisaillement dans ces couches (Figure 2.10). Du point de vue de l'élaboration, ces couches de résine proviennent d'une hétérogénéité d'imprégnation des nappes dans le procédé par voie liquide. Parmi tous les paramètres dont l'influence a été démontrée, l'élimination, ou pour être plus réaliste la réduction, de l'épaisseur de ces couches de résine est le point essentiel qui ne peut être maîtrisé directement. Dans ce contexte, l'apport de la modélisation du procédé RFI, voire plus simplement du mécanisme d'imprégnation transverse des *NCF*s, est un élément clef de compréhension, et donc d'optimisation, des paramètres du procédé en vue de la réduction de ces couches résiduelles. Le lien entre l'élaboration et les comportements critiques prend ici tout son sens. Une modélisation de ce procédé débute, dans le cadre de renforts multiaxiaux légèrement différents. Ce projet de recherche est présenté dans le chapitre 3 **Thème émergent - Procédés et problèmes connexes**, page 43 de ce mémoire.

Nous avons montré que les résistances en compression prévues par ces simulations recoupent assez bien les résultats expérimentaux obtenus avec des montages de compression directe. Il faut rappeler ici la difficulté de mener des tels essais. L'utilisation de montages de flambage rotulé permettrait de lever certaines difficultés, et l'étude présentée ici sur la simulation du comportement des *NCF*s peut s'étendre assez simplement à la réponse sous des chargements de flexion-compression. Finalement, compte-tenu des temps de calcul réduits, des séquences d'empilement complètes pourraient être modélisées, et, comme dans le cas des composites à fibres longues, une extension de ce modèle au 3D est envisageable. Qui plus est, à l'inverse des composites à fibres longues, la mesure

du défaut mésoscopique semble moins problématique dans les *NCF*s.

Dans les structures composites courantes, notamment dans le domaine des transports, les composites à fibres longues et les *NCF*s sont souvent utilisés en matériaux de peaux dans des sandwichs. Le comportement de ces structures particulières pourrait idéalement être étudié par des approches multi-échelles, telles que celle proposée dans les perspectives de la thématique 'Instabilités et effets d'échelle' (page 39). Les recherches présentées jusqu'ici ont permis d'établir des modèles capables de décrire les comportements critiques à l'échelle des stratifiés, que ce soit pour les composites à fibres longues, ou bien pour les *NCF*s. Il reste donc, avant de mettre en place une approche multi-échelle, à comprendre séparément le comportement en compression des sandwichs à peaux isotropes dans lesquels des instabilités géométriques peuvent se développer à deux échelles différentes. Ceci fait l'objet de la partie suivante de ce mémoire.

2.3 Instabilités et effets d'échelle dans les poutres sandwichs

Depuis plus d'un demi-siècle [Williams et al., 1941], les sandwichs ont été largement utilisés pour réaliser des structures secondaires, notamment dans le domaine des transports où leur rigidité spécifique de flexion élevée induit des gains de masse directement convertibles en charges payantes, *i.e.* en passagers supplémentaires transportés. Depuis une vingtaine d'années, on assiste à l'utilisation croissante des sandwichs dans les structures primaires. Le dimensionnement de ces nouvelles applications structurelles, soumises à des sollicitations alternées, exige donc une parfaite connaissance du comportement mécanique des sandwichs, qui sont des assemblages hétérogènes constitués de deux peaux fines et rigides connectées par une âme épaisse et légère. Le dimensionnement des sandwichs en flexion, cisaillement, ou tension est généralement correctement appréhendé par des approches basées sur les concepts élémentaires de la mécanique des structures. Par contre, le comportement en compression est aujourd'hui un comportement critique qui pose de nombreux problèmes au concepteur, tant du point de vue de la prévision que de la mesure [Teti and Caprino, 1989]. En effet, les instabilités dans ces structures peuvent apparaître aussi bien à l'échelle du sandwich (Figure 2.12-a) qu'à l'échelle locale des constituants (Figure 2.12-b/-c), et interagir. Comme dans les composites à fibres longues, l'hétérogénéité géométrique et matérielle des constituants, qui permet d'atteindre des propriétés spécifiques élevées, est également à l'origine, sous un chargement déstabilisant, d'instabilités à deux échelles différentes.

Si les instabilités dans les sandwichs ont été étudiées depuis l'introduction de ces matériaux [Williams et al., 1941], le comportement en compression plane reste mal cerné. On rejoint ici la problématique générale introduite dans le cas des composites à fibres longues, où par manque d'outils de description adaptés et de moyens expérimentaux adéquats, la résistance en compression devient une propriété dimensionnante. On constate par exemple que l'approche proposée par Allen en 1969 [Allen, 1969] est toujours largement utilisée, associée à des coefficients de sécurité variant

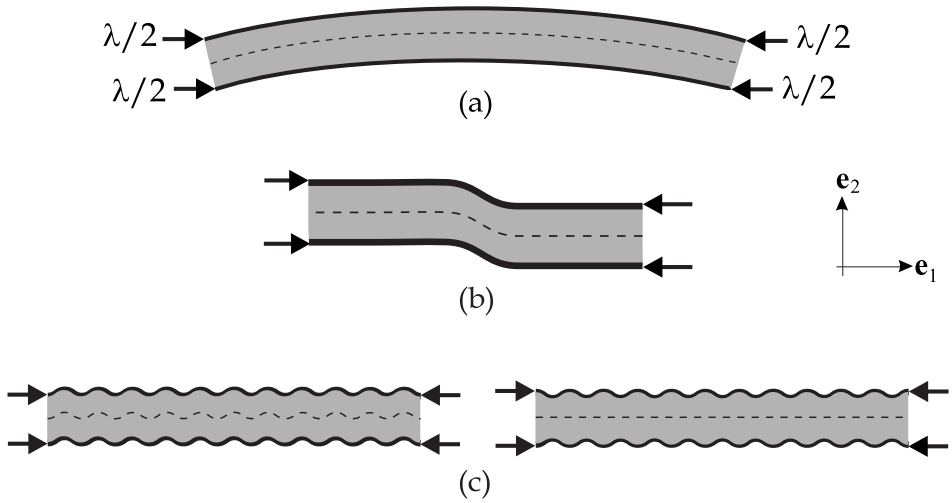

FIG. 2.12: Formes de flambage des structures sandwichs : (a) flambage global, (b) *shear crimping* et (c) *wrinkling* symétrique et antisymétrique.

du *simple au double* pour les charges d'apparition des instabilités locales, dites *wrinkling*, établies avec des modèles de poutre sur fondation élastique :

$$\lambda_{class} = 2bh_pQ\sqrt[3]{E_pE_aG_a} \tag{2.5}$$

avec b la largeur de la poutre, h_p l'épaisseur des peaux, Q un coefficient variant de 0,4 à 0,9 selon les auteurs, E_p le module d'Young des peaux, E_a le module d'Young de l'âme, et G_a son module de cisaillement. On notera que cette expression (Eq. 2.5) ne dépend que de paramètres matériaux. Par ailleurs, le flambage global est traité avec un modèle d'Euler pour une poutre macroscopique possédant une rigidité de cisaillement. La simplicité de cette approche explique certainement son utilisation car il est peu aisé de vérifier expérimentalement ses prévisions, les essais de compression directe étant encore plus délicats à mettre en œuvre que dans le cas des composites monolithiques. Bien qu'elle ait été améliorée depuis sa parution, cette approche reste intrinsèquement une approche découplée où les instabilités globale et locales sont traitées à travers des modèles distincts dont les limites de validité ne sont pas clairement définies. De plus, un problème essentiel de ces approches découplées a trait à l'impossibilité de représenter l'interaction possible entre les modes se développant aux deux échelles (*flambage interactif*), phénomène pourtant observé dés le début de l'utilisation structurelle des sandwichs [Williams et al., 1941].

Il semble pourtant qu'un modèle mécanique bien posé devrait être en mesure de représenter l'apparition des instabilités à ces deux échelles, en prenant en compte l'ensemble des paramètres pertinents pour chacune des formes. Un tel modèle est un préalable à l'optimisation des sandwichs vis-à-vis de la résistance en compression. Quelques modèles complets existent qui tentent d'aborder ce problème à deux échelles à travers une approche *unifiée*, malheureusement ils sont peu aisés à mettre en œuvre [Hunt et al., 1988], incomplets [Frostig and Baruch, 1993] ou sources de singularités dans les simulations numériques [Starlinger, 1990]. L'objectif final du travail de recherche

présenté ici, développé dans la thèse de Lionel Léotoing soutenue en novembre 2001, était de proposer des outils simples, de nature analytique et numérique, de dimensionnement en compression des structures sandwich par rapport aux instabilités globales et locales, mais également par rapport au flambage interactif.

2.3.1 Modèle unifié de poutre sandwich

Afin de fonder cette approche sur des bases bien maîtrisées, un modèle analytique de poutre a été mis en place (Léotoing *et al.*, 2002 a - Annexe 2.6). Pour construire ce modèle, nous considérons une poutre sandwich symétrique de hauteur h et le longueur L, telle que représentée schématiquement sur la Figure 2.12, constituée de matériaux élastiques isotropes, et dont les peaux du bas et du haut seront indicées 'b' et 'h' respectivement dans les relations suivantes, et l'âme sera indicée 'a'.

Cinématique

Pour simplifier l'approche, nous choisissons de formuler le problème en déplacements, à l'échelle des peaux et de l'âme. La cinématique choisie pour ce modèle doit être suffisamment riche pour représenter toutes les formes d'instabilité, mais aussi suffisamment simple pour permettre d'extraire des solutions analytiques. La cinématique dans les peaux est de type Bernoulli, incluant le terme de rotation modérée pour pouvoir rendre compte de l'apparition des instabilités géométriques locales. La cinématique dans l'âme est quant à elle primordiale car elle contrôle la réponse locale du sandwich.

[Lo et al., 1977] ont montré que pour une poutre homogène, lorsque la longueur caractéristique de variation du chargement est de l'ordre de grandeur de l'épaisseur de la poutre, une cinématique d'ordre supérieur doit être utilisée. Il est également établi, dans les modèles de plaques ou coques sandwich par exemple, qu'une théorie d'ordre supérieur est nécessaire pour décrire le gauchissement des sections, c'est-à-dire la variation parabolique du cisaillement à travers l'épaisseur qui est observée expérimentalement. Dans la thèse de Laurent Dufort soutenue en janvier 2000, nous avons également établi, analytiquement, par éléments finis, et expérimentalement, la nécessité d'une théorie d'ordre supérieur dans le cas de poutres composites épaisses en flexion trois points (Dufort *et al.*, 2001 - Annexe 2.9). Ces solutions analytiques permettent de décrire, même sous des conditions sévères de faible élancement et pour des rapport d'orthotropie élevés, les profils identifiés expérimentalement, tout en supprimant la singularité de distribution du cisaillement sous le point d'application de l'effort. Finalement, pour notre poutre sandwich dans laquelle les instabilités locales sont caractérisées par la flexion des composants sur des longueurs d'onde faibles, se rapprochant d'une flexion de poutre de faible élancement, il est raisonnable de choisir une cinématique d'ordre supérieur dans l'âme.

Équilibre

La cinématique de la poutre complète est définie à l'aide de onze inconnues cinématiques, fonctions uniquement de la position dans la longueur de la poutre. Pour simplifier l'approche, la continuité des contraintes est vérifiée aux interfaces peaux-âmes, et la contrainte de cisaillement est prise, en première approximation, linéaire dans l'épaisseur de l'âme afin de réduire la taille du problème. On montre d'ailleurs que tous les modes ne seraient pas décrits avec une contrainte de cisaillement constante dans l'épaisseur du sandwich (Léotoing *et al.*, 2002 a - Annexe 2.6). Ensuite, les puissances virtuelles sont explicitées, en limitant les contributions à la contrainte normale dans les peaux ($\mathbf{S}^{\alpha} = S_{11}^{\alpha}\mathbf{e}_1 \otimes \mathbf{e}_1$ avec $\alpha = b, h$) et aux cisaillement transverse et contrainte normale transverse dans l'âme ($\mathbf{S}^{a} = S_{12}^{a}\mathbf{e}_1 \otimes \mathbf{e}_2 + S_{22}^{a}\mathbf{e}_2 \otimes \mathbf{e}_2$). Le PPV est complètement défini, et les équations d'équilibre s'en déduisent. On aboutit finalement à cinq équations d'équilibre non-linéaires pour la poutre sandwich. Ces cinq équations correspondent aux cinq inconnues cinématiques restantes (voir détails dans Léotoing *et al.*, 2002 a - Annexe 2.6) qui sont $\mathbf{u}^{\alpha}(x_1) = u^{\alpha}(x_1)\mathbf{e}_1 + v^{\alpha}(x1)\mathbf{e}_2$ les deux composantes du déplacement dans les deux peaux, et $\phi(x_1)$ un gradient de rotation dans l'âme.

Charges critiques

Avec l'objectif de proposer des expressions analytiques des charges de flambage, la solution de ce système fortement non-linéaire ne peut être recherchée simplement. Par contre ces charges critiques peuvent être calculées à l'aide du problème linéarisé, obtenu à partir des équations d'équilibre en considérant un état de pré-flambage linéaire, et en négligeant les termes de rotations modérées dans les résultantes de membrane et de courbure.

Pour résoudre ce problème linéarisé, nous proposons de rechercher les déplacements solutions sous formes de série d'harmoniques qui vérifient les conditions aux limites cinématiques. Finalement un problème aux valeurs propres est formulé. Sa résolution conduit à l'expression de deux valeurs propres strictement positives fonctions du nombre d'onde n, associées à un mode symétrique ($\lambda_S^{MU}(n)$) et à un mode antisymétrique ($\lambda_A^{MU}(n)$). Classiquement, pour expliciter les valeurs critiques de ces charges, on effectue une minimisation par rapport au nombre d'ondes qui détermine le nombre d'ondes critiques et donc la charge correspondante. Considérons le sandwich dont les propriétés sont définies dans le Tableau 2.1-a suivant et traçons les courbes de stabilité neutre pour deux épaisseurs de l'âme h_a de 30 et 60 *mm* (Figure 2.13).

On constate que pour la charge symétrique (Figure 2.13-a), le nombre d'ondes critique est élevé pour les deux épaisseurs considérées. Le mode critique possède donc une longueur d'onde faible, il s'agit d'un mode de wrinkling symétrique. Par contre, pour la charge antisymétrique (Figure 2.13-b), le nombre d'onde critique varie et vaut 1 pour h_a=30 mm, ce qui correspond à un mode de flambage global, et environ 34 pour h_a=60 mm, ce qui correspond à un mode de wrinkling antisy-

$E_p(MPa)$	50000	$h_p(mm)$	1
$E_a(MPa)$	70	$L(mm)$	600
$G_a(MPa)$	25	$b(mm)$	40

(a)

$E_p(MPa)$	70000	$h_a(mm)$	50
$E_a(MPa)$	175	$L(mm)$	470
$G_a(MPa)$	67,3	$b(mm)$	60

(b)

TAB. 2.1: Caractéristiques du sandwich utilisé (a) pour tracer les courbes de stabilité neutre dans la Figure 2.13 et (b) pour les calcul non-linéaires § 2.3.2.

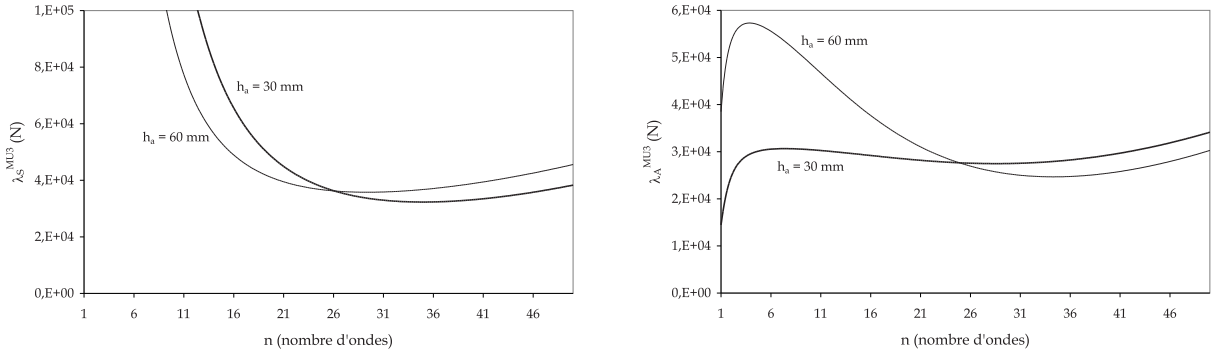

(a) (b)

FIG. 2.13: Courbes de stabilité neutre en fonction de l'épaisseur de l'âme ($h_a = 30$ *mm*, $h_a = 60$ *mm*) associées à (a) λ_S^{MU} et (b) λ_A^{MU} pour la configuration donnée dans le Tableau 2.1.

métrique. Notre modèle est donc bien en mesure de représenter, sans hypothèses supplémentaires que celles posées initialement, les trois principaux modes d'instabilité. La condition d'existence du wrinkling antisymétrique peut s'écrire explicitement, par contre pour la charge critique associée une expression approchée est proposée (Eq. 2.8). La comparaison de ces résultats avec les charges données par des modèles spécifiques de wrinkling, plus lourds ou au contraire trop simplistes [Allen, 1969], montrent que les expressions tirées de notre approche contiennent tous les effets nécessaires pour prévoir l'apparition des deux modes locaux. Les détails de ces comparaisons sont donnés dans Léotoing *et al.*, 2002 a - Annexe 2.6.

À partir des expressions des charges, des calculs de sensibilité peuvent être menés, dans le but notamment de cerner l'influence des paramètres et de leur combinaison sur l'apparition des trois modes (Léotoing *et al.*, 2002 c - Annexe 2.8). Il ressort de cette analyse que les modes de wrinkling dépendent tous deux des mêmes paramètres, l'épaisseur des peaux et les modules de l'âme, ce qui confirme que l'approximation de ces phénomènes par des modèles de poutre sur fondation est valide lorsque l'épaisseur des peaux apparaît dans l'expression des charges, contrairement à la charge utilisée habituellement (Eq. 2.5). Le mode global lui est principalement relié à l'élancement de la poutre, ce qui est pleinement justifié par l'aspect macroscopique de cette instabilité. Afin de cerner plus globalement l'évolution des charges en fonction des nombreuses combinaisons de paramètres géométriques et matériaux, nous introduisons quatre coefficients adimensionnés qui

suffisent à exprimer les trois charges :

$$\begin{aligned} \rho_L &= \frac{L}{\pi h_a} \text{ (élancement)} & \rho_h &= \frac{h_p}{h_a} \text{ (rapport des épaisseurs)} \\ \rho_E &= \frac{E_a}{E_p} \text{ (rapport des modules)} & \rho_\nu &= \frac{G_a}{E_a} = \frac{1}{2(1+\nu_a)} \text{ (rapport des modules de l'âme)} \end{aligned} \tag{2.6}$$

En utilisant ces coefficients, les expressions des charges critiques se simplifient et s'écrivent :

$$\lambda_{AG}^{MU} = B\left[\frac{\rho_h}{\rho_L^2} + \left(\frac{6\rho_E}{\frac{\rho_h}{\rho_\nu} + \frac{\rho_h}{12\rho_L^2} + 2\rho_E\rho_L^2}\right)\left(\frac{1}{\rho_h} + \rho_h + 2\right)\right] \tag{2.7}$$

$$\lambda_{AL}^{MU} = B\left[12\left(\sqrt{2\rho_E\left(\frac{1}{\rho_h}+2\right)} - \frac{\rho_h}{\rho_\nu}\right)\right] \quad \text{si} \quad \frac{2{h_p}^3 E_p E_a}{{G_a}^2{h_a}^2(h_a+2h_p)} < 1 \tag{2.8}$$

$$\lambda_{SL}^{MU} = B\left[4\sqrt{6}\sqrt{\frac{\rho_E}{\rho_h}} + \frac{2\rho_E\rho_\nu}{\rho_h^2}\right] \tag{2.9}$$

Le coefficient B commun aux trois expressions précédentes (Eqs. 2.7, 2.8 et 2.9) est défini par $B = b\rho_h E_p h_p/6$, son signe est donc toujours positif.

Diagramme de sélection

En comparant les charges deux à deux, nous pouvons facilement dégager des « zones de prédominance » dans lesquelles chacune des instabilités apparaîtra pour la charge appliquée la plus faible. Ceci peut se mettre sous la forme d'outils graphiques de sélection des configurations de sandwichs vis-à-vis des instabilités locales ou globales (Léotoing *et al.*, 2002 c - Annexe 2.8). Parmi les quatres paramètres adimensionnés, le rapport des modules de l'âme peut être fixé, on montre que son influence est négligeable sur l'évolution des charges, et le rapport d'aspect peut également être fixé dans un premier temps. La différence des charges ne dépend plus que de deux paramètres libres, elle peut être tracée facilement à partir des expressions analytiques (Eqs. 2.7, 2.8 et 2.9) sur des graphiques $\rho_E - \rho_h$.

On montre que la charge de wrinkling symétrique est systématiquement plus faible que la charge de wrinkling antisymétrique. Un seul diagramme est donc utile pour isoler les configurations dans lesquelles sont susceptibles de se développer le flambage global ou le wrinkling qui est antisymétrique (Figure 2.14). Pour un élancement ρ_L donné, trois zones peuvent être isolées,

elles sont représentées sur la Figure 2.14. La première zone, **LOCAL**, correspond aux configurations sandwich pour lesquelles le phénomène de wrinkling antisymétrique va apparaître pour des charges inférieures à la charge critique de flambage global de la poutre. En revanche, dans la deuxième zone, **GLOBAL**, le mode de flambage global sera prépondérant devant le mode local. Une troisième zone est matérialisée sur ce diagramme ($\lambda_{AL}^{MU} \nexists$), elle correspond à la validité de la condition d'apparition du wrinkling antisymétrique (Eq. 2.8), phénomène qui n'est de toute façon pas critique à cet endroit. Grâce à ce diagramme, on vérifie bien que lorsque l'élancement augmente, les instabilités globales sont susceptibles d'apparaître pour les charges les plus faibles, ce qui confirme bien les résultats énoncés avec les calculs de sensibilité. Sans aucune considération d'ordre matériel, on peut affirmer que lorsque $\rho_L > 8$, la poutre sandwich soumise à des efforts de compression plane se comportera comme sa représentation homogène équivalente, *i.e.* aucune forme d'instabilité locale ne sera susceptible d'apparaître.

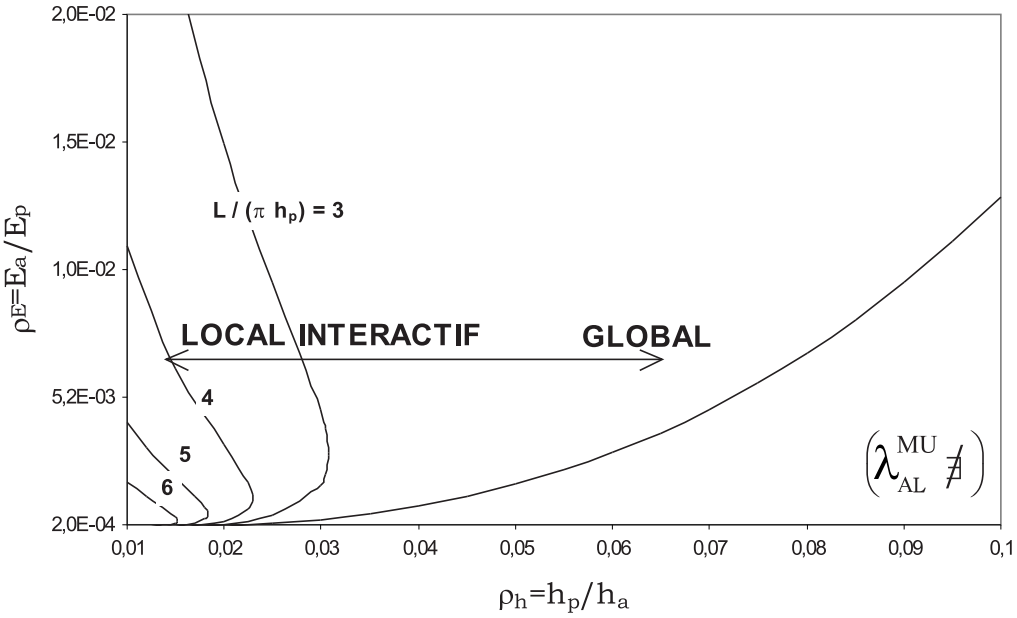

FIG. 2.14: Zones de prédominance pour la charge de wrinkling antisymétrique λ_{AL}^{MU} et la charge globale λ_{AG}^{MU}, en fonction de la valeur de l'élancement ρ_L.

Bilan des développements analytiques

L'intérêt de cette approche analytique est donc manifeste. Les charges critiques ainsi déterminées constituent des outils simples en terme d'évaluation du type d'instabilité susceptible de se développer pour une configuration de poutre sandwich donnée. L'introduction de rapports adimensionnés permet de simplifier l'écriture des charges critiques et de représenter graphiquement les zones de prédominance de chacune de ces instabilités. Ces diagrammes de conception sont très

simples d'utilisation, en calculant seulement l'élancement de la poutre et les rapports des épaisseurs et des modules, on est capable de prédire rapidement si le sandwich sera instable localement ou globalement. On note également qu'autour des lignes $\rho_L = C^{ste}$, la différence des charges est faible (**INTERACTIF**). Pour ces configurations, les charges locales et globale sont très proches, et on vérifie par ailleurs qu'elles sont maximales (Léotoing *et al.* 2002 a - Annexe 2.6). Ce sont donc des configurations optimales vis-à-vis du flambage, et classiquement [Byskov and Hutchinson, 1977] le flambage interactif se développera préférentiellement dans ces sandwichs.

Nous allons maintenant étendre cette étude de la résistance en compression des sandwichs à des approches plus complètes incluant des non-linéarités géométriques et matériaux. Pour mettre en place ces modèles, nous pourrons utiliser les résultats analytiques comme référence afin de construire un modèle numérique bien fondé, induisant des temps de calcul suffisamment faibles dans la perspective des calculs non-linéaires.

2.3.2 Stabilité et résistance en compression

Par souci d'efficacité, nous souhaitons utiliser un code de calcul commercial, en l'occurrence ABAQUS. Se pose alors le problème de la continuité des contraintes aux interfaces peaux/âme qui ne peut être assurée systématiquement par des éléments formulés en déplacement. Cette approximation doit donc être évaluée soigneusement. Il faut, de plus tenir compte des contraintes de taille des problèmes à traiter. Le détail de la mise en place de ces modèles éléments finis se trouve dans Léotoing *et al.*, 2002 b - Annexe 2.7 et Léotoing *et al.*, 2002 c - Annexe 2.8.

Pour mettre en place ces modèles, le premier point à traiter est l'introduction de charges et la prise en compte des conditions aux limites, qui du point de vue numérique, comme du point de vue expérimental d'ailleurs, peuvent induire des effets locaux dans ces zones critiques. Pour lever cette difficulté, nous avons reproduit une solution technologique qui consiste à rigidifier ces bords, ce qui se traduit dans nos calculs par une contrainte cinématique (*MPC) sur tous les nœuds du bord qui doivent rester alignés. Cette ligne pouvant se dilater et tourner autour d'un nœud de référence est utilisée pour appliquer les conditions aux limites cinématiques et statiques (Figure 2.15-a).

Pour la discrétisation, nous avons d'abord considéré une discrétisation bidimensionnelle de la poutre sandwich avec des éléments bilinéaires en contraintes planes. Des études de convergence ont montré que les charges critiques se stabilisent pour environ trois éléments dans l'épaisseur des peaux, ce qui correspond à des maillages allant de 40 000 à 200 000 ddls au total pour le modèle. Cette taille de maillage n'est pas acceptable pour conduire des calculs non-linéaires géométriques et matériaux. Nous avons donc recouru à une approche similaire à la superposition d'éléments utilisée avec les NCFs (Drapier & Wisnom, 1999 a et b - Annexes 2.4 et 2.5), qui consiste ici à discrétiser les peaux avec des éléments de poutre linéaires de Timoshenko et l'âme avec des éléments bilinéaires en contraintes planes. Ces éléments utilisant les mêmes degrés de libertés, quelques précautions doivent être prises afin qu'un élément de poutre ne puisse pas flamber sur

l'élément 2D car les rotations sont libres dans la poutre. Cette condition fixe la taille maximale des éléments de poutre, la taille minimale est quant à elle imposée par la nécessité de représenter correctement les modes locaux, en imposant par exemple au minimum 4 éléments de poutre par onde. Connaissant les longueurs d'onde établies analytiquement (Léotoing *et al.*, 2002 a - Annexe 2.6), le maillage final est construit, sa taille comprise entre 2 000 et 10 000 *ddl*s est réduite par 20 par rapport à la discrétisation complète.

Les calculs de valeurs propres (Figure 2.15) menés sur plusieurs configurations de sandwichs ont montré que les résultats fournis par les deux modèles éléments finis étaient en bon accord avec les résultats analytiques, tant du point de vue des charges que des longueurs d'onde (Léotoing *et al.*, 2002 c - Annexe 2.8). De plus, des comparaisons énergétiques ont permis de montrer clairement que le maillage simplifié non-conforme possède un état de contraintes très proche de celui du modèle complet, ce qui est une assurance pour de futurs calculs incluant la plasticité. La principale différence entre les calculs numériques et analytiques peut être attribuée à la distribution des contraintes de cisaillement qui est linéaire dans l'épaisseur pour le modèle analytique, tandis que cette répartition est parabolique dans le calcul par éléments finis complet. Ceci confirme notre précédente remarque sur la nécessité d'une cinématique d'ordre supérieur dans l'âme.

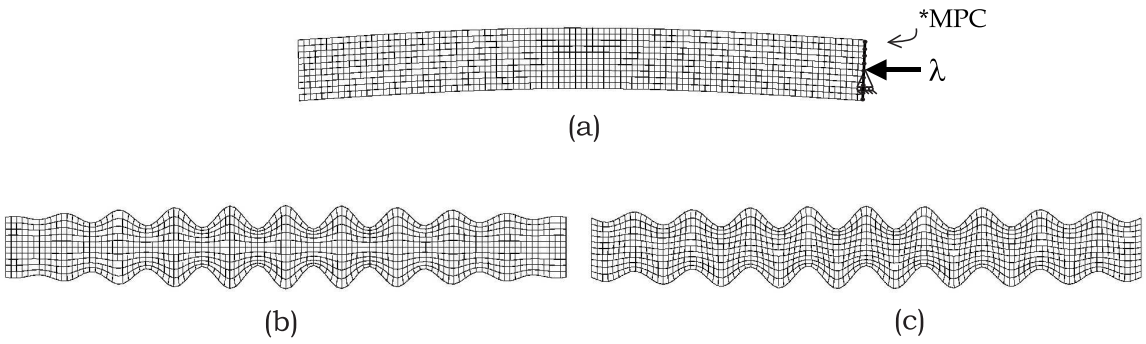

FIG. 2.15: Modes propres établis avec le modèle par éléments finis simplifié : (a) flambage global, (b) wrinkling symétrique des peaux, (c) et wrinkling antisymétrique des peaux.

Post-flambage élastique

Le modèle numérique étant validé sur des calculs de valeurs propres, nous pouvons mener des simulations plus complètes incluant les non-linéarités géométriques et matériau (Léotoing *et al.*, 2002 b - Annexe 2.7). Pour traiter ces problèmes par éléments finis, nous utilisons un pilotage à longueur d'arc permettant de passer les points de rebroussement et les points limites.

En premier lieu, nous pouvons, grâce au diagramme de sélection (Figure 2.14), choisir des configurations types telles que les instabilités locales, globale et le flambage interactif puissent être caractérisés. Pour cela, partant de la configuration dont les caractéristiques sont données dans le Tableau 2.1-b, nous considérons une épaisseur des peaux de 1, 1,5 et 2,5 *mm*, conformément à la

représentation schématique de la Figure 2.14. Avant de déterminer la réponse de ces configurations, il reste à préciser le type d'imperfection géométrique que nous introduisons. Ces imperfections nous permettent d'abord de régulariser le problème de flambage, mais surtout, leur rôle sur la stabilité est primordial.

Pour de très faibles amplitudes des imperfections prises sur le mode critique (< 0,2% de l'épaisseur totale), les configurations LOCAL et GLOBAL présentent des réponses sur-critiques en fonction du chargement, caractérisées par une première partie linéaire liée à l'état fondamental, suivie par un point de bifurcation correspondant à une amplification du mode avec la charge. Notons que ces modes obtenus pour des imperfections de faibles amplitudes correspondent bien aux modes attendus, ce qui confirme la validité du diagramme de sélection proposé. Lorsque l'amplitude de l'imperfection initiale est augmentée, la charge de flambage diminue, et la réponse post-flambée reste stable. Par contre, la réponse post-bifurquée est instable si la longueur d'onde du défaut n'est pas du même ordre de grandeur que la longueur d'onde du mode critique, *i.e.* un défaut global dans la configuration LOCAL et inversement.

Au contraire des réponses précédentes, pour la configuration INTERACTIF optimale vis-à-vis du flambage, on observe comme attendu une réponse plus complexe qui se décompose en trois parties (Figure 2.16). Pour un défaut trés faible, le début de la réponse est classique pour une poutre homogène par exemple, avec un état fondamental suivi d'un premier point de bifurcation correspondant à l'amplification du mode global. Ensuite, quasiment à charge constante, une bifurcation secondaire caractérise l'apparition d'un mode local dans l'intrados de la courbure induite par la première instabilité globale. La seconde branche est sous-critique, et on assiste au développement de localisations géométriques. Ce phénomène de flambage interactif est évidemment influencé par l'amplitude de l'imperfection initiale prise sur le mode global. Dans ce cas, la réponse tend à s'éloigner de la réponse fondamentale, et la bifurcation secondaire apparaît à l'intersection entre la branche primaire et la branche secondaire qui reste inchangée (Figure 2.16).

En fait, l'apparition de la seconde bifurcation est presque indépendante de la première, elle correspond à l'apparition de wrinkling lorsque la contrainte normale induite dans l'intrados dépasse la charge limite de wrinkling. Ce type de réponse peut donc être attendu dans les poutres courbes, sans toutefois l'effet de la précontrainte dont l'intensité est égale à la charge critique globale qu'il est nécessaire de dépasser ici pour obtenir la courbure. Dans [Léotoing, 2001], nous avons proposé un modèle analytique capable de rendre compte du flambage interactif, en présence d'un défaut global. Ce modèle s'appuie sur l'analyse, à l'aide de notre modèle unifié, de la redistribution des efforts dans les deux peaux du sandwich pendant le post-flambage global. La stabilité de la seconde branche est recherchée par une méthode de perturbation appliquée à une poutre sur fondation caractérisant la peau dans l'intrados de la courbure globale, la raideur de la fondation étant également issue de notre modèle (Léotoing *et al.*, 2002 a - Annexe 2.6). Les résultats analytiques et numériques sont en excellent accord.

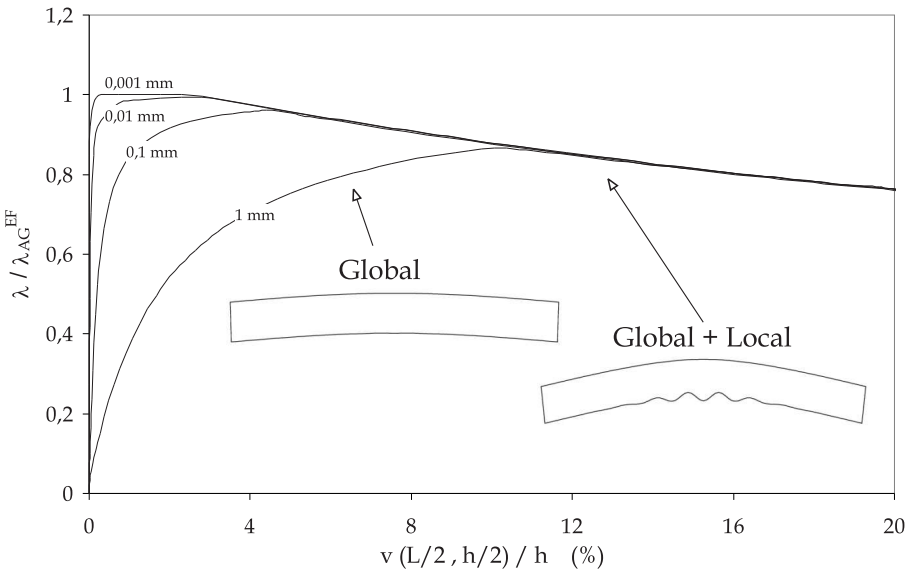

FIG. 2.16: Évolution du chargement en fonction de la flèche au centre de la poutre sandwich possédant un défaut initial sur le mode global : flambage interactif .

De manière générale, on constate que la perte de rigidité de la poutre sandwich est très souvent associée à l'apparition d'une forme de flambage interactif. La stabilité est liée principalement à la 'symétrie' que la déformée peut conserver. Quand les modes se développent de la même façon sur les deux peaux, le comportement est sur-critique. En revanche, l'apparition de localisations géométriques entraîne une dissymétrie qui conduit rapidement à un comportement sous-critique. Compte-tenu du caractère prépondérant de ces localisations géométriques, il est légitime d'introduire dans ces calculs un comportement non-linéaire matériau pour l'âme qui supporte les localisations géométriques dans les peaux.

Post-flambage plastique

Pour représenter le comportement non-linéaire matériau de l'âme, nous choisissons de la modéliser comme une mousse Divinicell H130 dont les propriétés sont disponibles dans la littérature. Le comportement est approché par une loi élastique parfaitement plastique. Les réponses élastoplastiques montrent que pour nos sandwichs on observe le résultat classique de l'introduction d'une loi de comportement non-linéaire dans un problème instable géométriquement (*cf* Figure 2.3). Les réponses deviennent systématiquement sous-critiques, indépendamment de l'amplitude et de la forme des imperfections dont l'effet vient se superposer à la réduction de charge limite induite par l'apparition de l'instabilité plastique. Comme on peut le voir sur la Figure 2.17, l'apparition de cette bifurcation plastique fortement sous-critique correspond à la résistance du sandwich mesurable expérimentalement.

Il est intéressant de noter que le phénomène observé sur cette Figure 2.17 correspond à un mode

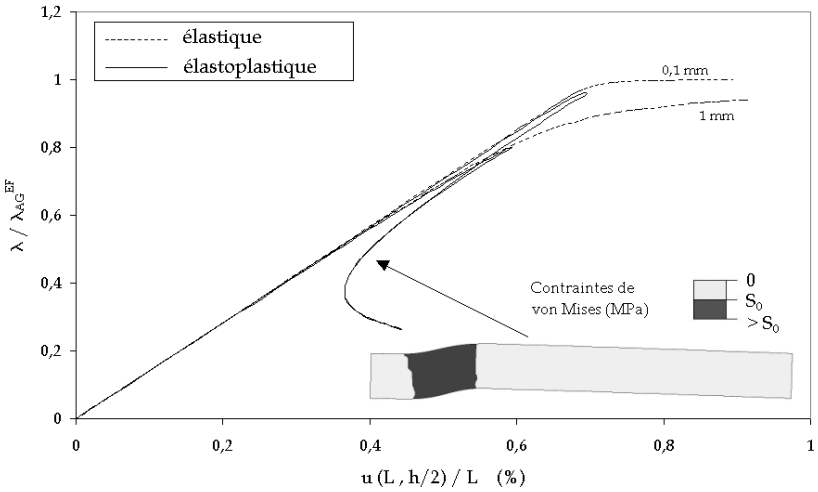

FIG. 2.17: Charge appliquée en fonction du raccourcissement global avec une loi élastoplastique dans l'âme : configuration GLOBAL et défaut sur le mode critique.

de rupture très répandu appelé *shear crimping* (Figure 2.12-b), soit rupture par cisaillement-pliage de l'âme. On vérifie grâce à nos calculs que ce mode de rupture n'est en fait que la conséquence observable de la rupture survenant après l'apparition de la bifurcation plastique dans un sandwich élancé possédant un défaut géométrique initial à l'échelle de la structure. Cette rupture survient à la suite de la localisation des déformations plastiques comme on peut le vérifier sur cette Figure 2.17. Pourtant, le critère de dimensionnement correspondant à ce mode de rupture est habituellement formulé à partir de données purement 'locales', c'est en fait la rigidité de cisaillement de la poutre, qui ne peut donc pas tenir compte de la réponse du matériau non-linéaire, ni de l'influence des défauts.

2.3.3 Conclusions et perspectives

Nous avons développé un modèle analytique unifié capable de rendre compte de l'apparition des instabilités aux échelles globales et locales dans les poutres sandwichs. Les charges critiques ont été établies rigoureusement, sans hypothèses supplémentaires, et leur limites de validité sont parfaitement maîtrisées. La richesse de ces solutions nous a permis dans un premier temps de mettre en place des diagrammes de sélection des configurations de sandwich par rapport aux instabilités globales et locales, mais aussi interactif. Ensuite, un modèle éléments finis simplifié a été mis en place et validé par comparaisons des modes et charges critiques avec les résultats analytiques, et les calculs d'un autre modèle éléments finis plus raffiné.

Les coûts de calculs très réduits nous ont permis de caractériser les réponses de post-flambage élastiques des diverses configurations de sandwichs affectées par des défauts géométriques de différente nature. Le flambage interactif a également été observé, il est caractérisé par un compor-

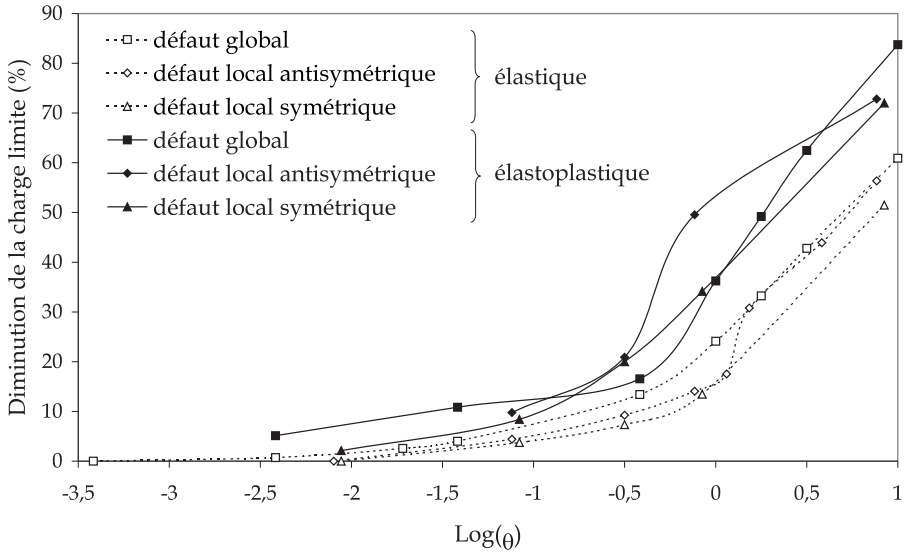

FIG. 2.18: Diminution de la charge limite par rapport à la charge critique de la poutre sandwich INTERACTIF, suivant le type et la taille du défaut (représenté par l'angle maximum par rapport à l'axe de la poutre) pour une âme élastique et élastoplastique.

tement post-bifurqué dont le caractère sous-critique provient du développement de localisations géométriques. Enfin, l'introduction d'une loi de comportement non-linéaire nous a permis de vérifier que l'apparition d'une instabilité géométrique s'accompagnait de la localisation de déformations plastiques, résultant en une réponse post-bifurquée fortement sous-critique, caractérisant par conséquent la résistance du sandwich. Une extension de ces calculs aux panneaux et aux poutres sandwich à peaux composites équilibrées a été brièvement introduite dans [Léotoing, 2001].

Pour conclure, nous pouvons évaluer, pour la configuration INTERACTIF, les diminutions de charge limite dues à la non-linéarité matériau et à la présence de défauts (Figure 2.18). On constate que les pertes de charge sont très comparables pour les trois types de défaut, mais qu'en moyenne, cette perte de charge est deux fois plus grande lorsque la loi de comportement élastoplastique parfaite est considérée dans l'âme. Enfin, on notera la somme importante de calculs nécessaires pour évaluer ces pertes de charges. Les temps de calcul mis en jeux justifient à eux seuls l'utilisation des diagrammes de sélection pour extraire les configurations optimisées en première approximation. Ensuite, les calculs de résistance des poutres peuvent être menés avec le modèle éléments finis simplifié. À moyen terme, l'introduction de peaux en composites dans cette approche étendue aux panneaux sandwichs devrait ouvrir la voie à une perspective élargie de dimensionnement puis d'optimisation multi-échelle des structures sandwichs. Ces perspectives sont décrites ci-dessous.

2.4 Perspectives du thème 'Instabilités et effets d'échelle dans les composites et les sandwichs'

La problématique de la résistance en compression des sandwichs que nous venons d'aborder rejoint sous de nombreux aspects la résistance en compression des composites à fibres longues. Outre les aspects techniques de mise en œuvre de modèles raffinés permettant de prendre en compte des paramètres à plusieurs échelles, la façon dont ont été traités ces comportements révèle des problèmes plus fondamentaux. En effet, ce qui était pendant longtemps considéré comme des propriétés matériaux se révèle être le résultat de l'interaction de mécanismes complexes à plusieurs échelles d'observation. C'est seulement la mise au point, en parallèle, de modèles et de moyens de caractérisation appropriés qui a permis de mieux cerner ces phénomènes, et donc de favoriser une utilisation plus rationnelle de ces matériaux.

On comprend bien qu'aborder la résistance en compression de ces structures hétérogènes comme elle peut l'être pour des matériaux macroscopiquement homogènes revêt un intérêt pratique certain. Lors de la conception, il est en effet plus commode de disposer de critères simples de dimensionnement, au risque de devoir sous-estimer les résistances réelles par des coefficients de sécurité élevés, intégrant le manque de connaissance des mécanismes mais aussi les incertitudes liées à l'identification. Le risque de surdimensionner les structures est indéniable, mais cela peut être encore plus pénalisant, voire constituer un point de blocage, par exemple pour des structures conçues en vue de subir de grandes déformations élastiques dans leur fonctionnement. Il faut donc mettre en place des approches spécifiques d'une part pour la conception, et d'autre part pour l'identification des résistances en compression.

Avec l'évolution des puissances de calcul actuelles, on peut envisager de mettre en place à moyen terme une approche multi-échelle qui permettra, partant des paramètres matériels et géométriques à l'échelle des constituants fibre/matrice, d'optimiser les structures sandwichs avec peaux composites sur la base de critères en résistance autant qu'en rigidité (Figure 2.19). Ces simulations ne peuvent être réalisées à n'importe quel coût, elles doivent donc être basées sur des formulations spécifiques du type de celles mises en place ici. Il faut prévoir d'abord de combiner les modèles de microflambage plastique et de sandwich présentés dans ce mémoire. Cette approche peut-être réalisée en premier lieu dans un cadre très simple de poutres sandwichs à peaux composites à base de plis croisés. À plus long terme, cette approche devrait être étendue aux panneaux, dont les premiers calculs avec le modèle EF simplifié confirment la faisabilité. En parallèle, l'approche structurelle du microflambage plastique devra être étendue au 3D, certainement en recourant à une approche non-conforme à base d'éléments finis standards de type solides et poutres. Dans ce cas la caractérisation tridimensionnelle du défaut sera un des paramètres essentiels de l'approche. Lorsque ce modèle de microflambage plastique 3D sera mis en place et couplé avec les modèles de panneaux sandwichs, il faudra ensuite penser aux coques, format de structure particulièrement répandu pour

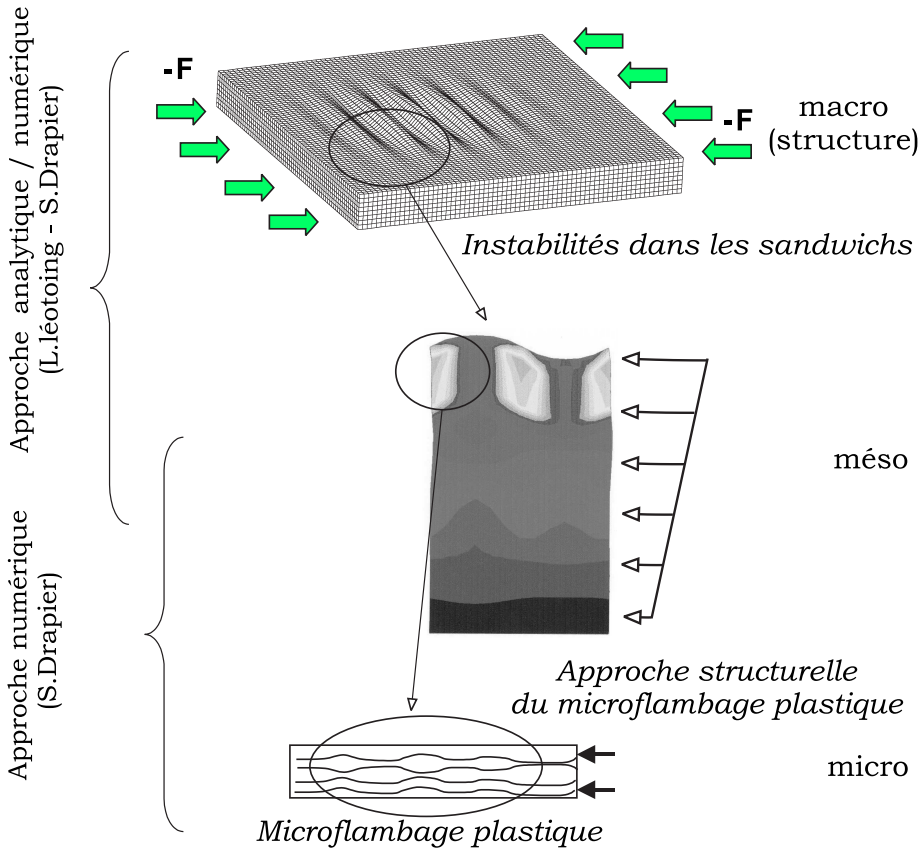

FIG. 2.19: Représentation schématique de la modélisation multi-échelle dans les sandwichs à peaux composites.

les sandwichs. Il semble probable que pour les coques, les calculs devenant trop lourds à mettre en œuvre dans le cadre de la conception, on recourt à des simulations en deux temps où les résistances de séquences d'empilement données sont calculées en fonction du gradient de chargement, et sont ensuite utilisées comme 'critère' de résistance locale dans les calculs non-linéaires géométriques et matériaux des structures sandwichs.

Bien évidemment, cette approche doit être réalisée en parallèle avec des essais adaptés. Notamment, l'utilisation d'essais de flambage rotulé est essentielle pour caractériser la résistance en fonction des paramètres structuraux. Il faut en premier lieu mettre en œure des essais sur sandwichs à peaux isotropes, d'abord pour des poutres puis pour des panneaux. Pour cela, les modèles numériques non-conformes de sandwich pourront être utilisés pour dimensionner les essais, et notamment pour étudier les conditions de frontière. Ces zones où sont introduites les charges et où les conditions aux limite sont imposées sont excessivement sensibles dans les sandwichs. Ensuite, des sandwichs à peaux composites seront considérés, tandis que les composites seront également caractérisés séparément. Dans ces essais, l'apport des méthodes de mesure de champ cinématique pourrait être riche, en nous permettant de cerner plus précisément les phénomènes locaux, rencontrés notamment aux points d'application des efforts et des conditions aux limites, mais aussi au

niveau des interfaces peaux-âme par exemple.

Au final, on peut penser que dans cette approche globale, seule pourrait subsister la caractérisation du défaut d'alignement des fibres dans les plis UDs. Ce problème pourrait toutefois devenir moins essentiel, puisque les semi-produits tels que les *NCF*s utilisés de plus en plus largement, sont surtout sensibles aux défaut à l'échelle des nappes. Toutefois cette utilisation croissante ne peut être soutenue que si les procédés accompagnant ces semi-produits sont parfaitement maîtrisés, et donc optimisés. Je débute actuellement la modélisation d'un de ces procédés de mise en œuvre. Ce projet de recherche est présenté dans la partie suivante de ce mémoire où sont exposées mes activités de recherche les plus récentes, liées aux procédés en général.

- 3 -

Thème émergent - Procédés et problèmes connexes

Cette seconde partie du mémoire aborde le thème des procédés à travers deux projets de recherche, qui traitent pour une part de la simulation d'un procédé d'élaboration par voie liquide de composites organiques, et d'autre part de l'étude de tricots élastomériques utilisés en grandes déformations pour générer des pressions de contention dans le domaine du bio-médical. Dans la thématique des procédés, ces projets sont complémentaires en ce sens que la modélisation thermique et physico-chimique est abordée dans le premier, tandis que dans le second le traitement des grandes déformations et des problèmes de contact est nécessaire. Ces projets de recherche reçoivent un soutien fort d'industriels de la région Rhône-Alpes, et deux thèses ont débuté respectivement en octobre 2000 et en octobre 2001 dans le cadre de ces projets. Il n'y a donc à ce jour que très peu de communications sur les premiers résultats des recherches. En conséquence, une attention particulière est portée dans ce document à la mise en lumière des problématiques et aux programmes de recherches mis en place. Comme dans l'ensemble des travaux de recherche présentés précédemment, la complémentarité simulation / caractérisation est ici un point clef.

Comme il a été rappelé à travers ce document, la modélisation des procédés d'élaboration répond au besoin de mieux comprendre les phénomènes mis en jeu lors de la fabrication. Dans le cas des procédés par voie liquide, l'un des objectifs est de mieux mesurer l'influence des divers paramètres d'élaboration sur l'imprégnation, dont dépendent les propriétés mécaniques du matériau final, mais qui conditionne également les temps des cycles. La spécificité de la modélisation des procédés pour les composites organiques est la nécessité de mettre en œuvre des connaissances de domaines aussi variés que la mécanique des fluides et des solides, la thermique, et la physico-chimie des polymères. Dans le procédé qui nous intéresse, appelé *RFI*, la modélisation complète nécessite de traiter de manière couplée des problèmes thermo-mécaniques et physico-chimiques

dans un domaine à frontière mobile, frontière évoluant pendant l'imprégnation des nappes sèches. Avant de mettre en place cette modélisation, il nous a fallu caractériser la perméabilité transverse qui conditionne très fortement la qualité et les temps d'imprégnation.

Pour le second projet de recherche, la modélisation des tricots élastomériques en grandes déformations, la problématique diffère. Ces tricots élastomériques sont utilisés pour la contention du système veino-lymphatique chez l'homme. L'étude que nous mettons en place actuellement a pour but de prévoir les distributions de pressions générées par les articles de contention, à partir de profils de membre et connaissant la réponse des tricots. Ceci pour palier aux problèmes de mesure *in-vivo* des faibles pressions induites par ces articles. Cette étude nous donne l'opportunité d'appliquer des outils de la mécanique des milieux déformables à ces matériaux du monde bio-médical, où tant du côté des concepteurs que des prescripteurs l'empirisme pré-domine. Dans le cadre de ces recherches coopératives, l'apport de la modélisation promet de soutenir des avancées considérables en terme de développement et d'utilisation de ces produits. Actuellement, les tricots en général sont étudiés essentiellement dans les renforts pour composites, mais très peu de travaux de recherche ont porté sur l'étude de ces tricots élastomériques dont l'utilisation entraîne des élongations de 80 à 130 %. Un programme de recherche spécifique a donc été mis en place, d'abord pour identifier la réponse des tricots en grandes déformations puis pour prendre en compte ce comportement dans des simulations par éléments finis.

3.1 Modélisation des procédés d'élaboration par voie liquide des composites organiques

Comme nous l'avons indiqué dans la partie 2.2 de ce mémoire, les procédés par voie liquide, plus particulièrement abordés ici, peuvent permettre de réaliser à moindre coût des structures composites épaisses tout en assurant de bonnes qualités de fabrication qui sont le gage de propriétés mécaniques optimales. Dans ces procédés, sous l'action d'une pression extérieure et du tirage du vide, la résine imprègne des préformes fibreuses sèches placées dans un moule rigide ou semi-rigide. Ensuite un cycle de température et de pression spécifique est appliqué à la structure pour amener la résine dans son état réticulé. Le plus répandu de ces procédés est le Resin Transfer Molding (*RTM*) dans lequel la résine est injectée à travers des orifices d'injection dans un moule fermé rigide. De nombreux travaux ont été, et sont encore, consacrés à l'étude de ce procédé, notamment concernant l'optimisation du placement des trous d'injection et des évents dans les moules. Plus récemment, le procédé dit Resin Film Infusion a été développé pour palier à ces problèmes d'injection. En effet dans le RFI l'imprégnation, ou plutôt l'infusion, des préformes est réalisée sur une large surface sous l'effet de la faible pression induite par le déplacement d'une partie mobile du moule. Cette particularité assure de très bonnes propriétés mécaniques finales résultant de l'excellente homogénéité de l'imprégnation réalisée. Par contre cette technologie en-

traîne également que l'épaisseur finale de la pièce à réaliser, et donc la fraction volumique de fibres dont dépendent très fortement les propriétés mécaniques finales, sont fonctions du jeu de paramètres pression-température appliqué. L'objectif de cette modélisation est donc de décrire, pour ensuite optimiser, ces conditions de fabrication en vue de maîtriser les propriétés mécaniques finales.

Nous avons débuté récemment, en collaboration étroite avec la société Hexcel Fabrics, la simulation du procédé *RFI* utilisé pour de nouveaux renforts multiaxiaux pour composites structuraux appelés *NC*2 (Non Crimp New Concept (*NC*2). Les *NC*2 diffèrent des *NCF*s par une très bonne homogénéité de leur mésostructure obtenue en utilisant des nappes homogènes au lieu de mèches placées côte-à-côte (Figure 2.8 page 20). Cette collaboration entre dans le cadre d'un programme régional thématique prioritaire 2000-2002 intitulé '*Optimisation du procédé de transformation de nouveaux renforts multiaxiaux pour composites structuraux*' dont je suis co-responsable avec A. Vautrin. Des laboratoires universitaires de l'université Claude Bernard de Lyon (L2M) et de l'université Jean Monnet de Saint-Étienne (LTSI) sont également nos partenaires dans ce projet. Outre les échanges scientifiques avec nos partenaires, le cadre de ce programme nous permet d'accéder aux nombreuses données matériaux (thermiques, mécaniques, physico-chimiques) nécessaires pour les simulations, caractérisant à la fois la résine, les renforts, et les multiaxiaux. Dans le procédé *RFI*, il faut en plus de ces paramètres caractériser la perméabilité transverse, paramètre essentiel qui contrôle l'imprégnation de la résine dans les préformes et donc les propriétés finales et les temps de cycles.

3.1.1 Mesure de la perméabilité transverse

Les paramètres matériaux nécessaires à la modélisation du *RFI* sont identifiés par Hexcel Fabrics, partenaire industriel de ce projet régional : viscosité en fonction de la température et du degré de réticulation, taux de réticulation en fonction de la température et du temps, coefficients de conductivité thermique des constituants. Par contre, la caractérisation de la perméabilité transverse a été menée au département Mécanique et Matériaux, d'abord dans le DEA d'Alexandre Pagot en 1999/2000 (Drapier *et al.*, 2002 - Annexe 2.10). Dans ce travail, un montage de mesure spécifique a été développé. Grâce à ce montage, on mesure la perte de charge induite lors du passage d'un fluide à travers l'épaisseur des matériaux, et on en déduit la perméabilité transverse par la relation de Darcy en 1D. Une des difficultés de ces mesures est que nous n'avons pas d'idée précise sur les vitesses que le fluide atteint dans le procédé réel puisque tout se passe sous presse. Nous avons donc pris le parti de tester une gamme assez large de vitesses.

Ce montage a permis de montrer, sur des *NC*2 biaxiaux, que ni la séquence d'empilement, ni le type de couture n'ont d'influence notable sur cette perméabilité. Des simulations par éléments finis ont permis de confirmer que c'est essentiellement la densité des points de couture qui a une influence significative sur la perméabilité transverse. Plus précisément, c'est la surface libérée par

les trous de couture qui permet au fluide de s'écouler. Ces trous agissent comme des porosités ouvertes dans le sens de l'écoulement. On peut également noter que la perméabilité des nappes seules, dont l'homogénéité assure d'excellentes propriétés mécaniques finales, est de l'ordre de 10^{-14} m^2 pour les nappes de carbone, soit environ 100 fois inférieures aux perméabilités longitudinales de plis UDs plus classiques. Au final les coutures transverses, qui sont essentiellement introduites pour utiliser des nappes de grammage élevé, ou pour une amélioration des propriétés mécaniques transverses, permettent d'atteindre des perméabilités de l'ordre de 10^{-13} m^2, plus propices à réaliser une imprégnation de bonne qualité et à réduire les temps de cycle (Drapier *et al.*, 2002 - Annexe 2.10).

Depuis octobre 2000, la thèse d'Othmane Elbouazaoui a débuté sur le thème de la caractérisation de la perméabilité transverse et de la modélisation du *RFI*. Dans ce travail, des mesures de perméabilité supplémentaires ont été réalisées pour divers types de *NC2*. La difficulté de l'approche concerne la variabilité des mesures effectuées sur trois grandes familles de matériaux qui se différencient par le type de fibres, les séquences d'empilement, et la couture utilisés. Il ne semble pas possible de déterminer, pour ces matériaux, un rapport direct entre la surface libérée par les trous de couture, estimée à l'aide d'appareils de microscopie par transmission, et la perméabilité transverse. Ces matériaux possèdent en effet des perméabilités différentes, bien que les surfaces de trous, avant et après la mesure de perméabilité, soient voisines. De plus, on a mis en évidence que la résistance à l'écoulement, et donc la perméabilité, notée K_{33}, n'est pas la même selon la face subissant la traversée du fluide (Figure 3.20). Nous menons actuellement des essais complémentaires pour tenter d'apporter une explication satisfaisante à ce phénomène.

On note que la densité de couture apparaît ici comme un nouveau paramètre de contrôle dans le procédé d'élaboration. Il ne faut toutefois pas négliger ses répercussions sur la modification de la mésostructure, et donc, comme nous l'avons vu dans le cas des *NCF*s, sur les comportements critiques.

3.1.2 Simulation

La difficulté de la simulation du procédé est l'aspect multi-physique du problème. Généralement, un des aspects seulement des procédés est abordé, par des spécialistes du domaine concerné. Comme dans les autres procédés en général, la pression (notée P) et la température (notée T) sont à la fois les paramètres physiques de contrôle mais également les grandeurs physiques (variables d'état) dont va dépendre la simulation. À ces deux grandeurs, on peut associer deux types de modélisation, qui dans un premier temps peuvent être considérées séparément : modèle thermo-mécanique de remplissage et modèle thermo-physico-chimique de réticulation. Quelques exemples existent dans la littérature pour chacun de ces modèles. Par exemple pour le remplissage, une première solution a été proposée récemment par [Joshi et al., 1999]. Et pour la réticulation [Blest et al., 1999] ont proposé une approche unidimensionnelle raffinée des phénomènes thermo-

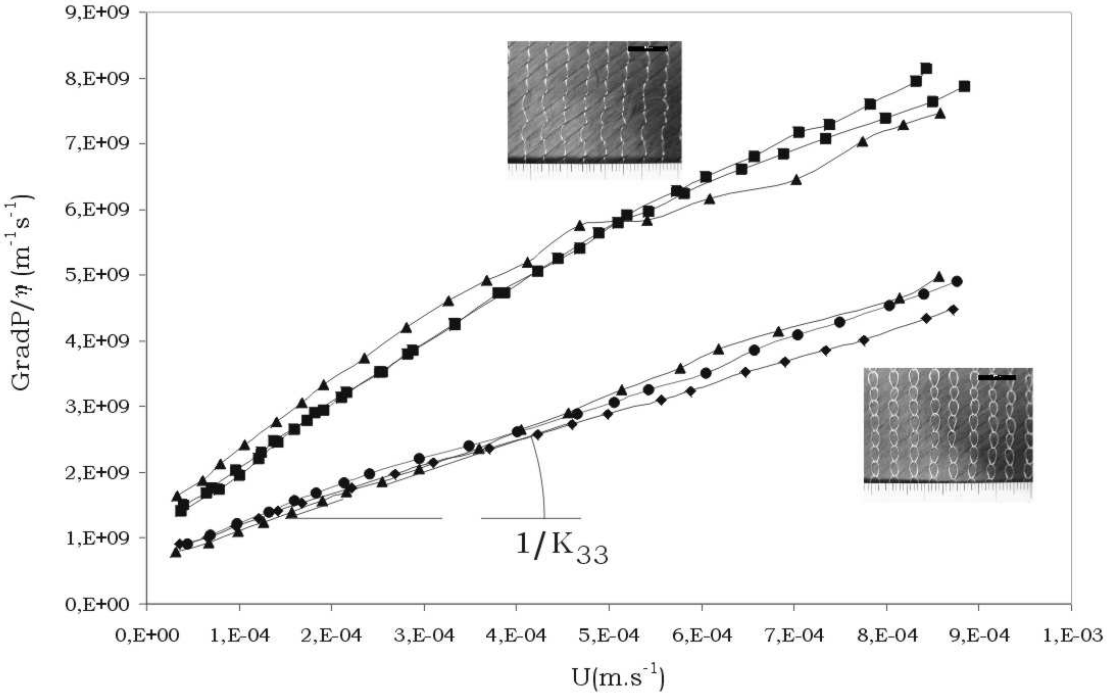

FIG. 3.20: Courbes de résistance à l'écoulement pour un matériau biaxiale *NC*2 [0,90] 2 $\times 215 g/m^2$, coutures 5x5.

physico-chimiques. Le lien entre ces deux modèles, pour des vitesses du fluide supposées faibles, provient de l'évolution de la viscosité de la résine, fonction du taux de réticulation atteint et de la température.

Récemment, O. Elbouazzaoui a mis en place une simulation par différences finies en 1D de la partie thermo-physico-chimique de la réaction de réticulation. L'équation de la chaleur pour le composite est modifiée pour intégrer le terme source prenant en compte l'exothermie de la réticulation de la résine. Elle s'écrit en 1D, dans la direcion **x** :

$$\frac{\partial T}{\partial t} = K_h \frac{\partial^2 T}{\partial x^2} + (1-f)\frac{H_R}{C_h}\frac{\partial \alpha}{\partial t} \tag{3.10}$$

où K_h est la diffusivité thermique du composite, H_R est la chaleur de réaction de la résine, et C_h est la capacité de chaleur spécifique du composite. L'évolution du degré de réticulation de la résine, noté α, est une fonction de la réticulation atteinte et de la température, qui s'écrit pour la résine Hercules 3501-6 considérée [Blest et al., 1999] :

$$\frac{\partial \alpha}{\partial t} = \begin{cases} (a_1 + a_2\alpha)(1-\alpha)(0,47-\alpha), & \text{si } \alpha \leq 0,3 \\ \\ a_3(1-\alpha), & \text{si } \alpha > 0,3 \end{cases} \tag{3.11}$$

où les différents coefficients a_i ($i = 1, \ldots, 3$) sont dépendants de la température et s'expriment de la façon suivante :

$$a_i(T) = A_i \exp\left(-\frac{\Delta E_i}{R\,T}\right)$$

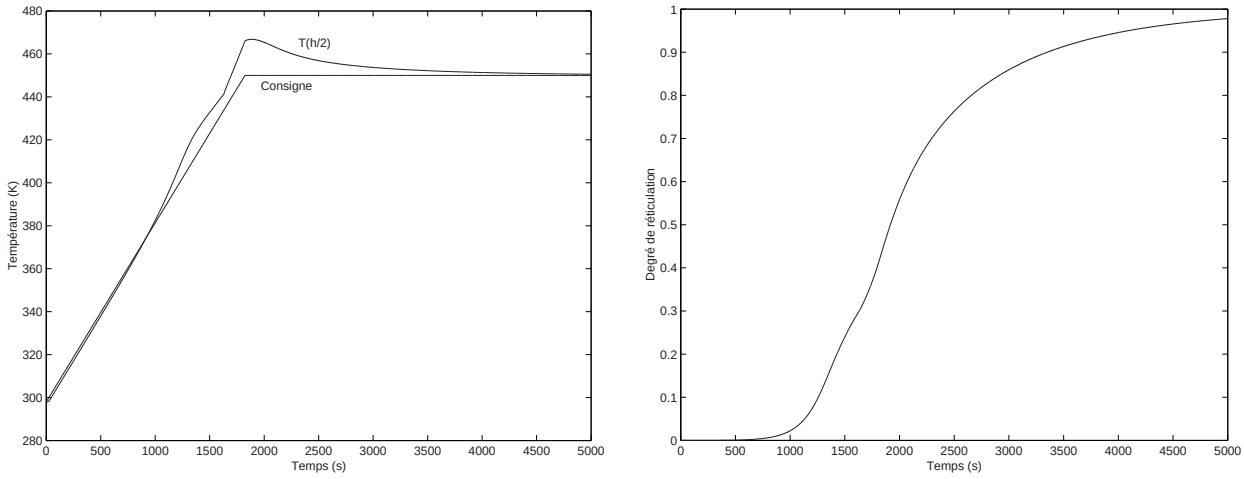

(a) (b)

FIG. 3.21: Simulation de la réticulation au cours du temps : (a) évolution de la température au centre du composite et consigne donnée par le cycle au bord du composite (b) évolution du degrés de réticulation au centre du composite.

avec les A_i des termes pré-exponnentiels, ΔE_i l'énergie d'activation et R la constante des gaz parfaits.

La résolution simultanée de ces deux équations conduit à un problème non-linéaire couplé par la réticulation de la résine. Ce système est discrétisé par différences finies centrées en temps et en espace, et le problème linéarisé est résolu avec un schéma itératif de Newton qui permet d'obtenir une convergence rapide de la solution. Afin de valider cette approche, nous avons repris les données matériaux utilisées par [Blest et al., 1999]. Nous simulons la réticulation dans un composite de 80*mm* d'épaisseur, représentant les applications visées par le *RFI*. Les conditions aux limites du composite sont en température imposée, égale à celle de l'autoclave fixée par le cycle de cuisson, soit une chauffe à 5K/min en partant de 300K jusqu'à atteindre 450K (soit pendant 1800s) et ensuite maintient de la température à 450K. La température initiale est homogène dans toute l'épaisseur du matériau et le taux de réticulation initial vaut 0. Les résultats obtenus pour la distribution de température (Figure 3.21-a) et le taux de conversion (Figure 3.21-b) pendant le cycle, sur des matériaux témoins extraits de la littérature, valident cette approche.

Cette modélisation a également été abordée dans le DEA de Bénédicte Régis en 2000/2001 qui s'est déroulé chez Bristish Aerospace (Filton, GB) et a porté pour la plus grande partie sur les tolérances dimensionnelles des assemblages de structures primaires et secondaires en composite. Les résultats sont confidentiels, mais on peut indiquer que le point délicat de ces assemblages concerne les pièces élaborées par *RFI*. Ceci ne fait que renforcer notre souhait de mieux comprendre ce procédé, dans lequel rappelons-le, les dimensions finales dépendent étroitement des paramètres d'élaboration. Notamment, l'application de la température et de la pression jouent un grand rôle puisque la viscosité évolue fortement dans les premiers temps du cycle. Si la viscosité est trop

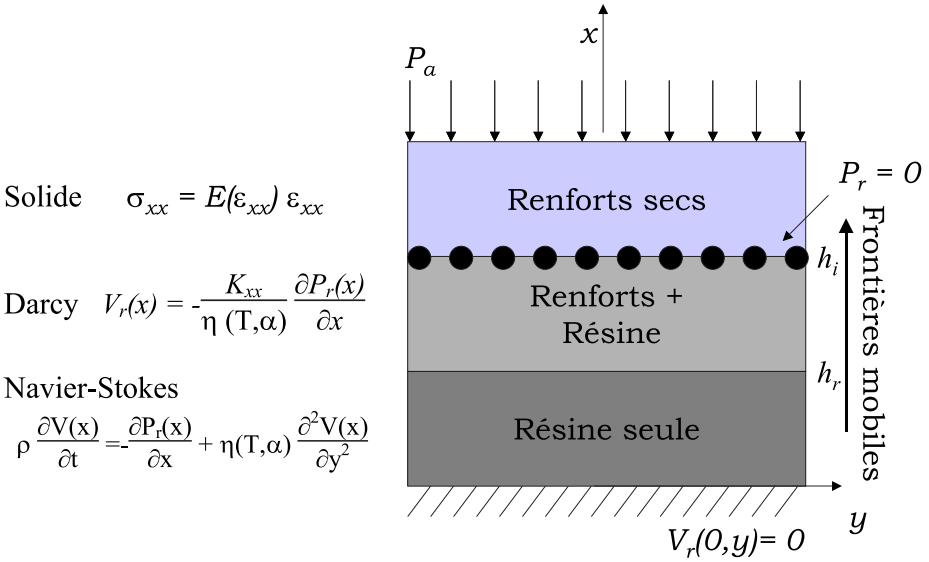

FIG. 3.22: Représentation schématique du problème de remplissage et équations 1D associées.

faible la résine sera chassée en excès, tandis que si la viscosité de la résine est trop élevée, l'imprégnation ne pourra se réaliser de façon homogène et des bulles d'air pourront être emprisonnées. La conséquence directe est un changement de l'architecture mésoscopique, qui se traduit par une modification du comportement mécanique.

3.1.3 Perspectives

La modélisation de la réticulation unidimensionnelle est validée, il faut maintenant mettre en place le modèle de remplissage qui fait intervenir le couplage de modèles de milieux solides, milieux poreux saturés, et fluide (Figure 3.22). Pour ces modèles, les réponses en compression des nappes sèches et saturées ont d'ores et déjà été établies. Nous travaillons actuellement sur le traitement de l'imprégnation des nappes par le fluide. Compte-tenu des faibles perméabilités des ces renforts ($<$ 1% de surface ouverte pour l'écoulement), les approches classiques rencontrées dans les milieux poreux ne sont plus en mesure de représenter ces écoulements. Les simulations numériques de type fluide-structure notamment doivent être mises en place à l'échelle des trous de couture.

La spécificité de l'approche proposée est donc le couplage, à terme, de la modélisation thermo-mécanique du remplissage avec la modélisation du problème thermo-physico-chimique de la réaction de réticulation. Ce type d'approche est à ce jour totalement absent de la littérature, et nécessitera certainement la mise en commun des compétences transverses à ces deux domaines pour mener à bien la modélisation complète. À travers ce thème, nous collaborons avec les universités Fédérico II de Naples et la Seoul National University en Corée.

Enfin, il faut noter que la caractérisation de ces procédés est un élément clef. Un travail de

recherche est actuellement en cours au département Mécanique et Matériaux sous la direction d'A. Vautrin, toujours dans le cadre du projet thématique prioritaire régional. Des capteurs à fibres optiques sont développés pour permettre d'une part de suivre le remplissage des préformes sèches par la résine, et d'autre part d'évaluer en temps réel la réticulation de la résine. Les premières informations attendues concernent les vitesses d'imprégnation que nous ne connaissons pas à l'heure actuelle et qui nous serviront pour évaluer les limites du modèle de remplissage (Figure 3.20). Ces capteurs pourraient également être utilisés pour évaluer l'état de contrainte interne du matériau.

3.2 Modélisation des distributions de pression générées par des tissus élastomériques en grandes déformations

Pour ce second projet de recherche, la modélisation des tricots élastomériques en grandes déformations est abordée. Plus particulièrement, ces matériaux sont utilisés dans les Bas Médicaux de Contention (*BMC*), une des composantes thérapeutiques de soin et/ou de prévention des déficiences veino-lymphatiques qui, en créant une contention le long de la jambe du patient, facilitent le reflux sanguin vers le cœur.

Dans l'objectif de traiter au mieux les déficiences du système veino-lymphatique, la contention doit être distribuée de façon calibrée et précise, en fonction des pathologies rencontrées. Les produits de contention doivent donc être utilisés de manière optimale, et de nouveaux produits sur-mesure devraient également être développés à terme. C'est à ce niveau qu'intervient l'apport des outils de modélisation et d'identification du champ de la mécanique, mis en œuvre dans ces matériaux très spécifiques : *rigidités faibles*, *grandes déformations*, *multimatériaux*. En effet, les propriétés mécaniques des *BMC* sont décrites à travers des modèles qui datent des années 70. Le comportement de ces matériaux n'a jamais été abordé dans des approches scientifiques rigoureuses. On peut mettre en lumière deux raisons essentielles qui expliquent cet empirisme. En premier lieu, l'utilisation des *BMC* se base essentiellement sur les connaissances acquises par les prescripteurs au cours des décennies, le besoin de connaître plus en détail les mécanismes de la contention étant réel mais perçu comme inextricable avec les outils classiques utilisés dans le monde médical. Pourtant de telles approches sont largement répandues dans l'étude des tricots et tissus de renforts pour composites [Huang et al., 2000], essentiellement d'ailleurs pour la mise en forme des préformes [Gasser et al., 1999]. En second lieu, les pressions induites par la contention sont de l'ordre de quelques hectoPascals, ce qui représente une difficulté majeure pour quantifier rationnellement les effets de contention de ces matériaux très spécifiques. Une modélisation du phénomène de contention représenterait une avancée de tout premier plan, permettant ainsi de quantifier son effet, et donc d'utiliser de manière adéquate les moyens de contention en fonction des pathologies rencontrées. L'idée originale de ce projet d'*associer les outils de la mécanique* et les *connaissances semi-empiriques des producteurs* de *BMC* doit permettre cette avancée signifi-

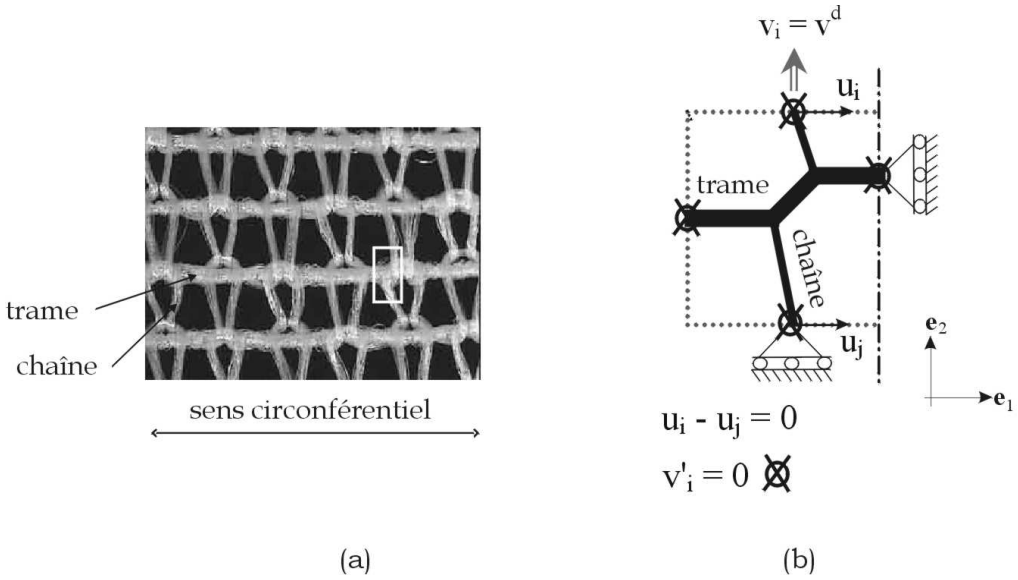

FIG. 3.23: (a) Maille réelle d'un tricot tramé et (b) modèle EF de la cellule représentative - Données confidentielles.

cative.

En préalable au démarrage de la thèse d'Issam Gaied en octobre 2001, j'ai abordé la mécanique de ces tricots, dont l'utilisation donne lieu couramment à des déformations de l'ordre de 80 à 130 %. Des essais de traction uniaxiale ont été mis en œuvre à la fois sur les fils de Lycra, chez Dupont-de Nemours, et sur les tricots eux-mêmes. En parallèle, des simulations EF de type cellule de base ont été menées au niveau d'une demi-maille (Figure 3.23), en utilisant la loi de comportement identifiée pour le Lycra seul. Les fils sont représentés par des éléments de type Hermite, et les conditions de périodicité aux limites de cette cellule sont réduites du fait du nombre restreint de *ddl*s (Figure 3.23-b). Dans ce cas très simplifié, les contacts sont fixes, et le fil de Lycra est représenté seul, alors qu'il est en réalité 'guipé' par un fil de polyamide, c'est-à-dire contraint par un fil torsadé sur sa circonférence. Les résultats ont permis de proposer une première estimation quantitative de la réponse du tricot, et de montrer la difficulté de maîtriser les conditions initiales d'essais sur ces matériaux de très faible rigidité (Figure 3.24). Notamment, d'un point de vue expérimental la viscoélasticité est problématique.

L'objectif de la thèse d'Issam Gaied est plus large et doit permettre dans un premier temps de comprendre en profondeur les mécanismes mis en jeu dans le phénomène de contention, pour ensuite proposer des *modèles prédictifs* des pressions induites par la contention sur les membres humains. Le programme de recherche mis en place pour atteindre cet objectif se décompose en deux phases distinctes relativement indépendantes.

La première phase consiste à prévoir, par une modélisation et des essais adéquats, le comportement non-linéaire orthotrope bidimensionnel du tissu constitutif des articles de contention. En col-

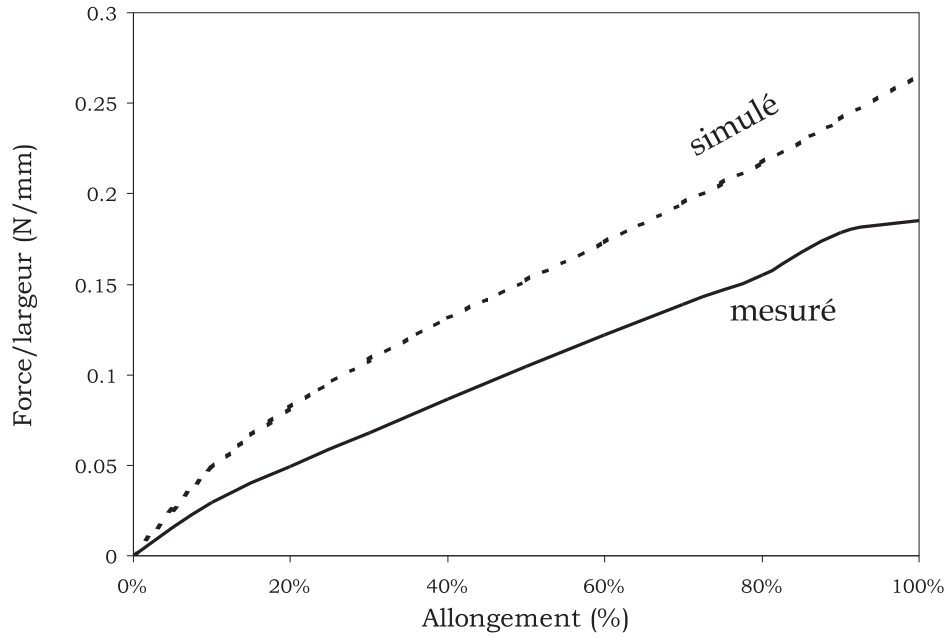

FIG. 3.24: Réponse en traction sens trame d'un tricot tramé : comparaisons mesures / simulations - Données confidentielles.

laboration avec Ganzoni France SA la caractérisation du comportement des tricots élastomériques a débuté, utilisant des méthodes de mesure sans contact disponibles au département Mécanique et Matériaux. Ces mesures de champ de déplacement reposent sur le traitement informatique de séquences d'images. La 'granularité' naturelle des tricots fait ici office de traceur. Actuellement, le montage de caractérisation a été conçu en s'appuyant sur des simulations par éléments finis utilisant la loi de comportement élastique non-linéaire identifiée lors de l'étude préliminaire (Figure 3.24). Les premiers essais de mesures des déformations par corrélation d'images nous laissent entrevoir d'excellentes perspectives. La loi de comportement à identifier est également à l'étude, notamment afin de pouvoir déterminer les temps de relaxation de ce matériau typiquement visco-élastique. De plus, le recours à des méthodes d'optimisation est nécessaire pour l'identification de cette loi à partir de mesures de champ. Sur ce point les compétences internes au laboratoire seront mises à contributions, notamment dans le domaine de l'optimisation.

La seconde phase aura pour but de fournir la répartition des pressions sur une jambe modèle, en s'appuyant sur des simulations par EF incluant des grandes déformations et du contact-frottement entre surfaces. Pour cette partie, des études préliminaires ont également été menées. Il faut noter que la formulation de la loi de comportement bidimensionnelle (phase 1) conditionne très fortement la précision et le réalisme des résultats qui seront issus de la simulation de la contention sur une jambe (phase 2).

- 4 -

Conclusion générale et perspectives

L'utilisation rationnelle des composites et des sandwichs repose sur des outils d'aide à la conception et à l'optimisation spécifiques. À travers la synthèse de mes travaux de recherche, j'ai voulu faire apparaître le préalable incontournable à la mise en place de ces outils : *la problématique du développement et de la connexion des modélisations de plus en plus fines des composites*. Notamment, nous avons vu que ces outils spécifiques doivent s'appuyer d'une part sur des *modèles mécaniques* décrivant de manière convenable les *comportements critiques*, et d'autre part sur des modélisations du procédé permettant de prendre en compte l'effet des *paramètres d'élaboration* sur les *caractéristiques initiales* des matériaux.

Compte-tenu de l'état actuel des recherches que j'ai menées ou encadrées, les perspectives à moyen et long terme devront permettre de coupler les différents modèles mécaniques entre eux, puis avec la modélisation des procédés d'élaboration. Le premier point pourrait aboutir à moyen terme, lorsque les calculs de microflambage plastique seront étendus au 3D en s'appuyant cette fois sur des éléments finis standards disponibles dans un code d'accueil. L'approche expérimentale de ces effets d'échelle est également un problème à traiter à moyen terme, à mener en parallèle avec le mise en place de l'approche numérique multi-échelle. La conception des essais pourra idéalement s'appuyer sur les modèles qui ont été présentés. À plus long terme, l'approche proposée devrait permettre d'améliorer de façon consistante la compréhension du comportement instable des panneaux et coques sandwichs à peaux composites. Il ne faut toutefois pas perdre de vue que les applications industrielles sont visées, un effort devra donc être fourni pour proposer des outils adaptés aux contraintes industrielles.

Concernant les procédés d'élaboration et la mise en forme, cette activité débute à travers deux projets de recherche et reçoit le soutien de la région Rhône-Alpes et d'industriels. À moyen terme, la modélisation du *RFI* devrait être complétée en couplant les modèles thermo-mécaniques et physico-chimiques, aboutissant à un modèle capable de prévoir l'évolution du matériau au cours du remplissage et de la cuisson. La distribution et la qualité de l'imprégnation doivent être simulées

compte-tenu de l'influence de ce paramètre sur les propriétés mécaniques, notamment sous des chargements déstabilisants. La modélisation des tricots élastomériques en grandes déformations quant à elle, abordée d'un point de vu expérimental et numérique, doit apporter à court terme les premiers éléments de réponses. La difficulté rencontrée dans ces deux approches porte sur les spécificités des phénomènes étudiés. Dans le cas de la modélisation du *RFI*, la modélisation de la phase de remplissage est critique car les frontières sont mobiles, et la viscosité de la résine évolue fortement pendant cette opération. Pour l'étude des tricots élastomériques, le frottement intra-maille, et entre le tricot et la peau de membres humains, peut être à l'origine de variations de comportement, et excessivement complexe à évaluer.

En résumé, l'objectif à plus long terme est de prévoir l'influence des paramètres de fabrication sur l'état initial du matériau, et donc sur les caractéristiques géométriques et mécaniques initiales qui pilotent le comportement aux différentes échelles, de façon encore plus notoire sous des sollicitations déstabilisantes souvent dimensionnantes. Nous avons mis en place des modèles de comportement incluant plusieurs échelles d'observation qui peuvent être couplés à moyen terme, et des essais doivent être mis en place pour appuyer cette démarche multi-échelle. La simulation des procédés d'élaboration quant à elle débute, mais est confrontée à la même problématique de mise en œuvre simultanée de simulations et d'identifications. D'ores et déjà, la connexion des instabilités et des procédés d'élaboration peut se faire dans le cas particulier des multiaxiaux, semi-produits utilisés de plus en plus largement, dans lesquels l'architecture mésoscopique ne dépend pas directement de la simulation des procédés mais peut être identifiée à partir de l'assemblage des renforts sélectionnés.

Bibliographie

[Allen, 1969] ALLEN, H. (1969). *Analysis and design of structural sandwich panels*. Robert Maxwell, M.C., M.P. 2.3, 2.3.1

[Anthoine-Rahier, 1998] ANTHOINE-RAHIER, O. (1998). « *Amélioration des montages d'essai de caractérisation de la résistance en compression des composites stratifiés* ». Thèse de Doctorat, Université de Metz - France. 2.1.3, 2.7

[Anthoine-Rahier et al., 1998] ANTHOINE-RAHIER, O., GRANDIDIER, J.-C., and DARIDON, L. (1998). « Pure compression testing of advanced fibre composites ». *Comp. Sci. Technol.*, 58(5) :735–740. 2.1.4

[Backhouse, 1998] BACKHOUSE, R. (1998). « Multiaxial Non-Crimp Fabrics : charaterisation of manufacturing capability for composite aircraft structure applications ». Master's thesis, Cranfield University, School of Industrial and Manufacturing Science. 2.2, 2.8, 2.2, 2.2.2

[Blest et al., 1999] BLEST, D., MCKEE, S., ZULKIFLE, A., and MARSHALL, P. (1999). « Curing simulation by autoclave resin infusion ». *Comp. Sci. Technol.*, 59 :2297–2313. 3.1.2, 3.1.2, 3.1.2

[Budiansky, 1983] BUDIANSKY, B. (1983). « Micromechanics ». *Comp. Struct.*, 16(1) :3–12. 2.1

[Byskov and Hutchinson, 1977] BYSKOV, E. and HUTCHINSON, J. (1977). « Mode interaction in axially stiffened cylinfrical shells ». *AIAA Journal*, 15(7) :941–948. 2.3.1

[Dransfield et al., 1994] DRANSFIELD, K., BAILLIE, C., and MAI, Y.-W. (1994). « Improving the delamination resistance of CFRP by stitching - a review ». *Comp. Sci. Technol.*, 50 :305–317. 2.2.1

[Frostig and Baruch, 1993] FROSTIG, Y. and BARUCH, M. (1993). « High-order buckling analysis of sandwich beams with transversely flexible core ». *J. of Eng. Mech.*, 119(3) :476–495. 2.3

[Gardin and Potier-Ferry, 1992] GARDIN, C. and POTIER-FERRY, M. (1992). « Microflambage des fibres dans un matériau composite à fibres longues : Analyse asymptotique 2-D ». *Compt. Rend. de l'Acad. des Sci. Paris*, 315 :1159–1164. 2.1.1

[Gasser et al., 1999] GASSER, A., HANKLAR, S., BUET-GAUTIER, K., SOULAT, D., and BOISSE, P. (1999). « Comportement mécanique des tissus de fibres à l'échelle de la maille ». Dans *Actes du 14ième Congrés Francais de Mécanique - Toulouse, septembre 1999*, volume 1, pages 25–36. 3.2

[Grandidier, 1991] GRANDIDIER, J.-C. (1991). « *Compression et microflambage dans les matériaux composites* ». Thèse de Doctorat, Université de Metz - France. 2.1.2

[Grandidier et al., 1992] GRANDIDIER, J.-C., FERRON, G., and POTIER-FERRY, M. (1992). « Microbuckling and strength in long-fiber composites : Theory and experiments ». *Int. J. Solids Struct.*, 29(14/15) :1753–1761. 2.1, 2.1, 2.1.1

[Grandsire-Vinçon, 1993] GRANDSIRE-VINÇON, I. (1993). « *Compression des composites unidirectionnels : mèthodes d'essais et approche micromécanique* ». Thèse de Doctorat, ENS de Cachan - France. 2.1, 2.1

[Huang et al., 2000] HUANG, Z., RAMKRISHNA, S., and TAY, A. (2000). « Modeling the stress/strain behavior of knitted fabric-reinforced elastomer composite ». *Comp. Sci. Technol.*, 60 :671–691. 3.2

[Hunt et al., 1988] HUNT, G., DA SILVA, L., and MANZOCCHI, M. (1988). « Interactive buckling in sandwich structures ». *Proceedings of the Royal Society of London*, 417A :155–177. 2.3

[Hutchinson, 1974] HUTCHINSON, J. (1974). « Plastic buckling ». *Adv. Appl. Mech.*, 14(12) :67–144. 2.1.2

[Jochum, 1999] JOCHUM, C. (1999). « *Microflambage des fibres lors de la cuisson des composites stratifiés à fibres longues* ». Thèse de Doctorat, Université de Metz. 2.1.4

[Jochum et al., 1999] JOCHUM, C., GRANDIDIER, J.-C., and POTIER-FERRY, M. (1999). « Modelling approach of microbuckling mechanism during cure in a carbon epoxy laminate ». In MASSARD, T. & VAUTRIN, A., éditeurs, *Proceedings of ICCM12 - Paris 5-9 july 1999*, page 317. 2.1.4

[Joshi et al., 1999] JOSHI, S., LIU, X., LAM, Y., and SHERIDAN, J. (1999). « Simulation of resin film infusion process using Finite Element / Nodal Control Volume approach ». *Advanced Composite Letters*, 8(3) :101–104. 3.1.2

[Kyriakides et al., 1995] KYRIAKIDES, S., ASCULARATNE, R., PERRY, E., and LIECHTI, K. (1995). « On the compressive failure of fiber reinforced composites ». *Int. J. Solids Struct.*, 32(6/7) :689–738. 2.1, 2.1.2

[Léotoing, 2001] LÉOTOING, L. (2001). « *Modélisation du flambage global, local et interactif dans les structures sandwich en compression* ». Thèse de Doctorat, École Nationale Supérieure des Mines de Saint-Étienne et Université Jean Monnet - France. 2.3.2, 2.3.3

[Lo et al., 1977] LO, K., CHRISTENSEN, R., and WU, E. (1977). « A high-order theory of plate deformation, part 1 : homogeneous plates ». *J. Appl. Mech.*, pages 663–668. 2.3.1

[Miller, 1996] MILLER, A. (1996). « The Effect of Microstructural Parameters on the Mechanical Properties of Non-Crimp Fabric Composites ». Master's thesis, Cranfield University, School of Industrial and Manufacturing Science. 2.8, 2.2, 2.2.1, 2.2.2, 2.2.2

[Rosen, 1964] ROSEN, B. (1964). « *Mechanics of composite strengthening* », pages 37–75. Am. Soc. Metals Seminar, Metal Parks, Ohio. 2.1, 2.1

[Starlinger, 1990] STARLINGER, A. (1990). « *Development of efficient finite shell elements for the analysis of sandwich structures under large deformations and global as well as local instabilities* ». Thèse de Doctorat, Vienna University of Technology - Austria. 2.3

[Teti and Caprino, 1989] TETI, R. and CAPRINO, G. (1989). « Mechanical behavior of structural sandwiches ». Dans OLSSON, K. & REICHARD, R., éditeurs, *Proceedings of Sandwich Constructions 1*, pages 53–68. Engineering Materials Advisory Services Ltd. 2.3

[Williams et al., 1941] WILLIAMS, D., LEGGETT, D., and HOPKINS, H. (1941). « Flat sandwich panels under compressive end loads ». Technical Report 1987, R.A.E. 2.3, 2.3, 2.3

[Wisnom, 1991] WISNOM, M. (1991). « The effect of the specimen size on the bending strength of unidirectional carbon fibre-epoxy ». *Comp. Struct.*, 18 :47–63. 2.1, 2.1.3, 2.5

[Wisnom, 1993] WISNOM, M. (1993). « Analysis of shear instability in compression due to fibre waviness ». *J. of Rein. Plast. Comp*, 12(11) :1171–1189. 2.1.3, 2.2.1

Annexe 1 : Notice Individuelle

- A -

Curriculum Vitæ

Sylvain Drapier

Maître Assistant

Centre Science des Matériaux et des Structures
Département Mécanique et Matériaux
École Nationale Supérieure des Mines de Saint-Étienne
http ://www.emse.fr/∼drapier

Décembre 2002

Mécanique des Matériaux et des Structures / Matériaux Composites

État civil / Coordonnées

Sylvain Drapier
né le 29 juillet 1968, marié, 1 enfant

Coordonnées Professionnelles
Centre *SMS*, dépt. *Mécanique et Matériaux*
École Nationale Supérieure des Mines de Saint-Étienne
158, Cours Fauriel
42023 Saint-Étienne cedex 02

Tél : 04-77-42-00-79
Fax : 04-77-42-02-49
mèl : drapier@emse.fr

Coordonnées Personnelles

23 A, Impasse de la Vivaraize
42100 Saint-Étienne

Tél : 04-77-47-94-26
Portable : 06-18-41-35-68
mèl : sylvain.drapier@wanadoo.fr

Parcours professionnel

Octobre 97 → actuellement *Maître Assistant* à l'ENSM.SE, dépt. Mécanique et Matériaux :

→ Enseignement : mécanique des matériaux, des solides et des structures en $2^{ième}$ et $3^{ième}$ cycle : Licence/Maîtrise de Mécanique, cursus des Ingénieurs Civils des Mines, DEA Génie Mécanique et Génie Civil.

→ Thématiques de recherche : (co)-auteur de 13 publications et 25 communications
- instabilités et effets d'échelle dans les matériaux composites à fibres longues et les sandwichs,
- modélisation de systèmes fortement couplés : *thèmes émergents*
  - procédés de mise en oeuvre par voie humide de nouveaux composites organiques
  - pressions de contact générées par des tricots élastomériques en grandes déformations,
  - modélisation des contraintes internes de service dans les plaques stratifiées de dimensions finies.

→ Relations industrielles/universitaires : participant/porteur de projets régionaux (1 en cours, 1 fini) en relation avec des partenaires industriels et universitaires, collaborations industrielles contractuelles, suivis de DEA/TFE et thèses en relation et dans des industries.

Post-Doctorat (Octobre 96 → Septembre 97) : "Research associate" au département "Aerospace Engineering" de l'Université de Bristol (Prof. M.R. Wisnom) : modélisation des instabilités dans les nouveaux renforts NCF pour composites structuraux - collaboration avec Airbus/BAe.

Thèse de Doctorat (Octobre 93 → Septembre 96) en Sciences pour l'Ingénieur, soutenue le 20/09/1996, Univ. de Metz - LPMM / Groupe Calcul de Structures, co-direction des profs. M. Potier-Ferry et J.-C Grandidier : "Prévision de la résistance en compression des composites à fibres longues : approche structurelle du microflambage plastique". *Très honorable avec félicitations du jury*.

Formation

- 1992 - 93 : D.E.A. Mécanique - Matériaux - Structure, Université de Metz (*Mention Bien*).
- 1990 - 92 : M.S.T. Conception et Fabrication Mécaniques Assistées par Ordinateurs, Université de Metz (*Mention Bien, major de promotion les 2 années*).
- 1988 - 90 : DEUG Science et Structure de la Matière, Université de Metz.

- B -

Activités d'enseignement

Les enseignements que j'ai été amené à effectuer, d'abord à l'université de Metz de 1993 à 1996 en tant que moniteur d'enseignement supérieur, puis à l'École Nationale Supérieure des Mines de Saint-Étienne depuis février 1998 en tant que Maître-Assistant, portent sur la mécanique en général et la mécanique des solides et des structures en particulier. L'augmentation graduelle du volume d'enseignement depuis mon arrivée à l'ENSM.SE correspond à la création et la mise en place d'enseignements divers (Dynamique, Homogénéisation, Mise en œuvre des composites, RdM, Mécanique des Structures, ...). Pour la rentrée 2002, je suis chargé de mettre en place un *axe scientifique Mécanique* de 120h en $2^{ième}$ année du cursus des Ingénieurs Civils des Mines (ICM).

L'encadrement de projets d'étudiants et de stages d'étudiants en entreprise est également une composante importante de mon implication dans l'enseignement. En parallèle à ces enseignements en formation initiale, j'ai également pu aborder par deux fois la formation continue.

B.1 Enseignement dispensé en formation initiale

B.1.1 Synthèse des enseignements

Le Tableau 2.2 sur la page suivante synthétise les enseignements assurés de 1993 à ce jour en formation initiale, indiquant les intitulés et le volume horaire correspondant, en heure équivalent TD (h Éq. TD)[1]. Le contenu de ces enseignements est détaillé dans le syllabus suivant, page 65.

Dans ces enseignements, les publics visés sont de niveau licence/maîtrise (30 à 40 étudiants, et ponctuellement 100 à 120 étudiants), et année 2 et 3 du cycle des ICM (20 et 40 élèves ingénieurs en 2A, et 15 à 30 élèves ingénieurs en 3A). Pour les cours les plus denses (Dynamique, RdM, Homogénéisation), des supports dactylographiés ont été mis en place.

[1] Heures Éq. TD : 1 h de cours ⇔ 1,5 h Éq. TD, 1 h de TP ⇔ 0,75 h Éq. TD

Année	Établis.	Matière enseignée	Niveau	Vol.	Réf. syllabus
1993→1996	Univ. Metz	**Calcul des Structures** (93/94 et 94/95)	Maîtrise	64	*[CdS]*
		Résistance des Matériaux 1995/96	Licence	64	*[RdM1]*
début 1998	ENSM.SE	**Conception des Structures Composites**	3A / DEA	27	*[CSC]*
1998/1999	ENSM.SE	Conception des Struct. Composites	3A / DEA	27	*[CSC]*
		Initiation à la CAO	2A	13	*[CAO]*
		APPEX	1A	3	*[APPEX]*
1999/2000	ENSM.SE	Conception des Struct. Composites	3A / DEA	18	*[CSC]*
		Dynamique des Solides&Structures	3A / DEA	27	*[DSS]*
		Initiation à la CAO	2A	4,5	*[CAO]*
		Mise en Œuvre des Composites	2A	13,5	*[MOC]*
		Éléments Finis et Structures	2A	9	*[EF]*
		APPEX	1A	3	*[APPEX]*
2000/2001	ENSM.SE	Dynamique des Solides&Structures	3A / DEA	27	*[DSS]*
		Homogénéisation et Méthodes de Changement d'Échelles	3A / DEA	22,5	*[HMCE]*
		Instabilités des Structures	3A / DEA	4,5	
		Initiation à la CAO	3A / DEA	2,5	*[CAO]*
		Relations μstructure - Propriétés	2A	2,5	
		Mise en Œuvre des Composites	2A	9	*[MOC]*
		Résistance des Matériaux	2A	18	*[RdM2]*
		APPEX	1A	3	*[APPEX]*
2001/2002	ENSM.SE	Dynamique des Solides&Structures	3A / DEA	27	*[DSS]*
		Homog. et Changement d'Échelles	3A / DEA	22,5	*[HMCE]*
		Instabilités des Structures	3A / DEA	4,5	
		Relations μstructure - Propriétés	2A	2,5	
		Mise en Œuvre des Composites	2A	9	*[MOC]*
		Résistance des Matériaux	2A	18	*[RdM2]*
		APPEX	1A	3	*[APPEX]*

TAB. 2.2: Synthèse des activités d'enseignement par année et par type, et volume horaire correspondant en h Éq. TD. Les enseignements en gras indiquent la création et la mise en place du module.

B.1.2 Syllabus des enseignements

[CdS] Calcul des structures, cours/TD/TP, 64 h Éq. TD, niveau maîtrise
Objectif : donner aux étudiants les outils et méthodes nécessaires pour être critiques par rapport aux résultats de simulations par éléments finis. Des rappels de calculs variationnels (21 h) précèdent les cours et TD de RdM qui permettent de formuler des éléments finis simples (21 h), utilisés ensuite dans des applications mises en place lors de TPs (Abaqus) sur station de travail (22 h).

[RdM1] Résistance des Matériaux, TP/TD, 64 h Éq. TD, niveau licence
Objectif : formuler en TD (30 h) les problèmes de RdM classiques utilisés dans les structure simples, et les mettre en oeuvre dans des expériences simples (TP, 34 h).

[CSC] Conception des structures composites, cours/TD/TP, 27 h Éq. TD, niveau ICM 3A / DEA
Objectif : dimensionnement de structures composite simples (poutres, cylindres) à l'aide d'outils de RdM et logiciels dédiés puis caractérisation expérimentale, pour ensuite mener une confrontation prédictions / résultats expérimentaux.

[CAO] Initiation à la CAO, cours/TD/TP, 14 h Éq. TD, niveau ICM 2A
Objectif : apporter une connaissance élémentaire de l'apport de la CAO dans le métier d'ingénieur. Présentation des grandes lignes de la CAO, puis utilisation d'un système de CAO de type paramètrique (Pro-Engineer), couplage avec un code de calcul (ANSYS) pour de l'optimisation de forme.

[APPEX] Activité Personnelle en Physique Expérimentale, 3 h Éq. TD, niveau ICM 1A
Objectif : amener les élèves ingénieurs, par trinômes, à construire une réflexion leur permettant de caractériser rigoureusement des phénomènes physiques qui peuvent paraître aléatoires *a priori*. Application au cas du flambage des poutres sur 7×3 h.

[EF] Éléments finis en mécanique des structures, cours, 9 h Éq. TD, niveau ICM 2A
Objectif : faire le lien entre la mécanique des poutres et la formulation d'éléments finis. Rappels, approximations cinématiques, formulation d'élément de type Lagrange et Hermite.

[DSS] Dynamique des solides et des structures, cours, 27 h Éq. TD, niveau ICM 3A / DEA
Objectif : à l'issue de ce cours les étudiants doivent être capables de réaliser la mise en équation d'un problème de dynamique, de le résoudre de façon analytique ou numérique, et d'analyser et d'interpréter les résultats obtenus.

[MOC] Mise en œuvre des composites, cours/TD/TP, 9 h Éq. TD, niveau ICM 2A
Objectif : présentation à travers des cours et des TPs, en 15h, des moyens de fabrication les plus courants qui peuvent être mis en oeuvre pour les composites organiques ; illustrer l'intéraction entre fabrication et conception dans le cas des composites à fibres longues.

[HMCE] Homogénéisation et méthodes de changement d'échelle, cours/TD, 22,5 h Éq. TD, niveau ICM 3A / DEA
Objectif : introduire les techniques courantes permettant de relier le comportement d'un milieu, à une échelle d'observation donnée, aux propriétés de ses constituants connues à une

échelle d'observation inférieure ; propriétés linéaires des milieux périodiques, présentation des estimations d'ordre 1 et 2.

[RdM2] Résistance des Matériaux, cours/TD, 18 h Éq. TD, niveau ICM 2A
Objectif : donner les outils de base pour la formulation des problèmes de poutres en traction, flexion, torsion, flambage.

[Proj] Projets "industriels", de 30 à 50 h pour ICM 2A et de 40 à 120h pour ICM 3A
Objectif : ce travail en binôme permet aux étudiants de traiter un problème, de nature généralement appliqué, dans le cadre d'un des axes d'enseignement. Le rôle de l'encadrant consiste à proposer des sujets renouvelés et à suivre l'évolution du travail, et si nécessaire le recadrer. Ces projets sont sanctionnés par une soutenance orale

[stage2A] Stage industriel, de 16 semaines minimum ICM 2A
Objectif : ce stage dit d'application technique permet aux élèves ingénieurs de mettre en œuvre les concepts scientifiques et techniques introduits durant leur cursus. Le rôle du tuteur consiste très souvent à conseiller l'étudiant sur son choix de stage, et/ou proposer des stages. Ces stages sont sanctionnés par une soutenance orale préparée avec l'encadrant. Généralement, dans les domaines techniques, l'encadrant se déplace sur le lieu du stage pour faire des bilans réguliers de l'avancement du travail.

[TFE] Stage industriel, de 16 semaines minimum ICM 3A
Objectif : ce stage permet aux élèves ingénieurs une immersion dans un environnement professionnel. Le rôle du tuteur consiste à encadrer et/ou proposer des stages, puis à suivre l'évolution du travail dans un cadre professionnel. Ces stages sont sanctionnés par une soutenance orale préparée avec l'encadrant. Ce type de stage permet également au tuteur de nouer et/ou pérenniser des relations avec les acteurs du monde économique.

B.2 Activités d'encadrement

Les activités d'encadrement sont intégrées à la scolarité des $2^{ième}$ et $3^{ième}$ année ICM et peuvent se décomposer en 3 catégories distinctes : encadrement de projets *[Proj]*, encadrement de stage en entreprise (*[TFE]*, *[stage-2A]*), et accueil et envoi d'étudiants en scolarité à l'étranger (*[Acc-étr]*, *[Scol-étr]*). Ci-dessous le Tableau 2.3 synthétise ces activités d'encadrement par type et présente une estimation en h Éq. TD basée sur les mesures horaires en vigueur à l'ENSM.SE. Ces estimations horaires attribuent forfaitairement à l'encadrant 20 % du volume horaire du projet pour des projets standards (50h) soit environ 10 h Éq. TD, 10 % du projet pour les projets longs (120h) soit 12 h Éq. TD, 4 h Éq. TD pour les TFE, et enfin 2 h Éq. TD pour les stages 2A .

Les projets et stages encadrés portent sur la mécanique au sens large, appliquée tant aux matériaux et structures homogènes qu'aux composites. La mécanique des fluides est également traitée, dans les problèmes liés aux procédés d'élaboration notamment. L'aspect modélisation est prépondérant, mais le recours à l'expérimentation est très fréquent.

	1998/99	1999/00	2000/01	2001/02
Travail de Fin d'Études (3A)*[TFE]*	2	4	1	
Stage de DEA + TFE (3A)		1	1	
Stage de 2^{ième} année *[stage-2A]*	2	1	1	1
Pré - Travail de Fin d'Études (3A - 120h) *[Proj]*	2	1	3	
Projet 2A et 3A ($\sim$50h) *[Proj]*	2	3	2	1
Scolarité d'ICM 3A à l'étranger *[Scol-étr]*	2	3	1	1
Étudiant étranger à l'ENSM.SE *[Acc-étr]*	1	1	1	2
h Éq. TD	**102**	**118**	**167**	**57**

TAB. 2.3: Synthèse des activités d'encadrements par année et par type, et estimation des h Éq. TD.

B.3 Enseignement dispensé en formation continue

- En 1998, formation continue d'un ingénieur de la société Hexcel Composites : Mécanique des Structures (30 h),
- en 2000/2001, *création et enseignement* d'un 1/2 module CNAM (30h) - Multimatériaux et Composites Hautes Performances :
  - Présentation générale des composites et des multimatériaux (4h),
  - Mécanique des composites HP (8h),
  - Dimensionnement de base avec les composites - théorie des poutres stratifiées (14h),
  - Moyens d'élaboration (4h).

B.4 Synthèse

L'ensemble des activités d'enseignement présentées dans cette partie B est synthétisé dans le Tableau (2.4) ci-dessous en termes de volume horaire par année et par type.

		→1996	déb. 98	1998/99	1999/00	2000/01	2001/02
Formation initiale	Cours/TD/TP	64/an	27	43	75	89	86
	Encadrements	-	-	102	118	167	57
	Total	**64/an**	**27**	**145**	**193**	**256**	**143**
Format. continue*			**30**			**30**	

TAB. 2.4: Synthèse des activités d'enseignement par année et par type en h Éq. TD (sauf *,cours)

- C -

Activités scientifiques

Dans cette partie du dossier, les activités de recherche sont présentées de façon *condensées*. La liste complète des publications est quant à elle donnée dans le Chapitre F page 77 de cette annexe, mais dans le but de faciliter la lecture du dossier, un tableau synthétique des publications produites et soumises est proposé ci-dessous (Tableau 3.5 - page 70).

C.1 Mémoires et diplômes dirigés

Dés mon arrivée au département Mécanique et Matériaux en février 1998, j'ai été impliqué dans le (co)-encadrement de travaux scientifiques. Après avoir participé à l'encadrement d'une thèse soutenue en janvier 2000 (L.Dufort), j'ai co-dirigé une thèse qui a été soutenue en novembre 2001 (L.Léotoing). J'assure actuellement la co-direction de trois autres thèses. J'ai également encadré deux DEAs pendant cette période :

- Thèses de doctorat soutenues :
  - L.Dufort, thèse soutenue en janvier 2000 : *Étude expérimentale et théorique du gauchissement des sections dans les poutres composites*, participation à l'encadrement $\approx$ 30 % (M. Grédiac),
  - L.Léotoing, thèse soutenue en novembre 2001 : *Modélisation du flambage global, local et interactif dans les structures sandwich en compression*, co-encadrement $\approx$ 80 % (A.Vautrin).
- Thèses en cours, co-encadrement avec A.Vautrin :
  - O.Elbouazzaoui, début octobre 2000 : *Modélisation thermo-mécanique et physique du process de fabrication de* NC2 *par infusion* - lien avec le programme thématique prioritaire *NC2* (*cf* C.3 Implication / Responsabilités dans des projets de recherche), co-encadrement $\approx$ 90 %,

  - I. Gaied, début octobre 2001 : *Modélisation et prévision des distributions de pressions générées par les articles de contention sur les membres humains inférieurs*, en collaboration avec Ganzoni (*cf* E Relations industrielles), co-encadrement ≈ 90 %,
  - M. Gigliotti, début en octobre 2001 : *Modélisation des contraintes internes de service dans les plaques stratifiées de dimensions finies*, co-encadrement ≈ 20 %.
- DEAs, encadrement à 100 % :
  - A.Pagot, soutenance en septembre 2000 : *Étude de l'influence des points de couture sur la perméabilité de nouveaux renforts multiaxiaux pour composites structuraux*,
  - B.Régis, soutenance en septembre 2001 : *Élaboration de composites structuraux par le procédé RFI : effet de la qualité de fabrication sur les tolérances et les propriétés mécaniques finales*.

C.2 Synthèse des publications

Ci-dessous est donnée, dans le Tableau 3.5, la synthèse des publications et communications issues des activités de recherche. La liste complète se trouve au Chapitre F de cette Annexe 1.

	→1996	1997	1998	1999	2000	2001	2002	Total
Revues int. avec CL	1	1	1	3		2	3(+ 1)	11 (+ 1 révisé)
Contrib. ouvrage				1				1
Congrés. int. *invités*	1		2	1		1	1	6
Congrés int. avec actes	2			2	1		2	7
Congrés int. résumés	1				3			4
Actes congrés nat.	6				1			7
Lettre d'information	1							1
Rapports techn./sci.		3		1		1	2	7

TAB. 3.5: Nombre de communications par année et par type.

C.3 Implication / Responsabilités dans des projets de recherche

- Implication dans un programme 1998/2000 d'*assistance technique à l'étude du dimensionnement de produits et structures composites* auprès de la société Hexcel Composites,
- Co-responsable avec le professeur A.Vautrin d'un projet de formation *CAO/Conceptique* sur 1999/2000 visant à *faciliter la pénétration des composites dans les PME/PMI en s'appuyant sur les outils informatiques*, mené en partenariat avec l'association Mécapôle de

Saint-Étienne (association locale des industries de la mécanique). Budget global du projet de 1040 kF, soutien à hauteur de 765 kF du FEDER/FSE sur 1999/2000,

– Co-responsable avec le professeur A.Vautrin d'un programme régional 'Thématique Prioritaire 2000/2002' intitulé *Optimisation du procédé de transformation de nouveaux renforts multiaxiaux pour composites structuraux*. Le département MeM est porteur de ce projet mené en collaboration avec le L2M de l'Université Claude Bernard - Lyon, le LTSI de l'Université Jean Monnet - Saint-Étienne, et la société Hexcel Fabrics située aux Avenières (38). Budget global du projet de 3260 kF, aide de la région de 900 kF.

C.4 Reviewing

Reviewer pour la revue *International Journal of Fracture* - 2 articles.

C.5 Organisation / Participation

– Chairman d'une session *Composite Materials* au $4^{ième}$ Euromech Solid Mechanics Conference, Metz-France 26-30 juin 2000,

– Participation à des jurys de thèse au département MeM :

  – L. Dufort, le 12 janvier 2000, *Étude expérimentale et théorique du gauchissement des sections dans les poutres composites*, Université Blaise Pascal - Clermont-Ferrand,

  – L. Léotoing, le 26 novembre 2001, *Modélisation du flambage global, local et interactif dans les structures sandwich en compression*, École Nationale Supérieure des Mines de Sain-Étienne et Université Jean Monnet.

– Participation à des jurys de DEA au département MeM :

  – S. Avril, le 28 septembre 1999, *Contribution à la conception d'une structure de siège ferroviaire en matériaux composites*, DEA Matériaux, Structures, Fiabilité,

  – A. Pagot le 21 septembre 2000, et B. Régis le 18 septembre 2001, DEA Matériaux, Structures, Fiabilité (en 1999/2000, puis Génie Mécanique et Génie Civil à partir de 2000/2001) - étudiants sous ma direction à 100 % (*cf* C.1 Mémoires et diplômes dirigés),

  – J.-C. Minni, le 18 septembre 2001, *Étude de la stabilité dimensionnelle des tissus utilisés dans les circuits imprimés multicouches*, DEA Génie Mécanique et Génie Civil.

C.6 Sociétés savantes

– Membre de l'AUM (devenue GTT 'Universitaires et Chercheurs' de l'Association Française de Mécanique (AFM)) depuis 1997,

- Membre de l'Association Française pour les Matériaux Composites (AMAC) depuis 1998,
- Membre de l'Association Calcul de Structures et Modélisation (CSMA) en 1995,
- Membre de la European Society of Composite Materials (ESCM) en 1996 et 2002.

- D -

Activités d'administration / Responsabilités

D.1 Responsabilités en enseignement

- Responsable pour le DEA Génie Mécanique et Génie Civil de 3 cours, communs avec la 3^{ième} année du cycle ICM
  - en 1998/99 et 1999/2000 responsable pour le site de l'ENSM.SE de 'Conception des Structures Composites' *[CSC]*[1],
  - depuis 1999 responsable pour le site de l'ENSM.SE de 'Dynamique des solides et des structures' *[DSS]*,
  - depuis 2000 responsable pour le DEA de 'Homogénéisation et méthodes de changement d'échelle' *[HMCE]*.
- Responsable à partir de 2002 d'un **axe scientifique Mécanique** pour la 2^{ième} année du cycle ICM : création et mise en place de cet axe de 120h,
- Responsable pour la 2^{ième} année du cycle ICM de 3 UPs (Unités Pédagogiques)
  - en 1998/99 et 1999/2000, Introduction à la CAO *[CAO]*,
  - depuis 1999, Mise en oeuvre des composites *[MOC]*,
  - à partir de septembre 2002 Mécanique des Structures *[MSt]*.
- Responsable des échanges SOCRATES avec des universités étrangères - gestion administrative, suivi pédagogique et encadrement des stages longs au département MeM :
  - depuis 1998, Bristol (GB), Bath (GB),
  - depuis 1999, Moscow (Idaho, USA),
  - depuis 2000, Naples (Italie).
- Responsable scientifique de la formation d'un ingénieur de la société Hexcel Composites, en 1998 (Mécanique des structures / Mécanique des composites - 140 h),
- Membre d'un groupe de travail formé en 1999/2000 pour refondre les enseignements de 3^{ième} année du centre SMS. Nouvelle option CIME mise en place à la rentrée 2000.

[1] voir Syllabus des enseignements, page 65

D.2 Responsabilités dans le département Mécanique et Matériaux /centre SMS

- Recrutements, en 1999, 2000 et 2001, avec le directeur de MeM (A.Vautrin) des doctorants,
- Animateur en 1999/2000 d'un groupe de travail de 7 personnes (GT calculs) - choix des moyens de calculs scientifiques du centre SMS pour les 5 ans à venir.

D.3 Organisation

- Co-organisateur, avec le professeur A.Vautrin, des Journées de l'Association Universitaire de Mécanique (AUM) 98, 8-9 septembre à l'ENSM.SE. Thème *Le transfert technologique entre l'enseignement supérieur et les entreprises de la mécanique*. 75 participants dont 25 industriels,
- pour décembre 2003 organisation d'un congrès Euromech 453 *Internal stresses in polymer composite processing and service life*, en collaboration avec l'université Federico II de Naples (I).

D.4 Responsabilités collectives

- Représentant élu, en 1995 et 1996, des doctorants au conseil de laboratoire du LPMM, Université de Metz,
- **Membre élu**, 2002-2004, des personnels scientifiques au **Comité de la Recherche** de l'ENSM.SE.

- E -

Relations industrielles

- Prestations pour des PME-PMI lorraines en collaboration avec le CRITT Apollor - Nancy (40 kF - 94-96),
- Prestations pour un bureau d'étude en génie civil (35 kF - 94-95),
- Adwest OCI - La Tallaudière (42)
  en juin 1999, rapport d'étude "Commande de boîte de vitesse : modélisation du contact dans les câbles de commande et modélisation d'un actionneur électromagnétique",
- Alstom - Le Creusot (71)
  - en 1999, encadrement d'un TFE chez Alstom - "conception d'une transmission courte en composites",
  - en 1998/1999/2000, représentant de l'École Nationale Supérieure des Mines de Saint-Étienne au *Cercle Technique Bogie* (Alstom / partenaires universitaires).
- Hexcel Composites - Dagneux (01)
  - en 1998/1999, assistance technique au développement de produits en composites,
  - en 1998, responsable scientifique de la formation d'un ingénieur Hexcel à la conception de structures composites (Mécanique des structures / Mécanique des composites - 140 h).
- Mécapôle (42) - association d'entreprises de la mécanique du bassin stéphanois
  - implication de Mecapôle dans le déroulement des Journées AUM98 dont j'étais l'organisateur,
  - de 1999 à 2000, porteur d'un projet de formation continue 'CAO/Conceptique' pour les PME/PMI. Soutien sur 1999-2000 du FEDER et du FSE.
- Ganzoni France SA - Andrézieux (42)
  - en 2000, encadrement d'un TFE sur la modélisation et la caractérisation des tissus élastomériques en grandes déformations,

  - en 2001, signature d'un accord cadre de collaboration. Projet de modélisation des distributions des pressions générées par les produits de contention - soutien de 300 KF sur 2 ans. Début en octobre 2001 de la thèse d'I.Gaied en co-encadrement (A.Vautrin / S.Drapier) sur ce sujet.

- Hexcel Fabrics - Les Avenières (38)
  - en 2000, encadrement d'un TFE / DEA (A.Pagot) sur la caractérisation et la modélisation de la perméabilité de nouveaux renforts cousus (NC2),
  - en octobre 2000, début de la thèse d'O.Elboazzaoui début en octobre 2000 en co-encadrement (A.Vautrin / S.Drapier) dans le cadre d'un programme régional 'Thématique prioritaire *NC2*' sur 2000-2002.
- British Aerospace (GB) : 2 TFE en 1999/2000 et 2000/2001.

- F -

Production scientifique

F.1 Revues internationales à comité de lecture

1. S. Drapier, J.-C. Grandidier, C. Gardin, & M. Potier-Ferry. Structure effect and microbuckling. *Comp. Sci. Technol.*, 56(7) :861–867, 1996.
2. S . Drapier, J.-C. Grandidier, & M. Potier-Ferry. Theoretical study of structural effects on the compressive strength of laminate composites. *Compt. Rend. Acad. Sci. Paris*, 324 :219–227, 1997.
3. S. Drapier, J.-C. Grandidier, & M. Potier-Ferry. Non-linear numerical approach to microbuckling. *Comp. Sci. Technol.*, 58(5) :785–790, 1998.
4. S. Drapier, J.-C. Grandidier, & M. Potier-Ferry. Towards a numerical model of the compressive strength for long fibre composites. *Eur. J. Mech. A/Solids*, 18 :69–92, 1999.
5. S. Drapier & M.R. Wisnom. Finite-element investigation of the compressive strength of non-crimp-fabric-based composites. *Comp. Sci. Technol.*, 59(8) :1287–1297, 1999.
6. S. Drapier & M.R. Wisnom. Finite element investigation of the interlaminar shear strength of non-crimp fabric based composites. *Comp. Sci. Technol.*, 59(16) :2351–2362, 1999.
7. S. Drapier, J.-C. Grandidier, & M. Potier-Ferry. A structural approach of plastic microbuckling in long fibre composites : comparison with theoretical and experimental results. *Int. J. Solids Struct.*, 38 :3877–3804, 2001.
8. L. Dufort, S. Drapier, & M. Grédiac. The cross section warping in short beams under three point bending : an analytical study. *Compos. Struct.*, 52(2) :233–246, 2001.
9. L. Léotoing, S. Drapier, & A. Vautrin. First applications of a novel unified model for global and local buckling of sandwich columns. *Eur. J. Mech. A/Solids*, 21 :683–701, 2002.
10. L. Léotoing, S. Drapier, & A. Vautrin. Nonlinear interaction of geometrical and material properties in sandwich structures instabilities. *Int. J. Solids Struct.*, 39(13-14) :3717–3739, 2002.

11. L. Léotoing, S. Drapier, & A. Vautrin. Using new close form solutions to setup design diagrams and numerical models for the global and local buckling of sandwich beams, *J. of Sand. Struct. and Mat.*, 2002. Accepté, *à paraître*.

12. S. Drapier, A.Pagot, A. Vautrin, & P. Henrat. Influence of the stitching density on the transverse permeability of Non-Crimped New Concept (*NC2*) multiaxial reinforcements : measurements and predictions, *Comp. Sci. Technol.*, 62(15) :1979–1991, 2002. .

Contribution à un ouvrage collectif - numéro spécial de revue

13. S. Drapier, C. Jochum, J.-C. Grandidier, & M. Potier-Ferry. Structural plastic microbuckling and compressive strength of long-fibre composite materials, pages 125–136 dans *G.Maugin* éditeur *Continuum thermomechanics : the art of science and modelling material's behaviour*. Kluwer Academic Publisher, 2000.

F.2 Congrès internationaux

Congrès internationaux sur *Invitation*

Conférences où j'ai présenté une communication suite à une invitation personnelle du comité scientifique.

14. S. Drapier, J.-C. Grandidier, & M. Potier-Ferry. A microbuckling model for long fibre composites, including structural effects, material non-linearities and fibre waviness. Dans *Stability and Bifurcation in Solids Mechanics, Euromech 347 - Paris 13-15 May 1996*, 1996.

15. S. Drapier, J.-C. Grandidier, & M. Potier-Ferry. Prediction of long-fibre compressive strength : a structural approach of microbuckling. Dans *Proceedings of the 13th US National Congress on Applied Mechanics, Gainseville-Florida 21-26 June 1998*, page WB11, 1998.

16. S. Drapier & M.R. Wisnom. Finite element investigation of non-crimp fabric based composites. Dans *Proceedings of the 13th US National Congress on Applied Mechanics, Gainseville-Florida 21-26 June 1998*, page RB11, 1998.

17. S. Drapier, L. Léotoing, & A. Vautrin. Instabilities and scale effects in composites. Dans R.C. Batra et E.G. Henneke, éditeurs, *Proceedings of ASME 1999 Mechanics and Materials Conference, Blacksburg- Virginia 27-30 June 1999*, page 296, 1999.

18. L. Léotoing, S. Drapier, & A. Vautrin. Nonlinear interaction of geometrical and material properties in sandwich structures instabilities. Dans S.Kyriakides et N.Tirantafyllidis, editeurs, *Book of abstracts of the IUTAM symposium Material Instabilities and the Effect of Microstructure, Austin - Texas, May 7-11 2001*, page 15, 2001.

19. S. Drapier, L. Léotoing, & A. Vautrin. Global, local and interactive buckling in sandwich structures Dans B.H.V. Toping, éditeur, *Proceedings of Computational Structure Technology 2002 - Pragues 4-6 September 2002*, CST83.

Congrès internationaux avec actes

20. S. Drapier, J.-C. Grandidier, & M. Potier-Ferry. Non-linear numerical approach of microbuckling. Dans Composite Division Institute of Material, éditeur, *Proceedings of ECCM7 - Londres 14-16 mai 1996*, volume 2, pages 39–44. Woodhead Publishing Ltd, 1996.
21. S. Drapier, L. Daridon, & J.-C. Grandidier. Influence of some structural parameters on both theoretical and experimental compressive strength of laminates. Dans T. Massard & A. Vautrin, éditeurs, *Proceedings of ICCM12 - Paris 5-9 July 1999*, page 300 - ref 418 Cd-Rom, 1999.
22. S. Drapier and M.R. Wisnom. Investigation of the non-crimped fabrics compressive and interlaminar shear behaviours. Dans T. Massard & A. Vautrin, éditeurs, *Proceedings of ICCM12 - Paris 5-9 July 1999*, page 799 - ref 389 Cd-Rom, 1999.
23. L. Léotoing, S. Drapier, & A. Vautrin. Closed-form solution for local, global buckling in sandwich stuctures. Dans H.R. Meyer-Pienning & D. Zenkert, éditeurs, *Proceedings of Sandwich Construction 5 - Zurich 5-7 September 2000*, volume 1, pages 25–36. E-mas publishing, 2000.
24. L. Léotoing, S. Drapier, & A. Vautrin. Global, local and interactive buckling in sandwich structures Dans A.Cardon, éditeur, *Proceedings of ECCM10 - Bruges 3-7 June 2002* paper 433.
25. S. Drapier, A.Pagot, O.Elbouazzaoui, A. Vautrin, & P.Henrat. Assessment and prediction of the influence of the stitching density on the transverse permeability of NC2 multiaxial reinforcements Dans A.Cardon, éditeur, *Proceedings of ECCM10 - Bruges 3-7 June 2002* paper 281.

Congrés internationaux avec résumé seul

26. S. Drapier, J.-C. Grandidier, & M. Potier-Ferry. A microbuckling model for long fibre composites, with structural effects, material non-linearities and fibre waviness. Dans *Book of Abstracts of Stability and Bifurcation in Solids and Structures, ASME Mechanics and Materials conference - Baltimore 12-14 June 1996*, 1996.
27. S. Drapier, J.-C. Grandidier, & M. Potier-Ferry. Influence of structural effects on the compressive failure of composite materials. Dans *Proceedings of XIXth ICTAM, Kyoto 25-31 August 1996*, 1996.
28. S. Drapier, L. Léotoing, & A. Vautrin. Interactive buckling in sandwich structures. Dans *Proceedings of 4th Euromech Solid Mechanics Conference, Metz-France 26-30 June 2000, Metz-France*, page 265, 2000.
29. S. Drapier, L. Léotoing, & A. Vautrin. Influence of scale effects on the buckling of sandwich structures. Dans *Proceedings of XXth ICTAM, Chicago 27 August -1 September 2000,* page 78.
30. S. Drapier, J.-C. Grandidier, & M. Potier-Ferry. A structural approach of plastic microbuckling in long fibre composites. Dans *Proceedings of XXth ICTAM, Chicago 27 August -1 September 2000*, page 118.

F.3 Actes de congrés nationaux

31. S. Drapier, C. Gardin, J.-C. Grandidier, & M. Potier-Ferry. Comportement mécanique des structures composites en compression. Dans A.Vautrin, éditeur, publication AMAC, *Actes des JNC9, Saint-Étienne 22-24 novembre 1994*, pages 741–750, 1994.
32. S. Drapier, J.-C. Grandidier, & M. Potier-Ferry. Rupture en compression des composites à fibres longues et effet de structure. Dans J.M. Berthelot, éditeur, publication AMAC, *Acte des Journées Scientifiques et Techniques organisées par l'AMAC : Micromécanique et mécanismes de l'endommagement des composites, ENSAM PARIS 30-31 mai 1995*, volume 1995/4.
33. S. Drapier, C. Gardin, J.-C. Grandidier, & M. Potier-Ferry. Approche numérique non-linéaire du microflambage dans les composites. Dans L.Zilliox, éditeur, publication AUM,*Actes du 12ème Congrés Français de Mécanique AUM, Strasbourg 4-8 septembre 1995*, volume 1, pages 345–348. AUM, 1995.
34. S. Drapier, C. Gardin, J.-C. Grandidier, & M. Potier-Ferry. Effet de structure et microflambage des composites. Dans F. Léné, éditeur, Éditions Hermès, 1995. *Actes du Deuxième Colloque National en Calcul des Structures, Giens 16-19 mai 1995*, volume 1, pages 95–100.
35. S. Drapier, C. Gardin, J.-C. Grandidier, M. Potier-Ferry, & O. Rahier. Résistance en compression des stratifiés, une confrontation entre théorie et expériences. Dans Publication AMAC, *Actes des Journées Scientifiques et Techniques organisées par l'AMAC : Interaction Modèle Expériences dans les Composites, ONERA Châtillon 29 mai 1996*, 1996.
36. S. Drapier, C. Gardin, J.-C. Grandidier, & M. Potier-Ferry. Approche numérique non-linéaire du microflambage. Dans D.Baptiste et A.Vautrin, éditeur, publication AMAC, *Actes des JNC10, Paris 29-31 octobre 1996*, volume 2, pages 817–828.
37. L. Léotoing, S. Drapier, & A. Vautrin. Flambage et effets d'échelle dans les structures sandwich. Dans O.Allix, C.Cluzel, et J.Lamon, éditeurs, publication AMAC, *Actes des JNC12, Paris 15-17 Novembre 2000*, volume 1, pages 343–352.

F.4 Autres

Articles dans une lettre d'information

38. S. Drapier, J.-C. Grandidier, & M. Potier-Ferry. Comportement mécanique des structures composites en compression. *La lettre d'Apollor*, mars - avril(24), 1994.

Rapports Scientifiques / Rapports de contrat

39. S. Drapier & M.R. Wisnom. Non-crimped fabrics composites compressive strength F.E. modelling. Technical report, University of Bristol, Aerospace Engineering Dept., 1997. *64 pages, INFACS-Activity 3 report.*

40. S. Drapier & M.R. Wisnom. F.E. modelling of non-crimp fabric based composites interlaminar shear behaviour. Technical report, University of Bristol, Aerospace Engineering Dept., 1997. *64 pages, INFACS-Activity 3 report.*
41. S. Drapier & M.R. Wisnom. Fibre placement and structures (Infacs) - finite element modelling of non-crimped fabric composites. Technical report, University of Bristol, Aerospace Engineering Dept., 1997. *EPSRC contract report.*
42. S. Drapier. Commande de boîte de vitesse : modélisation du contact dans les câbles de commande et modélisation d'un actionneur électromagnétique. Rapport Technique, ENSM.SE, département Mécanique et Matériaux, 1999. *26 pages, Rapport d'étude*.
43. S. Drapier. Activités modélisation et caractérisation liées au projet Thématique Prioritaire - NC2. Rapport Technique, ENSM.SE, département Mécanique et Matériaux, 2001. *34 pages dans Rapport d'activité année 1 du programme Thématique Prioritaire NC2*.
44. S. Drapier. Activités modélisation et caractérisation liées au projet Thématique Prioritaire - NC2. Rapport Technique, ENSM.SE, département Mécanique et Matériaux, 2002. *27 pages dans Rapport d'activité année 2 du programme Thématique Prioritaire NC2*.
45. I. Gaied & S. Drapier. Étude des tricots élastomériques en grandes déformations. Rapport Technique, ENSM.SE, département Mécanique et Matériaux, 2002. *76 pages, Rapport de contrat Ganzoni France*.

Mémoires en vue de soutenance de diplômes

46. Conception d'un élément fini de microflambage. Université de Metz, juin 1993. *Rapport de DEA*.
47. Prévision de la résistance en compression des composites à fibres longues : approche structurelle du microflambage plastique. Université de Metz, septembre 1996. *Thèse de Doctorat de l'Université de Metz en Sciences pour l'ingénieur*.

Logiciel

48. Logiciel de calcul développé en Fortran pour les besoins des recherches sur les instabilités géométriques locales plastiques dans les composites à fibres longues, et comprenant :
    - formulation d'un élément fini 1 D $\frac{1}{2}$ (EF 1D + harmoniques 1D) en rotations modérées,
    - prise en compte du comportement non-linéaire matériau local, de type Ramberg-Osgood ou discret, et homogénéisation associée,
    - calculs de valeurs propres et détermination automatique par dichotomie des charges critiques,
    - pilotage adaptatif à longueur d'arc du problème non-linéaire (passage de points de rebroussements),
    - pré et post-traitement.

F.5 Synthèse

	→1996	1997	1998	1999	2000	2001	2002	Total
Revues int. avec CL	1	1	1	3		2	3(+ 1)	11 (+ 1 révisé)
Contrib. ouvrage				1				1
Congrés. int. *invités*	1		2	1		1	1	6
Congrés int. avec actes	2			2	1		2	7
Congrés int. résumés	1				3			4
Actes congrés nat.	6				1			7
Lettre d'information	1							1
Rapports techn./sci.		3		1		1	2	7

TAB. 6.6: Nombre de communications par année et par type.

Annexe 2 : Articles représentatifs

▷ **Annexe 2. 1** S. Drapier, C. Gardin, J.-C. Grandidier, & M. Potier-Ferry. Structure effect and microbuckling. *Comp. Sci. Technol.*, 56(7) :861–867, 1996.

▷ **Annexe 2. 2** S. Drapier, J.-C. Grandidier, & M. Potier-Ferry. Towards a numerical model of the compressive strength for long fibre composites. *Eur. J. Mech. A/Solids*, 18 :69–92, 1999.

▷ **Annexe 2. 3** S. Drapier, J.-C. Grandidier, & M. Potier-Ferry. A structural approach of plastic microbuckling in long fibre composites : comparison with theoretical and experimental results. *Int. J. Solids Struct.*, 38 :3877–3804, 2001.

▷ **Annexe 2. 4** S. Drapier & M.R. Wisnom. Finite-element investigation of the compressive strength of non-crimp-fabric-based composites. *Comp. Sci. Technol.*, 59(8) :1287–1297, 1999.

▷ **Annexe 2. 5** S. Drapier & M.R. Wisnom. A finite-element investigation of the interlaminar shear behaviour of non-crimp-fabric-based composites. *Comp. Sci. Technol.*, 59(16) :2351–2362, 1999.

▷ **Annexe 2. 6** L. Léotoing, S. Drapier, & A. Vautrin. First applications of a novel unified model for global and local buckling of sandwich columns. *Eur. J. Mech. A/Solids*, 21 :683–701, 2002.

▷ **Annexe 2. 7** L. Léotoing, S. Drapier, & A. Vautrin. Nonlinear interaction of geometrical and material properties in sandwich structures instabilities. *Int. J. Solids Struct.*, 39(13-14) :3717–3739, 2002.

▷ **Annexe 2. 8** L. Léotoing, S. Drapier, & A. Vautrin. Using new closed-form solutions to set up design rules and numerical investigations for global and local buckling of sandwich beams. *J. of Sand. Struct. and Mat.*, 2002. Accepté, *à paraître*.

▷ **Annexe 2. 9** L. Dufort, S. Drapier, & M. Grédiac. Closed-form solution for the cross-section warping in short beams under three-point bending. *Compos. Struct.*, 52(2) :233–246, 2001.

▷ **Annexe 2. 10** S. Drapier, A.Pagot, A. Vautrin, & P. Henrat. Influence of the stitching density on the transverse permeability of Non-Crimped New Concept (*NC2*) multiaxial reinforcements : measurements and predictions. *Comp. Sci. Technol.*, 62(15) :1979–1991, 2002.

- G -

Annexe 2. 1

S. Drapier, C. Gardin, J.-C. Grandidier, & M. Potier-Ferry.

Structure effect and microbuckling.

Comp. Sci. Technol. **, 56(7) :861–867, 1996.**

ELSEVIER

S0266-3538(96)00033-4

Composites Science and Technology **56** (1996) 861–867

0266-3538/96/$15.00

STRUCTURE EFFECT AND MICROBUCKLING

Sylvain Drapier, Catherine Gardin, Jean-Claude Grandidier & Michel Potier-Ferry*

Laboratoire de Physique et Mécanique des Matériaux, URA CNRS 1215, Institut Supérieur de Génie Mécanique et Productique, Université de Metz, Île du Saulcy, 57045 Metz Cedex 01, France

(Received 22 November 1994; accepted 6 October 1995)

Abstract

At the present time, it is clearly established that the compressive failure in the direction of fibers of a unidirectional ply is not intrinsic to the material but depends on the structure (stacking sequence, thickness of the ply and loading). This dependence can be explained by the appearance of fiber microbuckling. The purpose of this work is the 'exact' calculation of the microbuckling modes which may appear in the laminate. Unlike the local models from the literature, the complete microstructure of a laminate is represented and the modes are sought in the form of harmonics in the direction of fibers. The following parametric study clearly shows the effect of the ply thickness, the boundary conditions, the loading, the stacking sequence and the presence of damage, on the mode and on the critical strain of microbuckling. Moreover, these results lead to a very reliable homogenized model which gives the possibility of taking into account the effect of fiber alignment defects and the appearance of plasticity inside the matrix. © 1996 Elsevier Science Limited

Keywords: failure, compression, microbuckling, structure effect, 2-D models

1 PRESENTATION OF THE PROBLEM

Thirty years of intensive research has permitted us to understand and model the behaviour of composites, especially the behaviour of long-fiber laminates. However, some doubts still remain about the compressive behaviour and strength in the direction of fibers in the case of carbon/epoxy composites. The unidirectional ply presents both stiffness and strength losses in compression by comparison with traction. At the present time, there remain problems in experiments, modelling and understanding of phenomena.

1.1 The problem seen from the experimental side

From the experimental point of view, it seems difficult to measure the failure stress precisely with available compression devices; moreover it is not reasonable to dissociate the measured strengths from the tests used. On the other hand, the results of bending or bending–compression tests are less scattered and the devices used in different laboratories lead to similar values.[1–3] From these studies, it appears that the compressive failure strain of unidirectional ply composites depends on the stacking sequence of the specimen and on the loading, since the failure data are generally greater in bending or bending–compression than in pure compression. In brief, the failure data of unidirectional composites are not intrinsic to the material but depend on the structure (stacking sequence of the laminate and applied loading).

1.2 The problem seen from the modelling side

Initially, authors have tried to model the loss of strength that was observed in pure compression tests. The first model was proposed by Rosen;[4] in his opinion, this phenomenon is due to the appearance of a local instability process: fiber microbuckling. Using a model constituted by a superimposition of stiff and soft layers, he showed that when instability occurs, the stress is approximately equal to the effective shear modulus, G, in the plane of fibers. The comparison with the experimental data is not satisfying because the critical strains are markedly greater than the experimental failure strains. Following Rosen, authors have tried to decrease the critical load by taking into account initial fiber misalignments, physical matrix non-linearity and/or damage at the interface.[5–7]

Unlike Rosen, Budiansky[8] considered that the yield stress corresponds to the arising of a plastic instability in the matrix, which appears in the form of a shear band. This approach is based on the existence of an initial alignment defect which produces a shear stress inside the matrix. Some authors improved on this model by adding an elasto-plastic law[9] and fiber bending. The correlation between the predictions given by these models and the experimental failure stresses is good. However, some questions remain, because these models are local and cannot account for the structural effect that is established by the experiments (in particular, it is not possible to estimate the microbuckling wavelength). Conse-

* To whom correspondence should be addressed.

quently, previous results cannot be used as local failure criteria for laminates submitted, for example, to mixed compression–bending.

Thus, it is essential to integrate the influence of the mesoscopic scale into the model. The basic idea is that the instability (mode and critical load) which appears in a ply is influenced not only by the presence and the stiffness of neighbouring plies,[3,10] but also by the stress distribution. Different models[3,10,11] express naturally the critical microbuckling stress and the wavelength in the direction of fibers as explicit functions of the boundary conditions imposed at the mesoscopic scale. In these studies, the shape of the mode through-ply thickness is given *a priori*. In order to fill this gap, we have developed a numerical model where the complete microstructure of the laminate is discretized. Our objective is first to characterize correctly the microbuckling modes, and secondly to propose a homogenized model with the idea of introducing the effect of initial defects and matrix plasticity on the instability.

2 A MODEL TO COMPUTE THE EXACT MICROBUCKLING MODES OF THE COMPLETE MICROSTRUCTURE

2.1 A classical model of the microstructure

Because it is not possible to perform a parametric study by using classical tridimensional finite elements, the modes are sought in the (x_1,x_2) plane, where x_1 is the principal direction of loading (0°) and x_2 is the transverse direction through-the-thickness. The 0° plies are represented by a 2-D superimposition of stiff and soft layers (fiber/matrix), and their thickness is chosen according to the real microstructure. More precisely, the thickness of stiff layers is equal to the diameter of fibers, and the thickness of soft layers is chosen in order to obtain a laminate whose volume fraction of fibers, f, is the same as in the real ply. As for the 90° or 45° plies, they are represented by an equivalent homogeneous material, whose characteristics are calculated by use of the mixture rule. The constitutive laws of each material in this laminate are supposed linear, elastic and orthotropic (Fig. 1). The limit of stability of an equilibrium state is reached when the quadratic part of the potential energy, P_2, changes sign, that is to say when $\delta P_2 = 0$. In the framework of linear buckling, the quadratic part of the potential energy reduces to:

$$P_2 = -\lambda \int_{2\text{-D}} \gamma \mathbf{L}(x_2) \gamma_{\text{pre-buckling}} \mathrm{d}S + \frac{1}{2} \int_{2\text{-D}} \varepsilon \mathbf{L}(x_2) \varepsilon \mathrm{d}S \qquad (1)$$

where $2\varepsilon = {}^t\nabla\mathbf{u} + \nabla\mathbf{u}$ and $2\gamma = {}^t\nabla\mathbf{u}\cdot\nabla\mathbf{u}$ ($\mathbf{u}$ being the increment of displacement towards the equilibrium position). The term $\gamma_{\text{pre-buckling}}$ is the strain tensor at equilibrium and λ is the load parameter. Two different pre-loadings are considered in this study (Fig. 1): a pure compression state (constant strain through the thickness) and a bending loading (linear strain in the compression zone).

In the case of long-fiber laminates, the length of the specimen in the x_1 direction of fibers is much greater than the thickness in the x_2 direction. It is then possible to work within the context of cellular instabilities and search harmonic modes in the x_1 direction:

$$\begin{cases} u(x_1,x_2) = U(x_2)\cos kx_1 \\ v(x_1,x_2) = V(x_2)\sin kx_1 \end{cases} \qquad (2)$$

where k denotes the wavenumber and $U(x_2)$, $V(x_2)$ the amplitudes of the displacement field. The bifurcation criterion leads to a unidimensional eigenvalue problem, where each layer of the material represented in Fig. 1 is discretized only in its thickness. For each prescribed value of the wavenumber, the first eigenvalue, λ_c, is computed. The minimum of the neutral stability curve, $\lambda_c(k)$, corresponds to the critical load and the critical wavenumber of microbuckling.

2.2 Structure effect and microbuckling

2.2.1 Effect of the loading and the boundary conditions

The amplitudes $U(x_2)$ and $V(x_2)$ of the microbuckling mode are plotted in Fig. 2 in the case of a unidirectional ply whose characteristics are given in Table 1.

In Fig. 2(a), the stack is submitted to compression, and only the bottom face is clamped. A boundary layer is observed near the top face, concerning principally the amplitude U. Inside the ply, U is nearly periodic in x_2, and V is nearly linear in x_2. U is distinctly lower than V.

In Fig. 2(b), the top face is clamped too, which changes the shape of the mode. More precisely, the amplitude $V(x_2)$ is similar to the function $\sin(\pi x_2/\text{thickness})$. This result is in good agreement with the shape of the mode proposed by Grandidier.[3] But in the case where only the bottom face is clamped, Grandidier supposed the mode of the shape of $\sin(\pi x_2/2 \times \text{thickness})$, which is partly false. Indeed, the characteristic length in the clamped–free case is much greater than twice the thickness (see Fig. 2(a)).

A bending loading has also been considered and the corresponding microbuckling mode is represented in Fig. 2(c) (only the bottom face is clamped). This is a

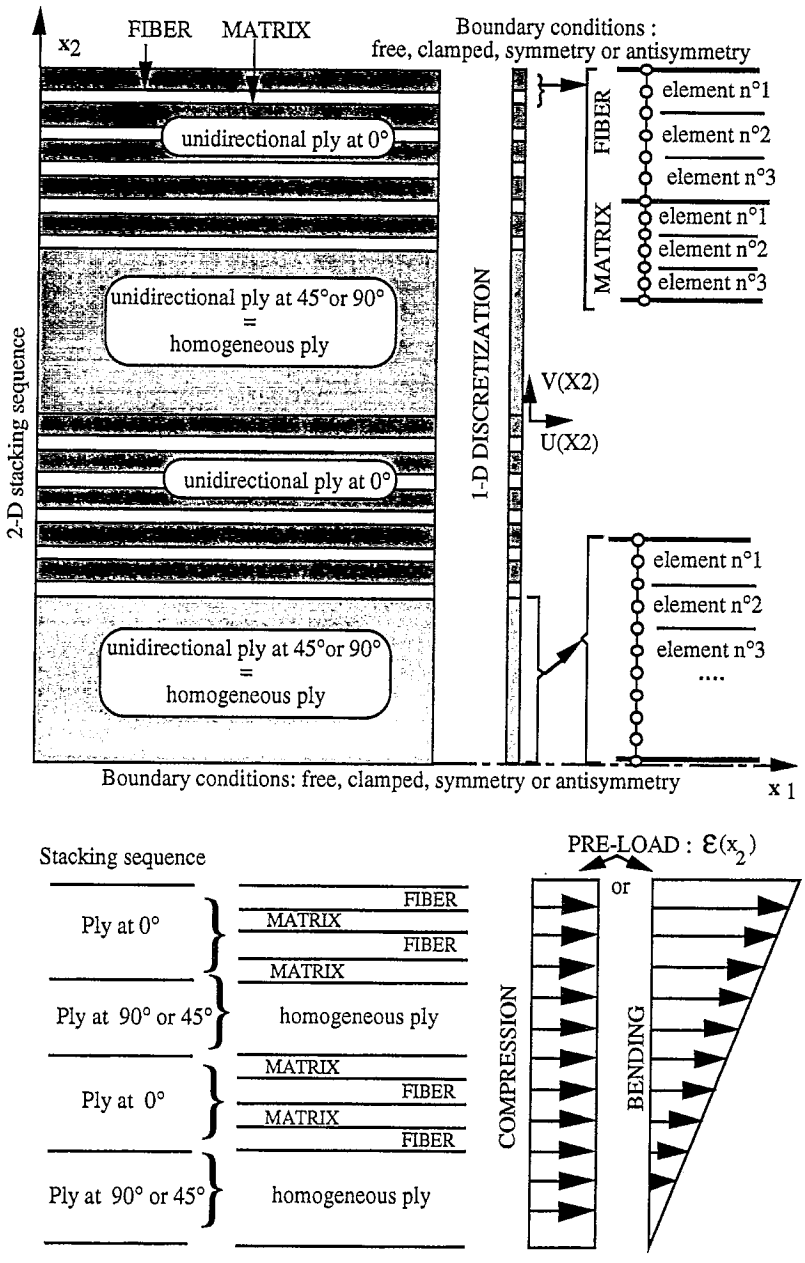

Fig. 1. Discretization of the complete 2-D microstructure and pre-buckling loading.

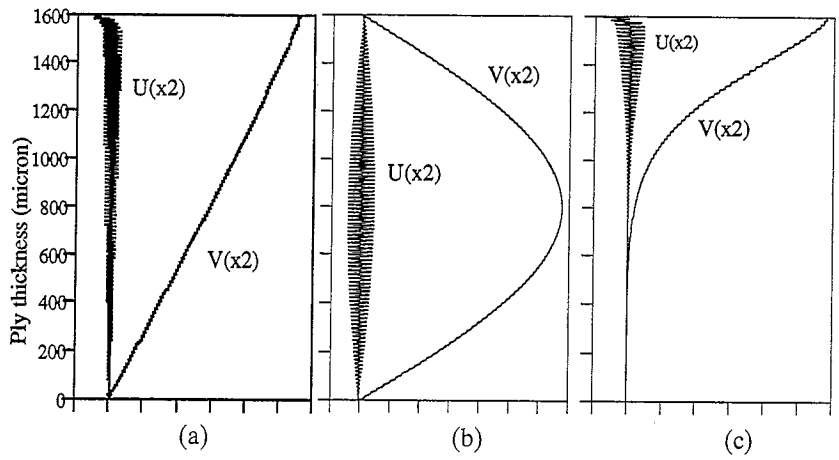

Fig. 2. Modal displacements for a 1600 μm thick UD, submitted to (a, b) compression, and (c) bending.

Table 1. Mechanical characteristics of the unidirectional ply

Isotropic matrix	Anisotropic fiber	
$E_M = 4{\cdot}5$ GPa	$E_f = 240$ GPa, $E_{tf} = 15$ GPa	Volume fraction, $f = 0{\cdot}625$
$G_M = 1{\cdot}6$ GPa	$G_f = 92$ GPa	Diameter of fibres, $d_f = 10\ \mu$m
$\nu_M = 0{\cdot}4$	$\nu_f = 0{\cdot}3$	Ply thickness, $h = 1600\ \mu$m

new result which, to our knowledge, has never been presented in the literature.

To each of these modes correspond a critical strain and a critical wavelength. These values are given in Table 2, which shows the effect of the boundary conditions and the loading. The critical strain of microbuckling is greater and the wavelength lower under bending than under pure compression.

2.2.2 Effect of the thickness

A whole series of computations has been performed on the same unidirectional composite (UD) with different thicknesses. It is evident from Fig. 3 that the critical strain and wavelength are strongly dependent on the ply thickness in both cases of boundary conditions. For any thickness, the critical strains are higher in the clamped–clamped case than in the clamped–free case.

It is clear that the boundary conditions have a great influence on the critical strain level when the ply thickness is small. But when the ply thickness is greater than 500 μm, the strains tend to the value given by Rosen's model[4] ($\varepsilon_{crit\ Rosen} = 2{\cdot}8\%$). Indeed, Rosen considers an infinite and perfectly periodic medium, and clearly shows that, sufficiently far from the faces and for large thicknesses, the displacement field is periodic (see Fig. 2). On the other hand, when the thickness decreases, the boundary conditions provide sizeable boundary layers, and the result is an increase in the critical strain. More precisely, the transverse strain, ε_{22} in the matrix plays a more and more important part when the thickness decreases. That is the reason why the critical strains increase and become different from the strain obtained by Rosen, who neglects the effect of the ε_{22} strain on the microbuckling. We note that this effect of the transverse strain on the microbuckling is taken into account in some models.[3,10,11]

2.2.3 Effect of the stacking sequence

Three different stacking sequences are considered: $[UD]_8$, $[90_4,0_4]$ and $[90,0]_4$ of T300/914. These three laminates have the same thickness and the same boundary conditions (free top face and clamped bottom face). The modal amplitudes are plotted in Fig. 4. It is noted that the 90° layers behave like elastic supports in the x_2 direction. According to this feature, microbuckling appears unexpectedly in plies within the laminate. On the other hand, these 90° plies make the axial displacement $u(x_1,x_2)$ concentrated in the 0° neighbouring plies. Also the critical strain is closely related to the thickness of the 0° ply nearest the free face. The critical strains are always greater under bending than under compression. From a qualitative point of view, this agrees with the experiment.

2.2.4 Effect of the mechanical characteristics of the matrix

A set of computations was performed with different mechanical characteristics of the matrix. It turns out that the critical strains decrease as the matrix stiffness (E_M and G_M) decreases as well. However, the variations of the critical strain and wavelength as a function of the ply thickness are similar in all cases of matrix characteristics. In the case of thick plies, all the critical strains tend to the value obtained by Rosen,[4] which decreases when G_M decreases as well.

The influence of an initial localized damage in the matrix was also studied. It turns out that the mode is very disturbed, and that in some particular situations such as superficial damages, the presence of damages can inhibit the effect of the stacking sequence. The critical strains depend not only on the number of localized damages but especially on their position. In the case of superficial damage, the critical strain can reach a value less than 1%. This result explains the external microbuckling that we observed on glass/epoxy specimens badly polymerized on their faces.

2.3 Discussion

A 2-D heterogeneous numerical simulation of linear buckling has permitted us to derive original microbuckling modes and to study the influence of many parameters (geometry, boundary conditions, stacking sequence and defects) on the instability. But

Table 2. Critical strain and wavelength of the unidirectional ply

	Compression, clamped bottom face	Compression, clamped bottom and top faces	Bending, clamped bottom face
Critical strain	0·028	0·030	0·033
Wavelength (μm)	654	427	390

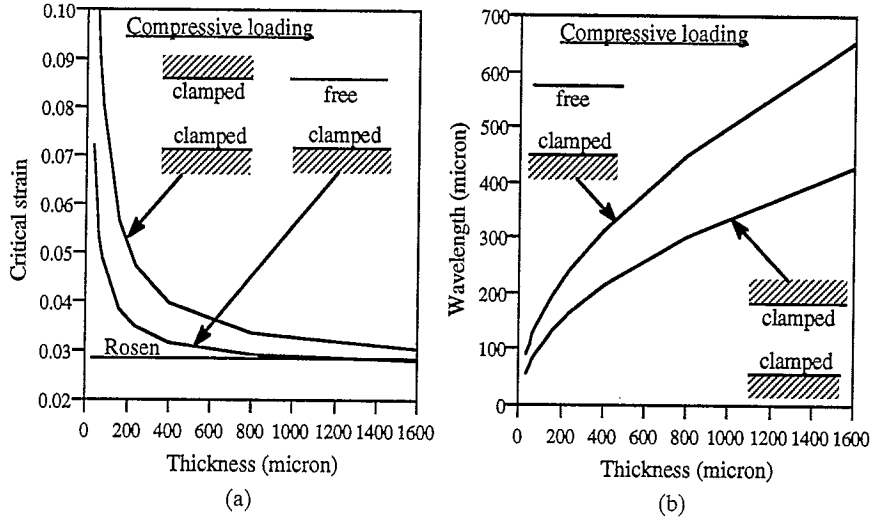

Fig. 3. Critical values versus thickness of the UD under compressive loading: (a) critical strains and (b) critical wavelengths.

the efficient prediction of the compressive failure of a real composite will only be possible by including the effect of fiber initial misalignment and the effect of the matrix non-linear behaviour (plasticity) in the microbuckling mechanism. As it is not reasonable to keep a complete description of the microstructure in the modelling of a real laminate, we propose a 2-D homogenized model developed from the previous analysis. It allows us to understand properly the structural effects and can easily be developed with the aim of integrating the effects of defects and plasticity.

3 A HOMOGENIZED MICROBUCKLING MODEL

3.1 Presentation of the homogenized model

After careful examination of the modal strains computed by complete discretization, we suppose, as a first approximation, the following:

- In the fiber, ε_{11} and S_{11} are quasi-linear in x_2, and the shear stress, S_{12}, is neglected in comparison with the main stress, S_{11}. Thus, the fiber is submitted to a bending–compression state and its displacement field is of the Bernoulli type. Consequently, it is classical to split up the strain energy into a bending energy plus a membrane energy.
- The strains are supposed constant in x_2 in the matrix and in the fiber (only for the membrane part) as well. So as a first approximation, the following identities are assumed:

$$\varepsilon_{11}^{\text{fiber}} \doteq \varepsilon_{11}^{\text{matrix}} = \langle \varepsilon_{11} \rangle = \frac{\partial u}{\partial x_1} \tag{3}$$

$$\varepsilon_{\alpha 2}^{\text{fiber}} = 0 \quad (\alpha = 1,2) \tag{4}$$

$$\langle \varepsilon_{\alpha 2} \rangle = \varepsilon_{\alpha 2}^{\text{matrix}}(1-f); \quad \langle \varepsilon_{22} \rangle = \frac{\partial v}{\partial x_2} \tag{5}$$

and

$$\langle \varepsilon_{12} \rangle = \frac{1}{2}\left(\frac{\partial u}{\partial x_2} + \frac{\partial v}{\partial x_1}\right)$$

The pre-load tensor is calculated by use of the mixture rule, but as the fiber stiffness is much greater than the matrix one, the pre-buckling stresses are neglected in the matrix. Accounting for all these

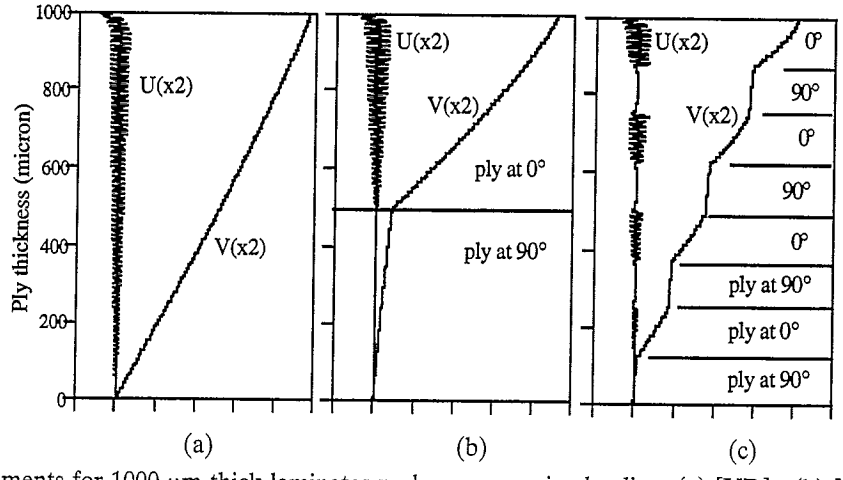

Fig. 4. Modal displacements for 1000 μm thick laminates under compressive loading: (a) $[UD]_s$, (b) $[90_4, 0_4]$ and (c) $[90,0]_4$.

results, the quadratic part of the homogenized potential energy is written as follows:

$$P_2 = \frac{1}{2}\int_{2\text{-D}} \langle\varepsilon\rangle \mathbf{L}_{\text{equiv}}^{\text{homog}} \langle\varepsilon\rangle \mathrm{d}S - \frac{1}{2}\int_{2\text{-D}} \lambda f E_f \varepsilon_{11}^{d}(x_2)\left(\frac{\partial^2 v}{\partial x_1^2}\right)^2 \mathrm{d}S + \frac{1}{2}\int_{2\text{-D}} f E_f r_{gf}^2 \left(\frac{\partial^2 v}{\partial x_1^2}\right)^2 \mathrm{d}S \quad (6)$$

where

$$r_{gf} = \sqrt{\frac{I_f}{S_f}}$$

and $\mathbf{L}_{\text{equiv}}^{\text{homog}}$ is the stiffness tensor of the homogeneous material equivalent to the UD ply. The term $\langle\varepsilon\rangle$ represents the mean microscopic strain tensor in the matrix, and the mean membrane strain tensor in the fiber. The bending energy developed by all the fibers is distributed in the 2-D domain.

3.2 Resolution of the stability equations in the case of a constant load through the thickness applied on a unidirectional ply

In the case of a UD ply submitted to pure compression, an analytical solution of the stability equations was obtained by dividing the problem into three parts: two problems in the boundary layers near the top and bottom faces, and the third inside the ply. The critical stress and the corresponding wavenumber are expressed as:

$$k_{\text{crit}} = \sqrt[4]{\frac{E_M}{(1-\nu_M^2)f(1-f)E_f}}\sqrt{\frac{\pi}{Hr_{gf}}} \quad (7)$$

and

$$\sigma_{\text{crit}}^{\text{fiber}} = \frac{G_M}{f(1-f)} + \sqrt{\frac{E_M E_f}{(1-\nu_M^2)f(1-f)}}\frac{\pi}{H}(2r_{gf}) \quad (8)$$

It is important to remark that the thickness, H, is a direct function of the boundary conditions imposed on the two faces of the ply. We have already introduced this characteristic length,[3] but now H can be derived analytically.

4 RESULTS AND COMPARISON BETWEEN THE TWO MODELS OF MICROBUCKLING

The results of the homogenized model are systematically in very good agreement with the results of the complete discretization, for any thickness and boundary conditions. As for the mode, the mean distribution of the displacement through the thickness is well represented by the homogenized model. The homogenized model describes correctly the distribution of the displacement in the boundary layer near the top face, although the thickness of the boundary layer is small in comparison with the heterogeneity size. The critical strains obtained by complete discretization and by the homogenized model are very close together for thick plies, while a slight difference is observed for thin plies (<200 μm). This is due to the presence of the boundary layer. The comparison between the wavelengths obtained by both models is excellent.

5 CONCLUSION

The results confirm the ideas that we have been defending for several years[3,12] and throw new light on the concept of microbuckling, which had not very much advanced since the work of Rosen[4] and Budiansky.[8] It is clear that microbuckling is a structural instability which strongly depends on the geometry of the laminate and on the loading through-the-thickness. With that kind of structural model, it becomes evident that the failure mechanism depends on the stacking sequence, on the thickness of the specimen or on the loading. This means that the idea of failure strain 'intrinsic to the material' must be given up, since on the one hand it is established that the failure yield depends on structural data, and on the other hand that the fiber strength estimated by Grandsire-Vinçon[1] is very high (failure strain from 3 to 4%), thus much greater than the strength of „to 4%), thus much greater than the strength of laminates (about 1% in compression, a little more than 2% in bending).

REFERENCES

1. Grandsire-Vinçon, I., Compression des composites unidirectionnels. Méthodes d'essais et approche micromécanique. PhD thesis, ENS Cachan, France, 1993.
2. Wisnom, M. R., The effect of specimen size on the bending strength of UD carbon fiber epoxy. *Comp. Struct.*, **18** (1991) 47–63.
3. Grandidier, J. C., Ferron, G. & Potier-Ferry, M., Microbuckling and strength in long fiber composites: Theory and experiments. *Int. J. Solids Struct.*, **29** (1992) 1753–1761.
4. Rosen, B. W., Mechanics of composite strenghtening. In *Fiber Composite Materials*, American Society for Metals, 1964.
5. Effendi, R. & Guedra-Degeorges, D., Étude expérimentale de la dégradation en compression des composites unidirectionnels fibre de carbone-matrice organique et simulation numérique associée. *Proc. 8th Journées Nationales sur les Composites,* Palaiseau, France, 1992, pp. 29–40.
6. Guynn, E. G., A parametric study of variables that affect fiber microbuckling initiation in composite laminates: Part I. Analyses. *J. Comp. Mater.*, **26** (1992) 1594–1616.
7. Wisnom, M. R., Analysis of shear instability in compression due to fibre waviness. *J. Reinf. Plast. Comp.*, **12** (1993) 1171–1189.
8. Budiansky, B., Micromechanics. *Computers and Structures*, **16** (1983) 3–12.

9. Budiansky, B. & Fleck, N. A., Compressive failure of fiber composites. *J. Mech. Phys. Solids*, **41** (1993) 183–211.
10. Swanson, S. R., A micro-mechanics model for in-situ compression strength of fiber composite laminates. *J. Engng Mater. Technol.*, **114** (1992) 8–12.
11. Schaffers, W. J., Buckling in fiber-reinforced elastomers. *Textile Res. J.* (1976) 502–512.
12. Gardin, C. & Potier-Ferry, M., Microflambage des fibres dans un matériau composite à fibres longues: Analyse asymptotique 2-D. *Compt. Rend. Acad. Sci. Paris*, **315** (1992) 1159–1164.

- H -

Annexe 2. 2

S. Drapier, J.-C. Grandidier, & M. Potier-Ferry.

Towards a numerical model of the compressive strength for long fibre composites.

Eur. J. Mech. A/Solids **, 18 :69–92, 1999.**

Eur. J. Mech. A/Solids 18 (1999) 69–92

Towards a numerical model of the compressive strength for long fibre composites

Sylvain Drapier [a]*, Jean-Claude Grandidier [b], Michel Potier-Ferry [c]

[a] *Département Mécanique et Matériaux, Centre de Sciences des Structures et des Matériaux, École Nationale Supérieure des Mines de Saint-Étienne, 158 cours Fauriel, 42023 Saint-Étienne cedex 2, France*
[b] *Laboratoire de Modélisation en Mécanique et Mathématiques Appliquées, SP2MI, Boulevard 3, Téléport 2, BP 179, 86960 Futuroscope cedex, France*
[c] *Laboratoire de Physique et Mécanique des Matériaux, URA CNRS 1215, Institut Supérieur de Génie Mécanique et Productique, Université de Metz, Ile du Saulcy, 57045 Metz cedex 01, France*

(Received 16 June 1997; revised and accepted 19 March 1998)

Abstract – The compressive failure of long fibre composites is tackled as a structural instability that is initiated by plastic microbuckling. A homogenised model is proposed to take into account the fibre initial waviness, the non-linear matrix behaviour and some structural effects. The problem is formulated at the ply scale by using a two-scale displacement field and a specific finite element is developed to reduce the extent of computations. This numerical tool permits us to rapidly determine the failure of various unidirectional ply configurations by use of a maximum load criterion. The results establish the influence of some structural parameters on the compressive failure strains, as has been observed in related experiments. They also explain the high compressive strength achieved under flexural loading. © Elsevier, Paris

long fibre composite / numerical model / compressive strength / structural instability / compressive failure

1. Introduction

The compressive strength of long fibre composites has given rise to numerous articles. It is now well established that failure in the fibre direction is initiated by fibre microbuckling, which leads in a catastrophic way to the emergence of a kink band. The main parameters influencing this mechanism are the matrix non-linear behaviour and the fibre initial waviness. The models proposed in the literature correctly take into account these two phenomena. Yet this local instability seems to be also strongly influenced by some structural parameters such as the stacking sequence, the gradient of longitudinal loading across the thickness and the ply thickness.

1.1. Microbuckling model

The first approach, presented by Rosen in 1964, showed that in an elastic framework the microbuckling stress is approximately equal to the composite shear modulus. Since this value is much greater than those experimentally observed, it became necessary to take into account the presence of fibre initial curvature and the matrix non-linear behaviour. Argon (1972) and later Budiansky (1983) estimated the load leading to the catastrophic emergence of a kink band in a fibre bundle having an initial inclination angle ϕ_0 with respect to the 0° loading axis. In this way, they established a failure criterion including the effects of both the imperfection

* Correspondence and reprints

and the matrix plasticity. In Budiansky's article (1983) the matrix is supposed to be elastic perfectly plastic, which results in the failure stress expression

$$\sigma_c = \frac{G}{1 + \frac{\phi_0}{\gamma_y}} \tag{1}$$

where γ_y is the composite shear yield strain and G its shear modulus.

Later, Budiansky and Fleck (1993) improved this expression by introducing a strain hardening law, and Fleck et al. (1995) added the fibre bending stiffness in the model. Recently, some micro-heterogeneous numerical modelling approaches have confirmed the influence of the *fibre imperfection* coupled with the *matrix non-linear behaviour* (Effendi, 1993; Fleck and Shu, 1995; Kyriakides et al., 1995) on the compressive strength.

1.2. Comparison with experiments

By adjusting some parameters such as the initial imperfection magnitude and the matrix constitutive law, the models discussed above yield strength values comparable to those measured with various pure compression devices. Nevertheless, failure values observed experimentally indicate that failure may also be influenced by the parameters at the component scale. For instance, Grandsire-Vinçon (1993) clearly showed that for UD plies the compressive strength depends at the same time on the type of loading prescribed and on the laminate stacking sequence (*figure 1*). The failure values are greater in bending than those measured under compression. In fact, this can be assigned to the gradient of longitudinal strain across the ply thickness (Grandidier et al., 1992; Wisnom, 1992, 1997). Moreover, Wisnom (1991) experimentally established that the strength under compression also depends on the ply thickness. These results bring to the fore the effects of the stacking sequence, the type of loading and the ply thickness on the compressive strength. The influence of these parameters will be grouped under the generic term *effect of the structure,* or similarly '*structural effects*'. It is one of the key elements of compressive failure, yet none of the models to date is able to properly account for this effect. Indeed, micromechanical models are basically only local ones whereas micro-heterogeneous models would induce prohibitive computation amounts.

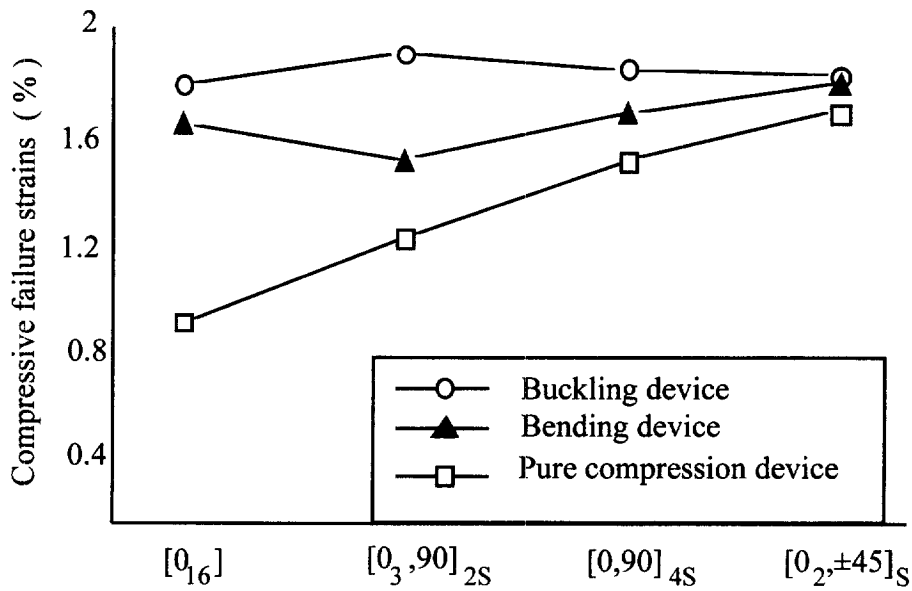

Figure 1. Ultimate compressive strain of an outer UD ply in a laminate versus stacking sequence and experimental device. The material is a carbon/epoxy T400/6376 (from Grandsire-Vinçon, 1993); —○— buckling device; —▲— bending device; —□— pure compression.

1.3. Models with structural effects

Following the previous remarks, the microbuckling approach must be carried out at the scale of the ply thickness, also referred to as the mesoscopic scale. Recent works (Grandidier and Potier-Ferry 1990; Grandidier et al. 1992; Gardin and Potier-Ferry 1992; Drapier et al. 1997) have shown that provided the mode is variable across the ply thickness and the fibre bending stiffness is taken into account, the structural effects appear naturally. The wavelength in the fibre direction and the critical compressive stress are then explicit functions of both the conditions on the ply boundaries and the ply thickness. Schaffers (1977) was the first to propose a model including both transverse shear effect and fibre bending by studying a fibre bundle. Swanson (1992) proposed a similar model, including fibre initial curvature. The solution obtained by the Rayleigh–Ritz method provided results which described pure compression test results quite well (Swanson and Colvin, 1993).

It is clear that in these structural models the characteristic transverse length plays a major role. Up to now, it was introduced in the solution which was sought as an analytical function that also depended on the ply thickness. Yet this evolution of the solution across the thicknes, which actually depends on structural parameters, was given a priori. This restriction has been removed by Drapier et al. (1996), who clearly established the influence of the ply thickness, the stacking sequence and the loading on elastic microbuckling. The present paper can be considered as an extension of that analysis in the plastic range in the presence of initial geometrical imperfections.

In the study conducted by Kyriakides et al. (1995), the entire microstructure is also discretised. By doing so, the influence of the material parameters and the effect of the structural parameters could be taken into account. However, the computation times required to solve these non-linear problems are very large because of the vast number of degrees of freedom. We shall establish that similar predictions of failure strains can be addressed with the help of a homogenised model.

In the present paper is introduced a numerical model able to predict the occurrence of fibre microbuckling, and thus provide the failure loads of long fibre composites with low computational cost. It provides a means of accounting for both fibre waviness and matrix non-linear behaviour. By comparison with the most complete models (Kyriakides et al., 1995) three kinds of simplification are made. First, the basic equations are those of a homogeneous continuous medium; but when introducing the fibre bending stiffness, the resulting equations look like those of a Cosserat medium (Cosserat and Cosserat, 1909). Secondly, the local character of the instability is taken into account by introducing kinematics with two scales. This finally enables us to apply a Ritz method in the fibre direction coupled with a finite element discretisation across the composite thickness. In the present article the numerical applications are limited to instabilities appearing in single plies. These first results explain qualitatively why the failure strain is not the same under bending as under compression, and how the latter also depends on the ply thickness. To complete this work, an extensive quantitative comparison with both existing models and experimental results will be presented.

2. Local formulation of the microbuckling problem

In this section, we introduce a non-linear microbuckling model wherein the effects of the initial waviness imperfection, of the matrix non-linearity and of the structure are taken into account. A formulation of the problem at the mesoscopic scale is established. Its advantage is to allow a simulation of the non-linear evolution of microbuckling at the ply scale with limited computational effort.

2.1. Formulation of the problem including imperfection and non-linear constitutive law

It is assumed that the microstructural behaviour can be represented by an equivalent homogeneous medium upon which is distributed the fibre bending energy. This modelling approach of the heterogeneous medium is

similar in idea to that proposed by Fleck and Shu (1995). These authors have used a Cosserat medium to predict the bidimensional development of a kink-band. Various justifications of this representation have been presented within a linear buckling analysis, (see Gardin and Potier-Ferry, 1992; Drapier et al., 1996).

As we aim to examine the effect of some structural parameters on plastic microbuckling only up to the onset of instability, it is assumed that the rotations in the medium remain moderate. On the other hand, many authors have established that the longitudinal loading gradient across the thickness and the ply thickness itself are two parameters which greatly influence the mechanism. Consequently, for this study we place ourselves in the general framework of a bidimensional problem expressed for plane stress in Lagrangian configuration.

In the following, the fibre direction is denoted $\mathbf{e}_1$, the transverse direction $\mathbf{e}_2$, and the corresponding displacement components are u and v. Stresses are represented with the aid of the second Piola–Kirchhoff tensor identified by $\mathbf{S}$. As far as strains are concerned, the Green–Lagrange tensor denoted by γ, corresponding to moderate rotations, is used. The medium equilibrium is satisfied via the principle of virtual works. The virtual displacement field is denoted by $\delta\mathbf{u}$, and the virtual strain tensor by $\delta\gamma(\mathbf{u})$. As has been mentioned, the microstructural behaviour is represented by an equivalent homogeneous medium upon which is distributed the fibre bending. In this framework, the virtual work of the internal efforts ($P_{\text{int}}(\delta\mathbf{u})$) is expressed in the following manner

$$P_{\text{int}}(\delta\mathbf{u}) = -\int_{\Omega}\left\{fm_f\frac{\delta\partial^2 v}{\partial x_1^2} + \mathbf{S}\cdot\delta\gamma\right\}d\Omega \tag{2}$$

The first term, where f is the fibre volume fraction, represents the virtual work developed by the internal efforts due to the fibre bending moment (m_f) that was previously distributed on the whole domain. The second term corresponds to the work developed by the in-plane internal efforts. It is assumed that the virtual work of the external efforts is a linear form, denoted by $< >$, of the virtual displacement field. Its expression is that of a classical medium

$$P_{\text{ext}}(\delta\mathbf{u}) = \langle\mathbf{F}, \delta\mathbf{u}\rangle \tag{3}$$

where vector $\mathbf{F}$ represents the set of efforts applied to the medium. Concerning the strain tensor, we have chosen to reduce the non-linear part to the only component in the fibre direction, for the other terms induce computation amounts that are too large in comparison with the limited additional accuracy they bring about

$$\gamma(\mathbf{u}) = \varepsilon(\mathbf{u}) + \gamma(\mathbf{u})^{\text{NL}} = \begin{pmatrix} \dfrac{\partial u}{\partial x_1} & \dfrac{1}{2}\left(\dfrac{\partial u}{\partial x_2} + \dfrac{\partial v}{\partial x_1}\right) \\ \dfrac{1}{2}\left(\dfrac{\partial u}{\partial x_2} + \dfrac{\partial v}{\partial x_1}\right) & \dfrac{\partial v}{\partial x_2} \end{pmatrix} + \begin{pmatrix} \dfrac{1}{2}\left(\dfrac{\partial v}{\partial x_1}\right)^2 & 0 \\ 0 & 0 \end{pmatrix} \tag{4}$$

In what follows, derivatives with respect to the fibre direction are denoted

$$(\,)' = \frac{\partial}{\partial x_1} \text{ and } (\,)'' = \frac{\partial^2}{\partial x_1^2}$$

In the presence of a geometric imperfection, represented by function $v_0(\mathbf{x})$ defining the 2-D distribution of initial fibre position, the Green–Lagrange strain tensor is expressed in the following manner

$$\gamma(\mathbf{u}) = \varepsilon(\mathbf{u}) + \gamma(\mathbf{u})^{\text{NL}} = \begin{pmatrix} \dfrac{\partial u}{\partial x_1} & \dfrac{1}{2}\left(\dfrac{\partial u}{\partial x_2} + \dfrac{\partial v}{\partial x_1}\right) \\ \dfrac{1}{2}\left(\dfrac{\partial u}{\partial x_2} + \dfrac{\partial v}{\partial x_1}\right) & \dfrac{\partial v}{\partial x_2} \end{pmatrix} + \begin{pmatrix} \dfrac{1}{2}\left(\dfrac{\partial v}{\partial x_1}\right)^2 + \dfrac{\partial v}{\partial x_1}\dfrac{\partial v_0}{\partial x_1} & 0 \\ 0 & 0 \end{pmatrix} \tag{5}$$

where v is now the fibre transverse displacement taken from the initial position defined by v_0. Using the symbol $\otimes$ for the tensorial product, the strain tensor is written

$$\gamma(\mathbf{u}) = \varepsilon(\mathbf{u}) + \gamma(\mathbf{u})_{11}^{\mathrm{NL}} \mathbf{e}_1 \otimes \mathbf{e}_1 \tag{6}$$

and the corresponding virtual strains are given by

$$\delta\gamma(\mathbf{u}) = \delta\varepsilon(\mathbf{u}) + (v' + v_0')\delta v' \mathbf{e}_1 \otimes \mathbf{e}_1 \tag{7}$$

The constitutive behaviour is modelled by a non-linear relation between homogenised stresses and strains. We use the following general expression

$$\mathbf{S}(\gamma) = \mathbf{L}(\gamma) \cdot \gamma \tag{8}$$

This relation is built by homogenising the matrix and fibre mechanical characteristics. Details of this operation are presented in Section 3.4 [see (45)]. To build this homogenised law we have chosen to represent the matrix behaviour by a non-linear isotropic law of 'deformation theory' type. This simplistic law does not account for some potential unloadings, but it was checked subsequently that the loading continuously increases in the matrix whereas unloadings take place only in the fibres. Moreover, this law is known to be more reliable for describing pure bifurcations in the plastic range (Hutchinson, 1974). So the constitutive modelling seems to be the best possible approach in the small imperfection case. According to the current practice in structural stability analysis, a flow theory could have been applied in the large imperfection case. As for the fibres, they are supposed to have an elastic linear behaviour, as it has been shown that taking into account the fibre non-linear behaviour would not affect the failure mechanism (Kyriakides et al., 1995). Consequently the bending moment distribution m_f is related to the curvatures by the following classical relation

$$m_f = E_f r_{gf}^2 v'' \tag{9}$$

where E_f is the Young's fibre modulus and r_{gf} its gyration radius (Gardin and Potier–Ferry, 1992).

Finally, the equilibrium in presence of fibre imperfection and for non-linear matrix behaviour is expressed as

$$-\int_\Omega \{f\, E_f r_{gf}^2 v'' \delta v'' + \mathbf{S}(\gamma) \cdot \delta\varepsilon + S_{11}(\gamma)\delta\gamma_{11}^{\mathrm{NL}}\} d\Omega + \langle \mathbf{F}, \delta\mathbf{u} \rangle = 0, \ \forall\, \delta\mathbf{u} \tag{10}$$

On the basis of this first formulation of the problem, it is possible to characterise the non-linear microbuckling development. However, this instability is a short wavelength phenomenon when compared to the macroscopic dimensions, and the discretisation of the problem as it is presented above would require too many degrees of freedom to enable a parametric study to be made. Consequently, it was chosen to formulate the microbuckling problem at the mesoscopic scale by introducing kinematics with two scales

2.2. Two scale kinematics

The solution of the microbuckling problem is sought under the form of a displacement evolving on the structural scale (denoted $\mathbf{u}_G$), *very locally modulated* by a displacement evolving at the ply scale (denoted $\mathbf{u}_L$) (*figure 2*)

$$\mathbf{u}(\mathbf{x}) = \mathbf{u}_G(\mathbf{x}) + \mathbf{u}_L(\mathbf{x}) \tag{11}$$

When introducing the displacement field (11) in the strain tensor (6), we get a new form of the strain tensor

$$\gamma(\mathbf{u}) = \varepsilon(\mathbf{u}_G) + \varepsilon(\mathbf{u}_L) + \gamma(\mathbf{u}_G + \mathbf{u}_L)_{11}^{\mathrm{NL}} \mathbf{e}_1 \otimes \mathbf{e}_1 \tag{12}$$

and the virtual strains from (7) are presented by

$$\delta\gamma(\mathbf{u}) = \delta\varepsilon(\mathbf{u}) + (v_G' + v_L' + v_0')\delta v' \mathbf{e}_1 \otimes \mathbf{e}_1 \tag{13}$$

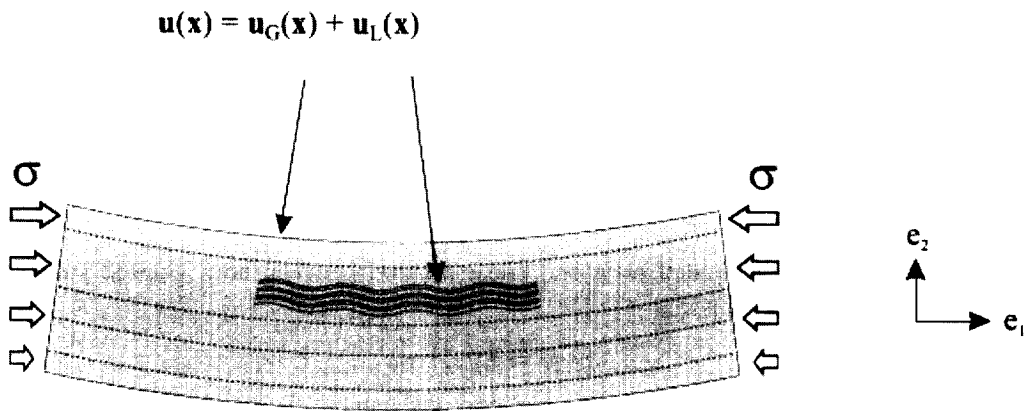

Figure 2. Scheme showing microbuckling in a ply under bending and associated displacement field.

Then the structure equilibrium is written as

$$\int_\Omega \{fE_f r_{gf}^2 v_G'' \delta v'' + fE_f r_{gf}^2 v_L'' \delta v'' + \mathbf{S}(\gamma) \cdot \delta\varepsilon + S_{11}(\gamma)(v_G' + v_L' + v_0')\delta v'\} d\Omega \\ -\langle \mathbf{F}, \delta\mathbf{u}\rangle = 0, \ \forall \delta\mathbf{u} \tag{14}$$

2.3. Mesoscopic formulation of the microbuckling problem

As has been experimentally shown by Paluch (1994), the fibre imperfection wavelength has the order of magnitude of the ply thickness. The structure being assumed perfect at the global scale, the only imperfections in this problem are the fibre curvatures which influence only the evolution of the local field. From this remark, we define the global equilibrium as the response of the structure without any imperfection where the local instability is disregarded. Hence the global field $\mathbf{u}_G$ is a solution of

$$\int_\Omega \{fE_f r_{gf}^2 v_G'' \delta v'' + \mathbf{S}(\gamma(\mathbf{u}_G)) \cdot \delta\varepsilon + S_{11}(\gamma(\mathbf{u}_G)) v_G' \delta v'\} d\Omega - \langle \mathbf{F}, \delta\mathbf{u}\rangle = 0, \ \forall \delta\mathbf{u} \tag{15}$$

The first term of this expression represents the virtual work of the fibre bending moments induced by a displacement field evolving at the global scale. In classical laminate theory, this effect is neglected and the global field can be computed by a classical finite element code.

Simultaneously, the equilibrium related to the overall displacement field (10) and the equilibrium related to the global displacement field (15) must be verified. Consequently the local displacement field is a solution of the following problem

$$\int_\Omega \{fE_f r_{gf}^2 v_L'' \delta v'' + [\mathbf{S}(\gamma) - \mathbf{S}(\gamma_G)] \cdot \delta\varepsilon + [S_{11}(\gamma)(v_G' + v_L' + v_0') - S_{11}(\gamma_G) v_G'] \delta v'\} d\Omega = 0, \ \forall \delta\mathbf{u} \tag{16}$$

obtained by making the difference (14)–(15) and where γ_G stands for $\gamma(\mathbf{u}_G)$.

We define the stress associated with the local microbuckling problem (denoted $\mathbf{S}_L$) as the difference between the total stress ($\mathbf{S}(\gamma)$) and the stress corresponding to the solution of the global equilibrium problem ($\mathbf{S}(\gamma_G)$)

$$\mathbf{S}_L(\gamma) = \mathbf{S}(\gamma) - \mathbf{S}(\gamma_G) \tag{17}$$

Then the local equilibrium (16) is expressed in the following manner

$$\int_\Omega \{fE_f r_{gf}^2 v_L'' \delta v'' + \mathbf{S}_L(\gamma) \cdot \delta\varepsilon + [S_{11}(\gamma_G)(v_L' + v_0') + S_{L11}(\gamma)(v_G' + v_L' + v_0')] \delta v'\} d\Omega = 0, \ \forall \delta\mathbf{u} \tag{18}$$

2.4. Assumptions

It is assumed that even if the structure is extensively deformed (bent), the global curvature remains much lower than that induced by the fibre microbuckling which was observed to be a very short wavelength phenomenon (see *figure 2*)

$$\begin{cases} v'_L \gg v'_G \\ v'_0 \gg v'_G \end{cases} \tag{19}$$

Then the local longitudinal stress term is approximated by

$$S_{L11}(\gamma)(v'_G + v'_L + v'_0) \approx S_{L11}(\gamma)(v'_L + v'_0) \tag{20}$$

Thanks to these assumptions, we can also express a new form of the strain tensor

$$\gamma(\mathbf{u}) = \varepsilon(\mathbf{u}_G) + \varepsilon(\mathbf{u}_L) + \left[\left(\frac{v'^2_G}{2}\right) + \left(\frac{v'^2_L}{2} + v'_L v'_0\right)\right]\mathbf{e}_1 \otimes \mathbf{e}_1 \tag{21}$$

which can be rewritten as follows

$$\gamma(\mathbf{u}) = \varepsilon(\mathbf{u}_G) + \gamma_G(\mathbf{u}_G)^{NL} + \varepsilon(\mathbf{u}_L) + \gamma_L(\mathbf{u}_L)^{NL} \tag{22}$$

or

$$\gamma(\mathbf{u}) = \gamma_G(\mathbf{u}_G) + \gamma_L(\mathbf{u}_L) \tag{23}$$

In what follows, the virtual displacement field is taken as the local displacement field variation ($\delta\mathbf{u}(\mathbf{x})$ is noted $\delta\mathbf{u}_L(\mathbf{x})$). When introducing these notations in the local equilibrium (18), and putting together the local stress terms, the problem to be solved is finally written under the form

$$\int_\Omega \{f E_f r_{gf}^2 v''_L \delta v''_L + \mathbf{S}_L(\gamma_G, \gamma_L) \cdot \delta\gamma_L + S_{11}(\gamma_G)(v'_L + v'_0)\delta v'_L\} d\Omega = 0, \ \forall\, \delta\mathbf{u}_L \tag{24}$$

The constitutive law associated with this local problem is given by

$$\left.\begin{aligned} \mathbf{S}(\gamma) &= \mathbf{L}(\gamma) \cdot \gamma \\ \mathbf{S}_L(\gamma_G, \gamma_L) &= \mathbf{S}(\gamma_G + \gamma_L) - \mathbf{S}(\gamma_G) \end{aligned}\right\} \tag{25}$$

We notice that in this formulation the external loading does not appear any more, and that it is sufficient to know the global displacement field $\mathbf{u}_G$ for the ply scale problem to be solvable. In what follows, the macroscopic displacement field corresponds to compression or bending–compression states. Moreover, when placed within the framework of cellular instabilities, as previously suggested in Drapier et al. (1996) the local problem can be solved in a reduced domain corresponding to a multiple of the wavelength because the effect of the boundary conditions in the fibre direction does not influence very much the local response of the medium. In order to solve the problem on the local scale, we use a numerical method of finite element type a description of which is presented in the following section.

3. Numerical description

In this part we describe the non-linear numerical features implemented to solve the local problem associated with microbuckling. First the incremental problem is formulated in displacement, and then a specific finite element is presented. The discretised problem is solved in a classical manner with an 'arc-length' method to deal with the limit points both in load and in displacement.

3.1. Prescribed loading

To simplify our approach, we assume that the global problem is solved and that the global strain tensor is restricted to only the longitudinal component, which is sufficient to represent bending and compression states

$$\gamma_G = \gamma_{G11}\mathbf{e}_1 \otimes \mathbf{e}_1 \tag{26}$$

The global stress tensor is related to the global strain tensor by the constitutive relation (8). It can also be assumed uniaxial since the transverse stiffness is very small when compared to the axial stiffness

$$\mathbf{S}(\gamma_{G11}) = \mathbf{e}_1 \otimes \mathbf{e}_1 \mathbf{L}_{1111}(\gamma_{G11})\gamma_{G11} \tag{27}$$

3.2. Literal formulation in displacement

To solve the non-linear geometrical and material problem, a classical iterative method associated with a Newton type linearisation is used. The loading is successively incremented and the solution of the corresponding equilibrium is sought from the linearised problem. The incrementation is introduced by a load parameter λ applied on the global strain prescribed in the fibre direction

$$\gamma_G = \gamma_{G11}(x_2)\mathbf{e}_1 \otimes \mathbf{e}_1 = \lambda\gamma_{11}^d(x_2)\mathbf{e}_1 \otimes \mathbf{e}_1 \tag{28}$$

The local problem to be solved, also called residual, is expressed in the form

$$\Psi(\mathbf{u}_L, \lambda; \delta\mathbf{u}_L) = \int_\Omega \{fE_f r_{gf}^2 v_L'' \delta v_L'' + \mathbf{S}_L(\gamma_G, \gamma_L) \cdot \delta\gamma_L\} d\Omega + \int_\Omega \{S_{11}(\gamma_G)(v_L' + v_0')\delta v_L'\} d\Omega \tag{29}$$

With a Newton linearisation, we shift from a steady state A defined by $(\mathbf{u}_L(A), \lambda_A)$, to a neighbouring steady state $(\mathbf{u}_L(B), \lambda_B)$ by the following relation

$$\Psi(\mathbf{u}_L(B), \lambda_B; \delta\mathbf{u}_L) = \Psi(\mathbf{u}_L(A), \lambda_A; \delta\mathbf{u}_L) + \frac{\partial\Psi(\mathbf{u}_L, \lambda; \delta\mathbf{u}_L)}{\partial u_L}_{|A} \Delta\mathbf{u}_L + \frac{\partial\Psi(\mathbf{u}_L, \lambda; \delta\mathbf{u}_L)}{\partial\lambda}_{|A} \Delta\lambda + \ldots \tag{30}$$

We respectively note the stiffness matrix and the right-hand side term of the incremental problem in the form

$$\left.\begin{aligned} \frac{\partial\Psi(\mathbf{u}_L, \lambda; \delta\mathbf{u}_L)}{\partial u_L}_{|A} \Delta\mathbf{u}_L &= k_t(\mathbf{u}_L(A), \lambda_A; \delta\mathbf{u}_L, \Delta\mathbf{u}_L) \\ \frac{\partial\Psi(\mathbf{u}_L, \lambda; \delta\mathbf{u}_L)}{\partial\lambda}_{|A} &= f_\lambda(\mathbf{u}_L(A); \delta\mathbf{u}_L) \end{aligned}\right\} \tag{31}$$

In our case, since the global displacement is fixed, only the local displacement can vary, i.e. $\Delta\gamma_G = 0$. The stiffness matrix and the right-hand side term are put in the form

$$\begin{aligned} &k_t(\mathbf{u}_L, \lambda; \delta\mathbf{u}_L, \Delta\mathbf{u}_L) \\ &\quad = \int_\Omega \{fE_f r_{gf}^2 \Delta v_L'' \delta v_L'' + \Delta[\mathbf{S}_L(\gamma_G, \gamma_L)] \cdot \delta\gamma_L + \mathbf{S}_L(\gamma_G, \gamma_L) \cdot \Delta(\delta\gamma_L) + S_{11}(\gamma_G)\Delta v_L' \delta v_L'\} d\Omega \end{aligned} \tag{32}$$

$$f_\lambda(\mathbf{u}_L; \delta\mathbf{u}_L) = \int_\Omega \left\{ \frac{\partial\mathbf{S}_L(\gamma_G, \gamma_L)}{\partial\lambda} \cdot \delta\gamma_L + \frac{\partial S_{11}(\gamma_{G11})}{\partial\lambda} (v_L' + v_0')\delta v_L' \right\} d\Omega \tag{33}$$

If $\mathbf{L}^T(\gamma)$ stands for the tangent constitutive law deduced from $\mathbf{L}(\gamma)$ the constitutive law of the equivalent homogeneous medium, the local stress increment and the right-hand side term are obtained by using (25)

$$\Delta[\mathbf{S}_L(\gamma_G, \gamma_L)] = \Delta[\mathbf{S}(\gamma_G + \gamma_L) - \mathbf{S}(\gamma_G)] = \frac{\partial\mathbf{S}(\gamma_G + \gamma_L)}{\partial\gamma} \cdot \Delta\gamma_L = \mathbf{L}^T(\gamma_G + \gamma_L) \cdot \Delta\gamma_L \tag{34}$$

$$\frac{\partial \mathbf{S}_L(\gamma_G,\gamma_L)}{\partial\lambda} = \frac{\partial \mathbf{L}(\gamma)}{\partial\gamma}\frac{\partial(\lambda\gamma_{11}^d(x_2)\mathbf{e}_1\otimes\mathbf{e}_1+\gamma_L)}{\partial\lambda} - \frac{\partial \mathbf{L}(\gamma_G)}{\partial\gamma_G}\frac{\partial(\lambda\gamma_{11}^d(x_2)\mathbf{e}_1\otimes\mathbf{e}_1)}{\partial\gamma} = \gamma_{11}^d(x_2)[\mathbf{L}^T(\gamma_G+\gamma_L)-\mathbf{L}^T(\gamma_G)]\,.\,\mathbf{e}_1\otimes\mathbf{e}_1 \tag{35}$$

$$\frac{\partial S_{11}(\gamma_G)}{\partial\lambda} = \frac{\partial S_{11}(\gamma_{G11})}{\partial\gamma_{G11}}\frac{\partial(\lambda\gamma_{11}^d(x_2)\mathbf{e}_1\otimes\mathbf{e}_1)}{\partial\lambda} = \mathbf{e}_1\otimes\mathbf{e}_1\,.\,\mathbf{L}^T(\gamma_{G11})\,.\,\mathbf{e}_1\otimes\mathbf{e}_1\gamma_{11}^d(x_2) \tag{36}$$

When introducing the intermediary calculations (34)–(36) and the constitutive law (25), the residual, the tangent stiffness and the right-hand side term are written

$$\Psi(\mathbf{u}_L,\lambda;\delta\mathbf{u}_L) = \int_\Omega \{fE_f r_{gf}^2 v_L''\delta v_L'' + \gamma_L\,.\,\mathbf{L}(\gamma_G+\gamma_L)\,.\,\delta\gamma_L\}d\Omega + \lambda\int_\Omega\{\gamma_{11}^d(x_2)[\mathbf{L}(\gamma_G+\gamma_L)\,.\,\delta\gamma_L - \mathbf{L}(\gamma_G)\,.\,\delta\varepsilon_L]\,.\,\mathbf{e}_1\otimes\mathbf{e}_1\}d\Omega$$

$$k_t(\mathbf{u}_L,\lambda;\delta\mathbf{u}_L,\Delta\mathbf{u}_L) = \int_\Omega\{fE_f r_{gf}^2\Delta v_L''\delta v_L'' + \Delta\gamma_L\,.\,\mathbf{L}^T(\gamma_G+\gamma_L)\,.\,\delta\gamma_L + \gamma_L\,.\,\mathbf{L}(\gamma_G+\gamma_L)\,.\,\mathbf{e}_1\otimes\mathbf{e}_1\Delta v_L'\delta v_L'\}d\Omega + \lambda\int_\Omega\{\gamma_{11}^d(x_2)\mathbf{e}_1\otimes\mathbf{e}_1\,.\,\mathbf{L}(\gamma_G+\gamma_L)\,.\,\mathbf{e}_1\otimes\mathbf{e}_1\Delta v_L'\delta v_L'\}d\Omega \tag{37}$$

$$f_\lambda(\mathbf{u}_L;\delta\mathbf{u}_L)\Delta\lambda = \Delta\lambda\int_\Omega\{\gamma_{11}^d(x_2)[\mathbf{L}^T(\gamma_G+\gamma_L)\,.\,\delta\gamma_L - \mathbf{L}^T(\gamma_G)\,.\,\delta\varepsilon_L]\,.\,\mathbf{e}_1\otimes\mathbf{e}_1\}d\Omega$$

3.3. Displacement approximation

The incremental problem being described, the displacement approximation used in the finite element solution remains to be decided. If a classical bidimensional discretisation were chosen several problems would be raised. The internal virtual work (2) is made up of two terms. The first represents the virtual work of the bending moments present in the fibres, and its approximation requires a Hermite type interpolation along the longitudinal direction. On the other hand, the second term representing the virtual work developed by the in-plane internal stresses can be approximated by a Lagrangian type interpolation. Therefore, the discretisation of (37) would require a non-classical Hermite–Lagrange finite element. That is why, by situating this in a cellular instability framework, it is proposed to combine a Ritz method in the fibre direction with a unidimensional finite element discretisation across the thickness. Therefore the displacement field approximation is chosen as the product of amplitudes in the ply thickness and Ritz basis functions in the fibre direction. This hypothesis of cellular instability also allows the mesoscopic domain Ω to be restrained to a wavelength in the fibre direction (*figure 3*). This reduces significantly the amount of computation required. The choice of the Ritz basis functions used in the displacement approximation is conditioned by the two following criteria. On the one hand, the displacement field must be able to reproduce the elastic microbuckling modes previously obtained with a basis made up of simple harmonics (Drapier et al., 1996). On the other hand, the latter must be completed to take into account the geometrical non-linearity. The new functions are sought as complementary harmonics that enable a quasi-constant buckling stress to be obtained in the fibres. Indeed, it is known that the post-buckling stress is nearly constant for slender structures. Finally, the displacement approximation suggested is

$$\mathbf{u}(\mathbf{x}) = \begin{cases} U_1(x_2)\cos(kx_1) + U_2(x_2)\sin(2kx_1) \\ V_1(x_2)\sin(kx_1) + V_2(x_2)\sin(3kx_1) \end{cases} \tag{38}$$

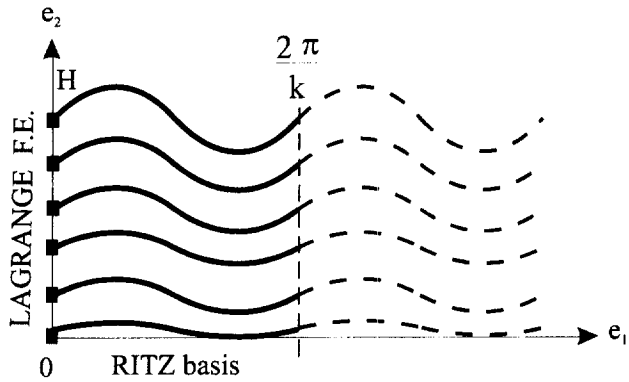

Figure 3. Reduced domain and displacement approximation.

where k is the wavenumber and $U_i(x_2)$, $V_i(x_2)$ are the displacement field amplitudes which are discretized with a classical interpolation. The interpolation functions of the element are Lagrangian in type; thus one element is made up of three nodes, that is to say twelve nodal amplitudes. Displacements are written as

$$\begin{cases} U_i(x_2) = N_1(x_2)q_{1i} + N_2(x_2)q_{3i} + N_3(x_2)q_{5i} \\ V_i(x_2) = N_1(x_2)q_{2i} + N_2(x_2)q_{4i} + N_3(x_2)q_{6i} \end{cases} \tag{39}$$

with $N_j(x_2)$ expressing the quadratic displacement interpolation functions and q_{ji} the nodal amplitudes.

It is assumed that the imperfection possesses a form similar to that of the displacement with a magnitude which can vary across the thickness. This choice can be justified by experimental measures achieved by Paluch (1994) on unidirectional composites. The latter author established that the imperfections measured can be assimilated to a simple sine wave for a percentage of fibres ranging from 42 to 85 % depending on their type. Moreover, it was determined that all the fibres were subject to a harmonic imperfection, but a single harmonic is not always sufficient to model it. In our case it will be taken as the combination of two sine waves, the wave numbers of which are k and $3k$ respectively

$$v_0(\mathbf{x}) = V_{01}(x_2)\sin(kx_1) + V_{02}(x_2)\sin(3kx_1) \tag{40}$$

In short, the imperfection is characterised by the wavenumber k and the magnitudes V_{01} and V_{02}.

The computation of the various integrals making up the tangent stiffness matrix, the residual and the right-hand side term is carried out by a Gauss integration technique. The displacement approximation is unidimensional, but as the constitutive law of the material is non-linear it is necessary to define a bidimensional distribution of Gauss points to account for the matrix plastic flow heterogeneities in the 2-D domain. In the fibre direction the number of divisions is chosen so as to correctly approximate the Ritz basis harmonic functions. This network of Gauss points can be built up by defining a bidimensional pseudo-mesh and pseudo-nodes, as shown in *figure 4.*

3.4. Taking the matrix plasticity into account

The last step in our approach consists of introducing the influence of the matrix plasticity and its coupling with the initial imperfection in the homogenised model. The non-linear behaviour can be introduced at two different levels, i.e. that of the ply or that of the microstructure. The first solution involves the homogenised values, and the constitutive law must be established for a unidirectional orthotropic ply. This requires significant experimental characterisation work. On the contrary, the second solution permits the change in the equivalent homogeneous medium to be taken into account by assuming an isotropic constitutive law only for the matrix. In counterpart, a further localisation/homogenisation process is required to relate the local and mesoscopic characteristics. First, in order to apply the local law the matrix strains must be deduced by localisation from the

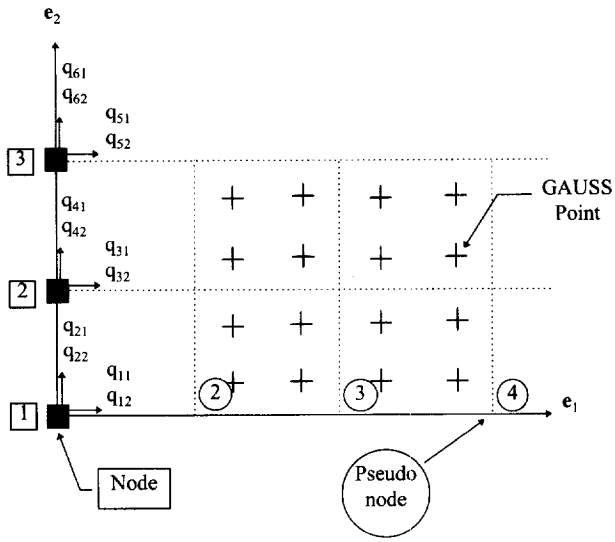

Figure 4. Microbuckling finite element.

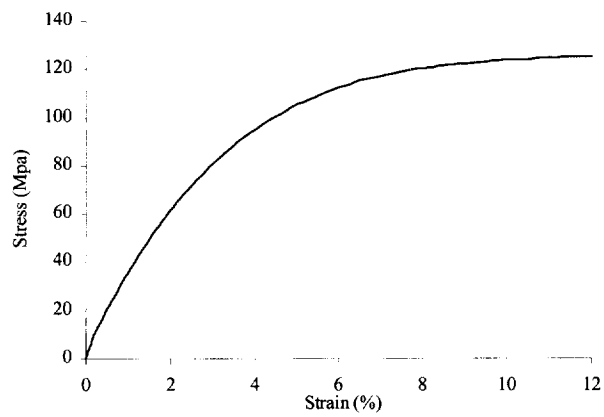

Figure 5. Resin 914 stress–strain law (from Wisnom, 1991).

mesoscopic strains. Second, the equivalent homogeneous medium behaviour must be updated by homogenisation to account for the change in the matrix mechanical characteristics. This second solution is chosen and the matrix behaviour is represented with a classical non-linear elastic constitutive law of 'J_2 deformation theory' type. The matrix behaviour is assumed to be isotropic, and using the indicial notation the secant law is presented under the form (see for instance Hutchinson, 1974)

$$\gamma_{ij}^m = \frac{1+\nu_m}{E_m} S_{ij}^m - \frac{\nu_m}{E_m} S_{kk}^m \delta_{ij} + \frac{h_2(J_2)}{E_m} s_{ij}^m \tag{41}$$

with E_m and ν_m which are respectively the Young's modulus and the Poisson's ratio of the matrix. The matrix stress tensor is $\mathbf{S}^m$, γ^m is the matrix strain tensor, $\mathbf{s}^m$ is the matrix stress deviator and J_2 its second invariant.

The strain-hardening function h_2 is classically related to the matrix secant modulus E_{ms} which can be obtained from a unixial tension test (*figure 5*)

$$h_2(J_2) = \frac{3}{2}\left(\frac{E_m}{E_{ms}} - 1\right) \tag{42}$$

To apply this constitutive law, it is necessary first to establish the matrix strains by localisation. We assume that at the microscopic scale the axial strain is the same in the two constituents, whereas both transverse and shear strains are mainly undergone by the matrix. These assumptions have been justified within a linear microbuckling framework by Drapier et al. (1996). On the grounds of these hypotheses, microscopic strains are related to macroscopic strains which are the sum of both global and local strains (23). Finally, the matrix strains, denoted by γ^m, can be written versus the loading and the local strains

$$\left.\begin{aligned} \gamma_{11}^m &= \lambda\gamma_{11}^d(x_2) + \gamma_{L11} \\ \gamma_{22}^m &= \frac{\gamma_{L22}}{1-f} \\ \gamma_{12}^m &= \frac{\gamma_{L12}}{1-f} \end{aligned}\right\} \tag{43}$$

When the matrix strains are known, the corresponding J_2 is solution of a scalar non-linear equation relating the strain deviator to the stress deviator via their second invariants

$$I_2 - \left(\frac{1+\nu_m+h_2(J_2)}{E_m}\right)^2 J_2 = 0 \quad \text{where } I_2 = \frac{1}{2}\left(\gamma_{ij}^m - \frac{1}{3}\gamma_{kk}^m\delta_{ij}\right)\left(\gamma_{ij}^m - \frac{1}{3}\gamma_{kk}^m\delta_{ij}\right) \tag{44}$$

This scalar equation is solved with a predictor–corrector scheme. From J_2 corresponding to the strain state, the new secant and tangent constitutive laws in plane stress case are then derived from (41). Using the rule of mixtures we deduce the secant and tangent laws of the equivalent homogeneous medium. The expression of the secant law is (45)

$$\begin{Bmatrix} S_{11}^m \\ S_{22}^m \\ S_{12}^m \end{Bmatrix} = \begin{bmatrix} fE_f + (1-f)\dfrac{E_{ms}(J_2)}{1-\nu_m^2} & \dfrac{E_{ms}(J_2)\nu_m}{1-\nu_m^2} & 0 \\ \dfrac{E_{ms}(J_2)\nu_m}{1-\nu_m^2} & \dfrac{E_{ms}(J_2)}{(1-f)(1-\nu_m^2)} & 0 \\ 0 & 0 & \dfrac{G_{ms}(J_2)}{1-f} \end{bmatrix} \cdot \begin{Bmatrix} \gamma_{11}^m \\ \gamma_{22}^m \\ \gamma_{12}^m \end{Bmatrix} \tag{45}$$

The tangent constitutive law includes the stress deviator tensor derivative and its expression is rather intricate. Hence we have chosen to establish it with a formal calculation code.

The shear behaviour of the equivalent homogeneous medium is essential in predicting the compressive strength. To accurately represent this non-linear shear behaviour, a 3-D homogenisation calculation should be carried out on a repeating cell at the constituent level. That is to say, a complementary FE calculation should be required at every Gauss point for each update of the constitutive law. However, as everything so far has been done to address the maximum efficiency of our numerical approach, we cannot include such a prohibitive additional calculation therein.

Therefore we will use the simple law derived from the homogenisation of the elastic characteristics (45). In *figure 6* the pure shear response of the equivalent homogeneous medium can be compared with an experimental response for a T300/914 UD ply with the same fibre volume fraction (60 %). The authors realise that the response obtained from (45) underestimates the shear stiffness for shear strains $< 2.3\,\%$, and overestimates it for strains $> 2.3\,\%$. But the relative discrepancy in terms of stresses ranges from $-7\,\%$ up to $22\,\%$ for a $4\,\%$ shear strain. Therefore this representation is thought to be accurate enough for carrying out the qualitative comparison which is the target of this paper.

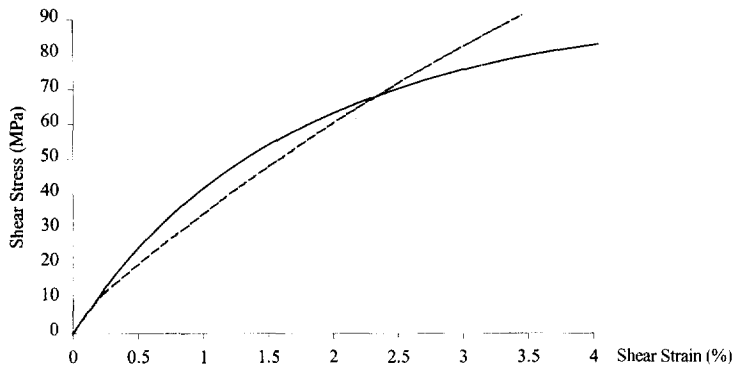

Figure 6. Pure shear stress–strain laws for a T300/914 UD ply: (—) experimental approach from Ditcher (1981) and (- - -) solution used in the present paper.

4. Results

With this numerical approach the response of a unidirectional carbon epoxy ply has been studied. We wish to demonstrate the ability of the model to explain the structural effects. The imperfection has a fixed wavelength equal to 200 $\pi\mu m$, its magnitude is constant through the thickness and is equal to 1 μm when not specified. The mechanical properties employed correspond to a T300/914 composite (*table I*), and the non-linear matrix constitutive law is given in Wisnom (1991) (*figure 5*). As introduced in Grandidier and Potier-Ferry (1990) and Swanson (1992), the position of the ply across the laminate thickness is taken into account with boundary conditions prescribed on its faces which represent, if necessary, the displacement prevented by adjacent plies.

Table I. Mechanical characteristics for a UD carbon-epoxy T300/914.

Isotropic matrix	Anisotropic fibre	
$E_M = 4.5$ GPa	$E_{1f} = 240$ GPa, $E_{2f} = 15$ GPa	Fibre volume fraction: $f = 0.625$
$G_M = 1.6$ GPa	$G_f = 92$ GPa	Fibre diameter: $d_f = 10$ μm
$\nu_M = 0.4$	$\nu_f = 0.3$	

The mesh consists of a regular subdivision of the domain independent of the constituent size, for the formulation is a homogenised one. For the set of results presented in this section, the choice of a regular mesh across the thickness might be debatable when the ply is located near the face of the laminate. In this case, near the free face a limit layer appears which would require a more refined mesh. But many tests have shown that both the limit strain and stress are correctly approximated when the domain is subdivided into twelve divisions in the fibre direction and twenty elements in the ply thickness (*figure 7*). This mesh represents in total 273 pseudo-nodes for 164 degrees of freedom. The computation times are in the order of a few minutes to establish the complete response of a ply, and < 1 minute to predict its failure strain.

4.1. Effect of plasticity and imperfection

The first computations concern a relatively thick layer (1.6 mm) under pure compression loading, in which case structural effects are limited. The goal is to validate the simplified model that has been developed. In a linear elastic framework the responses of unidirectional plies with different waviness amplitudes were computed. With a sufficiently small amplitude of the initial geometrical imperfection, we were able to find the modes as well as the critical strains and wavelengths which were established in Drapier et al. (1996). When the imperfection

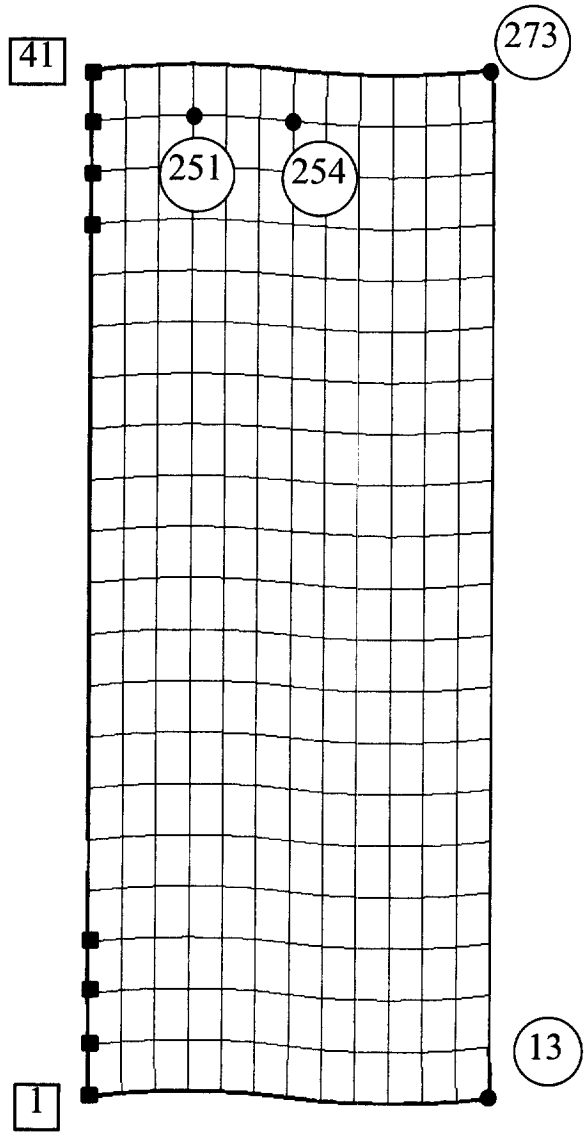

Figure 7. Mesh of 12 subdivisions in the fibre direction and 20 elements across the ply thickness. Initial imperfection 1 μm $\times$ 100 to be visible on this 1.6 mm-thick ply.

magnitude increased, a drop in ply stiffness could be observed, as seen in *figure 8*. These results validate the assumptions on the geometrical non-linearities and on the displacement field.

Next this imperfection was coupled with the non-linear behaviour of the matrix. This led to the occurrence of a sharp limit point especially for small imperfections (*figure 9*). This limit point is determined by the sign change of one of the stiffness matrix pivots and can be associated with the catastrophic character of the failure observed experimentally for these materials (Effendi, 1993). The responses presented in *figure 9* are similar to the calculations made by Kyriakides et al. (1995), who proposed a complete micro-heterogeneous modelling.

On the other hand, we have determined that the matrix plastic flow is mainly due to the shear induced by the fibre bending. In *figure 10*, one can observe the strong connection between the bending which is large at

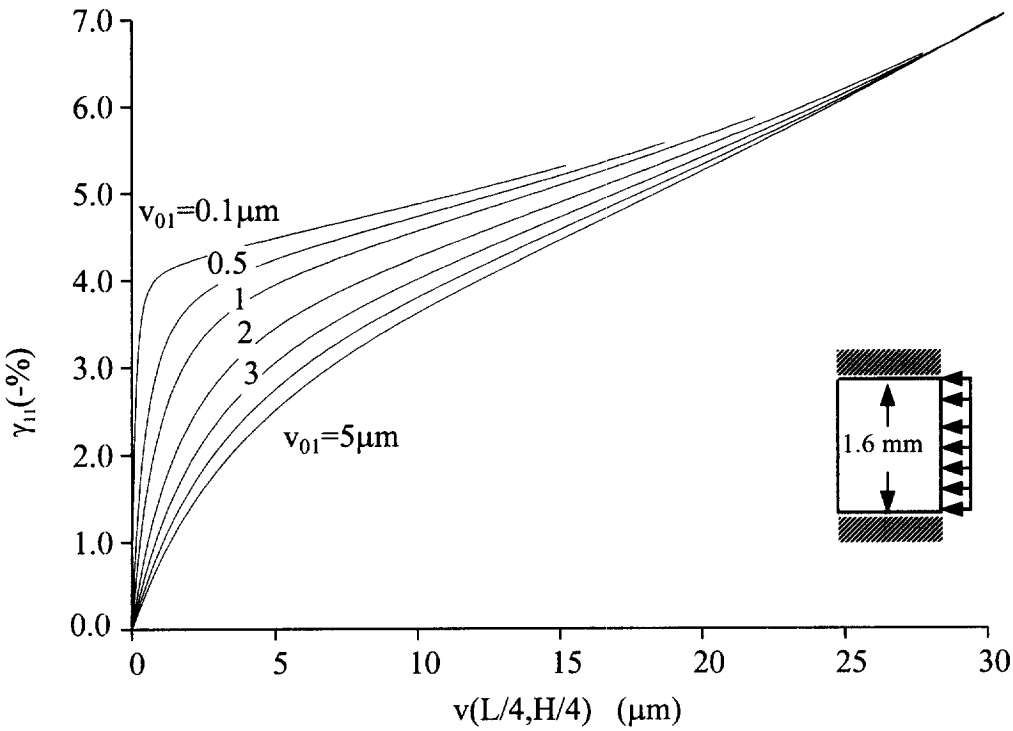

Figure 8. Prescribed strain versus a point displacement of the ply for an imperfection ranging from 0.1–5 μm. Elastic matrix behaviour; compression loading, clamped–clamped faces.

the waviness maximum curvature location (pseudo-node 251), and the shear induced at the waviness maximum slope location (pseudo-node 254). In this figure it is clear that when increasing the load, the matrix plastic flow develops in 254; meanwhile, the fibre bending increases in 251. When approaching the limit load (1.176%), a sharp increase in the equivalent stress in the matrix takes place which is accompanied by a decrease in fibre bending. This shows that fibre instability occurs due to the sharp decrease in the matrix shear modulus induced by the occurrence of plastic flow. This stage corresponds to the lower slope in the response prior to the limit load occurrence (*figure 9*). This mechanism keeps on developing and results in such a low overall stiffness that a decrease in both stress and loading (strain) is required in order to reach a new equilibrium. It corresponds to the cusp-like shape of the response in *figure 9* exhibited for the smallest imperfections. For larger waviness amplitudes, the mechanism leads to a more gradual decrease in the overall stiffness induced by a balance developing between the fibre bending and the change in matrix properties, as can be seen in the responses in *figure 9*.

Our model does not allow an accurate description of the stages following the occurrence of fibre microbuckling which correspond to the development of kink-bands. Some studies have been devoted to this specific stage of kink-band development (Fleck et al. 1995; Kyriakides et al., 1995). As for our model, the hypotheses of moderate rotations along with the J_2 deformation theory do not permit any localisation/rotation to be accounted for which is necessary to the kink-band formation modelling. But this is consistent with the present approach which mainly aims at predicting the limit load and hence failure with the lowest computational effort in order to analyse the effect of some structural parameters on the compressive strength.

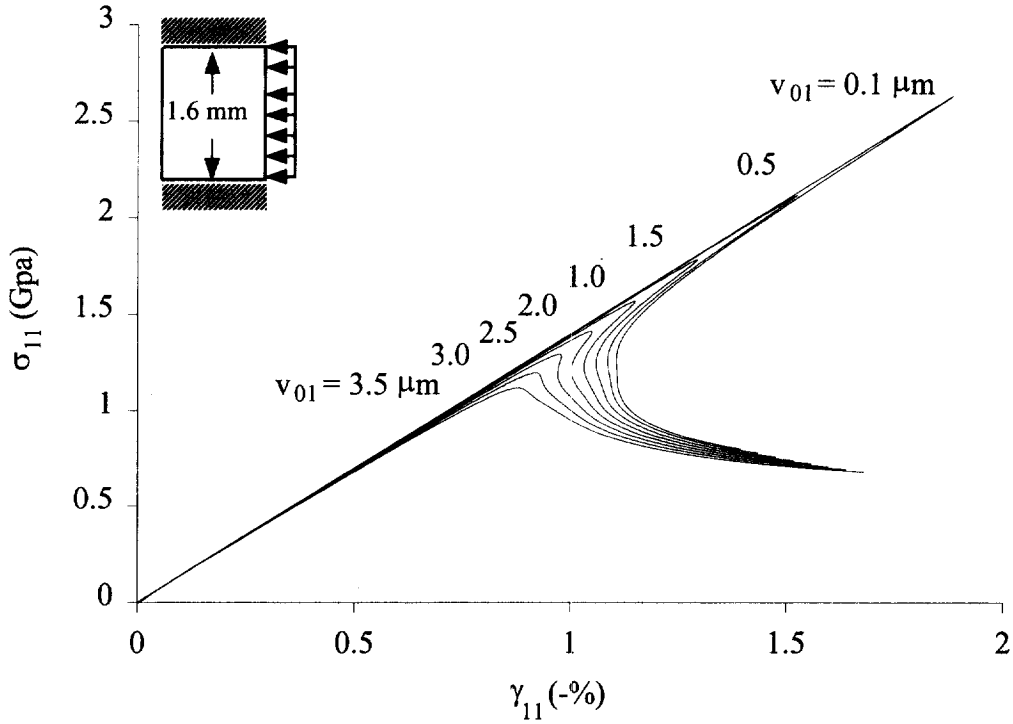

Figure 9. Mean stress in the fibre direction versus loading. The imperfection magnitude v_{01} ranges from 0.1–3.5 μm. Plastic matrix behaviour; compression loading, clamped–clamped faces.

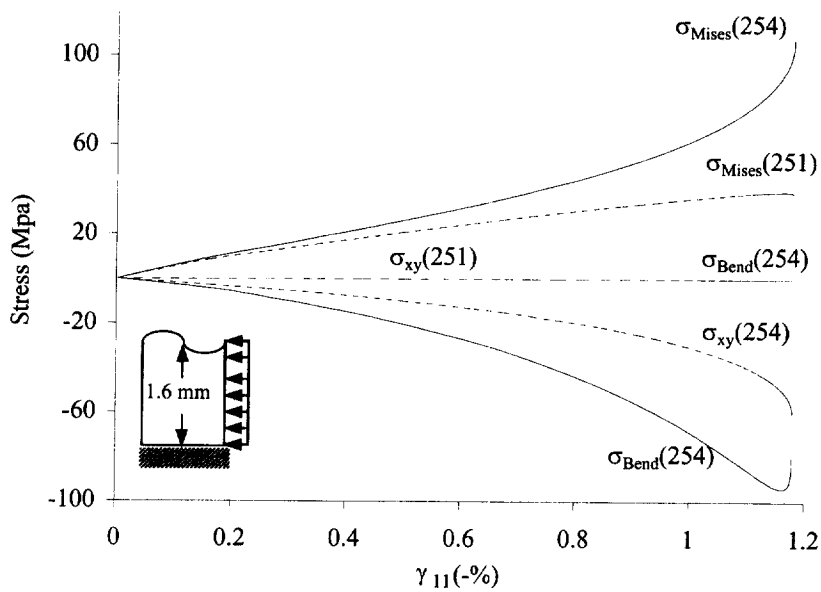

Figure 10. Bending, shear and von Mises matrix stresses and fibre bending stress versus loading up to the limit point for pseudo-nodes 251 and 254.

4.2. Structural effects

In this part, the influence of the ply structure on the development of plastic microbuckling and on the critical load has been discussed. A ply with a fixed thickness of 1.6 mm is discretised across its thickness and the interaction of neighbouring plies is represented by the boundary conditions prescribed on its faces (as proposed by Grandidier and Potier-Ferry (1990) and Swanson (1992)). Two cases are investigated. In the first, the ply is located inside the laminate and the displacements on its faces can be assumed to be restrained by the transverse contiguous plies. In the second case the ply is located on the laminate surface and only one face must verify some null displacements conditions, whereas the other face is free.

4.2.1. Boundary conditions

Whatever the boundary conditions, the basic mechanism is similar to that presented in the previous Section. The strong connection between fibre bending and matrix shear can still be observed, but the process development is heterogeneous across the thickness and it largely depends on the boundary conditions. In the case of a ply located on the laminate surface, a stress gradient appears close the free face (*figure 11*) and within the ply the stress field decreases progressively when coming near the clamped face. These results confirm those of Drapier et al. (1997) and the limit layer is similar to that obtained in the microbuckling modes detailed in Drapier et al. (1996). This region is strongly loaded (see also Drapier et al., 1997) and it tends to prematurely weaken the whole ply strength. We can associate these results with the experimental observations of fibre bundles in which microbuckling leads to superficial debonding (Grandidier et al., 1992).

When the ply is within a laminate, the microbuckling evolves in the middle of the ply (*figure 12*). Stresses are maximum in this region and decrease near the clamped faces. The stress distribution in the ply is very different from the previous case, and the support provided by the neighbouring plies stiffens the structure and delays the development of plasticity. Consequently the maximum stress withstood depends on the boundary conditions prescribed and for the reasons given above, this value is greater in the case where both faces are clamped. This new result explains the high failure stresses observed experimentally when the unidirectional ply is enclosed between cross-plies (Sigety, 1996) and also the influence of the stacking sequence observed by Grandsire-Vinçon (1993) and Colvin and Swanson (1993).

4.2.2. Type of loading

A bending-compression load was also considered which represents half a UD under pure bending. This loading is characterised by a linear load distribution across the thickness that is zero on the bottom face. Many simulations show that whatever the boundary conditions considered, microbuckling evolves in a domain that is more reduced than in the compression load case. The bottom part is almost not loaded, and can provide an effective support to the top part which is strongly loaded (*figure 13*). Therefore the ply strength is increased. This result provides a plausible explanation for the high strength observed during bending experiments carried out by Grandidier et al. (1993), Wisnom (1992) and Grandsire-Vinçon (1993) for instance. The boundary conditions effect is also more pronounced. Indeed, if the top face is clamped the support of the neighbouring ply prevents microbuckling, though this region is highly loaded. On the contrary, if the top face is free the limit layer effect is increased by the bending loading. Consequently the difference in strength between the clamped–clamped and clamped–free cases is more important under a bending loading.

4.2.3. Thickness

Some plies with different thicknesses were also analysed. It was established that the ply strength is greater when its thickness decreases, and the effect of the boundary conditions and of the loading type is as much

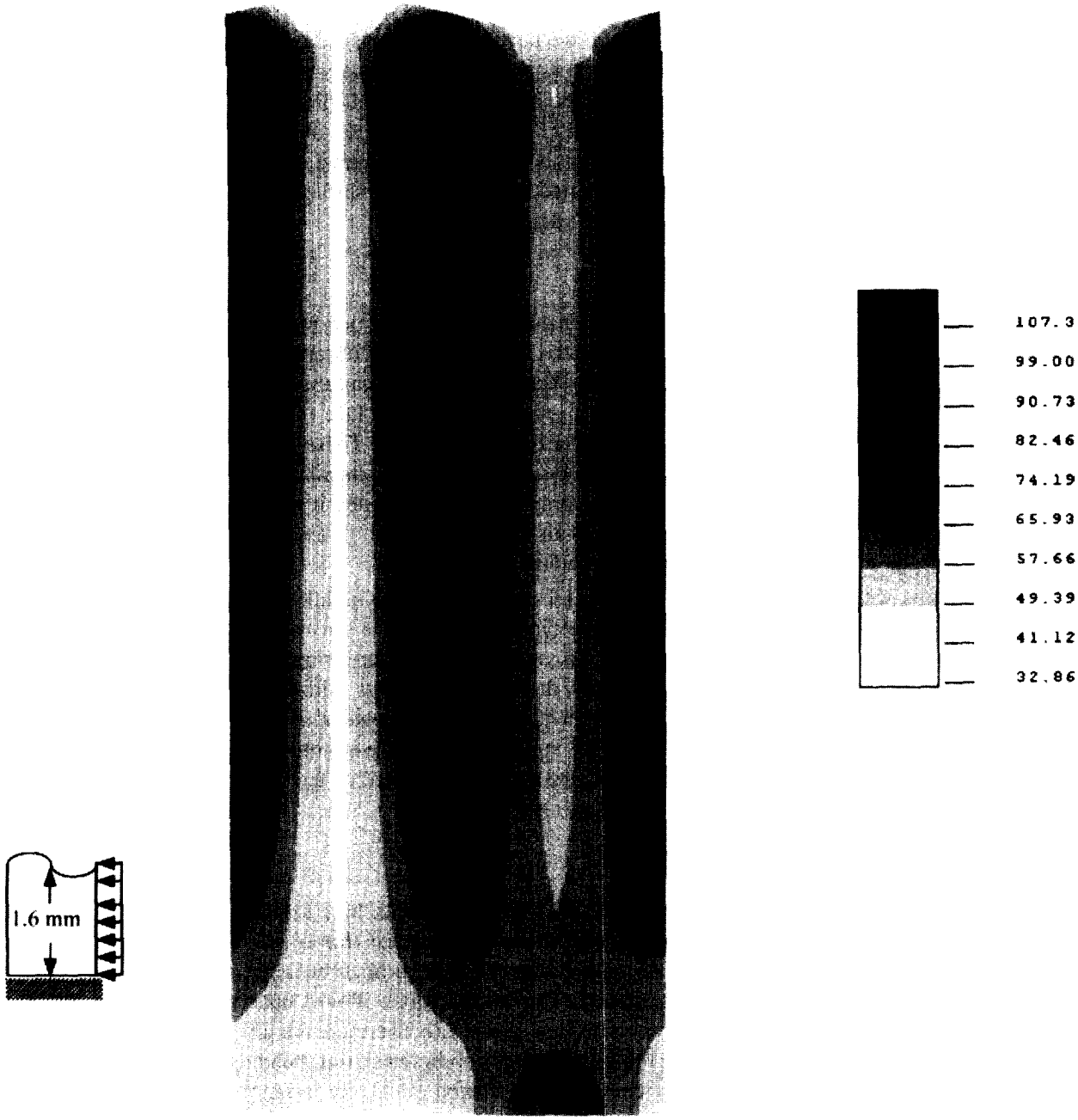

Figure 11. Von Mises matrix stress distribution (MPa) at maximum strain (–1.18 %). Pure compression loading, clamped-free boundary conditions. Deformed shape*10.

pronounced (*figure 14*). The stress distributions in the ply are very different in the case of a thick and a thin ply. For instance, for a 1.6 mm thick ply with both faces clamped, the maximum stresses are localised in the mid-zone (*figure 12*). On the contrary, for a similar ply 0.4 mm thick, the maximum stresses are located near the clamped faces (*figure 15*). It is the same for the limit layer present in a free-face case: when the

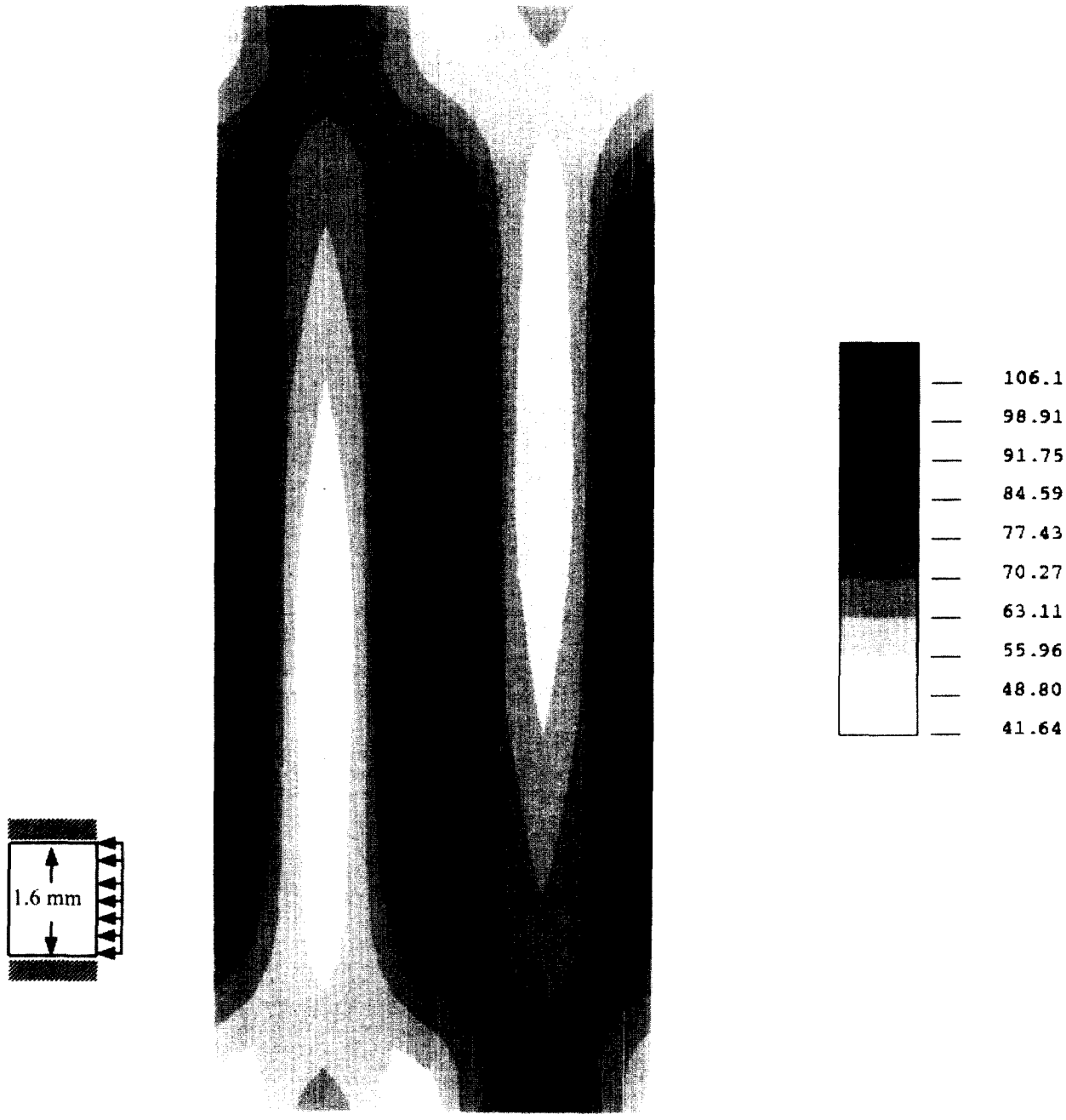

Figure 12. Von Mises matrix stress distribution (MPa) at maximum strain (−1.29 %).
Pure compression loading, clamped–clamped boundary conditions. Deformed shape*10.

ply becomes thin, this limit layer tends to fill up the whole domain (*figure 16* and *figure 17*). It results in an increase in strength when the thickness decreases, but this is less pronounced for the clamped–free case than for the clamped–clamped case.

In the case of the bending loading, the thickness also defines the load gradient across the thickness and therefore the stress gradient and the thickness of the strongly loaded zone. For thin plies (*figure 17*) the

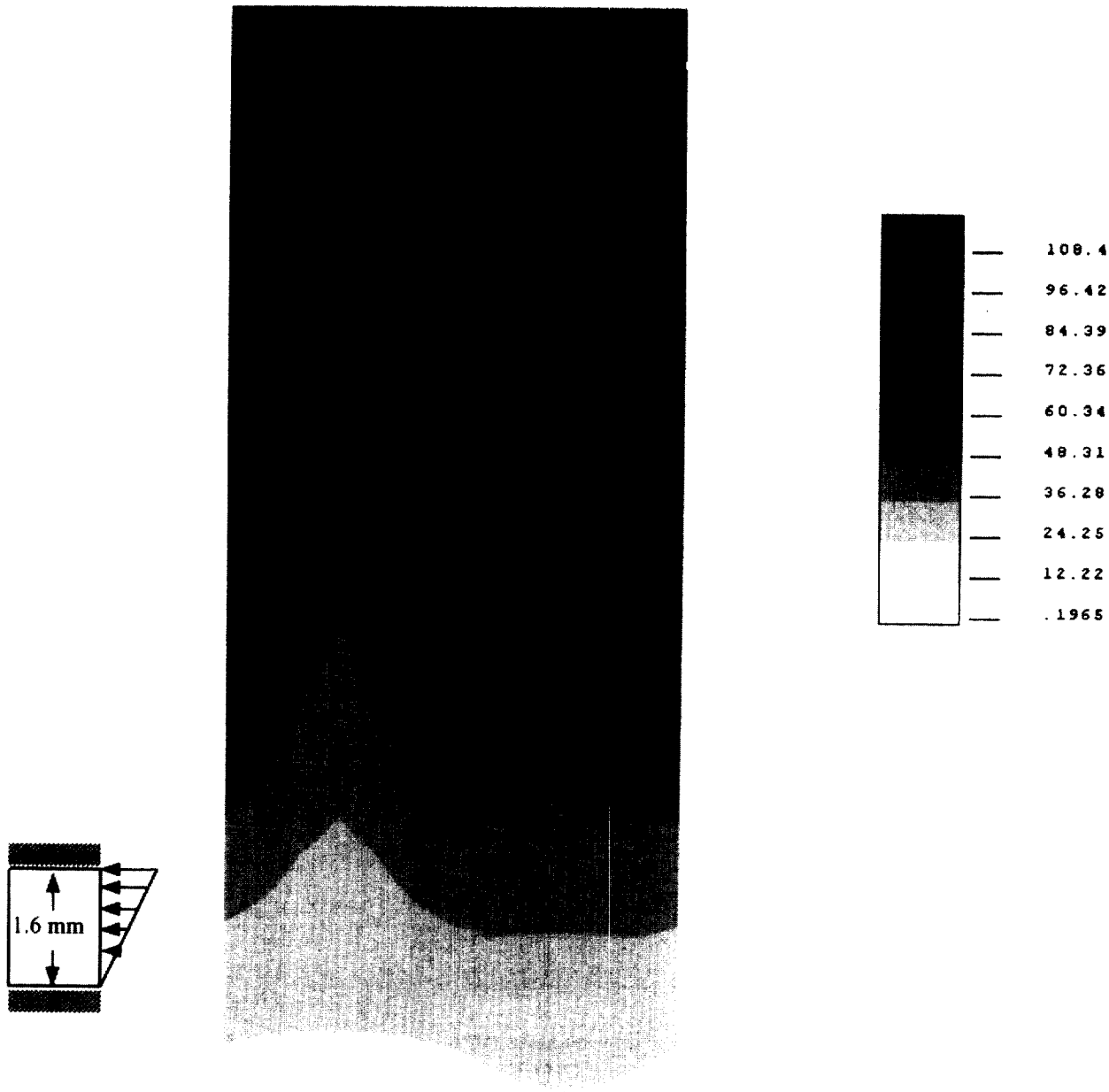

Figure 13. Von Mises matrix stress distribution (MPa) at maximum strain (–2.04 %). Bending-compression loading, clamped–clamped boundary conditions. Deformed shape*10.

microbuckling evolves over a very small height and the strength is consequently very high. When the ply becomes thick, the stress gradient across the thickness decreases and the strength tends towards failure values achieved under compression. The same influence of thickness on failure strain has been experimentally observed by Wisnom (1991) under bending load and by Colvin and Swanson (1993). Grandidier et al. (1992) and most recently Wisnom (1997) have clearly established the effect of stress gradient by using particular devices, and it appears that the experimental strength evolves in accordance with our predictions.

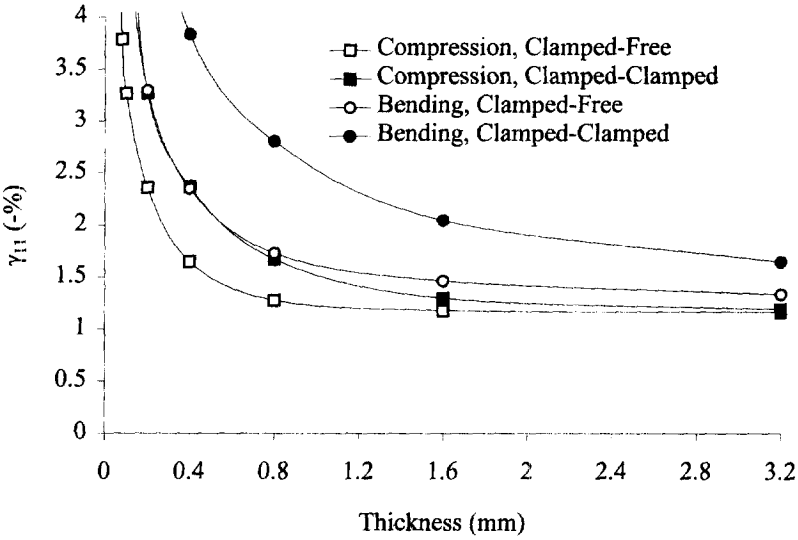

Figure 14. Maximum prescribed strain on top face versus the UD ply thickness. Imperfection amplitude 1 μm for several boundary conditions and loading combinations: —□— compression, clamped–free; —■— compression, clamped–clamped; —○— bending, clamped–free; —●— bending, clamped–clamped.

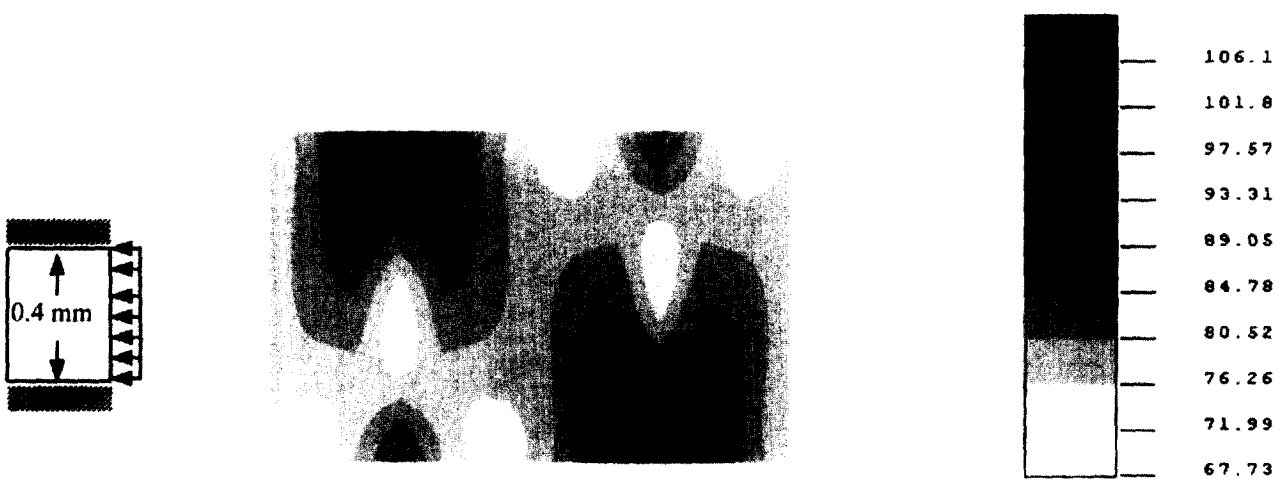

Figure 15. Von Mises matrix stress distribution (MPa) at maximum strain (–2.37 %). Pure compression loading, clamped–clamped boundary conditions. Deformed shape*10.

4.2.4. Influence of the local mechanism compared to structural effects

The previous results establish that the ply strength strongly depends on the boundary conditions, applied loading and ply thickness. For a fixed thickness of 1.6 mm, several imperfection amplitudes in a range of 0.1–3.5 μm have been considered. In *figure 18*, it is observed that the influence of structural parameters on the maximum strain is comparable to the effect of fibre waviness.

This is reinforced by the fact that the maximum von Mises matrix stress reached in *figure 10–13* and *15–17* is around 106–110 MPa. This indicates that the same local mechanism leads to the overall ply instability. Therefore the change in the stress field topography at instability can only be related to the structural parameters. Consequently it is clearly established that the structural parameters, together with local parameters, define the

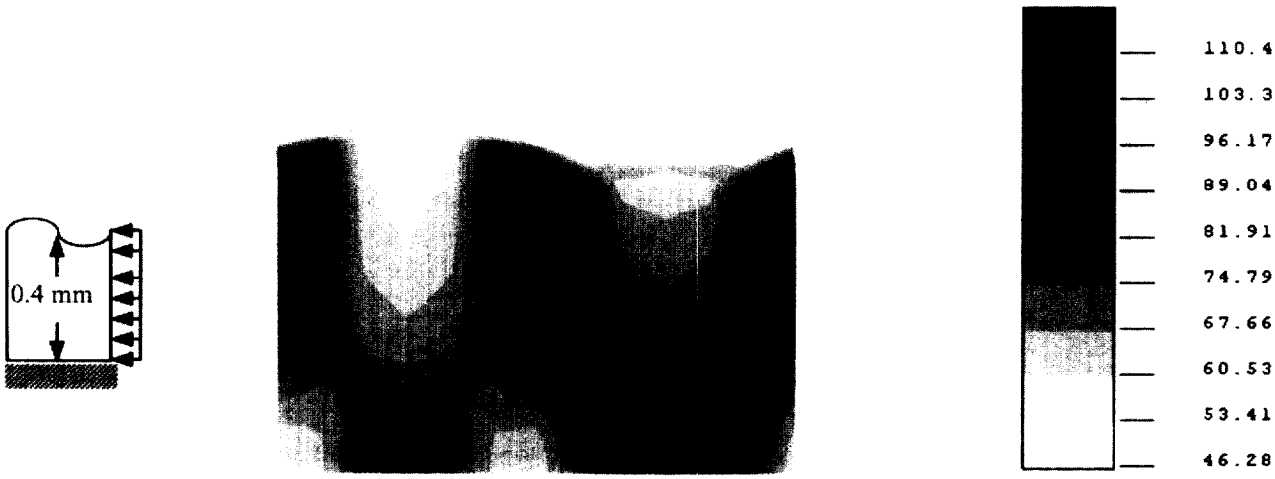

Figure 16. Von Mises matrix stress distribution (MPa) at maximum strain (–1.65 %). Pure compression loading, clamped–free boundary conditions. Deformed shape*10.

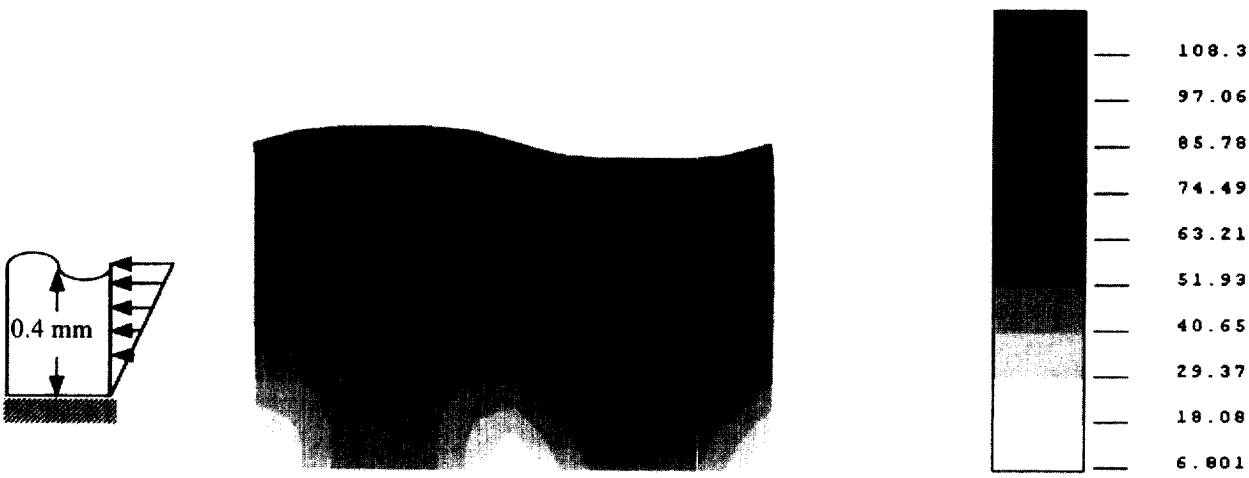

Figure 17. Von Mises matrix stress distribution (MPa) at maximum strain (–2.35 %). Pure compression loading, clamped-free boundary conditions. Deformed shape*10.

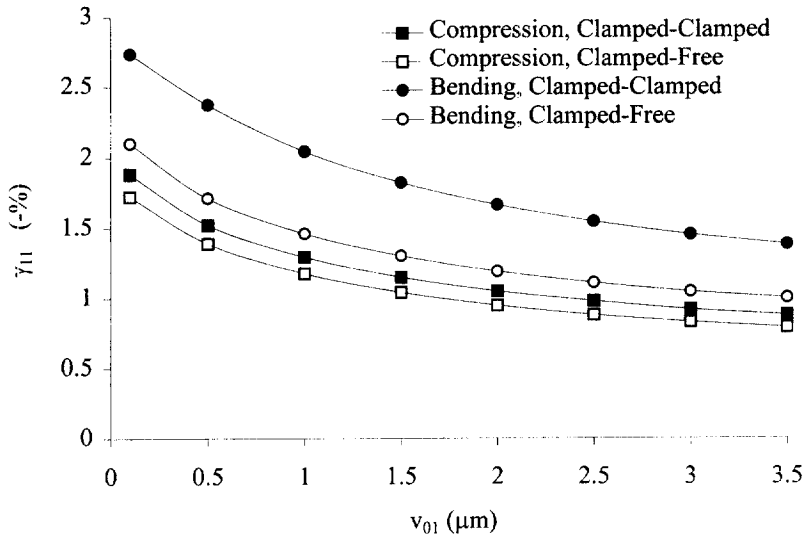

Figure 18. Maximum strain on top face versus fibre imperfection ranging from 0.1–3.5 μm for a UD ply 1.6 mm thick with several boundary conditions and loading combinations: —■— compression, clamped–clamped; —□— compression, clamped–free; —●— bending, clamped–free; —○— bending, clamped–free.

compressive strength. This final result shows that it is of the utmost importance to consider the structural parameters in the modelling of the microbuckling mechanism.

Let us notice that with 2 μm amplitude imperfections, the strengths predicted are $\approx$1 % under compression and, depending on the ply position across the laminate thickness, between 1.2–1.7 %. under bending. These values are comparable to experimental results (Wisnom, 1991; Grandidier et al., 1992; Grandsire Vinçon, 1993).

5. Conclusions

In this paper a numerical tool was built to predict the failure of composites under compressive loading applied in the fibre direction. The mechanism of microbuckling was simulated by using a homogenised medium including the fibre bending stiffness. The modelling was established on the scale of a unidirectional ply which allows us to take into account not only the influence of matrix plasticity and of initial fibre waviness, but also the effect of the ply meso-structure (ply thickness, boundary conditions and loading type) on the microbuckling. In a framework of cellular instabilities, we have proposed an original finite element which enables computationally efficient analyses to be achieved.

The responses of plies with different imperfections and including plasticity in the matrix are similar to those reported in the literature. The matrix plastic flow is mainly due to the shear induced by fibre bending. We have shown that the development of microbuckling is heterogeneous across the thickness and depends on the boundary conditions prescribed on the two faces of the ply, on the loading and on the thickness. Those effects can qualitatively explain why the strength is very high in bending and depends on the stress gradient, the thickness and the stacking sequence. Further applications of the present model will be reported in subsequent papers.

References

Argon A.S., Fracture of composites, Treat. Mater. Sci. Technol., 1, Academic Press, New York, 1972.
Budiansky B., Micromechanics, Comput. Struct., 16, (1), (1983), 3–12.

Budiansky B., Fleck N.A., Compressive failure of fiber composites, J. Mech. Phys. Solids, 41(1), (1993), 183–211.

Colvin G.E., Swanson S.R., In situ compressive strength of carbon epoxy AS4/3501-6 laminates, J. Eng. Mater. T ASME, 115, (1993), 122–128.

Cosserat E., Cosserat F., Théorie des corps déformables, Herman et Fils, Paris, 1909.

Ditcher A.K., The nonlinear stress–strain behaviour of carbon-reinforced plastics and its effect on the analysis of laminated plates and sandwich beams, PhD thesis, Department of Aerospace Engineering, University of Bristol, 1981.

Drapier S., Grandidier J.-C., Gardin C., Potier-Ferry M., Structure effect and microbuckling, Spec. JNC9, Compos. Sci. Technol., 56, (1996), 861–867.

Drapier S., Grandidier J.-C., Potier-Ferry M., Theoretical study of structural effects on the compressive strength of laminate composites, C.R. Acad. Sci. Paris, sér. II-b, 324, (1997), 219–227.

Effendi R.-R., Analyse des mécanismes de dégradation en compression des composites unidirectionnels, fibres de carbone – matrice organique et modélisation associée, Thèse de Doctorat de l'École Nationale Supérieure de l'Aéronautique et de l'Espace, 1993.

Fleck N.A., Shu J.Y., Microbuckle initiate in fibre composites: a finite element study, J. Mech. Phys. Solids, 43, 12, (1995), 1887–1918.

Fleck N.A., Deng L., Budiansky B., Prediction of kink width in fiber composites, J. Appl. Mech., 62, (1995), 329–337.

Gardin C., Potier-Ferry M., Microflambage des fibres dans un matériau composite à fibres longues : analyse asymptotique 2-D, C.R. Acad. Sci. Paris, Sér. II, 315, (1992), 1159–1164.

Grandidier J.-C., Potier-Ferry M., Microflambage des fibres dans un matériau composite à fibres longues, C.R. Acad. Sci. Paris, Sér. II, 310, (1990), 1–6.

Grandidier J.-C., Ferron G., Potier-Ferry M., Microbuckling and strength in long-fiber composites: theory and experiments, Int. J. Solids Struct., 29, 14/15, (1992), 1753–1761.

Grandsire-Vinçon I., Compression des composites unidirectionnels: méthodes d'essais et approche micromécanique, Thèse de Doctorat de l'ENS Cachan, 1993.

Hutchinson J.W., Plastic buckling, Adv. Appl. Mech., 14, 12, (1974), 67–144.

Kyriakides S., Arseculeratne R., Perry E.J., Liechti K.M., On the compressive failure of fiber reinforced composites, Int. J. Solids Struct., 32, 6/7, (1995), 689–738.

Paluch B., Analyse des imperfections géométriques affectant les fibres dans un matériau composite à renfort unidirectionnel, Rech. Aéronautique, 6, (1994), 431–448.

Rosen B.W., Mechanics of composite strengthening, Fibre Composite Materials, Am. Soc. Metals Seminar, Metal Parks, Ohio, 37–75, 1964.

Sigety P., Internal communication, Office National des Études et des Recherches Aérospatiales, 1996.

Schaffers W.J., Buckling in fiber reinforced elastomer. Text. Res. J., July, (1977), 502–512.

Swanson S.R., A micro-mechanics model for in situ compression strength of fiber composite laminates, J. Eng. Mater. ASME, 114, (1992), 8–12.

Swanson S.R., Colvin G.E., Compression failure in reduced adhesion fiber laminates, J. Eng. Mater. T. ASME, 115, (1993), 187–192.

Wisnom M.R., The effect of the specimen size on the bending strength of unidirectional carbon fibre-epoxy, Comp. Struct., 18, (1991), 47–63.

Wisnom M.R., On the high compressive strains achieved in bending tests on unidirectional carbon fibre epoxy, Compos. Sci. Technol., 43, (1992), 229–235.

Wisnom M.R., Constrained buckling tests show increasing compressive strain failure with increasing strain gradient, Compos. Sci. Technol., 29, 11, (1997), 959–964.

- I -

Annexe 2. 3

S. Drapier, J.-C. Grandidier, & M. Potier-Ferry.

A structural approach of plastic microbuckling in long fibre composites : comparison with theoretical and experimental results.

Int. J. Solids Struct. **, 38 :3877–3804, 2001.**

PERGAMON

International Journal of Solids and Structures 38 (2001) 3877–3904

INTERNATIONAL JOURNAL OF SOLIDS and STRUCTURES

www.elsevier.com/locate/ijsolstr

A structural approach of plastic microbuckling in long fibre composites: comparison with theoretical and experimental results

S. Drapier [a,*], J.-C. Grandidier [b], M. Potier-Ferry [c]

[a] *Department of Mechanical and Materials Engineering, ÉNS des Mines de Saint-Étienne, 42023 Saint-Étienne Cedex 02, France*
[b] *L3MA-SP2MI, Téléport 2, boulevard Pierre et Marie Curie, BP30179, 86962 Futuroscope Chasseneuil Cedex, France*
[c] *Laboratoire de Physique et Mécanique des Matériaux, ISGMP, Île du Saulcy, 57045 Metx Cedex 02, France*

Received 24 January 2000

Abstract

The aim of this paper is to compare some predictions obtained from a structural plastic microbuckling model presented in detail by Drapier et al. (1999), with theoretical and experimental results from the literature. After a short presentation of this model, it is established that with our approach it is possible to find the elastic modes determined by Drapier et al. (1996) on the composite microstructure. The plastic instability mechanism is then investigated and its understanding is refined. Some simulations are carried out varying the fibre initial imperfection, and the results are detailed and compared with predictions from a kink-band model (Budiansky and Fleck, 1993). Compared to the present knowledge, the understanding of the influence of the imperfection shape and of its distribution across the ply thickness is improved and new results are exposed. Validation of the present approach is completed by comparing the influence of both matrix and fibre behaviours as predicted by Budiansky and Fleck (1993) with the ones obtained from our numerical tool. Results demonstrate the influence of the change in the matrix tangent stiffness.

Secondly, we have quantified the effects of the applied loading, thickness and stacking sequence on the compressive strength of laminates. Numerical predictions provide new results that yield a proper justification of the very high compressive strength measured with bending tests. These predictions also fit well experimental measurements from the literature showing the effects of the thickness (Wisnom, 1992) and of the stacking sequence (Grandsire-Vinçon, 1993) on the compressive strength. For the first time, the effect of the gradient of loading across the laminate thickness is predicted. Results are shown to correlate well with experimental results from Wisnom et al. (1997).

Keywords: Compression; Long-fibre composites; Non-linear plastic microbuckling; Mesoscopic model; Structural effects

* Corresponding author. Tel.: +33-04-77420079; fax: +33-04-77420249.
E-mail addresses: drapier@emse.fr (S. Drapier), jcg@13ma.univ-poitiers.fr (J.-C. Grandidier), potier-ferry@lpmm.univ-metz.fr (M. Potier-Ferry).

0020-7683/01/$ - see front matter
PII: S0020-7683(00)00247-X

1. Introduction

Characterising and predicting the compressive strength of long-fibre composites originated lots of papers. It is now well established that failure is initiated by a fibre instability called microbuckling (Rosen, 1964) that leads to the catastrophic formation of a kink-band (Argon, 1972; Budiansky, 1983). The main parameters that influence this mechanism are the matrix physical non-linearity and the presence of fibre initial wavy imperfections. The most comprehensive models proposed in the literature very well account for these effects. For instance, Budiansky and Fleck (1993) starting from a kink-band model gave a simple expression of the compressive stress at failure corresponding to an increase in the kink-band rotation:

$$\sigma_c = \frac{G}{1 + n\left(\frac{3}{7}\right)^{1/n}\left(\frac{\bar{\phi}/\gamma_y^c}{n-1}\right)^{(n-1)/n}}, \tag{1}$$

where G is the elastic shear modulus of the composite and $\bar{\phi}$ is the initial inclination angle of the kink band. In this work, the non-linear response of the matrix is modelled through a constitutive law of Ramberg–Osgood's type whose strain hardening coefficient is denoted by n and yield strain in shear is γ_y^c. These authors compared some predictions given by expression (1) with some experimental results measured in various pure compressive tests. It is clear that amplitudes of the initial wavy imperfection and mechanical characteristics of the matrix that lead to a good correlation with the experimental results have both realistic values.

Despite their efficiency, the kink-band models cannot provide any explanation to the high strength of unidirectional plies measured with bending devices. As an example, under a bending loading T300/914 unidirectional plies can withstand compressive strains greater than 2%, whereas under a pure compression loading, this strength is lower than 1.2% (t'Hart et al., 1991). This observation can lead to hypothesis that pure compression tests yield a very poor estimation of the compressive strength, as suggested by the results from t'Hart et al. (1991). Recently, Anthoine et al. (1998) demonstrated, thanks to a numerical simulation, that even from a theoretical point of view, it is really difficult to set up pure compression tests on thin laminates. Then, the comparison with experimental results presented in many papers must be examined cautiously. Without questioning the dispersive character of pure compression tests observed experimentally, one can postulate that the local plastic microbuckling instability is influenced by the structure at the ply scale. This hypothesis is verified experimentally by several experimental works (Wisnom, 1991, 1992; Grandidier et al., 1992; Colvin and Swanson, 1993; Grandsire-Vinçon, 1993; Wisnom et al., 1997), which demonstrate the effect of the stacking sequence, loading and ply thickness on the resulting compressive strength.

The influence of these structural parameters on failure can be tackled by discretising the whole microstructure of the ply. For instance, Drapier et al. (1996) have clearly established by this way the influence of the ply thickness, loading and stacking sequence on the elastic microbuckling modes. On the basis of a heterogeneous bidimensional representation, Kyriakides et al. (1995) described the complete process of the microbuckling occurrence followed by a kink-band formation. However, the large number of degrees of freedom that is required in a discretisation of the whole ply does not allow us to account for the influence of the structural parameters on the failure. Conversely, this can be avoided if the microstructural behaviour is represented through an homogeneous equivalent medium (HEM) that efficiently accounts for the fibre bending, as shown by Grandidier et al. (1992) and Fleck et al. (1995a).

Thanks to homogeneous models of plies several authors (Schaffers, 1977; Swanson, 1992; Grandidier and Potier-Ferry, 1990; Grandidier et al., 1992) investigated the instability at the scale of unidirectional plies. The microbuckling amplitude is sought as a function of both the fibre position across the thickness and the boundary conditions prescribed on the two faces of the ply in which the instability takes place. These structural models establish clearly the major role of the transverse characteristic length along with

the fibre bending. In most of these works, the change of the solution across the thickness, which depends on structural data, is given a priori. More recently, Drapier et al. (1999) proposed a homogenised model including the fibre bending and was able to represent the effect of both fibre initial imperfection and matrix non-linear behaviour. The strongly non-linear development of the instability across the whole ply thickness is simulated numerically thanks to a specific finite element whose interest is to reduce largely the computation efforts. This model and the numerical resolution associated with are detailed in Drapier et al. (1999), where many simulations showed that the structural parameters must be taken into account, in the same manner as the imperfection and the matrix plasticity are. These computations permitted for the first time to demonstrate the influence on plastic microbuckling, of the loading (bending or compression), of the ply thickness, and the location of the ply in the laminate (on the edge or between cross-plies). A qualitative comparison with experimental results of the literature has been proposed and the high strength obtained under bending has been explained.

However, with the aim of making this work complete, we want to compare quantitatively the predictions obtained from this model with bending and compression test results carried out on unidirectional (UD) plies and laminates. Moreover, it is necessary to validate this method by comparing the predictions from our approach with others from the literature.

After a short presentation of our model, its ability to grasp the elastic modes is established by comparing them with the modes determined by Drapier et al. (1997). Then the role of the initial imperfection and the influence of the mechanical characteristics on the microbuckling mechanism is then detailed. The very low computation requirements enable one to demonstrate the effect of the initial imperfection shape along with its spatial distribution. The influence of both the fibre initial imperfection and the matrix non-linearity is presented and compared with the trends provided by the kink-band model of Budiansky and Fleck (1993). Eventually, a comparison with the experimental results demonstrate the ability of the present model to capture the effect of the structural parameters on the compressive strength of laminates observed experimentally. The various results confirm the necessity to account for these structural parameters in predicting the compressive strength of laminates. They also improve the understanding of the plastic microbuckling phenomenon.

2. A structural plastic microbuckling model

The equations of the problem and the numerical model are presented in Drapier et al. (1999) which the reader should refer to for technical details. The idea underlying this model is to have the stress and strain at failure (when microbuckling occurs) with very small amounts of computations while taking into account precisely all the parameters governing the phenomenon: size and shape of the initial imperfection, stiffness drop associated with the matrix plastic behaviour, and structural data across the plate thickness (thickness, bending or compression loading, stacking sequence). For further computation reductions, this model is limited to the moderate rotation framework and therefore, aims only at determining the response of laminates up to the occurrence of plastic microbuckling.

2.1. Formulation of the mesoscopic problem

In this model, only compression and bending loadings are considered. A bidimensional representation of a laminate is used (Fig. 1), where $\mathbf{e}_1$ is the 0° direction corresponding to the loading direction. In what follows, derivatives with respect to the fibre direction are denoted as $X' = \partial X/\partial x_1$ and $X'' = \partial^2 X/\partial x_1^2$.

Displacement along $\mathbf{e}_1$ is $u(\mathbf{x})$ and displacement along $\mathbf{e}_2$ is $v(\mathbf{x})$. Stresses (second Piola–Kirchhoff tensor) are denoted as $\mathbf{S}$ and Green–Lagrange's strain tensor is $\boldsymbol{\gamma}$. Based on the works of Grandidier et al. (1992), a

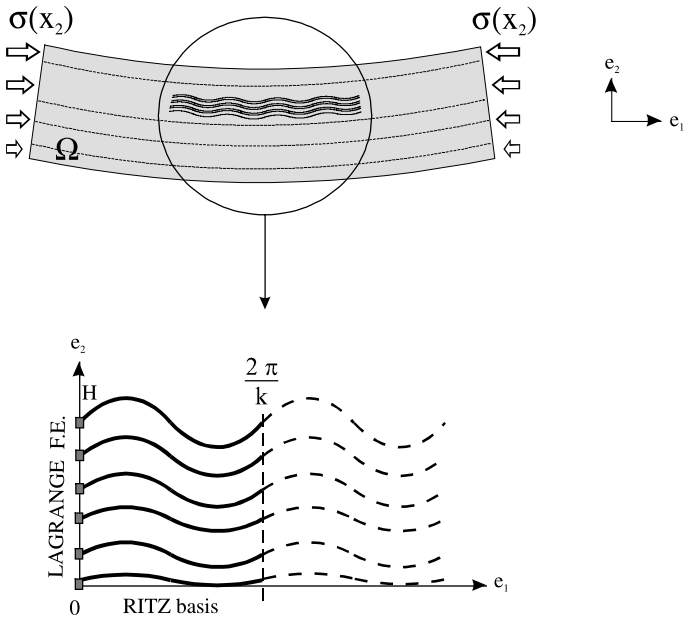

Fig. 1. Bidimensional domain studied.

formulation of the plastic microbuckling problem can be proposed where the virtual works developed in any virtual displacement field $\delta\mathbf{u}(\mathbf{x})$ is given as follows (2):

$$-\int_{\Omega}\left\{fE_{\mathrm{f}}r_{\mathrm{gf}}^{2}v''\delta v''+\mathbf{S}\cdot\delta\boldsymbol{\gamma}\right\}\mathrm{d}\Omega+\langle\mathbf{F},\delta\mathbf{u}\rangle=0\quad\forall\,\delta\mathbf{u}, \tag{2}$$

where f is the fibre volume fraction, E_{f}, the fibre Young modulus and r_{gf}, the fibre gyration radius. $\mathbf{F}$ represents the external loading, and the corresponding virtual work is assumed to depend linearly on the virtual displacement field through the scalar product noted $\langle,\rangle$.

The constitutive law (3) is of anisotropic type, the secant modulus tensor $\mathbf{L}$ being obtained from explicit homogenisation formulas based upon the constituents behaviour (Gardin and Potier-Ferry, 1992). Plasticity is defined at the microscopic scale to describe simply the anisotropy induced by fibre microbuckling. Then, only the matrix material is non-linear and follows an isotropic law of J2 deformation type that yields good predictions of plastic buckling (Hutchinson, 1974):

$$\mathbf{S}(\boldsymbol{\gamma})=\mathbf{L}(\boldsymbol{\gamma})\cdot\boldsymbol{\gamma}. \tag{3}$$

This medium is not classical due to the first term of Eq. (2) which represents the fibre bending energy. This is essential in predicting the effect of the structural data (Gardin and Potier-Ferry, 1992; Drapier et al., 1999) and also to predict the microbuckling wavelength (Grandidier et al., 1992). The micropolar medium was also presented by Fleck and Shu (1995b) and differs mainly by the constitutive law and choice of moderate rotations. The presence of this bending term has been justified by a homogenisation study using the multi-scale method (Gardin and Potier-Ferry, 1992) and also by comparing modes and buckling loads from this approach with micro-heterogeneous modelling results (Drapier et al., 1996). In the case of a laminate, this effect of the fibre bending will be taken into account only in 0° plies. In the other plies, the equivalent behaviour will be calculated from a classical rule of mixtures.

Considering mainly uniaxial loadings, non-linear terms in the strain tensor are reduced to the terms in the loading direction. The fibre initial misalignment is represented through a 'deflection field' $v_0(\mathbf{x})$ defining the fibre initial position in the domain Ω. Then, the strain tensor is given as follows (Eq. 4):

$$\boldsymbol{\gamma}(\mathbf{u}) = \boldsymbol{\varepsilon}(\mathbf{u}) + \boldsymbol{\gamma}(\mathbf{u})_{11}^{\mathrm{NL}}\ \mathbf{e}_1 \otimes \mathbf{e}_1$$
$$\text{with}\quad \boldsymbol{\varepsilon}(\mathbf{u}) = \begin{pmatrix} \frac{\partial u}{\partial x_1} & \frac{1}{2}\left(\frac{\partial u}{\partial x_2} + \frac{\partial v}{\partial x_1}\right) \\ \frac{1}{2}\left(\frac{\partial u}{\partial x_2} + \frac{\partial v}{\partial x_1}\right) & \frac{\partial v}{\partial x_2} \end{pmatrix} \text{ and } \boldsymbol{\gamma}(\mathbf{u})_{11}^{\mathrm{NL}} = \frac{1}{2}\left(\frac{\partial v}{\partial x_1}\right)^2 + \frac{\partial v}{\partial x_1}\frac{\partial v_0}{\partial x_1}. \tag{4}$$

2.2. Mesoscopic formulation of the microbuckling problem

Usually a numerical approach can be deduced from the continuous formulation through an adequate discretisation. In the present case, a further refinement is introduced which leads to a tractable model. Indeed, the microbuckling and imperfection wavelengths are of the order of some hundreds of micrometers, which is comparable to the ply thickness but much smaller than the size of composite structures. Then, a double-scale kinematics is introduced to represent at the ply scale this local short-wavelength phenomenon. The solution of the microbuckling problem is sought under the form of a displacement field (5) evolving at the scale of the structure (denoted $\mathbf{u}_{\mathrm{G}}$), very locally modulated by a displacement field evolving at the ply scale (denoted $\mathbf{u}_{\mathrm{L}}$),

$$\mathbf{u}(\mathbf{x}) = \mathbf{u}_{\mathrm{G}}(\mathbf{x}) + \mathbf{u}_{\mathrm{L}}(\mathbf{x}). \tag{5}$$

With the hypothesis of quick variations of $\mathbf{u}_{\mathrm{L}}$ and slow variations of $\mathbf{u}_{\mathrm{G}}$, the strain tensor can be simplified (Eq. 6) as:

$$\boldsymbol{\gamma}(\mathbf{u}) = \boldsymbol{\gamma}_{\mathrm{G}}(\mathbf{u}_{\mathrm{G}}) + \boldsymbol{\gamma}_{\mathrm{L}}(\mathbf{u}_{\mathrm{L}}),$$
$$\text{with}\quad \begin{cases} \boldsymbol{\gamma}_{\mathrm{G}}(\mathbf{u}_{\mathrm{G}}) = \boldsymbol{\varepsilon}(\mathbf{u}_{\mathrm{G}}) + \left(\frac{v_{\mathrm{G}}'^2}{2}\right)\mathbf{e}_1 \otimes \mathbf{e}_1 \\ \boldsymbol{\gamma}_{\mathrm{L}}(\mathbf{u}_{\mathrm{L}}) = \boldsymbol{\varepsilon}(\mathbf{u}_{\mathrm{L}}) + \left(\frac{v_{\mathrm{L}}'^2}{2} + v_{\mathrm{L}}' v_0'\right)\mathbf{e}_1 \otimes \mathbf{e}_1. \end{cases} \tag{6}$$

With these approximations (4) and (6) and assuming that the displacement $\mathbf{u}_{\mathrm{G}}$ is a known solution of the equilibrium equations (2) and (3), one gets the variational equation describing the mesoscopic equilibrium, the solution of which is $\mathbf{u}_{\mathrm{L}}(\mathbf{x})$ (Eq. (7)):

$$\int_{\Omega} \{f E_{\mathrm{f}} r_{\mathrm{gf}}^2 v_{\mathrm{L}}'' \delta v_{\mathrm{L}}'' + \mathbf{S}_{\mathrm{L}}(\boldsymbol{\gamma}_{\mathrm{G}}, \boldsymbol{\gamma}_{\mathrm{L}}) \cdot \delta\boldsymbol{\gamma}_{\mathrm{L}} + S_{11}(\boldsymbol{\gamma}_{\mathrm{G}})(v_{\mathrm{L}}' + v_0')\delta v_{\mathrm{L}}'\} \mathrm{d}\Omega = 0 \quad \forall \delta\mathbf{u}_{\mathrm{L}}, \tag{7}$$

where $\mathbf{S}_{\mathrm{L}}(\boldsymbol{\gamma}_{\mathrm{G}}, \boldsymbol{\gamma}_{\mathrm{L}}) = \mathbf{S}(\boldsymbol{\gamma}_{\mathrm{G}} + \boldsymbol{\gamma}_{\mathrm{L}}) - \mathbf{S}(\boldsymbol{\gamma}_{\mathrm{G}})$.

One may notice that in this mesoscopic formulation (7), the external loading no longer appears and is replaced by the global field through the global strain tensor $\boldsymbol{\gamma}_{\mathrm{G}}(\mathbf{u}_{\mathrm{G}})$ (Eq. (6). In order to simplify the problem, the global strain tensor is limited to its axial component (8), corresponding to a global displacement induced by compression or bending-compression states:

$$\boldsymbol{\gamma}_{\mathrm{G}}(x_2) = \gamma_{\mathrm{G}11}(x_2)\mathbf{e}_1 \otimes \mathbf{e}_1. \tag{8}$$

2.3. Displacement approximation

As we aim at the greatest efficiency, the number of degrees of freedom has to be minimum. In the framework of cellular instabilities, the displacement field approximation is chosen as a product of

amplitude across the ply thickness with few Ritz basis functions in the fibre direction. This hypothesis also allows for a reduction of the bidimensional mesoscopic domain Ω studied to a single wavelength in the fibre direction (Fig. 1), greatly reducing the amount of computations.

Ritz basis functions are selected so that microbuckling elastic modes obtained by Drapier et al. (1996) can be reproduced, and that a quasi-constant buckling stress can be obtained. Let us notice that the hypothesis of buckling with a constant stress is classical for slender structures. Eventually, the displacement approximation is (9):

$$\mathbf{u}(\mathbf{x}) = \begin{cases} U_1(x_2)\cos(kx_1) + U_2(x_2)\sin(2kx_1), \\ V_1(x_2)\sin(kx_1) + V_2(x_2)\sin(3kx_1), \end{cases} \tag{9}$$

where k is the wavenumber and functions $U_i(x_2)$, $V_i(x_2)$ are the magnitudes of the displacement field which are discretised by a three-noded finite element of Lagrange type (Fig. 1). The imperfection is assumed to have a similar form. Here it is considered as a combination of two sinusoids with a variable amplitude ($V_{01}(x_2)$, $V_{02}(x_2)$) across the thickness and with wavelengths of k and $3k$ respectively (10):

$$v_0(\mathbf{x}) = V_{01}(x_2)\sin(kx_1) + V_{02}(x_2)\sin(3kx_1). \tag{10}$$

There is thus no limitation in describing the change in the displacement fields and the imperfection across the laminate thickness. This is important in order to account for the influence of the structural parameters. Conversely, the Ritz approximation in the axial direction is more restrictive and this is what limits a proper representation of the localisation of the instability. Representing both localisation in the fibre direction and structure effect across the thickness would require a too large model. Consequently, the model focuses on the response up to the maximum load corresponding to the instability occurrence.

2.4. Elastic modes

In order to validate our approach of microbuckling, elastic computations have been carried out on UD plies. The mechanical characteristics are similar to the ones used by Drapier et al. (1996) and correspond to a T300/914 material (Table 1). The imperfection is chosen as constant across the thickness and its wavelength is 0.63 mm ($k = 0.01$). In Fig. 2 are represented, versus the prescribed strain, the change in the transverse displacement of a fibre located at the three fourth of the 1.6 mm ply thickness. The various lines correspond to plies whose amplitude V_{01} varies from 0.1 to 7 μm, whereas V_{02} is null. One can notice that the smaller the amplitude, the closer the response from the fundamental microbuckling path. In Fig. 3, one can observe that for these small amplitude values the displacement field distribution across the thickness is similar to the one obtained by Drapier et al. (1996) who characterised the elastic microbuckling mode by discretising the whole microstructure of the ply. The boundary layer observed close to a free face (top face here) is properly represented by our homogenised model. These results demonstrate the ability of our model

Table 1
Characteristics of T300/914 material and data used by default for the microbuckling mechanism study (Section 3)

Fibre T300 (isotropic)	Matrix 914 (isotropic)	Composite T300/914	Imperfection
$E_f = 230$ GPa	$E_m = 4500$ MPa	$E = 139{,}800$ MPa	$\lambda_0 = 200\ \pi$ μm
$r_f = 3.5$ μm	$G_m = 1600$ MPa	$G = 3817$ MPa	$V_{01} = 1$ μm
$f = 0.6$	$\nu_m = 0.4$		$V_{02} = 0$
			$\phi_0 = 1°$
	Strain hardening (isotropic)		
	$n = 3$	$n = 4.5$	
	$\varepsilon_y^m = 2\%$	$\gamma_y^c = 2.4\%$	

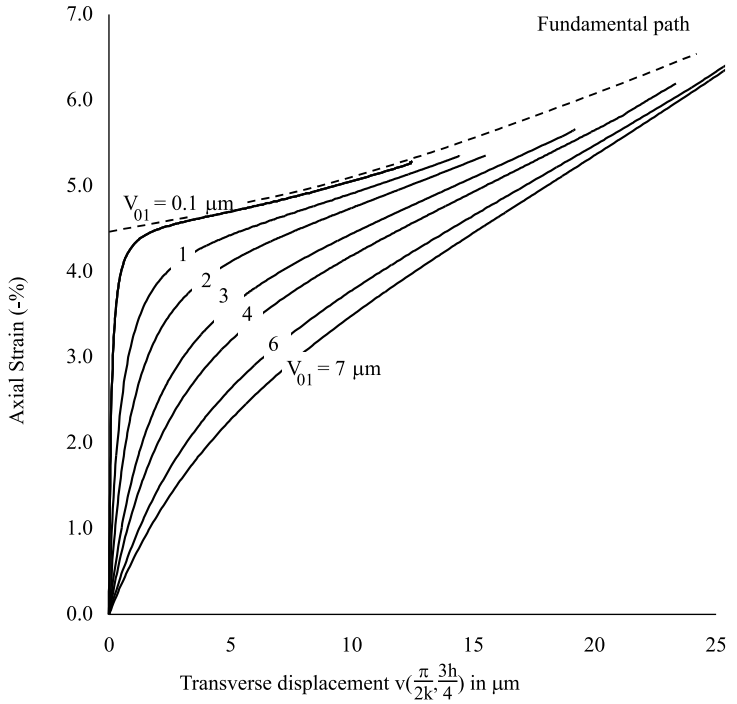

Fig. 2. Elastic response of a UD 1.6 mm thick ply under compression loading.

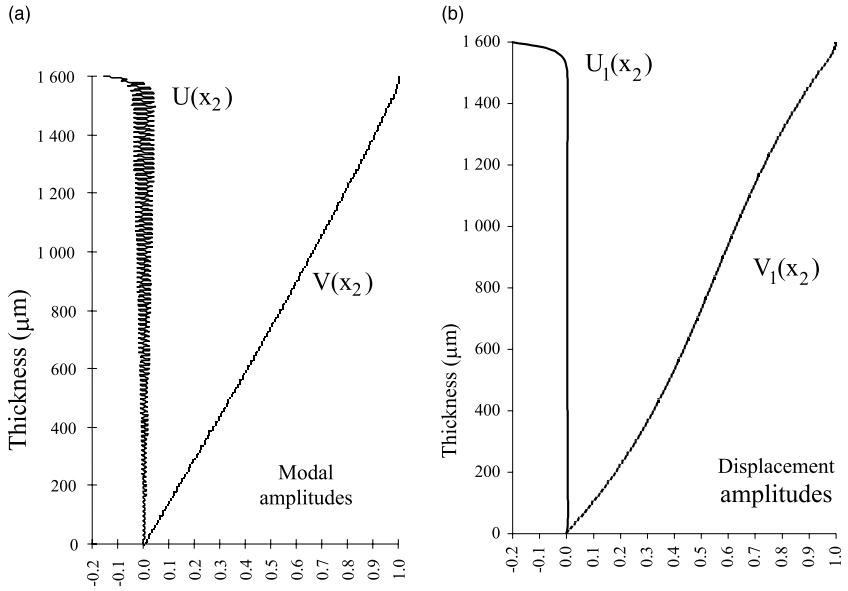

Fig. 3. Displacements for a UD under compression loading; thickness, 1.6 mm, bottom face clamped, top face free (a) modes from the complete discretisation (Drapier et al., 1996), (b) displacements from the present homogenised model $-V_{01} = 0.01$ μm.

to represent later the plasticity development across the thickness and more precisely in the boundary layer. This precaution is essential since it was demonstrated by Drapier et al. (1997) that the plasticity distribution is influenced by the presence of a free edge. For larger imperfection amplitudes, the solution deviates from the fundamental path and the ply stiffness drops drastically for amplitudes greater than 1 μm. Several thicknesses and boundary conditions prescribed on both faces have been investigated and it is found that systematically both the elastic modes and critical loads established by Drapier et al. (1996) can be determined.

In short, our approach permits to characterise properly the elastic microbuckling modes at the ply scale and emphasizes the influence of the imperfection on the elastic response of the ply. These results confirm the validity of the homogenised model proposed here and validates the splitting of the displacement field used to solve the problem at the ply scale.

3. Influence of the material mechanical characteristics

In the present part, the plastic microbuckling mechanism is thoroughly investigated. First, the mechanism is described in detail for a set of given mechanical and geometrical parameters. Afterwards, the influence of the imperfection parameters, i.e. amplitude, shape and distribution across the thickness, are presented and compared with some results obtained through the kink-band model proposed by Budiansky and Fleck (1993). Then, the role of the matrix and fibre mechanical characteristics is described and compared with the trends given by the kink-band model. On the basis of the results from Drapier et al. (1997, 1999), a very thick UD ply (5 mm) is studied whose top and bottom faces are clamped. With this geometry, the effects of the ply structure and boundary layer developing close to any free-edge are prevented. Moreover, a compression loading is considered to avoid any gradient effect induced by the loading. The material studied is of T300/914 carbon–epoxy type, whose matrix behaviour is modelled through a Ramberg–Osgood's type law. The characteristics taken by default are reported in Table 1 and the 914 resin stress–strain curve is plotted in Fig. 4.

3.1. The plastic microbuckling mechanism

In order to focus on the basic mechanism only, a UD ply is studied in which the imperfection wavelength is equal to 0.63 mm and has a constant amplitude across the thickness. The amplitude component V_{01}

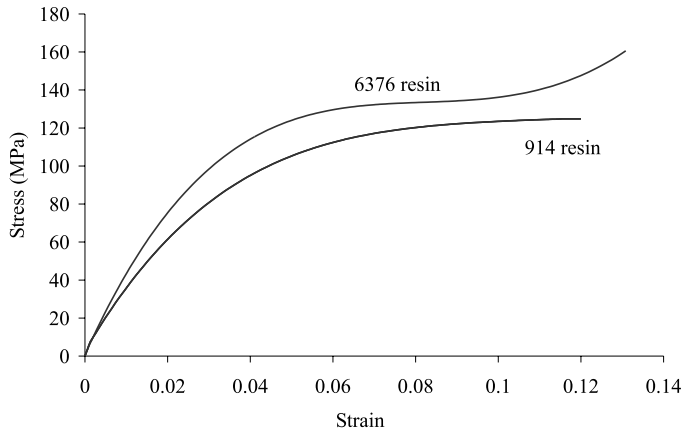

Fig. 4. Stress–strain curves used for resins 914 and resin 6376.

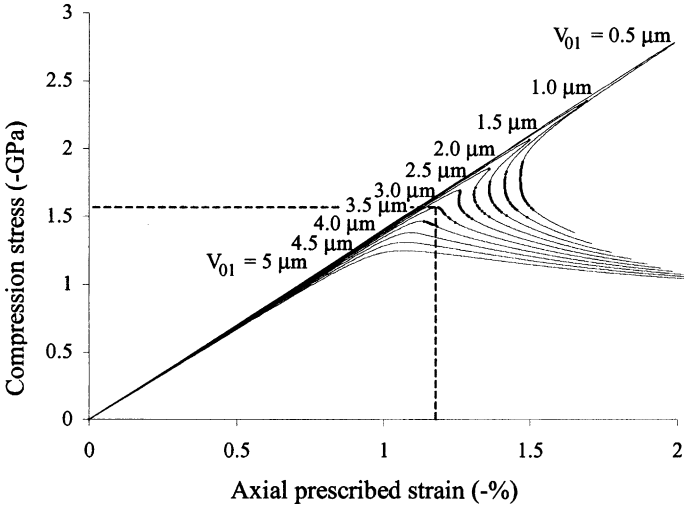

Fig. 5. Plastic response for a UD ply. The imperfection magnitude V_{01} ranges from 0.5 to 5 μm.

ranges from 0.5 to 5 μm, whereas V_{02} is zero. The observations reported in this particular configuration apply equally to the whole set of simulations that follows.

Responses under compression are plotted in Fig. 5 and are identical to the ones obtained by Kyriakides et al. (1995) who performed some finite element computations on a fully discretised region of a UD ply. One can clearly distinguish the stable and unstable responses towards the prescribed strain. Indeed, whereas the solution always exhibits a limit point in load, the limit point in strain is visible only for imperfection amplitudes lower than 3 μm. This value holds only for the present example.

It is assumed that experimentally, the occurrence of the plastic instability leads to the composite failure, since after the limit point neither a load control nor a displacement control can permit to drive the behaviour at the ply scale. By extension, the maximum stress point will be associated with the composite failure and then will be used to define both stress and strain at failure. It must be pointed out that in composites based on high stiffness fibres (GY70 for instance), the fibre failure might trigger the instability occurrence. In the present approach, the fibre fracture is not accounted for due to two main reasons. First, no evidence of such fracture appeared when taking this phenomenon into account in the present model, and second, one faces a lack of data relative to the fibre strength especially in compression.

After Tvergaard (1980), the type of behaviour reported in Fig. 5 is representative of structures that after the limit point exhibit a development of the localisation of plastic deformations. As stated previously, our model cannot represent this localisation, since the solution is sought in a restricted space defined by the displacement field approximation (9). But up to the instability, i.e. at failure, the present model is able to predict quantitatively the ply behaviour.

For fixed mechanical characteristics, the different behaviours for small or large imperfection amplitudes lie mainly on the stress ratios and distributions that lead the unreinforced material in its plastic state. In the next paragraphs are detailed the stress distributions in the mid-ply for both 1 and 4 μm imperfection amplitudes. Only the central part of the ply is studied for plastic microbuckling spreads all over this region. In Figs. 6–9, both developments and distributions are plotted versus both loading and locations along the fibre direction, for the two imperfection amplitudes considered. In those plots, σ_{11} is the HEM longitudinal stress, σ_{12}, the HEM shear stress, σ_{22}, the HEM transverse stress, σ_{Mises}, the von-Mises stress in the matrix and σ_{Bend}, the pure bending stress in the fibre.

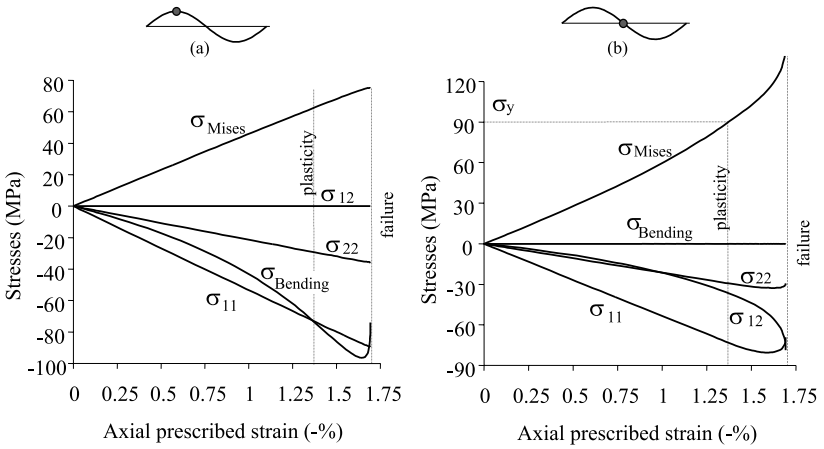

Fig. 6. Stresses versus loading up to the limit point at (a) the point of largest curvature and (b) the point of largest slope. The imperfection magnitude v_{01} is 1 μm.

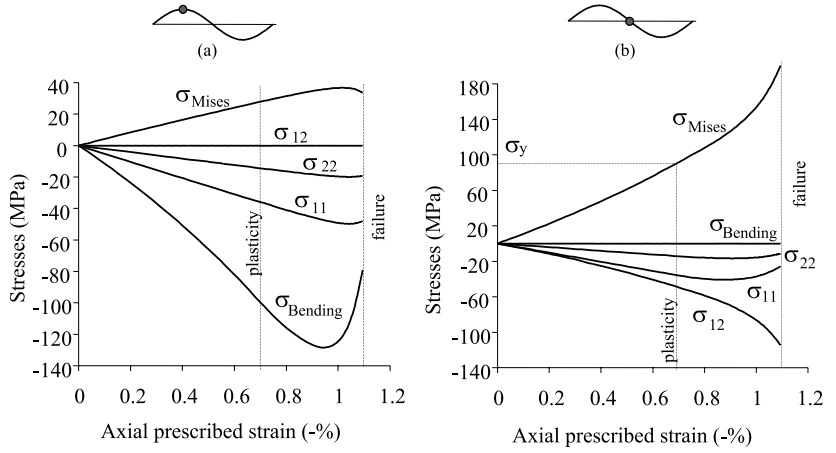

Fig. 7. Stresses versus loading up to the limit point at (a) the point of largest curvature and (b) the point of largest slope. The imperfection magnitude v_{01} is 4 μm.

3.1.1. Failure induced by the ply instability

In Fig. 6 (a) and (b), it can be seen that for small imperfections the fibre bending yields very little matrix shear at the beginning of loading. The direct compressive stress induced by the loading is predominant and leads the matrix in its plastic state for a prescribed strain of −1.37%. Indeed, over a large region of the studied zone, the plastic limit (σ_y, ε_y) is exceeded for the von-Mises stress and nearly reached for the direct compression stress. After this limit the resin stiffness drops quickly which induces a continuous increase of the bending stress at the largest curvature point (Fig. 6(a)). Meanwhile, the shear stress becomes more and more preponderant at the largest slope point (Fig. 6(b)). Just before the instability occurs, a sudden unloading takes place in the fibres (Fig. 6(a)). It is due to the geometrical instability that appears suddenly, inducing a very sharp response of the ply that is mainly controlled by the axial stiffness. This result confirms clearly that it is actually the connection between the fibre bending and the matrix non-linear shear response that originates the instability. After the limit point, the longitudinal compression stress slightly drops at the

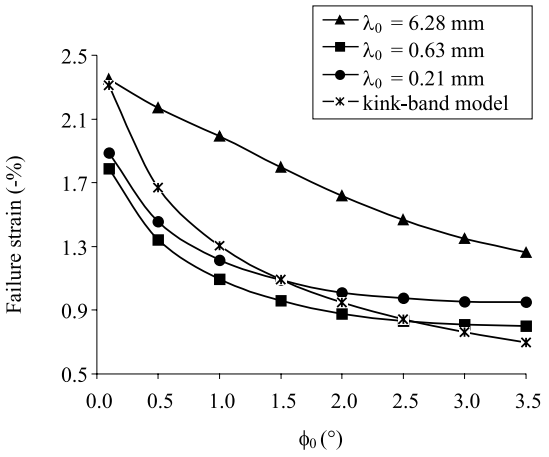

Fig. 8. Strain at failure versus the imperfection angle ϕ_0 for several wavelengths λ_0.

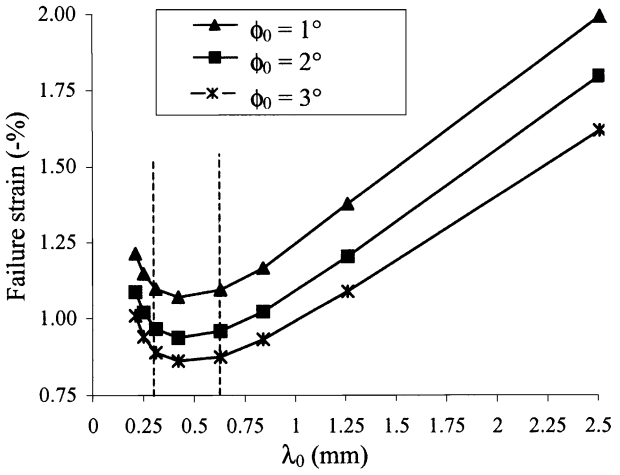

Fig. 9. Strain at failure versus the wavelength λ_0 for several imperfection angles ϕ_0.

largest slope point and the von-Mises stress is continuously increasing all over the domain. This increase is explained by the initiation of plastic shear strain localisation that takes place out of the longitudinal and transverse strains. The maximum load point corresponds to a change in the plastic flow path, which justifies the use of J2 deformation theory type that is efficient enough in characterising such plastic instabilities (Hutchinson, 1974).

3.1.2. Failure induced by a limit load

For a large initial imperfection, the fibre bending (Fig. 7(a))–matrix shear (Fig. 7(b)) connection is the basis of the microbuckling development. Compared to the small imperfection case, the resin is less compressed but it is more heavily loaded in shear as can be seen when observing Figs. 6 and 7. The yield stress is reached in particular locations of the domain for an applied strain of -0.69%. More precisely, the plastic strains localize at the point of maximum slope (Fig. 7(b)). At the beginning of loading, there is a gradual increase of the transverse displacement induced by the growth of fibre bending (Fig. 7(a)) up to the

maximum load. This bending induces high shear strains in the resin (Fig. 7(b)) that give rise to the development of plastic zones, where the mechanical properties quickly drop. This weakening of the matrix induces a larger displacement of the fibres, similar to the occurrence of a geometrical instability of low amplitude. With a 4 μm imperfection, the instability occurs very gradually, since the yield stress is exceeded only at the largest slope points, mainly driven by shear.

After the limit point, the fibre deflection increases gradually and the initiation of plastic strain localization comes along with locally a progressive decrease in the fibre bending stresses. The von-Mises stress is also subjected to a very slight decrease, but only where the plastic limit is not exceeded. Therefore, our hypothesis of no unloading, that justifies the use of a non-linear elastic law to simulate a plastic behaviour, is perfectly well founded.

3.1.3. Synthesis

The mechanism of plastic microbuckling depends essentially on the ratio of the fibre bending stiffness and its elasto-plastic support. Two regimes can be distinguished depending on the initial imperfection amplitude. When the imperfection is low, the matrix plasticity spreads homogeneously all over the domain under the action of the compression stress. This induces the sudden occurrence of the instability. For large imperfections, plasticity develops heterogeneously from the beginning of loading due to the shear induced by the increase of the initial waviness. Then, the fibre deflection increases gradually and a limit point in load is reached. It can be noticed that for large imperfections, it is the yield stress in compression that controls the plastic flow, whereas for small imperfections it is the yield stress in shear.

3.2. Influence of the initial imperfection

3.2.1. Influence of the imperfection wavelength

Previously, it has been demonstrated that the point of maximum slope corresponds to the region with the more pronounced plastic flow. This result on its own justifies why numerous authors assumed that the key parameter in the microbuckling mechanism is the angle made by the fibres with respect to the loading direction. In order to assess this assumption, the effect of both the amplitude, ϕ_0, and wavelength, λ_0, of the imperfection are investigated.

In Fig. 8, failure strains are reported versus the imperfection angle for three different wavelengths. In this figure are also reported the predictions calculated through relation (1) proposed by Budiansky and Fleck (1993) with identical mechanical properties. One can notice that for increasing imperfections, the failure strain decreases whatever be the wavelength predicted by Argon (1972) and Budiansky (1983) and as calculated from relation (1). However, our calculations show that the failure strain is also influenced by the imperfection wavelength. More precisely, it appears a 'critical' wavelength ($\approx$0.5 mm) for which failure strains are the lowest (dotted lines in Fig. 9). In a range around this 'critical' value (0.3–0.6 mm), the failure strain in first approximation depends only on the angle of imperfection, which defines a domain where the kink-band models are valid. But for large (>3 mm) or small (<0.2 mm) wavelengths, failure strains increase significantly, especially for large wavelength imperfections. Consequently, out of the 'critical' range, both parameters (angle and wavelength) must be considered to be of equal importance in defining the imperfection. In the numerous computations carried out on this 'test' ply, the transition between failures characterised by limit points and limit loads always occurs for an imperfection angle of 1.75°, whatever be the wavelength considered.

As shown in Fig. 8, the failure strains calculated from our model are comparable to the predictions from the kink-band model. Let us notice that for fixed wavelengths, the effect of the imperfection angle is not as much pronounced in our model as in Budiansky and Fleck's model (1993). But on the other hand, the 'critical' range of wavelengths (0.3–0.6 mm) lies above the measurements made by Paluch (1994) in a T300/914 material. The wavelengths measured in that study vary from 0.6 to 1.16 mm. Therefore, in order to

yield proper predictions of failure one must take into account both angle and wavelength of the imperfection.

3.2.2. Influence of the imperfection shape

Previous results showed that both wavelength and magnitude of the imperfection affect the microbuckling development. Mainly, these characteristics affect the stress field distribution in the matrix and thus the distribution of matrix plasticity. One can, therefore, expect the distribution of imperfection across the thickness to affect the microbuckling mechanism too. However, at the moment, very little is known about the imperfection distribution in composites. Hardly a couple of studies have been devoted to the measurements of imperfection amplitudes and wavelengths of few tens of fibres. Paluch (1994) has shown that the imperfections do not have a perfect configuration in the fibre direction. However, one can attempt to evaluate the effect of the spatial distribution of the imperfection on the compressive strength of UD plies.

Fibre waviness is first modelled with a single harmonic (wave number k). All the fibres are affected by the same imperfection which can vary in three manners across the thickness. First, the distribution is constant, second, the distribution follows the elastic mode shape and third, the distribution is opposite to that mode. The structure studied is a UD ply, 1.6 mm thick, with two sets of boundary conditions that represent the position of this ply in a laminate stacking sequence. First, both top and bottom faces are clamped and second, only the bottom face is clamped. The imperfection angle is 1° or 2.5° and its wave length is 0.63 mm. These choices must permit to split up in the development of plastic microbuckling, the contribution of the initial imperfection distribution (and therefore, the matrix plastic flow heterogeneity) from the contribution of the elastic buckling mode (purely geometrical non-linearity).

In Fig. 10 are reported the failure strains for both sets of boundary conditions and both imperfection angles. It is clear that the lowest strength is obtained from the constant distribution across the thickness which yields the largest zone affected by the highest matrix plastic flow. This result confirms that the role of the imperfection distribution is essential in setting the spatial distribution of the zones wherein plasticity develops. Comparison of the strains at failure calculated with modal and anti-modal distributions show that the plastic microbuckling development results from a combined effect of the distribution of geometrical instability and material non-linearity, as suggested by Drapier et al. (1997). These remarks hold for both sets of boundary conditions and imperfection angles. This suggests that it is a systematic character of these results.

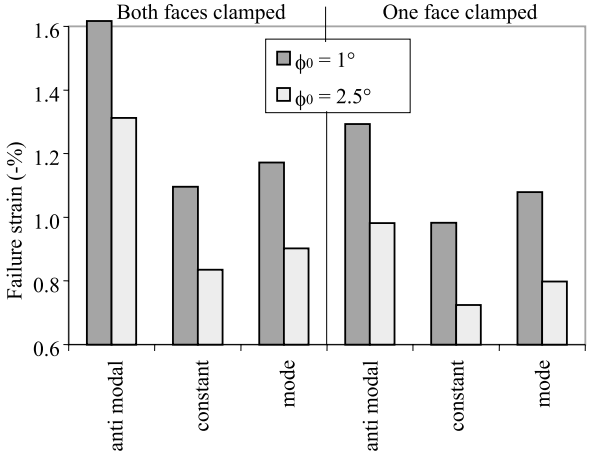

Fig. 10. Effect on the failure strain of the imperfection distribution across the thickness.

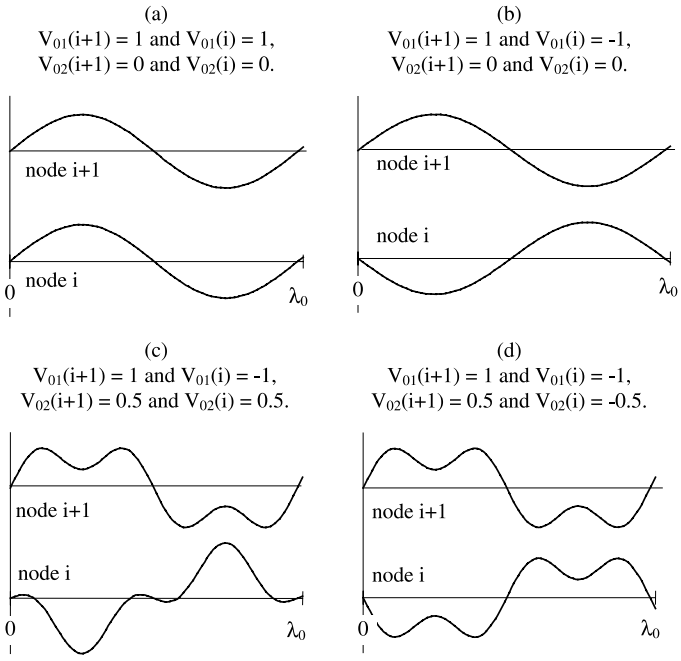

Fig. 11. Shape of the imperfection built with several amplitudes V_{01} and V_{02} (μm).

In this second part, four distributions along the fibre direction are chosen and are plotted in Fig. 11, where they are referred to as (a)–(d). The complete description of the imperfection over the domain is obtained by repeating periodically each of the four patterns in transverse and axial directions. The structure studied is a 1.6 mm thick ply whose faces are clamped and the imperfection wave number is here $k = 0.01$. Whatever be the distribution considered, the ply response remains identical, only the strains at failure vary significantly. The lowest failure strains are obtained with imperfections (a) and (c) (1.69% and 1.63%, respectively). Let us notice that the in-phase imperfection (a) does not yield the smallest failure strain as could be expected. Conversely, the phase-opposition imperfection (b) yields the highest strength (2.14%) and (d) distribution leads to an intermediate value of 1.93%. In these results appear again the major role of the bending-induced shear on the instability development. Indeed, configurations (a) and (c) that correspond to the lowest strength induce high matrix shear that facilitates the plastic flow. The other distributions induce a more complex strain state in the matrix that delays the plasticity development. The discrepancy on failure strains between configurations (a) and (c) is far from negligible (0.51%). We think that the large difference between the in-phase and phase-opposition distributions is mainly due to the contribution of the elastic mode, i.e. the geometrical non-linearity on its own (Drapier et al., 1997).

These results confirm the central role played by the imperfection. Thanks to the various capabilities of the present model, we establish not only the effect of the imperfection angle and imperfection wavelength but also the spatial distribution of this imperfection (both across the thickness and in the fibre direction). As far as the authors know, these are new results.

3.3. Influence of the constituents mechanical characteristics

As numerous authors pointed out, the microbuckling mechanism is strongly influenced by the matrix plastic behaviour. For instance, in the kink-band model considered here for comparison, an analytical

expression of the failure stress (1) was proposed as a function of the composite yield stress and the composite shear strain hardening. Predictions from this model are in good agreement with some experimental results and in the present paragraph, they are compared with the ones obtained from the present numerical tool.

In order to minimise the effects of the structural parameters, the various computations are carried out on a 5 mm thick UD ply, whose both faces are clamped. The influence of each material parameter is studied independently from the others.

3.3.1. Matrix

In Budiansky and Fleck (1993), the composite behaviour is modelled through a law of Ramberg–Osgood's type. The composite shear strain γ is related to the composite shear stress τ by the following constitutive law (11):

$$\gamma = \frac{\tau}{G}\left(1 + \frac{3}{7}\left(\frac{\tau}{G\gamma_y^c}\right)^{n-1}\right), \tag{11}$$

where G is the composite elastic shear modulus, n is the strain hardening coefficient and γ_y^c is comparable to a yield strain in perfect plasticity for the composite. With the form of the non-linear law (11), the authors proposed an analytical expression of the stress at failure. But with this expression, the response non-linearity is a complex function of both parameters n and γ_y^c. Indeed, this can be seen in Fig. 12(a), where the shear stress is plotted versus the shear strain for various values of n. It can be noticed that below the limit γ_y^c, the loss of stiffness is less important for large n, whereas above γ_y^c, the stiffness change versus n is inverted. In order to avoid this drawback, a law with a threshold is chosen (Fig. 12(b)) for the unreinforced material. Then, in our approach, the drop in stiffness depends only on a strain hardening coefficient, denoted by m, and it takes place when the equivalent strain exceeds the matrix yield strain ε_y^m. This particular choice (Fig. 12(b)) permits to evaluate separately the influence of each parameter (yield strain, elastic stiffness, strain hardening change, etc.).

It is important to notice that a couple in the present approach (m, ε_y^m) corresponds to a couple in the kink-band model (n, γ_y^c). In the results presented in the next paragraph, parameters (n, γ_y^c) are chosen such that the matrix constitutive law in shear is similar for both models of the plastic behaviour. In such a framework, the predictions yielded by the kink-band model and by our model can be compared quantitatively. Since in our numerical tool, the development of microbuckling is tackled through an incremental scheme driven by the prescribed macroscopical strain, the latter is used to compare our results to those

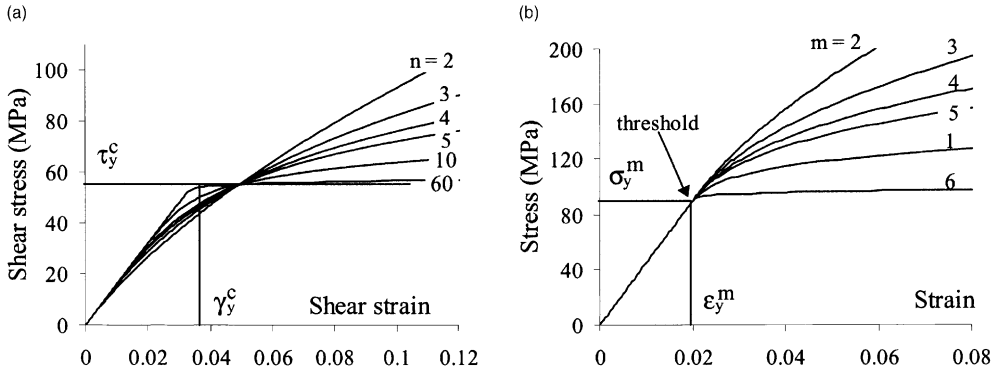

Fig. 12. Constitutive laws used: (a) in Budiansky and Fleck (1993) and (b) in the present approach.

from the kink-band model. From the expression of the failure stress (1) the (macroscopical) failure strain is easily derived with the following relationship:

$$\varepsilon_c = \frac{G}{E}\left(\frac{1}{1+n\left(\frac{3}{7}\right)^{1/n}\left(\frac{\bar{\phi}/\gamma_y^c}{n-1}\right)^{(n-1)/n}}\right), \tag{12}$$

where E is the composite Young's modulus.

3.3.1.1. Strain hardening coefficient. First, the matrix yield strain ε_y^m is set to 2%, and elastic (initial) stiffnesses of both constituents are fixed, whereas the matrix strain hardening coefficient (m) varies from 2 to 20. Two imperfection angles of 1° and 2.5° are considered, their distribution is constant across the thickness and their wavelength is 0.2 mm.

In Fig. 13, are reported failure strains calculated from both models. It can be noticed that our predictions are always larger than the ones from kink-band model. This discrepancy is natural since when the fibre bending stiffness is accounted for in the process of kink band formation, predictions (1) and (12) must be raised from 5 to 10% as stated in Fleck et al. (1995a). This is justified by the results presented here and in Section 3. For both imperfection amplitudes, the contribution of the fibre bending in the microbuckling process is essential (Figs. 6 and 7), but more markedly for large imperfections. This latter effect is not taken into account in the kink-band theories and justifies the discrepancies observed in Fig. 13.

Second, for strain hardening coefficients larger than 8, failure strains hardly vary and are quite close for both models. They tend towards a finite value that corresponds to the composite strength, whose matrix would be ruled by a perfectly plastic law. Conversely, for strain hardening coefficients lower than 8 predictions from both models diverge. The maximum discrepancy between predictions from both models is observed for a large imperfection and small strain hardening coefficients. It seems that plies affected by a 2.5° imperfection angle are slightly more sensitive to the changes in the non-linear response of the matrix. As has been demonstrated previously, for large imperfections, the instability is induced by the drop in shear mechanical characteristics and therefore, the behaviour depends strongly on the matrix response. Whereas for small imperfections, the instability arises from the coupling of the stiffness drop with the geometrical non-linearity induced by fibre bending. Thus, changes in the matrix response are not fully passed on to the composite behaviour for small imperfections.

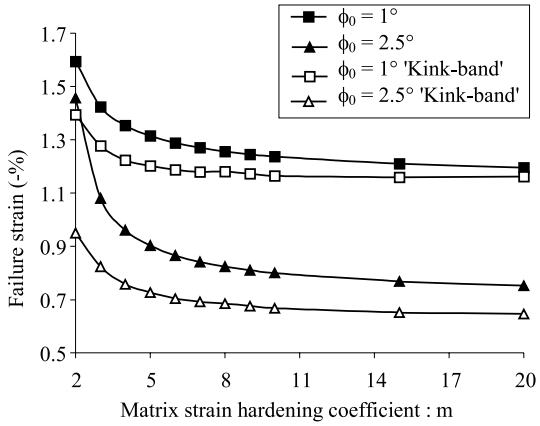

Fig. 13. Failure strain versus the strain hardening coefficient of the matrix m.

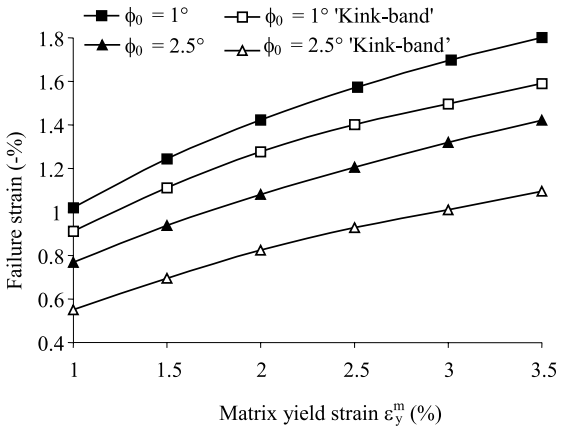

Fig. 14. Failure strain versus the matrix yield strain ε_y^m.

It is important to point out that the influence of the strain hardening coefficient presented here is a new result. Indeed, when relation (12) is used with several strain hardening coefficients n (Fig. 13), only a very feeble difference can be observed (Budiansky and Fleck, 1993). This is based on the expression of the constitutive law whose elastic threshold depends on the combination of both strain hardening and yield strain, as explained previously in this section.

3.3.1.2. Yield strain. These results demonstrate that the central role of the elastic threshold proposed by many authors is to be reconsidered. To validate this, the influence of the yield strain on the strength is quantified (Fig. 14). The matrix strain hardening coefficient is set to 3. Comparing the changes in strength when the yield strain varies (Fig. 14) with those presented previously (Fig. 13), one can notice that both effects are of the same order of magnitude. When the yield strain increases, the stress necessary to increase the plastic flow also increases. It results in an improvement of the ply strength whatever be the imperfection angle. If failure strains predicted by our model are larger than those from the kink-band model, the changes are similar.

Previous results demonstrate the central role of the change in tangential stiffness. This idea is reinforced by the curves plotted in Fig. 15, where an improvement of the strength can be seen when the matrix elastic stiffness increases. In that case, the tangential stiffness drop is delayed as a direct consequence of the yield stress increase since both yield strain and strain hardening coefficients are fixed to 2% and 3, respectively. Failure strain changes that are predicted here are similar to the ones from the kink-band model for both imperfection angles considered. Again, the discrepancy between the predictions from both models (Figs. 14 and 15) can be attributed to the fibre bending stiffness since the largest difference is systematically observed for large imperfections.

To summarise, the relative variation of failure strains versus the various parameters demonstrates that the matrix plays actually a central role. But unlike the statements made by several authors, it appears that the instability is mainly influenced by the change in the tangential stiffness. This latter effect is a direct function of the matrix mechanical characteristics, but depends also on the tridimensional stress state when plasticity occurs which differs for small and large imperfections.

3.3.2. Fibres

The intrinsic fibre characteristics come into play twice in the compressive failure. As seen previously, the fibre bending has a destabilising effect and hence participates in the failure mechanism. But it has to be

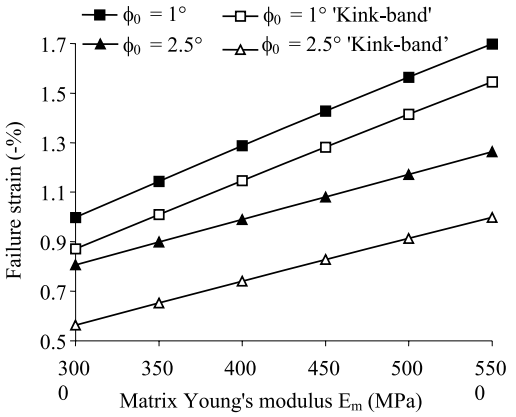

Fig. 15. Failure strain versus the matrix Young's modulus E_m.

noticed that the ply response before the instability strongly depends on the fibre modulus. Three fibre stiffnesses are considered here (230, 290 and 350 GPa) and the 5 mm thick ply response is established for two imperfections (1° and 2.5°). Observation of stresses and strains taken at the failure of the ply show that the ratio of fibre bending to matrix plasticity is fairly constant. Also, it can be noticed that the fibre bending stresses at the limit point are constant for the three moduli considered. It results in a very low dependence (variation lower than 4%) of the failure stresses to the fibre Young's modulus (Fig. 16). Conversely, since the ply elastic stiffness is based on the fibre elastic stiffness, the failure strain strongly decreases for increasing fibre moduli. This clearly appears in Fig. 16 where it can also be seen that predictions from the kink-band model lead to similar changes in failure strains for both imperfections considered.

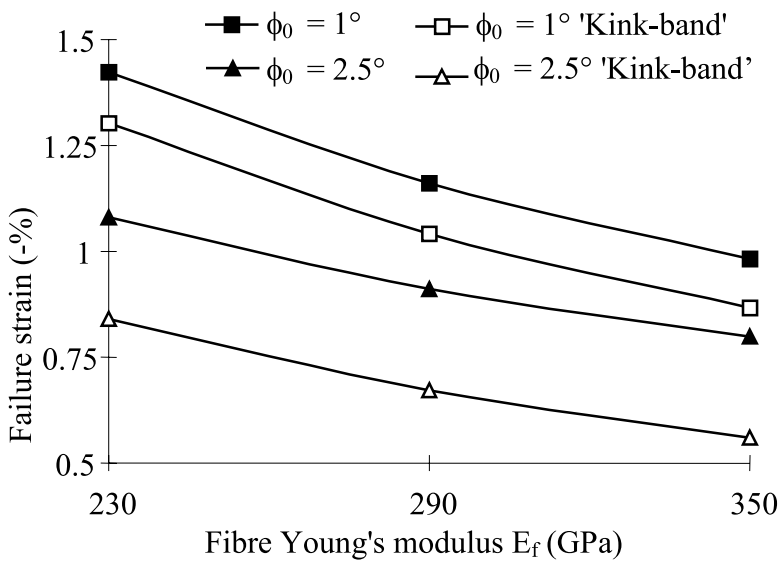

Fig. 16. Failure strain versus the fibre Young's modulus E_f.

3.4. Synthesis

The mechanism of compressive failure is characterised by two different regimes depending on whether the imperfection is small or large. But in both cases the equilibrium between the fibre bending and the matrix stiffness is the basis of plastic microbuckling occurrence. The difference is due to the way in which the matrix reaches its plastic state. For small imperfections, it is mainly the compression stress that originates plasticity whereas for larger imperfections, it is the shear induced by the fibre waviness increase that initiates it.

The fibre initial imperfection is a key element of the plastic microbuckling mechanism. It can be characterised by the maximum angle measured between the fibre and its theoretical (straight) axis, i.e. the point, where the localisation of plastic strains develops, which leads to the ply failure. However, this simplification of the imperfection is valid only in a range of wavelengths for which failure strains are minimum and remain almost constant for the given imperfection angles. For small and large wavelengths, such as the ones measured experimentally, both parameters (angle and wavelength) are necessary to represent the effect of the imperfection on the plastic microbuckling mechanism.

The influence of the mechanical characteristics that we predict is in perfect accordance with the literature. Choosing a threshold function permits to split up the role of the strain hardening from the role of the yield strain (stress). It appears that the change in tangential stiffness is the main parameter that affects the instability mechanism. If the fibre bending influences the failure stress little, it is opposite for the failure strain that increases largely for increasing fibre moduli.

4. Influence of the structural parameters and comparison with experimental results

In the work by Drapier et al. (1999), the influence of the loading, ply thickness and boundary conditions prescribed on bottom and top faces have been extensively described. A complementary part is developed here, where the microbuckling is studied in a complete laminate. The whole thickness of the composite is discretised and free faces conditions are prescribed on both faces. Characteristics of the fibre initial imperfection are very rare and therefore a range of imperfection angles is considered. The other characteristics of the imperfection are not very well known either, or not known at all. Consequently, first, several imperfection angles are considered to grasp at the best the actual compressive strength of the material. Second, because no experimental information can be found that describe the imperfection distribution across the ply thickness, a parabolic distribution is chosen with the largest waviness amplitude located at mid-height.

As has been demonstrated that the imperfection plays a great role in triggering microbuckling, the distribution across the thickness is essential in predicting structural plastic microbuckling development. Then, the imperfection distribution that is chosen is driven by the understanding gained in the field of the imperfection birth and growth (Jochum et al., 1999). More precisely, fibre waviness seems to result from the occurrence of fibre microbuckling induced by the resin shrinkage during the reticulation stage. If this chemical reaction is exothermal and thermo-stimulated, then the shrinkage is larger for fast reactions. This is confirmed by experiments carried out on single-fibre specimens. Consequently, a relationship does exist between the resin shrinkage, fibre initial waviness, and temperature distribution across the ply thickness during cure. Studying thermal exchanges during the curing process shows first that temperature is maximum at mid-thickness and second that the distribution is parabolic in first approximation. Hence one can postulate that the resulting fibre imperfection will be parabolic with the largest amplitude at mid-thickness. This distribution will be used throughout the present section.

In the present framework, the influence of the loading, thickness and stacking sequence on the compressive strength is studied. Since the whole ply is discretised, no hypothesis on the interaction between plies

Table 2
Data for T400 fibres and 6376 resin

Fibre T400 (isotropic)	Matrix 6376 (isotropic)
$E_f = 250$ GPa	$E_m = 4.5$ GPa
$r_f = 3.5$ μm	$G_m = 2.91$ GPa
$f = 0.6$	$\nu_m = 0.33$
	Strain hardening (isotropic)
	$n = 6.5$
	$\varepsilon_y^m = 1.8\%$

is necessary unlike in Drapier et al. (1999). Moreover, the constitutive laws used are based on realistic characteristics of the components such that comparisons can be made between results from our computations and experimental results from the literature. Fibre and resin characteristics are detailed in Tables 1 and 2 and experimental stress–strain curves used for both 914 and 6376 resins are plotted in Fig. 4.

4.1. Loading

Experimental bending tests have demonstrated that a T300/914 composite can locally withstand more than 2% of compression. Conversely, if the same material is tested under pure compression, its strength is about 1.2% (t'Hart et al., 1991). In order to explain this difference, two configurations are investigated here for a 3.2 mm thick UD ply. In the first case, the loading is constant across the thickness (pure compression), whereas in the second case the loading varies linearly through the thickness and vanishes at mid-thickness (pure bending). The imperfection angles range from 0.1° to 2° and the wavelength remains equal to 0.9 mm according to Paluch's measurements (1994) ranging from 0.6 to 1.16 mm.

In Fig. 17 are reported strain at failure for several computations carried out on a T300/914 like material. One can notice that with both loadings the larger the imperfection, the lower the laminate compressive strength. Also, the strength is systematically higher under pure bending loading. With imperfection angles close to 0.5°, our prediction of the compressive strength correlates very well with experimental measurements (t'Hart et al., 1991) for both compression (1.2%) and bending (1.95%). Predictions obtained through

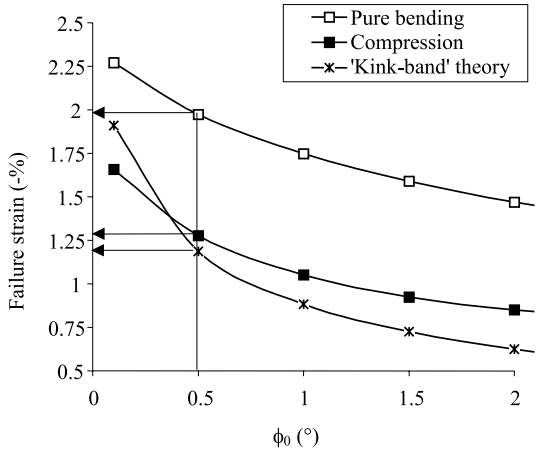

Fig. 17. Failure strain versus the imperfection angle ϕ_0 for compression and pure bending loadings.

the kink-band model are close to the ones obtained under pure compression (Fig. 17), which supports the validity of relation (1) under simple conditions.

The influence of the imperfection angle on the compressive strength is similar for both compression and bending loadings. This result clearly demonstrates that the scattering of results that pure compression devices exhibit (t'Hart et al., 1991) must be essentially attributed to the compression rigs themselves rather than to the fibre misalignment imperfection. Indeed, if fibre initial imperfections can initiate scatterings in measurements, from the simulation, this discrepancy should be observed for the bending devices too, but this is not the case. This conclusion is confirmed by results from the simulation of pure compression devices carried out by Anthoine–Rahier and Grandidier (1996). These authors have shown that testing devices are very sensitive to any manufacturing and positioning imperfection. These imperfections induce tridimensional stress states in the grips that lead to the premature failure of the material in these places.

In Fig. 17, it can also be noticed that the difference in strength obtained from the two loading configurations is rather constant whatever the angular imperfection. This result is justified by the displacement and stress distributions across the ply thickness which are proper to each loading and are independent of the imperfection. Under pure compression loading, both strain and stress distributions are fixed by the imperfection distribution across the thickness. Indeed, matrix plasticity develops in the central zone of the UD ply but does not localize in the boundary layer close to the free face, as could be expected. The maximal von-Mises stress is reached in the centre at the largest slope points (Fig. 18). Conversely, under bending this zone in which plasticity develops is reduced to a third of the ply thickness, and it is situated in the part undergoing compression (Fig. 19). More precisely, a boundary layer appears according to the presence of the free edge. It seems that the loading counterbalances the effect of the imperfection distribution which is no longer predominant in setting the microbuckling distribution. The characteristic transverse length, i.e. the dimension of the zone in which microbuckling will develop and thus control the laminate response, is fixed by the gradient of loading.

To summarise, in the presence of imperfection distributions, under pure compression loading, plastic microbuckling will develop accordingly to the maximal misalignment amplitude. Conversely, under bending loading, the gradient of loading is predominant in setting the plastic microbuckling development. Therefore, the imperfection distribution will play only a minor role regarding the spatial distribution of microbuckling.

4.2. Thickness

In order to evaluate the influence of the thickness on the characteristic transverse dimension, computations have been carried out for UD plies whose thickness ranges from 0.25 to 12.8 mm. Angular imperfections considered are 0.5° and 1.5° with the same wavelength of 0.9 mm. Results from the simulations are compared with measurements from bending experiments achieved by Wisnom (1991) on XAS/913 material. Data for this type of fibre and resin are quite close to the ones from T300/914 material and consequently these latter data will be used for the present comparison.

It can be observed in Fig. 20 that under pure compression the thickness has very little influence on the laminate strength. This result can be justified first by the homogeneous strain and stress distributions, and second because the influence of the boundary layers close to the free faces is limited by their small size. Only for very thin composites, the region in which plasticity develops is of the same size as boundary layers, and this induces a slight decrease in the compressive strength. Therefore, except the influence of the boundary layers for very thin laminates, there is no structural effect under compression since there is no characteristic transverse length prescribed: both faces are free and the loading is constant across the thickness. From there, only a distribution of imperfection across the thickness can induce a structural effect as it was demonstrated in Section 3.2.2.

Conversely, under a bending loading, a decrease in thickness yields an increase in failure strain for both imperfections angles considered. This strength increase is induced by the decrease of the zone undergoing

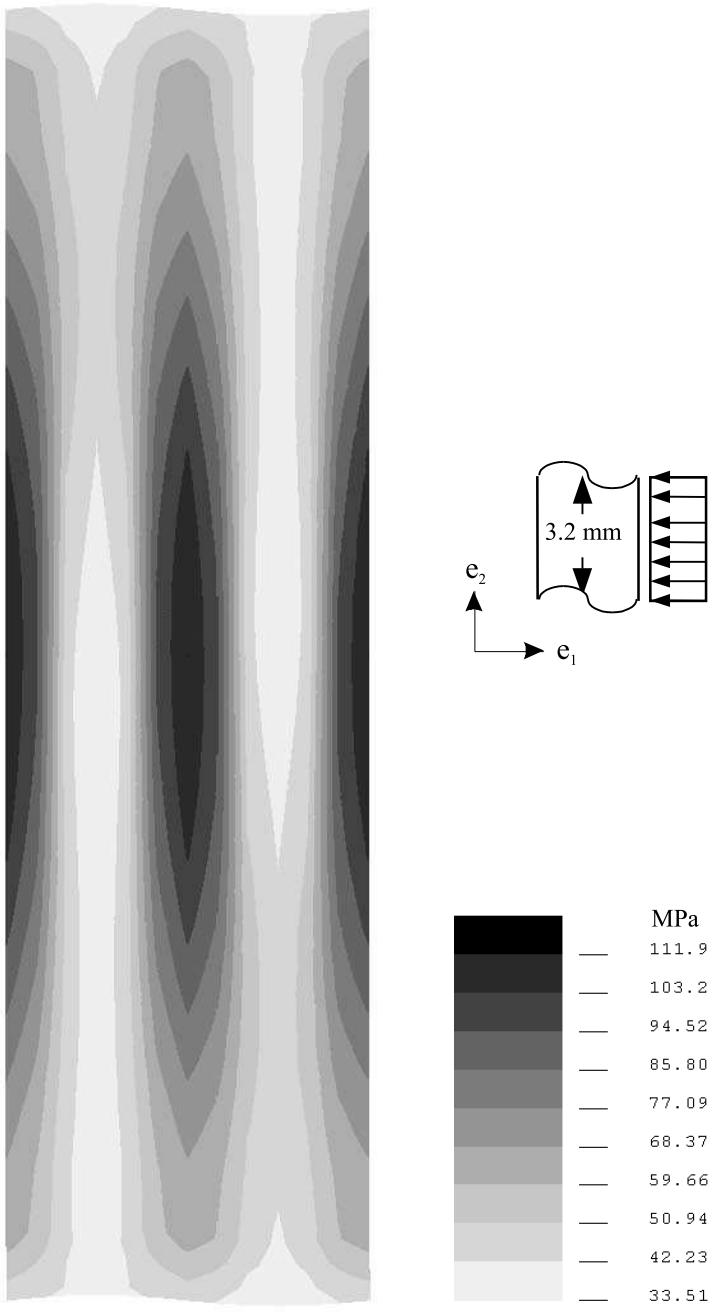

Fig. 18. Von-Mises stress distribution (MPa) in the resin at failure load. Case of compression loading for a 3.2 mm thick ply. Deformed shape × 10.

compression when the thickness decreases. In other words, when the gradient of loading increases beyond 3.2 mm, the influence of the thickness becomes small which confirms the results from Drapier et al. (1999).

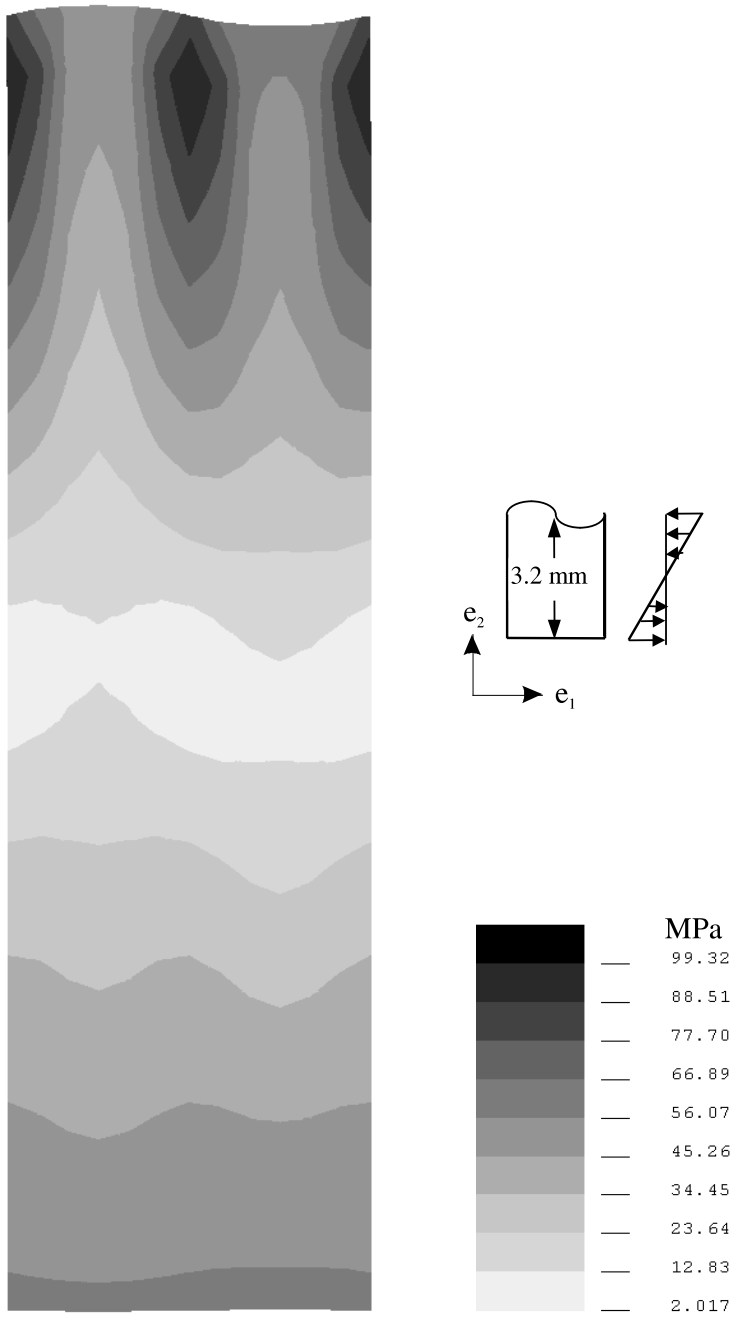

Fig. 19. Von-Mises stress distribution (MPa) in the resin at failure load. Case of pure bending loading for a 3.2 mm thick ply. Deformed shape × 10.

Wisnom (1991) tested UD carbon–epoxy XAS/913 with 60% volume fraction of fibres. Specimens were manufactured with pre-impregnated material 0.125 mm thick and 25, 50 and 100 layers which lead to

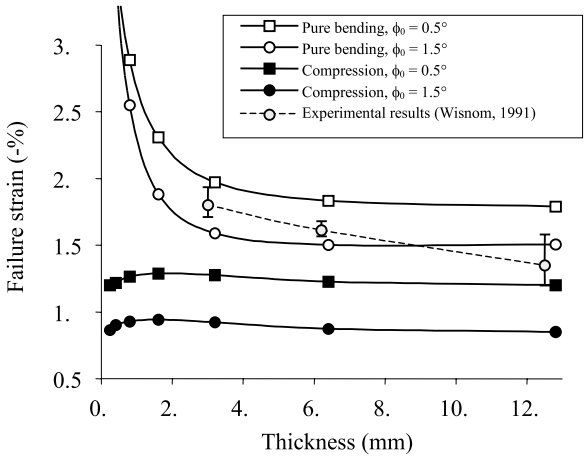

Fig. 20. Failure strain versus the UD thickness.

measured thicknesses of 3.175, 6.35 and 12.38 mm respectively. Failure strains were measured in tension and compression with a pin-ended-buckling test and a four-points bending rig. For this comparison, only failure which occurred on the compressed face were considered. In Fig. 20, it clearly appears that our predictions can correlate the experimental results at least for the two thinner plies for which the gradient is the most pronounced. For thick specimens, a drop in measured strength is observed that is related either to manufacturing defects or to the presence of larger waviness amplitudes as suggested by our computations. Also, as pointed out by the author (Wisnom, 1991), the cure process used for the thicker specimen is different from the process used for the thinner ones. Eventually, it is worthwhile pointing out that the imperfections considered here are restrictive and that further information is required to improve the comparison between theory and experiments. Especially if one realises that fibre initial imperfections are controlled by both geometrical and processing parameters.

4.3. Gradient of loading

It was demonstrated previously that both the loading and thickness of UD plies has a great influence on the compressive strength. The combination of these two parameters results in setting the gradient of loading across the thickness. This confirms the work of Grandidier et al. (1992) who established through a combination of experiments and computations on glass/epoxy material that high gradients of loading yield higher strength. In an elastic framework, a model was proposed which led to qualitative prediction of this phenomenon.

Variation of this parameter can result from the combination of a varying thickness with constant maximum load applied, but also from a bending state that is no longer pure bending. In this part are compared predictions from our model with experimental results of Wisnom et al. (1997) who tested with pin-ended buckling rigs some T800/924 material. In this work, specimens of various dimensions were tested, especially the thickness and length varied which led to gradients of loading across the thickness ranging from 0.325% to 3.83% mm^{-1}.

Characteristics considered here for the computations are similar to those for a T300/914 material (Table 1). In Fig. 21, it can be seen that our predictions correlate well with the experimental results of Wisnom et al. (1997) which in first approximation relates linearly the compressive strength to the gradient of loading. The small discrepancy that exists between predictions and experiments may be related to imperfections that are

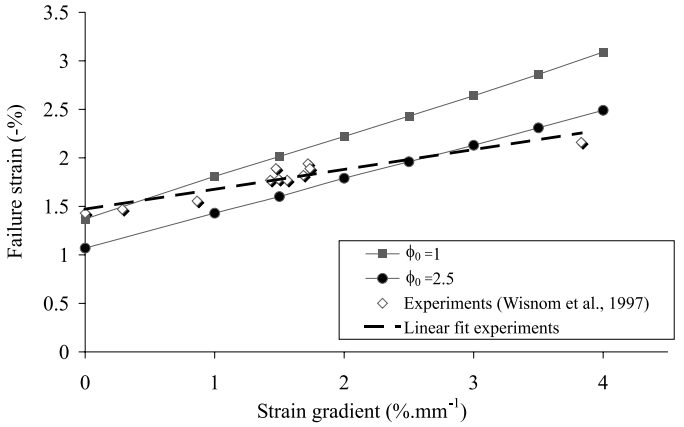

Fig. 21. Failure strains versus the gradient of loading for UD plies, for experimental results (Wisnom et al., 1997) and predictions from the present model.

not in reality as homogeneous as considered in the model. From the effect of the loading and thickness, it is clear that the effect of the gradient of loading is to set the characteristic length upon which microbuckling develops. This role of the gradient of loading is in agreement with the work of Drapier et al. (1996), who studied the elastic microbuckling mode at ply scale, but also with the work of Drapier et al. (1997) who reached the same conclusion on single UD plies.

This comparison demonstrates first, the ability of our model to account for the effect of structural parameters. Second, with reasonable imperfection angles a quantitative prediction of the effect of the gradient of loading is proposed. This effect is the very one that affects the compressive strength, although its influence can appear either through varying thickness or loading. This explains why demonstrating its influence is not straightforward and very sparsely considered in the literature. And as far as the authors know, the effect of the gradient of loading on the compressive strength of composites has never been predicted either qualitatively or quantitatively.

4.4. Stacking sequence

In this part, the influence on the instability of the stacking sequence and of the cross plies (90° and 45°) stiffness is investigated. Six laminates are considered which are made up of 16 plies: $[0_{16}]$, $[0_3,90]_{2S}$, $[0_2,45_2]_{2S}$, $[0_2,90_2]_{2S}$, $[0,90_3]_{2S}$ and $[0,90]_{4S}$. Among these sequences, four families can be distinguished, which are characterised by a similar number of neighbouring 0° plies (16 plies, 3 plies, 2 plies and one ply).

It is evident that whatever the loading considered the thicker the consecutive neighbouring 0° plies, the lower the compressive strength (Fig. 22). The presence of transverse plies at 90° or 45° set the characteristic transverse length by clamping the fibre transverse displacement close to the interface between the 0° ply and the transverse ply. Let us notice that regarding the instability, the support provided by transverse plies is similar since the compressive strength of $[0_2,45_2]_{2S}$ and $[0_2,90_2]_{2S}$ laminates are identical. On the contrary, the transverse plies thickness does play a role, since in $[0,90]_{4S}$ laminate microbuckling develops in both internal and external 0° plies. This yields a slight drop in strength when compared to $[0,90_3]_{2S}$ laminate for which microbuckling occurs in the external plies only.

The difference in strength between compression and bending is maximum for the $[0_{16}]$ stacking. This is due to the fact that the difference in size of the zone where plasticity develops is larger between the two loadings for UD plies. In the case of laminates, the dimension of the plastic zone is essentially influenced by the thickness of the 0° consecutive plies. When this latter becomes small, the loading no more influences the

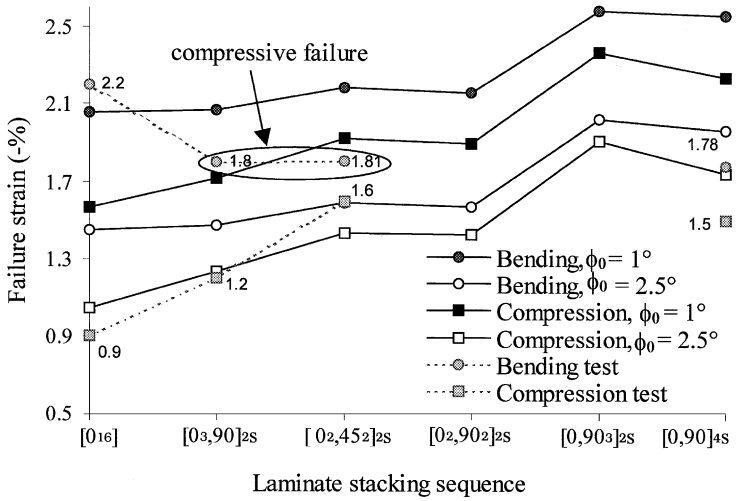

Fig. 22. Theoretical and experimental failure strains versus laminate stacking sequences.

strength. It must be pointed out that contrary to the previous section, there appears a structure effect under compression loading which is induced by the thickness of consecutive 0° plies.

The comparison attempted here with experimental data is partial, since very few works can be found in the literature which deal with this problem. The present approach considered from Grandsire-Vinçon (1993) was carried out on T400/6376 material whose behaviour is represented through the data given in Table 2 and in Fig. 4. Laminates were tested using pure compression and pin-ended buckling experiments. Results from experimental measurements are reported in Fig. 22. It appears that our predictions are in good agreement with the experimental tendencies, but these new results must be validated by a consistent experimental work that is in progress at the moment.

5. Conclusion

In this article, the compressive strength of composite laminates has been investigated, thanks to a specific finite element. The model underlying this numerical tool permits for the first time to capture the development of the plastic microbuckling mechanism in laminates while taking into account the effect of structural parameters.

In terms of response, systematically two characteristic responses of the ply can be observed. For small fibre imperfections, the matrix plasticity appears homogeneously in the material under the action of the compressive stress. This leads quickly to the sudden occurrence of the geometrical instability characterised by a limit point both in loading and displacement. For larger imperfections, plasticity appears heterogeneously from the start of the loading under the action of shear induced by the initial waviness. Then, fibre waviness increases progressively and a limit point in load is reached.

Those results confirm that the fibre initial wavy imperfection is one of the key parameters for failure induced by plastic microbuckling. It can be characterised by the maximum angle that exists between the fibre and its theoretical direction (loading direction). However, as it has been demonstrated, this simplification of the imperfection holds only for a narrow range of wavelengths, for which failure strains are minimum and depend only on the angle. This range of wavelengths has proved to differ from measurements of imperfections made on actual composites. Then, both parameters (wavelength and amplitude) are necessary in order to get realistic predictions of the compressive strength limited by the plastic micro-

buckling mechanism. Our approach also permitted us to quantify the influence of the spatial distribution of the imperfection. Simulations led to the conclusion that the lowest failure strains correspond to a constant imperfection across the thickness. But the comparison of failure strains obtained when considering a modal and anti-modal imperfection distribution demonstrates that the elastic (geometrical) mode participates too in the development of plastic microbuckling. The form of the imperfection in the loading direction influences significantly the strength. This is a result that calls for a better understanding of the fibre initial imperfection.

A parametric study was carried out on the constituent mechanical characteristics which validates our model and completes the results from kink-band theories. Clearly, the combination of fibre imperfection with matrix plasticity is a central element of failure induced by plastic microbuckling. The constitutive law with a threshold that was used for the matrix has permitted to grasp the influence better, of the yield strain (and stress), strain hardening, and elastic stiffness on the compressive strength. The results show that the central role that many authors assign to the threshold must be reconsidered since a tangent stiffness criterion seems more appropriate in predicting the compressive failure. Comparison with the kink-band theory demonstrates that our approach, which does not aim at describing in deep details the plastic microbuckling mechanism, permits to tackle very properly this instability.

Then, our structural model, including also the effect of the local parameters, was used to demonstrate and explain the effect of both thickness and loading. Computations carried out on UDs provided a rigorous explanation of the high strength of composites achieved under bending loading. Combination of the loading along with the laminate thickness results in setting the dimension of the zone in which microbuckling develops and consequently sets the strength of the whole ply. More precisely, for a UD ply under bending loading, the thinner the ply the larger its strength. Beyond 3 mm, the effect of the thickness is no longer significant. Under pure compression, no structure effect can be observed on the UD ply since no transverse characteristic length is prescribed. In accordance with some experimental evidences, the compressive strength was shown to depend in first approximation linearly on the loading across the UD thickness. For the first time, the effect of the gradient of loading on the compressive strength of composites was demonstrated from a theoretical point of view.

In laminates made up with transverse plies, the key parameter is the combination of the number of consecutive 0° plies (thickness) with the gradient of loading across the laminate thickness. More precisely, it is the gradient of loading across the thickness of these contiguous plies that sets the transverse characteristic length of the phenomenon and therefore, it influences the mechanism under both pure compression and pure bending.

These results provide some clear explanations of the influence of the structure on the compressive strength. In order to draw definitive conclusions, further experimental investigations must be carried out, especially bending experiments on laminates are being achieved. Also, it would be interesting to predict both distribution and amplitudes of the fibre initial imperfection, the only parameter which is still not sufficiently known but was shown to control strongly the local plastic microbuckling mechanism. A comparison with experimental measurements must rely on such information that is hard to quantify today.

References

Anthoine-Rahier, O., Grandidier, J.C., Daridon, L., 1998. Pure compression testing of advanced fibre composites. Comp. Sci. Tech. 58 (5), 735–740.

Argon, A.S., 1972. Fracture of Composites. Treatise of Materials Science and Technology, vol. 1, Academic Press, New York.

Budiansky, B., 1983. Micromech. Comput. Struct. 16 (1), 3–12.

Budiansky, B., Fleck, N.A., 1993. Compressive failure of fiber composites. J. Mech. Phys. Solids 41 (1), 183–211.

Colvin, G.E., Swanson, S.R., 1993. In-situ compressive strength of carbon–epoxy AS4/3501-6 laminates. J. Engng. Mat. Tech. 115, 122–128.

Drapier S., Grandidier, J.-C., Gardin, C., Potier-Ferry, M., 1996. Structure effect and microbuckling. Special JNC9, Comp. Sci. Tech. 56, 861–867.

Drapier, S., Grandidier, J.-C., Gardin, C., Potier-Ferry, M., 1997. Theoretical study of structural effects on the compressive failure of laminate composites. Compt. Rend. de l'Acad. des Sci. Paris, Série II b 324, 219–227.

Drapier, S., Grandidier, J.-C., Potier-Ferry, M., 1999. Towards a numerical model of the compressive strength for long fibre composites. Eur. J. Mech/A Solids 18, 69–92.

Fleck, N.A., Deng, L., Budiansky, B., 1995a. Prediction of kink width in fiber composite. J. Appl. Mech. 62, 329–337.

Fleck, N.A., Shu, J.Y., 1995b. Microbuckle initiate in fibre composites: a finite element study. J. Appl. Mech. Phys. Solids 43 (12), 1887–1918.

Gardin, C., Potier-Ferry, M., 1992. Microflambage des fibres dans un matériau composite à fibres longues: analyse asymptotique 2-D. Compt. Rend. de l'Acad. des Sci. Paris, Série II 315, 1159–1164.

Grandidier, J.-C., Potier-Ferry, M., 1990. Microflambage des fibres dans un matériau composite à fibres longues. Compt. Rend. de l'Acad. des Sci. Paris, Série II 310, 1–6.

Grandidier, J.-C., Ferron, G., Potier-Ferry, M., 1992. Microbuckling and strength in long-fiber composites: theory and experiments. Int. J. Solids Struct. 29 (14/15), 1753–1761.

Grandsire-Vinçon, I., 1993. Compression des Composites Unidirectionnels: Méthodes d'Essais et Approche Micromécanique. Thèse de Doctorat de l'ENS Cachan.

Jochum, C., Grandidier, J.-C., Potier-Ferry, M., 1999. Modelling approach of microbuckling mechanism during cure in carbon/epoxy laminates. Proceedings of ICCM12, Paris, July 5–9, 1999.

Hutchinson, J.W., 1974. Plastic buckling. Adv. Appl. Mech. 14 (12), 67–144.

Kyriakides, S., Arseculeratne, R., Perry, E.J., Liechti, K.M., 1995. On the compressive failure of fiber reinforced composites. Int. J. Solids Struct. 32 (6/7), 689–738.

Paluch, B., 1994. Analyse des Imperfections Géométriques Affectant les Fibres dans un Matériau Composite à Renfort Unidirectionnel. La Recherche Aéronautique 6, 431–448.

Rosen, B.W., 1964. Mechanics of Composite Strengthening. Fibre Composite Materials, Am. Soc. Metals Seminar, Metal Parks, Ohio, 37–75.

Schaffers, W.J., 1977. Buckling in fiber reinforced elastomer. Text. Res. J. 502–512.

Swanson, S.R., 1992. A micro-mechanics model for in-situ compression strength of fiber composite laminates. ASME J. Engng. Mat. Technol. 114, 8–12.

t'Hart, W.J.G., Aoki, R., Bookholt, H., Curtis, P.T., Krober, I., Marks, N., Sigety, P., 1991. Garteur Compression Behaviour of Advanced CRFP. AGARD Report 785. The Utilisation of Advanced Composites in Military Aircraft. 73rd Meeting of the AGRAD Structures and Materials Panel held in San Diego, October 7–11.

Tvergaard, V., Needlemann, A., 1980. On the localization of buckling patterns. J. Appl. Mech. 47, 613–619.

Wisnom, M.R., 1991. The effect of the specimen size on the bending strength of unidirectional carbon fibre–epoxy. Comp. Struct. 18, 47–63.

Wisnom, M.R., 1992. On the high compressive strains achieved in bending tests on unidirectional carbon fibre/epoxy. Comp. Sci. Tech. 43, 229–235.

Wisnom, M.R., Atkinson, J.W., Jones, M.I., 1997. Reduction in compressive strain to failure of unidirectional carbon fibre–epoxy with increasing specimen size in pin-ended buckling tests. Comp. Sci. Tech. 57 (9/10), 1303–1308.

- J -

Annexe 2. 4

S. Drapier & M.R. Wisnom.

Finite-element investigation of the compressive strength of non-crimp-fabric-based composites.

Comp. Sci. Technol. **, 59(8) :1287–1297, 1999.**

ELSEVIER

Composites Science and Technology 59 (1999) 1287–1297

COMPOSITES SCIENCE AND TECHNOLOGY

Finite-element investigation of the compressive strength of non-crimp-fabric-based composites

Sylvain Drapier [a,*], Michael R. Wisnom [b]

[a] *Mechanical and Materials Engineering Department, Ecole des Mines de Saint-Etienne, 158, cours Fauriel, F-42023 Saint-Etienne Cedex 02, France*
[b] *Department of Aerospace Engineering, University of Bristol, University Walk, Bristol BS8 1TR, UK*

Received 7 August 1998; accepted 2 October 1998

Abstract

The compressive strength of composites based on non-crimped fabric (NCF) under axial loading has been investigated. The objectives are firstly to give insight into the mechanisms leading to failure, !and secondly to provide guidelines for the fabric structure to optimise the NCF properties. The modelling approach is at the blanket scale where the main microstructural parameters can be accounted for based on experimental characterisation of the NCF composites (A.J. Miller, School of Industrial and Manufacturing Science, 1996). Using a two-dimensional repeating finite-element model through the thickness of a biaxial fabric, we relate the NCF compressive properties to the geometrical and mechanical characteristics of the constituents. It is established that mesobuckling of the 0°-oriented tows leads to an overall shear instability of the model that can be associated with the experimental occurrence of failure. The coupling of tow crimp and material properties, especially the resin mechanical characteristics, is shown to very much modify the NCF compressive strength. The 90° tow shape is also relevant as it defines the support provided against the 0° tow plastic mesobu!ckling. Finally, it is seen that in order to improve the NCF compressive strength, the stitching tension during the manufacturing stage should be kept low so that the tows can spread. Thus, mesobuckling is delayed owing to the improvement in 90° tow support and the reduction in 0° tow crimp. These guidelines are consistent with compressive strength measurements carried out on NCF made during manufacturing trials (R. Backhouse, Eng D. Thesis, 1998). Improvement of the resin characteristics is also shown to bring about substantial improvement in predicted NCF compressive strength.

Keywords: Non-crimp fabric composites; Structure-property relation; Finite element model; Compression; Plastic buckling; Parametric study

1. Introduction

In an attempt to improve the damage resistance of carbon-fibre-reinforced plastics (CFRP) whilst reducing manufacturing costs and weights, new types of composite are being de!veloped. The so-called non-crimp fabric (NCF) materials respond to this demand. These composites are obtained by stacking blankets which are typically made up from two to four layers of fibre stitched together through their thickness. This process is represented in Fig. 1 where it can be seen that the layers, which can be oriented in several directions, are made up of tows of fibres placed side by side. In terms of cost reduction, the improvement comes both from the easier handling/lay-up process and from the use of cheaper tows containing up to 64,000 fibres.

The other main issue to be addressed with stitching is the improvement in resistance against delamination. NCF composites show definite improvements in damage tolerance [6] which surprisingly are not necessarily attributed through the thickness reinforcement provided by the stitching. Indeed, Backhouse et al. (1995) established that the heterogeneous character of the fibre! distribution could be responsible for this improvement, as experiments showed irregular fracture paths with cracks propagating around the tows, leading to an enhanced area of fracture.

On the other hand the introduction of stitching has strong drawbacks as it induces heterogeneity at the scale of the tows. Imperfections are introduced such as resin pockets forming between tows or fibre breakage induced by the penetration of needles into the tows [6]. In Miller [21], various other geometrical imperfections such as tow crimp (Fig. 2) are also observed in the final composite. In this study devoted to the NCF characterisation, a very

* Corresponding author. Tel.: 0033 0 4-77420079; fax: 0033 0 477420000; e-mail: Drapier@emse.fr

0266-3538/99/$ - see front matter
PII: S0266-3538(98)00165-1

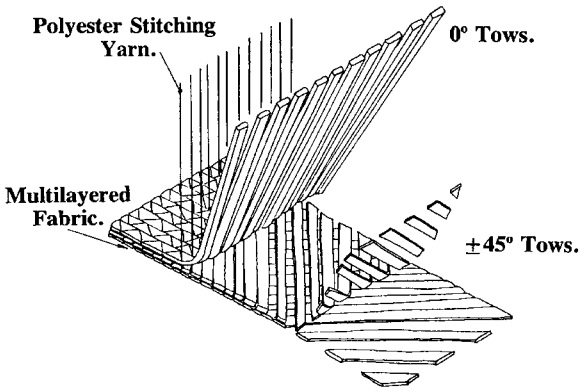

Fig. 1. Schematic of a NCF manufacturing.

strong correlation was observed between the compressive strength and some of the parameters measured at the scale of the blanket, especially the tow crimp level and the size of resin-rich pocket!s.

In the literature NCFs are mostly studied from an experimental point of view [16,2], although some research on modelling other kinds of through-the-thickness reinforced composites has been carried out [4] [10]. Extensive studies have been devoted to the examination of multiaxial warp-knit (MWK) materials which are very similar to NCF in terms of the manufacturing process. The mechanical properties of these materials have been characterised experimentally [18], but most of the work has been devoted to studying the feasibility of MWK [9,17,19] in terms of packing. One study has been reported relating the mechanical properties of the MWK to those of the yarns as a function of their orientation [17].

The behaviour of these new composites is not that well understood, and no established modelling approach exists to relate the NCF properties to the constituents' characteristics. The use of these new materials requires a better understanding, espec!ially of their behaviour under axial compression loading which is usually a major design driver for composites. Consequently an investigation of NCF compressive strength is presented here. Finite element modelling has been carried out at the blanket scale based on the knowledge gained in the field of compressive behaviour of homogeneous composites [23,7]. In the present study every medium making up the NCF composites is assumed to be homogeneous. A representative bidimensional unit cell is defined at the blanket scale, taking into account the main geometrical and material parameters at this level likely to affect the overall instability responsible for failure.

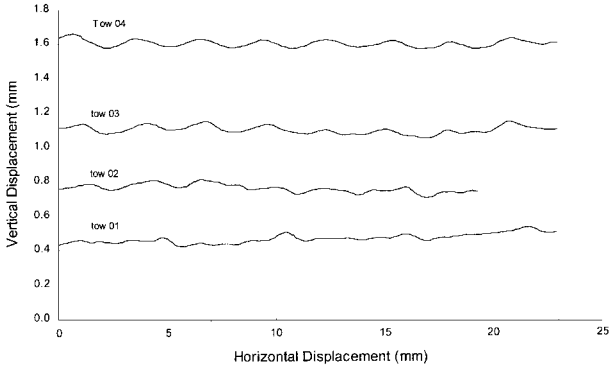

Fig. 2. 0° tow crimp measured in a biaxial NCF based composite [21].

2. Mesoscopic approach of biaxial NCF

From the measurements and experimental results of Miller [21], a relationship was found to exist between the tow crimp and the parameters of the surrounding layers of tows. Based on this assumption of 'nesting' of the tows in gaps in the compl!ementary direction (detailed below in Section 2.1, see Fig. 3) a unit cell was defined which includes the main imperfections: the tow crimp level and the resin pockets. It was decided to focus on the simplest NCF, i.e. biaxial 0°/90°, in order to investigate the basic mechanisms. Connection of displacements on the cell edges permits simulation of the deformation in a finite medium. The finite element approach involves a combination of beam and continuum elements in order to properly account for the change in behaviour of the 0° tows under compression. The 0° tows, 90° tows and resin are all assumed homogeneous, and non-linear properties were deduced from a single stress–strain curve of the resin. Generalised plane-strain theory was used to represent the three-dimensional medium with a two-dimensional finite-element analysis of a slice of unit thickness.*2.1. NCF mesostructure*

From measureme!nts at the blanket scale [21], it appears that the crimp level of the tows in the so called non-crimped fabrics can be very large, some way between unidirectional and woven composites. The measurement of this crimp is defined by its wavelength (λ) and its amplitude which is represented by the standard deviation of the orientation (SDO) with respect to the theoretical direction. As a statistical tool, the SDO was checked to be relevant and it can be shown to be simply related Eq. (1) to the maximum angle of misorientation (ϕ_{max}) if the crimp is sinusoidal

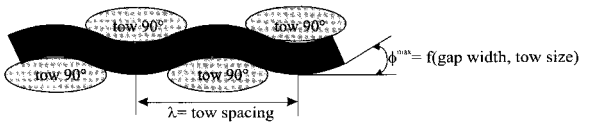

Fig. 3. Schematic of NESTING defining tow crimp.

$$\phi_{max} = \pm\sqrt{2}\,\mathrm{SDO}. \quad (1)$$

From the measurements it is clear that the tow crimp depends essentially on the arrangement of the tows in the complementary direction. This is most obvious in the case of the biaxial blankets. Due to the inherent disposition of tows placed side by side during manufacturing, gaps remai!n between them which are filled by resin. Under the pressure applied during the cure, tows in one direction (e.g. 0°) tend to nest into the gaps left in the complementary direction (resp. 90°). This nesting phenomenon is schematically represented in Fig. 3. This is very clear when comparing crimp angles and wavelengths [21]. The crimp wavelength is set by the spacing of tows in the complementary direction, whereas the misalignment angle depends on the width of the gaps left in this complementary direction (Fig. 3). These gaps are directly related to the number of fibres in the tow, since for a given overall fibre content bigger tows will leave 'deeper' gaps. Finally, the larger the 90° spacing, the larger the 0° crimp wavelength, and the wider the 90° gap (larger tow size), the greater the 0° tow misalignment angle.

Manufacturing trials [3] showed that very tight stitching could induce well developed resin channels in NCFs. This suggests that the stitching tension might modify t!he final geometry of the NCF. Also when the stitching was removed before curing, the tows could spread and the crimp level was halved. Moreover, a strong correlation was found between the mean resin-rich area size (resin pockets) and the crimp level, which tends to reinforce the assumption of nesting: the more the material is 'gappy', the larger the crimp and the resin-rich areas.

It was also established [3] that changes in the stitching tension would not modify significantly the compressive strength measured. However, a relatively loose stitching is recommended as far as compressive performance is concerned. It seems that the stitching can carry part of the load when delamination occurs, but under compressive loading the stitching is not directly involved. For the present study it was assumed that the stitching could be ignored when modelling NCF compressive strength, as it primarily changes the crimp level (which is for us an input data from measurements) but does no!t participate in terms of stiffness.

2.2. Mesoscopic bidimensional repeating cell

From these studies [3,21], it can also be noticed that the variation of 0° tow cross-section (area and shape) in the fibre direction due to the stitching is sufficiently low (for normal stitching) for the 0° tow mechanical characteristics not to vary significantly along the loading direction. Moreover, the variation of the parameters in the 90° direction is assumed low and can be simplified by taking into account only the effect of a direct strain in that direction. Lastly, the stitching has no direct effect on the compressive behaviour. Consequently, a 2D model defined through the thickness and along the 0° tow direction was sufficient and neither the stitching thread nor its stiffness was taken into account (Fig. 4).

Following the previous remarks, the nesting phenomenon defines the mode!l frame where, by symmetry, only half of the crimp wavelength needs to be studied. In order to represent a wide range of cases, the unit cell is defined with two 0° tows. The resin rich areas are directly defined by the room left between the 90° tows and the 0° tows. In this model the tows are represented in the 0° direction by an homogeneous band across the width. Tows along the 90° direction are represented by an ellipse of equivalent cross-sectional area depending on the tow size used (3 k, 6 k, 12 k, 24 k). Tow crimp is assumed sinusoidal and the maximum angle with respect to the theoretical 0° direction defines the crimp level (Fig. 4). This crimp is constant across the NCF width but different for both 0° tows. Voids are neglected and therefore every medium is assumed to be continuous.

Boundary conditions are prescribed in order to simulate a repeating cell in the loading and thickness directions, located in a medium of finite dimensions: !the sides transverse to the loading direction stay straight (u, the displacement in direction $\mathbf{e}_1$ is the same along ver-

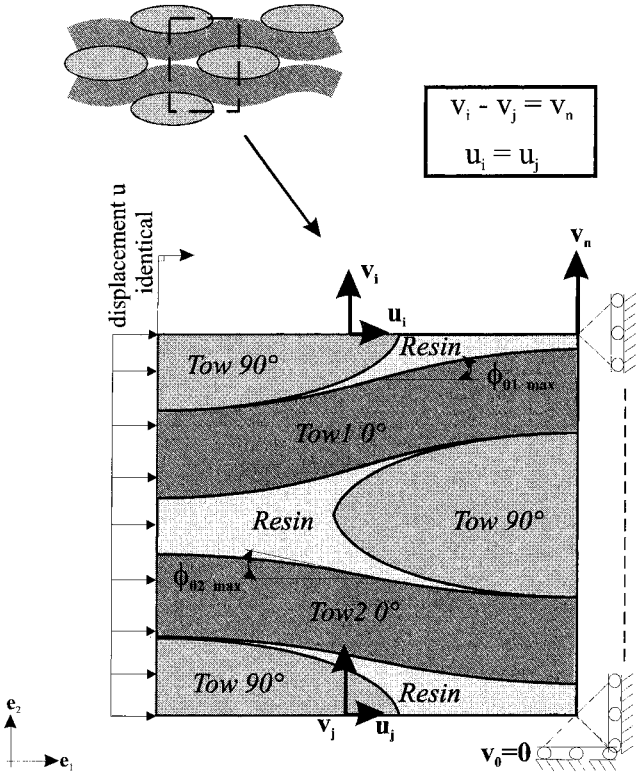

Fig. 4. Bidimensional repeating cell: geometry, parameters and boundary conditions.

tical and horizontal sides), and displacements v across the thickness on both horizontal sides are coupled together but accounting for the Poisson's ratio effect displacement (Fig. 4).

2.3. Tow modelling

For reasons of simplicity of the model, we decided to assume homogenous media. As far as the 0° tows are concerned, it is well known that compression gives rise to stability problems with which only very few homogeneous models are able to deal. These few modelling approaches assume that the equivalent behaviour of UD plies under compression is split into two superimposed parts: fibre bending and an equivalent homogeneous medium. This behaviour can be mathematically demonstrated [7,13,14] or treated from a mechanical point of view [12,23,24].

Among these three solutions, our approach [23,24] is the most directly suitable for FE analysis with existing elements. Its principle is to rebuild an homogeneous equivalent medium from standard finite elements provided in ABAQUS® [1]: beams without shear flexibility which withstand the compressive load and provide bending stiffness, superimposed on planar elements which bear shear and transverse loads (Fig. 5). Beam displacements along $\mathbf{e}_1$ and $\mathbf{e}_2$, respectively u and v, are constrained to be identical to those of the plate. On the contrary, the rotation θ is left free. A specific constitutive law has to be introduced to rebuild the equivalent behaviour from the two media properties, which is addressed in a UMAT subroutine.

The equivalent constitutive law of the 0° tows is determined from the resin stressstrain curve and the fibre content based on a simple layered model. The behaviour is assumed non-linear in shear, but linear in the fibre and transverse directions (see Appendix A). For the 90° tows, the fully non-linear planar constitutive law is also deduced from the same resin curve (see Appendix B) taking account of the fibre volume fraction, and assuming a Von–Mises equivalent plastic principle. The same equivalent plastic behaviour is used for the regions of unreinforced resin.

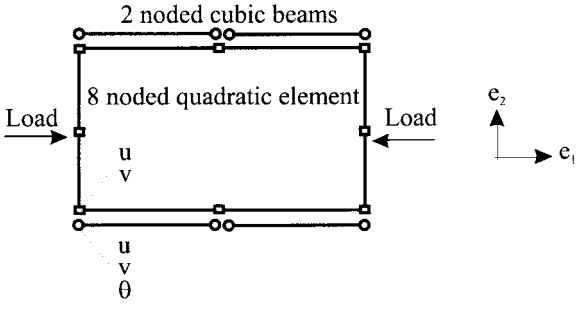

Fig. 5. Pseudo-element used by Wisnom [23] [24].

2.4. Meshes/computations

The cell size depends on the 0° tow crimp, the tow thicknesses and the crimp wavelength. Moreover the areas occupied respectively by the 3 media (resin, 0° tow, 90° tow) must match the volume fractions prescribed. With the geometry we chose we cannot control the resin rich area volume fraction independently and therefore we allowed it to be free, depending on the area occupied in the mesh. But for the tows, we can imagine several ways to obtain at the same time the correct dimensions and volu!me fractions.

As a parametric study is to be carried out, we chose a simple solution: keeping the thicknesses of the 0° and 90° tows constant. In NCF manufacturing the fibre volume fraction can be relatively easily controlled, thus the condition to be met by the mesh is that the overall fibre content matches the measurement. Since the behaviour of laminates under compression is dependent on the fibre content, the volume fraction in the 0° tows (direction of loading) is more important than the 90° tow volume fraction. Therefore we keep it constant, and the 90° tow fibre volume fraction is allowed to vary so as to meet the requirement of the given overall fibre volume fraction. Consequently, for every new geometry of the cell, the areas occupied by the three media have to be estimated and the 90° tow fibre volume fraction calculated to match the correct overall fibre content.

The 2D mesh (Fig. 6) was generated with FEMGEN® [11], a commercial mesh generator. In order to best represent a 3D medium with a 2D model, quadratic planar elements with generalised plane strain theory were used. This allows a direct strain in the 90° direction (out of the plane of the model) to be taken into account, which could play a role in the plastic behaviour of the media. An 'arc-length' path-following method was used to cope with the limit points expected to appear, as classical laminates exhibit sharp snap-back responses under compression. Data used for the computations are those for a T300/914 composite, with an estimated fibre volume fraction of 0.55. The fibres and matrix were both assumed to be isotropic (Table 1).

3. Parametric study

A baseline case was used (Fig. 6(a)), corresponding to a composite made up of biaxial NCF. Angular imperfections were $+2°$ for tow 1 (top of cell) and $-6°$ for tow 2 (bottom of cell). Dimensions of the tows were deduced from their volume fraction in the composite, their content in fibres (3 k) and the measurement of their width [21]. The 0° tow thickness was calculated to be 0.298 mm and the 90° tows were 0.244 mm thick and 1.1 mm wide. The crimp wavelength was the one measured in [21] for this case, i.e. 1.4 mm, and !the overall

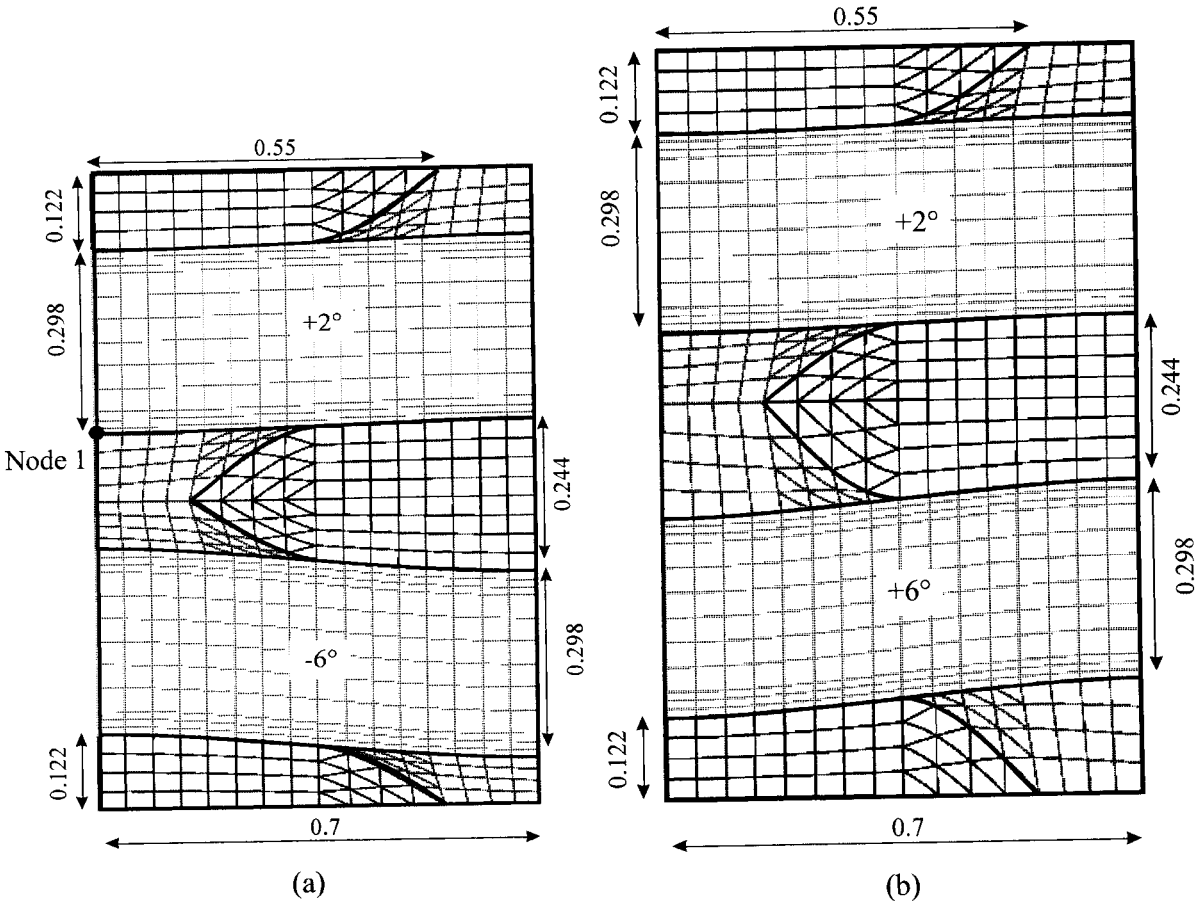

Fig. 6. Mesh, two imperfections $\phi_{01}^{max} = +2°$, $\phi_{02}^{max} = \pm 6°$. For tow thicknesses given, the cell height depends on the crimp level.

fibre fraction was 0.44. The fibre volume fraction in the 0° tows for the baseline mesh was 0.547, and the value in the 90° tows was 0.41 for that configuration of crimp. The corresponding resin-rich region volume fraction was 0.12.

When compressive loading is applied to the baseline cell, the response is to a first approximation linear up to the point where an instability occurs (Fig. 7). From an experimental point of view, neither load control nor displacement control would permit this point to be passed, which then represents failure and defines the critical load that the NCF can be expected to withstand.

Occurrence of this instability corresponds to an overall shear of the cell (Fig. 8(a)). T!his is clearly related to the development of shear stresses across the thickness.

Table 1
Mechanical characteristics used for computations. !Indices 'f' and 'm' refer, respectively, to fibres and matrix, and 'c' stands for composite

Constituents	Composite ($V_f = 0.55$)
$E^f = 230$ GPa	$E_{11}^c = 129$ Gpa
$V^f = 0.25$	$E_{22}^c = 9.77$ Gpa
$E^m = 4.5$ GPa	$\nu_{12}^c = 0.32$
$\}\nu^m = 0.4$	$\}\nu_{23}^c = 0.45$

From equilibrium, the shear stress distribution must be continuous when going across the thickness from one medium to another. It is verified here and the slight discontinuity observed can be related to the small amount of shear that is carried by the beams of the 0° tows at an angle. This distribution is more heterogeneous in the fibre direction where stresses go from zero on the vertical free edges (which are planes of symmetry) to a maximum value in the centre. Moreover

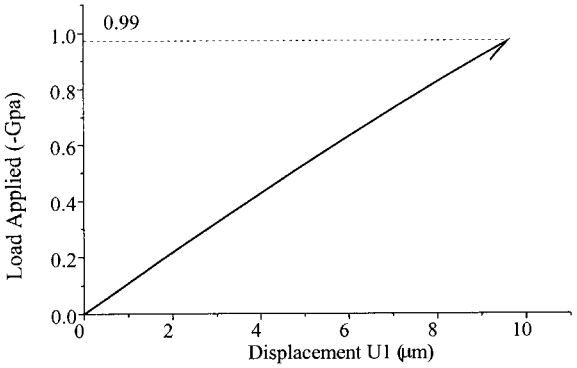

Fig. 7. Displacement of node 1 for the baseline case versus the load applied.

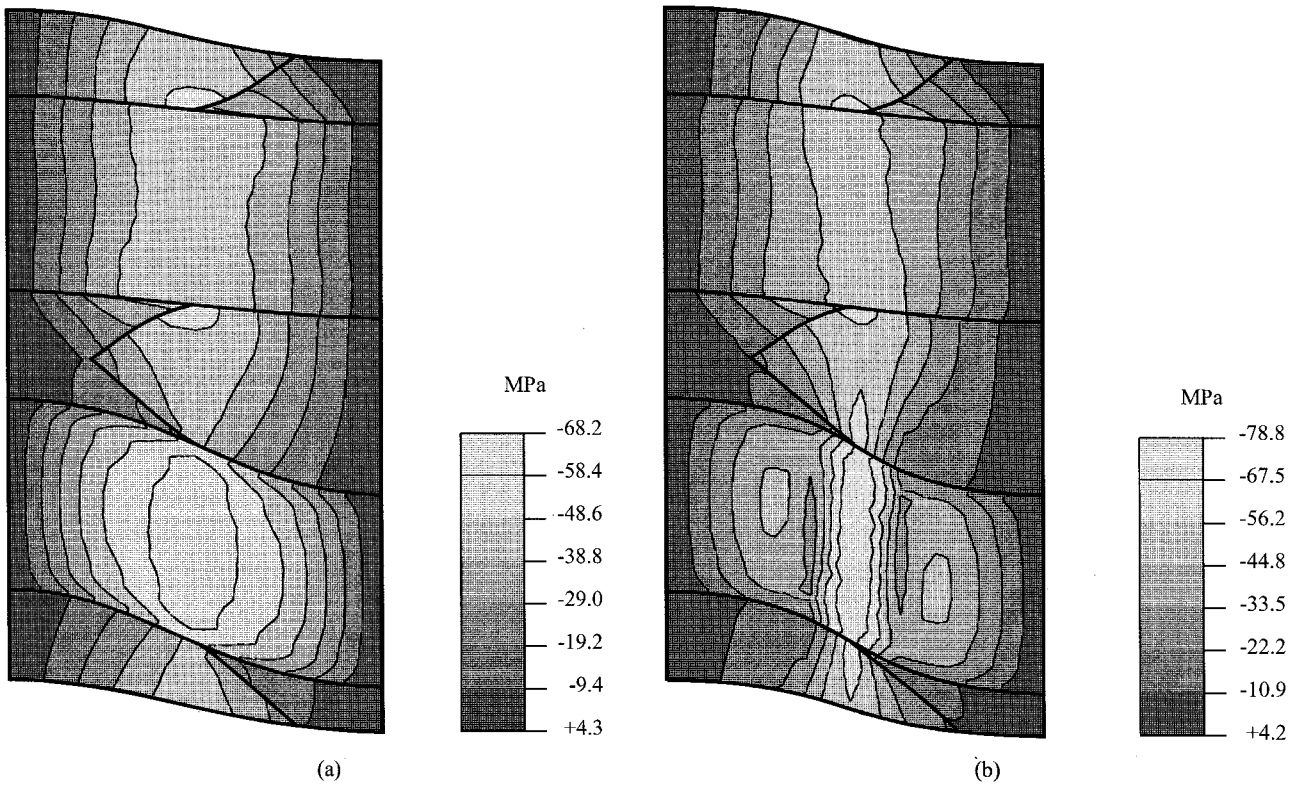

Fig. 8. Shear stress distribution on deformed shap{\text e}*10; for the baseline case (a) at instability, (b) after instability.

the resin pockets are very favourable to heterogeneous development of shear as 3 media with very different mechanical characteristics are neighbouring in those locations. Also, close to the tip of this triangular part of the pockets the highest shear stresses in the 0° tows arise.

After the instability (Fig. 8(b)), localisation of very high shear stresses develops in the centre of the cell. It can be noticed that c!onsistent with the shear behaviour of the media, the resin shear yield stress is not exceeded. However, shear strains must be very high as shown by the zone which tends to shrink in the centre of the 0° tows, especially in the most crimped tow. From this stress distribution, it is clear that at the scale of the tows, high shear stresses develop which are related to both the 0° tow maximum misalignment angle and the 0° tow non-linear shear behaviour. Consequently, by analogy with fibre microbuckling, we call this phenomenon leading to the overall instability 0° *tow plastic mesobuckling*, and it is shown to control the predicted overall response of the NCF.

From these observations, we can describe the mesobuckling mechanism leading to the occurrence of overall shear instability. When the load is applied, high shear stresses are induced by the geometry of the crimped 0° tows, which tends to weaken first the part of the cell with the largest imperfection angle (here the bottom part). Afterwards the rest of the c!ell is more and more highly loaded, particularly the second 0° tow where bending increases too. Then shear stresses spread between the 0° tow mesobuckling zones across the resin pockets and 90° tows. Finally shear develops in the centre all over the cell, and leads to a plastic overall shear instability. At this point high shear stresses (Fig. 8) are also observed in the narrow region of resin between the 0° tows and 90° tows. After the instability, the highest stresses localise in the mid region over the thickness of the cell (Fig. 8(b)) and form a kind of kink-band, especially in the 0° tow with the largest imperfection.

3.1. *Effect of angular imperfections*

It can be noticed that the deformed shape of the cell in Fig. 8 follows the orientation of the largest imperfection (−6° for the 0° tow in the bottom of the cell). If we observe the effect on the NCF response of the imperfection in the second 0° tow, it is cl!ear that the larger it is, the lower the critical load of the NCF (Fig. 9). This is consistent with unidirectional laminate imperfection sensitivity (see for instance [23]) as mesobuckling which controls the NCF strength is also a geometrical instability occurring in the fibre direction and accompanied by resin shear plastic flow.

For the case with +2°/+6° angular imperfections (mesh in Fig. 6(b)), the deformed shape is opposite to the baseline case, and therefore shear stresses are

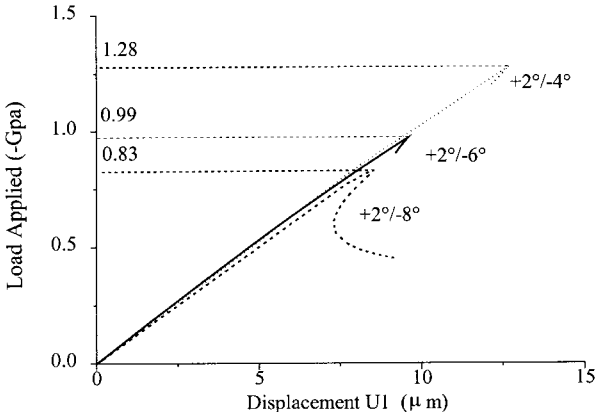

Fig. 9. NCF response for three imperfections of tow 2 ($\phi_{02}^{max} = -4°, -6°, -8°$.) in the baseline case; tow 1 angular imperfection is $+2°$.

opposite in sign (Fig. 10). The critical load is als!o lower: -0.65 instead of -0.99 GPa for the baseline case. This is due to the sign of the initial imperfections, as in the present case both 0° tow misalignments are positive, and under a compressive loading these angles increase and lead to an overall shear of the cell. Conversely, in the baseline case 0° tow plastic mesobuckling first occurs for the larger absolute imperfection ($-6°$), but the other 0° tow whose imperfection is $+2°$ provides support against it. This results in a higher critical load when imperfections have opposite signs. In the case where the two angles are identical in amplitude but opposite in sign, the strength is maximum as the tows are providing symmetrical support one to the other.

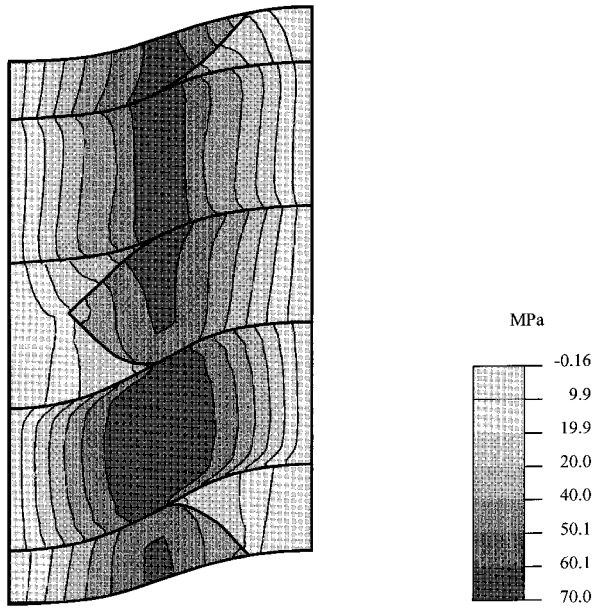

Fig. 10. Shear stress distribution on deformed shape *10 at instability. The maximum angular imperfections are $+2°$ for tow 1 and $+6°$ for tow 2.

Other pairs of angles have been considered. Following Miller [21] who measured a mean maximum angle of 3° for a 12° range, angles considered range here from $-8°$ to $+8°$. In Fig. 11 a series of results for these angles is reported. For instance, let us follow the results for $\phi_{01}^{max} = +2°$. When $\phi_{02}^{max} = -2°$, the strength is maximum and if $|\phi_{02}^{max}|$ increases the strength drops. Therefore, not only do the misalignment angles modify the NCF compression strength, but also the larger the difference between the imperfection angles of the 0° tows, the lower the strength.

3.2. Tow width effect

Due to the way NCFs are manufactured, the 90° tow shape can be changed, for instance by altering the 90° tow size or the stitching tension (which produces tow bunching). The 90° tow width is most relevant in our model as it defines the resin pocket size, and therefo!re it is the only parameter that is modified here. Following our procedure of keeping the overall fibre content fixed, the fibre content of the 90° tow has to be updated when changing the tow width, as resin is assumed to flow into or out from the resin pockets. In the baseline case, if the 90° tow width is halved, the 90° tow fibre content goes from 0.41 to 0.76 so as to keep the 0° tow fibre fraction at 0.547 for an overall fibre content of 0.44.

When the 90° tow width is halved, the critical load drops from -0.99 to -0.83 GPa. The corresponding shear stress distribution (Fig. 12) clearly shows that similarly to the baseline case, an overall shear of the cell leads to instability. However, we !can notice that the highest shear stresses reached in the 0° tows are not as spread out. Not only are the 90° tows reduced in size, but also the resin pockets are too weak compared with the 90° tows to prevent 0° tow mesobuckling. Thus the overall shear instability which depends mainly on this mesobuckling occurs at lower loads. If the 90° tows do

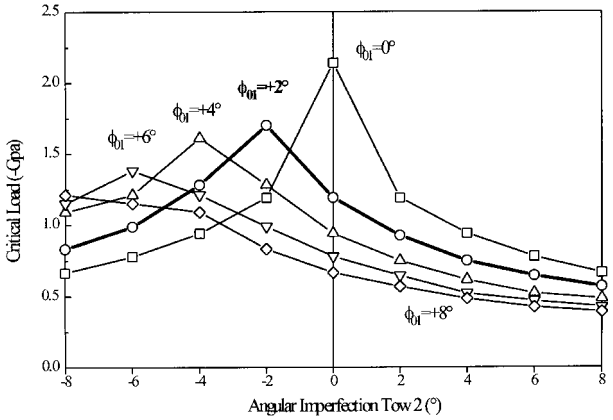

Fig. 11. Critical load versus imperfections of tow 2 ranging from $-8°$ to $+8° \cdot \phi^{max}{}_{01} = +2$.

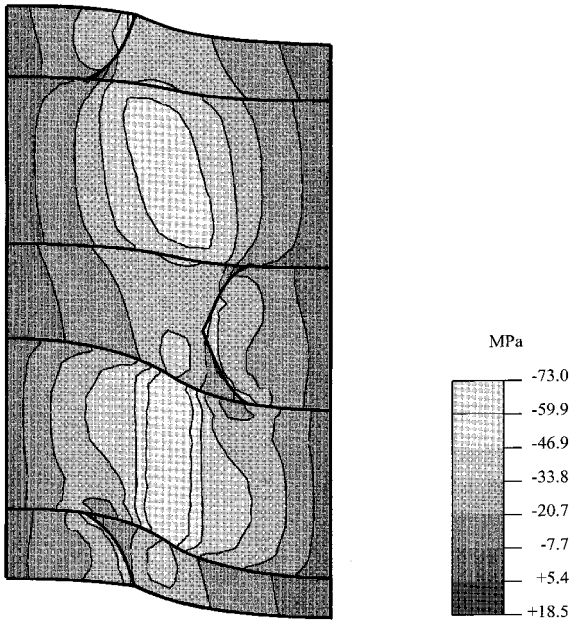

Fig. 12. Shear stress distribution at instability for smallest 90° tow width (deformed shape *10). The maximum angular imperfections are +2° for tow 1 and −6° for tow 2.

not cover the centre part of the cell, the strength is lower, even though the 90° tow fibre content is higher.

3.3. Effect of the fibre content

The fibre content in the NCF can be modified in the manufacturing process, for instance by adding extra resin layers before curing. In order to test the influence of this change on the strength, firstly the fibre volume fraction of only the 0° tows was modified, since it is the 0° tow plastic mesobuckling that was shown to control the NCF compressive strength. Secondly, the overall fibre content was also modified. Miller's measurements [21] have led us to fibre volume fractions in the tows of about 0.!55. We chose to consider a range of fibre content in the 0° tows from 0.5 to 0.65 applied to the baseline case. Following our procedure of keeping the overall fibre volume fraction constant, for the first series of analyses the corresponding 90° tow fibre contents range from 0.5 to 0.2.

Responses for these first four cases (V_{ft0} [0.5,0.65] − V_{ft90} [0.5,0.2]) (Fig. 13) verify that by increasing the 0° tow fibre content, the axial NCF stiffness is increased. This is the expected result for perfectly aligned laminates, but here the large 0° tow imperfections do not allow direct application of the rule of mixtures. However, this increase of the axial stiffness does not change th!e critical load because there is a corresponding decrease in the stiffness of the 90° tows, which reduces the support against mesobuckling of the 0° tows. This is confirmed by the results of a case with

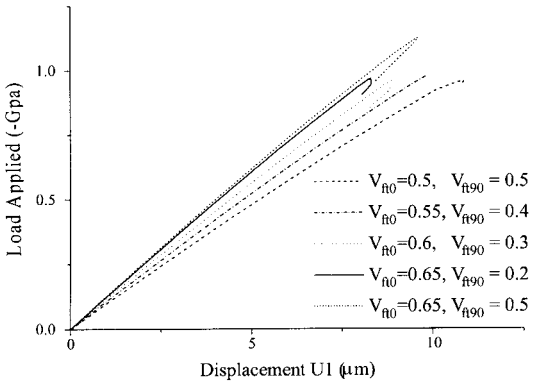

Fig. 13. NCF baseline case response for various fibre volume fraction in 0° tows.

$V_{ft0} = 0.65$, but keeping a value of $V_{ft90} = 0.5$ instead of 0.2 as previously. This corresponds to an increase of the overall fibre content from 0.44 to 0.55. We can see that this response is quite different from the others obtained previously (Fig. 13). Even if the overall stiffness varies very little compared with the 'normal' case ($V_{ft0} = 0.65$ and $V_{ft90} = 0.2$), the support provided by the stiff 90° tows improves the NCF strength. This means that if the fibre content is increased in every tow, the global NCF characteristics will be improved, due to the increase in stiffness firstly in the fibre direction and secondly in the transverse direction.

The increase of the overall fibre content in our case is from 0.44 to 0.55, and yields an improvement !in strength from 0.99 to 1.12 Gpa. This increase is relevant for our biaxial NCF whose fibre content is initially quite low (0.44), but for other composites whose fibre content is higher (0.5–0.55), the improvement in strength might be limited by the resin. As the mesobuckling stress increases with increasing overall fibre content, the 0° tows will undergo higher shear stresses and thus the resin could be unable to resist such high loads.

In summary, an increase in fibre volume fraction in the 0° tows improves the NCF stiffness but not the critical load. But if the fibre content is also increased in the 90° tows, NCF strength is improved in terms of critical strain as well as critical stress. Yet for sufficiently high fibre content this improvement could be limited by the resin strength.

3.4. Resin effect

The resin is an important factor in any composite under compressive loading, especially in those controlled by microbuckling. By analogy with those! laminates, we know that if plastic mesobuckling triggers failure, the resin must play a very important role.

We investigate resin whose modulus is 0.5 and 1.5 times the resin elastic modulus used in the baseline case ($E^m = 4.5$ GPa). The behaviour of the 90° and 0° tows is

also modified as it directly depends on the resin (See Appendix B). The yield stress remains the same although it is thought also to play a role, but probably less important compared to the modulus.

Critical loads are presented for three cases of imperfection couples ($+2°/+6°$, $+2°/0°$, $+2°/-6°$), and we can check that the change in strength is very similar whatever the imperfections considered (Fig. 14). !The results also confirm that the effect of the resin is most important for the 0° tow shear behaviour. Indeed, an increase of 50% of the resin modulus in the 0° tow shear leads to a strength improvement of about 20%. If the resin change is taken into account in the resin pockets and 90° tows too, the improvement is about 25%. Hence 80% of the improvement is brought about by the change of resin in the 0° tows' shear behaviour.

These results show that any change in the resin, especially in the 0° tow shear behaviour, is passed on to the NCF compressive strength. This sensitivity to resin changes in the 0° tow shear behaviour indicates that the 0° tows undergo mainly shear, which reinforces the idea that NCF compressive behaviour is controlled by 0° tow mesobuckling.

4. Conclusion

In this parametric study, we have tested the effect on the NCF compressive strength of the parameters defining the 2D mesoscopic model. The main result !is that the NCF compressive behaviour is controlled by 0° tow geometrical instability arising at the mesoscopic scale and accompanied by resin shear plastic flow. By analogy with fibre microbuckling, we call this instability mesobuckling, and we have clearly established that it leads to the overall shear of the model cell, which can be associated with failure.

We have demonstrated that as in any imperfection sensitive medium, the coupling of the imperfection with the 0° tow non-linear shear behaviour (hence resin behaviour) is the most important feature to be considered. The 90° tow shape has a smaller effect although these tows provide support against 0° tow plastic mesobuckling if they cover the centre of the cell where high shear stresses are located. NCF stiffness has been shown to depend on the fibres, whereas NCF strength is mainly dependent on parameters which control 0° tow plastic mesobuckling.

In order to improve the NCF compressive strength, the coupling of the geometrical imperfections with the non-lin!ear resin behaviour has to be avoided. Moreover, if the fibre volume fraction can be increased in the tows and if the 90° tows can provide better support to the 0° tows against mesobuckling, NCF strength can be increased provided the resin characteristics are high enough. Consequently, the NCF compressive strength will be improved when the crimp level is limited, the resin has high mechanical characteristics (especially a high modulus), tows are spread and the overall fibre content is increased.

In short, as far as compression is concerned, the NCF should tend towards a classical laminate (geometry and fibre content), and a high modulus resin should be used. From a manufacturing point of view, the resin could be replaced by one with a higher modulus, and the fibre content could also be slightly increased. As for the geometry, simple changes could improve strength. By increasing the 0° tow tension during the lay-up, the gaps should be limited and the resulting NCF sho!uld have lower tow crimp levels. More certainly by using a low stitching tension, tows would not bunch, and hence the crimp level would be lower (by limiting nesting) and the 90° tows would spread and thus provide full support against 0° tow mesobuckling. This indication for the stitching tension is confirmed by experimental results [3] which show that in order to improve the NCF compressive strength, the stitch tension should be kept low.

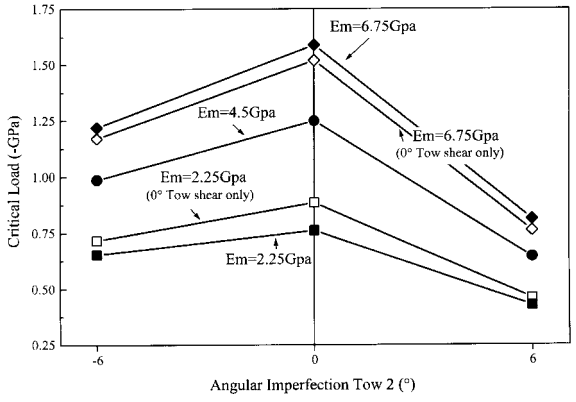

Fig. 14. Critical load versus angular imperfection of tow 2 for 3 resins moduli ($Em = 2.25$, 4.5, 6.75 GPa). $\phi^{max}_{01} = +2°$, $\phi^{max}_{02} = -6°$, 0°, +6°.

Acknowledgements

This work was achieved during the involvement of the authors in the Innovative Fabrics Aircraft Composites (INFACS) programme – Activity 3 Guidelines for Preforms/Fabric led by Cranfield University – School of Industrial and Manufacturing Science in collaboration with British Aerospace, Shorts, Dowty Aerospace, Ciba Composites, Tech Textiles, Imperial College and Queen Mary and Westfield College. The authors wish to acknowledge the support of the UK Engineering and Physical Science Research Council !under contract GR/K68516. As per the authors' request, references 8 and 15 have been deleted.

Appendix A. 0° tows' non linear shear constitutive law

The medium standing for the 0° tow is assumed isotropic transversely to the fibre direction and 2-3 is its plane of isotropy. As we work using a generalised plane strain theory, for the constitutive law of the planar element we have to use a full 3D expression but with only the in-plane shear. In the case of transverse isotropy the material is defined with four coefficients: E_{11}: the Young's modulus in fibre direction; E: the Young's modulus in isotropy plane ($=E_{22}=E_{33}$); ν_{12}: the Poisson's ratio in 1-2 plane ($=\nu_{13}$); ν: the Poisson's ratio in isotropy plane ($=\nu_{23}=\nu_{32}$).

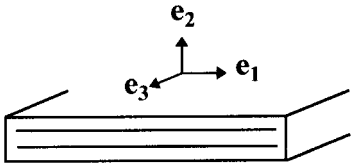

In this configuration the constitutive law of the transverse isotropic medium is:

$$\begin{pmatrix}\sigma_{11}\\ \sigma_{22}\\ \sigma_{33}\\ \sigma_{12}\end{pmatrix}=\begin{bmatrix}\frac{1-\nu^2}{E^2\delta} & \frac{\nu_{21}+\nu_{21}\nu}{E^2\delta} & \frac{\nu_{21}+\nu_{21}\nu}{E^2\delta} & 0\\ \frac{\nu_{21}+\nu_{21}\nu}{E^2\delta} & \frac{1-\nu_{12}\nu_{21}}{E_{11}E\delta} & \frac{\nu+\nu_{12}\nu_{21}}{E_{11}E\delta} & 0\\ \frac{\nu_{21}+\nu_{21}\nu}{E^2\delta} & \frac{\nu+\nu_{12}\nu_{21}}{E_{11}E\delta} & \frac{1-\nu_{12}\nu_{21}}{E_{11}E\delta} & 0\\ 0 & 0 & 0 & G_{12}\end{bmatrix}\cdot\begin{pmatrix}\varepsilon_{11}\\ \varepsilon_{22}\\ \varepsilon_{33}\\ \varepsilon_{12}\end{pmatrix}$$

with

$$\delta=\frac{1-2\nu_{12}\nu_{21}-\nu^2-2\nu\nu_{12}\nu_{21}}{E_{11}E^2}.$$

The composite axial modulus is taken into account in beams, therefore the sum of the planar element stiffness and of the beam stiffness must produce the correct overall material stiffness. That is to say the first component of the constitutive law above must be modified and gives

$$L[1,1]=\frac{1-\nu^2-E_1E^2\delta}{E^2\delta}.$$

This constitutive law is implemented in UMAT, and the composite shear modulus is deduced from a close form of a 914 resin shear stress–strain curve given in Ref. [22]. This law was derived from uniaxial compression tests on small blocks of resin and then curve fitted. The expression of the shear secant modulus of the resin (suffix m) versus the shear strain (in Pa) is

$$G^{\mathrm{m}}=\frac{1}{|\gamma^{\mathrm{m}}|}\left\{-57+109.5\left[1-\left(\frac{|\gamma^{\mathrm{m}}|-0.0935}{0.1095}\right)^2\right]^{1/2}\right\}$$

for $0\leqslant|\gamma^{\mathrm{m}}|\leqslant0.038$

$$G^{\mathrm{m}}=\frac{1}{|\gamma^{\mathrm{m}}|}\left\{-113.5+182.5\left[1-\left(\frac{|\gamma^{\mathrm{m}}|-0.1405}{0.1825}\right)^2\right]^{1/2}\right\}$$

for $0.038\leqslant|\gamma^{\mathrm{m}}|\leqslant0.13$.

The non-linear shear stress–strain curve of the 0° tows is deduced from this expression by assuming that the shear strain is proportional to the shear strain in the resin with respect to the fibre volume fraction (V_{f}). Moreover, it is well known that for a fibre volume fraction given a 2D approach underestimates the !actual shear stiffness [20] since distances between fibres are larger in 2D than in 3D. Finally the shear modulus of the 0° tows is equal to the matrix shear modulus expressed with respect to the shear strain in the matrix corrected for taking in account the 3D fibre distribution

$$G_{\mathrm{tow0}}(\gamma)=G^{\mathrm{m}}\left(\frac{1.5\gamma}{(1-V_{\mathrm{f}})}\right).$$

It leads to the following shear stress–strain response of the 0° tow

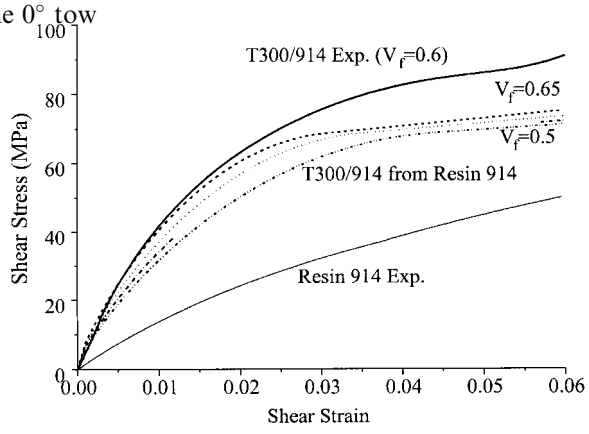

Comparison of shear behaviours for: T300/914 experimental (from [5]), T300/914 rebuilt from 914 resin shear, and 914 resin shear behaviour (from [22]).

Appendix B. 90° tows' non-linear constitutive laws

The 90° tows are assumed to be transversely isotropic with 1-2 (as referred to so far) being their plane of isotropy. With a simple rule of mixtures applied to a 2D stacking i!n plane 1-2 representing the composite, and with an hypothesis on fibre and resin stiffnesses [7], the expression of the moduli of the 90° tows can be deduced from the resin moduli.

Hypothesis. Fibre stiffness $\gg$ Resin stiffness: Thus, the mean strains in the composite are mainly concentrated in the matrix, and with a simple rule of mixtures, they write

$\gamma_{22} = \gamma_{22}^{m}(1 - V_f)$ and $\gamma_{23} = \gamma_{23}^{m}(1 - V_f)$,

where $\langle x \rangle$ stands for the mean of x on the fibre-matrix stacking or similarly it stands for the mesoscopic value of x. But due to the stress interface continuity in the layered model, the corresponding stresses are the same in both constituents ('f' corresponds to fibres and 'c'! to composite)

$$\sigma_{22} = \sigma_{22}^{m} = \sigma_{22}^{f} \quad \text{and} \quad \sigma_{23} = \sigma_{23}^{m} = \sigma_{23}^{f}.$$

Therefore we can deduce both transverse and transverse shear moduli for the composite. For instance, the composite transverse Young's modulus E_{22}^{c} is found by considering a pure transverse tension

$$\sigma_{22} = E_{22}^{c}\gamma_{22} = E_{22}^{c}\gamma_{22}^{m}(1 - V_f)$$

$$\text{and} \quad \sigma_{22} = \sigma_{22}^{m} = E_{22}^{m}\gamma_{22}^{m} \Rightarrow E_{22}^{c} = \frac{E_{22}^{m}}{(1 - V_f)}.$$

With the same demonstration, we can get the composite transverse shear modulus. By comparing the elastic moduli obtained with this simple approach with others got from different manners (Hahn formulas, Léné homogenisation [20]), it turns out that a simple correction with a constant gives a proper approximation. Finally:

$$E_{22}^{c} = \frac{E_{22}^{m}}{0.8(1 - V_f)} = \frac{E^{m}}{0.8(1 - V_f)} \quad G_{23}^{c} = \frac{G_{23}^{m}}{0.8(1 - V_f)} = \frac{G^{m}}{0.8(1 - V_f)}.$$

This correction is then extended to the non-linear !response of the 90° tows.

References

[1] ABAQUS, Hibitt, Karlsson and Sorensen Inc 100, Medway St, Providence, RI, 02906, USA

[2] Backhouse R, Blakeman C, Irving PE. Mechanisms of toughness enhancement in carbon fibre non-crimp fabrics. Third International Conference on Deformation and Fracture of Composites, UK: Surey, 1995. p. 307–12

[3] Backhouse R. Multiaxial non-crimp fabrics: characterisation of manufacturing capability for composite aircraft structure applications. Eng. D. thesis, Cranfield University, School of Industrial and Manufacturing Science, 1998.

[4] Dexter HB. An overview of the NASA textile composite program, Proceedings of the Sixth conference on advanced engineering fibres and textile structures for composites, Philadelphia, 1992. p. 1–31

[5] Ditcher AK. The non-linear stress–strain behaviour of carbon fibre reinforced plastic and its effect on the analysis of laminated plates and sandwich beams. Ph. D. thesis, University of Bristol, Department of Aerospace Engineering, Bristol, 1981

[6] Dransfield K, Baillie C, Yiu-Wing M. Improving the delamination resistance of CFRP by stitching – a review. Composites Science and Technology 1994;50:305–17

[7] Drapier S, Gardin C, Grandidier J-C, Potier-Ferry M. Structure effect and microbuckling. Composites Science and Technology 1996;56:861–7

[8] Deleted in proof.

[9] Du GW, Ko F. Analysis of multiaxial warp-knit preforms for composite reinforcement. Composites Science and Technology 1996;56:235–60

[10] Farley GL, Dickinson LC. Mechanical Response of composite materials with through-the-thickness reinforcement. Proceedings of Fifth conference on advanced engineering fibres an!d textile structures for composites, 1991. p. 123–43

[11] FEMGEN. Femsys Limited 158 upper new walk. Leicester LE1 7QA, UK

[12] Fleck NA, Shu JY. Microbuckle initiation in fibre composites: a finite element study. Journal of Mechanics and Physics of Solids 1995;43(12):1887–918

[13] Gardin C, Potier-Ferry M. Microflambage des Fibres dans un Matériau Composite à Fibres Longues: Analyse Asymptotique 2-D, Comptes Rendus de l'Académie des Sciences de Paris Tome 315, Série II, 1992. p. 1159–64

[14] Grandidier J-C, Ferron G, Potier-Ferry M. Microbuckling and strength in long-fiber composites: theory and experiments, International Journal of Solids and Structures, 1992; 29(14/15):753–1761

[15] Deleted in proof.

[16] Hogg PJ, Ahmadnia A, Guild JF. The mechanical properties of non-crimped fabric base composites. Composites 1993;24: 423–32.

[17] Ko F, Fang P, Pastore C. Multilayer multidirectional warp knit fabrics for industrial applications. Journal of Industrial Fabrics 1985;4(2):4–12

[18] Ko F, Kutz J. Multilayer warp knit for advanced composites. Proceedings of Fourth Annual Conference on Advanced Composites, US: Dearborn, Michigan, 1988. p. 73–7

[19] Ko F, Lei C, Rahman A, Du GW, Cai Y. Unit cell geometry of multiaxial preforms for structural composites. Final Report to NASA Langley Research Center (NASA-CR-197294), 1993

[20] Léné, F. Contribution à l'étude des matériaux composites et de leur en!dommagement. Thèse de Doctorat ès sciences de l'Université Pierre et Marie Curie, Paris VI, 1984

[21] Miller AJ. The effect of microstructural parameters on the mechanical properties of non-crimp fabric composites. M. Phil thesis, Cranfield University, School of Industrial and Manufacturing Science, August 1996

[22] Wisnom MR. The effect of fibre misalignment on the compressive strength of unidirectional carbon fibre/epoxy. Composites 1990;21(5):403–7

[23] Wisnom MR. Analysis of shear instability in compression due to fibre waviness. Journal of Reinforced Plastics and Composites 1993;12(11):1171–89

[24] Wisnom MR. The effect of fibre waviness on the relationship between compressive and flexural strengths of UD. Journal of Composite Materials 1994;28:66–76

- K -

Annexe 2. 5

S. Drapier & M.R. Wisnom.

A finite-element investigation of the interlaminar shear behaviour of non-crimp-fabric-based composites.

Comp. Sci. Technol. **, 59(16) :2351–2362, 1999.**

ELSEVIER

Composites Science and Technology 59 (1999) 2351–2362

COMPOSITES SCIENCE AND TECHNOLOGY

A finite-element investigation of the interlaminar shear behaviour of non-crimp-fabric-based composites

Sylvain Drapier [a,*], Michael R. Wisnom [b]

[a] *Mechanical and Materials Engineering Department, Ecole des Mines de Saint-Etienne, 158, cours Fauriel, F-42023 Saint-Etienne Cedex 02, France*
[b] *Department of Aerospace Engineering, University of Bristol, University Walk, Bristol BS8 1TR, UK*

Received 4 January 1999; received in revised form 5 June 1999; accepted 22 July 1999

Abstract

In this paper the interlaminar shear behaviour of non-crimped-fabric-based composites is investigated by using a finite-element approach. It is intended to provide an understanding of the basic mechanisms which control the NCF behaviour, together with manufacturing guidelines for the fabric structure to optimise the NCF properties. The present approach is based on a bi-dimensional mesoscopic model of a biaxial blanket developed in a previous study devoted to the compressive strength of NCF (Drapier, S, Winsom MR. Finite element investigation of the compressive strength of non-crimp fabric based composites. Composites Science and Technology, 1999;59:1287–97). This through-thickness repeating cell is completed with the proper boundary conditions representative of interlaminar shear loading. It is established that the NCF ILS behaviour is controlled by the development of high shear-strain concentrations induced by the combination of mechanical and mesoscopic geometrical characteristics. These shear-strain concentrations are very likely to lead to local damage that could affect the NCF load-bearing capacity. It is mainly the resin shear behaviour, and to a lesser extent the tow size, which are shown to control the ILS behaviour. Also, the presence of resin layers which can form between the tows during the manufacturing process increases these strain concentrations. From a manufacturing point of view, it comes out from this study that the resin should have high shear stiffness and yield stress, and that tow bunching should be prevented by limiting both the stitching tension and the size of the tows used. Finally, the formation of resin layers should be limited as far as possible.

Keywords: Non-crimp-fabric composites; Structure/property relation; Finite-element model; Interlaminar shear strength; Shear-strain concentrations; Parametric study

1. Introduction

A quick survey of the recent literature makes it clear that non-crimp-fabric (NCF) materials (Figs. 1 and 2) are becoming popular as they bring an improvement in damage tolerance [1], particularly against delamination [2–4], as well as substantial cost reductions. These improvements are obtained by introducing a stitching yarn through the thickness of a blanket made up of a stack of two to four layers of tows (Fig. 1). These layers are obtained from tows of fibres placed side by side. The blankets are then used as classical plies, stacked to give thicker composites and cured in a resin film infusion process.

Unfortunately, the improvements brought about by the NCF process in terms of damage tolerance come along with strong drawbacks. These are either inherent to the stitching, such as fibre breakage induced by needle penetrations, or they are caused by the heterogeneity of the constituents put together that lead to the formation of mesoscopic defects (Fig. 2) such as resin pockets and tow crimping. This last phenomenon can be rather important, and it was shown to control the compressive strength of the NCF both from a theoretical [5] and experimental point of view [2]. The presence of resin pockets is also thought to facilitate the development of strain concentrations.

So far, most of the studies devoted to the NCF composites have been either dedicated to their experimental characterisation [2,6], or to the investigation of their resistance to delamination [3,4]. Studies have been carried out on modelling other kinds of through-thickness

* Corresponding author. Tel.: +33-04-7742-0079; fax: +33-04-7742-0000.

E-mail address: drapier@emse.fr (S. Drapier), m.wisnom@bris.ac.uk (M.R. Wisnom).

0266-3538/99/$ - see front matter
PII: S0266-3538(99)00091-3

reinforced composites [7,8]. Multiaxial-warp-knit materials, which are very close to NCF in terms of manufacturing, have been extensively studied from an experimental point of view [9], and from a theoretical point of view in terms of packing [10–12] and tow misalignment/MWK property relationships [10].

The numerous studies devoted to both NCF characterisation and fabrication demonstrate an increasing interest in these materials. As NCF composites are not yet well understood from a theoretical point of view, we aim to give an insight into the underlying mechanisms which control their behaviour. As far as the compressive behaviour is concerned, we proposed an approach [5] at the mesoscopic scale that gave good correlation with experimental investigations [13]. Now the ILS behaviour of NCF is to be dealt with, on the basis of the same mesoscopic bi-dimensional FE model developed for the NCF compression. A parametric study is carried out to show the parameters which are most likely to influence the ILS behaviour of NCFs.

2. Mesoscopic modelling approach for biaxial NCF

In order to test the influence on the NCF ILS behaviour of the most relevant characteristics a model was developed. It is a mesoscopic FE model of NCF wherein geometry (tow crimp, tow width, resin layers) along with constituent properties (fibre-volume fraction and resin characteristics) can be represented.

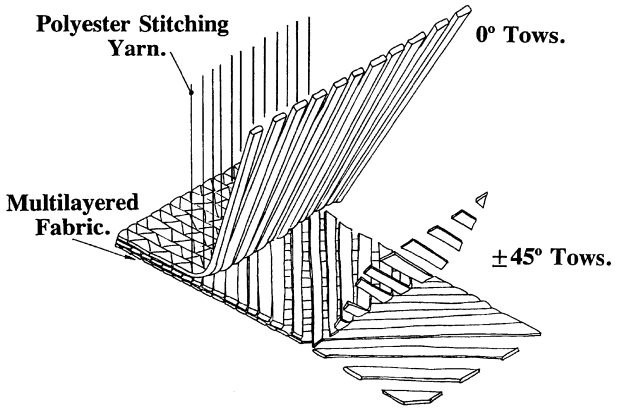

Fig. 1. Schematic of a NCF manufacturing.

Comprehensive justifications of the choices which led to the mesoscopic model upon which the present development is based are given in Drapier and Wisnom [5]. The key point is that this model was established at the mesoscopic scale. Of the four scales of observations of NCF (constituents scale, tow scale, blanket scale, composite scale), it is at the 'blanket scale' (or mesoscopic) that most of the parameters were measured [13,14] and were shown to be relevant as far as the basic mechanisms are concerned. This scale of observation could not have been considered without the use of equivalent homogeneous media to model the tows made up from 3000 to 24,000 fibres. This last issue was addressed thanks to the knowledge gained in the field of the representation of the behaviour of equivalent homogeneous media in non-uniform states of stress [15,16].

2.1. Nesting

From measurements at the blanket scale [14], it appears that the crimp level of the tows in the so called non-crimped fabrics can be very large, some way between unidirectional and woven composites. The measurement of this crimp can be assumed sinusoidally shaped and is defined by its wavelength (λ) and its amplitude, which is related to the maximum misalignment angle with respect to the theoretical direction (ϕ^{max}). When comparing crimp angles and wavelengths [14], it is seen that the tow crimp depends essentially on the arrangement of the tows in neighbouring layers. This is most obvious in the case of biaxial blankets. Under the pressure applied during the cure, tows in one direction (e.g. 0°) tend to 'nest' into the gaps left in the complementary direction (resp. 90°). In this nesting phenomenon schematically represented at the top of Fig. 3, the crimp wavelength is set by the spacing of tows in the complementary direction and depends on

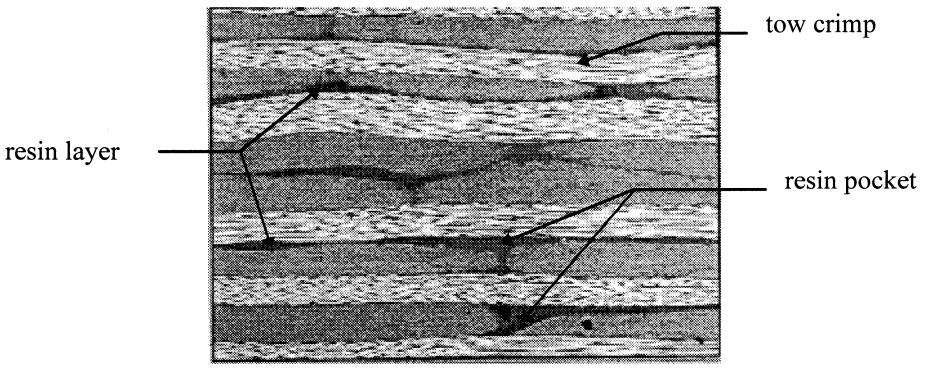

Fig. 2. Mescoscopic photograph of a biaxial NCF slice through thickness (from Miller [14]).

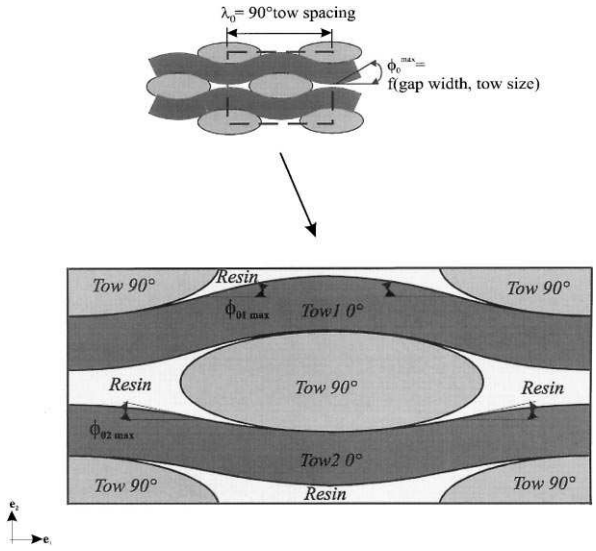

Fig. 3. Bi-dimensional model used for the interlaminar shear study of a biaxial NCF.

the tow size, whereas the misalignment angle (resp. amplitude) depends on the width of the gaps left in this complementary direction (depending on both the 90° tows spacing and size).

2.2. Stitching

Manufacturing trials [13] showed that very tight stitching could induce well-developed resin channels running parallel to the tows. Also, when the stitching was removed before curing, the tows could spread and the crimp level was halved. This suggests that the stitching tension might modify the final geometry of the NCF. Moreover, a strong correlation was found between the mean resin rich area size (resin pockets) and the crimp level, which tends to reinforce the assumption of nesting: the more the material is 'gappy', the larger the crimp and the resin-rich areas.

It has been shown that stitching plays a role when delamination propagates. The improvement of fracture toughness with stitching is up to 15 times for mode I [3], but 'only' 4 times for mode II [4]. Therefore, as far as mode II is concerned, i.e. interlaminar shear fracture, the contribution of the stitching is not as marked as for mode I. Moreover, one can think that the stitching stiffness will participate only if large deformations are experienced following the appearance of damage. For the present study which aims at understanding the mechanisms controlling initiation of damage in the NCF, it was assumed that the stitching could be ignored, as it primarily changes the crimp level (which is for us an input data from measurements) but does not participate markedly in terms of stiffness as long as the integrity of the meso-structure is conserved.

2.3. Mesoscopic bidimensional repeating cell

From the studies by Miller [14] and Backhouse [13], it emerges that most of the parameters likely to influence the NCF behaviour are measured at the mesoscopic scale, i.e. the scale at which the tows are seen as homogeneous media (Fig. 2). Therefore, the model was set up at this scale of observation for the simplest case of NCF, that is to say a biaxial one (0°/90°). In Miller [14] and Backhouse [13], the measured variation of 0° tow cross-section (area and shape) in the fibre direction is sufficiently low for us to consider that it does not affect significantly the 0° tow mechanical characteristics along this direction. Moreover, the variation of the parameters in the 90° direction is also assumed low and can be simplified by taking into account only the effect of a direct strain in that direction. Finally, as the stitching effect is not considered, a 2-D repeating cell defined through the thickness and along the 0° tow direction was sufficient and neither the stitching thread nor its stiffness was taken into account (Fig. 3).

Following the previous remarks, the model was based on the nesting phenomenon (Drapier and Wisnom [5]), i.e. the cell dimensions are set by the 0° tow-crimp wavelength and the tow thicknesses. The unit cell was defined with two 0° tows, and the resin pockets are directly defined by the room left between the 90° tows and the 0° tows. In this model tows are represented in the 0° direction by an homogeneous band across the width. Tows along the 90° direction are represented by an ellipse of equivalent cross-sectional area depending on the tow size used (3, 6, 12, 24 k). Tow crimp is assumed sinusoidal and the maximum angle with respect to the theoretical 0° direction defines the crimp level (Fig. 3). This crimp is assumed constant across the NCF width but different for both 0° tows. Voids were neglected and therefore every medium was assumed to be continuous.

2.4. Tow modelling — material representation

Tows were assumed to be homogeneous, and for the 0° tows the approach used to model their compressive behaviour was retained. Its principle is to rebuild an homogeneous equivalent medium from standard finite elements provided in ABAQUS® [17]: beams without shear flexibility which withstand the fibre direction load and provide bending stiffness, superimposed on planar elements which bear shear and transverse loads (Fig. 4). Displacements along $\mathbf{e}_1$ and $\mathbf{e}_2$, respectively u and v, are constrained to be identical for the beam and the plate, and the beam rotation θ is left free. A constitutive law has to be introduced to rebuild the equivalent behaviour from the properties of the two media, which was addressed in a UMAT subroutine (for details see Appendix 1 in [5]).

As previously [5], the non-linear behaviour of the three media (0° tows, 90° tows and resin pockets) was based upon the same non-linear experimental stress/strain curve for the resin (Fig. 5). The 0° tows were assumed to be non-linear in shear but linear in the fibre and transverse directions. Their shear behaviour was derived from the resin shear constitutive law using a simple layered model based on the fibre-volume fraction (Fig. 5). For the 90° tows, the fully non-linear planar constitutive law was also deduced from the same resin curve (for details see Appendix 2 in [5]) taking account of the fibre-volume fraction, and assuming a Von Mises equivalent plastic principle. The same plastic constitutive law was used for the regions of unreinforced resin. Hence, any change in the resin used in manufacturing can be reflected directly in the three media (resin, 0° tows, 90° tows) by changing only the resin shear response.

2.5. Boundary conditions

The study of the shear behaviour requires the boundary conditions used for the compression investigation [5] to be modified. First, we must represent a repeating cell in the fibre and through-thickness directions; this implies that the displacements perpendicular to the boundaries on opposite edges must be equal (Fig. 6a). Second, the boundary conditions must represent the anti-symmetry of the shear. That is to say, the displacements inducing shear must be equal and opposite with respect to the centre of the cell. Moreover, we choose to prescribe this displacement to be equal for all the points on the same edge in order to represent an even shear strain applied along the edges (Fig. 6b). Finally, it remains to prevent any rigid-body rotation, which is achieved by constraining, at a single point, the displacements u and v to be equal (Fig. 6c).

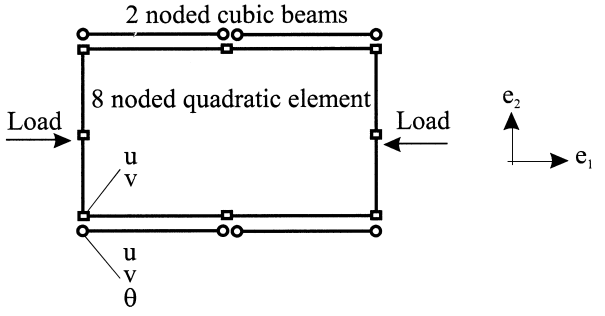

Fig. 4. Pseudo-element similar to that used by Wisnom [15,19].

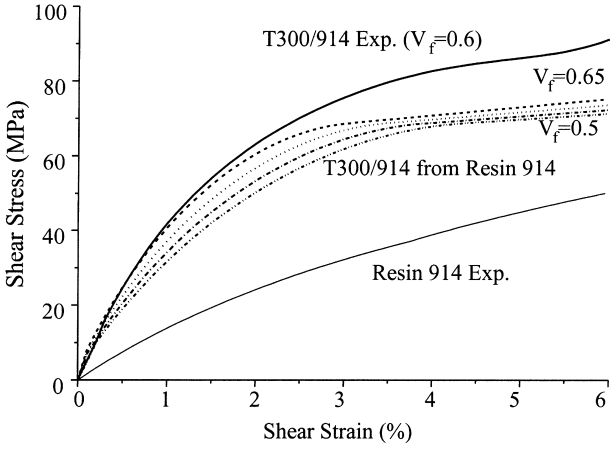

Fig. 5. Comparison of shear behaviours for: T300/914 experimental (from [20]), T300/914 rebuilt from 914 resin shear, and 914 resin shear behaviour (from [21]).

2.6. Meshes

The cell size depends on the 0° tow crimp, the tow thicknesses and the crimp wavelength. Moreover, the areas occupied respectively by the three media (resin, 0° tow, 90° tow) must match the volume fractions prescribed. With the geometry we chose, the volume fraction of unreinforced material is not controlled for it depends on the area occupied by the resin pockets in the mesh. But for the tows, we can imagine several ways to obtain at the same time both the correct dimensions and volume fractions, and so certain parameters must be fixed. As a parametric study is to be conducted, we chose a simple solution, similar to that adopted in the NCF compressive behaviour investigation [5]: the thicknesses of the 0° and 90° tows is kept constant. The 0° tow volume fraction (V_{ft0}) is also initially held constant according to the measurements, and these parameters are calculated from both the number of fibres in the tows and the tow geometry. Then, depending on the area occupied by the media in the mesh, the volume fraction of the 90° tows (V_{ft90}) is evaluated so as to meet the given overall fibre content of the cell. In the previous study, the fibre-volume fraction of the tows in the loading direction was critical in modelling compression, but here the choice of fixing V_{ft0} is justified only by the need to have a single parameter to control.

The 2D mesh (Fig. 7) was generated with FEMGEN® [18], a commercial mesh generator. The geometry of the 90° tows was slightly simplified in order to avoid some problems with narrow elements which could form between the 0° and 90° tows. For a perfect case, i.e. without 0° tow crimp, this choice for the 90° tows fits with the assumption of Du and Ko [12] who assumed the 90° tows to have a 'race-track'-like cross-section (see also Fig. 2).

2.7. Computations

In order to best represent a 3-D medium with a 2-D model, quadratic planar elements with a generalised plane-strain theory were used. This allows a direct strain in the 90° direction (out of the plane of the model) to be

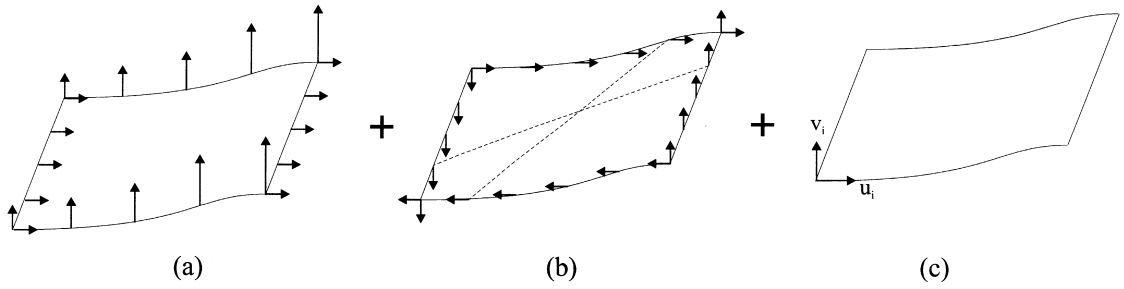

Fig. 6. Schematic of the boundary conditions for pure shear: (a) displacements coupled, (b) opposite displacements on opposite nodes, (c) rigid body motion prevented.

taken into account, which could play a role in the plastic behaviour of the media.

An 'arc-length' path-following method was used to cope with non-linear response of the NCF. Unlike the compression study, we did not expect the effect of large strains to be very significant, therefore a linear geometrical approach was sufficient.

The loading was applied via a force prescribed on a vertex, and because of the specific boundary conditions it corresponds to a distributed loading applied on the cell perimeter. Therefore, the corresponding stress can easily be calculated from the cell perimeter, and the overall shear strain is calculated from the displacement of the vertices with respect to the cell dimensions.

3. Baseline case

A *baseline case* was used (Fig. 7), corresponding to a biaxial NCF. Data used for the computations are those for T300/914, with an estimated fibre-volume fraction of 0.55. The fibres and matrix were both assumed to be isotropic (Table 1).

Angular imperfections were $+2°$ for tow 1 (top of cell) and $-6°$ for tow 2 (bottom of cell) (Fig. 7a). The dimensions of the tows were deduced from their volume fraction in the composite, their content in fibres (3 k) and the measurement of their width [14]. The 0° tow thickness was calculated to be 0.298 mm and the 90° tows were 0.244 mm thick and 1.1 mm wide. The crimp wavelength was 1.4 mm, as measured in Miller [14], and the overall fibre fraction was 0.44. The fibre content in the 0° tows for the baseline mesh was 0.55, and the value in the 90° tows was 0.41 for that configuration of crimp. The corresponding resin rich region volume fraction was 0.12.

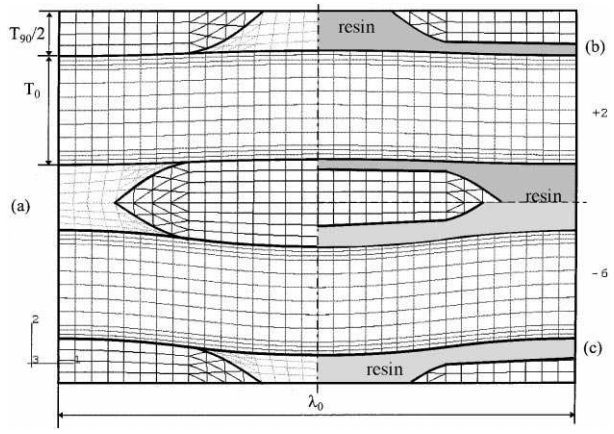

Fig. 7. Mesh with imperfections of $+2°$ for tow1 and $-6°$ for tow 2: (a) Baseline case, (b) with one resin layer, (c) with two resin layers.

3.1. NCF response

In Fig. 8 it can be seen that the overall shear response of the cell is fully non-linear. In this figure are also plotted responses of both the resin and the 0° tow on their own, respectively the softest and stiffest media in the cell. It is clear that the NCF overall shear stiffness depends on the contribution of the three media shear

Table 1
Mechanical characteristics used for computations[a]

Constituents	Composite ($V_f = 0.55$)
$E^f = 230$ Gpa	$E^c_{11} = 129$ Gpa
$v^f = 0.25$	$E^c_{22} = 9.77$ Gpa
$E^m = 4.5$ Gpa	$v^c_{12} = 0.32$
$v^m = 0.4$	$v^c_{23} = 0.45$

[a] Indices 'f' and 'm' refer respectively to fibres and matrix, and 'c' stands for composite.

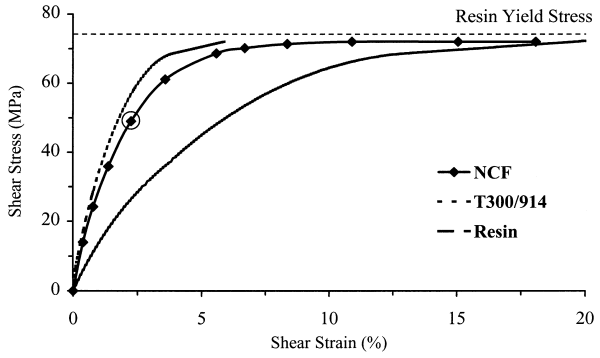

Fig. 8. Response for the baseline case (mesh Fig. 7a), resin 0° tows: shear strain versus shear stress.

stiffness. It is also especially relevant that the *resin yield stress limits the overall shear response* (~72 MPa in our experimental curve), since it is the same for the three media whose response reaches a plateau at this level of stress. This reinforces our idea that the resin should limit the tow behaviour, as is usually observed for other loadings.

Observation of the stress and strain distributions permits us to check first that, as we can expect from a medium loaded in pure shear, the fibre-direction (ε_{11}) and transverse-to-fibre strains (ε_{22}) are small when compared to the shear component (ε_{12}) and vary very little across the cell. ε_{11} and ε_{22} both remain relatively small ($< 1\%$) even for the prescribed load of 50 MPa (circled dot in Fig. 8) which is rather high for a shear loading. Therefore, these direct strains will no longer be considered in this study of the NCF ILS behaviour.

Second, the shear-stress distribution (Fig. 9) exhibits a quite gradual variation across the cell thickness and to a first approximation stresses are continuous across the interface between the different materials (see, for instance, the middle part of the cell). However, it can be observed that the largest gradient occurs through a narrow triangular region (between the tip of the 90° tows and the 0° tows), as a result of both the change in material characteristics and the small length over which this change takes place. As shear stresses are approximately continuous across the thickness, conversely strains are not. It is clear in Fig. 10, especially in the resin pockets, that there are some large drops in strain when going from the resin to the tows (from soft to stiff material). The variation in the fibre direction is less pronounced for both stresses and strains as the change in material is present only in the 'resin triangle'. Only a slight change of the shear stresses in the same medium is visible in the 0° tows which might be imputed to the misalignment of the corresponding elements in the mesh.

As shown in the deformed shape in Figs. 9 and 10, when loaded under shear the NCF behaves to a first approximation as a stack of soft (resin + 90° tows) and stiff (0° tows) layers. This becomes even clearer as the load is increased since, because of the non-linear shear behaviour of the resin, very high strains spread in the resin + 90° tow 'layer', emphasising the gradient of the strain distribution plotted in Fig. 10. Strains increase until finally the shear stress all over the cell has reached the same value, i.e. the yield stress of the resin. From now, we will focus only on results corresponding to loads of 50 MPa, high enough to get results close to the real situation at failure (the typical ILS strength measured in Miller [14] is about 50 MPa) but avoiding unrealistic shear strains, especially in the resin.

3.2. Strain localisation

When approaching the yield stress which limits the NCF shear response, shear strains are very high, with the highest shear strains developing in the tip of the very small 'triangle-like' region of the resin pockets between the tows. It can be noticed that by using a failure criterion, for instance a maximum shear strain criterion, the overall interlaminar shear stress could be predicted. However, a fracture analysis of this type would require experimental data which were not available at the time of this study and would represent a study on its own. This is far from the scope of the present study which aims mainly at understanding the basic mechanisms that finally lead to a drop of stiffness prior to failure. But the present approach allows a description of the shear-strain localisations that are representative of potential damage initiations.

In Fig. 11 the shear-strain distribution is plotted for the baseline case for strains greater or equal to 4%, the order of the failure strain typically measured for epoxy resins. This permits us to check quickly the locations where the highest strains develop which might lead to damage initiation. A close-up of the 'resin triangle' (Fig. 11) reveals sharp gradients of shear strains where the actual values are very likely to be mesh-dependent. These strain localisations which cannot be avoided are usually dealt with by considering strains and stresses at a distance away from the peak, e.g. in the centre of the elements (pointed by arrows in Fig. 11). It does not

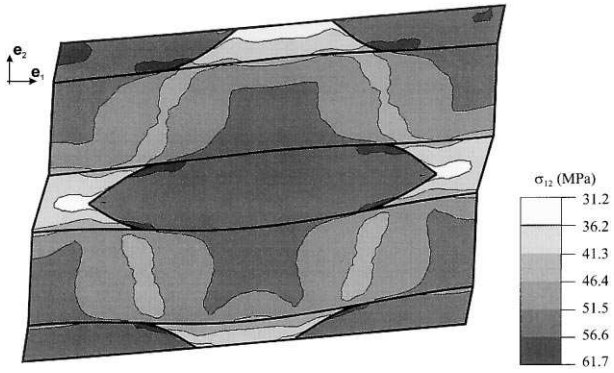

Fig. 9. Shear-stress distribution in the baseline case (+2°/−6°) for a prescribed stress of 50 MPa. Deformed shape×10.

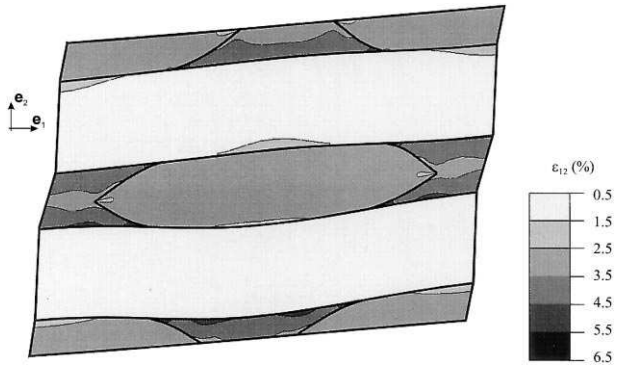

Fig. 10. Shear-strain distribution in the baseline case (+2°/−6°) for a prescribed stress of 50 MPa. Deformed shape×10.

eliminate the problem but it limits its influence on the interpretation of the results. In our case, the centroidal shear strains of the main elements in the 'resin triangle' reach 5.75%, whereas the maximum nodal value extrapolated from the Gauss points given in ABAQUS POST® [17] is 7.76%.

For the results following, the maximum centroidal shear strain will also be quoted in order to give a better indication of the shear strain reached excluding the highly localised peak values. This is already accounted for in Fig. 10 where the shear-strain distribution is plotted for strains lower or equal to 6.5% (instead of 7.76%), in order to have a relevant range of shear strains which can also be compared with other shear-strain distributions in the following. Indeed, as the changes in strains are larger than the changes in stresses which approach a constant value near the yield stress level, we will focus henceforth only on shear strains.

4. Parametric study

In this parametric study is investigated the influence of the most sensitive geometrical and material characteristics that can be changed by modifying either constituent properties or manufacturing parameters. The geometry of the resulting NCF can be changed through the stitching tension, therefore the influence of both 0° tows imperfection and 90° tow width was investigated. Then, fibre-volume fractions and resin characteristics were considered. Finally, the presence of resin layers was investigated, alone and also when accompanied by changes in the resin modulus.

4.1. Effect of the geometrical parameters

4.1.1. Angular imperfection

Recall that when the 0° tow crimp changes, the 90° tow fibre-volume fraction is updated in order to get the same overall fibre content of 0.44. Here four pairs of imperfections were investigated (tow1°/tow2°) : +2/−6, +8/0, −8/0 and +2/+6. This corresponds to fibre-volume fractions in the 90° tows of 0.405, 0.404, 0.495 and 0.483, respectively, and volume fraction of unreinforced material of 0.119, 0.118, 0.166 and 0.16, respectively.

In the compression study [5], it has been demonstrated that the crimp level and the combination of the crimp of the two tows plays a major role: the larger the crimp, the lower the compressive strength. If we observe the effect of the crimp on the response of the cell (Fig. 12), there is no significant difference when the crimp changes. Neither are the strain distributions of these cases worth showing since there is very little change. Similarly, the maximum shear strains remain almost identical through the four cases investigated.

4.1.2. Tow width

By changing either the size of the tows used or the stitching tension, the 90° tow shape can change. The length of 0° tow covered with the 90° tows (called 'contact length') has proved to play a major role in the NCF compressive strength [5]. We assume that when the contact length increases, the resin comes from the pockets into the 90° tows whose fibre-volume fraction is decreased such that the overall fibre content is matched. Moreover, when this dimension changes, the 90° tow width varies proportionally.

Let us consider a change in the 'contact length' in the baseline case in the range $[\lambda_0, 2\lambda_0/3, \lambda_0/2, \lambda_0/4]$ which corresponds to a change in the 90° tow fibre content of [0.209, 0.337, 0.405, 0.757] and a change in the unreinforced material content of [0, 0.059, 0.119, 0.257]. The corresponding responses are very similar, except for the case with the narrowest 90° tows whose response exhibit a slight softening. If we observe the shear-strain distribution for the case where the contact length is the smallest (Fig. 13a), it reveals that some higher strains can develop in the 0° tows, at the location where the

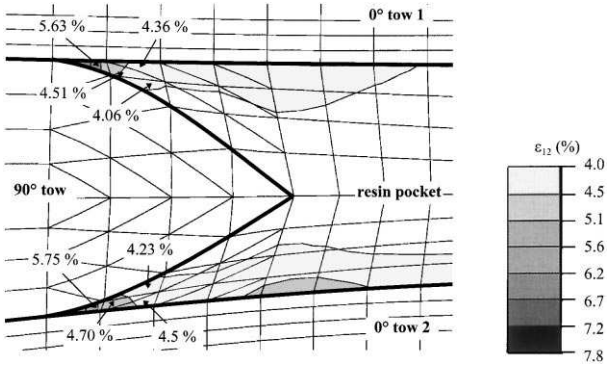

Fig. 11. Shear-strain distribution in the baseline case for a prescribed load of 50 MPa. Close up of the 90° tip in the centre part, only shear strains ⩾ 4% are plotted. Centroidal shear strain values of elements are pointed by the arrows.

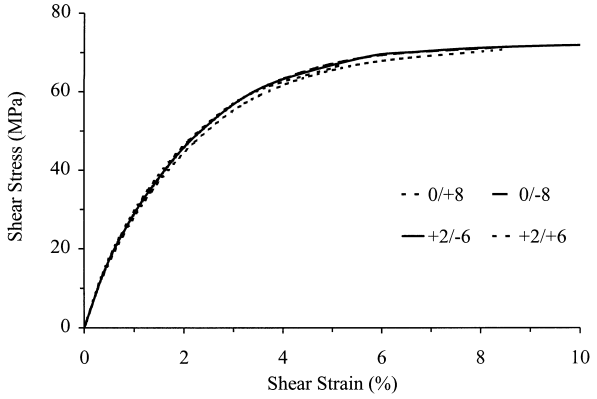

Fig. 12. Shear response for cells with different crimp imperfections combination.

misalignment angle is maximum. As the resin cannot provide as good a support to this region as the 90° tows in the baseline case, an advanced strain state results in an overall softening of the cell. Moreover, this explains why in the baseline case (Fig. 13b) some very high shear strains can be observed in the resin 'triangle'. In fact, these high shear strains in the resin come from both this 0° tow misalignment and the vicinity of the three media, i.e. the change in mechanical characteristics over short distances.

It could be thought that the effect of the misalignment might become more important in the case where the support provided by the 90° tows is not sufficient. But the main loading being shear, this effect is still small as differences in response occur only after about 50 MPa, when local shear strains are already relatively high.

It is interesting to compare the strain state for the baseline case and the case quoted above (Fig. 13b and 13a). The maximum centroidal shear strains are very close (5.75% for the baseline case and 5.92% in the present case) but the shear distribution is more disturbed when the 90° tows are shorter. Conversely, for the case where the 90° tows entirely cover the 0° tows (contact length $=\lambda_0$), i.e. the resin pockets are completely merged into the 90° tows, for the same overall stiffness as the baseline case the shear strain distribution is more even over the cell. This could give some interesting characteristics because of the homogeneous strain state as it avoids any high strain concentration which could initiate failure: the more spread the 90° tows, the more uniform the shear state.

4.2. Mechanical characteristics

4.2.1. Fibre-volume fraction

When changing the fibre-volume fraction in the 0° tows, the fibre-volume fraction of the 90° tows has to be changed in order to keep the correct overall fibre content. In our case, we increase the 0° tow fibre-volume fraction (V_{ft0}) from 0.55 to 0.65 which corresponds to a decrease in the 90° tow fibre-volume fraction (V_{ft90}) to 0.2. If V_{ft90} remains unchanged with respect to the baseline case value (0.41), the present increase in V_{ft0} is equivalent to an increase of the overall fibre content from 0.44 to 0.5.

It is clearly seen in the responses for these three cases (Fig. 14), that an increase of fibre content in the 0° tow by redistributing fibres from the 90° tows does not change at all the overall stiffness. Conversely, if the overall fibre content is increased, the overall stiffness is also increased. This could be predicted with a simple rule of mixtures. The result also shows that local mechanisms are not brought into play by this increase in fibre-volume fraction because only an increase in the entire cell has an effect on the overall response. This is confirmed by the shear-strain state which is virtually identical to that of the baseline case.

4.2.2. Resin characteristics

The resin is known to play a major role in the strength of composites under all loading conditions other than fibre-direction tension. We investigate in detail here the influence on the NCF behaviour of a change in the resin elastic modulus and in the resin yield stress. Increasing and decreasing the resin elastic modulus by 50%, i.e. with E^m in the range [2.25, 4.5, 6.75] GPa, once more we can see from the response of the cell (Fig. 15) that this change is passed directly on to the overall shear stiffness. That can be expected from the analysis of the shear-strain distribution in the baseline case (Fig. 10): the resin pockets are strongly shear loaded, and thus an increase in stiffness will strengthen these regions, as it will in the meantime also increase the tow stiffness. A slight difference can be observed between the change in the responses for a 50% increase and a 50% decrease of the modulus; the lowering of the overall stiffness is not as pronounced as the increase. This could be caused by some local mechanisms where the combination of geometrical and mechanical parameters emphasises more or less these changes of the resin elastic modulus. Secondly,

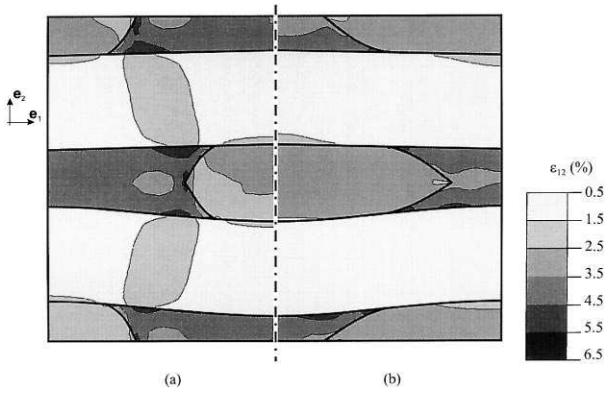

Fig. 13. Shear-stress distributions plotted on the initial shape for a prescribed load of 50 MPa: (a) contact length = 1/4 crimp wavelength, (b) baseline case.

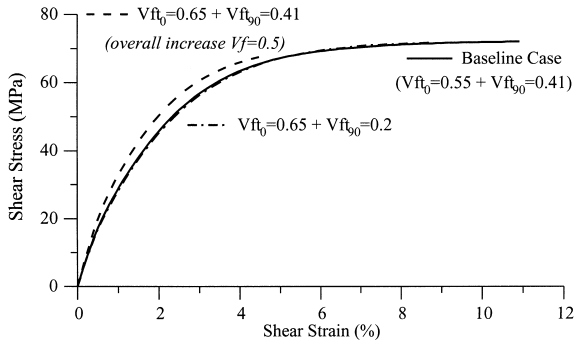

Fig. 14. Shear response for different fibre-volume fractions in the baseline case.

as could be expected, any change in the resin yield stress brings a similar change in the NCF ILS overall behaviour (Figs. 8 and 15) which is definitely controlled by the resin response.

In Fig. 16 one can see that the shear-strain distribution corresponding to a 6.75 GPa resin elastic shear modulus (Fig. 16a) is very close to the one for the baseline case with a 4.5 GPa resin (Fig. 16b). In fact, it looks as if only the range of representation of the strains has changed, with a general decrease of about 0.7%, although a bit more for the highest values located in the 'resin triangle' because of the non-linear behaviour. Strains extrapolated from the Gauss points go here from 0.77 to 6.2% instead of 1.43 to 7.76% for the baseline case and maximum centroidal values are 4.92% compared with 5.75%. The lowest strains are in the 0° tows, and the highest ones are in the resin pockets, with a very similar distribution for these regions when compared to the baseline case.

Even though we must interpret the highest values carefully, if we also consider the change in response brought about by the increase in the resin modulus (Fig. 15), we can reckon that the localisations in the 'resin triangle' are limited by the higher resin stiffness combined with a better load bearing of the surrounding tows. Conversely, this worsens when the modulus is decreased as the resin mechanical characteristics are already low and hence allow the localisation to occur for lower loads.

To conclude, the comparison of the strain distributions for the baseline case with 4.5 and 6.75 GPa shows an overall uniform decrease of the strains (Fig. 16) when the resin modulus is increased. Also, the overall stiffness increases with an increasing resin modulus. In short, the stiffer the resin, the stiffer the NCF shear response and the more even the shear state.

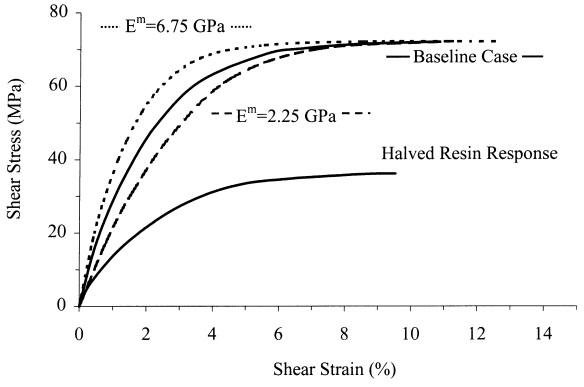

Fig. 15. Shear response for the cell with a 50% increase, genuine and halved resin elastic modulus, and for a response of the resin halved.

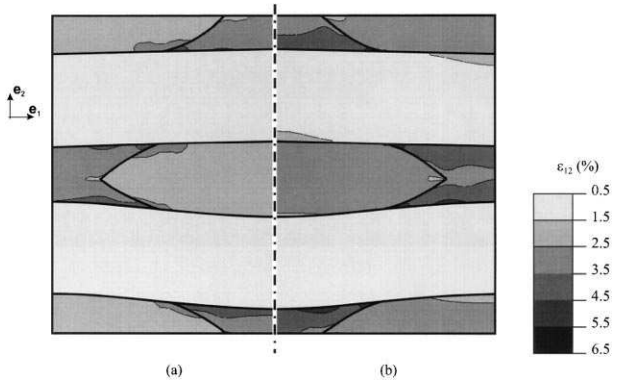

Fig. 16. Shear-strain distribution plotted on the initial shape for a prescribed load of 50 MPa. For the baseline case with (a) $E^m = 6.75$ GPa and (b) the genuine resin modulus of 4.5 GPa.

4.3. Presence of resin layers

4.3.1. Resin layers in the baseline case

Miller [14] has clearly shown that, after curing, resin layers tend to form parallel to the stacking plane. A linear correlation was found between decreasing ILS strength measurements and increasing thickness of these resin layers (Fig. 17). The mean resin layer thickness was measured by Miller [14] in biaxial NCFs to be 42 μm.

Here we aim to investigate the presence of such resin layers between the 0° and 90° tows, by replacing in the existing mesh of the baseline case one or two rows of elements on the 90° tows boundary with resin properties (see Figs. 7b and c). This corresponds to resin layer thicknesses of 30 and 60 μm. As previously, this is achieved by assuming implicitly that the resin filling these layers comes out from the 90° tows, leading to 90° tow fibre volume fraction of 0.58 and 0.83, respectively, for one and two rows of resin elements.

Overall responses for these three cases do not show a great difference, an increase in the thickness of the resin layer corresponding to a small drop in the overall shear stiffness. Therefore, it seems that the large change in the 90° tow fibre content (from 0.41 to 0.58 and 0.83) does

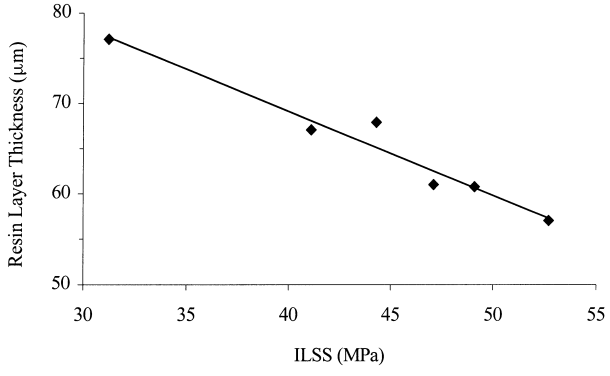

Fig. 17. Interlaminar shear strength versus resin layer thickness (Miller [14]).

not greatly affect the overall stiffness, which consequently depends primarily on the overall fibre content. Fig. 18 shows the response of the 60 μm resin layer case for 90° tow fibre-volume fractions both changed to 0.83 and kept at 0.41. The latter corresponds to an overall fibre content of 0.37. A further small reduction in stiffness is seen, confirming that the effects of the overall fibre-content modification and the presence of resin layer are cumulative as far as the overall stiffness is concerned. Therefore when the resin-layer thickness is increased alone, without any change in the overall fibre content, the observed drop of the overall stiffness can only be attributed to some local mechanisms induced by the presence of the resin layers.

These local effects of the resin layers are clearly visible in Fig. 19 where the shear-strain distributions for strains greater or equal to 4% are plotted for the two cases of resin-layer thickness. It is clear from Fig. 19a that high strains are reached in the cell, as the strains range now from 0.48 to 8.28% (7.03% for the centroidal value), instead of 1.43 to 7.76% (5.75% for the centroidal value) for the baseline case. Similarly to the baseline case, some high shear-strain gradients arise, but this time from the 90° tow edges, and therefore they can widely develop across the resin- layer thickness. From the response (Fig. 18) and the strain-distribution analysis (Fig. 19a) it is seen that the presence of the resin layer induces shear-strain gradients, large enough to both affect the overall stiffness and locally play a role in inducing failure.

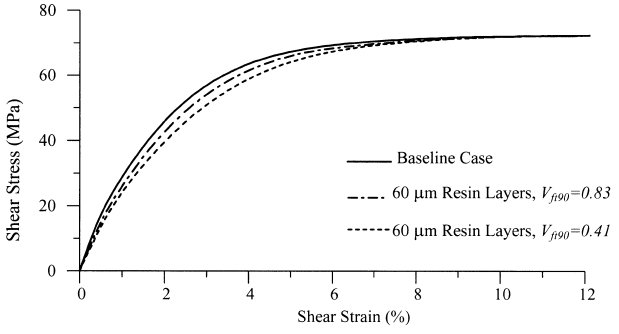

Fig. 18. Shear response for the cell with two layers of resin, with $V_{ft90}=0.41$ and $V_{ft90}=0.83$.

When increasing the resin-layer thickness from 30 to 60 μm, strains close to 4% (Fig. 19b and a, respectively) are more spread, but the largest difference between the two cases is in the resin layer itself. It can be seen in both cases that in the resin layer there is a strain concentration arising at the tip of the 90° tows, but it is more developed in the thicker resin layer. In fact, the resin layer acts like an intermediate medium through which the load is transferred from the 0° tows to the 90° tows. It is highly sheared and when the layer thickness is large enough some local stress concentrations occur at the particular points where the load transfer is most intense, inducing the largest strains in the cell. The idea that the NCF behaves under shear loading as a uniform stack of soft and stiff layers is no longer valid when the resin layers become large compared with the 90° tows, as stress concentrations grow with increasing resin-layer thickness.

The development of strain concentrations with the increasing layer thickness is confirmed by the increase of the maximum centroidal shear strain from 5.75% for the baseline case to 6.91% for a 30 μm resin layer and 7.03% for a 60 μm resin layer. This shows that failure is likely to take place at a lower load when the resin-layer thickness increases, which fits with the experimental observations reported in Fig. 17 [14]. Quantitative comparisons are more difficult because of the very localised nature of these strains, but the experimental trend is well captured by the analysis.

4.3.2. Resin layers and change in the resin modulus

So far, the parameters which were shown to be the most influential are the resin modulus, the fibre-volume fraction, and the presence of resin layers. This latter is a

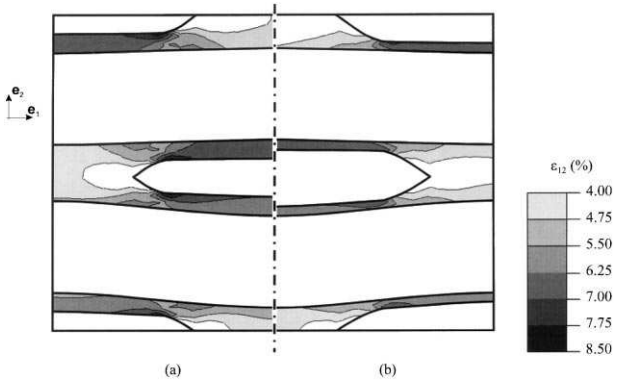

Fig. 19. Shear strain ⩾4% distribution plotted on the initial shape for a prescribed load of 50 MPa. For the baseline case with (a) two resin layers and (a) one resin layer.

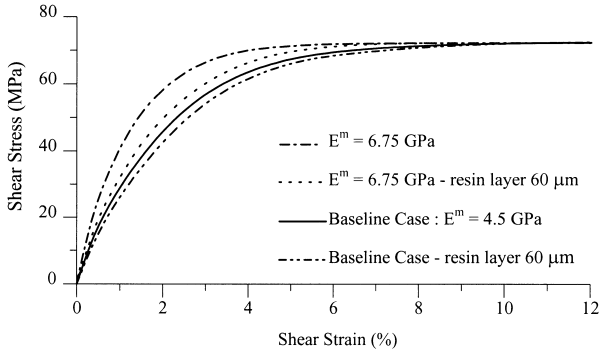

Fig. 20. Shear responses of: the baseline case with genuine and 50% increased resin modulus, the baseline case with resin layer with genuine and 50% increased resin modulus.

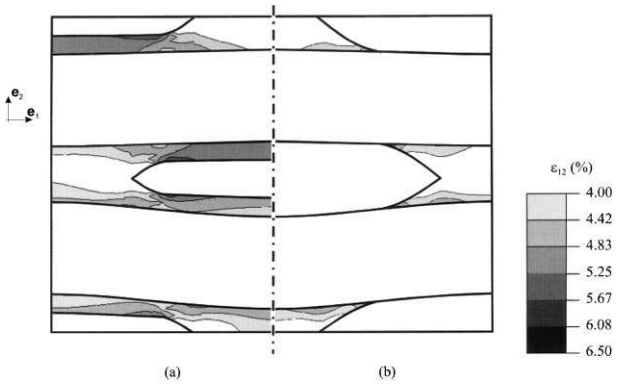

Fig. 21. Shear strain $\geqslant 4\%$ distribution plotted on the initial shape for a prescribed load of 50 MPa. For (a) the baseline case with two resin layers and $E^{m} = 6.75$ GPa and (b) the baseline case.

mesoscopic scale effect that cannot easily be controlled during the manufacturing. The effect of the resin modulus and the fibre-volume fraction is mainly on the overall stiffness. It is, however, worth looking at the effect which could arise from the combination of resin layers and a change in the resin modulus, as an attempt to limit the problems brought about by the resin layer presence could perhaps be made by using a stiffer resin.

From the responses in Fig. 20, it is clearly seen that the presence of the resin layer limits the improvement which can be brought about by increasing the resin modulus. It can also be noticed that the resin layer induces a drop in stiffness which is proportionally larger for a higher resin modulus. Indeed, for the case where the resin modulus is 4.5 GPa, the introduction of the resin layer does not change very much the overall stiffness, since it is already low as a result of the presence of strain localisations whereas, for the same load when the resin modulus is 6.75 GPa, strain localisations are limited by the higher mechanical characteristics of the resin and 90° tow. The NCF in this case is therefore intrinsically more sensitive to the introduction of the resin layer which facilitates the occurrence of strain localisations resulting in a drop of the overall stiffness.

These developments of high strains 'spoil' both the improvement of stiffness which comes with an increase of the resin modulus and, to a lesser extent, the homogeneity of the distribution of strains, as wider zones are available for high shear strains to develop. If we compare the baseline case (Fig. 21b) with the case where the resin modulus is increased to 6.75 GPa but with two resin layers (Fig. 21a), we clearly see that the maximum strains are very similar (maximum centroidal shear strains are 5.75 and 5.65%, respectively), but in the second case they are spread out over a larger area.

In short, the presence of resin layers almost eliminates the improvement brought about by the resin modulus increase. It is even worse as far as the strain distribution is concerned, since the highest strains develop over wider zones.

5. Conclusions

Using a bi-dimensional FE model of a bi-axial NCF, we have investigated the effect on the NCF pure shear behaviour of some mesoscopic mechanical and geometrical parameters. It has been verified first that under a pure shear loading the overall response is largely controlled by the resin response (non-linearity and yield stress) and second that the highest strains develop in the resin pockets which form between the tows. The analysis explains the mechanisms leading to strain localisations and the results for maximum shear strains indicate the points where failure is most likely to initiate.

It was demonstrated that heterogeneity of the meso-structure was the main parameter which affects significantly the NCF ILS behaviour. When changing the 90° tows shape or when including the presence of resin layers in the model, it was clearly demonstrated that the shear loading is transferred from tows to tows through regions of strongly varying mechanical characteristics. In these regions, high strain gradients can develop which may correspond to failure-initiation locations. Then the resin behaviour is the key parameter as the highest shear strains develop in unreinforced regions and also tows' behaviour depends mainly on it. Thus, it comes out that by improving the resin elastic modulus and the resin yield stress, the global response is improved in the same range, whereas increasing the fibre volume fraction improves the ILS stiffness only.

Consequently, the key parameters which can influence significantly the NCF ILS behaviour are the resin (resin pockets and resin yield stress), the 90° tow shape and the presence of resin layers which can form between plies. Therefore, in order to improve the NCF shear behaviour from a manufacturing point of view the *development of high shear strains has to be limited*. This can be addressed by suppressing the resin layers (or at least reducing their thickness), by using a resin with a high yield stress and a high modulus, and by limiting the stitching tension such that tows can spread in order to obtain a homogeneous meso-structure and therefore avoid shear localisations.

Acknowledgements

This work was achieved during the involvement of the authors in the Innovative Fabrics Aircraft Composites (INFACS) programme — Activity 3 Guidelines for Preforms/Fabric led by Cranfield University — School of Industrial and Manufacturing Science in collaboration with British Aerospace, Shorts, Dowty Aerospace, Ciba Composites, Tech Textiles, Imperial College and Queen Mary and Westfield College. The authors wish to acknowledge the support of the UK Engineering and Physical Science Research Council under contract GR/K68516.

References

[1] Dransfield K, Baillie C, Yiu-Wing M. Improving the delamination resistance of CFRP by stitching — a review. Composites Science and Technology 1994;50:305–17.

[2] Backhouse R, Blakeman C, Irving PE. Mechanisms of toughness enhancement in carbon fibre non-crimp fabrics. 3rd international conference on deformation and fracture of composites, March 1995, Surrey (UK), 1995. p. 307–12.

[3] Dransfield K, Jain L, Mai Y-W. On the effects of stitching in CFRPs — I. Mode I delamination toughness. Composites Science and Technology 1998;58:815–27.

[4] Jain L, Dransfield K, Mai Y-W. On the effects of stitching in CFRPs — II. Mode II delamination toughness. Composites Science and Technology 1998;58:829–37.

[5] Drapier S, Wisnom MR. Finite element investigation of the compressive strength of non-crimp fabric based composites. Composites Science and Technology, 1999;59:1287–97.

[6] Hogg PJ, Ahmadnia A, Guild JF. The mechanical properties of non-crimped fabric base composites. Composites 1993;24:423–32.

[7] Dexter HB. An overview of the NASA textile composite program. Proc. of the 6th conference on advanced engineering fibres and textile structures for composites, Philadelphia, October 1992, 1992. p. 1–31.

[8] Farley GL, Dickinson LC. Mechanical response of composite materials with through-the-thickness reinforcement. Proc. of 5th conference on advanced engineering fibres and textile structures for composites, 1991. p. 123–43.

[9] Ko F, Kutz J. Multilayer warp knit for advanced composites. Proceedings of the 4th annual conference on advanced composites, Dearborn, MI, September 1988. p. 73–7.

[10] Ko F, Fang P, Pastore C. Multilayer multidirectional warp knit fabrics for industrial applications. Journal of Industrial Fabrics 1985;4(2):4–12.

[11] Ko F, Lei C, Rahman A, Du GW, Cai Y. Unit cell geometry of multiaxial preforms for structural composites. Final report to NASA Langley Research Center (NASA-CR-197294), November 1993.

[12] Du GW, Ko F. Analysis of multiaxial warp-knit preforms for composite reinforcement. Composites Science and Technology 1996;56:235–60.

[13] Backhouse R. Multiaxial non-crimp fabrics: charaterisation of manufacturing capability for composite aircraft structure applications. Eng D. thesis, Cranfield University (UK), 1998.

[14] Miller AJ. The effect of microstructural parameters on the mechanical properties of non-crimp fabric composites. M. Phil thesis, Cranfield University, School of Industrial and Manufacturing Science, August 1996.

[15] Wisnom MR. Analysis of shear instability in compression due to fibre waviness. Journal of Reinforced Plastics and Composites 1993;12(11):1171–89.

[16] Drapier S, Gardin C, Grandidier J-C, Potier-Ferry M. Structure effect and microbuckling. Composites Science and Technology 1996;56:861–7.

[17] ABAQUS. Hibitt, Karlsson and Sorensen Inc., 100, Medway St, Providence, RI, 02906, USA.

[18] Femgen. Femsys Limited, 158 Upper New Walk, Leicester LE1 7QA, UK.

[19] Wisnom MR. The effect of fibre waviness on the relationship between compressive & flexural strengths of UD. Journal of Composite Materials 1994;28:66–76.

[20] Ditcher AK. The non-linear stress-strain behaviour of carbon fibre reinforced plastic and its effect on the analysis of laminated plates and sandwich beams, Ph.D. thesis, University of Bristol, Department of Aerospace Engineering, Bristol, 1981.

[21] Wisnom MR. The effect of fibre misalignment on the compressive strength of unidirectional carbon fibre/epoxy. Composites 1990;21(5):403–7.

- L -

Annexe 2. 6

L. Léotoing, S. Drapier, & A. Vautrin.

First applications of a novel unified model for global and local buckling of sandwich columns.

Eur. J. Mech. A/Solids **, 21 :683–701, 2002.**

ELSEVIER

European Journal of Mechanics A/Solids 21 (2002) 683–701

First applications of a novel unified model for global and local buckling of sandwich columns

L. Léotoing, S. Drapier *, A. Vautrin

Mechanical and Materials Engineering Department – SMS Division, École Nationale Supérieure des Mines de Saint-Étienne, 42023 Saint-Étienne cedex 02, France

Received 26 February 2001; revised and accepted 4 April 2002

Abstract

Due to the intrinsic heterogeneity of sandwich structures, phenomena at various scales can co-exist in these layered-like assembly of thick-soft and thin-stiff materials. Especially under in-plane compression loadings, geometrical instabilities can occur at both global (structure) and local (skins) scales. Therefore, the in-plane compressive response of sandwich structures is of major concern in designing structural applications. In the present paper, the first applications of a novel unified model for sandwiches are presented, with closed-form solutions for both global and local buckling. For the perfect structure, analytical critical loads are extracted for a simply supported beam, through the calculation of two eigenvalues leading to three buckling modes: it appears that the eigenvalue associated with the antisymmetrical mode can correspond to the occurrence of either global or local (wrinkling) buckling. These global and local loads from the present unified model are shown to compare very well with the predictions given by the most complete specific models from the literature. Moreover, it is shown that conversely to the classical models, our approach yields critical loads that depend only on rigorous well-founded mechanical hypotheses. The simple but general analytical expressions from the unified model permit to select quickly configurations against local and global buckling. In this simplified framework, conclusions can be drawn from this unified model capable of properly predicting the phenomena at both scales. This simplified study is essential in getting an insight in the role played by each geometrical and material parameter, the combination of which is of importance for subsequent non-linear interactive post-buckling analyses (Léotoing et al., 2001).

Keywords: Sandwich structure; Stability; Scale effects; Analytical model; Closed-form eigenvalues

1. Introduction

Since the early 40s, sandwich structures have been very widely used in building lightweight structures, especially in the fields of transportations where their high specific flexural stiffness leads to consistent weight savings. Classically, these layered-like materials are ideally employed as lagging or floor elements in applications which belong to aeronautics and astronautics where gaining *pay-loads* is a major driver in designing. Therefore sandwich structures have been historically associated with leading edge applications, and the use of these materials in other fields of engineering has received attention only since the mid 80s. This renewal of interest can be related to a better understanding in the sandwich behaviour, to new manufacturing processes which permit nowadays to build some integral parts out of sandwiches for structural units, but also to the integration of new materials such as composites. Classical loadings like tension, shear or bending are easily integrated in the design process

* Correspondence and reprints.
E-mail address: drapier@emse.fr (S. Drapier).

0997-7538/02/$ – see front matter
PII: S0997-7538(02)01229-9

Nomenclature

$(\mathbf{e}_1, \mathbf{e}_2, \mathbf{e}_3)$	reference basis
(u_1, u_2, u_3)	components of the displacement field $\mathbf{u}$
(u_1^l, u_2^l, u_3^l)	displacements of the sandwich lower skin
(u_1^u, u_2^u, u_3^u)	displacements of the sandwich upper skin
(x_1, x_2, x_3)	point coordinates
α	$= b$ (bottom face) or t (top face)
b	sandwich column width
D	equivalent flexural stiffness of the sandwich column
E_c	core Young's modulus
E_s	skin Young's modulus
$\eta_{\alpha b}$	$= 1$ if $\alpha = b$ and -1 if $\alpha = t$
$\boldsymbol{\gamma}(\mathbf{x})$	Green–Lagrange strain
G_c	transverse shear modulus of the core
k_y^s	shear transverse rigidity of a two-parameter foundation
k_z^e	normal transverse rigidity of a two-parameter foundation
L	sandwich column length
λ	external applied load
λ_{AG}^{um}	critical load of the global buckling mode
λ_{AL}^{um}	critical load of the antisymmetrical wrinkling mode
λ_{SL}^{um}	critical load of the symmetrical wrinkling mode
λ_{EHB}	critical load of the equivalent homogeneous sandwich column
λ_{class}	classical wrinkling load
ν_c	core Poisson's coefficient
ϕ_i	kinematical functions ($i = 1, \ldots, 5$)
Φ^n	amplitude of the kinematical function ϕ
Q	multiplicative coefficient for λ_{class}
$\mathbf{S}(\mathbf{x})$	2nd Piola–Kirchhoff stress tensor
S	transverse shear stiffness of the sandwich column
t_c	core thickness
t_s	skin thickness
U_i^n	amplitude of modal displacements
ξ	dimensionless factor $= (1/2 + t_s/t_c)$

of sandwich-based structures, but other loading configurations such as in-plane compression still present some difficulties for designers. Such destabilizing loadings necessitate conservative criteria for designing imperfection-sensitive panels and shells, to ensure a sufficient safety margin able to take into account the presence of potential imperfections.

The difficulties in studying sandwich structures lie in their intrinsic heterogeneity, both material and geometrical. Indeed, these materials are made up of three different components, two thin stiff skins separated by a thick weaker core. The nature of this assembly is responsible for the (co-)existence of phenomena at several distinct scales: at the global scale of the assembly, at the local scale of components, and also at the fibre and ply scales when skins are made up of composites. This complex behaviour is mostly enhanced under destabilizing loadings such as in-plane compression, where configurations at those various scales can interact, even if the occurrence of mechanisms at the ply or fibre scales are usually not included when studying composite skin-based sandwiches.

1.1. Sandwich response under in-plane compression

Since their first introduction during the World War II (Williams et al., 1941), one of the major concerns for structural engineers has been to prevent sandwich structures from buckling. Since then, a large number of theoretical investigations of the geometrical instabilities in sandwich columns, panels and shells have been conducted (see for instance (Benson and Mayers, 1967; Allen, 1969; Librescu, 1970; Hunt et al., 1988; Vinson, 1989; Teti and Caprino, 1989; Starlinger and Rammerstorfer, 1992). The very few studies devoted to the measurements of buckling loads ((Teti and Caprino, 1989) for instance), along with

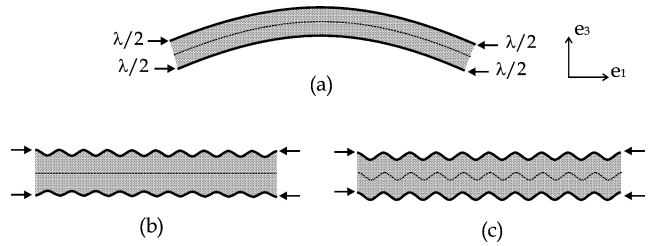

Fig. 1. Sandwich buckling at two scales: (a) global buckling (Euler's type), (b) symmetrical wrinkling of the skins, (c) antisymmetrical wrinkling of the skins.

the diversity of the numerous theoretical approaches perfectly demonstrates the difficulty of grasping the buckling phenomena in this type of layered materials.

In sandwich structures, buckling modes can appear at two different scales: global buckling (Fig. 1(a)) similar to Euler's buckling for columns, and some local forms of buckling of the skins called *wrinkling*. For this local instability, generally two distinct forms are considered which are the symmetrical mode (Fig. 1(b)) and the antisymmetrical mode (Fig. 1(c)). The classical approach of buckling in sandwiches is an uncoupled one (Williams et al., 1941; Hoff and Mautner, 1945; Allen, 1969; Zenkert, 1995) where two different models are proposed in order to describe the instability at each scale. From there, the designer has, for each case of instability, to cope with several conservative formulae. If these criteria yield rather good predictions for global buckling, not only are predictions for the wrinkling phenomenon very scattered, but also antisymmetrical wrinkling is very rarely described. This led some authors to attempt a more unified approach, focusing mainly on the interactive buckling of sandwich structures (Hunt et al., 1988; Starlinger, 1990; Frostig and Baruch, 1993).

1.2. Global buckling

The global buckling mode of a sandwich column is generally studied thanks to an equivalent homogeneous column in which the transverse shear effect is taken into account (Allen, 1969). The equivalent flexural and transverse shear stiffnesses are calculated from 'strength of materials' considerations where shear effects are included. The Euler critical load is then corrected by taking into account the shear effect, through the shear stiffness thereafter denoted by S. The critical load of the equivalent homogeneous column λ_{EHB} is then given by

$$\frac{1}{\lambda_{\mathrm{EHB}}} = \frac{1}{\lambda_{\mathrm{E}}} + \frac{1}{\lambda_{\mathrm{S}}}, \tag{1}$$

where λ_{E} is the classical Euler's critical load and λ_{S} is the critical load when only shear is considered:

$$\lambda_{\mathrm{E}} = \frac{\pi^2 D}{L^2}, \qquad \lambda_{\mathrm{S}} = S. \tag{2}$$

For a simply supported column, the Euler load is given by Eq. (2) and the shear buckling load is equal to the equivalent transverse shear stiffness S. For a symmetrical sandwich, the most common expressions for the equivalent flexural stiffness D, and for S, are:

$$D = \frac{E_s b t_s (t_c + t_s)^2}{2}, \qquad S = \frac{G_c b (t_c + t_s)^2}{t_c}, \tag{3}$$

where E_s is the skin Young's modulus, b is the column width, t_s and t_c are respectively the skin and core thicknesses, and G_c is the transverse shear modulus of the core.

1.3. Local buckling – wrinkling

The local buckling of faces is usually dealt with through a different model where one of the skins is considered as a beam resting on an elastic foundation standing for the core (Fig. 2). Therefore the main difficulty of these local approaches lies in the ability of the assumed equivalent behaviour of the core to properly reproduce the actual core mechanical behaviour which partly controls the local buckling mechanisms.

In the simplest model of this type the core is treated as a set of linear, uniformly distributed springs: this is the so-called one parameter foundation. This model can be improved by introducing a second parameter able to account for shear interactions between the loaded skin and the core (Thomsen, 1992; Hassinen and Martikainen, 1995) (Fig. 2). Another approach consists in representing cores, including honeycomb cores, as elastic isotropic continuous media characterized by Airy's function (Allen,

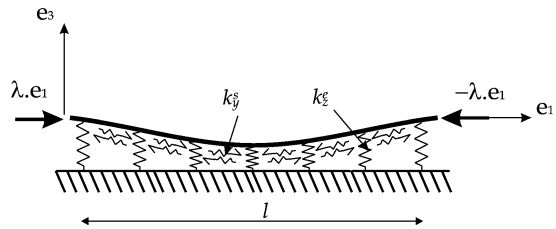

Fig. 2. Buckling of a beam resting on a two-parameters elastic foundation: k_y^s is the foundation response in shear and k_z^e is the foundation response in extension.

1969; Niu and Talreja, 1999). The main difficulty of these approaches is to postulate the Airy's function which must be sufficiently complete to consider all the interactions between the components, and usable for a possible analytical determination of simple critical criteria. From those models, the classical formula for the wrinkling of the skins is given by

$$\sigma_{\mathrm{CR}} = Q\sqrt[3]{E_s E_c G_c}, \tag{4}$$

where E_c is the transverse normal modulus of the core and Q is a constant. The value of Q varies from 0.4 to 0.9, depending on the authors and on the studied case (wrinkling of one face, symmetrical wrinkling or antisymmetrical wrinkling). Usually, a value of 0.5 is taken for Q, for all the wrinkling cases, in order to obtain a conservative formula for designers (Vinson, 1992; Zenkert, 1995).

Although this formula has merit due to its simplicity, there are numerous limits for these local models of the wrinkling phenomena. Indeed, experimental investigations have shown that correlations between Eq. (4) and experiments is rather difficult (Teti and Caprino, 1989) and according to these results, the value of Q can not be considered as constant. Second, this kind of approach should be employed only either for symmetrical wrinkling where the mean line of the sandwich remains flat, or for thick cores and thin skins where the core thickness can be assumed to be infinite with respect to the skin thickness, i.e. when the deformation of the mean line does not interact with the skin displacements.

1.4. Interactive buckling

An attempt has been made in the last few years to develop some more complex models, in order to account for the effect of interactions between the configuration at both scales onto the elastic buckling of sandwiches. One can mention the analytical and semi-analytical approaches of Hunt (Hunt et al., 1988) and Frostig (Frostig and Baruch, 1993) or the numerical approach of (Starlinger, 1990). For Hunt and co-authors (Hunt et al., 1988), the interaction between both skins is considered through a superposition of a global and two local modes (symmetrical and antisymmetrical). The main drawback of Frostig's model (Frostig and Baruch, 1993) is the absence of antisymmetrical wrinkling. Starlinger (1990), in a sandwich shell element, considers the local degradation due to the appearance of local phenomena and then modifies the global rigidity of the structure to reach a new equilibrium. This is implemented in an efficient tool to compute structures, but this treatment yields severe problems of convergence after the drastic reduction induced by local buckling. Moreover, there is no geometrical characterization of the local instability. One concludes that very few models actually deal properly with the interaction between the two scales of the sandwich materials and that all of them present some limits.

There is still a need for a unified approach able to deal with the interactive buckling in sandwich structures. Our final aim is to propose a simple tool which will permit to make efficient calculations for the design of such structures. The first step of this approach is to set up a unified model for a perfect structure. This unified model is detailed here. It is used to predict the linear buckling of sandwich columns at both scales, yielding tractable closed-form solutions for the critical loads. These simple design formulae are then compared, on a working example, with the classical expressions (Eqs. (1) and (4)) for global and local (symmetrical and antisymmetrical) instabilities. A more refined local model from (Niu and Talreja, 1999) is also used for comparison.

2. Presentation of the unified model

In this part a unified model is presented. First the displacement fields are chosen to represent the displacement of skins and core. Then, through the Principle of Virtual Work (PVW), the governing equations are derived. For the sake of simplicity, a symmetrical sandwich column is considered in which both faces and core are made up of homogeneous isotropic linear elastic materials.

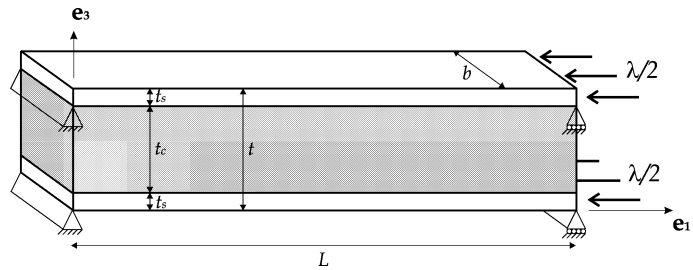

Fig. 3. Notation for a simply supported sandwich column.

Let us consider a bidimensional model as represented in Fig. 3 in which the position of any point is given by $\mathbf{x} = x_1\mathbf{e}_1 + x_3\mathbf{e}_3$ in the domain $\Omega = [0, L] \times [0, t]$. The column height is designated by $t = 2t_s + t_c$. Components of the displacements $\mathbf{u}(\mathbf{x})$ are respectively $u_1(\mathbf{x})$ along $\mathbf{e}_1$ and $u_3(\mathbf{x})$ along $\mathbf{e}_3$. Stresses are represented by the second Piola–Kirchhoff tensor, denoted by $\mathbf{S}(\mathbf{x})$, and strains are represented by the Green–Lagrange tensor $\boldsymbol{\gamma}(\mathbf{u})$ limited to the moderate rotation terms as far as the non-linear strains are concerned. The linear elastic constitutive law is reduced to the Young's modulus (E_s) for the skins, and to the elastic moduli for the isotropic core (E_c, G_c), according to the notations used so far.

2.1. Displacement fields

For the sake of simplicity, a model formulated in displacements is established. The only difficulty raised by this formulation is to choose kinematics sufficiently rich to observe all the potential forms of instability, but simple enough to get analytical and tractable design criteria. Lo et al. (1977) have shown that the use of higher-order theories is required for the problems where the external loads can vary over characteristic dimensions of the order of the column thickness. As far as sandwiches are concerned, face wrinkling has a wavelength on the order of the sandwich thickness. Therefore it can be assumed that a higher-order theory must be used for the displacement fields of the core which was shown to govern the local response of the sandwich. This assertion is confirmed by Finite Element computations in which the change in the longitudinal displacement field across the column thickness is cubic-shaped for an antisymmetrical mode with short wavelength (Léotoing, 2001). Higher-order theories have already been used by several authors, for example, (Benson and Mayers, 1967; Kim and Hong, 1988; Frostig and Baruch, 1993).

Classically, the displacements of any point of a column are represented through combinations of the displacements and rotations measured on the column mean line. In the present model, other kinematical components are chosen such that the expressions of the displacements remain simple enough:

$$
\begin{aligned}
0 < x_3 < t_s: \quad & u_1^l(x_1, x_3) = u_1^b(x_1) - x_3 \frac{\mathrm{d}u_3^b}{\mathrm{d}x_1}(x_1), \\
& u_3^l(x_1, x_3) = u_3^b(x_1); \\
t_s < x_3 < t_c + t_s: \quad & u_1^c(x_1, x_3) = u_1^m(x_1) - (x_3 - t_s)\phi_1(x_1) - (x_3 - t_s)^2\phi_2(x_1) - (x_3 - t_s)^3\phi_3(x_1), \\
& u_3^c(x_1, x_3) = u_3^m(x_1) - (x_3 - t_s)\phi_4(x_1) - (x_3 - t_s)^2\phi_5(x_1); \\
t_c + t_s < x_3 < t: \quad & u_1^u(x_1, x_3) = u_1^t(x_1) - (x_3 - t)\frac{\mathrm{d}u_3^t}{\mathrm{d}x_1}(x_1), \\
& u_3^u(x_1, x_3) = u_3^t(x_1),
\end{aligned}
\tag{5}
$$

where suffices ^{b} and ^{t} stand respectively for the data concerning the bottom and top of the column and can be thereafter replaced by suffix α ($\alpha = b, t$) to reduce the expressions including these data. According to the previous remarks, a higher-order theory is chosen for the core, as presented in Eq. (5), following the notations in Fig. 3. As for the skins, the displacements are chosen linear in x_3 for the $\mathbf{e}_1$-direction and constant in x_3 for the $\mathbf{e}_3$-direction (Eq. (5)). It can be noticed that the shear effects in the skins are not taken into account. This can be postulated because the influence of the shear effects on the buckling loads of a beam resting on a two-parameter elastic foundation (see Fig. 2) does not exceed 5% for classical isotropic sandwiches. This hypothesis will permit to keep the resolution simple enough to remain analytical. The core displacement field is described thanks to seven unknown functions of x_1 which are to be determined: $u_1^m(x_1)$, $u_3^m(x_1)$ which will be shown to correspond to the displacements of the lower skin/core interface, and ϕ_i ($i = 1$ to 5) some additional unknowns.

2.2. Reduction of the number of unknowns

The reduction of the number of unknown functions leads to a simplification of the resolution of the problem but also to a better characterization of the mechanical behaviour of the sandwich column thanks to a good estimate of the stress distribution across the thickness. Further relationships between the displacement fields components can be postulated, provided that they remain physically acceptable. It is inferred that the two interfaces between the skins and the core are perfect, thus the continuity of the displacement fields is verified on either side of the interfaces:

$$u_1^l(x_1,t_s)=u_1^c(x_1,t_s),\qquad u_1^u(x_1,t_c+t_s)=u_1^c(x_1,t_c+t_s),\qquad u_3^l(x_1,t_s)=u_3^c(x_1,t_s),$$
$$u_3^u(x_1,t_c+t_s)=u_3^c(x_1,t_c+t_s). \tag{6}$$

From these continuity equations, four relationships can be written between the unknowns. Let us consider functions $\mathbf{u}^m(x_1)$, $\phi_1(x_1)$ and $\phi_4(x_1)$ which are to be eliminated from the complete displacement fields (Eq. (5)):

$$u_3^m(x_1)=u_3^b(x_1),\qquad u_1^m(x_1)=u_1^b(x_1)-t_s\frac{\mathrm{d}u_3^b(x_1)}{\mathrm{d}x_1},\qquad \phi_4(x_1)=\frac{u_3^b(x_1)-u_3^t(x_1)}{t_c}-t_c\phi_5(x_1),$$
$$\phi_1(x_1)=\frac{u_1^b(x_1)-u_1^t(x_1)}{t_c}-\frac{t_s}{t_c}\left(\frac{\mathrm{d}u_3^b(x_1)}{\mathrm{d}x_1}+\frac{\mathrm{d}u_3^t(x_1)}{\mathrm{d}x_1}\right)-t_c\phi_2(x_1)-t_c^2\phi_3(x_1). \tag{7}$$

In other approaches of unified theories (Benson and Mayers, 1967; Kim and Hong, 1988; Frostig and Baruch, 1993), the displacement fields are derived by integrating the static equilibrium equations in the core, and the continuity relationships at the interfaces are used to determine the integration constants. However, the difficulty of those approaches lies in the existence of four continuity relationships for three constants only. For those authors the problem is circumvented by introducing an additional equation in the set of the governing equations of the problem (Frostig and Baruch, 1993) or by the introduction of Lagrange multipliers (Benson and Mayers, 1967; Kim and Hong, 1988). Our approach is rather different: the governing equations are derived, through the Principle of Virtual Work (PVW), from the displacements forms postulated such that local as well as global phenomena can be properly modeled.

In order to further reduce the number of unknown functions and to refine our theory, the shear stress distribution across the thickness can be postulated. Let us consider the first (along the $\mathbf{e}_1$-direction) static equilibrium equation prevailing in the core. Using the following notation for the derivatives: $\partial x/\partial x_i = x_{,i}$, we write:

$$S_{11,1}^c(\mathbf{x})+S_{13,3}^c(\mathbf{x})=0. \tag{8}$$

Commonly (Allen, 1969), the first term of Eq. (8) is neglected, this corresponds to a quasi-constant longitudinal stress state in the core at the onset of buckling, where compression prevails. When one considers this hypothesis, Eq. (8) is simplified and leads to the classical hypothesis that the transverse shear stress is constant across the core thickness.

For an antisymmetrical shape, this constant shear stress distribution would provide a sufficiently accurate approximation. On the contrary, for a symmetrical mode of deformation of the sandwich, the hypothesis $S_{13,3}^c(\mathbf{x})=0$ is no longer valid. Indeed, S_{13}^c written in displacement

$$S_{13}^c(\mathbf{x})=G_c\left(u_{1,3}^c(\mathbf{x})+u_{3,1}^c(\mathbf{x})\right) \tag{9}$$

shows that this stress follows and odd distribution with respect to x_3 since from a geometrical point of view it arises from the sum of two odd functions with respect to x_3: $u_{1,3}^c$ (the longitudinal displacements at the two interfaces are identical) and $u_{3,1}^c$ (the transverse displacements at the two interfaces are opposite). In this case, a constant shear stress distribution would lead to a null S_{13}^c whereas a FE evaluation of the energetic contribution of S_{13}^c and S_{33}^c clearly shows that these stresses are of the same order for a symmetrical shape. Then, in order to take into account the energetic contribution of S_{13}^c across the column thickness, it is inferred that a linear distribution with respect to x_3 will give a good approximation of its actual distribution for both antisymmetrical and symmetrical modes. Then, the assumed linear variation of S_{13}^c leads to two further relationships which permit to eliminate two additional unknowns in the displacement:

$$\phi_3(x_1)=-\frac{1}{3}\phi_{5,1}(x_1),\qquad \phi_2(x_1)=\frac{t_c}{2}\phi_{5,1}(x_1). \tag{10}$$

Finally the displacement fields can be rewritten thanks to the four unknown displacements of the skins $\mathbf{u}^\alpha(x_1)$ and to the gradient of rotation in the core $\phi_5(x_1)$, noted $\phi(x_1)$ thereafter:

$$0<x_3<t_s:\quad u_1^l(x_1,x_3)=u_l^b(x_1)-x_3u_{3,1}^b(x_1),$$
$$u_3^l(x_1,x_3)=u_3^b(x_1);$$

$$
\begin{aligned}
t_s < x_3 < t_c + t_s\colon\quad & u_1^c(x_1,x_3) = \frac{(x_3-t_s)}{t_c}u_1^t(x_1) + \left(1-\frac{(x_3-t_s)}{t_c}\right)u_1^b(x_1) + t_s\left(\frac{(x_3-t_s)}{t_c}\right)u_{3,1}^t(x_1)\\
& \qquad - t_s\left(1-\frac{(x_3-t_s)}{t_c}\right)u_{3,1}^b(x_1) + \frac{1}{6}(2x_3-t)(x_3+t_s-t)(x_3-t_s)\phi_{,1}(x_1),\\
& u_3^c(x_1,x_3) = \frac{(x_3-t_s)}{t_c}u_3^t(x_1) + \left(1-\frac{(x_3-t_s)}{t_c}\right)u_3^b(x_1) + (x_3-t_s)(-x_3+t_s+t_c)\phi(x_1);\\
t_c + t_s < x_3 < t\colon\quad & u_1^u(x_1,x_3) = u_1^t(x_1) - (x_3-t)u_{3,1}^t(x_1),\\
& u_3^u(x_1,x_3) = u_3^t(x_1).
\end{aligned}
\tag{11}
$$

2.3. Governing equations

The governing equations of the problem are derived from the Principle of Virtual Work (PVW) formulated in displacement thanks to the new displacement fields proposed above (Eq. (11)). The equilibrium of the sandwich column can be expressed as the sum, which must be null, of the virtual works done in the virtual displacement field $\delta\mathbf{u}(\mathbf{x})$: $\delta W_{\text{int}}(\mathbf{u})$ in Ω and $\delta W_{\text{ext}}(\mathbf{u})$ on the edge $\partial\Omega$ where the external loading is applied. Let the virtual field be the actual displacement field variation. Therefore boundary conditions are verified and prescribed displacements cancel, i.e. $\delta\mathbf{u}(\mathbf{x})$ is said Kinematically Admissible and henceforth noted $K.A.$. The internal virtual work can be calculated straightforwardly from the stresses $\mathbf{S}$ and the virtual strain tensor, denoted by $\delta\boldsymbol{\gamma}(\mathbf{u})$. It is assumed that the virtual work of the external efforts, denoted by $\langle\,\rangle$, is a linear form of the virtual displacement field. Finally, the general equilibrium of sandwich columns loaded by forces and moments $\mathbf{F}$ writes:

$$
\delta W_{\text{int}}(\mathbf{u}) - \delta W_{\text{ext}}(\mathbf{u}) = b\iint_{\Omega}\mathbf{S}:\delta\boldsymbol{\gamma}(\mathbf{u})\,\mathrm{d}\Omega - \langle\mathbf{F},\delta\mathbf{u}\rangle = 0,\quad \forall\delta\mathbf{u}(\mathbf{x})\ K.A.
\tag{12}
$$

The expression of the internal virtual work in the core and in the skins can be simplified by neglecting stresses whose energetic contributions are low. Therefore, in the skins only the longitudinal stress is considered: $\mathbf{S}^\alpha = S_{11}^\alpha\mathbf{e}_1\otimes\mathbf{e}_1$. In the core both the transverse normal stress S_{33}^c and the transverse shear stress S_{13}^c are taken into account: $\mathbf{S}^c = S_{33}^c\mathbf{e}_3\otimes\mathbf{e}_3 + S_{13}^c\mathbf{e}_1\otimes\mathbf{e}_3$. The corresponding Green–Lagrange strains in the skins are then expressed in the framework of small displacements and moderate rotations whereas in the core both displacements and rotations are small:

$$
\begin{aligned}
\gamma_{11}^b(\mathbf{x}) &= u_{1,1}^l(\mathbf{x}) + \frac{1}{2}\big(u_{3,1}^l(\mathbf{x})\big)^2, \qquad \gamma_{11}^t(\mathbf{x}) = u_{1,1}^u(\mathbf{x}) + \frac{1}{2}\big(u_{3,1}^u(\mathbf{x})\big)^2,\\
\gamma_{33}^c(\mathbf{x}) &= u_{3,3}^c(\mathbf{x}), \qquad \gamma_{13}^c(\mathbf{x}) = u_{1,3}^c(\mathbf{x}) + u_{3,1}^c(\mathbf{x}).
\end{aligned}
\tag{13}
$$

Then, these strains (Eq. (13)) can be written as functions of the five unknowns of the problem:

$$
\begin{aligned}
\gamma_{11}^\alpha(\mathbf{x}) &= u_{1,1}^\alpha(x_1) + \frac{1}{2}\big(u_{3,1}^\alpha(x_1)\big)^2 - \left(x_3 - \frac{1-\eta_{\alpha b}}{2}t\right)u_{3,11}^\alpha(x_1),\\
\gamma_{33}^c(\mathbf{x}) &= \frac{u_3^t(x_1)-u_3^b(x_1)}{t_c} - \big(2(x_3-t_s)-t_c\big)\phi(x_1),\\
\gamma_{13}^c(\mathbf{x}) &= \frac{u_1^t(x_1)-u_1^b(x_1)}{t_c} + \frac{x_3}{t_c}u_{3,1}^t(x_1) + \left(1-\frac{x_3-2t_s}{t_c}\right)u_{3,1}^b(x_1) + \frac{t_c^2}{6}\phi_{,1}(x_1),
\end{aligned}
\tag{14}
$$

where $\eta_{\alpha b} = 1$ if $\alpha = b$ and -1 if $\alpha = t$. The two different materials used for the sandwich column are assumed to be elastic linear and isotropic. Thus the internal virtual work is simply given by

$$
\delta W_{\text{int}}(\mathbf{u})/b = \iint_{\Omega_\alpha} S_{11}^\alpha\delta\gamma_{11}^\alpha(\mathbf{u})\,\mathrm{d}\Omega_\alpha + \iint_{\Omega_c}\big(S_{33}^c\delta\gamma_{33}^c(\mathbf{u}) + S_{13}^c\delta\gamma_{13}^c(\mathbf{u})\big)\,\mathrm{d}\Omega_c
\tag{15}
$$

the integral over Ω being splitted into the three distinct zones of the sandwich Ω_b, Ω_c, Ω_t respectively the bottom skin, the core, and the top skin ($\Omega = \Omega_\alpha\cup\Omega_c$). The external virtual work can be explicitly written from Eq. (12) using the unknown displacements $\mathbf{u}^\alpha(x_1)$. For the case shown in Fig. 3, the external virtual work is given by

$$
\delta W_{\text{ext}}(\mathbf{u}) = -\frac{\lambda}{2}\left(\delta u_1^b(L) - \frac{t_s}{2}\delta u_{3,1}^b(L)\right) - \frac{\lambda}{2}\left(\delta u_1^t(L) + \frac{t_s}{2}\delta u_{3,1}^t(L)\right).
\tag{16}
$$

Now, after a sufficient number of integrations by parts, the governing equations in the column and at its edges can be determined. In order to simplify the expression of the set of equations, the internal resultants of the skins $N^\alpha(x_1)$ and $M^\alpha(x_1)$,

respectively the membrane and bending generalized stresses, can be introduced. They are given by the following expressions:

$$\left.\begin{aligned} N^b(x_1) &= b\int_0^{t_s} S_{11}^b \,\mathrm{d}\Omega_b \\ N^t(x_1) &= b\int_{t_s+t_c}^{t} S_{11}^t \,\mathrm{d}\Omega_t \end{aligned}\right\} = E_s b t_s\left[\left(u_{1,1}^{\alpha} + \frac{1}{2}{u_{3,1}^{\alpha}}^2\right) - \eta_{\alpha b}\frac{t_s}{2}u_{3,11}^{\alpha}\right], \tag{17a}$$

$$\left.\begin{aligned} M^b(x_1) &= b\int_0^{t_s} x_3 S_{11}^b \,\mathrm{d}\Omega_b \\ M^t(x_1) &= b\int_{t_s+t_c}^{t} (x_3 - t) S_{11}^t \,\mathrm{d}\Omega_t \end{aligned}\right\} = E_s b {t_s}^2\left[\frac{\eta_{\alpha b}}{2}\left(u_{1,1}^{\alpha} + \frac{1}{2}{u_{3,1}^{\alpha}}^2\right) - \frac{t_s}{3}u_{3,11}^{\alpha}\right]. \tag{17b}$$

Since we have five kinematical unknowns, five equilibrium equations are determined which characterize the inner equilibrium of the sandwich column (suffix α stands for b and t). The dimensionless coefficient $\xi = (1/2 + t_s/t_c)$ is introduced:

$$\eta_{\alpha b}N_{,1}^{\alpha} + bG_c\left(\frac{u_1^t - u_1^b}{t_c} + \xi\left(u_{3,1}^t + u_{3,1}^b\right) + \frac{t_c^2}{6}\phi_{,1}\right) = 0, \tag{18a}$$

$$\begin{aligned} &\left(N^{\alpha}u_{3,1}^{\alpha}\right)_{,1} + M_{,11}^{\alpha} - \eta_{\alpha b}\frac{bE_c}{t_c}\left(u_3^t - u_3^b\right) \\ &\quad - bG_c\xi\left[u_{1,1}^t - u_{1,1}^b + \frac{t_c}{\xi}\left(\frac{2}{3(3+\eta_{\alpha b})} + \frac{t_s}{t_c}\left(1 + \frac{t_s}{t_c}\right)\right)u_{3,11}^t\right. \\ &\qquad \left. + \frac{t_c}{\xi}\left(\frac{2}{3(3-\eta_{\alpha b})} + \frac{t_s}{t_c}\left(1 + \frac{t_s}{t_c}\right)\right)u_{3,11}^b + \frac{{t_c}^3}{6}\phi_{,11}\right] = 0, \end{aligned} \tag{18b}$$

$$t_c E_c\phi - \frac{G_c}{2}\left(u_{1,1}^t - u_{1,1}^b + t_c\xi\left(u_{3,11}^t + u_{3,11}^b\right) + \frac{t_c^3}{6}\phi_{,11}\right) = 0. \tag{18c}$$

The system (Eqs. (18)) is non-linear since the resultants (Eqs. (17)) which appear in the first (Eq. (18a)) and second pair (Eq. (18b)) of equilibrium equations depend on both displacement components $u_1^{\alpha}(x_1)$ and $u_3^{\alpha}(x_1)$. The aim is now to evaluate the first point of bifurcation of the system, i.e. find the critical loads which characterize the transition from the flat unbuckled fundamental state to a buckled state. Since the buckling loads of both linearized and non-linear problem are the same (Léger et al., 1998), a linearized form of Eqs. (18) is sufficient to determine those loads.

2.4. Linear eigenvalue analysis

In order to solve analytically the system of equations (Eqs. (18)), it is necessary to linearize it through some hypotheses. A classical assumption consists in postulating that at the occurrence of the first geometrical instability, the linear relationship between the applied load and the internal resultants still holds, i.e. no deflection is observed and only the membrane terms exist. This is the so-called linear pre-buckling state assumption which permits one to linearize many bifurcations problems. In our case, it leads to a constant compressive resultant ($N_{,1}^{\alpha} = 0$) over the column length, which is directly identified from the governing equation on the edge at $x_1 = L$: $N^{\alpha}(L) + \lambda/2 = 0$. Therefore, in the buckling state the resultants $N^{\alpha}(x_1)$ are constant in Eq. (18b), this permits us to linearize this equation. Eq. (18a) is simply linearized by neglecting the moderate rotations in the expressions of the derivatives of the internal resultants which are supposed to depend on the linear strains only:

$$N_{,1}^{\alpha} = E_s b t_s\left(u_{1,11}^{\alpha} - \eta_{\alpha b}\frac{t_s}{2}u_{3,111}^{\alpha}\right), \qquad M_{,11}^{\alpha} = E_s b {t_s}^2\left(\eta_{\alpha b}\frac{u_{1,111}^{\alpha}}{2} - \frac{t_s}{3}u_{3,1111}^{\alpha}\right). \tag{19}$$

Then, the system (Eqs. (18)) can be rewritten by considering the linear pre-buckling state taken up. It is expressed versus the five unknown displacements only and no longer presents any coupling:

$$\eta_{\alpha b}E_s b t_s u_{1,11}^{\alpha} - \frac{bE_s {t_s}^2}{2}u_{3,111}^{\alpha} + bG_c\left(\frac{u_1^t - u_1^b}{t_c} + \xi\left(u_{3,1}^t + u_{3,1}^b\right) + \frac{t_c^2}{6}\phi_{,1}\right) = 0,$$

$$\frac{\lambda}{2}u^{\alpha}_{3,11} - \eta_{\alpha b}\frac{E_s b {t_s}^2}{2}u^{\alpha}_{1,111} + \frac{E_s b {t_s}^3}{3}u^{\alpha}_{3,1111} - \eta_{\alpha b}\frac{bE_c}{t_c}\left(u^t_3 - u^b_3\right)$$
$$- bG_c\xi\left[u^t_{1,1} - u^b_{1,1} + \frac{t_c}{\xi}\left(\frac{2}{3(3+\eta_{\alpha b})} + \frac{t_s}{t_c}\left(1+\frac{t_s}{t_c}\right)\right)u^t_{3,11} + \frac{t_c}{\xi}\left(\frac{2}{3(3-\eta_{\alpha b})} + \frac{t_s}{t_c}\left(1+\frac{t_s}{t_c}\right)\right)u^b_{3,11}\right.$$
$$\left. + \frac{{t_c}^3}{6}\phi_{,11}\right] = 0,$$
$$t_c E_c \phi - \frac{G_c}{2}\left(u^t_{1,1} - u^b_{1,1} + t_c\xi\left(u^t_{3,11} + u^b_{3,11}\right) + \frac{t_c^3}{6}\phi_{,11}\right) = 0. \tag{20}$$

Therefore, the system (Eqs. (20)) is linear and the critical loads are the eigenvalues of the corresponding eigenproblem. The displacements can be sought under the form of trigonometric series which are $K.A.$, i.e. which satisfy the restrictions on the kinematical boundary conditions. For a simply supported sandwich column, these displacements can be expressed with sine and cosine series:

$$u^{\alpha}_1(x_1) = \sum_n U^{\alpha n}_1 \cos\frac{n\pi x_1}{L}, \qquad u^{\alpha}_3(x_1) = \sum_n U^{\alpha n}_3 \sin\frac{n\pi x_1}{L}, \qquad \phi(x_1) = \sum_n \Phi^n \sin\frac{n\pi x_1}{L}. \tag{21}$$

Feeding these trigonometric approximations into the system (Eqs. (20)), we can formulate an eigenproblem in which the scalar parameter is the external load λ:

$$\left([A] - \lambda[B]\right)\{Y\} = \{0\}. \tag{22}$$

The defined problem (Eq. (22)) is valid for every n, therefore the obtained eigenvalues will be expressed with respect to the wavenumber. Matrix $[A]$ is symmetrical and its coefficients are given in Appendix A, with the notations $\omega = n\pi/L$. Matrix $[B]$ and vector $\{Y\}$ are expressed as follows:

$$B = \begin{bmatrix} 0 & 0 & 0 & 0 & 0 \\ 0 & 0 & 0 & 0 & 0 \\ 0 & 0 & \frac{1}{2}\omega^2 & 0 & 0 \\ 0 & 0 & 0 & \frac{1}{2}\omega^2 & 0 \\ 0 & 0 & 0 & 0 & 0 \end{bmatrix}, \qquad Y = \begin{Bmatrix} U^{tn}_1 \\ U^{bn}_1 \\ U^{tn}_3 \\ U^{bn}_3 \\ \Phi_n \end{Bmatrix}. \tag{23}$$

The determination of the eigenvalues consists in finding the roots of the characteristic polynomial, which results from $\det([A] - \lambda[B]) = 0$, the condition for not to have a trivial solution $\{Y\} = \{0\}$. The formal resolution leads to two strictly positive eigenvalues $\lambda^{um}_A(n)$ and $\lambda^{um}_S(n)$ corresponding respectively to an antisymmetrical eigenmode and to a symmetrical one:

$$\lambda^{um}_A = \frac{\omega^2 E_s t_s b}{6}\left(t_s^2 + \frac{72G_c E_c (t_c + t_s)^2}{\omega^4 E_s G_c t_s t_c^3 + 12\omega^2 E_s E_c t_s t_c + 24E_c G_c}\right), \tag{24a}$$

$$\lambda^{um}_S = \frac{\omega^2 E_s t_s^3 b}{6} + \frac{4E_c b}{\omega^2 t_c} + \frac{G_c t_c b}{3}. \tag{24b}$$

The corresponding stability curves are plotted for a sandwich column whose characteristics are given in Table 1 and for two different thicknesses (Fig. 4). As it can be seen in Fig. 4, the critical wavenumber of the antisymmetrical mode, i.e. the wavenumber for which the eigenvalue is minimum, depends on the thickness of the core, but obviously also on the other material and geometrical parameters. This very simple numerical application shows clearly an important capability of our model which highlights the existence of two distinct antisymmetrical modes characterized by very different wavenumbers. Depending on both geometrical and material parameters combinations, the critical mode can be either the global mode $n = 1$ or a local mode with a large wavenumber. For $t_c = 30$ mm the global mode ($n = 1$) will occur first (lower load), whereas for a core of thickness $t_c = 60$ mm the wrinkling mode ($n = 34$) is predominant.

One must point out that for kinematics with linear displacement fields in the core ($\phi_i = 0,\ i = 2, 3, 5$ in Eq. (5)) this minimum does not exist. As for the symmetrical case, there is only one possible critical load which corresponds to a local

Table 1
Sandwich characteristics of the plotted eigenvalues in Figs. 4 and 10–11

E_s (MPa)	50000	t_s (mm)	1
E_c (MPa)	70	L (mm)	600
G_c (MPa)	25	b (mm)	40

(a)

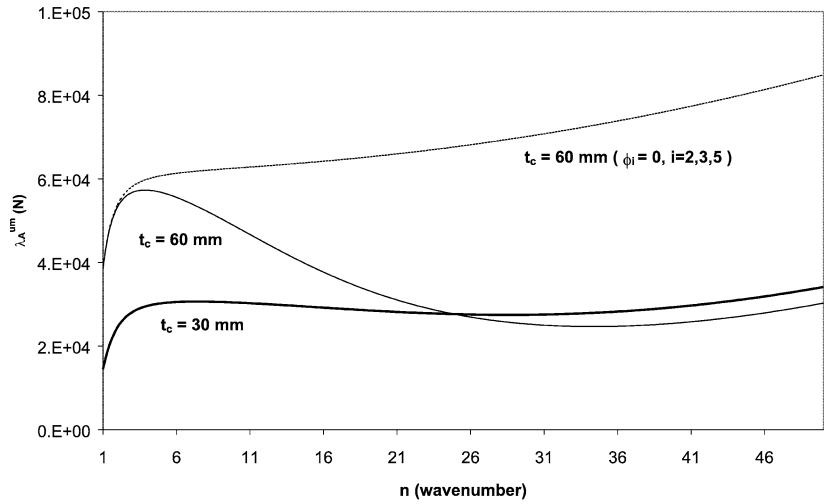

(b)

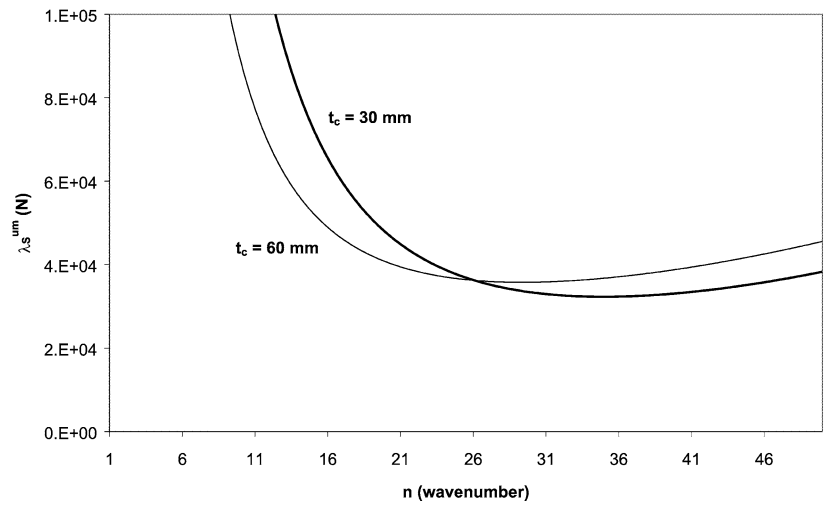

Fig. 4. Plots of λ_A^{um} (a), and λ_S^{um} (b), for two different thicknesses t_c of the core ($t_c = 30$ mm, $t_c = 60$ mm).

mode ($n \gg 1$). To summarize, this example demonstrates that depending on the sandwich configuration three distinct forms of instability can appear, a global one and two local ones. The aim of the following part is to give simple analytical formulae for the critical loads and to compare them with other approaches from the literature.

3. Analysis of the critical buckling loads

In this section, the proposed solutions for the three modes of instabilities are analysed in details. First, these expressions permit to illustrate the contributions and effects of the various geometrical and material parameters in the instabilities occurrence. Then the predictions yielded by the present approach are compared with other dedicated models from the literature. Eventually, design indications are extracted from the presented analytical forms.

The various plots used in this section correspond to the default sandwich configuration reported in Table 2. When necessary, the skin thickness (t_s) and core Young's modulus (E_c) vary to represent respectively a range of thickness and modulus ratios.

Table 2
Sandwich characteristics used by default for simulations plotted in Figs. 7–15 if not stated

E_s (MPa)	70000	t_c (mm)	50
E_c (MPa)	100	L (mm)	470
G_c (MPa)	35.7	b (mm)	60

When necessary t_s and E_c are varied accordingly to corresponding ratios.

3.1. Analytical expressions

3.1.1. Global buckling

The critical load corresponding to the global buckling mode is obtained from Eq. (24a) by taking $n = 1$, disregarding any other critical wavenumber for which $\lambda_A^{um}(n)$ may be minimum:

$$\lambda_{AG}^{um} = \frac{\pi^2 E_s t_s b}{6L^2}\left(t_s^2 + \frac{72 G_c E_c L^4 (t_c + t_s)^2}{\pi^4 E_s G_c t_s t_c^3 + 12\pi^2 E_s E_c t_s t_c L^2 + 24 E_c G_c L^4}\right). \tag{25}$$

3.1.2. Symmetrical wrinkling

The critical load corresponding to the local symmetrical mode is given by Eq. (24b) thanks to the determination of the minimum with respect to n. The formal calculation permits to find an explicit formulation of this critical value of n (n_S) which can be introduced in Eq. (24b) to get the sought analytical expression of the critical symmetrical wrinkling load:

$$\lambda_{SL}^{um} = \frac{2\sqrt{6}}{3} b \sqrt{\frac{E_c E_s {t_s}^3}{t_c}} + \frac{G_c t_c b}{3}. \tag{26}$$

The corresponding critical wavelength (L/n_S) is given by

$$\frac{L}{n_S} = \pi \sqrt[4]{\frac{E_s t_c {t_s}^3}{24 E_c}}. \tag{27}$$

These expressions were presented by Hoff and Mautner (1945) and Frostig et al. (1992), without the shear term of Eq. (26) for the latter. Observing the symmetrical wrinkling phenomenon (Fig. 1(b)), one can reckon that core shear will play a role in controlling the occurrence of symmetrical mode. Shear must consequently appear in the expression of the critical load. This can be verified in Fig. 5 where are plotted, versus the thickness ratio, the critical symmetrical loads of the default sandwich configuration calculated using the present approach both including and neglecting the core shear stiffness. It can be seen that

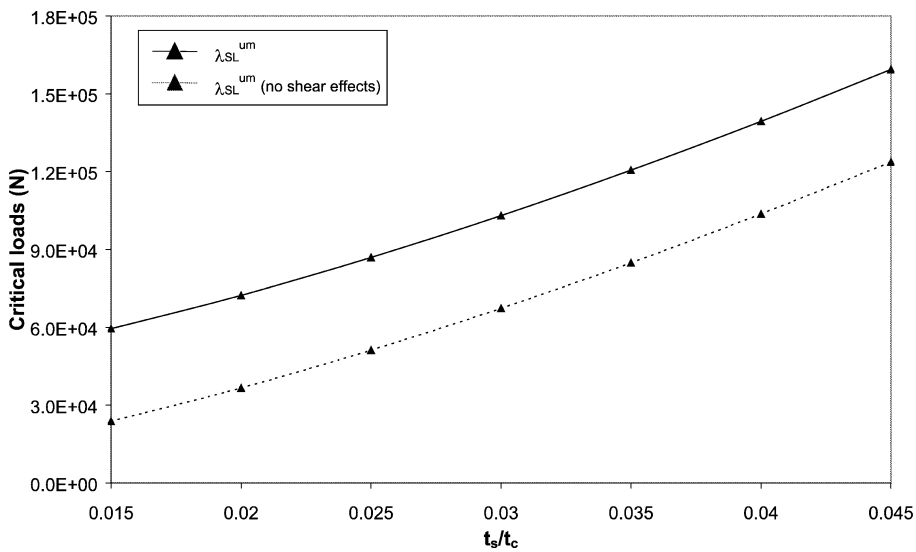

Fig. 5. Symmetrical wrinkling load versus thickness ratio t_s/t_c: effect of the core shear stiffness.

the effect of shear is constant and tends to 'stiffen' the sandwich against local symmetrical instabilities. This contribution of shear can thus represent up to 60% for the lowest loads corresponding to sandwiches with low thickness ratios (t_s/t_c), very sensitive to local phenomena. As a first explanation, this trend can be related to the change in the buckling loads of a beam resting on an elastic foundation, which will increase if the foundation can sustain shear. This 'correction' being constant, its effect will be especially visible for the sandwiches with the lowest loads.

3.1.3. Antisymmetrical wrinkling

The corresponding load of the antisymmetrical local mode is derived through the same procedure of minimization as for the symmetrical wrinkling. In this case, the difficulty lies in the complexity of the eigenvalue associated with the antisymmetrical mode (Eq. (24a)). Indeed, a formal calculation is possible but requires the resolution of an eighth degree polynomial in order to find the critical value of n. The resolution has been carried out with the software Maple V, but the analytical expression is untractable and cannot be considered as a simple design criterion. Therefore it is essential to simplify Eq. (24a) and under the following assumptions:

$$\left(\frac{t_c}{t_s}\right)^2 \gg 1, \qquad \left(\frac{t_s}{t_c}\right)\left(\frac{E_s}{E_c}\right) \gg \frac{1}{4} \tag{28}$$

which are completely satisfied for classical sandwich columns in which $t_c/t_s > 10$ and $E_s/E_c > 50$, a very simple analytical expression for the critical load is determined

$$\lambda_{AL}^{um} = \frac{2bt_s}{t_c}\left(\sqrt{2t_s E_s E_c(t_c + 2t_s)} - \frac{{t_s}^2}{t_c}\frac{E_s E_c}{G_c}\right). \tag{29}$$

The corresponding critical wavelength is given by

$$\frac{L}{n_A} = \pi \Big/ \sqrt{6\left(\frac{1}{t_s t_c}\sqrt{2\frac{E_c}{E_s}\left(\frac{t_c}{t_s} + 2\right)} - \frac{2E_c}{{t_c}^2 G_c}\right)}. \tag{30}$$

The evaluation of this critical load for different sandwich configurations shows that for some combinations of geometrical and material parameters, the antisymmetrical wrinkling does not exist. Hence, a relationship between the different parameters can be determined, the validity of which corresponds to the possible existence of this local form of instability. The extraction of this relation thanks to the exact solution is impossible due to the complexity of the expression (Eq. (24a)), but it is possible from the approximate load (Eq. (29)). Then a relation is isolated and corresponds mathematically to finding real roots in the minimization procedure

$$\frac{2{t_s}^3 E_s E_c}{{G_c}^2 {t_c}^2 (t_c + 2t_s)} < 1. \tag{31}$$

This relationship shows that antisymmetrical wrinkling is notably favored in sandwich configurations with a thick core and thin skins, since in first approximation it depends on the thickness ratio $(t_s/t_c)^3$. The simplified expression of the antisymmetrical wrinkling given by Eq. (29) is rather simple to use and manipulate, however it is interesting to estimate the relative discrepancy of the predictions yielded by this expression and the exact solution. Fig. 6 shows that the difference between the two loads for different geometrical and material ratios is very low (<0.1%). Some curves in Fig. 6 start for large t_c/t_s ratios because for the chosen sets of parameters Eq. (31) must be satisfied for the antisymmetrical wrinkling to occur.

If one observes the contribution of the core shear stiffness in the critical load associated with the antisymmetrical wrinkling (Fig. 7), it can be verified that it is non-linear and varies from less than 10% up to 50% of the critical load depending on the thickness ratio. But more importantly, the effect of shear tends here to 'soften' the sandwich column, conversely to the effect of shear in the symmetrical mode.

3.2. Comparison with existing models

In this section, the formulae given by the unified model are compared with the classical expressions of the critical loads for global buckling and (symmetrical) wrinkling presented in the introduction of this paper (Eqs. (1) and (4)).

3.2.1. Global instability

The critical load of the equivalent homogeneous sandwich column model for the global buckling (Eq. (1)) can be rewritten by feeding in the expressions of the equivalent stiffnesses D and S (Eq. (3)). This leads to the following equation:

$$\lambda_{\mathrm{EHB}} = \frac{\pi^2 E_s t_s b(t_s + t_c)^2 G_c}{2L^2 G_c + \pi^2 E_s t_c t_s}. \tag{32}$$

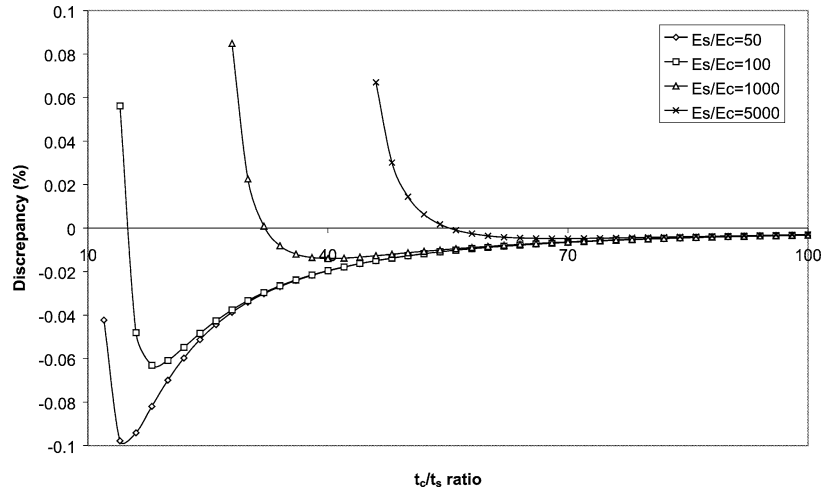

Fig. 6. Discrepancy between approximate (Eq. (29)) and exact antisymmetrical wrinkling load (Eq. (24a)) for the sandwich configuration in Table 1.

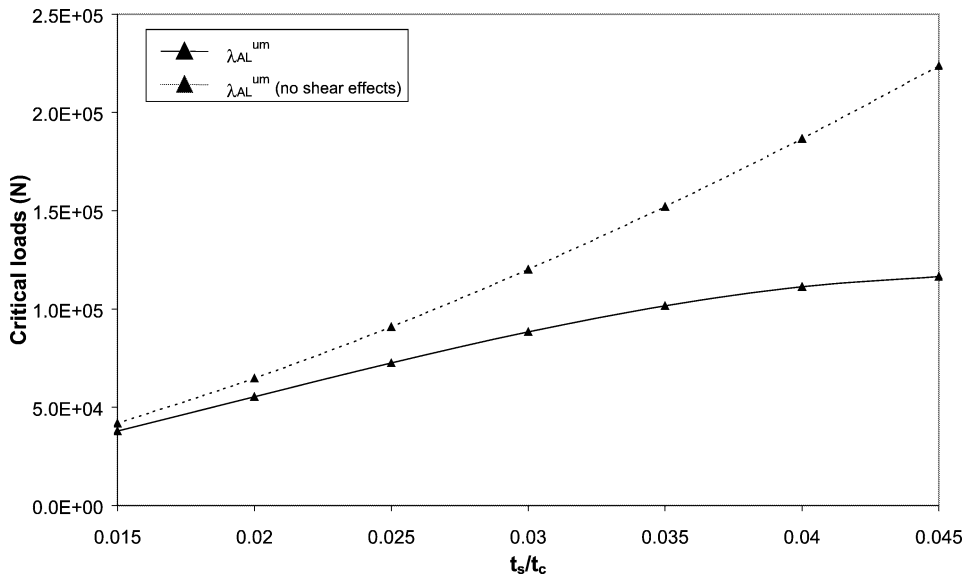

Fig. 7. Antisymmetrical wrinkling load versus thickness ratio t_s/t_c: effect of the core shear stiffness.

At first sight, it seems difficult to find a correlation between Eqs. (25) and (32). But when one estimates the two critical loads for multiple sandwich configurations, it appears that the relative difference between the two expressions does not exceed 1%, and is not therefore worth being shown here. So, the unified model is able to model properly the global buckling behaviour of sandwich columns. Also it can be noticed that the equivalent homogeneous column model, with the stiffnesses defined in Eq. (3), yields a good approximation of the global critical load.

3.2.2. Local modes

As stated below, the presented approach yields critical loads relying on well-founded hypotheses regarding structural mechanics. Conversely, we have quoted in the introductory part of this paper that the classical approaches of the local phenomena usually rely on local models of beams resting on elastic foundations, the parameters of the foundation being the keys in these models; see, for instance, (Thomsen, 1992; Hassinen and Martikainen, 1995; Allen, 1969; Niu and Talreja, 1999) for cores represented as elastic isotropic continuous media characterized by Airy's functions.

In Figs. 8 and 9 are plotted respectively the symmetrical (Eq. (26)) and antisymmetrical (Eq. (29)) critical wrinkling loads calculated with our approach and with the classical approach (Eq. (4)), for the default sandwich configuration reported

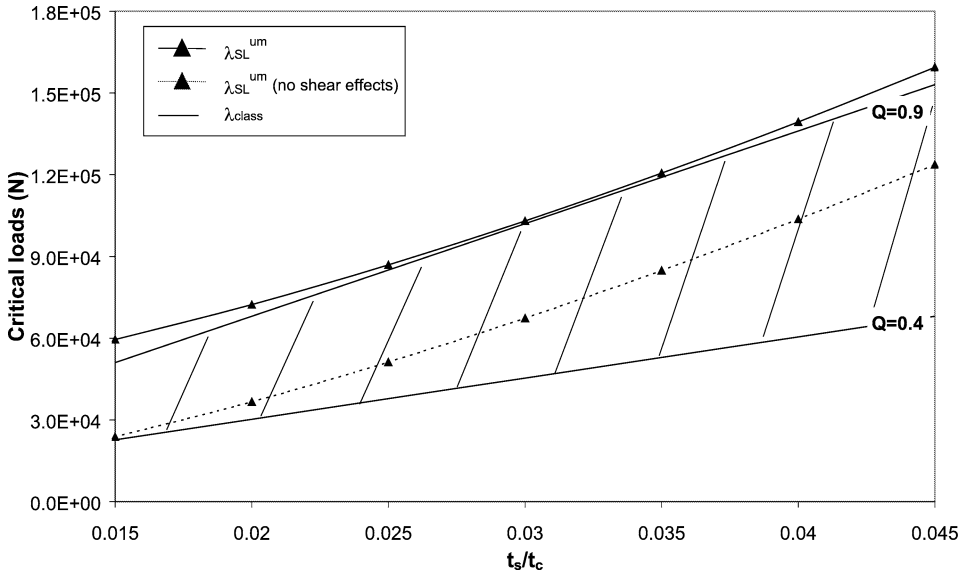

Fig. 8. Symmetrical wrinkling load versus thickness ratio t_s/t_c: effect of the core shear stiffness and comparison with classical wrinkling loads ($0.4 < Q < 0.9$ in Eq. (4)).

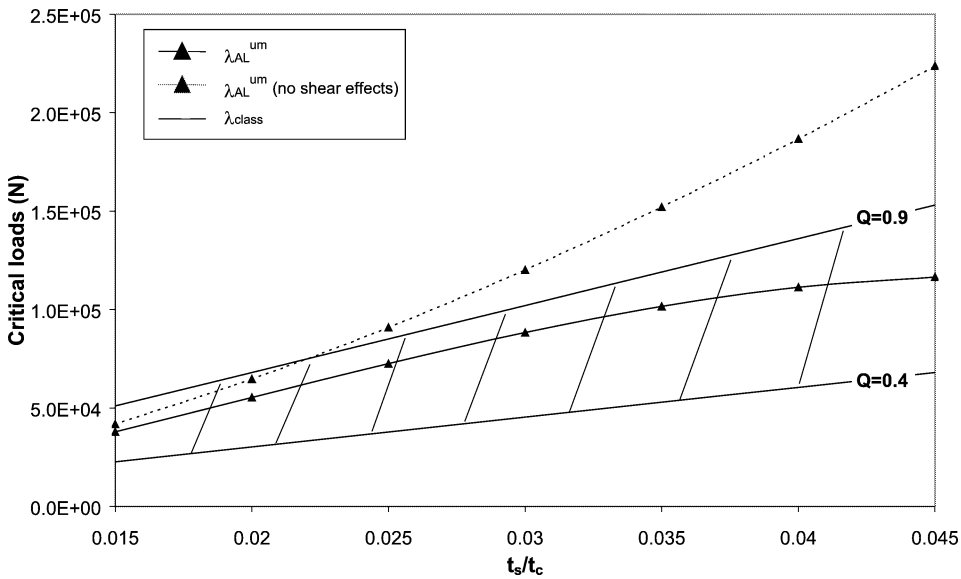

Fig. 9. Antisymmetrical wrinkling load versus thickness ratio t_s/t_c: effect of the core shear and comparison with classical wrinkling loads ($0.4 < Q < 0.9$ in Eq. (4)).

in Table 2. The critical load λ_{class} stands for the classical wrinkling load, deduced from Eq. (4), $\lambda_{\text{class}} = 2bt_s\sigma_{\text{CR}}$ with $Q \in [0.4, 0.9]$. It clearly appears that the dependence of the loads towards the core shear is of major concern. As seen before, the effect of the core shear on the instabilities is inverted for the symmetrical and antisymmetrical wrinkling. This may justify the use in the classical load (Eq. (4)) of correction coefficients that vary sufficiently (from 0.4 to 0.9) to cover the discrepancies between loads predicted by models with and without shear, especially for low thickness ratio sandwiches under symmetrical wrinkling. Moreover, it has to be noticed that conversely to the classical approach, the unified model approach yields critical loads (Eqs. (26) and (29)) which depend on both core and skin thicknesses, this is crucial even for a local phenomenon.

3.2.3. Comments on the symmetrical wrinkling load

As mentioned the symmetrical wrinkling of both skins can be represented through dedicated models provided the foundation parameters are properly determined. From the expression of the symmetrical wrinkling (Eq. (26)), we can propose the foundation parameters which must be used in such models to properly characterize the symmetrical wrinkling. Indeed, this expression (Eq. (26)) can be deduced thanks to a two-parameter foundation with the parameters defined by

$$k_z^e = \frac{4bE_c}{t_c}, \tag{33}$$

$$k_y^s = \frac{G_c t_c b}{3}. \tag{34}$$

3.3. Competition between local and global instabilities

3.3.1. Critical instabilities

The plots of the critical loads, versus parameters t_c and E_s are respectively given by Figs. 10 and 11, for the sandwich configuration given in Table 1 with a 30 mm core thickness. In these plots, the local loads are normalized over the global load, this permits to isolate easily the configurations for which global buckling or local buckling will prevail. For the antisymmetrical wrinkling, the comparison is carried out with the recent 'beam-elastic foundation' model of (Niu and Talreja, 1999) ($\lambda_{\mathrm{N\&T}}$ in figures), one of the very few model to represent properly antisymmetrical wrinkling. For the classical approach (λ_{class}) the correction coefficient is intermediate ($Q = 0.5$). Through these two representations, we can confirm the very conservative nature of Eq. (4) for the two local modes. Moreover, one can notice that the classical formula can be an admissible approximation of the symmetrical and antisymmetrical wrinkling only for thick cores, here ($t_c/t_s > 50$) in Fig. 10. For the antisymmetrical wrinkling, in Figs. 10 and 11, the tendencies of $\lambda_{\mathrm{N\&T}}$ and λ_{AL}^{um} are very close. But contrary to our approach the main drawback of the critical load $\lambda_{\mathrm{N\&T}}$ is the impossibility of isolating an analytical expression for a general sandwich configuration, due to the complex formulation of the stress function on which the model is built. It is interesting to notice that similarly to our model, although it is not mentioned by the authors, a condition exists for the existence of the antisymmetrical wrinkling and Fig. 10 shows a good correlation with our condition (Eq. (31)).

3.3.2. Design indications: sensitivity towards mechanical and geometrical parameters

If the symmetrical and global modes are properly represented through dedicated models, it is not the case for the antisymmetrical mode which is poorly addressed as it was explained previously. This can be crucial since the antisymmetrical wrinkling seems to yield lower loads than for the symmetrical wrinkling (Figs. 10 and 11). Then in order to compare the

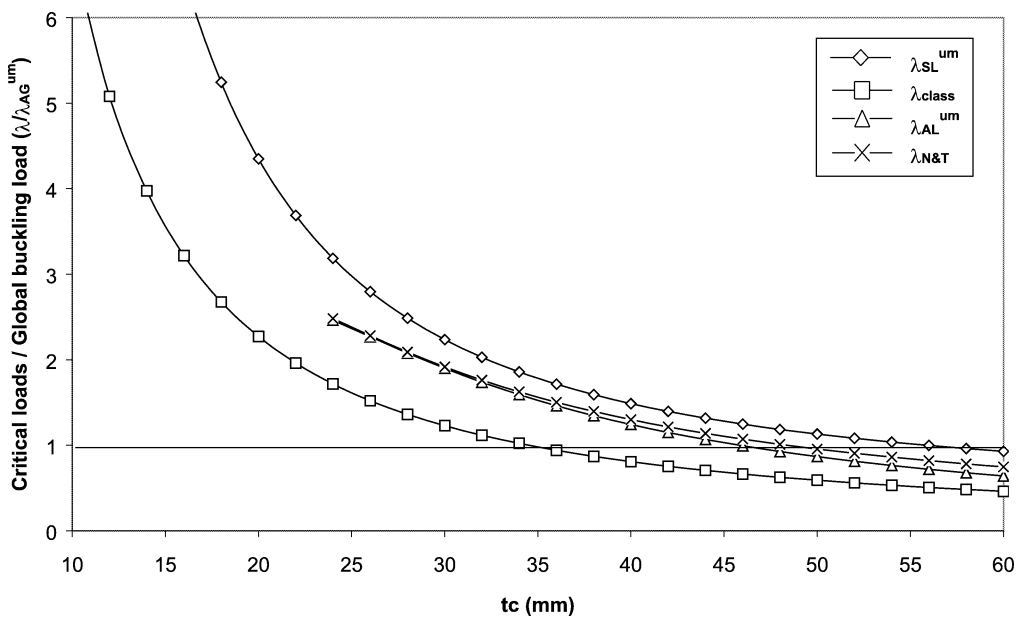

Fig. 10. Plot of the local critical loads (predicted by the present unified model and both classical approach and model from (Niu and Talreja, 1999)) versus the core thickness t_c.

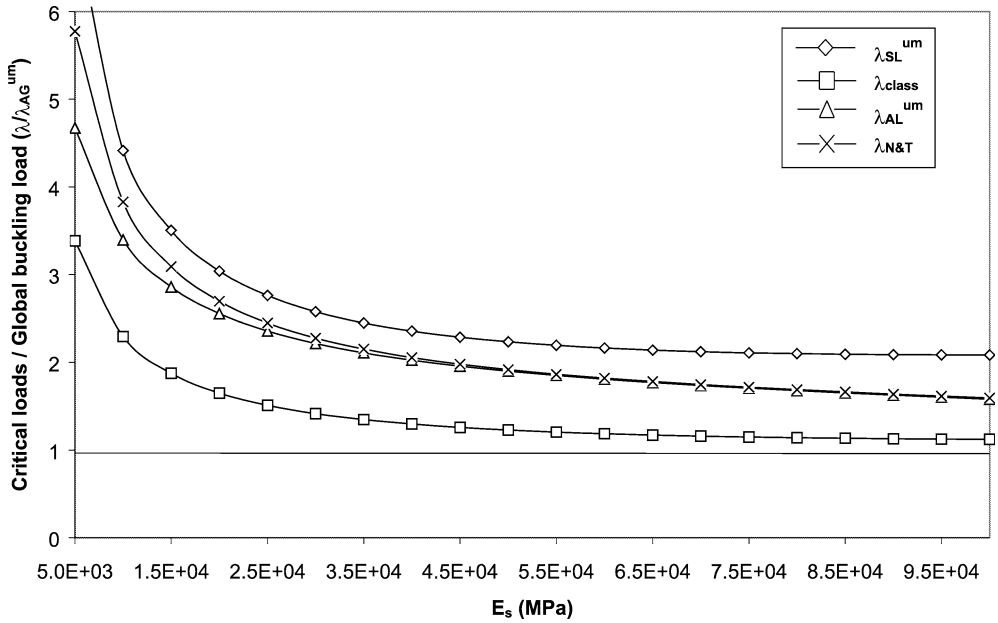

Fig. 11. Plot of the local critical loads (predicted by the present unified model and both classical approach and model from (Niu and Talreja, 1999)) versus the skin Young's modulus E_s.

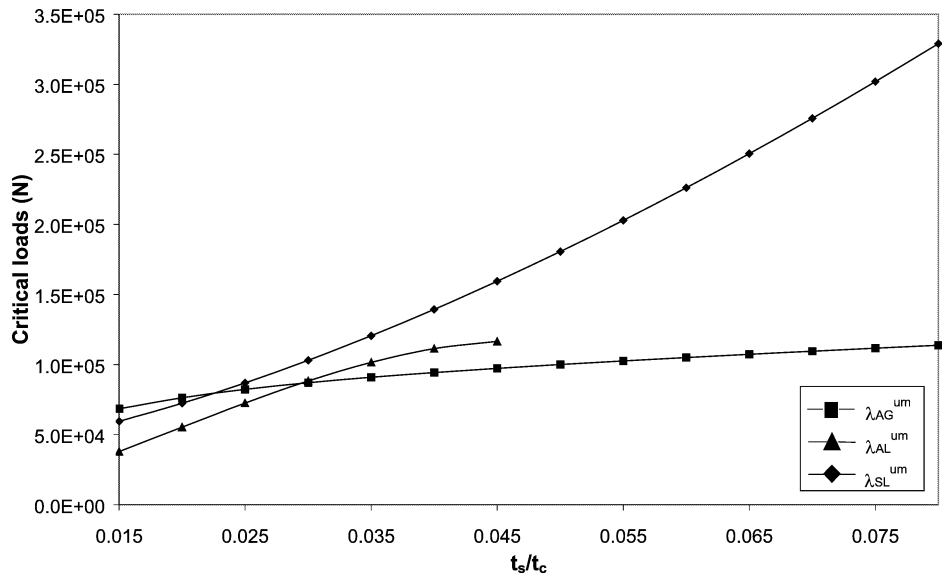

Fig. 12. Plot of the three presented critical loads versus t_s/t_c.

three instabilities, the loads deduced from the unified model will be used to compare quantitatively the three loads when varying thickness and modulus ratios. In Figs. 12 and 13, the three loads are plotted for the default sandwich configuration. One can notice that for sandwiches with low thickness ratios, local loads are quite close to each other and lower than the load for the global instability. When the skin thickness increases (Fig. 12), the global instability quickly prevails. As for the increase of the skin modulus (Fig. 13), local and global antisymmetrical instabilities would occur for very close load levels, with a predominance of local phenomena for rather medium skin moduli. The symmetrical wrinkling load is for both changes (thickness and modulus ratios) systematically larger than the load for antisymmetrical wrinkling. This can be established analytically from this unified model (Léotoing, 2001). The same conclusion was given by Niu and Talreja (1999) for their specific model.

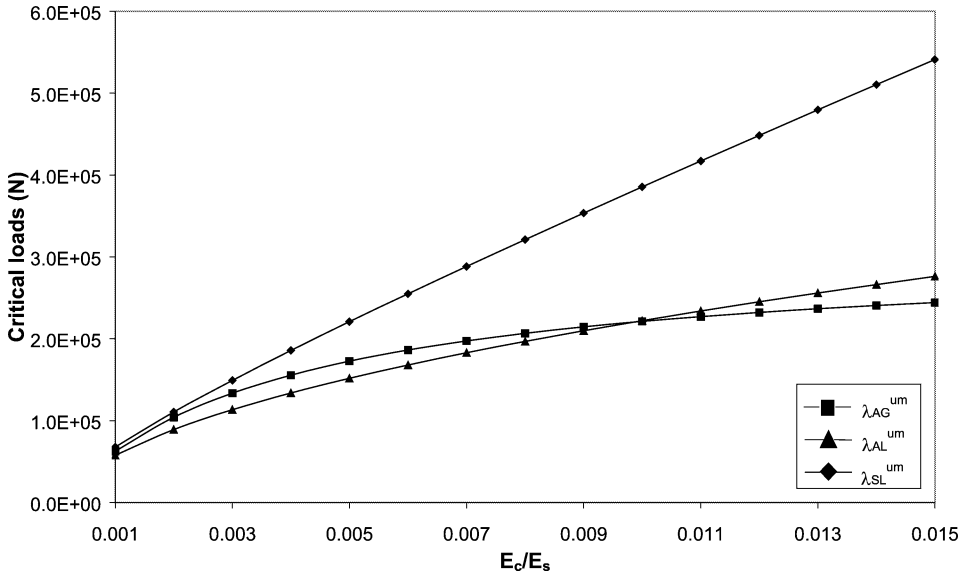

Fig. 13. Plot of the three presented critical loads versus modulus ratio E_c/E_s.

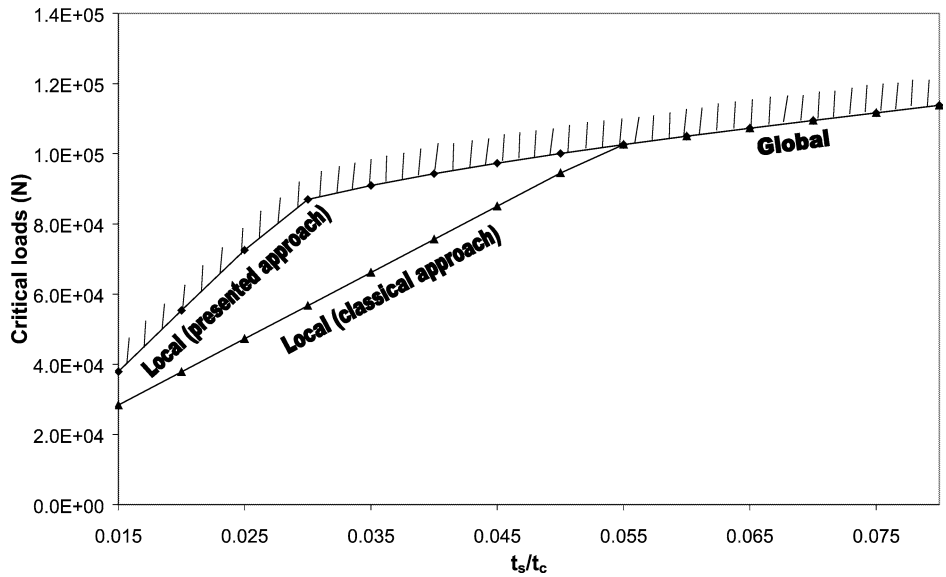

Fig. 14. Critical load of the sandwich column versus thickness ratio t_s/t_c: comparison between the presented approach and the classical one.

Finally, the expressions proposed for the prediction of buckling loads can be used to select sandwich configurations against compressive instabilities at both scales. It is proposed in Figs. 14 and 15 to visualize the zones where thickness and modulus ratios can be selected such that instabilities are avoided, for some given admissible load levels. It can be seen that according to the classical approach many configurations would be dismissed, depending only on the choice of a weighting coefficient Q. Conversely the proposed approach allows to isolate safely configurations which would be locally or globally stable. Further developments permit to express a general analytical condition for the selection of those configurations (Léotoing, 2001).

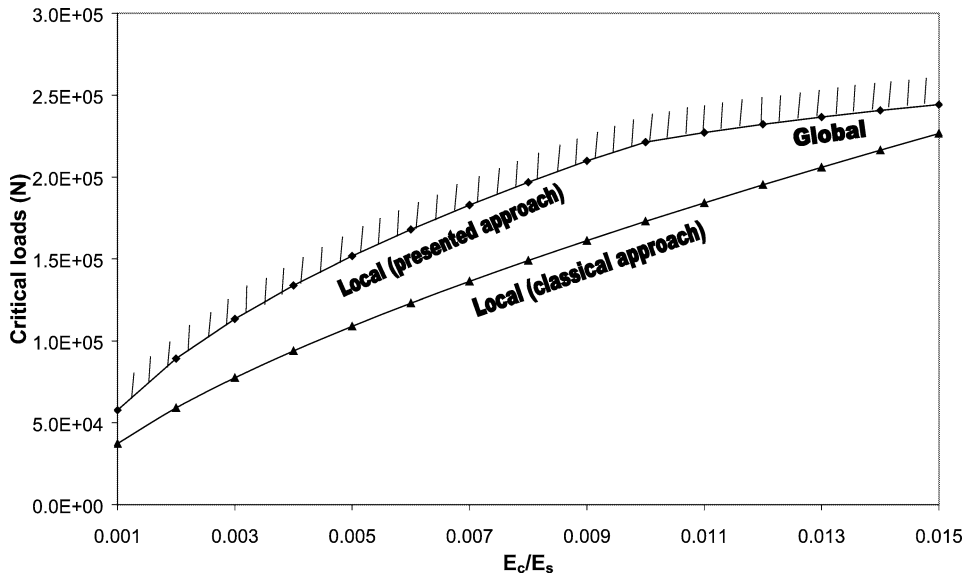

Fig. 15. Critical load of the sandwich column versus modulus ratio E_c/E_s: comparison between the presented approach and the classical one.

4. Conclusions

A unified model was presented which for a perfect linear structure demonstrated its ability to grasp both local and global geometrical instabilities. The critical loads extracted from this model through an eigenvalue calculation were compared, on given sandwich configurations, with the formulae usually employed for designing sandwich structures.

The global load was shown to agree with the approach of an equivalent homogeneous column. Then, the major role played by the core shear stiffness was underlined for both local forms. For the antisymmetrical instability, the predictions of the present approach were shown to perfectly fit the predictions obtained using the rigorous but complex formulas from (Niu and Talreja, 1999), exhibiting the same condition of existence. As for the symmetrical instability, the lack of accuracy of the classical approach was assessed.

Our unified model has been validated for a perfect linear structure. However, the existence of sandwich configurations has been shown for which critical loads associated with global and local instabilities are very close. This raises the need to extend the application of the model to the non-linear problem of post-buckling where interaction of local and global buckling should yield realistic unstable behaviours (Léotoing et al., 2001). Moreover, this unified model can be successfully used to characterize analytically the occurrence and the stability of an interactive buckling form (Léotoing, 2001).

Appendix A

The coefficients of the symmetrical matrix $[A]$ defined in Eq. (22) are given by

$$A_{11} = \frac{G_c}{t_c} + \omega^2 E_s t_s, \qquad A_{12} = -\frac{G_c}{t_c}, \qquad A_{13} = \omega G_c \xi + \omega^3 \frac{E_s t_s^2}{2}, \qquad A_{14} = \omega G_c \xi, \qquad A_{15} = \omega \frac{G_c t_c^2}{6},$$

$$A_{22} = \frac{G_c}{t_c} + \omega^2 E_s t_s, \qquad A_{23} = -\omega G_c \xi, \qquad A_{24} = -\omega G_c \xi - \omega^3 \frac{E_s t_s^2}{2}, \qquad A_{25} = -\omega \frac{G_c t_c^2}{6},$$

$$A_{33} = \frac{E_c}{t_c} + \omega^2 G_c t_c \left(\frac{1}{3} + \frac{t_s}{t_c}\left(1 + \frac{t_s}{t_c}\right)\right) + \omega^4 \frac{E_s t_s^3}{3}, \qquad A_{34} = -\frac{E_c}{t_c} + \omega^2 G_c t_c \left(\frac{1}{6} + \frac{t_s}{t_c}\left(1 + \frac{t_s}{t_c}\right)\right),$$

$$A_{35} = \omega^2 \frac{G_c t_c^3}{6} \xi, \qquad A_{44} = \frac{E_c}{t_c} + \omega^2 G_c t_c \left(\frac{1}{3} + \frac{t_s}{t_c}\left(1 + \frac{t_s}{t_c}\right)\right) + \omega^4 \frac{E_s t_s^3}{3}, \qquad A_{45} = \omega^2 \frac{G_c t_c^3}{6} \xi,$$

$$A_{55} = \frac{E_c t_c^3}{3} + \omega^2 \frac{G_c t_c^5}{36}.$$

References

Allen, H., 1969. Analysis and Design of Structural Sandwich Panels. Robert Maxwell, M.C., M.P.

Benson, A., Mayers, J., 1967. General instability and face wrinkling of sandwich plates – unified theory and applications. AIAA Journal 5 (4), 729–739.

Frostig, Y., Baruch, M., 1993. High-order buckling analysis of sandwich beams with transversely flexible core. Journal of Engineering Mechanics 119 (3), 476–495.

Frostig, Y., Baruch, M., Vilnay, O., Sheinman, I., 1992. Highorder theory for sandwich-beam behavior with transversely flexible core. Journal of Engineering Mechanics 118, 1026–1043.

Hassinen, P., Martikainen, L., 1995. Serviceability and ultimate limit states of continuous sandwich panels, in: Allen, H. (Ed.), Proceedings of Sandwich Construction 3. Engineering Materials Advisory Services, pp. 195–204.

Hoff, N., Mautner, S., 1945. Buckling of sandwich type panels. Journal of the Aeronautical Sciences 12 (3), 285–297.

Hunt, G., Da Silva, L., Manzocchi, M., 1988. Interactive buckling in sandwich structures. Proceedings of the Royal Society of London 417A, 155–177.

Kim, C., Hong, C., 1988. Buckling of unbalanced anisotropic sandwich plates with finite bonding stiffness. AIAA Journal 26 (8), 982–988.

Léger, A., Combescure, A., Potier-Ferry, M., 1998. Bifurcation, flambage, stabilité en mécanique des structures. Technical report, IPSI.

Léotoing, L., 2001. Modélisation du flambage global, local et interactif dans les structures sandwich en compression. PhD thesis, École Nationale Supérieure des Mines de Saint-Etienne et Université Jean Monnet.

Léotoing, L., Drapier, S., Vautrin, A., 2001. Nonlinear interaction of geometrical and material properties in sandwich beam instabilities. International Journal of Solids and Structures. Accepted for publication.

Librescu, L., 1970. On a geometrically nonlinear theory for elastic anisotropic sandwich-type plates. Revue Roumaine des Sciences Techniques. Série de Mécanique Appliquée 15 (2), 323–339.

Lo, K., Christensen, R., Wu, E., 1977. A high-order theory of plate deformation, part 1: Homogeneous plates. Journal of Applied Mechanics, 663–668.

Niu, K., Talreja, R., 1999. Modeling of wrinkling in sandwich panels under compression. Journal of Engineering Mechanics 125 (8), 875–883.

Starlinger, A., 1990. Development of efficient finite shell elements for the analysis of sandwich structures under large deformations and global as well as local instabilities. PhD thesis, Vienna University of Technology.

Starlinger, A., Rammerstorfer, F., 1992. A finite element formulation for sandwich shells accounting for local failure phenomena, in: Weissman-Berman, D., Olsson, K. (Eds.), Proceedings of Sandwich Constructions 2. Engineering Materials Advisory Services, pp. 161–188.

Teti, R., Caprino, G., 1989. Mechanical behavior of structural sandwiches, in: Olsson, K., Reichard, R. (Eds.), Proceedings of Sandwich Constructions 1. Engineering Materials Advisory Services, pp. 53–68.

Thomsen, O., 1992. Analysis of local bending effects in sandwich panels subjected to concentrated loads, in: Weissman-Berman, D., Olsson, K. (Eds.), Proceedings of Sandwich Construction 2, pp. 417–440.

Vinson, J., 1989. Comparison of optimized sandwich panels of various constructions subjected to in-plane loads, in: Olsson, K., Reichard, R. (Eds.), Proceedings of Sandwich Constructions 1. Engineering Materials Advisory Services, pp. 23–52.

Vinson, J., 1992. Analysis and optimization of composite and metallic sandwich cylindrical shells, in: Weissman-Berman, D., Olsson, K. (Eds.), Proceedings of Sandwich Constructions 2. Engineering Materials Advisory Services, pp. 377–400.

Williams, D., Leggett, D., Hopkins, H., 1941. Flat sandwich panels under compressive end loads. Technical report 1987, R.A.E.

Zenkert, D., 1995. An Introduction to Sandwich Construction. Engineering Materials Advisory Services.

- M -

Annexe 2. 7

L. Léotoing, S. Drapier, & A. Vautrin.

Nonlinear interaction of geometrical and material properties in sandwich structures instabilities.

Int. J. Solids Struct. **, 39(13-14) :3717–3739, 2002.**

PERGAMON

International Journal of Solids and Structures 39 (2002) 3717–3739

INTERNATIONAL JOURNAL OF SOLIDS and STRUCTURES

www.elsevier.com/locate/ijsolstr

Nonlinear interaction of geometrical and material properties in sandwich beam instabilities

L. Léotoing, S. Drapier *, A. Vautrin

Mechanical and Materials Engineering Department, SMS Division, École, Nationale Supérieure des Mines de Saint-Étienne, 158 Cours Fauriel, 42023 Saint-Étienne Cedex 02, France

Received 13 February 2002

Abstract

The first part of this paper is dedicated to the analytical and numerical characterization of local and global sandwich beam instabilities in a perfect linear framework. Analytical loads are extracted from an original unified model and used to understand in depth, through a parametric study, the role played by each geometrical and material parameter in the development of global as well as local instabilities. Also, the effects of the combinations of these characteristics is used to draw precious design indications. A low CPU time-consuming simplified model is then built and assessed. Critical loads and wavelengths computed from this model are shown to correlate very well with analytical predictions. It is established that this first approach is essential in order to lead to more detailed investigations in a numerical nonlinear framework which is the aim of the second part. The first geometrical nonlinear investigations in which linear elastic materials are considered permit to isolate sandwich configurations developing super- or sub-critical post-buckling behaviours. As a general trend, unstable behaviours are rather related to the occurrence of geometrical localizations along the beam. This is illustrated by the drastic effects of the so-called interactive buckling onto the whole stiffness of the sandwich beam. Moreover, it is shown that sandwiches are very sensitive towards imperfection sizes and forms. Eventually, an elastoplastic constitutive law is introduced for the core. It is demonstrated that plastic flow and strain localization in the core, combined with the occurrence of instabilities, are associated with a drastic drop in the global beam stiffness and with a strong decrease of the maximum limit load for some cases. The phenomenon of shear crimping is also observed which can be assimilated to a post-bifurcated development of the global buckling mode.

Keywords: Sandwich structure; Linear buckling loads; Scale effects; Post-buckling stability; Elastoplasticity; Imperfection sensitivity

1. Introduction

Sandwich structures have been widely used in aeronautics and astronautics since the early 1940s. The first theoretical works dedicated to the mechanical study of these materials are contemporary of their first applications (Williams et al., 1941). In the 1960s, the sandwich behaviour began to be studied in more detail

* Corresponding author. Tel.: +33-04-77-42-00-79; fax: +33-04-77-42-02-49.
E-mail address: drapier@emse.fr (S. Drapier).

0020-7683/02/$ - see front matter
PII: S0020-7683(02)00181-6

such as in the book by Allen (1969), which sets the basis of the mechanics of sandwich structures. But it is actually from the mid 1980s that the use of sandwich structures has moved from classical applications (sandwich are ideally employed as lagging or floor elements) towards structural components, and thus spread in other fields of engineering. The key point in using sandwich structures is the possibility of largely reducing weights while keeping the same equivalent stiffnesses. Then, it is mostly in transportations that their use leads to substantial weight savings straightfully translated into pay loads. This on-going spreading relies first on a better understanding of the mechanisms driving the response of such structures, and second on new manufacturing processes and materials which permit to build some integral parts out of structural units with sandwiches.

Unfortunately, since structural applications undergo multiaxial loadings, the design of sandwich structures must take into account various loadings such as bending, tension, compression, etc. Usually, classical layered material theories are sufficient for describing some of these mechanical sandwich behaviours. However, the heavy material and geometrical heterogeneity of the sandwich structures can be responsible for the existence of scale effects. More particularly the complex response under in-plane compressive loadings still presents some difficulties for designers. Indeed, under such a destabilising loading, the assembly of very different compounds involves the (co-)existence of buckling at two distinct scales: at the global scale of the assembly and at the local scale of the skins and core. For the global scale, the geometrical instability is similar to Euler's buckling for homogeneous beams (Fig. 1a). For the local scale, two forms are generally considered, which are the symmetrical mode (Fig. 1b) and the antisymmetrical mode (Fig. 1c), both corresponding to the local buckling of skins commonly referred to as wrinkling.

Then the complete understanding and characterization of buckling in such materials require to take into consideration geometrical instabilities at the two scales of observation. Since the mid of the last century, numerous theoretical studies have been conducted on buckling in sandwich beams, panels and shells (Williams et al., 1941; Allen, 1969; Vinson, 1989). The classical approach developed so far is to propose two distinct models associated, respectively, with the study of global and local buckling in an uncoupled way. The global mode of a sandwich beam is studied, thanks to an equivalent homogeneous beam in which the transverse shear effects must be considered. For the local forms, a beam (skin) resting on an elastic foundation (core), able to model the transverse normal and shear stiffnesses of the core, is generally used. The classical formula for the two local forms is given by Eq. (1), where E_c, G_c and E_s are material parameters standing, respectively, for the core transverse normal modulus, the core transverse shear modulus and the skin Young's modulus

$$\sigma_{\text{class}} = Q\sqrt[3]{E_c G_c E_s}. \tag{1}$$

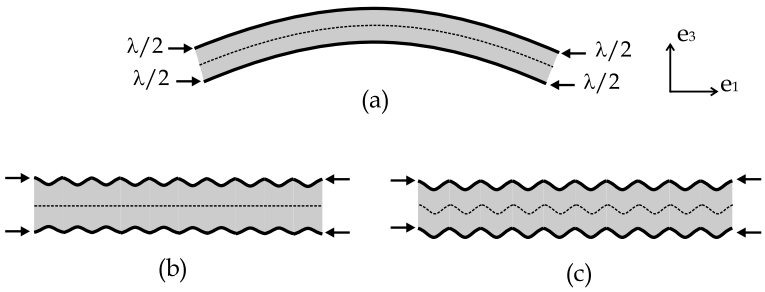

Fig. 1. Sandwich buckling at two scales: (a) global buckling (Euler's type), (b) symmetrical wrinkling of the skins, (c) antisymmetrical wrinkling of the skins.

The value of constant Q varies from 0.4 to 0.9 depending on the authors and the wrinkling case studied (Allen, 1969). The very simplified form of Eq. (1) and the considerable uncertainty concerning the value of Q both demonstrate the difficulty in characterizing instabilities in such structures. These approaches are often intuitive and only appropriate for special cases. Trying to clarify these approaches with experimental results would be of little use since experiments on buckling are by nature unstable and usually only the resulting failure can be observed. In the literature, very few studies are dedicated to the experimental characterization of wrinkling, and correlation can hardly be attempted with the theoretical approaches, unless assigning a variable character to the constant Q as suggested by Teti and Caprino (1989).

Then there is a need for more comprehensive modelling approaches able to first describe the different mechanisms prevailing at each scale, and second to account for a potential interaction of these instabilities at the two scales. Indeed, an optimization of sandwich structures against buckling at the two scales will lead to configurations where these buckling modes will appear at almost the same critical load (Byskov and Hutchinson, 1977). Such configurations will present an unstable post-buckling behaviour resulting of the combination of a global and a local mode (Hunt et al., 1988; Byskov and Hutchinson, 1977). Also these optimum configurations will tend to be very imperfection-sensitive. Some recent studies deal with the notion of interactive buckling but they remain very seldom and all present important limitations. They can be classified into two distinct classes, the analytical and semi-analytical approaches (Hunt et al., 1988; Sokolinsky and Frostig, 1999) and the numerical ones (Starlinger, 1990).

Eventually, it clearly appears that there is a real need for simple but reliable and rich design tools enabling to make rapid calculations for the use of sandwich materials in structural units. Our first aim is to develop a unified sandwich beam model able to grasp both local and global instabilities in a perfect framework. These analytical results are essential for the mechanical understanding of local and global phenomena, by getting an insight into the role played by the combinations of geometrical and material parameters at both scales. Through the analytical expressions associated with the three main forms of instability (Fig. 1), simple design diagrams can be established and sandwich configurations can be quickly selected against local and global buckling. Even if rich conclusions can be drawn in this very simple but mechanically rigorous framework, it is not sufficient for a complete description of the sandwich buckling behaviour. The second step is therefore to build a coherent finite element model in order to conduct rapid numerical investigations including geometrical and material nonlinearities, in other words in a more realistic framework. Finally, this well-founded numerical tool can be reliably used and nonlinear geometrical analyses with linear elastic materials are first led. They permit to identify the different post-buckling paths and isolate the buckling modes susceptible to develop super- or sub-critical regimes. The notion of interactive buckling is also described and it is shown, in agreement with Byskov and Hutchinson (1977), that the interaction between a global curvature and local wrinkling of the compressive skin induces a drop in the global stiffness of the beam. In the last part, more realistic calculations with a crushable core material (foam) show that the imperfection sensitivity of sandwich structures is still emphasized when plastic strains can develop, which lead to very sub-critical responses.

2. Linear buckling loads: analytical and numerical investigations

In this section, an analytical model is presented whose unified formulation and well-founded mechanical assumptions permit to establish reliable design criteria for the three main forms of instability. The accuracy of the corresponding predictions is assessed by FE evaluations. It is shown that these analytical expressions represent precious guides for the configuration selection of sandwich and for the use of an accurate numerical tool with low CPU time-consumption.

2.1. Analytical eigenvalues and design rules

2.1.1. Unified model

The following unified model is described in more detail in Léotoing et al. (2001a). For the sake of simplicity, a symmetrical sandwich beam of length L and width b is considered. Both skins and core are made up of homogeneous isotropic linear elastic materials, defined, respectively, by their Young's modulus E_s and E_c, and its shear modulus G_c for the core. Other notations used subsequently correspond to those introduced in Fig. 2. The model is formulated in displacements, consequently the main difficulty lies in the choice of proper kinematics, which must be rich enough to observe both global and local instabilities but simple enough to yield tractable closed form solutions. A higher-order theory is required in the core since it was shown to represent well the mechanical behaviour of short wavelength phenomena (Lo et al., 1977). For the skins, a simple Euler–Bernoulli beam model is used. By considering perfect skin/core interfaces and a linear transverse shear stress distribution across the beam thickness, the core displacement field $(\mathbf{u}^c(\mathbf{x}) = u_1^c(\mathbf{x})\mathbf{e}_1 + u_3^c(\mathbf{x})\mathbf{e}_3)$ can be written, thanks to the unknown displacements of the top $(\mathbf{u}^t(x_1))$ and bottom $(\mathbf{u}^b(x_1))$ of the sandwich beam and to a gradient of rotation $(\phi(x_1))$ in the core (Eq. (2))

$$\begin{aligned} u_1^c(x_1,x_3) &= \frac{(x_3-t_s)}{t_c}u_1^t(x_1) + \left(1-\frac{(x_3-t_s)}{t_c}\right)u_1^b(x_1) + t_s\left(\frac{x_3-t_s}{t_c}\right)u_{3,1}^t(x_1) \\ &\quad - t_s\left(1-\frac{(x_3-t_s)}{t_c}\right)u_{3,1}^b(x_1) + \frac{1}{6}(2x_3-t)(x_3+t_s-t)(x_3-t_s)\phi_{,1}(x_1), \\ u_3^c(x_1,x_3) &= \frac{(x_3-t_s)}{t_c}u_3^t(x_1) + \left(1-\frac{(x_3-t_s)}{t_c}\right)u_3^b(x_1) + (x_3-t_s)(-x_3+t_s+t_c)\phi(x_1). \end{aligned} \tag{2}$$

Then, using this displacement field, the corresponding stresses can be associated with through the linear constitutive laws. Stresses are represented by the second Piola–Kirchhoff tensor and strains by the Green–Lagrange tensor limited to the moderate rotation terms. Eventually, for a simply supported sandwich beam, a non-linear system of five differential governing equations is derived from the Principle of Virtual Works. Since the buckling loads of both the linearized and nonlinear problem coincide (Leger et al., 1998), a linearized form of the previous system is sufficient to determine those loads. The linearization is achieved by postulating a linear pre-buckling state which still holds at the occurrence of the first geometrical instability. Consequently, membrane and moment resultants depend on membrane strains only, and the whole governing equations become linear. The critical loads of this problem are the eigenvalues of the corresponding eigenproblem.

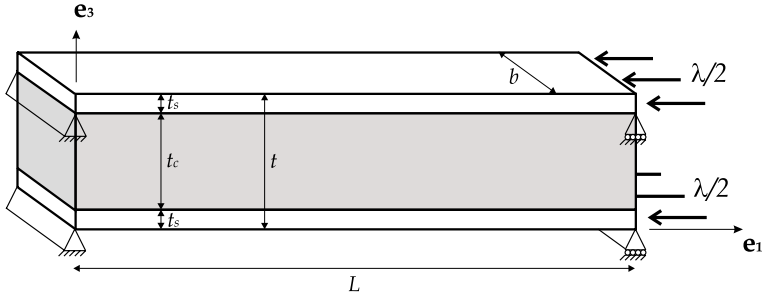

Fig. 2. Notations for a simply supported sandwich beam.

2.1.2. Analytical expressions

The formal resolution of the eigenproblem leads to two strictly positive eigenvalues corresponding, respectively, to an antisymmetrical eigenmode and to a symmetrical one. Through this calculation, three buckling modes and the corresponding loads (λ_X^{um}) can be isolated. Indeed, the eigenvalue associated with the antisymmetrical mode can correspond to the occurrence of either global (critical wavenumber is 1) (Eq. (3)) or local (high critical wavenumber—wrinkling) buckling (Eq. (4)), depending on the sandwich configuration. Moreover, for some combinations of geometrical and material parameters, the antisymmetrical wrinkling does not exist. A relationship (Eq. (4)) between the different parameters can be determined, the validity of which corresponds to the possible existence of this local form of instability. For the symmetrical case, there is only one possible critical load which corresponds to a local mode (Eq. (5)):

$$\lambda_{AG}^{um} = B\left[\frac{\rho_t}{\rho_L^2} + \left(\frac{6_{\rho_E}}{(\rho_t/\rho_v) + (\rho_t/12\rho_L^2) + 2\rho_E\rho_L^2}\right)\left(\frac{1}{\rho_t} + \rho_t + 2\right)\right], \tag{3}$$

$$\lambda_{AL}^{um} = B\left[12\left(\sqrt{2\rho_E\left(\frac{1}{\rho_t} + 2\right)} - \frac{\rho_t}{\rho_v}\right)\right] \quad \text{if} \quad \frac{2\rho_t^3}{\rho_v^2\rho_E(1+2\rho_t)} < 1, \tag{4}$$

$$\lambda_{SL}^{um} = B\left[4\sqrt{6}\sqrt{\frac{\rho_E}{\rho_t}} + \frac{2\rho_E\rho_v}{\rho_t^2}\right], \tag{5}$$

where the dimensionless ratios introduced are some independent combinations of the geometrical and material parameters ($\rho_L = L/(\pi t_c)$, $\rho_E = E_c/E_s$, $\rho_t = t_s/t_c$ and $\rho_v = G_c/E_c$). Factor B common to the three previous equations is expressed as $B = b\rho_t E_s t_s/6$ and has consequently a positive value.

The plots of the stability curves ($E_s = 50,000$ MPa, $E_c = 70$ MPa, $G_c = 25$ MPa, $t_s = 1$ mm, $L = 600$ mm, $b = 40$ mm) for two different core thicknesses (t_c) clearly illustrates the shift between a global and a local antisymmetrical mode (Fig. 3). One must point out that for kinematics with some linear displacement fields in the core, the minimum is always reached for $n = 1$ (Fig. 3), i.e. no antisymmetrical wrinkling can be represented. Fig. 4 represents the change in the critical load of the sandwich beam ($\min(\lambda_{AG}^{um}, \lambda_{AL}^{um}, \lambda_{SL}^{um})$)

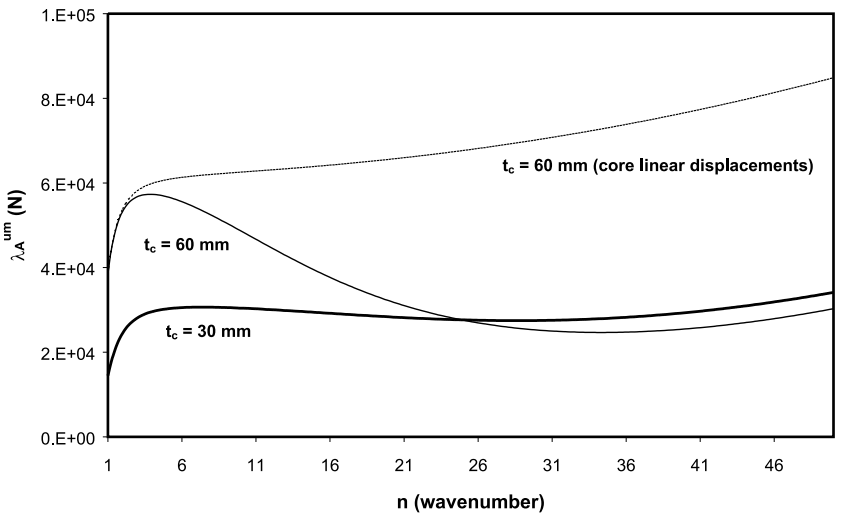

Fig. 3. Neutral stability curves for the critical antisymmetrical load (λ_A^{um}) for two different thicknesses t_c of the core ($t_c = 30$ mm, $t_c = 60$ mm), and for the analytical model based on a linear core displacement.

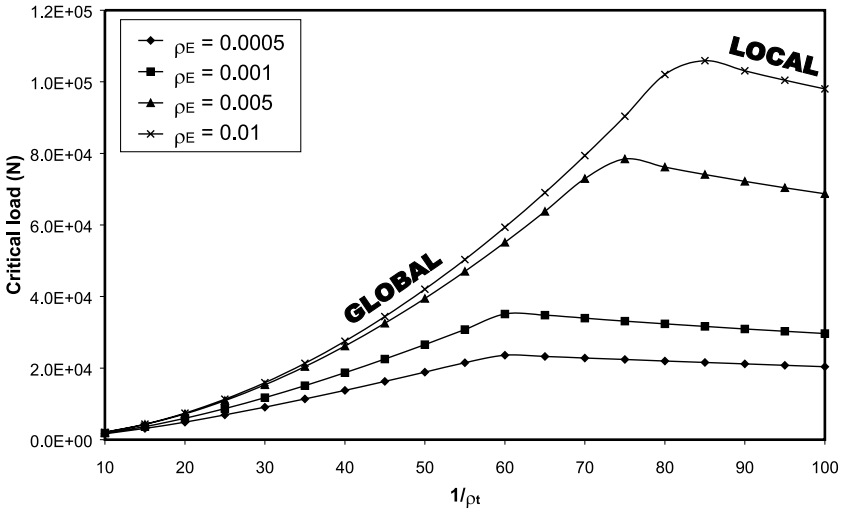

Fig. 4. Change in the critical load of the sandwich beam ($\min(\lambda^{um}_{AG}, \lambda^{um}_{AL}, \lambda^{um}_{SL})$) versus the thickness ratios $1/\rho_t$ and for different modulus ratios ρ_E.

versus the thickness ratios $1/\rho_t$ and for different modulus ratios ρ_E ($E_s = 70,000$ MPa, $t_s = 1$ mm, $L = 1000$ mm, $b = 50$ mm). One can notice that there exist very different configurations for which global or local instabilities will develop at the lowest loads. It clearly appears that the predominance zone of global or local buckling is strongly dependent on the sandwich configuration. Besides, for a fixed modulus ratio, the transition point between the two forms of instability corresponds to an optimized sandwich configuration against buckling. This observation fits a well-known result that the optimum design leads to configurations for which at least two buckling modes will appear at almost the same critical load (Byskov and Hutchinson, 1977). Following these authors, such configurations will present an unstable post-buckling behaviour resulting of the combination of a global and a local mode, and will tend to be very imperfection-sensitive. These configurations will receive a particular attention in the second part of the present contribution.

An alternative consequence of the existence of these instabilities at two scales is the need for designers to identify more systematically the configurations globally or locally unstable. This is achieved by understanding first the role played by each geometrical and material parameter, and second the weight of their combinations. Using the previous analytical expressions of the critical loads offers such a versatility.

2.1.3. Design rules

A sensitivity study was led in Léotoing et al. (2001b). The classical result of the high sensitivity of slender homogeneous beams towards global buckling was clearly demonstrated for sandwich beams. The calculation of the sensitivities for the two local forms are very comparable and their local nature is clearly confirmed by their independence towards the beam length. For the two forms, the key parameter is the thickness of the skins due to its cubic contribution in their flexural stiffness. Thus, t_s is rather associated with the local behaviour of the sandwich beam whereas t_c can be classified as a global parameter. The sensitivities towards the core moduli (E_c, G_c) are rather comparable for the two local modes and confirm the role played by both the transverse normal and shear stiffnesses on the occurrence of local phenomena.

Moreover, graphic tools were proposed (Léotoing et al., 2001b) to localize without any ambiguity the different zones of prevalence, i.e. when global buckling may appear rather than local buckling, and conversely. The three critical loads λ^{um}_{AG}, λ^{um}_{SL} and λ^{um}_{AL} can be compared by pairs, thus defining some zones of predominance for each and every phenomenon by evaluating the sign of the differences. For a given

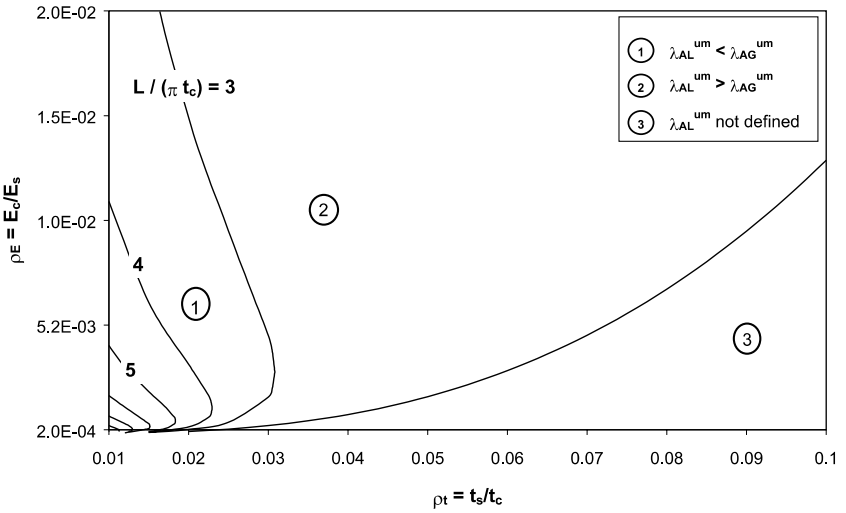

Fig. 5. Change in the predominance zones between antisymmetrical wrinkling and global buckling with $\rho_L = L/\pi t_c$ varying from 3 to 8.

Poisson's ratio, the parameter ρ_v is constant and then the zones can be easily plotted on a ρ_t–ρ_E graph, for different values of ρ_L. For the two local forms, the analysis of the inequality shows that the antisymmetrical wrinkling will unconditionally occur at lower loads than the symmetrical wrinkling, for ordinary engineering materials used in sandwich construction ($2 \times 10^{-4} < \rho_E < 2 \times 10^{-2}$ and $10^{-2} < \rho_t < 10^{-1}$). Then, predominance zones can be plotted for λ_{AG}^{um} and λ_{AL}^{um}, the two loads of interest. The corresponding graphic is given in Fig. 5, for the configuration previously used for Fig. 4. In Fig. 5 one can observe the change in the frontier between the two zones as a function of the slenderness (ρ_l). An additional zone (zone ③ in Fig. 5) is reported that bounds the configurations for which the condition of existence of the antisymmetrical wrinkling (Eq. (4)) is not valid.

Fig. 5 shows that the local forms are predominant in sandwich beam made up of weak and thick core (zone ①—low values of ρ_E and ρ_t). Moreover, one can observe that local instabilities disappear for slender sandwich beams. For a ratio $\rho_L > 10$, without any material consideration, it can be asserted that the sandwich beam will behave in compression as its equivalent homogeneous representation. These diagrams can be useful for a first dimensioning of sandwich beams under in-plane compression and can give some precious information on their buckling behaviour when a material or geometrical configuration is prescribed regarding other loading conditions.

2.2. Numerical eigenvalue buckling predictions

2.2.1. Finite Element sandwich beam model

In the literature, very few F.E. models are dedicated to sandwich modelling, and very rarely justified rigorously. This lack of reference model constrains us to try and use F.E. displacement-based models which intrinsically cannot ensure any stress continuity at the interfaces. Therefore, it is necessary to assess the quality and accuracy of such models. The first point in setting these models is to eliminate the local effects at the edges which induce complex and unrealistic linear buckling modes. Using a multi-point constraint, either edge is constrained to behave as a solid medium, i.e. the nodes are prescribed to move along a straight line connecting the two extreme nodes located on the top and bottom skins (Fig. 6). The line can stretch linearly and rotate around a central node, the degrees of freedom (d.o.f.) of which are used to apply the

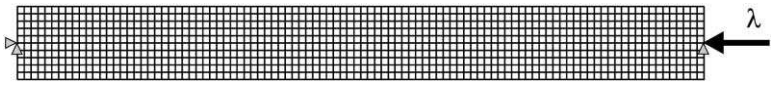

Fig. 6. Simplified F.E. model of the sandwich beam (1200 elements and approximately 2000 d.o.f.).

boundary conditions and loadings. This edge modelling is also suggested by the observation of real configurations of sandwich in which the edges are stiffened by close-outs in order to apply connections or loadings (HEXCEL, 1989).

The first way of modelling the sandwich beam can consist in a two-dimensional model for the whole beam. The skins and the core can be meshed with 4-noded bilinear plane stress solid elements. Various cases tested did not show any significant discrepancy for the eigenbuckling loads calculated with plane strain or plane stress elements. The point in this mesh is rather that in order to have some aspect ratios of the order of the unity, the small elements of the skins induce a large number of elements in the beam length. Then, this model is very heavy and will be CPU time-consuming for future nonlinear analyses. This model can be simplified by replacing the two-dimensional elements of the skins with linear and shear deformable beam elements, which reduces significantly the number of d.o.f. (Fig. 6). The slight loss in the global equivalent flexural stiffness due to the position of the skins that is closer than in the actual sandwich beam is corrected by modifying the beam width.

In this simplified model, the size of the beam elements is no longer controlled by the thickness of the skins, but the number of beam elements must be sufficient to observe the local instabilities. A convergence study has been carried out which showed that the local critical loads are strongly dependent on the length of the beam elements used. For example, Fig. 7 represents the eigenbuckling loads for the sandwich configuration from Table 1 versus the number of beam elements. The local critical loads can be overestimated if too few elements represent the skins, and the global mode becomes 'artificially' critical. Then, in practice, the beam number is selected by prescribing at least 8–10 elements over one wavelength, the expression of which is known analytically.

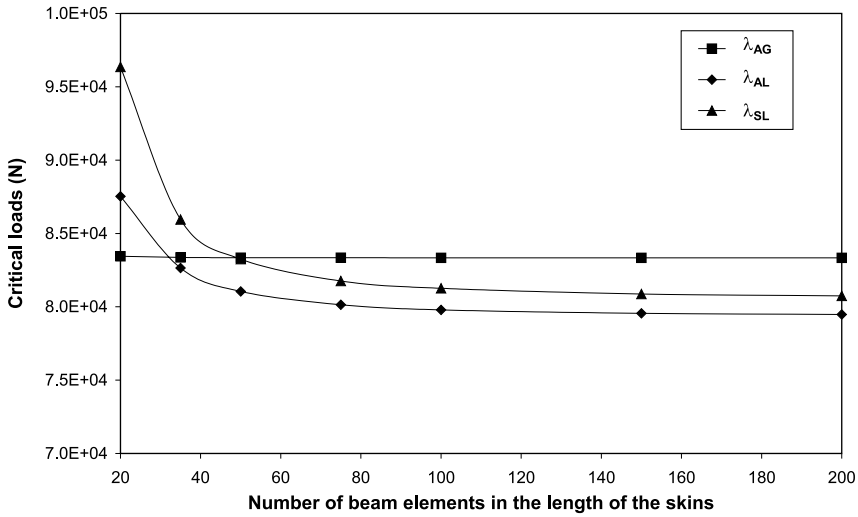

Fig. 7. Change in the three critical eigenbuckling loads versus the number of beam elements along the skins for the simplified model ($t_s = 1.25$ mm).

Table 1
Sandwich characteristics for the comparison between analytical and numerical eigenvalue buckling predictions

E_s (MPa)	70,000	t_c (mm)	50
E_c (MPa)	100	L (mm)	470
G_c (MPa)	35.7	b (mm)	60

A comparison can be made between the two F.E. models. In Table 2 the critical loads associated with the three buckling modes are reported for the simplified model and for two different mesh sizes of the complete model. Also, the total CPU time needed to extract 25 eigenvalues on 450 MHz/2 Gb RAM USparc II Sun workstations is reported. In this comparison, the parameters n_L and n_t stand, respectively, for the number of elements in the length and in the thickness of skins, the sandwich configuration considered is given in Table 1 with $t_s = 1.5$ mm. In Table 2, the global critical load does not vary significantly for the three F.E. models presented, whereas for the local forms the results of the complete model converge towards the critical loads of the simplified model for a large number of elements in the skins. The gain in CPU time for the simplified model is then clearly demonstrated (factor of $\sim$60). Moreover, an evaluation of the energetic contributions of every stress component for the two previous F.E. models have shown very similar behaviours. Consequently it can be assumed that the mechanical behaviour of the sandwich beam is well represented by this low CPU time-consuming simplified model (Léotoing et al., 2001b).

2.2.2. Comparison between analytical and numerical results

The three analytical buckling modes can be found using the previous F.E. model, thanks to an eigenvalue buckling analysis (Fig. 8). Numerical and theoretical critical loads for the antisymmetrical (global and local) and symmetrical (local) mode are plotted versus the thickness ratio, respectively, in Figs. 9 and 10, for the sandwich configuration given in Table 1. In Fig. 9, it can first be noticed the good correlation between analytical and F.E. predictions for the global load and for the antisymmetrical wrinkling mode. The

Table 2
Comparison between the eigenvalue buckling predictions for the two F.E. models

	Simplified model ($n_L = 100$)	Complete model ($n_L = 400$ and $n_t = 3$)	Complete model ($n_L = 1500$ and $n_t = 8$)
d.o.f.	2000	22,000	110,000
CPU time (s)	64	560	3700
λ_{AG} (kN)	83.3	83.8	83.5
λ_{AL} (kN)	79.8	85.6	78.7
λ_{SL} (kN)	81.3	87.7	79.8

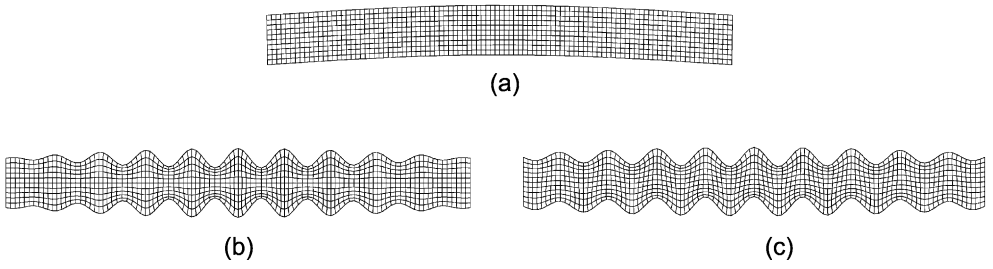

Fig. 8. F.E. beam sandwich buckling modes: (a) global buckling, (b) symmetrical wrinkling of the skins, (c) antisymmetrical wrinkling of the skins.

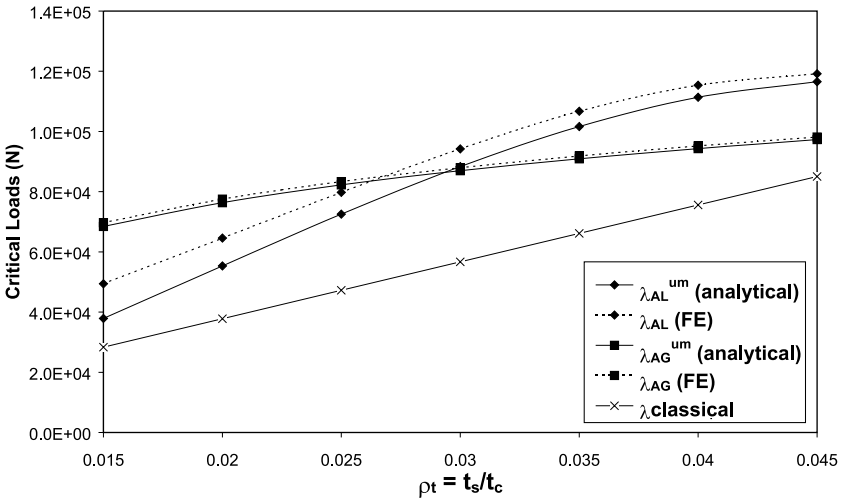

Fig. 9. Change in the analytical and numerical antisymmetrical critical loads for the global and local modes versus the thickness ratio.

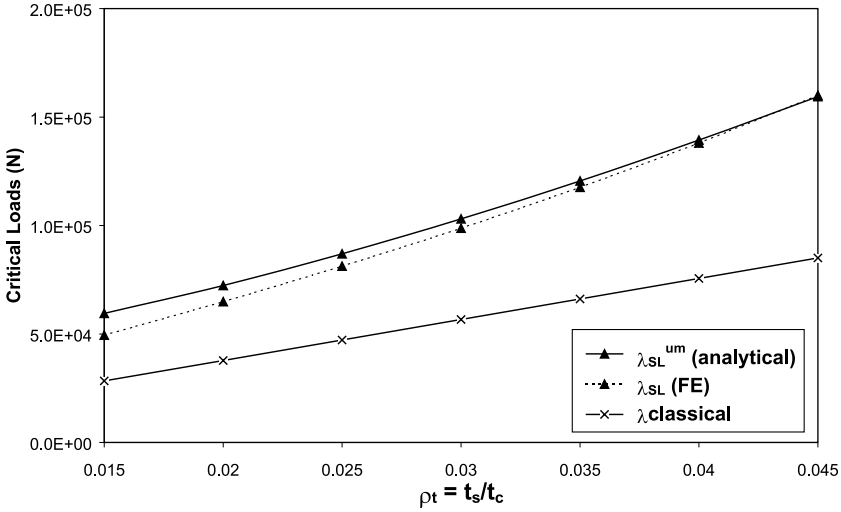

Fig. 10. Change in the analytical and numerical symmetrical critical loads versus the thickness ratio.

discrepancy between the two models does not exceed 22% for the configuration tested. For the symmetrical form (Fig. 10), the agreement is very good (discrepancy lower than 15%) and perfect for high thickness ratios. Anyway, the predictions for both local instabilities correlate rather well when observing the plot of the classical load for a classical and usual value of $Q = 0.5$ (Eq. (1)), the predictions of which are very conservative. The discrepancy between analytical and numerical results can be partly explained by the simplistic analytical shear stress distribution postulated which does not estimate accurately the actual energetic contribution of the shear stress (Léotoing et al., 2001b).

It is also essential to compare the analytical and numerical critical wavelengths. Indeed, if a good correlation is found, a time-optimum mesh will be used by controlling the number of beam elements along the

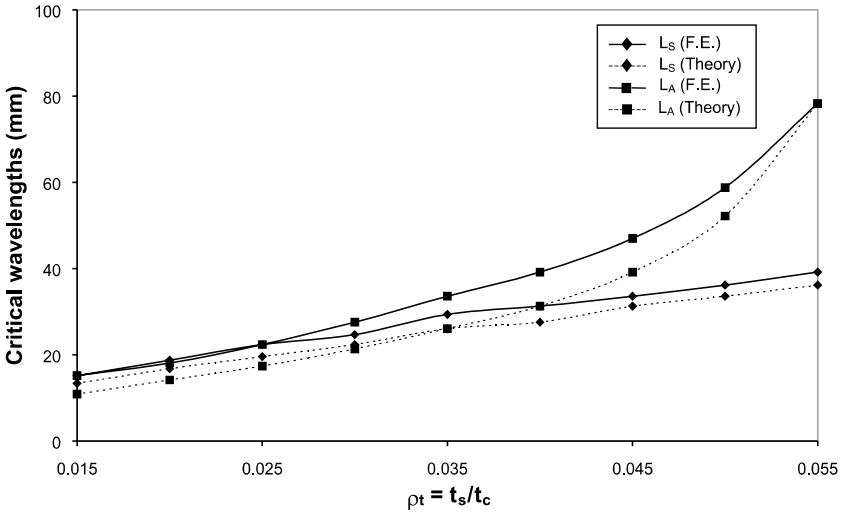

Fig. 11. Comparison between analytical and numerical critical wavelengths.

skins, based on the knowledge of the analytical wavelengths for symmetrical ($L_S = L/n_S$) and antisymmetrical ($L_A = L/n_A$) wrinkling (Eqs. (6) and (7))

$$n_S = \rho_L \sqrt[4]{\frac{24\rho_E}{\rho_t}}, \tag{6}$$

$$n_A = \rho_L \sqrt{6\left(\frac{1}{\rho_t}\sqrt{2\rho_E\left(\frac{1}{\rho_t}+2\right)}-\frac{2}{\rho_v}\right)}. \tag{7}$$

Fig. 11 illustrates the comparison between the two analytical wavelengths (Eqs. (6) and (7)) and the numerical ones, for the sandwich configuration given in Table 1. One can notice the good agreement between theoretical and F.E. predictions for the two wrinkling loads and the similar behaviour of L_S and L_A for small thickness ratios. Moreover, in Léotoing et al. (2001b), it was shown that the wavelength of the local phenomena is independent of the boundary conditions and that the minimum of the two theoretical wavelengths leads to a correct magnitude of the element size in the simplified mesh.

The results of the F.E. and analytical models are coherent. The presented F.E. model permits to find out the three main buckling modes, thanks to a special attention in the modelling of the boundary conditions and loadings. The aim of the following part is to study the post-buckling regime for several configurations.

3. Numerical nonlinear analyses of the post-buckling regime

In this section, first the complete response of elastic sandwich beams is studied. This approach permits to classify the type of response as super- or sub-critical depending on the sandwich configuration. The so-called interactive buckling also receives a special attention since it affects the whole beam stability. Then different geometrical imperfections are introduced on a given configuration and their effects on the beam stability is studied. In the second part, an elastoplastic constitutive law is introduced for the core. This

approach is required when observing geometrical localizations in elastic cores which may turn out to be emphasized when nonlinear materials are considered.

3.1. Linear elastic materials

3.1.1. Sandwich configurations

The existence of a bifurcation point is related to a non-uniqueness of the solution which numerically cannot be simply dealt with. In order to solve numerically the post-buckling problem, it is necessary to turn it in such a way that a continuous response exists. This is possible, thanks to the introduction of a very small geometrical imperfection. For the following investigations, the geometrical imperfections are the linear buckling modes derived from the eigenvalue buckling predictions. Since eigenvectors are defined with an arbitrary magnitude, the maximum displacement component is chosen as the mode amplitude. As a result, the smaller the imperfection, the more 'exact' the post-buckling regime. The geometrical nonlinear analyses are led with ABAQUS™ and the use of a Riks algorithm permits to investigate the post-buckling problems both with stable and unstable behaviours. Indeed, this method considers the applied load as an additional unknown, the problem is then solved simultaneously for loads and displacements.

The construction of the design diagrams has permitted to isolate the configurations in which global buckling is predominant with respect to the local phenomena (configuration 3 in Fig. 12) and conversely (configuration 1 in Fig. 12). But a third zone can be defined in which the three buckling loads are very close. This optimum configuration, denoted configuration 2 in Fig. 12, is also prone to exhibit some interactions between the instabilities at the two scales of the material, as verified for instance by Byskov and Hutchinson (1977). Then, thanks to the design diagram presented in Fig. 12, built for the configuration $t_c = 50$ mm, $E_s = 70,000$ MPa, $E_c = 175$ MPa and $L = 470$ mm, the variation of the thickness ratio allows the selection of three configurations with very different buckling behaviours. The aim of the following paragraph is to identify the bifurcated branches for the three presented configurations by introducing a very small geometrical imperfection corresponding to the first eigenmode.

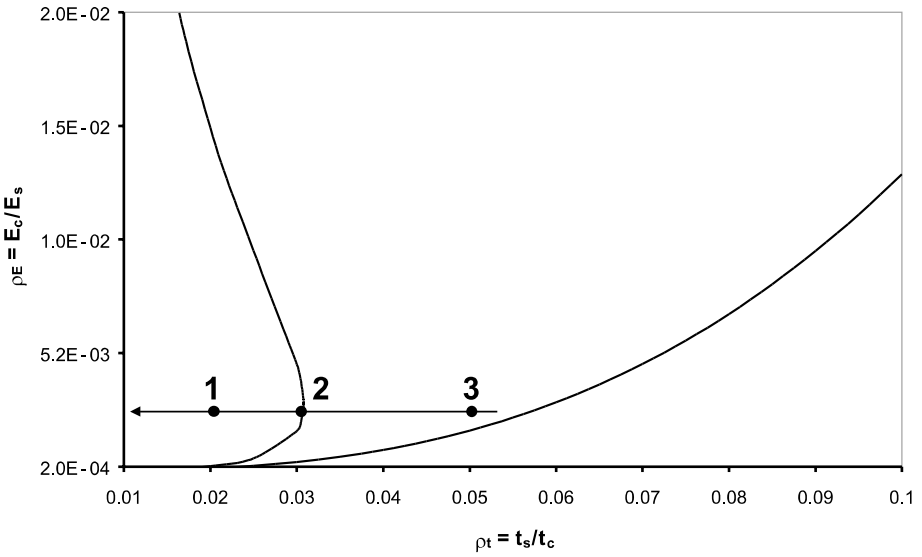

Fig. 12. Three geometrical and material sandwich configurations with different buckling behaviours.

3.1.2. Identification of the bifurcation branches

The numerical critical loads for the three configurations of Fig. 12 (t_s only varies) are given in Table 3. For the next plots, the change in the applied load (λ) is represented as a function of the global end shortening defined as the longitudinal displacement of the node where the load is applied in Fig. 6 normalized by the beam length ($u_1(L, t/2)/L$), or the global deflection defined as the transverse displacement of the node at mid-length and mid-thickness of the core normalized by the core thickness ($u_3(L/2, t/2)/t_c$). For the three configurations, the amplitude of the imperfection is 0.001 mm (0.0019% of the whole beam thickness).

Configuration 1 of Fig. 12 ($t_s = 1$ mm) is first considered. The lowest eigenvalue is associated with the antisymmetrical wrinkling mode for both analytical and numerical predictions (Table 3). A geometrical imperfection is then introduced on this local mode. Fig. 13 shows the corresponding load-end shortening response which exhibits two distinct regimes. The first part consists in a linear increase of the applied load versus the end shortening, up to the bifurcation point corresponding to the linear wrinkling load. After the bifurcation point, the post-buckling regime corresponds to an amplification of the antisymmetrical mode and the branch is super-critical (plate-like), i.e. the post-buckling regime of the sandwich beam is stable.

For configuration 2 in Fig. 12 ($t_s = 1.5$ mm), an imperfection associated with the critical global mode is introduced. The change in the applied load versus the global deflection is given in Fig. 14 which shows that the complete response can be divided into three parts. The first part corresponds to the fundamental 'flat' state of the beam undergoing only compressive deformations. The second part is associated with the post-

Table 3
Numerical linear buckling loads for the sandwich configurations presented in Fig. 12

	λ_{AG} (kN)	λ_{AL} (kN)	λ_{SL} (kN)
Configuration 1 ($t_s = 1$ mm)	115.1	96.8	96.9
Configuration 2 ($t_s = 1.5$ mm)	138.0	145.4	147.5
Configuration 3 ($t_s = 2.5$ mm)	167.5	219.7	262.4

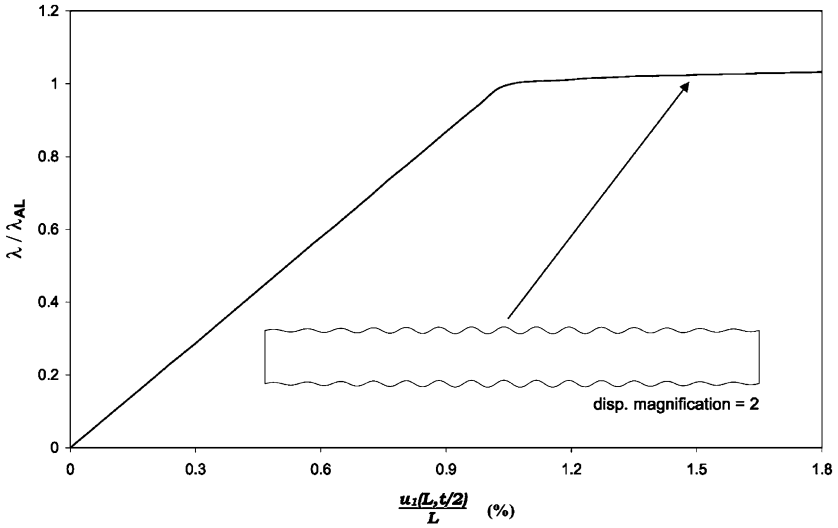

Fig. 13. Change in the applied load versus the global end shortening of the sandwich beam (configuration 1 of Fig. 12) for a geometrical imperfection of 10^{-3} mm on the antisymmetrical wrinkling mode.

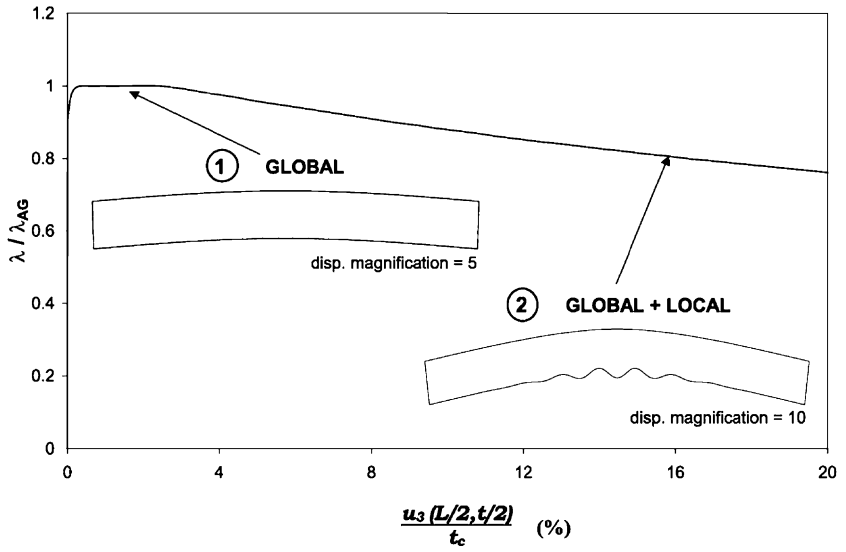

Fig. 14. Change in the applied load versus the global deflection of the sandwich beam (configuration 2 of Fig. 12) for a geometrical imperfection of 10^{-3} mm on the global mode.

buckling path of the equivalent homogeneous beam. This bifurcated branch is super-critical and the total applied load remains constant. The change in the deformed shape corresponds to the amplification of the global mode. But as the global deflection increases, and as it may be expected for this optimum configuration (Byskov and Hutchinson, 1977), a second bifurcation point is reached and the behaviour turns out to be strongly sub-critical (shell-like). The deformed shape of the sandwich beam is then made up of the previous global curvature onto which is superimposed a local wrinkling of the skin undergoing a compressive loading. The phenomenon of interactive buckling is here plainly illustrated. The interaction between the global mode and the wrinkling of one skin causes a geometrical localization responsible for a significant stiffness loss in the whole sandwich beam.

Finally, for the third configuration ($t_s = 2.5$ mm) a global imperfection is introduced, the corresponding load–deflection path is given in Fig. 15. Unlike the previous configuration, the amplitude of the global mode is amplified and no geometrical localization appears on the skins. This stable post-buckling behaviour is similar to that of the equivalent homogeneous sandwich beam.

3.1.3. Localization and stability

These first post-buckling investigations raise some interesting discussion points. To begin with, buckling modes and post-buckling regimes of a sandwich beam undergoing compressive loading are strongly dependent on its configuration. For configurations 1 and 3, in which, respectively, local and global buckling is predominant, the post-buckling behaviour is stable and only one bifurcation point is found. It must be noticed that the same geometrical imperfection can lead to two very different responses (global imperfection for configurations 2 and 3). This may, however, be due to the specificity of configuration 2, for which global and local critical loads are very close. In that case a form of interactive buckling is clearly observed and its harmful effects on the whole stability of the sandwich beam are demonstrated. Further investigations of this high imperfection-sensitive configuration are presented subsequently.

From this first approach, one can suggest that stability will depend on two main factors. The first one concerns the difference between the skin behaviours, i.e. when one skin is globally deformed while in the other one local phenomena develop. In this case, the sandwich beam is 'unbalanced', i.e. there is a breaking

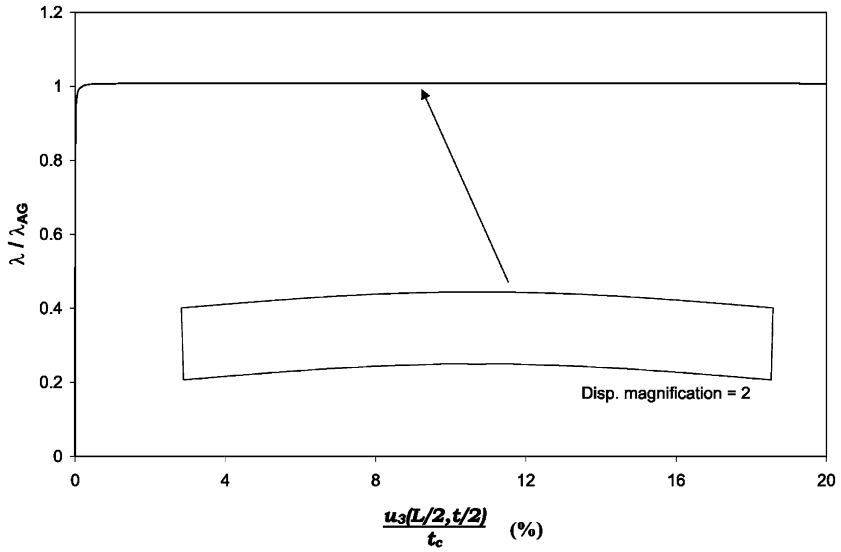

Fig. 15. Change in the applied load versus the global deflection of the sandwich beam for a global geometrical imperfection of 10^{-3} mm on sandwich configuration 3 of Fig. 12.

of the symmetry (Hunt et al., 1988), and unstable regimes are likely to develop. Second, the amplitude modulation (localization) along the deformed shape seems to play an important role, as it will be confirmed in the following part. About this localization of elastic deformations, a sensible analogy can be made with the post-buckling response of long one-dimensional beams resting on an elastic foundation (Wadee and Bassom, 2000). Indeed, the authors have shown that the periodicity of the deflected profile is characterized by a stable post-buckling behaviour. However, if periodicity is limited to a small region of the structure (sinusoidal bound by an exponentially decaying envelope, for example), the response will be sub-critical. One can expect this trend to be still emphasized when plasticity is considered (Tvergaard and Needleman, 1980).

3.1.4. Imperfection sensitivity

For the study of the imperfection sensitivity, various possibilities exist in the introduction of geometrical imperfections (form, size, combinations, etc.). The aim of this part is not to cover all the different cases, but simply to illustrate the main effects which can follow the introduction of a geometrical imperfection. Since interactive buckling may reveal most of the problems encountered separately in other configurations, sandwich configuration 2 in Fig. 12 is chosen and the three geometrical imperfections based on the three elastic buckling modes are, respectively, introduced. For the three cases, the amplitude of the imperfections are varied from 0.001 to 1 mm, that is to say from 0.0019% to 1.9% of the sandwich thickness. However, it is important to notice that the effects of a global geometrical imperfection with a given amplitude value are not directly comparable with the same local one. Indeed, for the global mode, an amplitude of 1 mm corresponds to a skin section rotation of 0.4° while for the symmetrical wrinkling, it becomes 8.4°. In this last case, the rotation magnitude is proportional to the wavenumber.

In Fig. 16, one can observe the variation of the applied load versus the global deflection of the sandwich beam for different values of the global imperfection amplitude. The first noteworthy point is that the existence of the two bifurcation points is still valid whatever the value of the geometrical amplitude. For the different imperfection values, the second branch remains unchanged and then a limit point in load is always

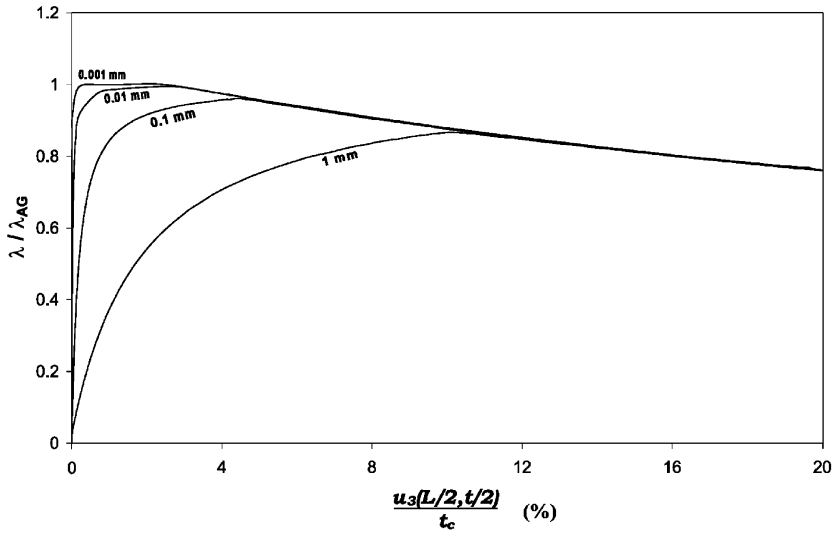

Fig. 16. Change in the applied load versus the global deflection of the sandwich beam for different global geometrical imperfection amplitudes in sandwich configuration 2.

reached. Therefore, by evaluating the first part of the post-buckling regime which corresponds to the behaviour of the equivalent homogeneous beam with a global imperfection, it is possible to find graphically the intersection between the two branches and to isolate the value of the maximum limit load. When increasing the imperfection, the value of the limit load decreases whereas the second bifurcation point deflection becomes larger. In Table 4, it can be seen that the drop in the limit load can be significant since for a rather low imperfection amplitude of 1 mm (1.9% of the total thickness), it exceeds 13%. Whereas the deflection associated with the second bifurcation point is multiplied by more than four for the same imperfection.

For the symmetrical imperfection (Fig. 17), the deformed shape is independent of the amplitude and still corresponds to an amplification of the symmetrical mode. Accordingly to the previous conclusions, as long as symmetry of the skins' behaviour is maintained and amplitude modulation is not significant, the global stability is ensured (by analogy with the antisymmetrical imperfection in configuration 1—Fig. 13). However, the effects of the symmetrical imperfection amplitude are particularly perceptible for low end shortenings (Fig. 17). For instance, increasing the imperfection amplitude from 0.001 to 1 mm induces a reduction by 2 of the load that can be withstood for an end shortening of 5 mm (1% of the beam length).

For the antisymmetrical imperfection case, the imperfection size effects are really noteworthy. Indeed, in addition to a drop in the limit load, the increase of the geometrical imperfection amplitude leads to some

Table 4
Change in the limit load and corresponding deflection for different values of the global imperfection amplitude in sandwich configuration 2

Global imperfection amplitude (mm)	*0.001*	*0.01*	*0.05*	*0.1*	*1*
Amplitude/total thickness (%)	*0.0019*	*0.019*	*0.096*	*0.19*	*1.9*
Limit load (kN)	140.2	139.2	136.6	134.6	121.4
Second bifurcation point deflection (mm)	1.25	1.58	2.00	2.48	5.39
Load decrease (%)	0	−0.7	−2.6	−4	−13
Deflection increase (%)	0	26	60	98	330

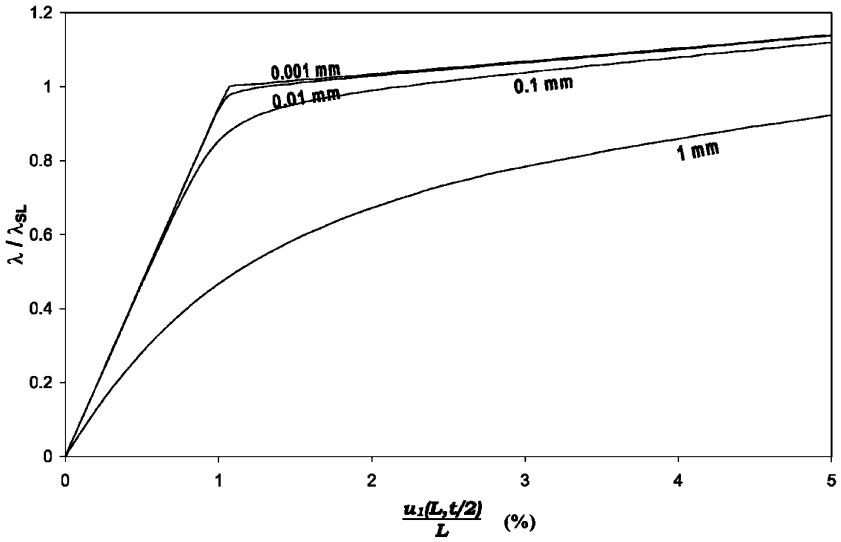

Fig. 17. Change in the applied load versus the global deflection of the sandwich beam for different amplitudes of the local symmetrical geometrical imperfection in sandwich configuration 2.

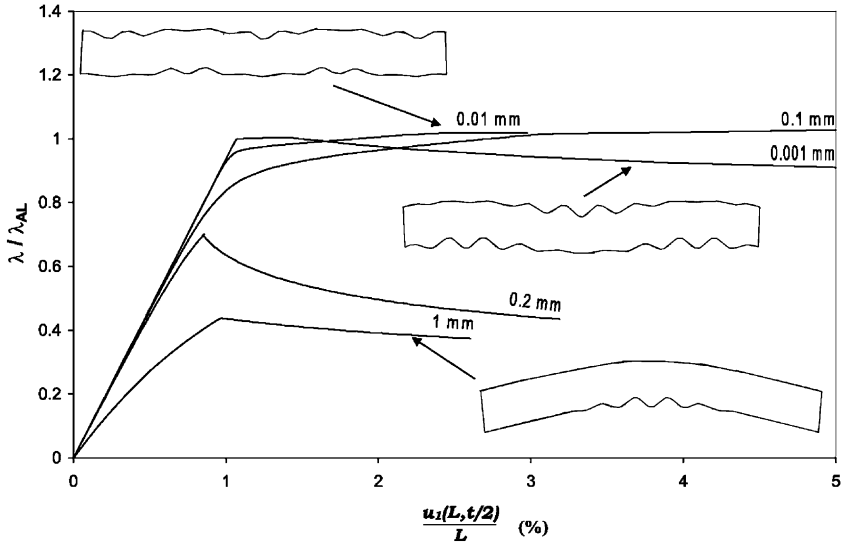

Fig. 18. Change in the applied load versus the global deflection of the sandwich beam for different local antisymmetrical geometrical imperfection amplitudes in sandwich configuration 2.

changes in the post-buckling response and then in the whole stability (Fig. 18). For a low amplitude of 0.001 mm, after a short plateau corresponding to stability, the post-buckling behaviour is slightly sub-critical and one can notice the existence of geometrical localizations on the two skins. Similarly to the same configuration but with global imperfection (Fig. 16), geometrical localization is associated with a drop in sandwich beam stiffness. But the presence of localizations on the two skins reduces here this drop, and the beam seems to be more 'balanced', i.e. the tendency of the beam is to remain straight and not to bend under

unbalanced localizations. This sub-critical behaviour is replaced by a super-critical regime for the imperfections of 0.01 and 0.1 mm in which the amplitudes are more comparable and the geometrical localization is less severe. For larger imperfection amplitudes (0.2 and 1 mm) again the interactive buckling revealed in Fig. 14 occurs, resulting in the superimposition of a global curvature and a local wrinkling of the skin under compression. In this last case, a limit point in load is reached and corresponds to only half of the eigen-buckling load.

In Fig. 18, one can observe the deformed shape for (an imperfection) amplitude of 0.01 mm. It is a form very close to the one with a 0.001 mm amplitude, but the beam seems to be more balanced and the stable post-buckling behaviour can be related to a lack of real localization, since the amplitude is almost constant. As a conclusion, when geometrical localizations develop, a sub-critical response of the sandwich beam is observed. Conversely, as long as the wave amplitude is not modulated, stability is maintained. The effect of geometrical localization is especially emphasized in cases where they do not appear in both skins, the more the localizations produce an unbalanced deformed shape, the sharper the sub-critical response.

Thanks to the different forms and sizes of the introduced geometrical imperfections, a sharp imperfection-sensitivity was noticed. This is first observed through the significant decrease of the maximum loads for sub-critical behaviours, but also by the possible change from a slightly super-critical regime to a severe sub-critical one for a very small increase in the antisymmetrical wrinkling size imperfection. These first analyses led with linear elastic materials have clearly emphasized the existence of stable and unstable post-buckling regimes. Unstable behaviours are related to the appearance of geometrical localizations along the beam. Since plastic deformation localization is known to be also responsible for sub-critical behaviours, especially in softening materials (Tvergaard and Needleman, 1980), it is essential to incorporate a nonlinear constitutive law in cores for which the hardening may be large.

3.2. Elastoplastic core and linear elastic skins

3.2.1. Constitutive model for the core

A rigid closed-celled PVC foam is considered here, chosen for the availability of its properties in the literature (Branner, 1995). The difficulty in modelling the foam constitutive laws lies in the existence of different deformation mechanisms in compression and in tension. In uniaxial compression, a stress–strain curve can be divided into three parts, a linear response is first observed, followed by a long plateau corresponding to the cell wall buckling and a last part associated with the densification of the foam in which cell walls interact and increase the global foam stiffness. Meanwhile the tensile stress–strain curves show a brittle behaviour for which the yield stress is greater than the compressive one.

A crushable foam model is implemented in ABAQUS™ (Aba, 1997; Martikainen and Rammerstorfer, 1999) which could meet our modelling needs. The yield surface can be built with different properties in tension and compression and the foam can deform volumetrically in compression which justifies the dependence of the yield function towards the hydrostatic stress in addition to the deviatoric ones. However, this model is rather delicate to calibrate and numerous convergence problems exist in the case of the foams which are of interest to us and which exhibit a tensile strength higher than the compressive strength. Consequently, in a first approach, a perfect elastoplasticity model is used with a von Mises yield function. The constitutive law is calibrated from uniaxial test in compression which is the most restricting behaviour for the foam. The densification part is not taken into account since it appears for very large strains (>40%) which were verified subsequently not to be reached in our computations.

3.2.2. Effects of the elastoplastic core behaviour on the post-buckling regimes

We can first consider sandwich configuration 2, studied in the previous section, in order to well underline the effects of the introduction of the core elastoplastic law. The chosen foam for the core is a Divinycell® H130 with a compressive and tensile modulus of 175 MPa and a compressive yield stress $\sigma_0 = 2.6$ MPa

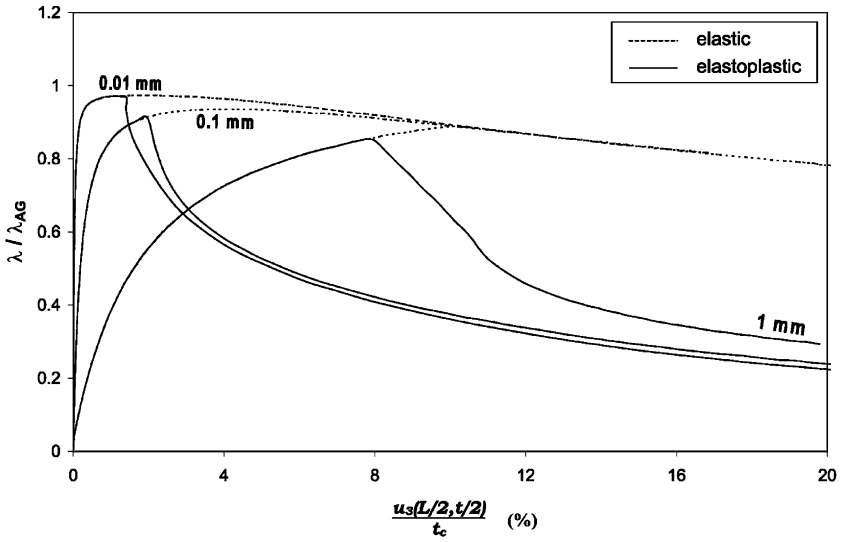

Fig. 19. Comparison of the change in the applied load versus the global deflection of the sandwich beam with a global imperfection, for elastic and elastoplastic constitutive law of the core.

(DIAB, 2001). The three previous geometrical imperfections are introduced and the effects of the core elastoplasticity are respectively discussed below. It must be noticed that due to the simplified F.E. formulation used, the complete elastoplastic post-buckling response of the 2000 d.o.f. sandwich beams is computed in about 20 min on the workstations described previously.

For a global geometrical imperfection, the evolution of the applied load versus the global deflection for different amplitudes is given in Fig. 19. The first noteworthy point is that the occurrence of a plastic flow is immediately followed by a drastic drop in the global stiffness of the sandwich beam. However, the value of the limit load is not really affected by this drop as it can be verified in Table 5. Concerning the deformed shape, after the bifurcation point, a strong localization of plastic deformations develop in the center of the sandwich beam (Fig. 20). The geometrical localization observed with an elastic core (Fig. 14) is here emphasized by the localization of plastic deformations.

The effects of the core elastoplasticity on the post-buckling behaviour of the sandwich beam with local symmetrical and antisymmetrical geometrical imperfections are, respectively, visible in Figs. 21 and 22. For the two cases, whatever the imperfection amplitude, the introduction of an elastoplastic constitutive law leads to a collapse of the sandwich beam. Experimentally, for the three forms of geometrical imperfection, the occurrence of the bifurcation point will be associated with the in-plane compressive strength of the beam, since neither a load control nor a displacement control will permit to reach an equilibrium without damaging the structure.

Table 5
Buckling load decrease between elastic and elastoplastic core for different values of the global imperfection amplitude in sandwich configuration 2

Global imperfection amplitude (mm)	*0.01*	*0.1*	*1*
Amplitude/total thickness (%)	*0.019*	*0.19*	*1.9*
Elastic limit load (kN)	133.4	128.2	121.8
Elastoplastic limit load (kN)	133.0	125.0	117.0
Load decrease (%)	−0.3	−2.5	−3.9

Fig. 20. Deformed shape and von Mises stress distribution in the sandwich beam (configuration 2) with elastoplastic core and global imperfection of 0.01 mm (deflection = 8 mm).

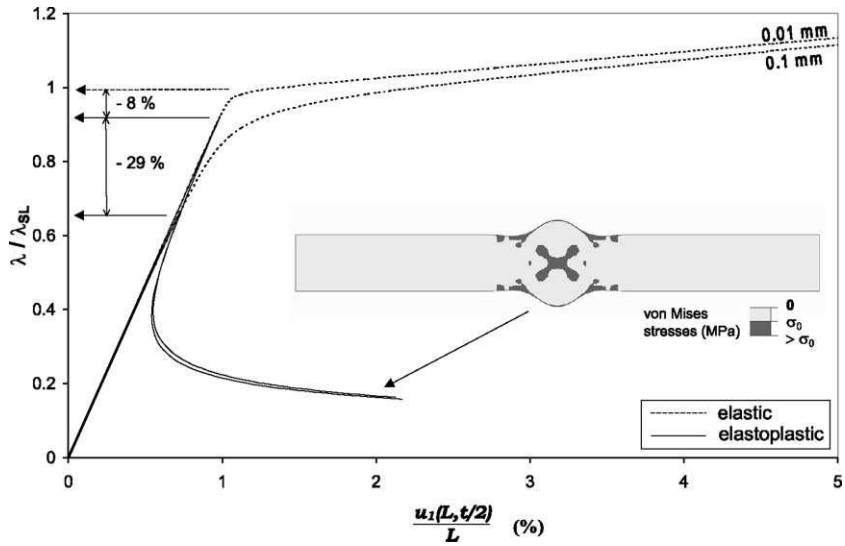

Fig. 21. Comparison of the change in the applied load versus the global deflection of the sandwich beam with sym-local imperfection, for elastic and elastoplastic core constitutive law.

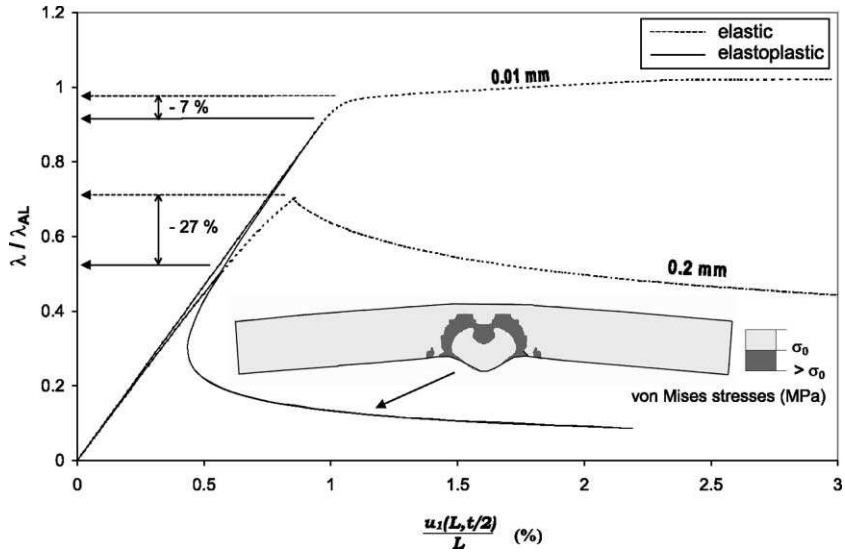

Fig. 22. Comparison of the change in the applied load versus the global deflection of the sandwich beam with anti-local imperfection, for elastic and elastoplastic core constitutive law.

For the two last cases (Figs. 21 and 22), the first important point is that the greater the imperfection amplitude, the larger the decrease of the observed critical load. Indeed, by increasing the imperfection amplitude from 0.01 to 0.1 mm, the limit load in comparison with the one for an elastic core has decreased from about 10% to 30% in both antisymmetrical and symmetrical cases. Furthermore, the post-bifurcated branch associated with the plastic flow is independent towards the imperfection size, and for the antisymmetrical case (Fig. 22), the elastic super and sub-critical behaviours observed in Fig. 18 are both replaced by the same bifurcated branch. For the deformed shape, a strain localization appears in the center of the beam. The initial symmetrical configuration maintains its symmetry while for the antisymmetrical form a global curvature appears due to the localization of deformations. A last point is that the distribution of the core von Mises stresses in Fig. 21 clearly demonstrates the predominance of shear in the plastic flow.

Eventually, for any imperfection, the response is highly sub-critical associated with strong plastic deformation localizations: responses which are stable with an elastic core are prone to undergo plastic deformation localization, while sub-critical responses caused by geometrical localization are further aggravated when the core plasticity is accounted for. One can assimilate this behaviour to shells' plastic buckling, the response of which is sub-critical and highly imperfection sensitive.

3.2.3. Shear crimping: a special case of global buckling

The previous numerical investigations have been made for sandwich configuration 2 of Fig. 12. In the present section, a global imperfection is introduced in a sandwich beam in which global buckling is prone to appear first (configuration 3 in Fig. 12). Calculations with a linear elastic constitutive law in the core have shown that whichever the size of the imperfection, the post-buckling regime is stable and corresponds to an amplification of the global buckling mode (Figs. 15 and 23). In this case, the post-buckling behaviour is that of the equivalent homogeneous beam without any local effect from the skins. The introduction of the elastoplastic law in the core affects this post-buckling behaviour and the occurrence of plastic flow gives rise to a strong drop in the global stiffness of the beam (Fig. 23). The corresponding deformed sandwich beam (Fig. 23) clearly exhibits a localization of the shear deformations in the beam, this is the so-called *shear crimping*. Shear failure will presumably appear in this region of weakness where the transverse shear stresses

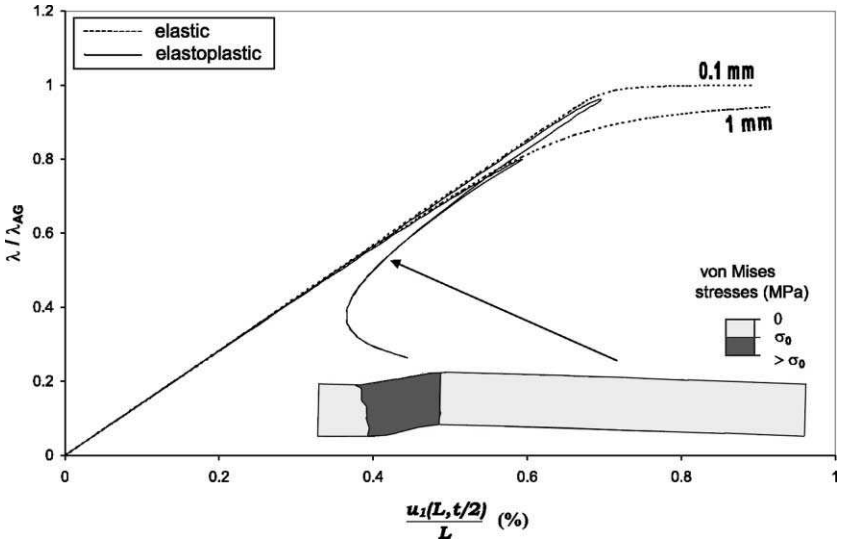

Fig. 23. Comparison of the change in the applied load versus the global deflection of the sandwich beam with global imperfection, for elastic and elastoplastic core constitutive law (sandwich configuration 3 of Fig. 12).

are maximum. This region is localized between the quarter of the beam length and its extremity, which are the zones of maximum shear stress, respectively, for a beam with clamped ends and for a simply supported beam. This last observation is in agreement with the F.E. model used in which edges are slightly stiffened by the chosen boundary conditions. In literature (Allen, 1969), the shear crimping is associated with a critical load which in fact corresponds to the equivalent transverse shear stiffness of the sandwich beam:

$$\lambda_{\text{shear}} = \frac{G_c b (t_c + t_s)^2}{t_c}. \tag{8}$$

In Fig. 23, one can observe that a limit load is reached when the shear crimping appears. This load is very sensitive to the size of the initial imperfection since for an imperfection of 1 mm, the decrease is 17% in comparison with a 0.1 mm imperfection amplitude. The value of λ_{shear} for the chosen geometrical and material parameters is 2.2×10^5 N. The limit loads computed for the two tested imperfection amplitudes (0.1 and 1 mm) correspond, respectively, to 70% and 60% of this too large value of the shear crimping load.

Eventually, due to the high numerical sensitivity of shear crimping towards the imperfection size and because of the large overestimation of λ_{shear}, Eq. (8) cannot be used as a design criterion against this phenomenon. Indeed, shear crimping is strongly dependent on the elastoplastic nature of the core material and cannot be accurately predicted by a simple combination of geometrical and material parameters. All the numerical investigations carried out have shown that shear crimping is in fact a consequence of the shear deformation localization following the occurrence of a global mode. This may explain why this phenomenon is very often considered as a special case of global buckling. Besides, the large influence of the imperfection amplitude on the value of the limit load justifies the problems met in the experimental characterization of shear crimping.

4. Conclusion

This study has been divided into two parts. The first part was dedicated to the characterization of sandwich beam instabilities in a perfect linear framework. It was shown that this simplified framework permits to identify, from a specific unified model, analytical criteria associated with both local and global instabilities. Thanks to these expressions, very rich conclusions can be drawn regarding the buckling modes at the two scales of a sandwich. Design diagrams were built and clearly demonstrated that local phenomena are predominant in sandwich beam made up of weak and thick cores, whereas global buckling prevails in slender beams. In order to lead more complex and realistic numerical analyses, a low CPU time-consuming simplified model was assessed. The numerical eigenvalue buckling predictions were shown to correlate very well the analytical results.

The second essential step was to characterize the post-buckling response of sandwich beams in order to identify the main bifurcation branches and then to isolate the configurations developing super- or sub-critical post-buckling behaviours. The geometrical nonlinear investigations, in which linear elastic materials are considered, have actually revealed the existence of stable and unstable post-buckling regimes. Unstable behaviours are related to the occurrence of geometrical localizations along the beam. This is still emphasized when localizations do not develop symmetrically on both skins, inducing a breaking of the symmetry that leads to a drastic drop of the load carrying capacities. A special case of 'unbalanced' buckling is the so-called interactive buckling, occurring in optimum configurations for which the critical loads are close. Interactive buckling yields a post-buckling behaviour highly sub-critical whereas it results from the interaction of global and local modes inherently stable. Besides, a very high sensitivity towards the imperfection sizes and forms was observed. The introduction of an elastoplastic constitutive law in the core emphasizes the sub-critical response observed in many cases with elastic materials. Plastic flows appear at

the onset of the instability occurrence, leading to very sub-critical regimes, followed by the development of plastic strain localization. Moreover, for some configurations, the value of the limit load from the elastoplastic analysis is strongly lower, up to 30%, than for linear elastic materials. The consideration of core elastoplasticity is then critical for these cases, as well as in the cases prone to exhibit interactive buckling.

Through these analyses, a very high sensitivity towards imperfections was demonstrated which corroborates the strong difficulties in obtaining reproducible experimental results. This is especially true for the characterization of shear crimping which was shown to be a post-bifurcated phenomenon that will appear in configurations in which global buckling is predominant.

Following the conclusions of Tvergaard and Needleman (1980) for inherently super-critical structures made up of elastoplastic materials, local imperfections will not affect significantly the load carrying capacity of the sandwich beam. Hence studying the maximum support load in the case of periodic modes and imperfections is still valid. Consequently, the complete analytical characterization of the elastic interactive buckling in sandwich is under achievement with the presented unified model.

References

Aba, 1997. ABAQUS Theory Manual. Hibbitt, Karlsson & Sorensen.

Allen, H., 1969. Analysis and Design of Structural Sandwich Panels. Robert Maxwell, MC, MP.

Branner, K., 1995. Capacity and lifetime of foam core sandwich structures. PhD thesis, Technical University of Denmark.

Byskov, E., Hutchinson, J., 1977. Mode interaction in axially stiffened cylindrical shells. AIAA Journal 15 (7), 941–948.

DIAB, 2001. Divinycell H grade. Technical Report, DIAB group.

HEXCEL, 1989. Mechanical properties of hexcel honeycomb materials. Technical Report TSB120.

Hunt, G., Da Silva, L., Manzocchi, M., 1988. Interactive buckling in sandwich structures. Proceedings of the Royal Society of London A 417, 155–177.

Leger, A., Combescure, A., Potier-Ferry, M., 1998. Bifurcation, flambage, stabilité en mécanique des structures. Technical Report, IPSI.

Léotoing, L., Drapier, S., Vautrin, A., 2001a. A novel unified model for sandwich: closed-form solutions for global and local buckling of beams. European Journal of Mechanics A/SOLIDS (submitted).

Léotoing, L., Drapier, S., Vautrin, A., 2001b. Using new closed-form solutions to set up design rules and numerical investigations for global and local buckling of sandwich beams (submitted).

Lo, K., Christensen, R., Wu, E., 1977. A high-order theory of plate deformation, part 1: homogeneous plates. Journal of Applied Mechanics, 663–668.

Martikainen, L., Rammerstorfer, F., 1999. Modelling the local failure modes in thin-faced sandwich panels. Strojnícky Časopsis 50, 241–252.

Sokolinsky, V., Frostig, Y., 1999. Boundary condition effects in buckling of "soft" core sandwich panels. Journal of Engineering Mechanics 125 (8), 865–874.

Starlinger, A., 1990. Development of efficient finite shell elements for the analysis of sandwich structures under large deformations and global as well as local instabilities. PhD thesis, Vienna University of Technology.

Teti, R., Caprino, G., 1989. Mechanical behavior of structural sandwiches. In: Olsson, K., Reichard, R. (Eds.), Proceedings of Sandwich Constructions 1. Engineering Materials Advisory Services Ltd., pp. 53–68.

Tvergaard, V., Needleman, A., 1980. On the localization of buckling patterns. Journal of Applied Mechanics 47, 613–619.

Vinson, J., 1989. Comparison of optimized sandwich panels of various constructions subjected to in-plane loads. In: Olsson, K., Reichard, R. (Eds.), Proceedings of Sandwich Constructions 1. Engineering Materials Advisory Services Ltd., pp. 23–52.

Wadee, K.M., Bassom, A.P., 2000. Restabilization in structures susceptible to localized buckling: an approximate method for the extended post-buckling regime. Journal of Engineering Mathematics 38 (1), 77–90.

Williams, D., Leggett, D., Hopkins, H., 1941. Flat sandwich panels under compressive end loads. Technical Report, 1987, R.A.E.

- N -

Annexe 2. 8

L. Léotoing, S. Drapier, & A. Vautrin.

Using new closed-form solutions to set up design rules and numerical investigations for global and local buckling of sandwich beams.

J. of Sand. Struct. and Mat. **, 2002. Accepté,** *à paraître***.**

Using new closed-form solutions to set up design rules and numerical investigations for global and local buckling of sandwich beams

L. Léotoing, S. Drapier [1] and A. Vautrin

Mechanical and Materials Engineering Department - SMS Division
École Nationale Supérieure des Mines de Saint-Étienne
42023 Saint-Étienne Cedex 02, France
Tel : (+33)(0)4 77 42 00 79 Fax : (+33)(0)4 77 42 02 49
E-mail : drapier@emse.fr

Abstract

This paper is dedicated to the study of global (at the sandwich scale) and local (at the component scale) buckling in sandwich structures. This approach relies on the basis of an analytical model able to capture both local and global instabilities [7]. Results from this model are used to provide simple design rules by assessing the combinations of geometrical and material parameters which control theses instabilities. From there, design diagrams are extracted which permit very quickly to select sandwich configurations more susceptible to develop local or global phenomena. Then, two distinct FE models are presented and compared. The ability of a reduced size FE model, to capture local as well as global instabilities is demonstrated. Eventually, the predicted loads and wavelengths from both FE simplified model and analytical model are shown to correlate very well. Thus, analytical wavelengths constitute a precious guide to evaluate the mesh element size for a low time-consuming but accurate FE model which can be easily extended to fully non-linear computations of sandwich panels.

Key words : sandwich structure, stability, scale effects, sensitivities, design diagrams, FE models

1 INTRODUCTION

Sandwich materials result from the assembly of very different compounds, providing to the resulting layered-like structure a very high specific flexural stiffness, that in turn can translate into significant weight savings. The use of these structures in many fields of engineering like transportations, aeronautics and aerospace where weight savings can be ideally converted into pay-loads, has been extended since the mid 80's. This renewal has been triggered mainly by the arising of new manufacturing techniques which permit nowadays to build some integral parts out of sandwiches for structural units. In turn, the use of sandwich in structural applications implies the need of a deeper knowledge of their mechanical behaviour, and more particularly the response under in-plane compressive loadings which still present some difficulties for designers. Under such destabilizing

[1] to whom correspondence should be addressed

loadings, the material and geometrical heterogeneity of these materials is responsible for the (co-)existence of buckling at several distinct scales : at the global scale of the assembly and at the local scale of the skins and core. These geometrical instabilities are namely the global buckling (Fig. 1-a) similar to Euler's buckling for beams, and some local forms of buckling of the skins called *wrinkling*. For this local instability, generally two distinct forms are considered which are the symmetrical mode (Fig. 1-b) and the antisymmetrical mode (Fig. 1-c).

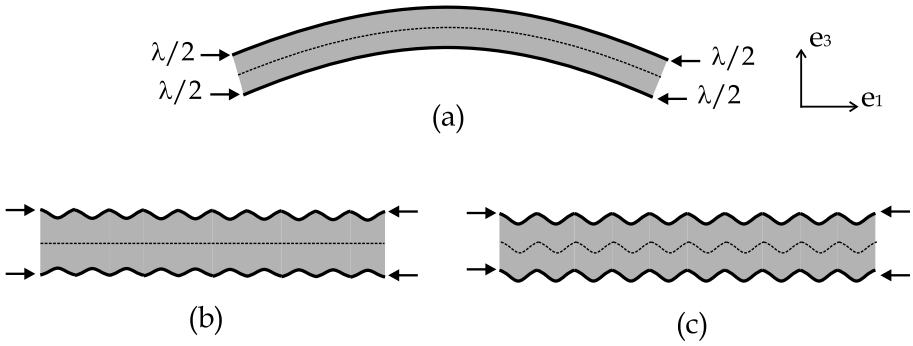

Figure 1: Sandwich buckling at two scales : (a) global buckling (Euler's type), (b) symmetrical wrinkling of the skins, (c) antisymmetrical wrinkling of the skins.

Since the early 40's, many theoretical studies have been dedicated to the occurrence of instabilities in sandwich structures (see for instance ([14], [1], [13]). In these classical approaches, two different models are proposed in order to characterize the instabilities at each scale. These models are respectively the equivalent homogeneous beam model for the global buckling and models of beams resting on an elastic foundation for the wrinkling of the skins. As a deeper knowledge is gained about these instabilities, the complete description of buckling and post-buckling in sandwich materials requires the development of more complex approaches accounting for the possible interactions between the two scales, defining the so-called interactive buckling.

Few studies deal with this notion of interactive buckling and can be divided into two distinct categories. One can isolate the analytical and semi-analytical approaches ([4], [10]) and the numerical ones ([11]). In spite of the limits induced by their formulation, the basic idea remains to study the influence of the occurrence of one type of instability onto the occurrence of other ones, and the resulting change in the whole beam stability. For Hunt [4] the global buckling appears first and can be followed by the appearance of a combination of global and local modes inauspicious for the stability of the sandwich beam. Starlinger ([11]) considers local degradations due to the appearance of local phenomena and then modifies the global rigidity of the structure to reach a new equilibrium. But for the former, the analytical approach gives only a partial view and cannot be easily extended to any sandwich beam. Whereas, for the latter, the numerical treatment of the local degradation yields severe problems of convergence and no geometrical characterization of the local instability is possible. So it clearly appears that there is a need for easy-to-use tools,

enabling to make rapid calculations for designing sandwich structures against instabilities under in-plane compression.

Our very aim is to develop such a simple numerical approach, in order first to select sandwich configurations against local as well as global buckling, and second to understand the effect of the possible interactions between these modes onto the sandwich stability. This approach will rely on the bases of an analytical sandwich beam model, briefly presented below, able to grasp both local and global instabilities in a perfect framework. This model will be used to assess the effect and combinations of the various geometrical and material parameters of the sandwich onto the instabilities.

1.1 A single model for local and global instabilities

The model briefly presented in this section is used to extract local as well as global buckling loads for the subsequent parametric study. This model has been more extensively detailed in [6] and [7]. For the sake of simplicity, a symmetrical sandwich beam is considered in which both faces and core are made up of homogeneous isotropic linear elastic materials (Fig. 2). The model is formulated in displacements and the first difficulty is to choose kinematics rich enough to describe all the potential forms of instability, but simple enough to get usable analytical design criteria. A higher-order theory is adopted for the core ($\mathbf{u}^c(\mathbf{x})$) which was shown to govern the local response of the sandwich. The use of such a theory is required for wrinkling wavelength magnitudes of the order of the beam thickness [8], which is the case for the local buckling of skins. For the upper ($\mathbf{u}^u(\mathbf{x})$) and lower ($\mathbf{u}^l(\mathbf{x})$) skins, the displacements in the $\mathbf{e_1}$-direction are chosen linear in x_3, while the displacements along the $\mathbf{e_3}$-direction are taken constant in x_3 (Eq. 1). Subsequently, suffices ^{b} and ^{t} stand respectively for the data concerning the bottom and top of the sandwich beam and can be thereafter replaced by suffix α ($\alpha = b,t$). Displacements in the core are then expressed thanks to five additional functions ($\phi_i,\ i = 1..5$) to be identified. Eventually, following the notations reported in Fig. 2, the complete displacement field writes :

$$
\begin{aligned}
&\underline{0 < x_3 < t_s} \\
&\quad u_1^l(x_1,x_3) = u_1^b(x_1) - x_3 \frac{du_3^b}{dx_1}(x_1) \\
&\quad u_3^l(x_1,x_3) = u_3^b(x_1) \\
&\underline{t_s < x_3 < t_c + t_s} \\
&\quad u_1^c(x_1,x_3) = u_1^m(x_1) - (x_3 - t_s)\phi_1(x_1) - (x_3 - t_s)^2\phi_2(x_1) - (x_3 - t_s)^3\phi_3(x_1) \\
&\quad u_3^c(x_1,x_3) = u_3^m(x_1) - (x_3 - t_s)\phi_4(x_1) - (x_3 - t_s)^2\phi_5(x_1) \\
&\underline{t_c + t_s < x_3 < t} \\
&\quad u_1^u(x_1,x_3) = u_1^t(x_1) - (x_3 - t)\frac{du_3^t}{dx_1}(x_1) \\
&\quad u_3^u(x_1,x_3) = u_3^t(x_1)
\end{aligned}
\tag{1}
$$

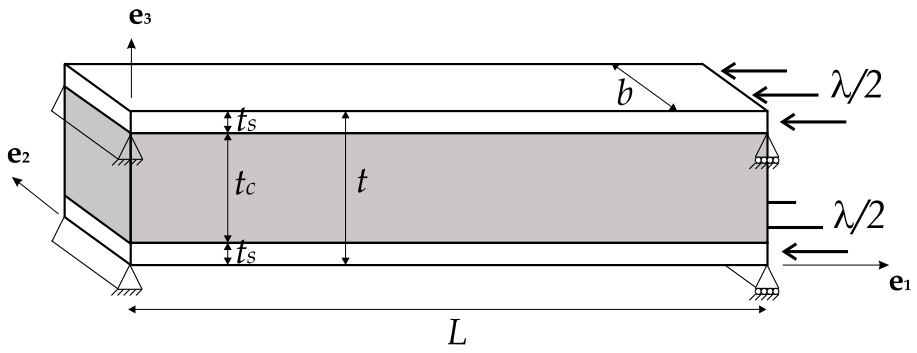

Figure 2: Notations for a simply supported sandwich beam.

The number of unknown functions can then be reduced by considering perfect interfaces and a linear transverse shear stress distribution across the beam thickness. This last assertion was confirmed by Finite Element computations. Finally the displacement fields can be written thanks to the four unknown displacements of the skins and to a gradient of rotation in the core.

Then, for a simply-supported sandwich beam (Fig. 2), the governing equations of the problem are derived from the Principle of Virtual Works. Stresses are represented by the second Piola-Kirchhoff tensor, denoted by $\mathbf{S}(\mathbf{x})$, and strains are represented by the Green-Lagrange tensor $\gamma(\mathbf{u})$ limited to the moderate rotation terms for the non-linear strain part. The expression of the internal virtual work in the whole beam is simplified by retaining stresses whose energetic contributions are predominant (the longitudinal stress in the skins, and the transverse normal stress and transverse shear stress in the core). A non-linear system of five differential equations is then determined which characterizes the inner equilibrium of the sandwich beam. Since the buckling loads of

both the linearized and non-linear problem coincide [5], a linearized form of the previous system is sufficient to determine those loads. The linearization is achieved by postulating that at the occurrence of the first geometrical instability, the linear relationship of proportionality between the applied load and the internal resultants still holds. Then the system can be rewritten by considering this linear pre-buckling state (Eqs. 2), in which $\eta_{\alpha b} = 1$ if $\alpha = b$ and -1 if $\alpha = t$, and $\xi = (1/2 + t_s/t_c)$.

$$
\begin{aligned}
/\delta u_1^\alpha : \quad & \eta_{\alpha b} E_s b t_s u^\alpha_{1,11} - \frac{b E_s {t_s}^2}{2} u^\alpha_{3,111} \\
& + b G_c \left(\frac{u_1^t - u_1^b}{t_c} + \xi (u^t_{3,1} + u^b_{3,1}) + \frac{t_c^2}{6} \phi_{,1} \right) = 0 \\
/\delta u_3^\alpha : \quad & \frac{\lambda}{2} u^\alpha_{3,11} - \eta_{\alpha b} \frac{E_s b {t_s}^2}{2} u^\alpha_{1,111} + \frac{E_s b {t_s}^3}{3} u^\alpha_{3,1111} - \eta_{\alpha b} \frac{b E_c}{t_c} (u_3^t - u_3^b) \\
& - b G_c \xi (u^t_{1,1} - u^b_{1,1} + \frac{t_c}{\xi} \left(\frac{2}{3(3+\eta_{\alpha b})} + \frac{t_s}{t_c} \left(1 + \frac{t_s}{t_c} \right) \right) u^t_{3,11} \\
& + \frac{t_c}{\xi} \left(\frac{2}{3(3-\eta_{\alpha b})} + \frac{t_s}{t_c} \left(1 + \frac{t_s}{t_c} \right) \right) u^b_{3,11} + \frac{{t_c}^3}{6} \phi_{,11}) = 0 \\
/\delta \phi : \quad & t_c E_c \phi - \frac{G_c}{2} \left(u^t_{1,1} - u^b_{1,1} + t_c \xi (u^t_{3,11} + u^b_{3,11}) + \frac{t_c^3}{6} \phi_{,11} \right) = 0
\end{aligned}
\tag{2}
$$

Therefore, the system (Eqs. 2) is linear and the critical loads are the eigenvalues of the corresponding eigenproblem. Parameters E_s, E_c and G_c stand respectively for the Young modulus of the skins and the normal and shear transverse core moduli. The displacements can be sought under the form of trigonometric series. The formal resolution leads to two strictly positive eigenvalues corresponding respectively to an antisymmetrical eigenmode and to a symmetrical one. Through this calculation, three buckling modes can be isolated thanks to the eigenvalue associated with the antisymmetrical mode which can correspond to the occurrence of either global (critical wavenumber is 1) (Eq. 3) or local (high critical wavenumber - wrinkling) buckling (Eq. 4), depending on the sandwich configuration. Moreover, for some combinations of geometrical and material parameters, the antisymmetrical wrinkling doesn't exist and then a relationship (Eq. 4) between the different parameters can be determined, the validity of which corresponds to the possible existence of this local form of instability. For the symmetrical case, there is only one possible critical load which corresponds to a local mode (Eq. 5).

$$
\lambda^{um}_{AG} = \frac{\pi^2 E_s t_s b}{6L^2} \left(t_s^2 + \frac{72 G_c E_c L^4 (t_c + t_s)^2}{\pi^4 E_s G_c t_s t_c^3 + 12 \pi^2 E_s E_c t_s t_c L^2 + 24 E_c G_c L^4} \right) \tag{3}
$$

$$
\lambda^{um}_{AL} = \frac{2 b t_s}{t_c} \left(\sqrt{2 t_s E_s E_c (t_c + 2 t_s)} - \frac{{t_s}^2}{t_c} \frac{E_s E_c}{G_c} \right) \quad \text{if} \quad \frac{2 {t_s}^3 E_s E_c}{{G_c}^2 {t_c}^2 (t_c + 2 t_s)} < 1 \tag{4}
$$

$$\lambda_{SL}^{um} = \frac{2\sqrt{6}}{3} b \sqrt{\frac{E_c E_s {t_s}^3}{t_c}} + \frac{G_c t_c b}{3} \tag{5}$$

In [7], the global load was shown to correlate perfectly with the predictions of an equivalent homogeneous beam approach in which shear is accounted for. For the antisymmetrical instability, the predictions of the presented approach were shown to perfectly fit with the dedicated but untractable approach from [9]. Moreover, in this previous paper, the lack of accuracy of the classical wrinkling critical load (Eq. 6) was demonstrated. Also the very conservative nature of this approach was underlined which is still emphasized by the value of the constant Q that varies from 0.4 to 0.9 depending on the authors in the literature.

$$\sigma_{class} = Q \sqrt[3]{E_c G_c E_s} \tag{6}$$

1.2 Present investigation

The first part of the present study permits to show that from these analytical elastic buckling loads, rich conclusions can be drawn for the characterization of the instabilities at the two scales and for the description of the interactive buckling concept. It is also shown that the sensitivity of the buckling loads towards both geometrical and material parameters yield precious guides for designing sandwich structures. Thereafter, the critical loads are expressed versus three independent dimensionless ratios only, and design diagrams are proposed which for wide ranges of materials and geometries permit to select configurations more likely to be unstable at either the global or the local scale. The second step is to build an accurate and coherent F.E. model with boundary conditions corresponding to realistic close-outs. It is shown that a good agreement can be found between predictions of a simplified model and the previous analytical results. The knowledge of the analytical local wrinkling wavelengths permits to estimate the maximum allowable length of the elements for a good representation of the local phenomena. From there, it is then possible to find the best compromise between the computation time and accuracy of the results. Adopting a reliable numerical tool is essential in order to carry out future efficient non-linear analyses.

2 PARAMETRIC STUDY OF THE ANALYTICAL CRITICAL LOADS

2.1 Sensitivities evaluation

The expressions of the presented buckling loads (Eqs. 3, 4 and 5) exhibit some complex combinations of mechanical and geometrical data, in a wide range of admissible values, which makes it tricky to get a general view of the influence of every parameter on the critical loads. The main idea

of this parametric study is to define, for a given sandwich configuration, an indicator able to provide a *weight* for each parameter. A dimensionless function is chosen, this so-called *sensitivity* can be defined for all the parameters and permits a comparison between the influence of the different parameters. For any parameter ζ, the dimensionless sensitivity is defined for a given geometrical and material configuration C_i (Eq. 7).

$$s_\zeta = \frac{\partial \lambda}{\partial \zeta}(C_i)\frac{\zeta}{\lambda(C_i)} \tag{7}$$

This numerical evaluation allows to identify the predominant parameters for each form of instability and to classify some of them as local or global, depending on which load they influence the more. The main drawback of this approach is the dependence of the calculated sensitivities towards the chosen sandwich beam configuration. The sandwich characteristics used are those of Table 1 with a 40 *mm* core thickness for which the values of the three critical loads are of the same order and then the sensitivities are more comparable. The diagram given in Fig. 3 presents the values of each sensitivity for the three considered critical loads.

$E_s(MPa)$	50000	$t_s(mm)$	1
$E_c(MPa)$	70	$L(mm)$	600
$G_c(MPa)$	25	$b(mm)$	40

Table 1: Sandwich characteristics of the sensitivity study

First, for the global critical load it is not surprising to notice that the preponderant parameter is the core thickness directly related to the global flexural stiffness of the beam, which increases in a quadratic way with the spacing between the skins. The length of the beam has also a large influence on the value of the global critical load. In fact, these two parameters can be associated with the slenderness of the beam and it is found again the classical result of the high sensitivity of slender beams towards global buckling.

The sensitivities for the two local forms are very comparable, this confirms the close nature of these two instabilities. First of all, their local nature is confirmed by their independence towards the length of the beam. For the two forms, the key parameter is the thickness of the skins due to its cubic influence in the skins flexural stiffness. Thus, t_s is rather associated with the local behaviour of the sandwich beam whereas t_c can be classified as a global parameter. The sensitivities towards the core moduli (E_c, G_c) are rather comparable for the two local modes and confirm the role played by both the transverse normal and shear stiffnesses on the occurrence of local phenomena.

Thanks to these sensitivities, conclusions have been drawn for each form of instability but now a comparison between the three critical expressions is necessary in order to isolate sandwich configurations more susceptible to develop local or global buckling. Indeed, two different sandwich

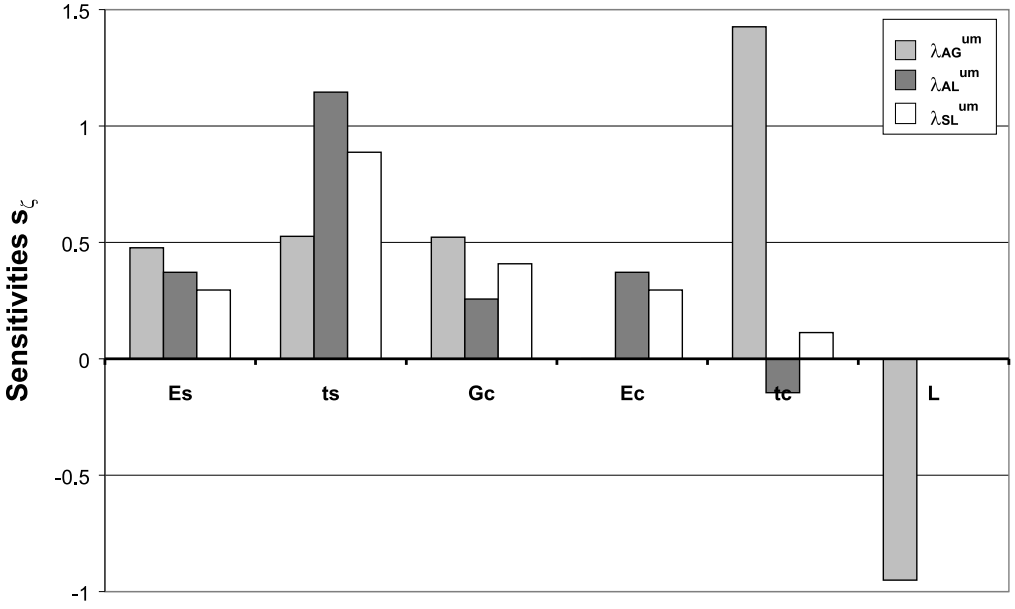

Figure 3: Sensitivities calculated for the three critical load expressions.

beams with the same equivalent flexural and shear stiffnesses can behave very differently under in-plane compression. A significant example is presented in Table 2. The critical loads calculated for these two configurations show that for the first one, global buckling will appear first contrary to the second configuration for which local instabilities are more susceptible to appear first. This numerical example underlines the need to study the local behaviour of sandwich beams and shows that the evaluation of the equivalent stiffnesses does not represent a safe design criterion for preventing such structures from buckling.

The sensitivity calculation or the plot of the critical loads versus one parameter give only a partial view of the predominant areas for each form of instability. The aim of the following section is to propose a graphic tool through which one is able to localize without any ambiguity the different zones of prevalence, *i.e.* when global buckling may appear rather than local buckling and conversely.

2.2 Graphic selection for the design of sandwich against buckling : Design diagrams

In order to propose a general view of the comparison between the critical loads, it is essential to reduce the number of parameters. Indeed, buckling loads depend upon the complex combinations of 6 parameters (L, t_s, t_c, E_s, E_c, G_c). Therefore we introduce new parameters which are some independent combinations of the previous ones. The following dimensionless ratios are introduced

	example 1	**example 2**
Skins	Aluminium	Thermoplastic
Core	Polyvinyl chloride	Polystyrene
$E_s\ (MPa)$	70000	6488
$E_c\ (MPa)$	70	25.9
$G_c\ (MPa)$	25	9.25
$t_s\ (mm)$	1	2
$t_c\ (mm)$	30	70
$b\ (mm)$	40	40
$L\ (mm)$	600	600
$D\ (N.mm^2)$	1.35 10^9	1.35 10^9
$S\ (N)$	9.6 10^5	9.6 10^5
$\lambda_{AG}^{um}\ (N)$	**17150**	15695
$\lambda_{AL}^{um}\ (N)$	29801	**13748**
$\lambda_{SL}^{um}\ (N)$	36399	17685

Table 2: Two different sandwich configurations with the same equivalent flexural and shear stiffnesses (respectively D and S), but with different critical loads

(Eq. 8) which permit to isolate easily the variation towards the 6 geometrical and material parameters. They are the slenderness of the beam ρ_L, the moduli ratio ρ_E, the thicknesses ratio ρ_t and the core moduli ratio ρ_ν where ν_c is the core Poisson's ratio.

$$\begin{aligned} \rho_L &= \frac{L}{\pi t_c} \\ \rho_E &= \frac{E_c}{E_s} \\ \rho_t &= \frac{t_s}{t_c} \\ \rho_\nu &= \frac{G_c}{E_c} = \frac{1}{2(1+\nu_c)} \end{aligned} \tag{8}$$

Then, Eqs. (3, 4 and 5) can be rewritten and yield Eqs. (9, 10 and 11).

$$\lambda_{AG}^{um} = B\left[\frac{\rho_t}{\rho_L^2} + \left(\frac{6\rho_E}{\frac{\rho_t}{\rho_\nu} + \frac{\rho_t}{12\rho_L^2} + 2\rho_E\rho_L^2}\right)\left(\frac{1}{\rho_t} + \rho_t + 2\right)\right] \tag{9}$$

$$\lambda_{AL}^{um} = B\left[12\left(\sqrt{2\rho_E\left(\frac{1}{\rho_t}+2\right)}-\frac{\rho_t}{\rho_\nu}\right)\right] \tag{10}$$

$$\lambda_{SL}^{um} = B\left[4\sqrt{6}\sqrt{\frac{\rho_E}{\rho_t}}+\frac{2\rho_E\rho_\nu}{\rho_t^2}\right] \tag{11}$$

Factor B common to the three previous equations is expressed as $B = b\rho_t E_s t_s/6$ and has consequently a positive value. Then, the interest of this formulation is to compare the three critical loads λ_{AG}^{um}, λ_{SL}^{um} and λ_{AL}^{um} by pairs, thus defining some zones of predominance for each and every phenomenon. The first studied difference is that of the two local forms and leads to the following relation (Eq. 12):

$$\lambda_{AL}^{um} < \lambda_{SL}^{um} \iff \rho_E^2\frac{\rho_\nu^2}{4\rho_t^2}+\rho_E\left(\frac{6\sqrt{6}}{\rho_t}\sqrt{2(1+\rho_t)}-36-\frac{21}{\rho_t}\right)+\frac{9\rho_t^2}{\rho_\nu^2} > 0 \tag{12}$$

Then, for a given Poisson's ratio, the parameter ρ_ν is constant and condition Eq. (12) can be easily plotted on a ρ_t-ρ_E graph, called *Design diagram*. But the resolution of this second degree polynomial shows that Eq. (12) is always valid for $\rho_t < 1/6$. Then for ordinary engineering materials used in sandwich construction ($0.0002 < \rho_E < 0.02$ and $0.01 < \rho_t < 0.1$), the antisymmetrical wrinkling load is always lower than the symmetrical one, *i.e.* according to our theory the antisymmetrical wrinkling will occur before the local symmetrical instability.

The same procedure is followed to study the difference between λ_{AG}^{um} (global) and λ_{SL}^{um} (symmetrical wrinkling), but unlike the previous case, an additional parameter ρ_L exists in the comparison between the two critical loads. Besides, the Poisson's ratio of classical isotropic cores (foams) doesn't vary a lot, therefore this parameter is chosen constant and equal to 0.4 for the next plots. The difficulty of this comparison lies in the complexity of the condition resulting from inequality $\lambda_{AG}^{um} < \lambda_{SL}^{um}$ (Appendix I). Then the limit of the predominance zones is found numerically thanks to Maple *V* through the resolution of the inequality. The condition presented in Appendix I is a function of three parameters, consequently for a given slenderness ρ_L, two zones can be isolated (Fig. 4). The first one, 1 , corresponds to sandwich configurations where symmetrical wrinkling is more likely to develop, whereas in sandwich configurations of zone 2 global buckling will prevail. In Fig. 5, one can observe the evolution of the frontier of the two zones of predominance of Fig. 4, for changes in the slenderness.

A similar condition can be isolated for λ_{AG}^{um} (global) and λ_{AL}^{um} (antisymmetrical wrinkling) (Appendix I). Fig. 6 represents the frontier between these two critical loads. It is important to notice that an additional zone (zone 3 in Fig. 6) is reported due to the validity of the condition of existence for the antisymmetrical wrinkling (Eqs. 4 and 13) as reported in [7]. Therefore only the global buckling exists in this zone. Fig. 7 shows the changes in these zones with the parameter ρ_L

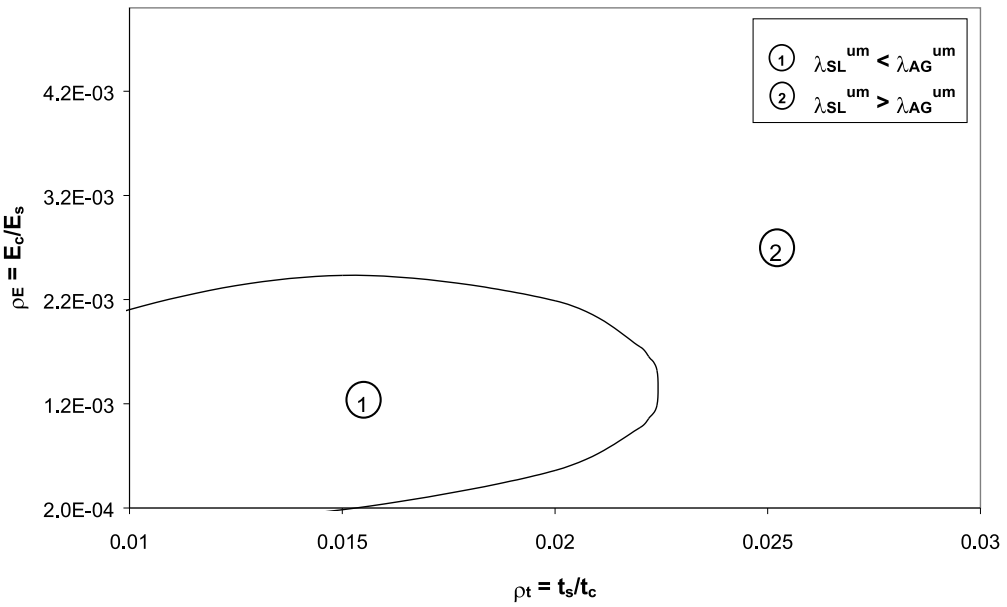

Figure 4: Design diagram : predominance zones between symmetrical wrinkling and global buckling for $\rho_L = 3$.

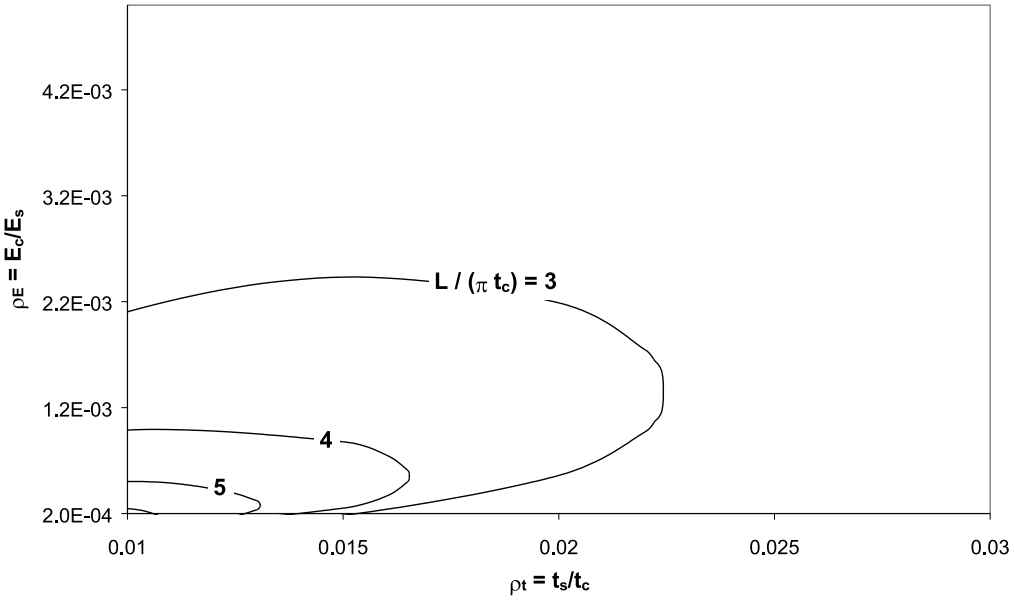

Figure 5: Design diagram : change in the predominance zones between symmetrical wrinkling and global buckling with ρ_L varying from 3 to 6.

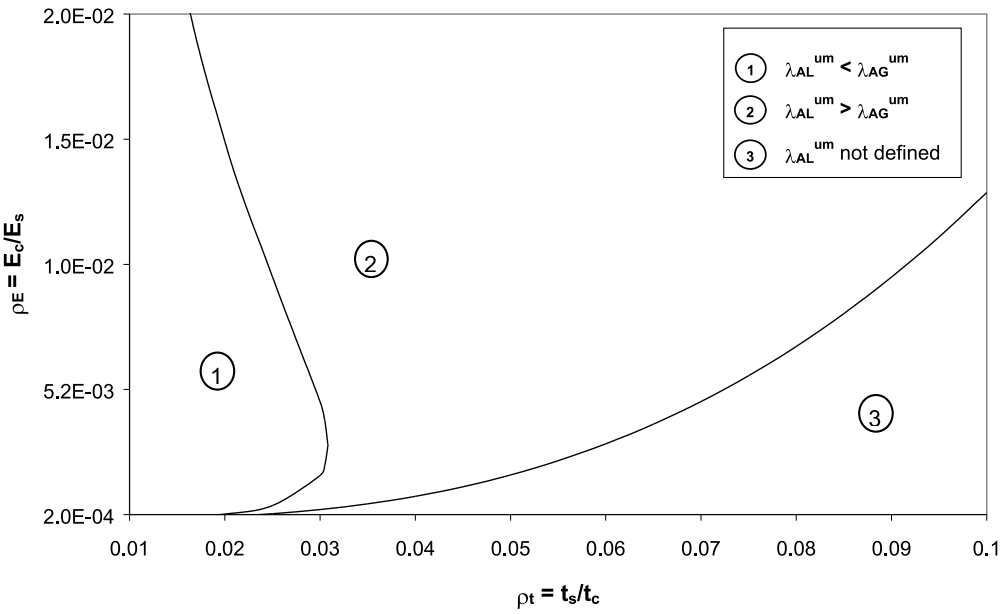

Figure 6: Design diagram : predominance zones between antisymmetrical wrinkling and global buckling for $\rho_L = 3$.

: zone 3 remains unchanged.

$$\frac{2{\rho_t}^3}{\rho_\nu^2 \rho_E (1+2\rho_t)} < 1 \tag{13}$$

Figs. 4 to 7 show that the local forms are predominant in reduced regions of sandwich configurations. Their localization clearly demonstrate that local phenomena are more susceptible to appear in "bulky" sandwich beam made up of weak and thick core (low values of ρ_E and ρ_t). Moreover thanks to Figs. 5 and 7, one can observe that local instabilities disappear for slender sandwich beams in which global buckling will occur first, for lower loads. For a ratio $\rho_L = L/\pi t_c > 8$, without any material consideration, it can be asserted that the sandwich beam will behave in compression as its equivalent homogeneous representation. Figs. 4 to 7 have been plotted with a constant Poisson's ratio of 0.4, but it is easily proved that a drop of this parameter very slightly increases the surface of predominance of local forms. This is represented for symmetrical wrinkling in Fig. 8.

These diagrams can be useful for a first design of sandwich beams under in-plane compression and can yield precious information on the buckling behaviour when a material or geometrical configuration is imposed. The general view given by the dimensionless ratios clearly shows the sandwich configurations which will develop local or global instabilities. This emphasizes the limits of one-parameter variation studies which give only a partial view.

The last curves (Figs. 4 to 7) highlight the existence of narrow domains in which the global critical load and the local ones are very close. This is represented in Fig. 9 where for a given thicknesses ratio ρ_t, a range of moduli ratio ρ_E exists for which local and global buckling loads

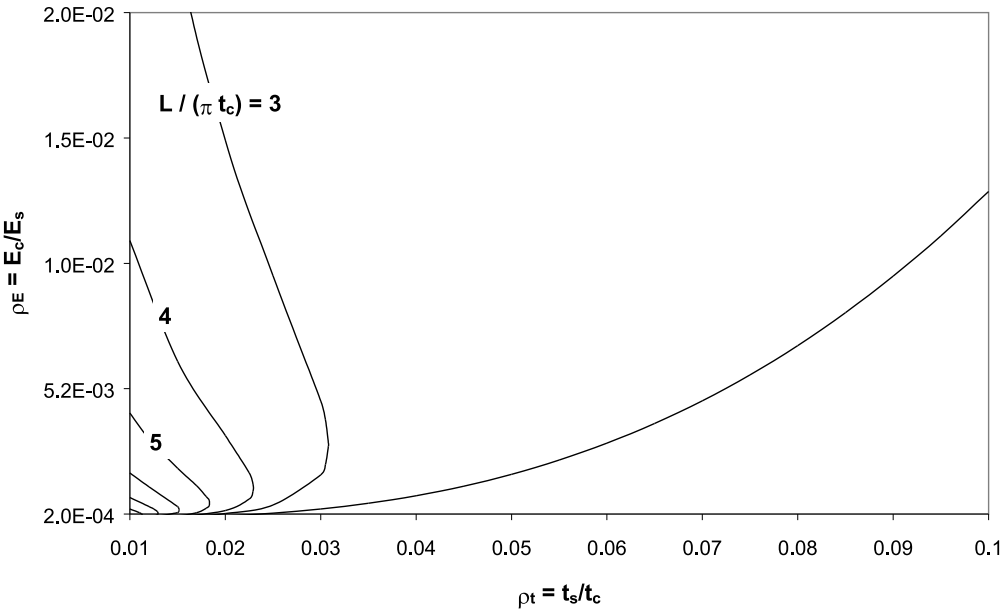

Figure 7: Design diagram : change in the predominance zones between antisymmetrical wrinkling and global buckling with ρ_L varying from 3 to 8.

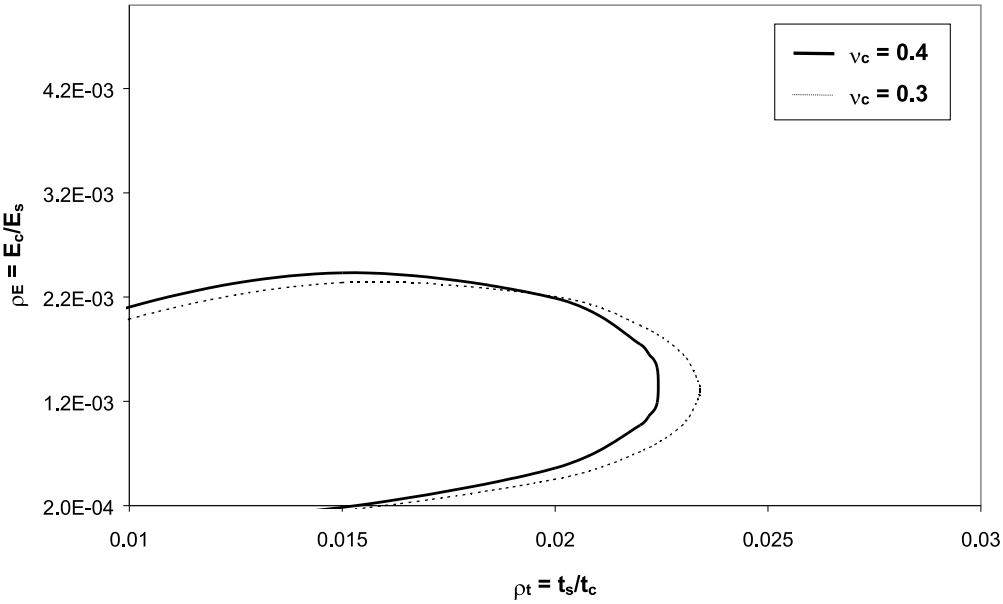

Figure 8: Design diagram : predominance zones between symmetrical wrinkling and global buckling with $\rho_L = 3$, for two values of the core Poisson's ratio (0.3 and 0.4).

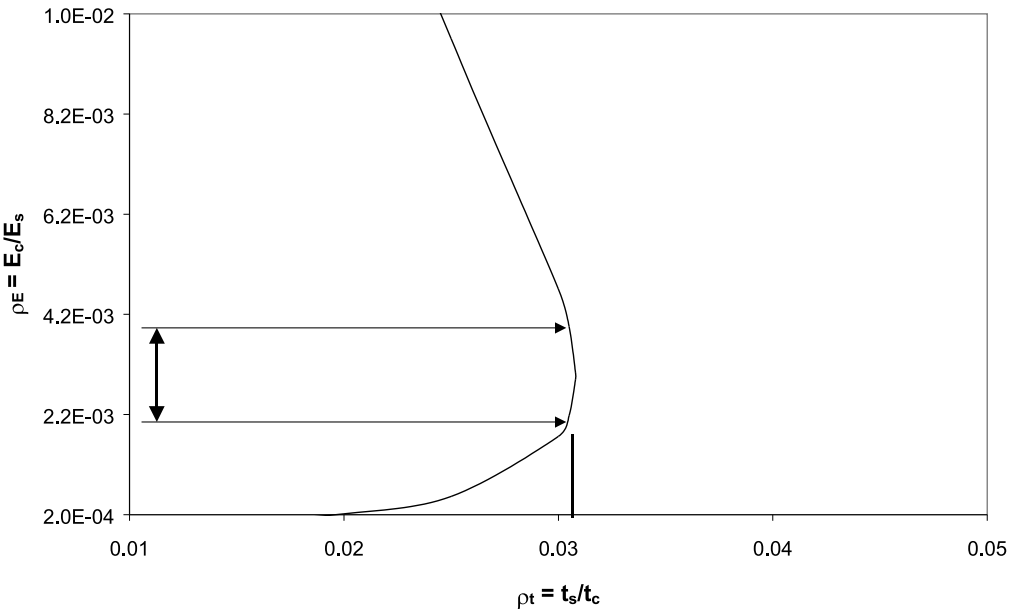

Figure 9: Range of moduli ratio ρ_E for which local antisymmetrical wrinkling and global buckling loads are identical for a given thicknesses ratio ρ_t.

are very close. The difficulty in studying the in-plane compressive behaviour of sandwich beams is then emphasized for these material and geometrical configurations. It raises the problem of interaction between the different modes since two bifurcation points exist close enough for a slight load increase to induce a shifting between local and global modes. Or more generally any mode combination can occur which then can no longer be qualified of either local or global and must receive special attention for it may be highly critical.

3 NUMERICAL INVESTIGATIONS

In this section, a numerical approach is led relying on two different beam models. A special attention is paid to the proper account of the boundary conditions. Besides a classical FE model, a simplified model is presented which yields large computation times reduction. Through this study, loads and wavelengths for both local and global instabilities are correlated with analytical results presented previously.

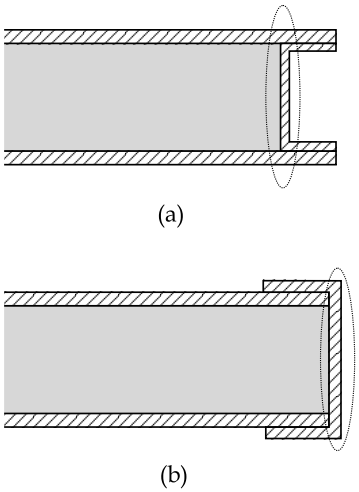

Figure 10: Two types of close-outs : incorporated into the beam (a) or attached to it (b).

3.1 Choosing a Finite Element model

3.1.1 Boundary conditions

The numerical investigations are led with $ABAQUS^{TM}$. Our first aim is to try to identify numerically the analytical buckling modes by eliminating the very local effects at the edges which induce very complex and unrealistic linear buckling modes. Consequently, the difficulty in setting the F.E. model is to represent the edges. This difficulty is naturally overcome when observing real configurations of sandwich, the edges of which are stiffened by close-outs in order to apply connections or loadings [3]. In Fig. 10, are sketched two different types of close-outs which can be incorporated into the sandwich structure (Fig. 10-a) or attached to it (Fig. 10-b). These stiffened-edges are represented in the F.E. model through kinematical restrictions on the displacements. Using a multi-point constraint, either edges are constrained to behave as a rigid medium, *i.e.* the nodes are prescribed to move along a straight line connecting the two extreme nodes located on top and bottom skins. This straight line can stretch linearly and rotate around a central node, the degrees of freedom (DOFs) of which are used to apply the boundary conditions and loadings (Fig. 11). Thus, perfect simply supported conditions are introduced, without any stresses concentrations which would involve very local buckling modes at the edges. The modeled part of the edges are encircled in Fig. 10.

3.1.2 The use of a simplified model

Due to the lack of F.E. reference model in the literature, F.E. displacement-based models are used which intrinsically cannot ensure any stress continuity at the skin/core interfaces. Therefore it is necessary to build a coherent model and assess its quality. The first way of modeling the sandwich beam can consist in discretising the skins and the core with bidimensional elements along the beam

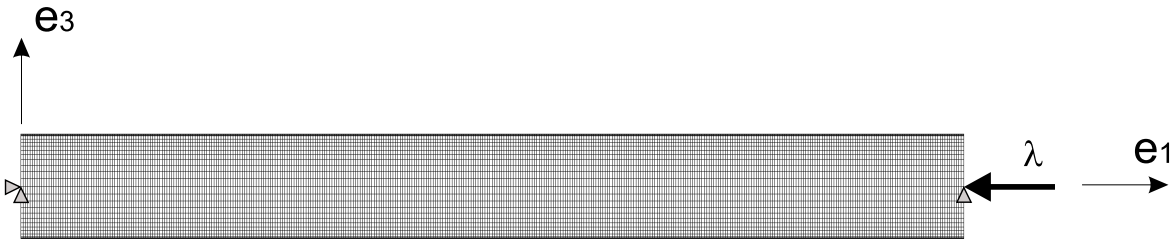

Figure 11: Complete F.E. model of the sandwich beam, approximately 22000 DOFs.

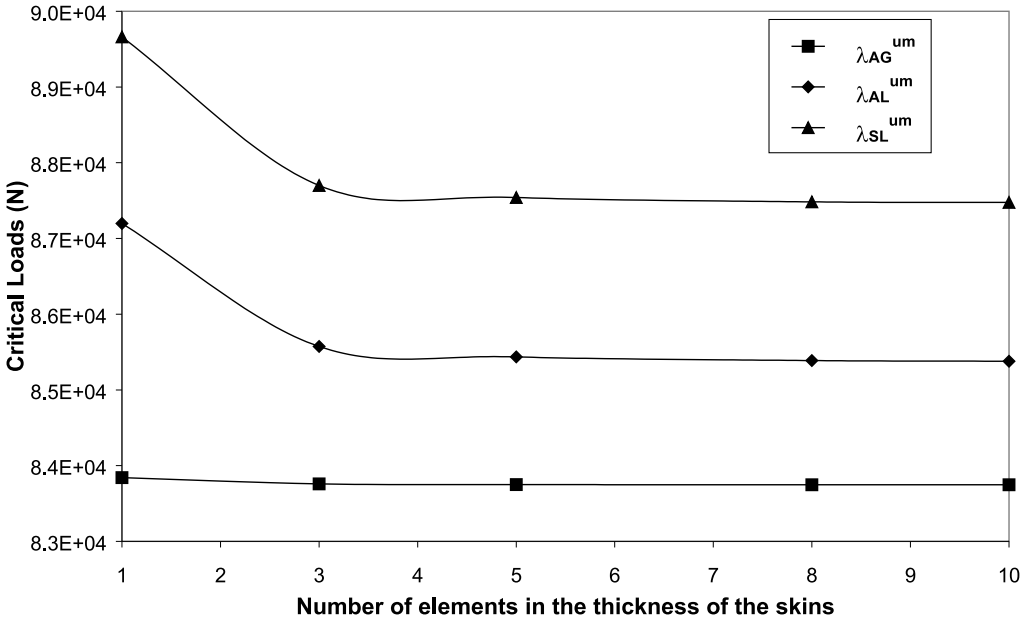

Figure 12: Change in the three critical loads versus the number of elements across the thickness of the skins for the two-dimensional model ($t_s = 1.25\ mm$).

length and across its thickness. 4-noded bilinear plane stress solid elements are used and in order to have aspect ratios of the order of the unity, the small elements of the skins induce a large number of elements on the whole beam (Fig. 11). In [12], only one element is used in the thickness of the skins, but it can be shown that critical loads corresponding to local phenomena are very sensitive to the number of elements in the two skins. In Fig. 12, the three critical loads are evaluated through eigenvalues calculations for this complete model with the sandwich configuration reported in Tab. 3. One can notice that the global critical load is independent on the number of element whereas a number of three elements in the thickness of the skins is necessary for a good accuracy of local wrinkling loads. This leads eventually to approximately 22000 DOFs for the entire model.

However, this model is very heavy and will be CPU time-consuming in subsequent fully non-linear analysis. Hence it is necessary to simplify it and ideally the number of degrees of freedom

$E_s(MPa)$	70000	$t_c(mm)$	50
$E_c(MPa)$	100	$L(mm)$	470
$G_c(MPa)$	35.7	$b(mm)$	60

Table 3: Sandwich characteristics for the F.E. evaluations

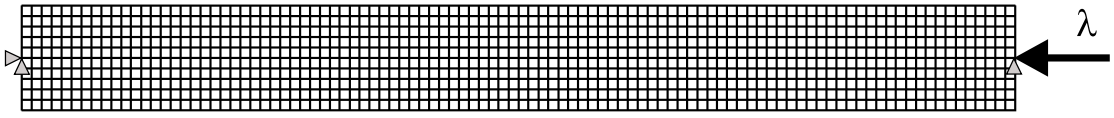

Figure 13: Simplified F.E. model of the sandwich beam, approximately 2000 DOFs.

can be reduced by replacing the two-dimensional elements of the skins by linear beam elements (Fig. 13). The use of linear elements ensures that they cannot buckle over the 2D-elements and then the beam rotation is not restricted. The principle is to connect these beam elements of the skins to the plane elements of the core, simply by using the same nodes. The main but slight drawback of this kind of model is that the centre line of the two skins are placed at a distance corresponding to the core thickness. This induces a loss in the global equivalent flexural stiffness since the skins are closer one to each other than in the actual sandwich beam. Heder [2] overcomes the problem by introducing a core thicker than the actual one. For a sandwich beam, one can also modify the width, and the determination of the same equivalent flexural stiffness leads to the following corrected width b' (Eq. 14). Due to the characteristic values of the sandwich ($0.01 < \rho_t < 0.1$), the effect of this change on the value of the critical loads is rather negligible ($b' \approx b$).

$$b' = b\,(1+\rho_t\,(2+\rho_t)) \tag{14}$$

The longitudinal size of the elements is no longer controlled by the thickness of the skins. So, the beam element length can be adjusted such that enough elements are present to observe the local phenomena. By controlling the number of elements a time-optimum mesh will be used. In Fig. 14, the evolution of the three critical loads is plotted versus the number of beam elements in the length of the skins (sandwich configuration from Tab. 3). One can notice that the value of the local critical loads are strongly dependent on this length. Any increase in the beam size elements results in a significant increase of the wrinkling loads. Consequently, for a small number of elements in the skins, the local critical loads can be overestimated (Fig. 14) and the global mode is then critical. In the simplified model, the whole number of degrees of freedom has significantly decreased and

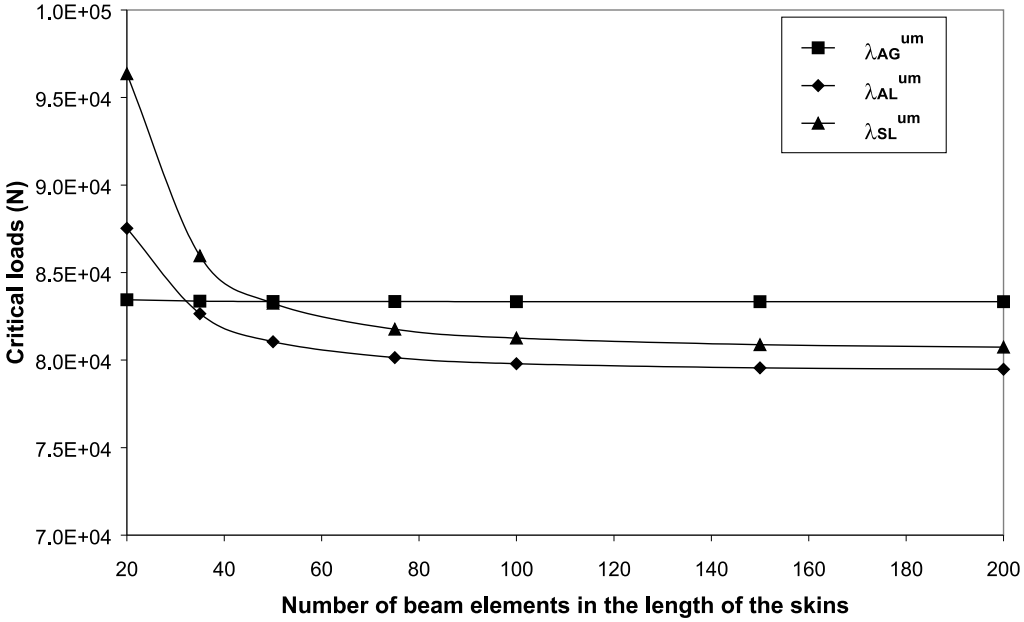

Figure 14: Change in the three critical loads versus the number of beam elements along the skins for the simplified model ($t_s = 1.25\ mm$).

reaches approximately 2000 DOFs for a number of 100 elements in the length (Fig. 13). Besides, due to the high wavenumber on the beam length for local phenomena, transverse shear effects in the beam elements must be taken into account. Comparisons between the energetic contributions of each stress component and stress distribution for the two previous F.E. models have shown very similar behaviours. Critical loads computed with these two F.E. models are compared in the next section.

3.1.3 Comparison between "complete" and "simplified" models results

The first important point is that the three analytical buckling modes can be found through a F.E. eigenbuckling analysis (Fig. 15). The geometrical and material parameters used for the F.E. evaluations are given in Tab. 3. The numerical critical loads from the "complete" and "simplified" FE models for the antisymmetrical (global and local) and symmetrical model, plotted versus the thickness ratio, are given respectively in Fig. 16 and Fig. 17. For the global mode (Fig. 16), the agreement is perfect. For the antisymmetrical (Fig. 16) and symmetrical (Fig. 17) wrinkling, the discrepancy between the two models never exceeds 20% for this configuration and a very good correlation is found for high thickness ratios. These figures clearly show a good correlation between the results of the two models. Consequently it can be assumed that the mechanical behaviour of the sandwich beam is well represented by this low CPU time-consuming simplified model, used thereafter.

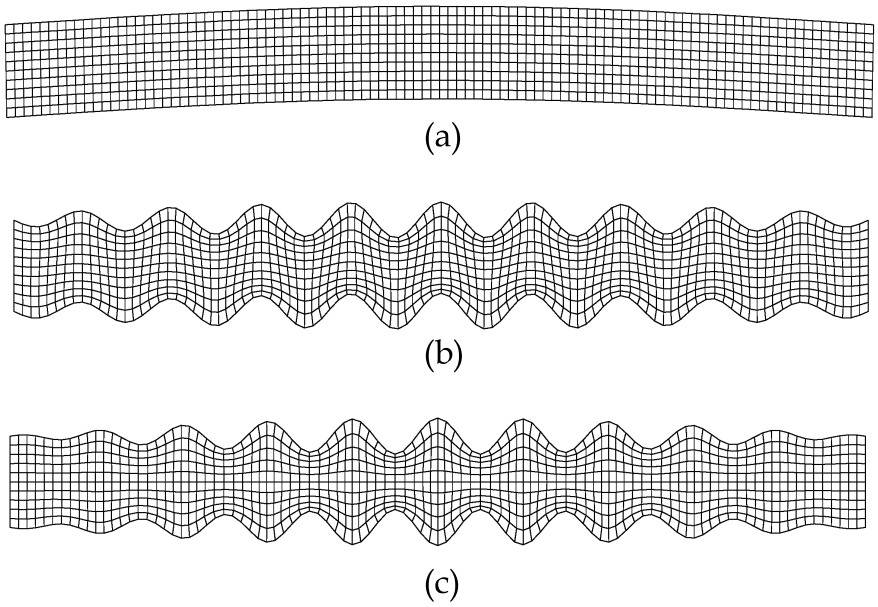

Figure 15: F.E. beam sandwich buckling modes for the simplified model : (a) global buckling, (b) antisymmetrical wrinkling of the skins, (c) symmetrical wrinkling of the skins.

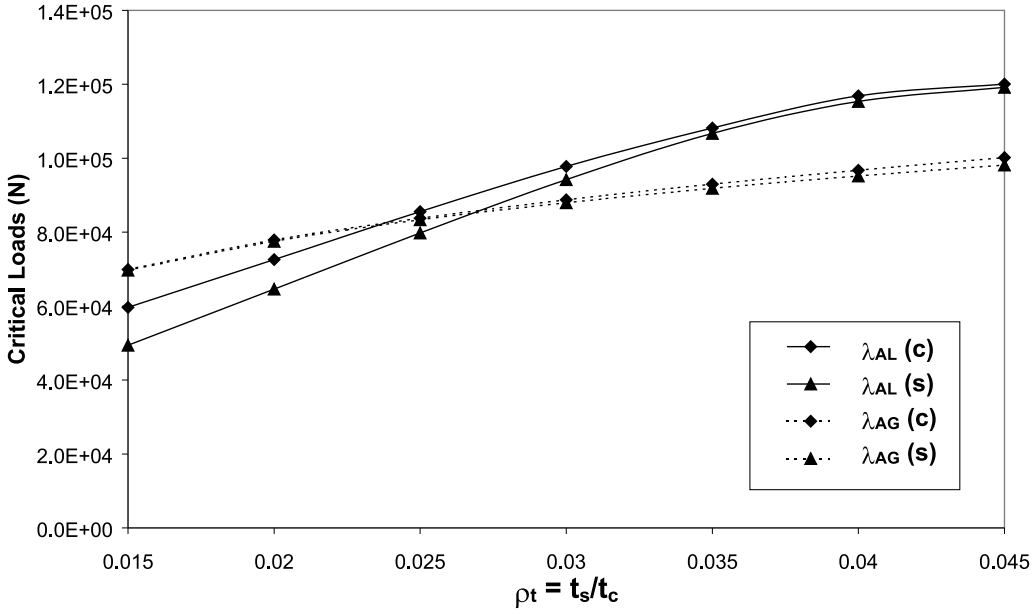

Figure 16: Change in the complete (c) and simplified (s) models of the antisymmetrical critical loads for the global mode and the local one, versus the thickness ratio.

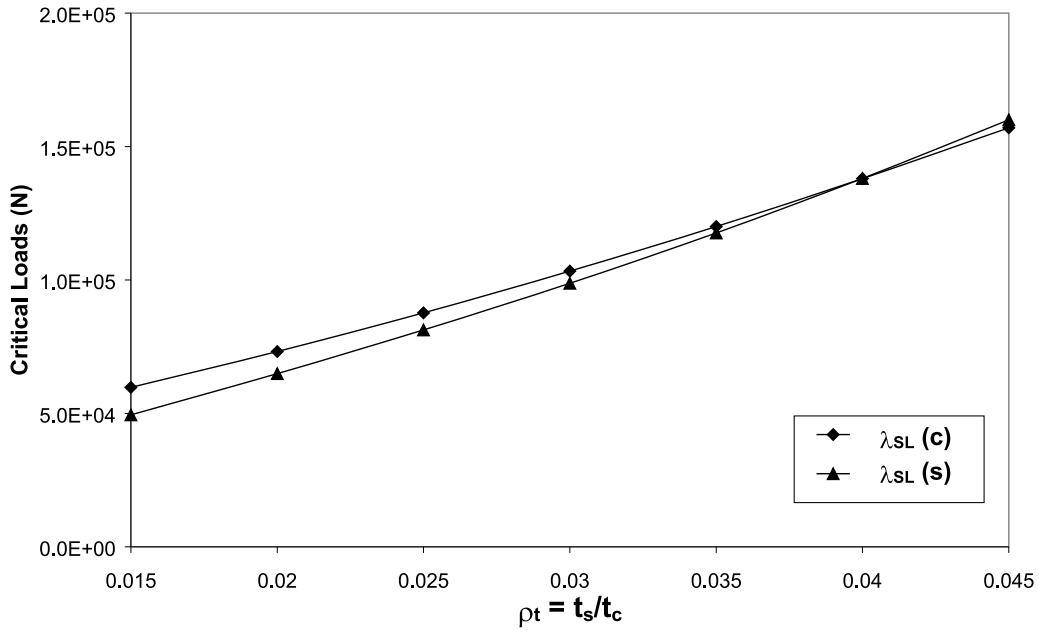

Figure 17: Change in the complete (c) and simplified (s) models of the symmetrical critical loads versus the thickness ratio.

Further comparisons are carried out in the following section where the analytical critical loads and wavelengths are compared with the numerical ones of the simplified model.

3.2 Comparison between analytical and numerical results

3.2.1 Critical buckling loads

Numerical and theoretical critical loads for the antisymmetrical (global and local) and symmetrical (local) mode are plotted versus the thickness ratio, respectively in Fig. 18 and Fig. 19. These plots permit to make a comparison between the configurations more susceptible to be unstable locally or globally. In Fig. 18, it can first be noticed the very good correlation for the global load (the largest difference is less than 2%). For the antisymmetrical wrinkling mode, the discrepancy between the numerical and the theoretical loads is rather constant and never exceeds 22% for this configuration. However, the comparison for this load is rather good when observing the plot of the classical load predictions (Eq. 6 with $Q = 0.5$) which is very conservative and presents a linear variation towards the thickness of the skins. For the symmetrical form (Fig. 19), the agreement is good (less than 15% of difference) and perfect for high thickness ratios. One can notice again the conservative nature of the classical wrinkling load unable to properly characterize the local phenomena.

An attempt can be made to explain the difference between the numerical and theoretical local loads by plotting the change in the transverse shear stress of the core for a given section where the

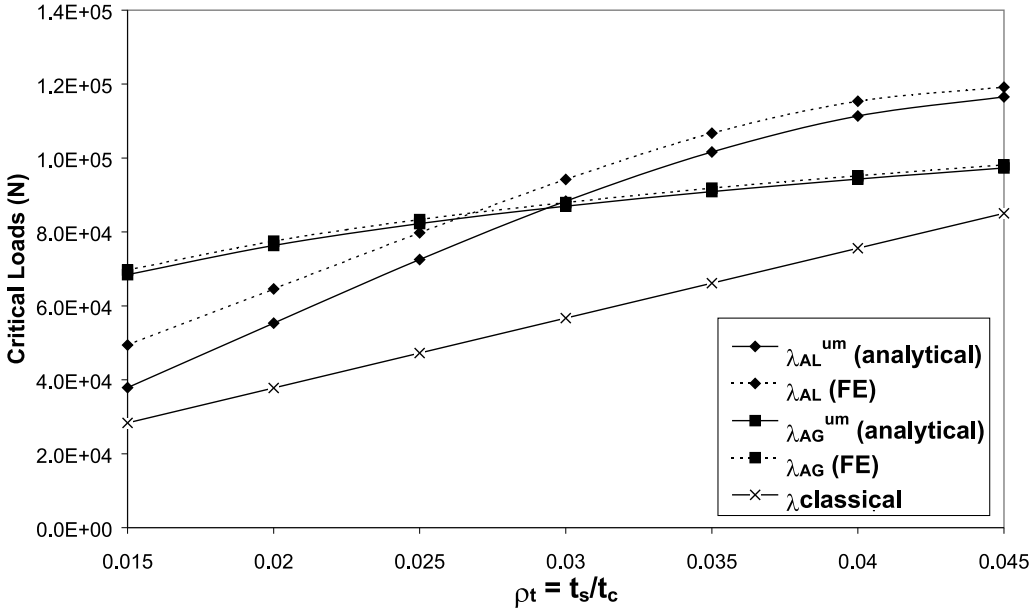

Figure 18: Change in the analytical and numerical antisymmetrical critical loads for the global mode and the local one, versus the thickness ratio.

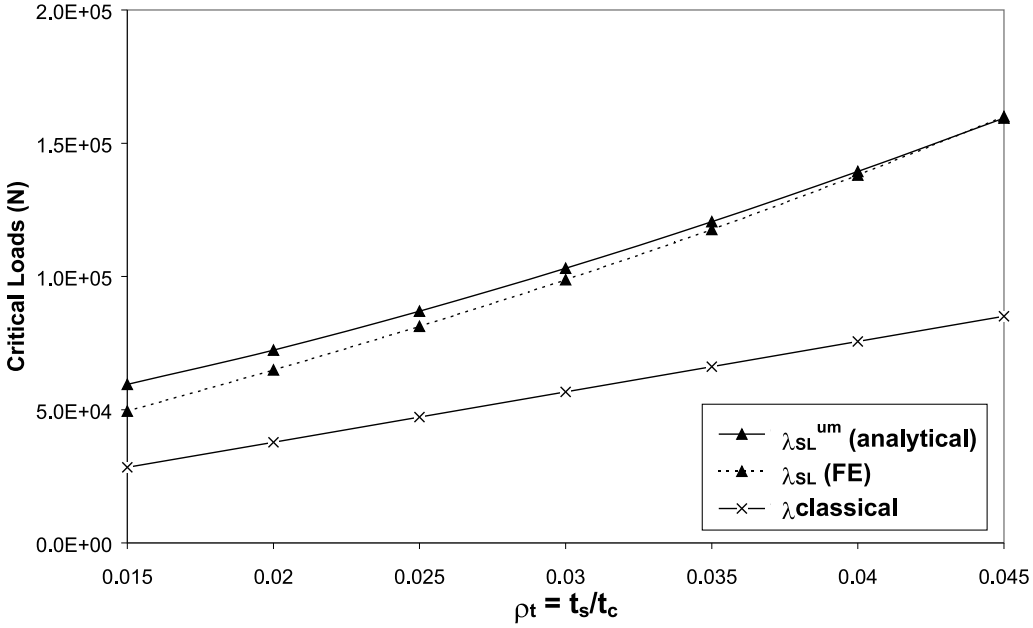

Figure 19: Change in the analytical and numerical symmetrical critical loads versus the thickness ratio.

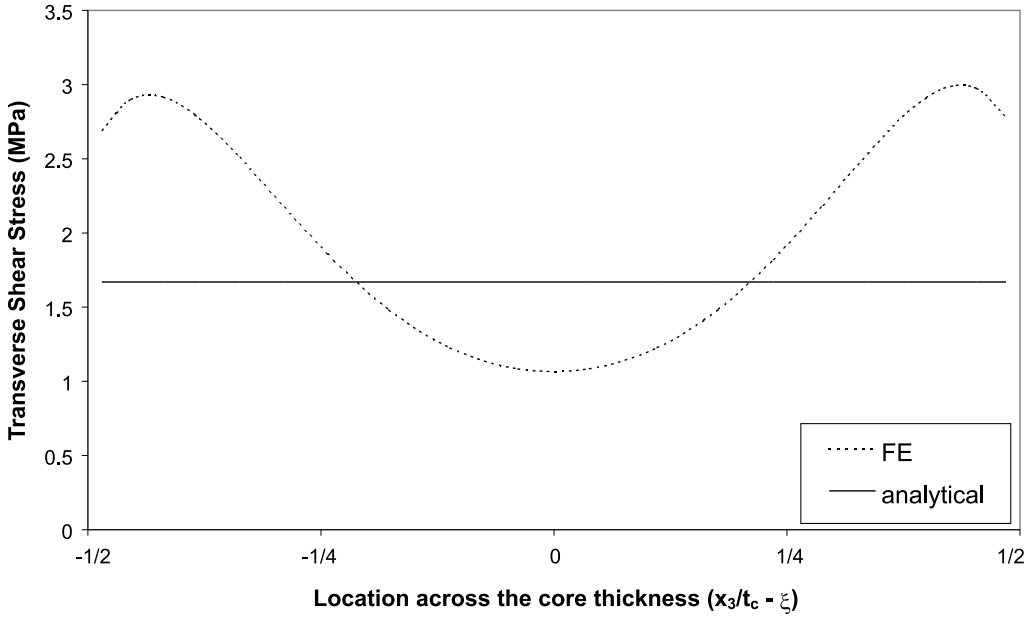

Figure 20: Comparison of the change in the analytical and numerical transverse shear stress across the core thickness for the antisymmetrical case.

shear effect is pronounced. The analytical model was built by approaching, as much as possible, the actual shear stress behaviour. For the antisymmetrical mode, the actual (F.E.) even distribution is modeled by a constant distribution and for the symmetrical mode, the actual odd distribution is approached with a linear change in the shear stress. This can be verified in Fig. 20 and Fig. 21 for respectively the antisymmetrical and the symmetrical wrinkling. In Fig. 20, it is easy to observe, by evaluating the surface under the curves, that the energetic contribution of the analytical shear stress is lower than the numerical one (-15%). Conversely, for the normal transverse stress, the contributions for the two models are closer. Thus we can infer that the lower analytical critical load for the antisymmetrical mode (Fig. 18) is related to a too simplistic distribution of the shear stress across the core thickness. The same observations can be made for the symmetrical mode (Fig. 21), but in this case the energetic contribution of the analytical shear stress is larger than the numerical one ($+30\%$) which can then justify the over-estimation of the analytical symmetrical load (Fig. 19).

The results of the F.E. model are coherent with those of the analytical one, they show that a correct evaluation of the transverse shear stress is required to well represent the mechanical behaviour of short wavelength phenomena. One can notice that the value of the analytical critical loads might be improved by introducing correction factors deduced from energetic considerations. Finally, the results of the numerical model and those of the analytical one are very close and they confirm that the analytical critical loads can be used as reliable design criteria.

3.2.2 Critical wavelengths

The comparison of the analytical and numerical critical wavelengths is very important. Indeed, a good correlation of the two models would mean that the optimum mesh element size can be properly determined by the analytical wavelengths alone and by choosing a sufficient number of elements per wave. The analytical wavelengths of the symmetrical and antisymmetrical wrinkling are respectively $L_S = L/n_S$ (Eq. 15) and $L_A = L/n_A$ (Eq. 16).

$$n_S = \rho_L \sqrt[4]{\frac{24\rho_E}{\rho_t}} \tag{15}$$

$$n_A = \rho_L \sqrt{6\left(\frac{1}{\rho_t}\sqrt{2\rho_E\left(\frac{1}{\rho_t}+2\right)}-\frac{2}{\rho_\nu}\right)} \tag{16}$$

Through the previous simplified model, the difference between analytical and numerical critical wavelengths can be evaluated. The values of the geometrical and material parameters used for this comparison are given in Tab. 3. Fig. 22 illustrates this comparison for the two wavelengths (Eqs. 15 and 16). First, one can notice the good agreement between theoretical and F.E. predictions for the two wrinkling modes. One can moreover underline the similar behaviour of L_S and L_A for small thickness ratios. In order to validate completely the use of the theoretical wavelengths to fix the element size, it is interesting to observe the evolution of the numerical wavelengths for different boundary conditions. Fig. 23 shows the comparison between the theoretical (Eqs. 15 and 16) and numerical wavelengths for a clamped sandwich beam. Then, one can see that the wavelength of the local phenomena is independent on the boundary conditions and the minimum of the two theoretical wavelengths gives a correct magnitude of the mesh element size. As an example, for the studied sandwich configuration, the analytical wavenumbers are respectively 22 and 20 for the symmetrical and antisymmetrical case. Therefore by fixing a number of 5 elements for a wave, the optimum number of elements for the whole length of the beam must be 110, which is coherent with the results of Fig. 14 where the sensitivity of the critical load towards the beam element size is assessed.

3.2.3 Design indications

The expressions proposed for the prediction of buckling loads (presented model, classical and F.E.) can be used to select sandwich configurations against compressive instabilities at both scales. It is proposed in Fig. 24 to visualize the zones where thickness ratios can be selected such that instabilities are avoided, for some given admissible load levels. It can be seen that according to the classical approach many configurations would be dismissed, depending only on the choice of the weighting coefficient Q (Eq. 6). In Fig. 24, the commonly used value of 0.5 for Q is chosen. The

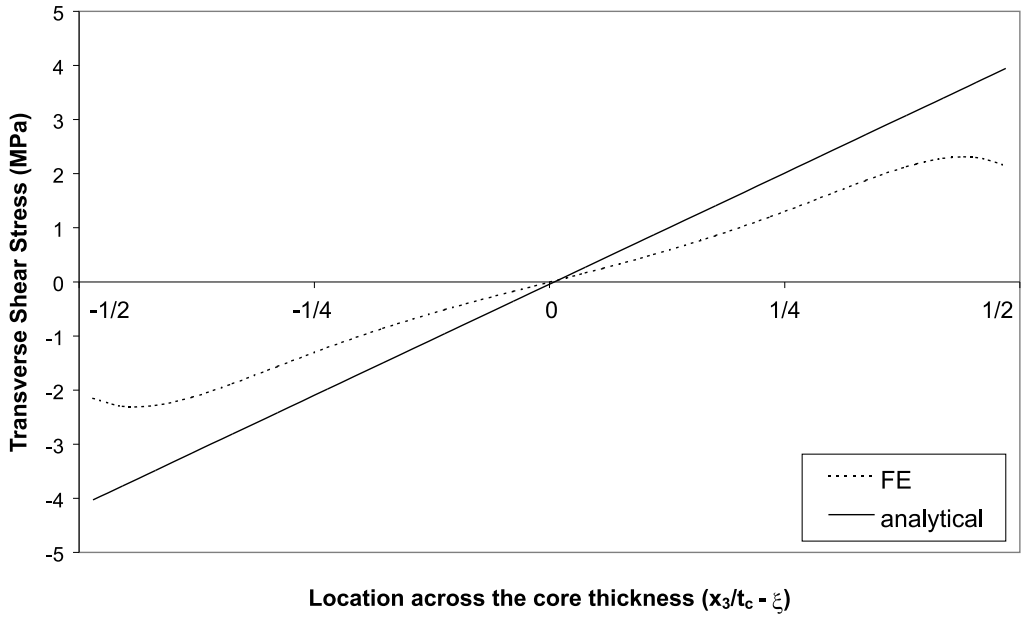

Figure 21: Comparison of the change in the analytical and numerical transverse shear stress across the core thickness for the symmetrical case.

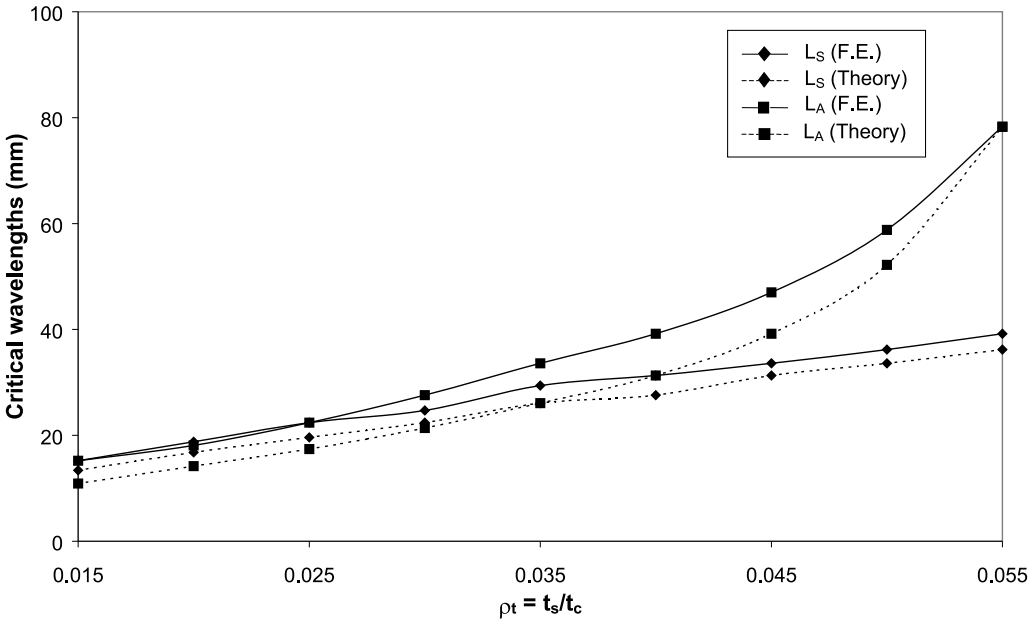

Figure 22: Comparison between analytical and numerical critical wavelengths.

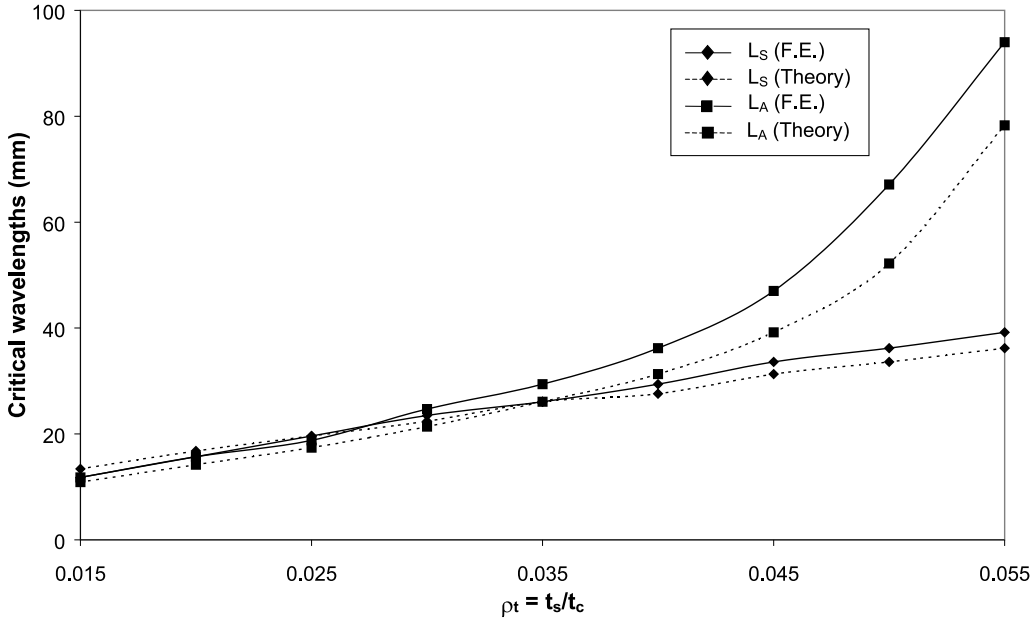

Figure 23: Comparison between analytical and numerical critical wavelengths for a clamped sandwich beam.

proposed approach and the numerical calculations allow to isolate nearly the same configurations. It is demonstrated that analytical expressions are reliable for isolating safely configurations which would be locally or globally stable.

4 CONCLUSION

A unified model has been built which in a perfect linear framework permits to grasp both local and global instabilities. Then, a parametric study was carried out in which the sensitivity of our formulae towards the geometrical and material parameters was assessed. Although the sensitivities might depend on the whole sandwich configuration, global buckling was shown to depend mainly on the core thickness, whereas wrinkling should be influenced mainly by the skin thickness. The design diagrams resulting from the introduction of dimensionless ratios clearly demonstrated that local phenomena are more susceptible to appear in "bulky" sandwich beams made up of weak and thick core, whereas global buckling prevails in slender beams.

The second step was to present a coherent Finite Element model with realistic boundary conditions and low CPU time-consumption, the final aim being to use this numerical model in a fully nonlinear framework. The correlation between the analytical and numerical critical loads associated with the main instability modes is actually good and the very conservative nature of the classical wrinkling load was underlined. It was shown that the key parameter for a low CPU

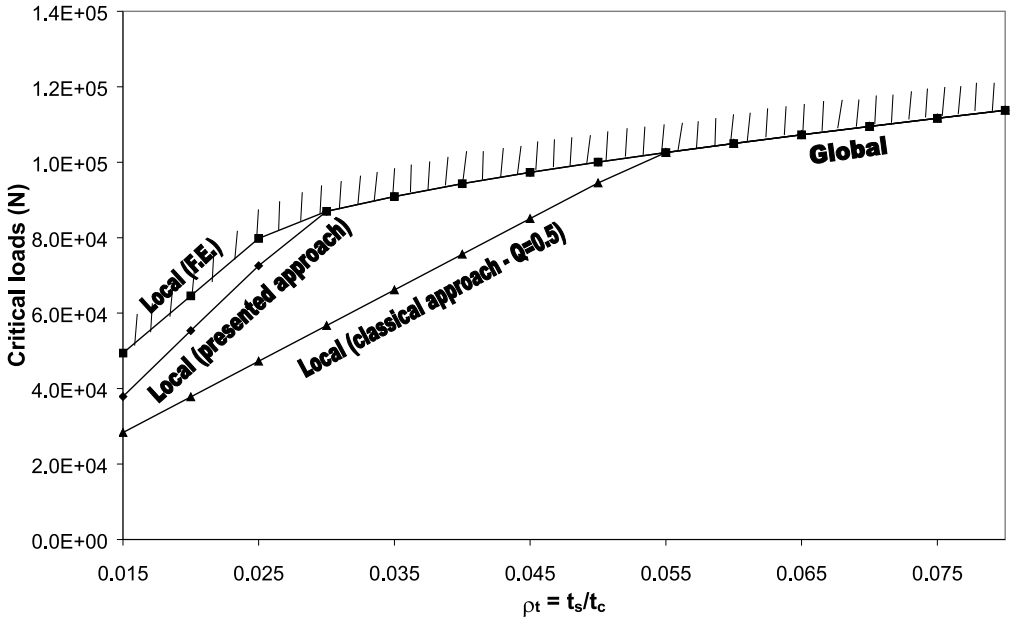

Figure 24: Critical load of the sandwich beam versus thickness ratio $\frac{t_s}{t_c}$: comparison between the presented approach, the classical and the numerical one.

time-consuming model is the length of the beam elements in the skins. But the good agreement between numerical and analytical wavelengths permits to postulate that the mesh element size can be evaluated from the analytical wavelengths.

Thus, the knowledge of the critical loads and their associated wavelengths constitutes an essential step in the complete characterization of the buckling behaviours of sandwich structures. Their analytical form permits to establish simple design rules for the choice of sandwich configurations more susceptible to develop local or global instabilities and to validate the use of an efficient numerical tool for future complex investigations of sandwich panels, including geometrical and material nonlinearities. Indeed, it is of prime importance to extend the application of the model to the non-linear problem of post-buckling where interaction of local and global buckling should yield very realistic unstable behaviours.

5 Appendix I

Comparison between the global critical load and the wrinkling loads.

$$\lambda_{SL}^{um} < \lambda_{AG}^{um} \iff$$
$$4\rho_E^2\rho_\nu\rho_L^2 + 2\rho_E\left(C_2\rho_\nu - 4\rho_t^3 - 3C_1\rho_t^2\right) + 4\sqrt{6\rho_E\rho_t^3}\left(C_2 + 2\rho_E\rho_L^2\right) - \frac{\rho_t^3}{\rho_L^2}C_2 < 0$$

$$\lambda_{AL}^{um} < \lambda_{AG}^{um} \iff$$
$$\rho_E^3 32C_1 + \rho_E^2(32C_1C_2 - C_3^2) - \rho_E 4C_2C_4 - 4C_2^4 < 0$$

with

$$C_1 = \frac{1}{\rho_t} + 2$$
$$C_2 = \frac{\rho_t}{\rho_\nu} + \frac{\rho_t}{12\rho_L^2}$$
$$C_3 = 4C_2 + C_1 + \rho_t$$
$$C_4 = 4C_2 - C_1 + \rho_t$$

References

[1] H.G. Allen. *Analysis and design of structural sandwich panels*. Robert Maxwell, M.C., M.P., 1969.

[2] M. Heder. Buckling of sandwich panels with different boundary conditions, a comparison between FE-analysis and analytical solutions. *Composites structures*, 19(4):313–332, 1991.

[3] HEXCEL. Mechanical properties of hexcel honeycomb materials. Technical Report TSB120, 1989.

[4] G.W. Hunt, L.S. Da Silva, and M.E. Manzocchi. Interactive buckling in sandwich structures. *Proceedings of the royal society of London*, 417A:155–177, 1988.

[5] A. Léger, A. Combescure, and M. Potier-Ferry. Bifurcation, flambage, stabilité en mécanique des structures. Technical report, IPSI, 1998.

[6] L. Léotoing, S. Drapier, and A. Vautrin. Closed-form solution for local, global buckling in sandwich stuctures. In H.R. Meyer-Pienning and D. Zenkert, editors, *Proceedings of Sandwich Construction 5 - Zurich 5-7 september 2000*, volume 1, pages 25–36. E-mas publishing, 2000.

[7] L Léotoing, S. Drapier, and A. Vautrin. A novel unified model for sandwich : closed-form solutions for global and local buckling of beams. *European Journal of Mechanics A/SOLIDS*, 2001. submitted.

[8] K.H. Lo, R.M. Christensen, and E.M. Wu. A high-order theory of plate deformation, part 1 : homogeneous plates. *Journal of Applied Mechanics*, pages 663–668, december 1977.

[9] K. Niu and R. Talreja. Modeling of wrinkling in sandwich panels under compression. *Journal of Engineering Mechanics*, 125(8):875–883, august 1999.

[10] V. Sokolinsky and Y. Frostig. Boundary condition effects in buckling of "soft" core sandwich panels. *Journal of Engineering Mechanics*, 125(8):865–874, august 1999.

[11] A. Starlinger. *Development of efficient finite shell elements for the analysis of sandwich structures under large deformations and global as well as local instabilities*. PhD thesis, Vienna University of Technology, 1990.

[12] M.A. Stiftinger and F.G. Rammerstorfer. Face layer wrinkling in sandwich shells-theoretical and experimental investigations. *Thin-Walled Structures*, 29:113–127, 1997.

[13] J.R. Vinson. Comparison of optimized sandwich panels of various constructions subjected to in-plane loads. In K.A. Olsson and R.P. Reichard, editors, *Proceedings of Sandwich Constructions 1*, pages 23–52. Engineering Materials Advisory Services Ltd., 1989.

[14] D. Williams, D.M.A. Leggett, and H.G. Hopkins. Flat sandwich panels under compressive end loads. Technical Report 1987, R.A.E., 1941.

- O -

Annexe 2. 9

L. Dufort, S. Drapier, & M. Grédiac.

Closed-form solution for the cross-section warping in short beams under three-point bending.

Compos. Struct. **, 52(2) :233–246, 2001.**

ELSEVIER

Composite Structures 52 (2001) 233–246

COMPOSITE STRUCTURES

www.elsevier.com/locate/compstruct

Closed-form solution for the cross-section warping in short beams under three-point bending

L. Dufort [a], S. Drapier [a], M. Grédiac [b,*]

[a] *École Nationale Supérieure des Mines de Saint-Étienne, SMS division, Mechanical and Materials Engineering Department, 158, Cours Fauriel, 42023 Saint-Étienne Cedex 2, France*

[b] *Laboratoire d'Etudes et de Recherches en Mécanique des Structures, Université Blaise Pascal, 24, Avenue des Landais, 63174 Aubière Cedex, France*

Abstract

The transverse shear behavior of composite beams can be critical and therefore must be properly represented by the various models of structures usually employed either to predict their behavior or to identify experimentally their properties. In this work, a simple analytical approach based on higher-order theories is proposed that accounts for the cross-section warping in beams. Then the solution of a beam under three-point bending is solved and the accuracy of both displacement and strain distribution predictions is shown through comparisons with the FE analysis results. In this formulation, the cross-section locking at mid-span is ensured owing to the dependence of the transverse shear strain upon the position along the beam axis. Eventually, comparisons with experimental measurements demonstrate the ability of these simple analytical solutions to grasp the main phenomena which control the response of composite beams under three-point bending loading, i.e. the arising of transverse shear.

Keywords: Thick composites; Transverse shear; Warping; Thick point bending

1. Introduction

The interlaminar shear is an important phenomenon in many problems of composite beams and plates under bending. This is mainly due to the relatively low value of both the transverse shear modulus and strength compared with the corresponding longitudinal values measured along the fibers. Determination of the transverse shear stress developed in beams and plates under bending is usually carried out under some well-known assumptions based on the displacement field across their thickness. Timoshenko's beam theory [1,2] assumes that plane cross-sections of the bent beam remain plane after loading. This so-called first-order theory was extended to elastic plates by Reissner [3] and Mindlin [4]. Higher-order theories including a warping of the cross section have then been proposed. These theories are more realistic, since they verify zero transverse shear stress conditions on the top and bottom boundaries of the structure, contrary to the Timoshenko and Reissner/Mindlin theories. In such higher-order theories, displacement along the axes of structures is usually assumed to be cubic, giving rise to a warping of the cross-section as well as to parabolic shear strain and stress distributions across the thickness. More recently, Touratier has showed that this cubic displacement could be refined with a sine [5,6].

There is an extensive literature on the use of the above theories in finite element formulations for beam and plate bending problems (see for instance [5,7,8]). When analytical solutions are addressed however, first-order theories are especially used. Considering for instance the classical problem of beams under three-point bending, the solution is usually found under the Timoshenko assumption if the influence of transverse shear is included. Two problems arise however with this classical solution. First, the shear stress is not zero at the top and bottom boundaries of the beam. The constant shear stress is therefore corrected a posteriori with a so-called 'correction' or 'shear factor' such that a parabolic shear distribution is quantitatively substituted to the linear distribution. Second, because of the symmetry of the displacement field, warping of the sections cannot occur at the center of the beam. It is therefore expected that

* Corresponding author. Tel.: +33-4-73-40-75-29; fax: +33-4-73-40-74-94.

E-mail address: grediac@lermes.univ-bpclermont.fr (M. Grédiac).

0263-8223/01/$ - see front matter
PII: S0263-8223(00)00171-9

the stress field and deflection are disturbed in the case of short beams because the Saint–Venant effect no more completely holds.

To the knowledge of the authors, it seems that this problem of properly representing the cross-section locking at mid-span has not been addressed and quantified in the literature through simple analytical resolutions. It must be emphasized that such short beam configurations are of prime importance for composite materials since the transverse shear strength of unidirectional fiber reinforced composites is often measured in the three-point short beam shear test [9]. The interpretation of such a test remains however problematic for the reasons described above or because of the non-linearity of the constitutive material (see for instance [10]). Hence, any improvement in the classical analytical solution is useful for a better interpretation of the standard ASTM test which in turn will contribute to a better characterization of composite materials. Moreover, an analytical solution yields an invaluable richness which cannot be easily met when using FE analyses (optimization, parametric study, etc.).

The aim of this paper is to propose a solution to the well-known problem of a beam under three-point bending including both a warping of the cross-section far away from the center, and a locking of this warping at the center of the beam. First, the equilibrium equations and the boundary conditions are obtained using a variational approach where three variables are used: the deflection, the rotation of cross-sections and its warping modeled through a warping function. The solution found in terms of deflection and through-thickness displacement is the usual one completed with an additional term that takes into account the warping of sections. Since symmetry of the displacement field is verified, the solution found is used to quantify the locking effect of warping at the center of the beam, both on the deflection and on the longitudinal displacement field in short composite beams. In the second part of the paper, one of the two equilibrium equations is used to find the transverse normal stress field due to the locking of warping. Eventually, a comparison between the experimental measurements shows that an analytical solution must account for the cross-section warping to properly represent the behavior of composite beams under three-point bending loading.

2. General governing equations associated with higher-order theories for beams

Let us consider a straight beam with a symmetrical cross-section made up of a homogeneous material. This beam has a plane of symmetry $(O, \mathbf{e}_1, \mathbf{e}_3)$, both in geometry and loading (Fig. 1). The present study is carried out within the framework of small perturbations. The

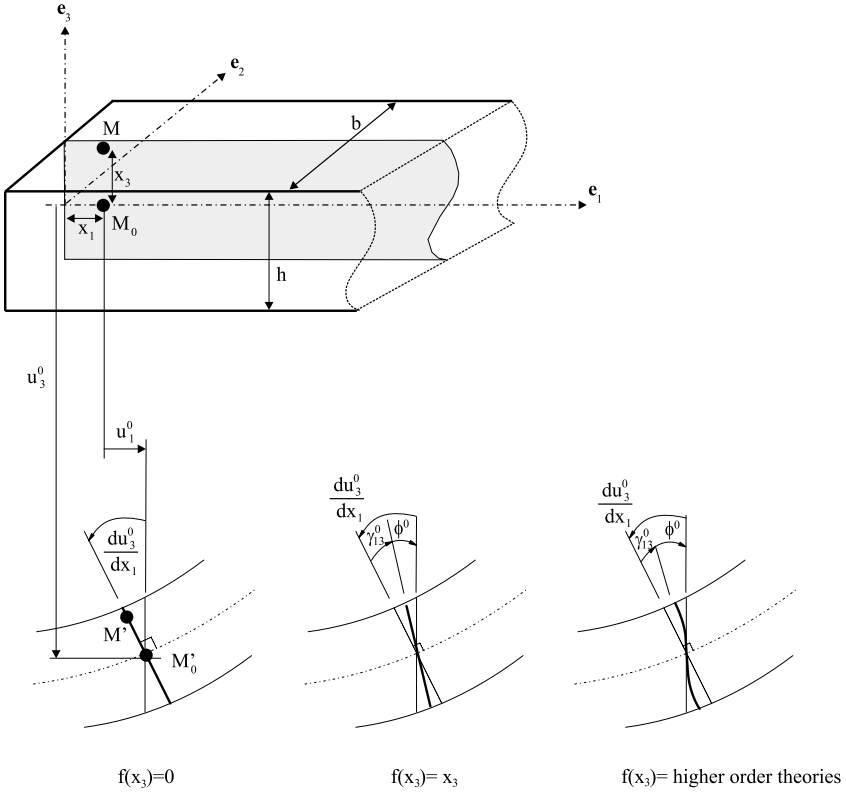

Fig. 1. Beam displacements and u_1 profile across the thickness vs. the form of $f(x_3)$.

constitutive material is assumed to be linear elastic and orthotropic.

2.1. Kinematics accounting for section warping

Usually, for this type of structural component, the corresponding displacement field relates the displacement $\mathbf{u}(M)$ of any point $M(x_1,x_3)$ of the bidimensional domain to the displacement $\mathbf{u}^0(M_0)$ of the corresponding point $M_0(x_1,0)$ on the neutral axis (see Fig. 1). Displacement components are, respectively, $u_1(M)$ along $\mathbf{e}_1$ and $u_3(M)$ along $\mathbf{e}_3$. In-plane component $u_1(M)$ can be splitted up into three parts (see Eq. (1)): first, the in-plane displacement, second, the displacement due to section rotation as defined in Euler–Bernoulli's classical beam theory that does not account for transverse shear, and third, a further refinement due to the distribution of shear strain through the thickness. This refinement leads to theories usually referred to as *higher-order*. Finally, the displacement field of any point in the beam writes:

$$\mathbf{u}(M)=\begin{cases} u_1(x_1,x_3)=u_1^0(x_1)-x_3u_{3,1}^0(x_1)+f(x_3)\gamma_{13}^0(x_1),\\ u_3(x_1,x_3)=u_3^0(x_1), \end{cases} \tag{1}$$

where $u_1^0(x_1)$ and $u_3^0(x_1)$ are the displacement components of a point M_0 located on the neutral axis (see Fig. 1) which moves to M_0'. $u_{3,1}^0(x_1)$ is the section rotation about $\mathbf{e}_2$ induced by bending. $X_{,i}$ with $i=1,2$ or 3 stands for the first derivative of any function X with respect to x_i, and similarly $X_{,ii}$ is the corresponding second derivative. $f(x_3)$ is an odd function of x_3 only which is to be defined, and $\gamma_{13}^0(x_1)$ is the transverse shear strain measured on the mean-line (Eq. (2)).

$$\gamma_{13}^0(x_1)=u_{3,1}^0(x_1)-\phi^0(x_1), \tag{2}$$

where $\phi^0(x_1)$ is the total section rotation measured on the mean-line (Fig. 1).

2.2. Strain and stress tensors

Within the framework of small perturbations, the linear Green–Lagrange strain tensor writes:

$$\begin{aligned} &\varepsilon_{11}(x_1,x_3)=u_{1,1}^0(x_1)-x_3u_{3,11}^0+f(x_3)\gamma_{13,1}^0,\\ &\gamma_{13}(x_1)=f_{,3}\gamma_{13}^0(x_1). \end{aligned} \tag{3}$$

According to classical beam theories, ε_{33} is neglected as a first approximation. Then the two strain components (Eq. (3)) are related to their corresponding stress components through the basic constitutive law:

$$\begin{aligned} &\sigma_{11}=E_{11}\varepsilon_{11},\\ &\sigma_{13}=G_{13}\gamma_{13}, \end{aligned} \tag{4}$$

where E_{11} is the Young's modulus of the constitutive material of the beam and G_{13} is the shear modulus.

2.3. Equilibrium equations and boundary conditions

A very systematic and safe way to establish governing and boundary equations of a model is to use the Principle of Virtual Work (PVW). Let us consider the general case of a medium $\mathscr{D}$ submitted to external loadings $\mathbf{f}^V$ and $\mathbf{f}^S$, respectively, body forces acting on $\mathscr{D}$ and surface forces acting on its external surface $\partial\mathscr{D}_f$. Then, the static equilibrium is achieved provided the sum of the internal (δW_{int}) and the external (δW_{ext}) virtual work developed in any virtual displacement field $\delta\mathbf{u}(M)$ is null (Eq. (5)). Let this virtual field be the actual displacement field variation (Eq. (8)), then kinematic boundary conditions are verified and prescribed displacements cancel. Such a displacement field is said to be Kinematically Admissible and henceforth noted K.A.

$$\delta W_{\text{ext}}(\delta\mathbf{u})+\delta W_{\text{int}}(\delta\mathbf{u})=0,\quad \forall\delta\mathbf{u}\ \text{K.A.} \tag{5}$$

with

$$\delta W_{\text{int}}(\delta\mathbf{u})=-\int_{\mathscr{D}}\sigma:\delta\epsilon\,\mathrm{d}V, \tag{6}$$

$$\delta W_{\text{ext}}(\delta\mathbf{u})=\int_{\mathscr{D}}\mathbf{f}^V\,\delta\mathbf{u}\,\mathrm{d}V+\int_{\partial\mathscr{D}_f}\mathbf{f}^S\,\delta\mathbf{u}\,\mathrm{d}S, \tag{7}$$

where $\delta\epsilon$ is the virtual strain tensor defined in Eq. (9) associated with $\delta\mathbf{u}(M)$.

2.3.1. Virtual fields

From its definition (Eq. (1)) and feeding in the shear strain (Eq. (2)), the virtual displacement field $\delta\mathbf{u}(M)$ writes in the basis $(\mathbf{e}_1,\mathbf{e}_2,\mathbf{e}_3)$:

$$\begin{aligned} \delta u_1(M)&=\delta u_1^0(x_1)-x_3\delta u_{3,1}^0(x_1)\\ &\quad+f(x_3)\Big[\delta u_{3,1}^0(x_1)-\delta\phi^0(x_1)\Big],\\ \delta u_3(M)&=\delta u_3^0(x_1). \end{aligned} \tag{8}$$

Similarly, the virtual strain components are:

$$\begin{aligned} \delta\varepsilon_{11}(M)&=\delta u_{1,1}^0(x_1)-x_3\delta u_{3,11}^0(x_1)\\ &\quad+f(x_3)\Big[\delta u_{3,11}^0(x_1)-\delta\phi_{,1}^0(x_1)\Big]\\ \delta\gamma_{13}(M)&=f_{,3}(x_3)\Big[\delta u_{3,1}^0(x_1)-\delta\phi^0(x_1)\Big]\\ &=f_{,3}(x_3)\delta\gamma_{13}^0(x_1) \end{aligned} \tag{9}$$

2.3.2. Internal and external virtual work

Within the framework of classical beam theories, loads prescribed on the beam can be of different types as recalled in Fig. 2: distributed loads, concentrated forces and moments. Assuming that the external loads are applied at $x_1=\ell$, the virtual work done on the beam of length ℓ writes:

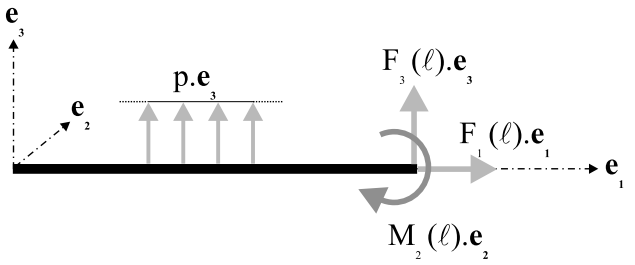

Fig. 2. Loads applied on the beam.

$$\delta W_{\text{ext}}(\delta\mathbf{u},\delta\phi) = \int_0^\ell p\delta u_3^0\,\mathrm{d}x_1 + F_3(\ell)\delta u_3^0(\ell) + F_1(\ell)\delta u_1(\ell) + M_2(\ell)\delta\phi^0(\ell). \tag{10}$$

Feeding the definitions of stresses (Eq. (4)) and virtual strain components (Eq. (9)) into Eq. (6) leads to the internal virtual work:

$$\begin{aligned}\delta W_{\text{int}}(\delta\mathbf{u},\delta\phi) &= -\int_0^\ell \left[\int_S \sigma_{11}\Big(\delta u_{1,1}^0(x_1) - x_3\delta u_{3,11}^0(x_1) + f(x_3)\delta\gamma_{13,1}^0(x_1)\Big)\,\mathrm{d}S + \int_S \sigma_{13}f_{,3}(x_3)\,\delta\gamma_{13}^0(x_1)\,\mathrm{d}S\right]\mathrm{d}x_1\\ &= -\int_0^\ell \Big[N(x_1)\delta u_{1,1}^0 + M(x_1)\delta u_{3,11}^0(x_1) + B(x_1)\delta\gamma_{13,1}^0(x_1) + H(x_1)\delta\gamma_{13}^0(x_1)\Big]\,\mathrm{d}x_1.\end{aligned} \tag{11}$$

$N(x_1)$ and $M(x_1)$ are the usual normal effort and bending moment, respectively:

$$N(x_1) = \int_S \sigma_{11}\,\mathrm{d}S = E_{11}A, \tag{12}$$

where A is the cross-sectional area of the beam.

$$\begin{aligned}M(x_1) &= -\int_S x_3\sigma_{11}\,\mathrm{d}S\\ &= -E_{11}\left[u_{1,1}^0(x_1)\int_S x_3\,\mathrm{d}S - u_{3,11}^0(x_1)\times\int_S x_3^2\,\mathrm{d}S + \gamma_{13,1}^0(x_1)\int_S x_3f(x_3)\,\mathrm{d}S\right]\\ &= c_1u_{3,11}^0(x_1) - c_2\gamma_{13,1}^0(x_1)\end{aligned} \tag{13}$$

with the following constants c_1 and c_2 defined as:

$$c_1 = E_{11}\int_S x_3^2\,\mathrm{d}S = E_{11}I_{22}, \tag{14}$$

$$c_2 = E_{11}\int_S x_3f(x_3)\,\mathrm{d}S, \tag{15}$$

c_1 depends on I_{22}, the second moment of the section with respect to $\mathbf{e}_2$. Extra resultants $B(x_1)$ (Eq. (16)) and $H(x_1)$ (Eq. (18)) are the non-usual terms induced by $f(x_3)$ in the displacement field. $B(x_1)$ is of the dimension of a moment and $H(x_1)$ of the dimension of a force.

$$\begin{aligned}B(x_1) &= \int_S f(x_3)\sigma_{11}\,\mathrm{d}S\\ &= E_{11}\left[u_{1,1}^0(x_1)\int_S f(x_3)\,\mathrm{d}S - u_{3,11}^0(x_1)\times\int_S x_3f(x_3)\,\mathrm{d}S + \gamma_{13,1}^0(x_1)\int_S f^2(x_3)\,\mathrm{d}S\right]\\ &= -c_2u_{3,11}^0(x_1) + c_3\gamma_{13,1}^0(x_1)\end{aligned} \tag{16}$$

with

$$c_3 = E_{11}\int_S f^2(x_3)\,\mathrm{d}S \tag{17}$$

$$H(x_1) = \int_S f_{,3}(x_3)\sigma_{13}(x_1)\,\mathrm{d}S = \left[G_{13}\int_S f_{,3}^2(x_3)\,\mathrm{d}S\right]\gamma_{13}^0(x_1) = c_4\gamma_{13}^0(x_1) \tag{18}$$

with

$$c_4 = G_{13}\int_S f_{,3}^2(x_3)\,\mathrm{d}S. \tag{19}$$

Constants c_2, c_3, c_4 are explicitly given in Table 1 in the case of a beam with a constant rectangular cross-section of width b and thickness h.

2.3.3. Governing equations

Governing equations of the present problem can be established by using expressions of the internal (Eq. (11)) and external (Eq. (10)) virtual work. The equilibrium expression can be rearranged, and once integrated by parts it writes:

$$\begin{aligned}&-\int_0^\ell \Big(N_{,1}\delta u_1^0 + \Big(((M+B)_{,1} - H)_{,1} - p\Big)\delta u_3^0 + (B_{,1} - H)\delta\phi^0\Big)\,\mathrm{d}x_1 + \Big[-N\delta u_1^0 + ((M+B)_{,1} - H)\\ &\times\delta u_3^0 - (M+B)\delta u_{3,1}^0 + B\delta\phi^0\Big]_0^\ell\\ &+ F_3(\ell)\delta u_3^0(\ell) + F_1(\ell)\delta u_1^0(\ell)\\ &+ M_2(\ell)\delta\phi^0(\ell) = 0 \quad \forall(\delta u_1^0, \delta u_3^0, \delta\phi^0)\ \text{K.A.}\end{aligned} \tag{20}$$

This equation holds for any virtual field K.A. defined by δu_1^0, δu_3^0 and $\delta\phi^0$.

Consequently, the governing equations are easily derived:

$$\begin{aligned}&N_{,1} = 0,\\ &B_{,1} - H = 0,\\ &-((M+B)_{,1} - H)_{,1} + p = 0.\end{aligned} \tag{21}$$

On the boundaries of the beam, i.e. at $x_1 = 0$ and $x_1 = \ell$, restriction can be set either on displacements or forces.

Table 1
Expression of the various coefficients vs. the form of function $f(x_3)$

	Euler–Bernoulli $f(x_3)=0$	Timoshenko $f(x_3)=x_3$	Cubic (C) $f(x_3)=x_3\left(1-\frac{4x_3^2}{3h^2}\right)$	Sine (S) $f(x_3)=\frac{h}{\pi}\sin\left(\frac{x_3\pi}{h}\right)$
c_1	0	$E_{11}b\frac{h^3}{12}$	$E_{11}b\frac{h^3}{12}$	$E_{11}b\frac{h^3}{12}$
c_2	0	$E_{11}b\frac{h^3}{12}$	$E_{11}b\frac{h^3}{15}$	$E_{11}b\frac{2h^3}{\pi^3}$
c_3	0	$E_{11}b\frac{h^3}{12}$	$E_{11}b\frac{17h^3}{315}$	$E_{11}b\frac{h^3}{2\pi^2}$
c_4	0	$G_{13}bh$	$G_{13}b\frac{8h}{15}$	$G_{13}b\frac{h}{2}$
ω	0	∞	$\frac{1}{h}\sqrt{\frac{G_{13}}{E_{11}}840}$	$\frac{1}{h}\sqrt{\frac{G_{13}\pi^6}{E_{11}\pi^4-96}}$
S_f	–	$\frac{1}{k}\left(\frac{h}{L}\right)^2\frac{E_{11}}{G_{13}}$[a]	$\left(\frac{h}{L}\right)^2\frac{E_{11}}{G_{13}\frac{5}{6}}$	$\left(\frac{h}{\ell}\right)^2\frac{E_{11}}{G_{13}\frac{\pi^6}{1152}}$

[a] $k=\frac{5}{6}$ for a rectangular homogeneous section.

Essential (Neumann) and natural (Dirichlet) boundary conditions then write, for instance at $x_1=\ell$ where concentrated loads are applied:

$$\delta u_1^0=0 \text{ or } -N+F_1=0,$$
$$\delta\phi^0=0 \text{ or } B+M_2=0,$$
$$\delta u_{3,1}^0=0 \text{ or } M+B=0,$$
$$\delta u_3^0=0 \text{ or } (M+B)_{,1}-H+F_3=0. \quad (22)$$

Complete formulation of a displacement field accounting for section warping is set. Its relevance is shown below in the simple case of a three-point bending test.

3. Solution associated with the three-point bending configuration

In this case, as sketched in Fig. 3, only a half of the beam is considered for the sake of symmetry, then the present problem is equivalent to the one used above simply by substituting ℓ for $\frac{L}{2}$ (see Fig. 2). In the framework of small perturbations and under this loading, only bending takes place. Consequently, one can use the above approach but where the in-plane terms $N(x_1)$ and $u_1^0(x_1)$ are ignored. Then the problem to solve reduces to the two last equations of Eq. (21) along with the three last boundary conditions in Eq. (22).

3.1. Boundary conditions

At $x_1=0$, the displacement is prevented along $\mathbf{e}_3$. At $x_1=L/2$ the section rotation is zero for the sake of symmetry:

$$u_3^0(0)=0,$$
$$u_{3,1}^0(L/2)=0,$$
$$\phi^0(L/2)=0. \quad (23)$$

Complementary natural conditions are derived from Eq. (22):

$$M_{,1}\left(\frac{L}{2}\right)+B_{,1}\left(\frac{L}{2}\right)-H\left(\frac{L}{2}\right)+\frac{F_3}{2}=0,$$
$$B(0)+M(0)=0,$$
$$B(0)=0. \quad (24)$$

3.2. Equation of equilibrium

3.2.1. Equilibrium in terms of displacement

The problem is completely defined with the boundary conditions in Eqs. (23) and (24) and with the equilibrium equations in Eq. (21). In order to be solved as a differential equation, it is rewritten as a function of the displacement field sought. Introducing definitions previously established for generalized forces and moments

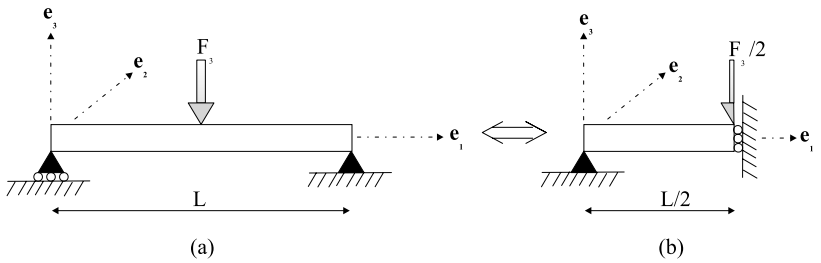

Fig. 3. Schematical three-point bending (a) half-model used for solving (b).

(Eqs. (13), (16) and (18)), the system built up with the two last equations in Eq. (21) becomes:

$$\begin{aligned}&(c_1-c_2)u^0_{3,1111}-(c_2-c_3)\gamma^0_{13,111}-c_4\gamma^0_{13,1}=0,\\&-c_2u^0_{3,111}+c_3\gamma^0_{3,11}-c_4\gamma^0_{13}=0,\end{aligned}\tag{25}$$

where the c_i's are constant terms defined in Eqs. (14), (15), (17) and (19).

Associated boundary conditions which deduce from Eq. (24) lead to:

$$\begin{aligned}&(c_1-c_2)u^0_{3,11}(0)-(c_2-c_3)\gamma^0_{13,1}(0)=0\\&-c_2u^0_{3,11}(0)+c_3\gamma^0_{13,1}(0)=0\\&(c_1-c_2)u^0_{3,111}(L/2)-(c_2-c_3)\gamma^0_{13,11}(L/2)\\&\quad-c_4\gamma^0_{13}(L/2)+\frac{F_3}{2}=0.\end{aligned}\tag{26}$$

Integrating the first equation of system (25) and combining it with the second one leads to the following system:

$$\begin{aligned}&-c_1u^0_{3,111}+c_2\gamma^0_{13,11}=A_1,\\&-c_2u^0_{3,111}+c_3\gamma^0_{13,11}=c_4\gamma^0_{13},\end{aligned}\tag{27}$$

where A_1 is an integration constant. Through a simple combination of these two equations, one obtains a differential equation where γ^0_{13} is unknown:

$$\gamma^0_{13,11}-\left[\frac{c_1c_4}{c_1c_3-c_2^2}\right]\gamma^0_{13}=-\left[\frac{c_2}{c_1c_3-c_2^2}\right]A_1\tag{28}$$

3.2.2. Solution of the differential equation

Solving the above differential equation requires to seek, first, one particular solution $\gamma^0_{13p}(x_1)$ of the whole equation and second, a general solution $\gamma^0_{13h}(x_1)$ of the associated homogeneous equation, i.e. Eq. (28) without the right-hand side term:

$$\gamma^0_{13h,11}-\frac{c_1c_4}{c_1c_3-c_2^2}\gamma^0_{13h}=0.\tag{29}$$

The particular solution $\gamma^0_{13p}(x_1)$ is constant and writes:

$$\gamma^0_{13p}(x_1)=\frac{c_2}{c_1c_4}A_1.\tag{30}$$

Hence the total solution writes:

$$\gamma^0_{13}(x_1)=\gamma^0_{13p}+\gamma^0_{13h}=\frac{c_2}{c_1c_4}A_1+\gamma^0_{13h}.\tag{31}$$

It clearly appears in Eq. (29) that the solution of this second equation depends on the sign of the term $\frac{c_1c_4}{c_1c_3-c_2^2}$. This sign can easily be determined by considering the definitions of these constants introduced in Eqs. (14), (15), (17), (19):

$$\frac{c_1c_4}{G_{13}}=\int_S f^2_{,x_3}\,\mathrm{d}S\,E_{11}\int_S x_3^2\,\mathrm{d}S>0,\tag{32a}$$

$$\frac{c_2^2-c_1c_3}{E_{11}}=\left(\int_S x_3f(x_3)\,\mathrm{d}S\right)^2-\left(\int_S x_3^2\,\mathrm{d}S\right)\times\left(\int_S f^2(x_3)\,\mathrm{d}S\right)<0.\tag{32b}$$

As $f(x_3)$ is an odd function positive defined, the numerator is the product of two positive integrals (Eq. (32a)) and therefore is always positive defined. The denominator (Eq. (32b)) shows that since the integral is a valid scalar product in the space of continuous functions, this inequality is of the Cauchy–Schwarz type. Since $f(x_3)$ is an odd function, the Cauchy–Schwarz property holds when elevated at the square and therefore the denominator is strictly positive. Eventually, the associated homogeneous equation (Eq. (29)) to be solved can be written as:

$$\gamma^0_{13h,11}-\omega_f^2\gamma^0_{13h}=0,\tag{33}$$

where ω_f is a scalar that depends on $f(x_3)$:

$$\omega_f=\sqrt{\frac{c_1c_4}{c_1c_3-c_2^2}}.\tag{34}$$

Then the solution of the differential equation of Eq. (27) writes:

$$\gamma^0_{13}(x_1)=\frac{c_2}{c_1c_4}A_1+\alpha\sinh(\omega_fx_1)+\beta\cosh(\omega_fx_1),\tag{35}$$

where α, β, A_1 are the three constants to be determined from the boundary conditions. At this stage, the sought displacement field must be expressed *vs.* the above form of the shear strain such that boundary conditions (Eqs. (23) and (24)) can be used to solve the problem. The third derivative of u_3 is obtained by introducing the complete solution (Eq. (35)) in the equilibrium equations written in terms of displacements (Eq. (27)). It is then integrated to obtain u_3. The section rotation $\phi^0(x_1)$ is finally obtained by using the relationship between the shear strain and section rotations of Eq. (2). Eventually, the solution writes:

$$\begin{aligned}u^0_3(x_1)=&\frac{c_2}{c_1}\frac{1}{\omega_f}[\alpha\cosh(\omega_fx_1)+\beta\sinh(\omega_fx_1)]\\&-\frac{A_1}{c_1}\frac{x_1^3}{6}+A_2\frac{x_1^2}{2}+A_3x_1+A_4,\\\phi^0(x_1)=&-\left(1-\frac{c_2}{c_1}\right)[\alpha\sinh(\omega_fx_1)+\beta\cosh(\omega_fx_1)]\\&-\frac{A_1}{c_1}\frac{x_1^2}{2}+A_2x_1+A_3-A_1\frac{c_2}{c_1c_4},\end{aligned}\tag{36}$$

where A_2, A_3, A_4, are the three additional constants to be determined. The six constants α, β, A_{1-4} are obtained from the boundary conditions written both in terms of displacements (Eq. (23)) and forces (Eq. (24)). They lead to the following six expressions:

$$\begin{aligned} A_1 &= \tfrac{F_3}{2}, & A_4 &= 0, \\ A_2 &= 0, & \alpha &= 0, \\ A_3 &= \tfrac{F_3}{2c_1}\left[\tfrac{c_2^2}{c_1c_4}\right], & \beta &= -\tfrac{c_2}{c_1c_4}\,\tfrac{F_3}{2}\,\tfrac{1}{\cosh\left(\omega_f\frac{L}{2}\right)}. \end{aligned} \tag{37}$$

After some calculations, the solution finally writes:

$$\begin{aligned} u_1(M) = &-x_3\frac{F_3}{2c_1}\left[-\frac{x_1^2}{2}+\left(\frac{c_2^2}{c_4c_1}+\frac{L^2}{8}\right)\right. \\ &\left.-\frac{c_2^2}{c_4c_1}\,\frac{\cosh(\omega_f x_1)}{\cosh\left(\omega_f\frac{L}{2}\right)}\right] \\ &+f(x_3)\frac{F_3}{2c_1}\,\frac{c_2}{c_4}\left[1-\frac{\cosh(\omega_f x_1)}{\cosh\left(\omega_f\frac{L}{2}\right)}\right] \\ u_3(M) = &\frac{F_3}{2c_1}\left[-\frac{x_1^3}{6}+\left(\frac{c_2^2}{c_4c_1}+\frac{L^2}{8}\right)x_1\right. \\ &\left.-\frac{c_2^2}{c_4c_1}\,\frac{1}{\omega_f}\,\frac{\sinh(\omega_f x_1)}{\cosh\left(\omega_f\frac{L}{2}\right)}\right] \end{aligned} \tag{38}$$

with

$$\begin{aligned} \phi^0(x_1) = -\frac{F_3}{2c_1}\,\frac{c_2}{c_4}\left[\left(\frac{c_2}{c_1}-1\right)\frac{\cosh(\omega_f x_1)}{\cosh\left(\omega_f\frac{L}{2}\right)}+\frac{c_4}{c_2}\,\frac{x_1^2}{2}\right. \\ \left.-\frac{c_2}{c_1}-\frac{c_4}{c_2}\,\frac{L^2}{8}+1\right]. \end{aligned} \tag{39}$$

3.3. Displacements and strains

These equations can be rewritten in a clearer fashion. Let us first introduce a term obtained from the classical theory of beams which represents the contribution of bending only. This term varies from 0 to L for x_1 ranging from 0 to $\frac{L}{2}$:

$$\Theta(x_1) = -x_1\left(4\left(\frac{x_1}{L}\right)^2-3\right). \tag{40}$$

Second, the part of this displacement field induced when taking shear into account depends on a dimensionless constant term which can be expressed vs. the c_i constants. Let this term be denoted by S_f and have the following form:

$$S_f = \frac{12}{L^2}\,\frac{c_2^2}{c_1c_4}. \tag{41}$$

Finally a function gathering the terms appearing when shear is accounted for is introduced. Let $\Psi_f(x_1)$ be this function that depends on $f(x_3)$ through ω_f defined in Eq. (34):

$$\Psi_f(x_1) = x_1 - \frac{1}{\omega_f}\,\frac{\sinh(\omega_f x_1)}{\cosh\left(\omega_f\frac{L}{2}\right)}. \tag{42}$$

Feeding equations (40), (42), and (41) and notation (equation (14)) in the displacement field (Eq. (38)) leads to:

$$\begin{aligned} u_1(M) = &-x_3\frac{F_3L^2}{48E_{11}I_{22}}\left[\Theta_{,1}(x_1)+2S_f\Psi_{f,1}(x_1)\right] \\ &+f(x_3)\frac{F_3}{2c_2}\,\frac{L^2}{12}S_f\Psi_{f,1}(x_1), \\ u_3(M) = &\frac{F_3L^2}{48E_{11}I_{22}}\left[\Theta(x_1)+2S_f\Psi_f(x_1)\right]. \end{aligned} \tag{43}$$

In the above expression of displacement, the first term of u_1 describes the solution of a simple bending case within the framework of Euler–Bernoulli's theory. The second and third terms both account for shear and cancel each other in the case of Timoshenko's theory. According to Eq. (3), by simple derivations of Eq. (43), one gets the strain components that write:

$$\begin{aligned} \varepsilon_{11}(M) = &-x_3\frac{F_3L^2}{48E_{11}I_{22}}\left[\Theta_{,11}(x_1)+2S_f\Psi_{f,11}(x_1)\right] \\ &+f(x_3)\frac{F_3L^2}{24c_2}S_f\Psi_{f,11}(x_1), \\ \gamma_{13}(M) = &f_{,3}\frac{F_3L^2}{24c_2}S_f\Psi_{f,1}(x_1). \end{aligned} \tag{44}$$

A general solution has been proposed for a beam under three-point bending loading. This solution holds for any odd function $f(x_3)$ and we shall use it to compare the solution obtained through different beam theories.

4. Assessment of the three-point bending solution for various warping functions

Here four different theories, namely the theories proposed by Euler–Bernoulli, Timoshenko [2], and two different higher-order theories are considered. These latter correspond, respectively, to cubic (denoted by C henceforth) and sine (S) warping function $f(x_3)$, they derive from plate theories described in [7] and [5]. Thus the main difference between these theories lies in the form of the function $f(x_3)$, i.e. the accuracy of the account of shear deformation in the sections (Eqs. (45a)–(45d)):

$$f(x_3) = 0, \tag{45a}$$

$$f(x_3) = x_3, \tag{45b}$$

$$f(x_3) = x_3\left(1-\frac{4x_3^2}{3h^2}\right), \tag{45c}$$

$$f(x_3) = \frac{h}{\pi}\sin\left(\frac{x_3\pi}{h}\right), \tag{45d}$$

where h is the beam thickness.

Henceforth, the beam is assumed to have a section of width $b = 30$ mm. First, let us consider a range over which the material and geometrical parameters can vary. The ratio of the Young's and shear moduli $\frac{E_{11}}{G_{13}}$ will belong to $[2.6, 40]$, i.e. materials represented will vary from steel to 60% carbon fiber unidirectional plies [11]. $\frac{L}{h}$ lies

between 5 and 20 to study the influence of the aspect ratio. The most common ratios used in the following are $\frac{E_{11}}{G_{13}} = 40$ with $E_{11} = 140$ MPa, and $\frac{L}{h} = 5$ with $L = 20$. A load $F_3 = 5000$ N applied at mid-span will be considered.

4.1. Displacement fields

4.1.1. Deflection u_3

From Table 1 the deflection (Eq. (43)) becomes for the different theories:

$$u_3(M) = \frac{F_3 L^2}{48 E_{11} I_{22}} \Theta(x_1), \tag{46a}$$

$$u_3(M) = \frac{F_3 L^2}{48 E_{11} I_{22}} [\Theta(x_1) + 2S x_1], \tag{46b}$$

$$u_3(M) = \frac{F_3 L^2}{48 E_{11} I_{22}} [\Theta(x_1) + 2S_C \Psi_C(x_1)], \tag{46c}$$

$$u_3(M) = \frac{F_3 L^2}{48 E_{11} I_{22}} [\Theta(x_1) + 2S_S \Psi_S(x_1)], \tag{46d}$$

where index $_f$ is now either $_C$ or $_S$ and denotes 'associated with' a cubic (like in Reddy's work) or a sine (like in Touratier's) warping function $f(x_3)$. S_C and S_S are defined from Eq. (41) and $\Psi_C(x_1)$ and $\Psi_S(x_1)$ from Eq. (42).

One can check that depending on the considered theory, both the classical and the higher-order results can be found. First, the Euler–Bernoulli's theory leads to the very well-known expression for simple bending without shear (Eq. (46a)). For Timoshenko's theory, the dimensionless shear coefficient S is introduced that allows for the shear to be taken into account (Eq. (46b)). It can be noticed that S is classically weighted by a constant $\frac{1}{k}$ (see Table 1) established usually from a shear energy equivalence between constant and parabolic shear distributions across the thickness [1,3]. k is equal to $\frac{5}{6}$ for a rectangular homogeneous section. Finally for higher-order theories (Eqs. (46c) and (46d)), it appears that the function $f(x_3)$ which is initially introduced to verify stress-free conditions on the top and bottom surfaces of the beam leads to a further dependence of the deflection upon the coordinate x_1 through $\Psi_f(x_1)$. This non-linear dependence tends to smoothen the slope of the deflected shape when compared to Euler–Bernoulli's and Timoshenko's theories (Fig. 4). This comes from the function $\Psi_f(x_1)$ which is not constant but varies gradually (Fig. 5) to reach a finite value at $x_1 = L/2$.

It can be noticed that deflections obtained for higher-order theory formulations are very close. This is due simply to the form of function $f(x_3)$ which in the case of a cubic warping function corresponds to a development in series up to the order 3 of function $\sin(x_3)$ used in [5]. Development of this function to higher order would probably not bring further accuracy to the results. Order 3 kept for a cubic function is sufficient to verify the slope

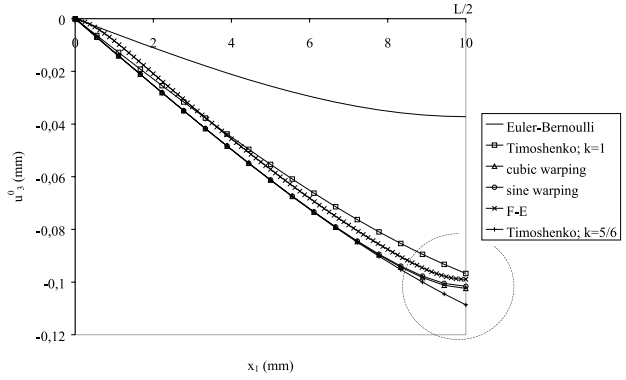

continuity at mid-span contrary to Timoshenko's theory (Fig. 4).

One can check in Fig. 4 that higher-order theories provide a solution that is very close to FE analyses carried out with the ANSYS 5.5 software. A parametric numerical model of a half-beam has been defined, the convergence of which is ensured by a sufficiently refined mesh made up of about 1300 eight-noded PLANE82 elements.

4.1.2. Longitudinal displacement u_1

From the general solution (Eq. (43)), expression of the longitudinal component $u_1(M)$ of the displacement field can be established (Eqs. (48a)–(48i)) for the four considered theories. In Fig. 6 where the corresponding displacement $u_1(M)$ are represented, the effect of section warping clearly appears. Higher-order theories lead to a profile which is made up of a cubic distribution superimposed onto the classical linear distribution of Euler–Bernoulli (identical to Timoshenko's in Fig. 6) through the thickness of the beam.

More precisely, displacement $u_1(M)$ can be represented as the sum of several terms. Indeed, from the initial expression of displacements (Eq. (1)) the longitudinal component depends on both deflection (Eqs. (47a) and (47b)) and warping (Eq. (47c)), respectively,

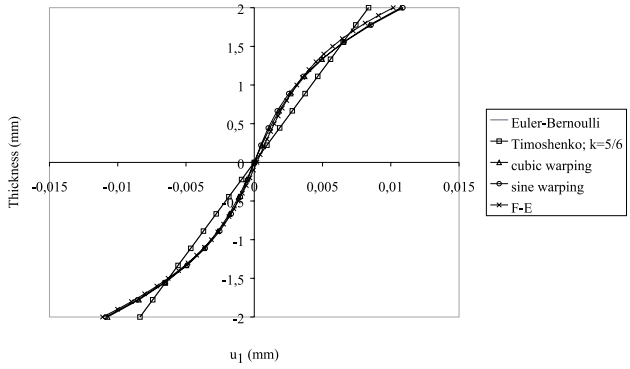

Fig. 6. Profile of displacement $u_1(M)$ at $x_1 = \frac{L}{4}$ for $\frac{E_{11}}{G_{13}} = 40$ and $\frac{L}{h} = 5$.

the second and third terms of Eq. (1) . The deflection (Eqs. (46a)–(46d)) also depends on a part of bending alone ($\Theta(x_1)$) yielding Eq. (47a), and on a shear contribution ($S_f \Psi_f(x_1)$) yielding Eq. (47b). Eventually, the longitudinal displacement $u_1(M)$ writes without in-plane displacement:

$$u_1(M) = -x_3 u^0_{3,1}\theta(x_1), \tag{47a}$$
$$-x_3 u^0_{3,1} S_f \Psi_f(x_1), \tag{47b}$$
$$+f(x_3)\gamma^0_{13}(x_1). \tag{47c}$$

In the framework of each of the four theories considered and following Eqs. (47a)–(47c), expressions of displacement $u_1(M)$ become:

$$u_1(M) = -x_3 \frac{F_3 L^2}{48 E_{11} I_{22}} \Theta_{,1}(x_1) \tag{48a}$$
$$u_1(M) = -x_3 \frac{F_3 L^2}{48 E_{11} I_{22}} [\Theta_{,1}(x_1) \tag{48b}$$
$$+2S] \tag{48c}$$
$$+x_3 \frac{F_3 L^2}{24 E_{11} I_{22}} S \tag{48d}$$
$$u_1(M) = -x_3 \frac{F_3 L^2}{48 E_{11} I_{22}} [\Theta_{,1}(x_1) \tag{48e}$$
$$+2S_C \Psi_{C,1}(x_1)] \tag{48f}$$
$$+x_3 \left(1 - \frac{4x_3^2}{3h^2}\right) \frac{F_3 L^2}{24 E_{11} I_{22}} \frac{5}{4} S_C \Psi_{C,1}(x_1) \tag{48g}$$
$$u_1(M) = -x_3 \frac{F_3 L^2}{48 E_{11} I_{22}} [\Theta_{,1}(x_1) \tag{48h}$$
$$+2S_S \Psi_{S,1}(x_1)] \tag{48i}$$
$$+\frac{h}{\pi} \sin\left(\frac{\pi x_3}{h}\right) \frac{F_3 L^2}{24 E_{11} I_{22}} \frac{\pi^3}{24} S_S \Psi_{S,1}(x_1). \tag{48j}$$

As can be seen in Fig. 7(a) Euler–Bernoulli's solution (Eq. (48a)) appears alone when shear is not considered. In Timoshenko's solution (Fig. 7(b)), contributions of shear both in deflection (Eq. (48c)) and warping (Eq. (48d)) cancel each other. This finally leads to the same displacement $u_1(M)$ as in Euler–Bernoulli's theory (Eq. (48a)) but for different deflections. In all these theories,

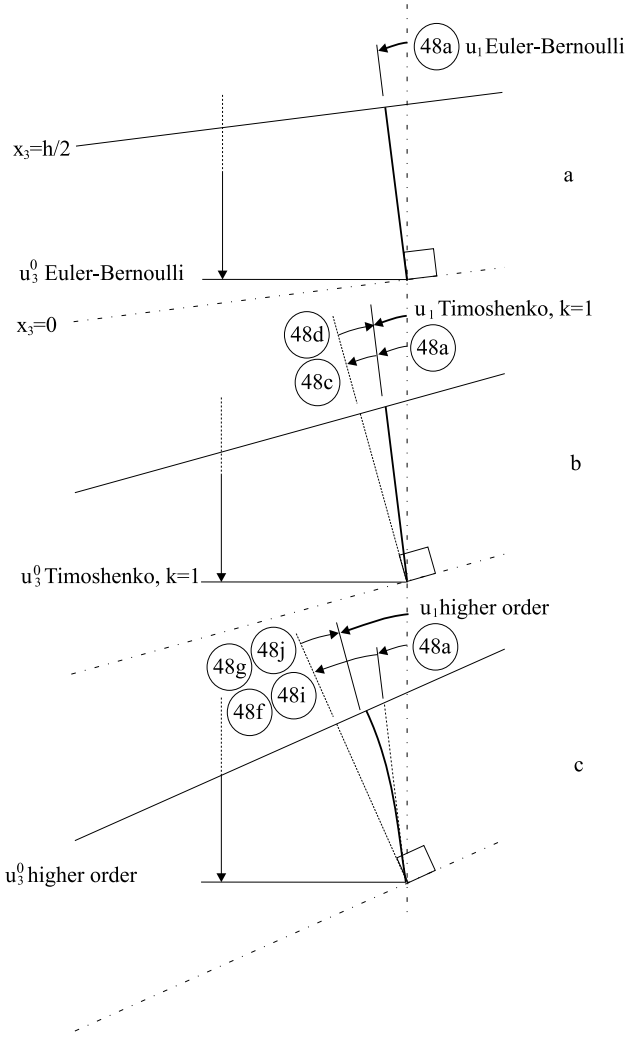

Fig. 7. Contribution of the various terms to the longitudinal displacement $u_1(M)$ on the top face of the beam for the different theories: (a) Euler–Bernoulli; (b)Timoshenko ($k = 1$); (c) higher-order.

the second part of the displacement $u_1(M)$ corresponding to Eq. (47b) linearly depends on a rotation induced by the contribution of shear in the deflection. This term is the rotation of the section required to get a deformed section perpendicular to the mean-line (Eqs. (48c), (48f) and (48i)).

The last part of displacement $u_1(M)$ (Eq. (47c)) corresponds to the contribution of warping which yields an opposite displacement that varies through the thickness (Fig. 7(c)) following the form of $f(x_3)$ (Eq. (48g) and (48j)). This corresponds to the evidence of section warping.

Owing to the dependence of displacement $u_1(M)$ upon x_1, especially through $\Psi_f(x_1)$, warping of the section varies along the mean-line. According to Fig. 8, the section warping amplitude is defined as the difference between the total displacement profile and a straight line connecting the displacements at the top and bottom skins.

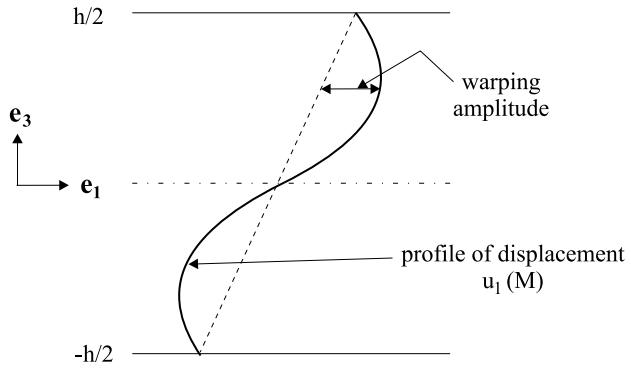

Fig. 8. Definition of the section warping amplitude.

The maximum warping amplitude, even if it is small, represents 16% of the total displacement $u_1(M)$ calculated at $x_3 = \frac{h}{2}$. As can be seen in Fig. 9, the warping amplitude is constant along the mean-line as long as x_1 is smaller than $\frac{L}{2}$, and then it quickly tends towards 0 when this limit is reached. This change is directly related to $\Psi_{f,1}(x_1)$ (Fig. 5), upon which $u_1(M)$ depends, which is different from zero only for higher-order theories and vanishes close to $\frac{L}{2}$. It lies between 1 and 0 for x_1 ranging from 0 to $\frac{L}{2}$.

4.1.3. Shear strain components

$\gamma_{13}(M)$ is obtained from Table 1 and from the general expression of transverse shear strain (Eq. (44)). One gets for the various forms of $f(x_3)$ (Eqs. (45a)–(45d)):

$$\gamma_{13}(M) = \frac{F_3}{2G_{13}bh}, \tag{49a}$$

$$\gamma_{13}(M) = \left(1 - \frac{4x_3^2}{h^2}\right)\frac{F_3}{2G_{13}bh}\frac{3}{2}\Psi_{C,1}(x_1), \tag{49b}$$

$$\gamma_{13}(M) = \cos\frac{\pi x_3}{h}\frac{F_3}{2G_{13}bh}\frac{48}{\pi^3}\Psi_{S,1}(x_1). \tag{49c}$$

It is no surprise that for Timoshenko's theory (Eq. (49a)), the shear strain is constant through the beam thickness all over the span. Conversely, cubic (Eq. (49b)) and sine (Eq. (49c)) theories lead to parabolic or cosine distributions of strain across the thickness (Fig. 10) which satisfy stress-free conditions on both skins.

The amplitude of this distribution vanishes very gradually (Fig. 11) at $x_1 = \frac{L}{2}$ owing to the term $\Psi_{f,1}(x_1)$ (Fig. 5). This smooth variation permits to avoid the shear strain discontinuity that appears classically at mid-span in Timoshenko's theory. This appears clearly in Fig. 11 where the accuracy of such theories can be directly compared with the FE analysis results.

A good correlation is observed between the higher-order theory solutions and the FE results. The variation of shear strains along the mean-line and the distribution through the beam are well represented, except the influence of the support at $x_1 = 0$ that was not accounted for in the present work.

4.2. Influence of material and geometrical characteristics on the solution

Various coefficients have been previously defined that depend on both geometry and constitutive material of the considered beam. Here the variations of the solution when these characteristics vary are investigated. Especially the different theories vary from one to another through the two terms S_f and $\Psi_f(x_1)$ which, respectively, represent the account of shear and the correction to shear brought by higher-order theories. Conversely

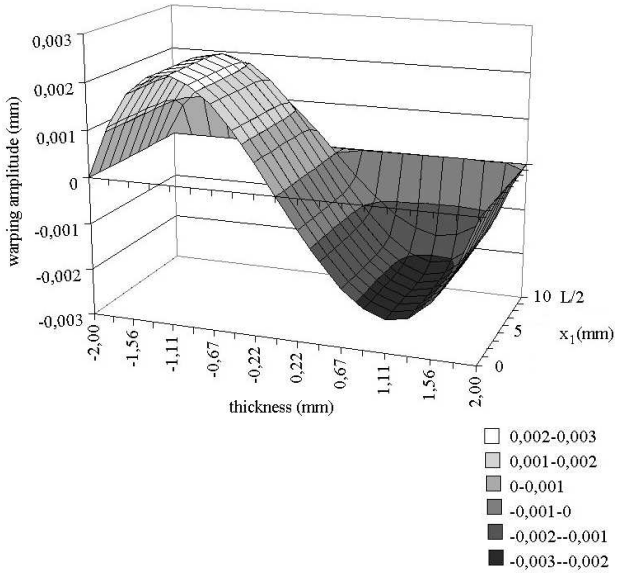

Fig. 9. Warping amplitude vs. x_1 for $\frac{E_{11}}{G_{13}} = 40$ and $\frac{L}{h} = 5$.

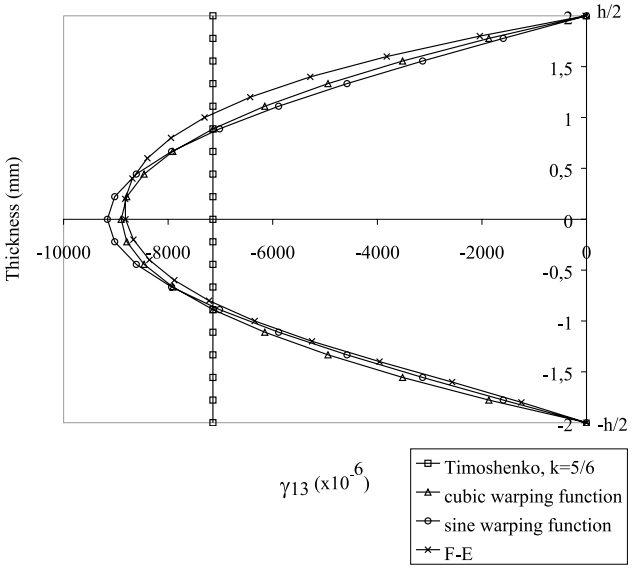

Fig. 10. Transverse shear strain across the beam thickness at $x_1 = \frac{L}{4}$ for $\frac{E_{11}}{G_{13}} = 40$ and $\frac{L}{h} = 5$.

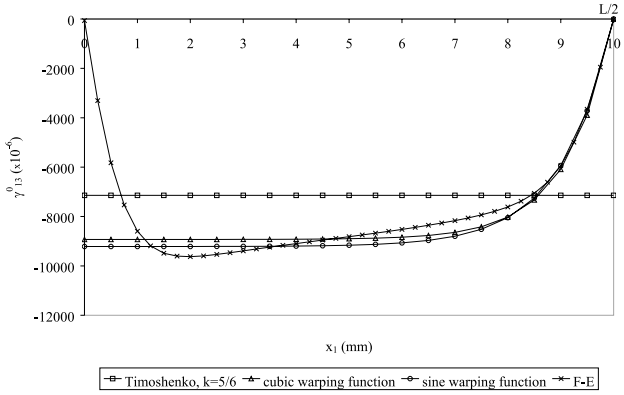

Fig. 11. Transverse shear strain on the mean-line for $\frac{E_{11}}{G_{13}} = 40$ and $\frac{L}{h} = 5$.

$\Theta(x_1)$ (Eq. (40)) that represents the bending contribution only depends on the beam span and not at all on the considered material.

4.2.1. Deflection

Let us recall that $\Theta(x_1)$ varies from 0 to L when x_1 ranges from 0 to $\frac{L}{2}$. The contribution of simple bending in the deflection (Eqs. (46a)–(46d)) through $\Theta(x_1)$ is therefore constant whatever the material and lengths considered. Conversely, when the shear is introduced there is a variation of S_f (Fig. 12 for Timoshenko's theory) when geometry and materials vary, i.e. the contribution of shear in the deflection changes.

In Timoshenko's solution (Eq. (46b)) this change increases the resulting deflection either for short beams or high moduli ratios, accordingly to classical results from strength of materials. This appears clearly when S varies: S greater than one in Eq. (46b), i.e. $2S\frac{L}{2} > \Theta(\frac{L}{2})$, means that the deflection induced by bending only becomes smaller than the deflection induced by shear.

As for higher-order theories (Eq. (46c) and (46d)), S_f is similar to S (see Table 1):

$$S_C = S,$$
$$S_S \approx S. \tag{50}$$

One can notice that S_f is equal to S in which a ratio of $\frac{5}{6}$ is already included according to classical beam theories for a homogeneous rectangular cross-section. This reinforces the idea that a parabolic distribution appears naturally from the stress-free face assumption originating higher-order theories which therefore do not require any shear correction factor fictitiously introduced.

Let us compare the expressions of deflection obtained for Timoshenko (Eq. (46b)) and higher-order theories (Eqs. (46c) and (46d)). The largest deflection is at mid-span where the contribution of shear is equal to $2S\frac{L}{2}$ for Timoshenko whereas it is $2S_f\Psi_f(\frac{L}{2})$ for higher-order theories. For ranges of aspect ratios and moduli that fit in beam theories, higher-order theories lead to deflections always lower than for Timoshenko's. For instance, using a cubic warping section, Eq. (50) and results plotted in Fig. 13 lead to the following inequality for both deflections due to shear:

$$2S \geqslant 2S\frac{\Psi_C(\frac{L}{2})}{\frac{L}{2}} \text{ with } \frac{\Psi_C(\frac{L}{2})}{\frac{L}{2}} \in \left[\frac{5}{6}, 1\right]. \tag{51}$$

The improvement brought about by using higher-order theories is shown in Fig. 14, where the ratio of the de-

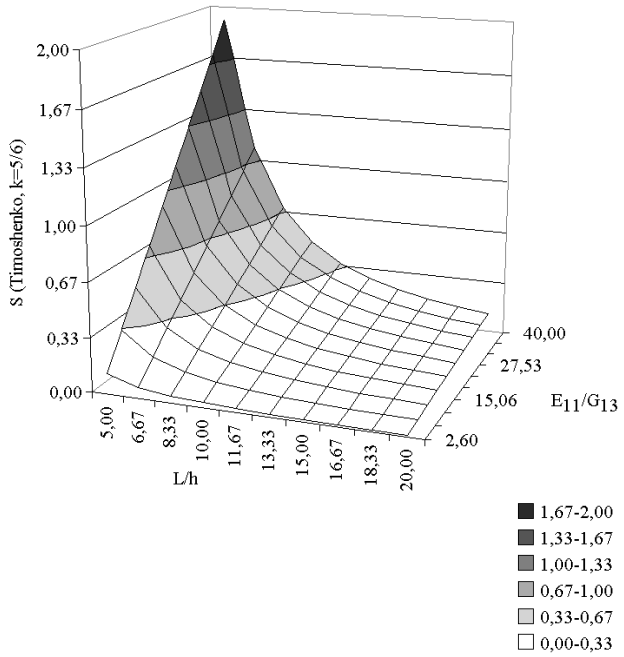

Fig. 12. Shear coefficient S vs. $\frac{E_{11}}{G_{13}}$ and $\frac{L}{h}$.

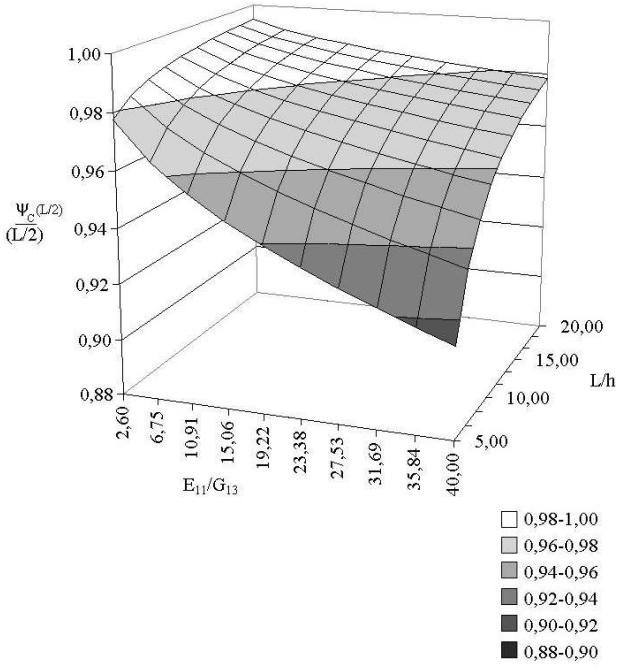

Fig. 13. $\frac{\Psi_C(L/2)}{L/2}$ vs. $\frac{E_{11}}{G_{13}}$ and $\frac{L}{h}$.

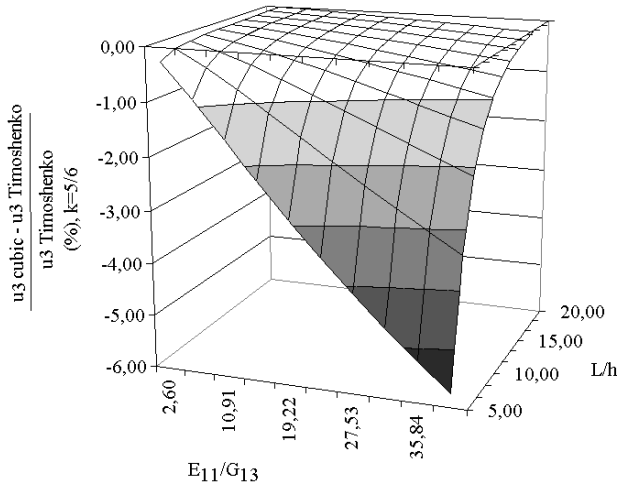

Fig. 14. Ratio of deflections obtained with a cubic warping function and Timoshenko's theory at $x_1 = \frac{L}{2}$ vs. $\frac{E_{11}}{G_{13}}$ and $\frac{L}{h}$.

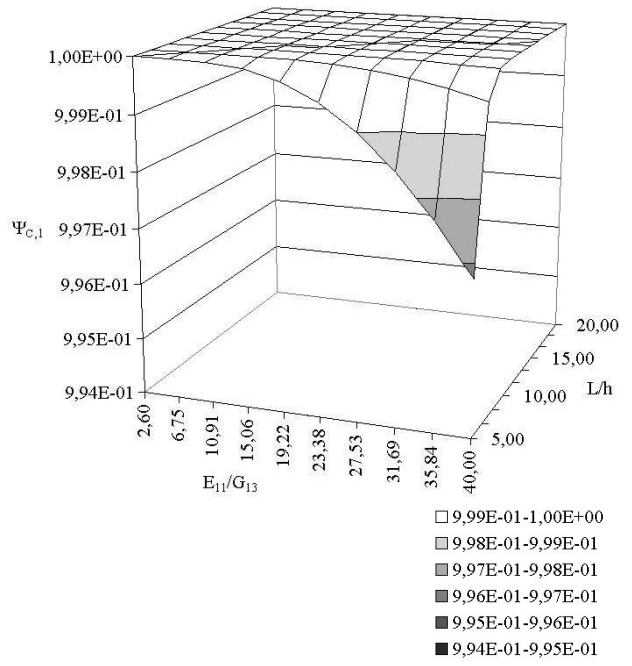

Fig. 15. $\Psi_{C,1}(x_1)$ vs. $\frac{E_{11}}{G_{13}}$ and $\frac{L}{h}$, $x = \frac{L}{4}$.

flections obtained with a cubic warping function and Timoshenko's theory are plotted. For high moduli ratios and small aspect ratios, i.e. when shear must be accounted for, a maximum difference of about 6% appears. We can see that the main improvement of these theories at this stage does not really come from a more accurate deflection prediction but from the continuity of strains at mid-span (Fig. 11).

4.2.2. Longitudinal displacement and transverse shear strains

Both longitudinal displacement $u_1(M)$ and transverse shear strain depend on $\Psi_{f,1}(x_1)$. This term modulates the shear part of the in-plane displacement and it can be seen in Fig. 15 that it depends on both geometry and material. Consequently, the way in which strain and displacement components vanish at mid-span varies with material and geometrical characteristics. This is clear when comparing Figs. 11 and 16 where only these characteristics are different. It can be seen that the part of the beam affected by the locking of warping increases as the ratio $\frac{E_{11}}{G_{13}}$ increases or $\frac{L}{h}$ decreases, that is to say when taking shear into account is no longer negligible compared to the bending contribution alone.

4.3. Conclusion

The results presented here clearly demonstrate that higher-order theories lead to more accurate predictions. They yield a better understanding of the section behavior and the results compare very well with the FE analyses. The most significant improvement is in terms of shear since the account of section warping is very rigorously established. The shear distribution across the thickness as well as the variation of amplitude along the mean-axis are properly represented. The main consequence of this dependence of the section warping upon the position on the mean-line is to avoid the singularity at mid-span of the beam which appears in Timoshenko' type theories. Also, it has been established that the precision of these predictions holds for a wide range of geometries and material data.

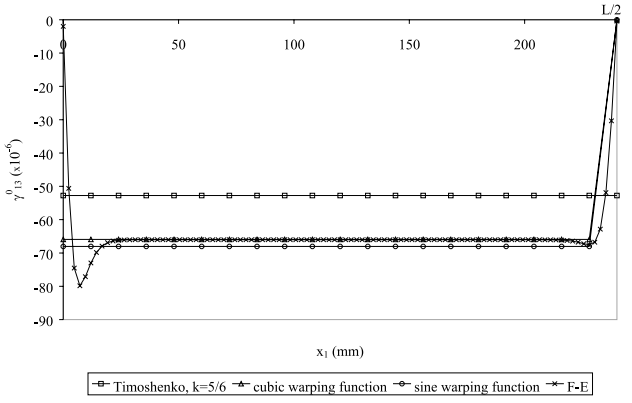

Fig. 16. Transverse shear strain on the mean-line for $\frac{E_{11}}{G_{13}} = 2.6$ and $\frac{L}{h} = 20$.

5. Comparison with experimental measurements

The validity of the proposed solution has been assessed through comparisons with experimental measurements presented in detail in [13]. Only the results which are relevant to illustrate this analytical approach are reported in the present section. Hence, configura-

Table 2
Characteristics of carbon/epoxy beams used to compare analytical predictions with experimental measurements and FE results

	Case 1	Case 2
Thickness h (mm)	20.27 mm	20.27 mm
Span L (mm)	125 mm	200 mm
Aspect ratio $\frac{L}{h}$	6.16	9.86
Loading for $u_3(\frac{L}{2}) = -1.75$ mm	22 kN	11.5 kN

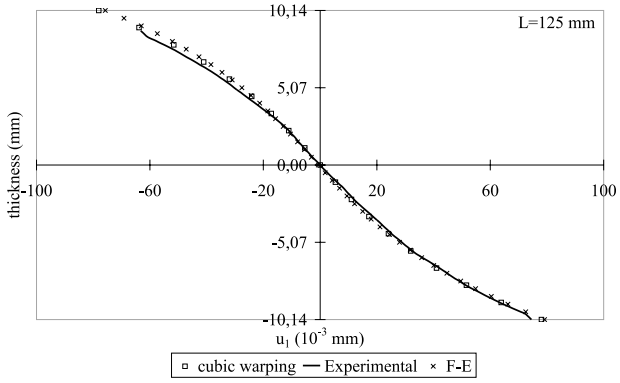

Fig. 17. Longitudinal displacement in $x_1 = \frac{3L}{4}$ for the 125-mm beam (see Table 2): analytical, FE and experimental measurements.

tions where the effect of transverse shear strains on the beam response prevails were selected. They correspond to small aspect ratio beams made up with a carbon/epoxy composite material which exhibits a high degree of anisotropy, i.e. an important $\frac{E_{11}}{G_{13}}$ ratio.

Experimentally, whole-field measurements of the displacement were performed onto the lateral surface of the bent specimens with a suitable optical method developed by Surrel and co-workers [12]. Experimental aspects of the method are not given here, full details can be found in [13].

For the present comparisons, a beam under three-point bending with two possible spans was considered. It is loaded in such a way that deflection at the center of the beam is -1.75 mm in both cases. The testing configurations and the loading magnitudes are both reported in Table 2. The beam moduli are $E_{11} = 115$ GPa and $G_{13} = 3$ GPa, leading to a high ratio $\frac{E_{11}}{G_{13}} = 38.3$.

In Fig. 17, a typical longitudinal displacement across the beam thickness is plotted for the 125-mm span. It can be verified that the analytical, FE and experimental results perfectly correlate. It must be pointed out that this refined scale of observation can only be reached experimentally thanks to an optical method.

In Fig. 18, for the two considered spans, the transverse shear strains of the mean-line in a window $[-23$ mm; 0] adjacent to the central loaded zone are plotted. The size of this window is directly controlled by the resolution of the CCD camera used to capture the grid positions. The strain is computed by differentiating numerically the displacement field with a suitable algorithm [14].

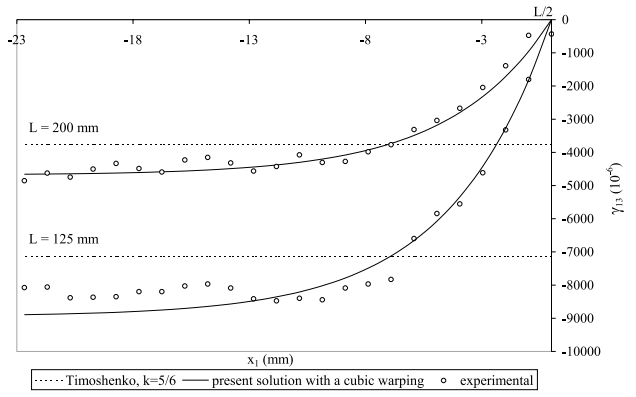

Fig. 18. Analytical and measured transverse shear strain on the mean-line for both 125 and 200 mm beams (see Table 2).

In this figure, it can be verified that the locking of the cross section warping is well represented by the simple analytical solution. Let us recall that the introduction of a warping function originates this dependence of the shear strain upon the position on the mean-line. Again, the measurements also perfectly correlate the analytical predictions. FE results are not plotted in this figure to keep it clear, but it was shown previously that analytical predictions fitted FE results (Figs. 11 and 16) well. Moreover, a similar perfect correlation was established by [13] for the transverse shear strain distributions through the thickness of the beam (as plotted in Fig. 10).

6. Conclusion

The results presented here clearly demonstrate the ability of higher-order theories to enhance predictions provided by classical beam theories. Comparisons of higher-order theories results with both FE analyses predictions and experimental measurements show a very good quantitative and qualitative correlation for homogeneous beams in terms of deflection as well as for shear strain distributions.

The most significant improvement is in terms of shear distribution since the account of section warping is very rigorously established. The shear distribution through the thickness as well as the variation of amplitude along the mean-axis are properly represented. Consequence of this dependence upon the position on the mean-line is to avoid the singularity at mid-span of the beam which appears in Timoshenko' type theories. Also, it has been established analytically that the precision of these predictions holds for a wide range of geometries and material data. Comparisons with the experimental measurements carried out on the most severe cases validated the accuracy of the analytical predictions.

Eventually these theories yield a realistic description of beam-like structures, even under severe loadings such as in three-point bending configurations where classical beam theories lack accuracy, for example in the case of short composite beams. Now, in order to assess all the effects which can appear in this type of severe loadings, refinements should be proposed to represent very local effects like indentation through enhanced beam models. This would finally lead to a beam theory able to capture the main phenomena which control the experimental identification of composite materials.

References

[1] Timoshenko SP. Strength of materials – Part I, 2nd ed. New York: D. Van Nostrand 1940. p. 170/71.
[2] Timoshenko SP, Gere JM. Mechanics of materials. New York: D.Van Nostrand; 1972.
[3] Reissner E. The effect of transverse shear deformation on the bending of elastic plates. J Appl Mech 1945;12:A69–77.
[4] Mindlin RD. Influence of rotatory inertia and shear on flexural motions of isotropic elastic plates. J Appl Mech 1951;18:31–8.
[5] Touratier M. An efficient standard plate theory. Int J Engng Sci 1991;29(8):901–16.
[6] Cheng S. Elasticity theory of plates and a refined theory. J Appl Mech 1979;46:644–50.
[7] Reddy JN, Liu CF. A higher-order shear deformation theory of laminated elastic shells. Int J Engng Sci 1985;23(3):319–30.
[8] Beakou A, Touratier M. A rectangular finite element for analysing composite multilayered shallow shells in statics vibration and buckling. Int J Num Meth Eng 1993;36:627–53.
[9] Standard test method for apparent interlaminar shear strength of parallel fiber composites by short-beam method. Technical Report D2344-84, ASTM Standard, 1995.
[10] Cui WC, Wisnom MR, Jones M. Failure mechanisms in three and four point short beam bending tests of unidirectional glass/epoxy. J Strain Anal 1992;27(4):235–43.
[11] Tsai WS, Hahn. Introduction to composite materials. Technomics, 1980.
[12] Surrel Y, Zhao B. Simultaneous u-v displacement field measurement with a phase-shifting grid method. Photomechanics 1994;2342:66–75.
[13] Dufort L, Grédiac M, Surrel Y. Experimental evidence of the cross-section warping in short composite beams under three-point bending. Comp Struct, 2000 (in press).
[14] Surrel Y. Design of algorithms for phase measurements by the use of phase stepping. Appl Opt 1996;35:51–60.

- P -

Annexe 2. 10

S. Drapier, A.Pagot, A. Vautrin, & P. Henrat

Influence of the stitching density on the transverse permeability of Non-Crimped New Concept (*NC2*) multiaxial reinforcements : measurements and predictions.

Comp. Sci. Technol. **, 62(15) :1979–1991, 2002.**

ELSEVIER

Composites Science and Technology 62 (2002) 1979–1991

COMPOSITES SCIENCE AND TECHNOLOGY

www.elsevier.com/locate/compscitech

Influence of the stitching density on the transverse permeability of non-crimped new concept (NC2) multiaxial reinforcements: measurements and predictions

S. Drapier[a,*], A. Pagot[a,1], A. Vautrin[a], P. Henrat[b]

[a] *Mechanical and Materials Engineering Department, SMS Division, École Nationale Supérieure des Mines de Saint-Étienne, 42023 Saint-Étienne Cedex 02, France*

[b] *Hexcel Fabrics, ZI Les nappes-38630 Les Avenières, France*

Received 29 April 2002; received in revised form 4 July 2002; accepted 8 July 2002

Abstract

New manufacturing processes arise for polymer-based composites which involve resin infusion through dry pre-forms. Modelling approaches of these processes require to assess new physical characteristics of the materials. In this paper, the transverse permeability of new multiaxial stitched materials, referred to as NC2, is investigated. First, in the framework of Darcy's flows, this permeability is assessed for various biaxial NC2 using a specific device. Through this approach it is shown that the transverse permeability depends strongly on the stitching density. Then, the results from a simplified FE study carried out at the blanket scale are shown to correlate quite well the experimental measurements and evidences established in the first part.

Keywords: Multiaxial reinforcements

1. Introduction

Till the early 1990s, high performance organic composite structures were mainly manufactured from pre-impregnated unidirectional plies. Since then, processes involving the resin impregnation in dry pre-forms have become very popular due to their versatility along with the cost reductions that they usually induce. Indeed, valuable cost cuts originate from the handling and storage cost reductions, since only the resin has to be cold-stored. But moreover in these processes thick/heavy multilayered preforms can be easily employed, this in turn induces material costs reductions.

In these manufacturing processes the impregnation stage is a key parameter [2,15]. Originally, liquid resins were injected through injection gates in molds containing the dry preforms. The most popular of these manufacturing processes, widely used, is the resin transfer molding (RTM). Modelling efforts, still continued, have permitted to optimise for the RTM the injection gates and events placements in the molds [12,14], in order for the mold to be completely filled and free of any air bubble which may be entrapped [15]. This injection takes place mainly in the preform plane and hence involves principally the longitudinal permeabilities properties of the preforms [3,19,22]. Other processes, involving rather resin infusion than resin injection and referred to as liquid composite molding (LCM), have been developed in the last few years. LCM processes permit us to overtake these problems of injection heterogeneities by impregnating the dry preforms over wide surfaces [11]. In this sense, lower pressures are involved, and the transverse permeability properties of the preforms become one of the key parameters to optimize the manufacturing cycles.

One of these processes is the resin film infusion (RFI) process in which films of neat resin are stacked, with dry preforms, in a mold. The use of a movable rigid perforated plate, or molds for more complex shapes, placed

* Corresponding author. Tel.: +33-04-77-42-00-79; fax: +33-04-77-42-49-02. (S. Drapier), Tel.: +33-04-74-33-88-60; fax: +33-04-74-33-99-02 (P. Henrat).

E-mail addresses: drapier@emse.fr (S. Drapier), vautrin@emse.fr (A. Vautrin), alexandre.pagot@ifp.fr (A. Pagot), patrick.henrat@hexcel-fabrics.fr (P. Henrat).

[1] Now at Institut Français du Pétrole, 1 et 4, avenue de Bois-Préau, 92852 Rueil-Malmaison Cedex, France.

0266-3538/02/$ - see front matter © 2002 Published by Elsevier Science Ltd.
PII: S0266-3538(02)00127-6

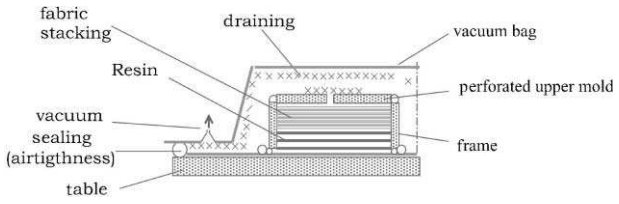

Fig. 1. Schematic of the resin film infusion process tooling.

on top of the stacking permits to ensure well-finished final surfaces. The whole stacking is then vacuum-bagged and usually placed in an autoclave to undergo a temperature-pressure cycle (Fig. 1). It is clear that the filling time and resin heterogeneity distributions in this process will depend mainly on the preform through-thickness permeability. This parameter is very seldom studied, since conversely to the longitudinal permeabilities, the length over which it can be measured is very small, of the order of 1 mm for single standard multiaxial reinforcements.

The present paper is dedicated to the study of the transverse permeability in long-fibre composites, more precisely in new multiaxial semi-products developed by Hexcel Fabrics. These non-crimped new concepts (NC2) multiaxial reinforcements are made up from very homogeneous planes of fibres stitched together through their thickness (see Fig. 2). The very high resulting homogeneity, essential to achieve high final mechanical properties, leads to very low permeabilities, much lower than the very few ones measured on other more classical materials. Then, in order to optimize the pressure-temperature cycles, the transverse permeability of single NC2 multiaxial fabrics must be input in some modelings of the impregnation process at the fabric scale.

In the present study, first, based on a quick survey of permeability measurements and fluid propagation in porous media, a specific set-up is designed to measure properly this permeability. This set-up is then used to assess the through-thickness permeability of biaxial NC2. These basic multiaxial fabrics are considered here to isolate the phenomena controlling the permeability. Then some simulations are presented at the blanket scale which focus on the effect of the stitching density onto the permeability. A good correlation is found between experimental measurements and predicted permeabilities regarding the stitching density influence.

2. The permeability phenomenon in composites

The transverse permeability phenomenon across composite multiaxial fabrics is introduced here, this permits to set up the basis of the principle of measurements. Then, longitudinal and transverse permeability measurements are presented.This yields some ideas for the set-up to be designed for the transverse permeability characterization. Finally, since a modelling approach is proposed in the second part of this paper, some representative models are presented which set the basis for the simulations.

2.1. Flow through porous media

The multiaxial fabrics studied here are intrinsically porous media, the pore size of which may be at the fibre level as well as at the stitching level (Fig. 2). The basics of flows through porous media can be found for instance in [13]. In these flows, the interconnected porosity is involved which restrains, at the microscopic scale, the fluid progression through 'channel-like' cavities. Hence, at this scale the classical laws of fluid mechanics will rule the flow. The two main laws commonly used are

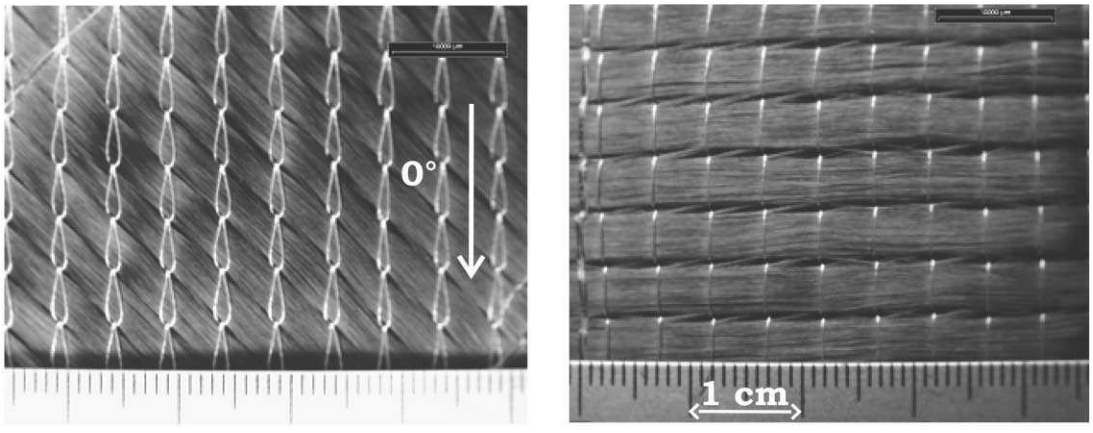

Fig. 2. Picture of a quadriaxial NC2 ([−45,0,45,90]) made up of dry carbon UD fabrics (Tenax HTS 5131/24 k tows 150 g/m 2), stitching pitch 5 mm × 5 mm: (a) −45° face and (b) 90° face.

the mass conservation equation and the Navier–Stokes equation, provided the fluid can be assumed as newtonian. When compared to a classical mass conservation equation, the volume fraction of any phase must be accounted for. Let us notice that in a wet fabric, the phases are either fluid for the resin in motion, or solid for the composite which can undergo deformation under the pressure generated by the flow. For this latter, the mechanical response must be determined too.

These two laws permit on their own to describe the fluid flow through the porous medium, where pressure and velocity are the parameters to determine in both phases. However, beyond the modelling efforts required for seeking the solution, the complexity of the porosity architecture does not allow in our case this system to be solved easily. Even numerically, the various porosity shapes which exist at the different scales cannot be easily represented without turning to more refined descriptions such those adopted in [7] or [10] for example. In the present approach, these equations will be solved through fluid mechanics finite element (FE) analysis in a simplified framework, following the experimental evidences demonstrated in the measurements.

2.2. Assessing permeabilities from flows in composites

In porous media, such as the fabrics of interest in composites, more convenient approaches can be led at the mesoscopic scale, i.e. the scale where the porous medium is seen as homogeneous. Several approaches exist which are used in the literature to model or to identify the permeability. The most popular approach relies on the Darcy's law, empirically established, which permits to relate in three dimensional cases the flow velocity to the gradient of pressure undergone by the fluid in the porous medium:

$$\mathbf{v} = -\frac{\widetilde{\mathbf{K}}}{\eta}\nabla P \tag{1}$$

where $\mathbf{v}$ is the flow rate vector, $\widetilde{\mathbf{K}}$ is the second order permeability tensor of the porous medium that usually depends on the fluid flowing through it represented here by its viscosity η, and ∇P is the pressure gradient. However, it must be pointed out that this empirical law has been established in a well defined frame. Indeed, the Darcy's law holds only for stationary regimes, and Reynolds (Re) numbers calculated for porous media must be lower than 1. Beyond this limit, the flow is inertial ($1 < \mathrm{Re} < 150$), and further ($300 < \mathrm{Re}$) turbulent. This Reynolds number maybe somehow hard to evaluate in porous media since it depends on a characteristic length of the medium [13], which in turn depends on the scale of observation considered.

For the experimental measurements the simplistic Darcy's approach is conveniently considered, either for longitudinal [1,10], transverse [3,22], or 3D permeability characterization [5]. Along with this flow rule, a usual restriction is made to the second order permeability tensor that is taken to be orthotropic. Moreover, it is assumed that no coupling exists between the permeabilities in the three principal directions. Finally, as a first approximation only three independent constants define the permeability tensor: two in-plane (longitudinal) permeabilities and one (through-thickness) transverse permeability. For uniaxial flows, a simplified form is deduced from Eq. (1) which relates the mean uniaxial velocity of the fluid to the pressure gradient undergone in the flow direction (for instance $\mathbf{e}_3$). The pressure gradient is here assumed to be linear, since it is deduced from the discrete measurements of the pressure loss along the flow. Moreover, it is assumed that the transverse direction is, in first approximation, a principal direction. Then, for an orthotropic medium, the uniaxial expression writes for a transverse flow :

$$D = -\frac{K_{33}A}{\eta}\frac{\Delta P}{e} \tag{2}$$

where D is the flux, K_{33} is the transverse permeability, A is the cross-sectional area of the flow, ΔP is the pressure variation, η is the fluid viscosity, and e is the flow length. All these quantities refer to the flow direction. In our case this approach will be used provided the permeability properties can depend on multiaxial architecture.

As for the NC2 material investigated here, it must be noticed that scientific papers devoted to permeability measurements of multiaxial composites mainly focus on woven or random reinforcements [3,6,10,16]. However, in some points multiaxial NC2 and woven fabrics have a close meso-structure, especially both exhibit an alternance of fibre tows and gaps. This meso-structure is important in setting the channels through which the resin will flow, either in injection or infusion. But this is mostly relevant in longitudinal permeability measurements. For the transverse permeability in NC2 materials, macropores are present due to the stitching. Consequently, the fluid will certainly flow through these channel-like connections and then continue either in the fabric planes or in the closest stitching upstream. This will be assessed in the second part dedicated to the transverse permeability modelling.

2.3. Longitudinal and transverse measurements

Permeability measurements can be carried out for either in-plane (for instance [3,17–19,22], transverse [3,22] or 3D flows [5]), in unsteady or steady regimes. The principle of measurement is common for both longitudinal and transverse measurements and is rather simple. A specific device is fed in with fluid under constant flux or pressure. Meanwhile pressure or velocity measurements are made in the dry (downstream) and

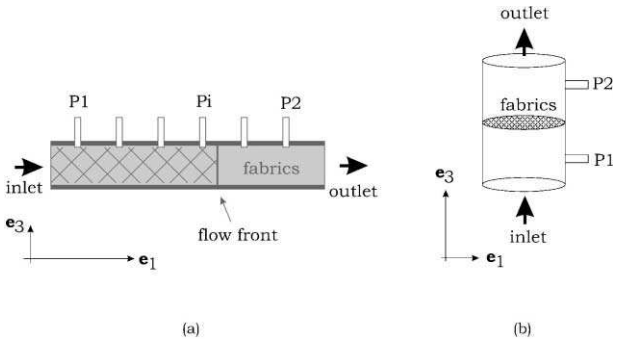

Fig. 3. Schematic of (a) longitudinal, and (b) transverse permeability measurements.

wet (upstream) regions, on either side of the flow front (Fig. 3a), or specimen location (Fig. 3b) in saturated regime. Permeability is then identified, using the Darcy's law [Eq. (1) or (2)] or more complex relationships in bidirectional or 3D cases, from the variations of velocity or pressure induced by the displacement of the fluid through the sample tested. For longitudinal measurements, rectangular or circular specimens are cut, respectively for unidirectional and bidirectional measurements, and fitted into a rigid mold.

For transverse measurements there is no such restrictions on the specimen shape, but usually circular cylindrical specimens are more conveniently used. This transverse measurement is very seldom studied [3,5,22] but tends to be more and more common due to the use of thicker fabrics. The very key point is in this case to realize the fluid injection while maintaining the specimen to be impregnated, but without disturbing the fluid flow. In [3] specimens are maintained on their edges, but this does not allow to control the specimen thickness. Therefore the fibre volume fraction, defined as the ratio of the fibre volume over the tested volume, could vary since the apparent fabric thickness may change. It must be pointed out that in the transverse permeability measurement, the fibre volume fraction is of great importance since it will influence the fabric permeability, i.e. will change the porosity configuration. In [22], the thickness can be controlled by compacting the specimen between 2 porous rigid plates allowing for the injection. The counterpart of this technological solution is that the pressure loss induced by the plate porosity may be higher than the one induced by the specimen itself, due to the reduced thickness involved. In either case, the measurement takes place in saturated regime since it is not possible to visualise the flow front over such a small length.

2.4. Through-thickness permeability predictions

As stated previously, commonly, permeability phenomena in composites rely on the treatment of their complex meso/micro-structure. Then idealized geometries are widely used, either to predict permeabilities in basic cases [13], or in an attempt to relate experimental permeabilities to micro, meso and macro scales [19]. In more refined approaches, such as the lattice Boltzmann model proposed by [20], phenomena can be represented at the mesoscopical scale whilst dealing with void formation in the tows. Results of transverse flows simulations over circular porous tows are proposed which describe the void entrapment in higher permeability regions for unsaturated flows. In our composite materials, saturated flow will be simulated, and consequently any entrapment will be ignored.

This qualitative analysis [20] applies also to more realistic pore architecture, the complexity of which has to be addressed if quantitative predictions are to be proposed. In the case of composites [10,21], starting from micrographs the identification of pores at micro and meso scales is deduced from the probabilistic treatment that a segment of length l fits in a pore in a given direction. For soils [7], the pore network is reconstructed from 3D image analyses, after skeletization and creation of a spatialized local pore size distribution. Then the 'conductivity' of the network is evaluated, especially fluid invasion is shown to be controlled by the connectivity between the largest pores. In our materials, where at least two pore scales exist, such a result reinforces our choice of modelling the flow at the mesoscopical scale where the largest pores are seen.

Eventually, homogenization methods exist which are the most relevant regarding the permeability of media with a regular micro/meso-structure [4,23]. These methods rely on the behaviour of a representative volume element on which are prescribed boundary conditions ensuring its periodicity. In our case, NC2 fabrics cannot be easily represented through a succession of elementary cells at the microscopical level. However, the idea of using a representative volume element can be adapted to the simulation of transverse permeability at the mesoscopical scale. Eventually, finite element approaches are in our case the most easily suitable for the predictions of transverse permeability using a representative mesoscopical cell, and will be subsequently used.

3. Assessment of the NC2 transverse permeability

Using the knowledge gained in the previous survey, an apparatus has been designed to measure the transverse permeability of fabrics. This experimental device is presented and then used to assess the NC2 transverse permeability, and further to demonstrate how this permeability varies with the stitching density.

3.1. Experimental apparatus

The principle of measuring the pressure loss induced by the flow of the fluid through the specimen is the basis

of the permeability measurement. The specific apparatus developed here is based on this principle (Figs. 4 and 5). Following [22], aluminium honeycombs are selected to maintain the specimen in the apparatus. Indeed, after some FE simulations, the channels formed naturally by the honeycomb structure were shown to make the flow become steady even for high fluid velocities. Hence, the use of honeycombs will allow for the thickness of the tested volume to be controlled while smoothing the flow. The second key point of the apparatus is the pressure measurement which is realized with two pressure probes. Let us notice that the location of the probes along the flow is optimized such that pressures are measured in steady flow regions before and after the honeycombs (Fig. 4b).

Another very important point, as explained previously, is the porosity volume fraction of the tested medium that will depend on the compression required to maintain the specimen. Conversely to the processes involving resin injection, the reinforcement deformation during impregnation appears very rarely in infusion processes [24]. In our case, the specimen thickness will be controlled during the measurements with integrated verniers, and the porosity will be deduced from the specimen surfacic mass. Furthermore, the paper of [17], dedicated to the repeatability measurements for longitudinal permeability, states that some discrepancies of the order of 15% may result from heterogeneities in the material as well as from the material deformability. The deformability of the specimen will especially take place during the cutting. Following this evidence, the specimen cutting is integrated to our apparatus such that specimens will not be handled at all [Figs. 4(a) and 5(b)].

This insitu cutting implies that the airtightness, required both to prevent the fluid from leaking and to isolate the chambers, has to be mobile. This is achieved in the presented apparatus as shown in Figs. 4(b) and 5(a). For further simplifications, the specimens tested were chosen circular, 100 mm in diameter. The specimen diameter was fixed such that for the lowest stitching density (10×10 mm), statistically at least 96% of the stitching points would be submitted to the flow for any random placement of the specimen.

Eventually, for the impregnating fluid a lubrication oil NEUTRAL was selected, the behaviour of which is newtonian. The oil was chosen such that its viscosity was as close as possible to the resin viscosity encountered in the RFI process, taking into account that the gear-pump used for the feeding [Fig. 4(b)] would not stand fluid viscosities larger than 10 Pa s. The oil viscosity is perfectly known as a function of temperature, and is given in the Appendix. The fluid temperature is evaluated through a thermo-couple placed between the pump and the fluid inlet, and any apparent thickness variation is assessed using an LVDT displacement sensor. An interface-card is used for data acquisition on a PC, for pressures, temperature, displacement, and flow rate.

3.2. Protocol

Measurements are carried out with the presented apparatus (Fig. 5). The flow length related to the fibre

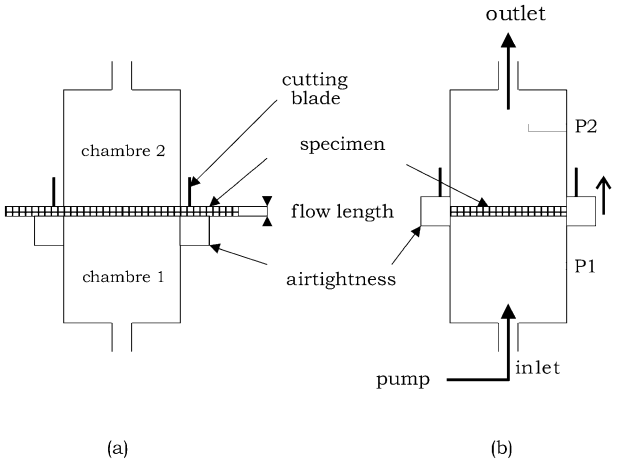

Fig. 4. Schematic of the through-thickness permeability measurement device, in the 2 main stages of the protocol: (a) cutting stage, and (b) measurement stage.

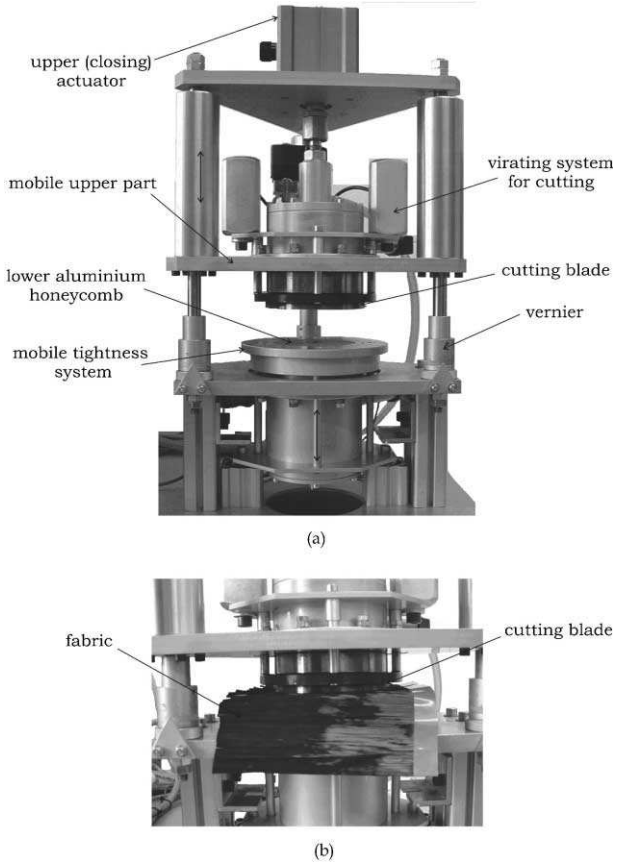

Fig. 5. Apparatus designed for transverse permeability measurements: (a) description, (b) cutting stage prior to measurements.

volume fraction of the specimen is set by the verniers, close to commonly used values. As for the velocity range, it is rather hard to know exactly the velocities encountered in the manufacturing processes. Hence, in order to cover the wider velocity range, it was chosen to stop to increase the fluid velocity (flux) when the upper actuator used to maintain the upper chamber was no longer able to sustain the pressure induced by the flow across the fabric. The pressure applied for maintaining the system closed is 7.5 bars, similar to the pressure which is used in the industrial RFI process.

The following protocol was used for the measurements. A multiaxial fabric is placed on the lower honeycomb and the upper mobile part comes down in contact with the verniers. The vibrating cutting system is turned on and maintained until the blade has completed the cut [Figs. 4(a) and 5(b)]. The airtightness mobile system can then move upward to ensure both the absence of air in the fluid flow and leaks out of the chambers [Fig. 4(b)]. In the first times of the cycle, a low fluid velocity is prescribed to the servo-gear pump which feeds in the apparatus with fluid. In this stage the lower chamber is filled, and then the fabric is impregnated. Once the second pressure probe can measure the fluid flow, the servo-gear pump is stopped, and then a complete test cycle can be started in which the fluid velocity is increased step by step. Every step is continued until pressures stability is reached.

3.3. Assessment of the transverse permeability

3.3.1. Permeability measurement

A typical measurement is presented in Fig. 6 for a biaxial *N*C2 made up from 2 × Tenax HTS5131 267 g/m^2 carbon fabrics stitched 10 mm × 10 mm. In this figure the resistance provided by the fabrics against the flow, i.e. the pressure gradient deduced from the pressure loss and flow length $e\left(\frac{\Delta P}{e}\right)$ over the fluid viscosity η, is plotted as a function of the fluid velocity (v). It is verified that the largest Reynolds number of the flow encountered is lower than 1:

$$\mathrm{Re}^{\max} = \frac{\rho v^{\max} d}{\eta} = 1.75 \cdot 10^{-2} << 1 \tag{3}$$

with ρ the volumic mass of the oil $\left(\rho = 877 \mathrm{kg\ m^{-3}}\right)$, $v^{\max}$ the maximum fluid velocity encountered $\left(v^{\max} \leqslant 3 \cdot 10^{-3}\ \mathrm{m\ s^{-1}}\right)$. d is the largest characteristic length of the *N*C2 taken as the largest stitching hole diameter measured from micrographs ($d \leqslant 0.4$ mm) and $\eta = 0.06$ Pa.s is the fluid viscosity at room temperature. Darcy's approach is then valid for these measurements. Then, simply by using the Darcy's law for uniaxial flows [Eq. (2)], the transverse permeability (K_{33}) can be identified from these data.

One will notice that this resistance of the fabric does not depend linearly on the fluid velocity as one would

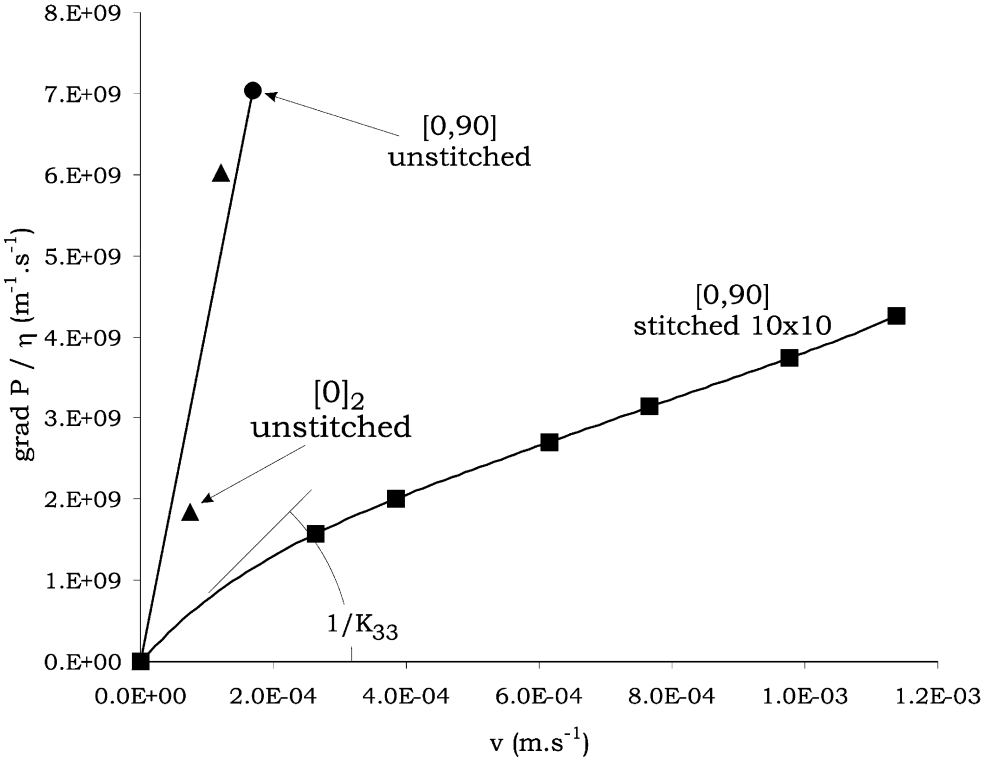

Fig. 6. Resistance of fabrics to the fluid flow versus the fluid velocity for fabrics 2 × 267 g/m^2: $[0]_2$ unstitched, [0,90] unstitched, and [0,90] stitched 10 mm × 10 mm.

expect. Conversely, in other more 'rigid' materials tested, such as woven fabrics and metallic lattices, a linear relationship is observed between the resistance and the fluid velocity. Therefore, this non-linearity seems to reflect some intrinsic properties of the NC2 materials. Further studies are currently under progress to clarify this point. However, one wishes to make a productive use of the data given by this first approach of the NC2 transverse permeability. Consequently, the nominal transverse permeability is assessed as the permeability prevailing at the onset of flowing in the NC2 (Fig. 6). At that stage the fibre volume fraction is perfectly controlled and the meso-structure is not disturbed. Eventually, for the present study, the nominal apparent permeability will be identified as the inverse of the initial slope (Fig. 6).

3.3.2. Measurement repeatability

The assessment of measure repeatability has been achieved for 2 types of biaxial NC2, made up of identical UD Tenax fabrics 267 g/m^2 (HTS 5131/24 k tows), but with different stitching pattern. The first biaxial was stitched with a 10 mm × 10 mm pattern and the other one with a 5 mm × 5 mm pattern, both were stitched with PA 6.6 78 tex stitching yarn. The largest discrepancies are for the 10 mm × 10 mm stitching pattern. The secant apparent permeability, deduced from the current slope of a given point on the resistance curve, reaches about 20% of variation (Fig. 7) for the fluid velocity tested. However, one must point out that the work of [17], dedicated to the repeatability measurements for longitudinal permeability reports some discrepancies of the order of 15%, but for longitudinal flows over several hundreds of millimeters (300 mm). In our case, transverse measurements are made over some lengths of the order of one millimeter or less. Moreover, transverse permeabilities are of the order of 10^{-13} m^2, whereas longitudinal permeabilities are at least one decade higher, of the order of 10^{-12} m^2.

3.4. Influence of the stitching density

The transverse permeability of NC2 is assessed with the presented dedicated apparatus, using the protocol introduced. Essentially, biaxial materials are tested, all of them made up from the same Tenax HTS 5131 UD dry fabrics. The stitching, when reported, is realized with a PA 6.6 78 tex stitching yarn. This kind of biaxial material permit to reveal many specificities of NC2 multiaxial fabrics without involving too much complexity related to tricky stacking sequences or architectures.

Assessing the influence of the stitching onto the transverse permeability is the main issue of the present work. To achieve this, 6 types of biaxial fabrics were tested. First $[0]_2$ and [0,90] fabrics, both unstitched, were tested. Then, biaxial [0,90] NC2, made up of the same fabrics were manufactured but with 3 different balanced stitching patterns of 10 mm × mm, 5 mm × 5 mm, and 2.5 mm × 2.5 mm, corresponding respectively to stitching

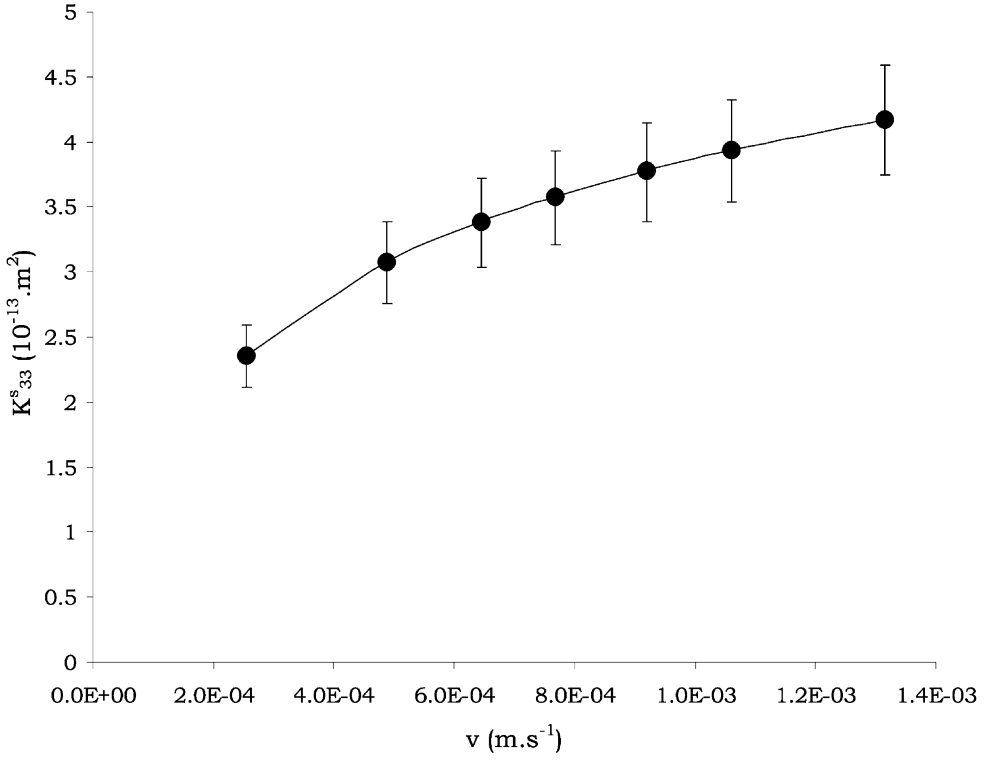

Fig. 7. Secant permeability measurements (K^s_{33}) versus the fluid velocity (v) for a biaxial [0,90] NC2 2 × 267 g/m^2 stitching pitch 10 mm × 10 mm.

densities of 10^4, 4.10^4, and 16.10^4 stitches per m^2. Eventually, biaxial [+45,−45] NC2 with a 5 mm × 10 mm stitching pattern were tested. Since the same UD blankets are used, the fibre volume fraction is set to 0.65 for all the materials tested.

First, permeabilities for the $[0]_2$ and [0,90] unstitched biaxial are very close (Fig. 6). Unfortunately, the very low permeability (of the order of $2 \cdot 10^{-14}$ m^2) of these UD fabrics may, under a 7.5 bars closure pressure, cause leaks in the apparatus even for a moderate flux. Therefore, only few flow rates can be tested but which are sufficient to draw some clear trends about these measurements. The curves obtained for both unstitched materials tend to coincide. The similarity between these material responses demonstrates that the resulting transverse permeability does not depend at all on the stacking sequence. At the opposite, the introduction of stitching (10 mm × 10 mm) seems to increase greatly the permeability which jumps from $0.24{\cdot}10^{-13}$ m^2 to $1.1{\cdot}10^{-13}$ m^2.

This strong influence is confirmed by the curves for the other material tested (Fig. 8) which clearly show that the permeability largely depends upon the stitching. But first, it must be pointed out that the differences between theses experimental results are much higher than the repeatability of the measures themselves. Therefore, these variations can be interpreted as intrinsically related to the material tested. More precisely, this permeability can even be related directly to the stitching density only since actually the independence of the transverse permeability upon the stacking sequence is again confirmed by the [+45,−45] NC2 measurement (Table 1). Indeed, in that material stitched 5 mm × 10 mm, only the stitch density seems to control the permeability comprised between the permeabilities for the biaxials [0,90] stitched 10 mm × 10 mm and 5 mm ×5 mm.

Table 1
Transverse permeability measurements for the 6 materials tested

Material	$[0]_2$ unst.	[0,90] unst.	[0,90] 10×10	[0,90] 5×5	[0,91] 2.5×2.5	[±45] 5×10
Stitching density (10^4 pts m^{-2})	–	–	1	4	16	2
K_{33} ,measured (10^{-13} m^2)	0.21	0.24	1.1	6.37	15.1	2.47

The stitching density seems to control the transverse permeability, this is clearly illustrated in Fig. 9 where the permeability is shown to vary, linearly in first approximation, with the stitching density. In fact, mesoscopical measurements of the fabric geometry reveal that only the holes left around the stitching pitches are open pores, the size of which are quite comparable for the various fabrics tested (∼0.4 mm). In first approximation this suggests that mainly these spaces will allow for the fluid to pass through. It can be easily reckoned that permeability depends on the amount of surface spaces for the fluid to flow, directly related to the stitching density. One will notice that, although the gap geometry is not exactly the

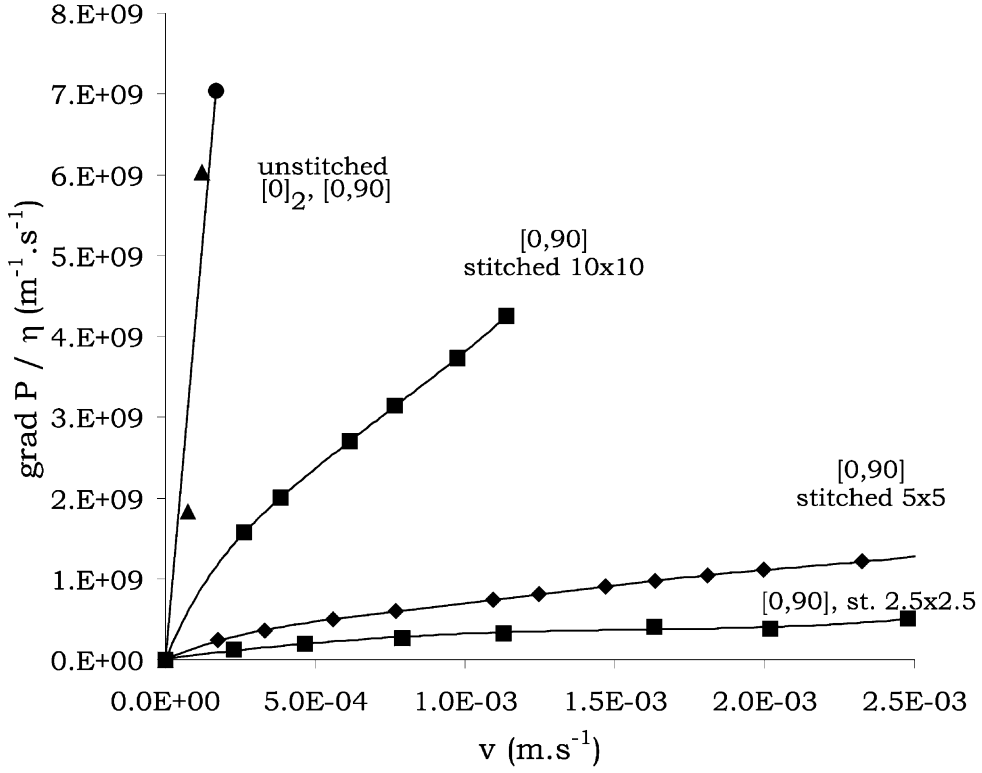

Fig. 8. Resistance to the fluid flow versus the fluid velocity for fabrics 2 × 267 g/m^2: $[0]_2$ unstitched, biaxial [0,90] unstitched and stitched 10 mm × 10 mm, 5 mm × 5 mm, and 2.5 mm × 2.5 mm.

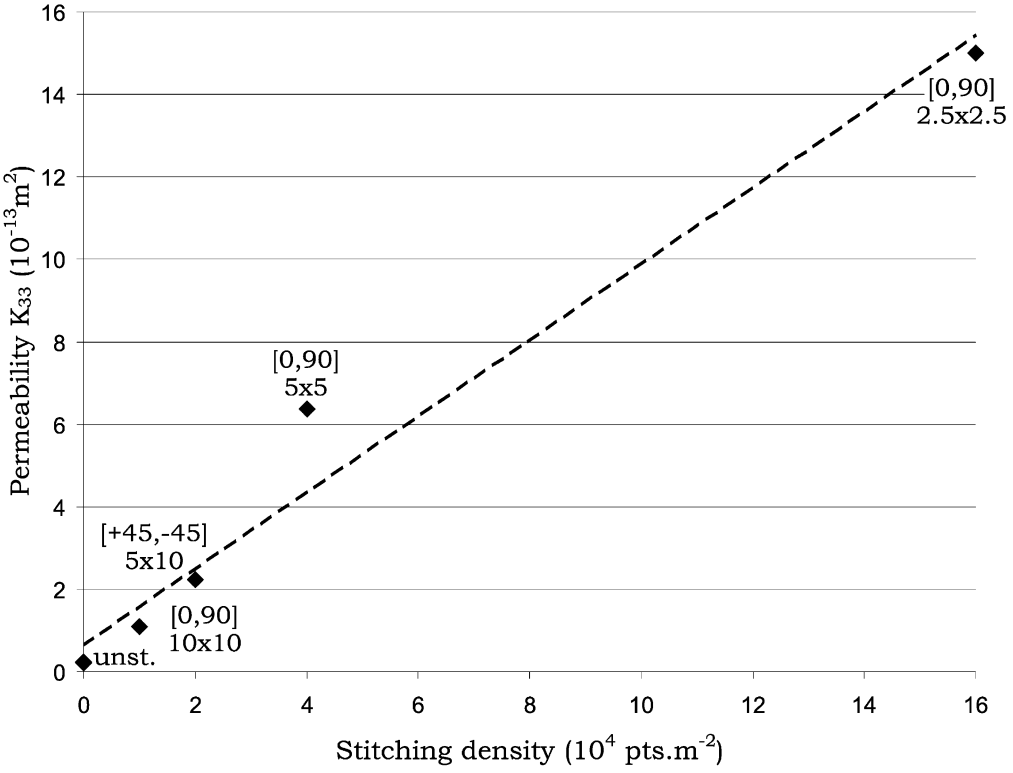

Fig. 9. Permeability of the materials tested vs their stitching density.

same for the [+45,−45] biaxial NC2 as for [0,90] [see in Fig. 2(a) and (b)], the effective (open pores) surface spaces may depend essentially on the stitching yarn itself.

From these results, it can be concluded that the stitching density is of prime importance regarding the transverse permeability of NC2. Although this stitching is introduced mainly to improve the handability and the mechanical properties of the resulting structural component, it appears to be also very helpful in increasing the permeability. Indeed, with a stitching density of 10^4 pts m^{-2}, the transverse permeability is increased by a factor of 5 with respect to the same unstitched biaxial. By increasing further the stitching density by 16 (from 10 mm × 10 mm to 2.5 mm × 2.5 mm), a similar increase is reached for the permeability. Regarding the very low permeability of unstitched materials, this increase of the permeability is essential in achieving proper manufacturings. There is obviously a limit in increasing the stitching density since the mechanical counterpart is that a decrease in the material properties is expected due to the geometrical imperfections resulting from the introduction of stitches, as it can be observed at larger amplitudes in NCF materials [8, 9].

4. Permeability predictions

The aim of this simulation is to model the influence of the stitching density onto the transverse permeability. The Ansys FE package is used to model the permeability response at the mesoscopical level, on a representative volume element of the biaxial [0,90] fabric tested previously.

4.1. Representative volume element

FE simulations are carried out on the biaxial NC2 characterized experimentally. In order to avoid very demanding computations, we use the principle of homogenization techniques based on repeating representative volume elements (RVE). It is assumed that the response of this volume element is representative of the response of the entire medium, provided proper boundary conditions are prescribed on its edges to represent neighbouring volume elements. For the modelling, the scale of observation has to be chosen first. The choice of this scale must permit to grasp the main features which may influence the permeability. For this choice, first one can notice that there is the formation of inter-tow spaces (gaps) (Fig. 2), independently on the direction of the stitching with respect to the fibre orientation. These gaps are similar to the ones developing in NCF manufactured with the Liba process for instance, but with a minor amplitude. Secondly, the other main features which may influence the transverse permeability are the stitches that were shown to strongly control the permeability (Fig. 9). Lastly, as saturated flow simulations are considered here, any air entrapment in the tows can be

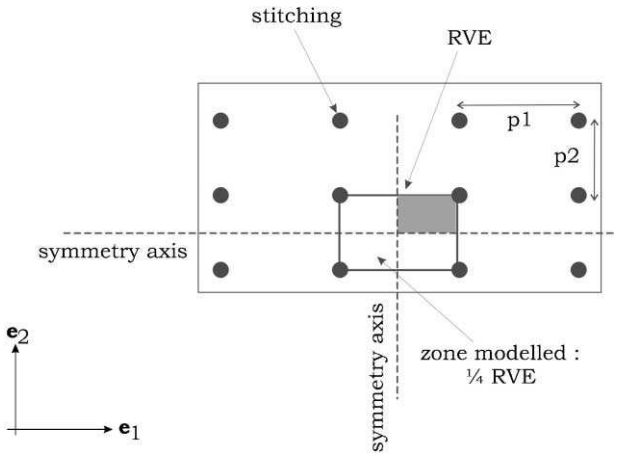

Fig. 10. Representative volume element for the biaxial NC2 permeability simulation.

neglected. Consequently, it seems natural to set up the model at the mesoscopical scale where gaps and stitches can be accounted for, and where tows are seen as homogeneous porous media. Therefore, in our biaxial material a RVE is easily extracted, the planar dimensions of which are equal to the stitching pattern used (Fig. 10) and its thickness corresponds to the fabric thickness. By applying proper boundary conditions, detailed below, the permeability of the equivalent infinite fabric can be computed.

4.2. Computations

For the sake of simplicity, the chosen RVE has been idealized. By symmetry, only a quarter of this RVE must be represented. Also, gaps between the tows induced by the stitching yarns (see Fig. 2) are represented as parallelepipeds [Fig. 11(a)], resulting from the space left between the planes standing for the 0 and 90° tows [Fig. 11(b)]. For the stitching, a space is considered as the union of the space left by the circular cylindrical stitching and the gap between the tows [Fig. 11(a)]. Stitching densities are represented by varying the cell dimensions (p1,p2) corresponding to the stitching pitch respectively along $\mathbf{e}_1$ and $\mathbf{e}_2$ directions.

The inter-tow gaps and the stitch hole are modeled with fluidic elements in which the Navier–Stokes equation prevail. For modelling tows, i.e. the porous medium, the Darcy's law is employed instead of the previous laws. Both media are meshed with quadratic isoparametric finite elements. Let us notice that in every article where permeability is simulated for a reinforcement, tows are supposed not to be permeable. However, due to the fabric homogeneity, in our case macropores are much less numerous. It is then possible that flow takes place through the tows as it can be observed in the RTM process [3]. Tow permeability is defined through a diagonal tensor. This is what prevented us from computing the

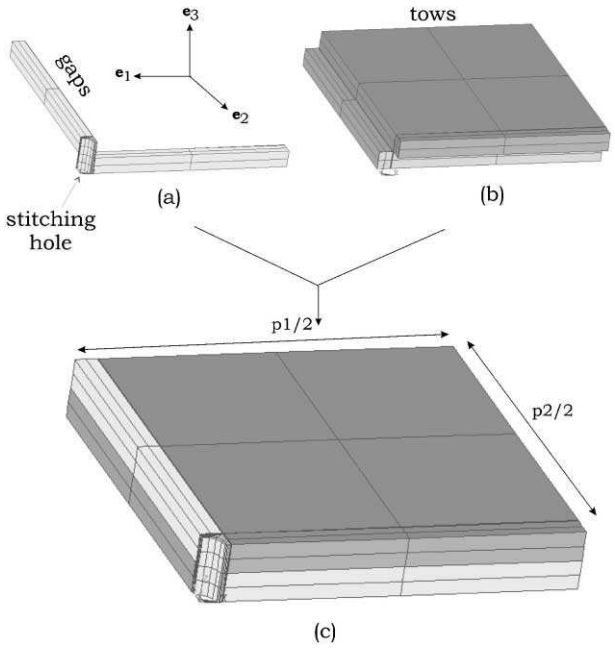

Fig. 11. RVE mesh used for FE simulations: (a) mesh of the gaps with fluidic elements, (b) mesh of the tows with solid porous elements, and (c) complete mesh of the RVE.

[+45,−45] biaxial NC2 permeability. The transverse permeability of the tows is the one assessed for a UD fabric (2.25×10^{-14} m^2), and in the fibre direction it is taken equal to 10^{-12} m^2 following the estimations from [17]. As for the fluid viscosity, it is equal to the viscosity of the lubrication oil used for experiments measured at room temperature ($\eta = 0.06$ Pa s) .

As can be seen in Fig. 11 the stitch hole is not represented, it is instead modeled with zero normal flux conditions, i.e. no fluid can penetrate the stitching yarn but the flow along this yarn is allowed. Indeed, implicitly it is assumed that the stitching yarn induces a hole, the diameter of which (0.3 mm) corresponds exactly to the yarn diameter deduced from its linear mass and its density. The other boundary conditions are zero normal flux conditions on the lateral faces of the cell. To represent the pressure drop induced by the flow through the fabric, a 1 bar pressure is applied on the upper face of the RVE while on the lower face pressure is null. Permeability is calculated through the Darcy's law [Eq. (2)] from both the pressure differential prescribed and the mean fluid velocity deduced from the massic flux computed.

4.3. Results—comparison with experiments

Permeabilities are computed for [0,90] fabrics considering the 3 stitching densities tested. The results reported in Table 2 are also plotted in Fig. 12 where can be seen the good correlation between the predicted permeabilities and the ones measured. The maximum discrepancy of about 25% is reached for the highest

Table 2
Transverse permeability predicted and measured for the 4 stitched biaxial materials tested

Material	[0,90] 10×10	[±45] 5×10	[0,90] 5×5	[0,90] 2.5×2.5
Stitching density (10^4 pts m^{-2})	1	2	4	16
K_{33} computed (10^{-13} m^2)	1.19	–	4.75	19.1
Predictions/measurements	−8%	–	−25%	27%
K_{33} analytical [Eq. (4)] (10^{-13} m^2)	1.19	2.38	4.76	19.1

stitching densities (4 and 16.10^4 pts m^{-2}), whereas for the lowest density it is 8% (1·10^4 pts m^{-2}).

The most important effect confirmed by these computations is the effect of the stitching density on the permeability. The simulations reveal that the fluid flows through the fabric (Fig. 13) only across the stitching holes. Indeed, whatever the stitching density simulated, the flow rate of fluid across the tows remains low. The tows are so little permeable that the fluid cannot flow across and passes almost in totality through the stitching holes. This is illustrated by the distribution of the transverse fluid velocity plotted in Fig. 13. Transverse velocities in the tows are 2 decades lower than the transverse velocities in the stitching hole. More particularly the fluid circulate in the narrow region between the gaps and the stitching yarn.

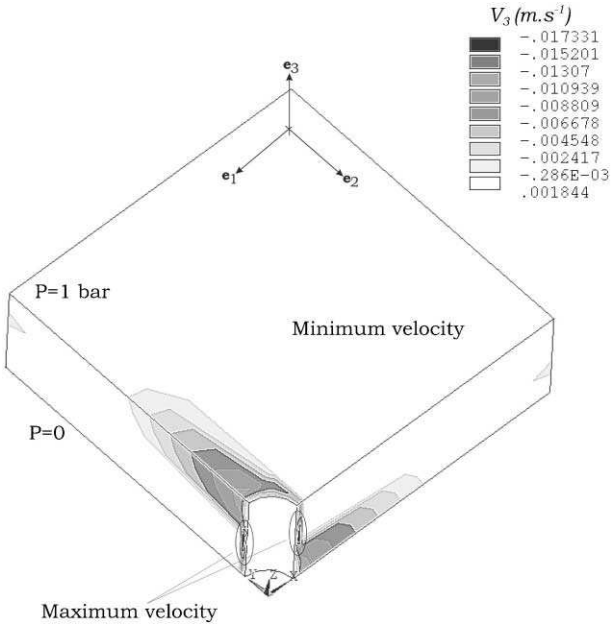

Fig. 13. Distribution of the transverse fluid velocity (V_3) in m s^{-1} for the [0,90] NC2 5 mm × 5 mm stitching pitch.

Assuming that the stitching pitches remain large enough, the interaction between flows in the stitching cylinders is negligible. Then, one can propose a very simple relationship that would relate the transverse permeability for a given stitching density $d_1(K_{33}^{d1})$ to the

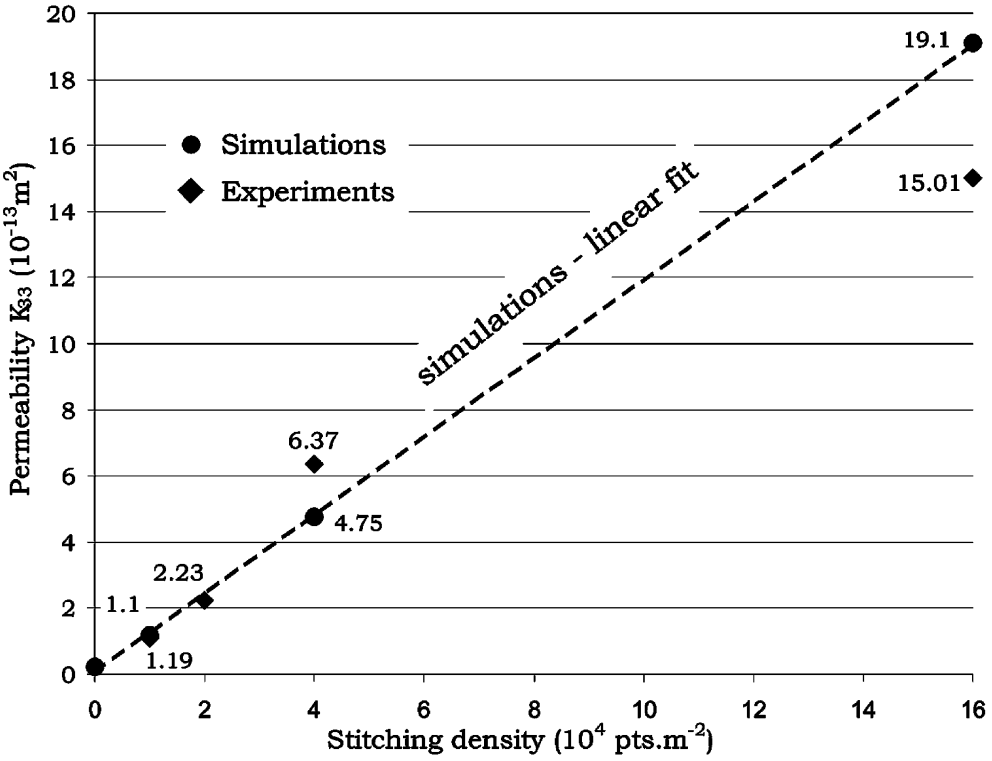

Fig. 12. Permeability predicted and measured, for the materials tested, vs their stitching density.

permeability of the same fabric but with a stitching density $d_2\left(K_{33}^{d2}\right)$ [Eq. (4)]. Predictions with this very basic relationship compare well with the FE results (Table 2).

$$K_{33}^{d1} = K_{33}^{d2}\frac{d_1}{d_2} \tag{4}$$

As a conclusion, both experimentally and theoretically, it is established that the fluid flows almost exclusively through the stitching holes. Some discrepancies exist between predicted and measured permeabilities, however regarding the very low permeabilities identified these moderate differences are acceptable for current industrial applications. Then, as a rule of thumb, assuming that the stitching hole geometry and the gap size will not depend on the stitching density, a linear relationship exists between the transverse permeability and the stitching density. For industrial applications, stitching densities are at least 10,000 pts m^{-2} but will usually not exceed 40,000 pts m^{-2} . This ensures that flow across the tows may be negligible, and that in turn this linear approximation will hold.

5. Conclusion

The first study of the influence of the stitching density on the transverse permeability of NC2 was carried out. The main mechanisms which control the flow of a fluid across NC2 were assessed. Eventually, predictions were shown to compare well with experimental results. First, a specific apparatus was designed to measure the transverse permeability in multiaxial fabrics. The key point of this system is to maintain properly the specimen, using aluminium honeycombs, while ensuring the fibre volume fraction control. Also, the specimen cutting is integrated to the apparatus which ensures that the fabric deformability will not yield any meso-structure variation. This apparatus allows to evaluate the transverse permeability through the uniaxial Darcy's law, knowing both pressure loss induced by the specimen resistance to the fluid flow, and fluid velocity.

Experiments were carried out on 6 different fabrics, both unstitched and stitched, and with several stacking sequences and stitching patterns. Experimentally it was demonstrated that neither the stacking sequence nor the stitching pattern would influence the transverse permeability. Conversely, the stitching density was shown to control greatly the permeability. Indeed, changing the stitching pitch from 10 mm × 10 mm to 2.5 mm × 2.5 mm, i.e. increasing by 16 the stitching density, permits to increase the permeability by about the same amount, from 1.1×10^{-13} to 15.1×10^{-13} m^2. From a manufacturing point of view, this improvement of the transverse permeability ensures a good fibre impregnation, and consequently optimum final mechanical characteristics.

This main result was found also by the FE simulations carried out at the mesoscopical scale on a representative volume element of [0,90] biaxial fabrics. Permeabilities were assessed by measuring the flux as a response to a differential of pressure applied to the fluid crossing the porous media standing for the tows. It was established that mainly the fluid flowed along the stitching yarn, in the stitching holes. Then, in first approximation, it is the surfacic ratio of spaces left by the stitching points which controls the permeability. This provides a clear explanation to the experimental dependence of the transverse permeability upon the stitching density. Eventually, as a first approximation, the permeability for any admissible stitching density can be extrapolated linearly from a single permeability known for a given stitching density.

Based on the knowledge gained here, this permeability study should be extended to tri and quadri-axial NC2. For the measurements, these materials will be tested with the apparatus developed here. As for the simulations, some problem may arise due to the non-diagonal terms of the permeability tensor which will appear for non cross-plies.

Acknowledgements

The authors wish to acknowledge the Rhône-Alpes Region for its support to this work through the programme 'Thématique Prioritaire 2000–2002'.

Apendix. Fluid viscosity

The fluid used, a lubrication oil (NEUTRAL), appeared to vary in viscosity with the ambient temperature. The characterization of this viscosity over a wide range of temperatures yields the following results (Table A1 and Fig. A1).

This viscosity can be fitted by the following fourth degree polynomial [Eq. (5)] leading to at most 1.1% of discrepancy, and 0.44% in the range 15–25 °C of interest here (Fig. A1):

$$\eta(T)\left(10^{-3}\text{Pa s}\right) = 9.6955E^{-6}T^4 - 1.4803E^{-2}T^3 + 0.88167T^2 - 25.782T + 3.4761 \tag{5}$$

Table A1
Oil viscosity vs. temperature

Temperature (T in °C)	5	15	18	20	22	25	30	40	50
Viscosity (η in 10^{-3} Pa s)	239	113.7	93.2	82	72.5	60.7	46	28	18.3

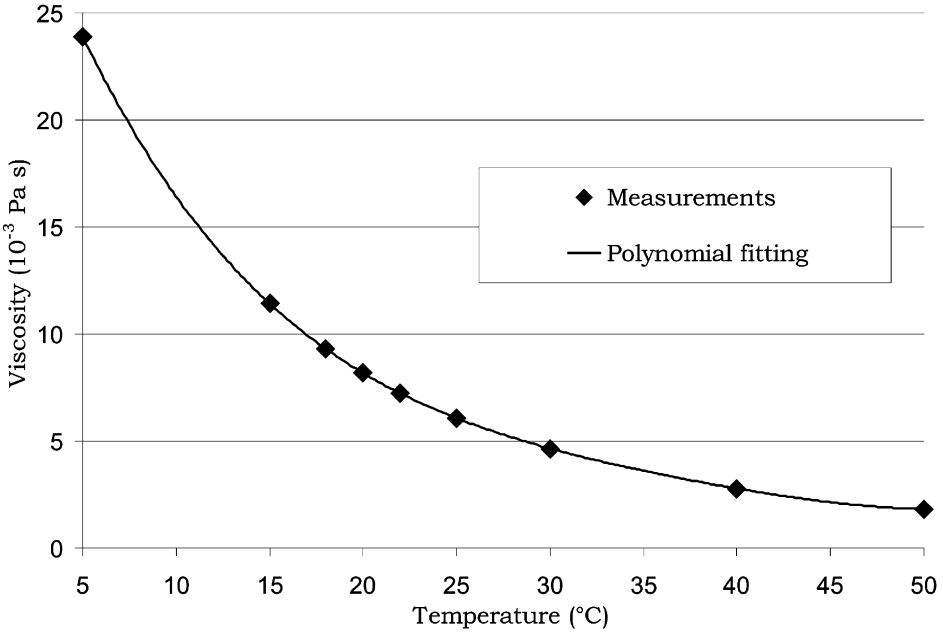

Fig. A1. Variation of the oil viscosity vs. temperature.

References

[1] Adams KL, Miller B, Rebenfeld L. Forced in-plane flow of an epoxy resin in fibrous networks. Polym Eng Sci 1986;26(20):1434–41.

[2] Avila R, Matthews FL. An experimental investigation of the isothermal impregnation of fibrous preforms. In: Institute of Material Composite Division, editor. Proceedings of ECCM9, Brighton 4–7 June 2000.

[3] Binétruy C, Pabiot J. Effects of fabrics architectural heterogeneities on effective and satured permeabilities in RTM. In: Massard T, Vautrin A. editors. Proceedings of ICCM12—Paris 5–9 July 1999. No. 178, p. 682.

[4] Boutin C. Study of the permeability by periodic and self-consistent homogenisation. Eur J Mech A/Solids 2000;19:603–32.

[5] Bréard J, Saouab A, Bouquet g. Mesure de la perméabilité spatiale d'un renfort tridimensionnel pour matériaux composites à matrice polymére. Eur Phys J AP 1998;1:269–78.

[6] Caba AC, Rattazzi RB, Loos AC. Verification of a simulation model for resin film infusion of complex shaped composite structures. J Rein Plast Comp 1999;18(16):1465–77.

[7] Delerue JF, Perrier E, Yu ZY, Velde B. New algorithms in 3d image analysis and their application to the measurement of a spatialized pore size disctribution in soils. Pys Chem Earth (A) 1999;24(7):639–44.

[8] Drapier S, Wisnom MR. Finite-element investigation of the compressive strength of non-crimp-fabric-based composites. Compos Sci Technol 1999;59(12):1287–97.

[9] Drapier S, Wisnom MR. Finite-element investigation of the interlaminar shear strength of non-crimp-fabric-based composites. Compos Sci Technol 1999;59(16):2351–62.

[10] Henzel, Y, Bréard J, Trochu F, Blanlot R. A standard characterisation of satured and unsatured flow behaviours in porous media. In: Massard T, Vautrin A, editors. Proceedings of ICCM12—Paris 5–9 July 1999. No. 604, p. 690.

[11] Joshi SC, Liu XL, Lam YC, Sheridan J. Simulation of resin film infusion process using finite element/nodal control volume approach. Advanced Composite Letters 1999;8(3):101–4.

[12] Kang MK, Jung JJ, Lee WI. Analysis of resin transfer moulding process with controlled multiple gates resin injection. Composites/A 2000;31:407–22.

[13] Kaviany S. Principle of heat transfert in porous media. New York: Springer-Verlag; 1991.

[14] Kenny JM, Trivisano A, Molina G. Mathematical modelling of resin trans-fer molding of composites for automotive applications. In: Miravette A, editor. Proceedings of ICCM9—Madrid July 1993. Woodhead Publishing Ltd., 1993. Vol. 3, p. 513–5.

[15] Lam YC, Joshi SC, Liu XL. Numerical simulation of the mould-filling process in resin-transfer moulding. Compos Sci Technol 2000;60(6):845–55.

[16] Lim ST, Kang MK, Lee WI. Modelling of void formation during resin transfer molding. In: Massard T, Vautrin A. editors. Proceedings of ICCM12-Paris 5–9 July 1999. No. 627, 544.

[17] Lundström TS, Stenberg R, Bergström R, Partanen H, Birkeland P.-A. Inplane permeability measurements : stability, repeatability and reproductibility. In: Massard T, Vautrin A. editors. Proceedings of ICCM12—Paris 5–9 July 1999. No. 309, pp. 696.

[18] Robitaille F, Long AC, Souter BJ, Rudd CD. Permeability modelling of industrial preforms: simulations and practical aspects. In: Institute of Material Composite Division, editor. Proceedings of ECCM9, Brighton 4–June 2000.

[19] Shih C-H, Lee LJ. Effect of fiber architecture on permeability in liquid composite molding. Polym Compos 1998;19(5):626–39.

[20] Spaid MAA, Phelan Jr FR. Lattice boltzmann methods for modeling microscale flow in fibrous porous media. Phys Fluids 1997;9(9):2468–74.

[21] Stavrov VP, Kremenevskaya EI, Stavrov VV, Tkachev VM. Effect of the structure of a fibrous layer on its permeability for a nonlinearly viscous fluid. Mech Compos Mater 1997;33(4):554–63.

[22] Trevino L, Rupel K, Young WB, Liou MJ, Lee LJ. Analysis of resin injection molding in molds with preplaced fiber mats: permeability and compressibility measurements. Polym Compos 1991;12(1):20–9.

[23] Velten, K. Drag measurement and evaluation in impregnation processes. In: Institute of Material Composite Division, editor, Proceedings of ECCM9, Brighton 4–7 June 2000.

[24] Walsh TJ, Morse CT, Ochoa OO. Composite auto bumper : design and process evaluation. In: Miravette A. editor. Proceedings of ICCM9—Madrid July 1993. Woodhead Publishing Ltd., 1993. Vol. 6, p. 252–259.